MEG application for pediatric epilepsy and epileptic syndrome

Hiroshi Otsubo[1*], Ayako Ochi[1*], Sylvester H, Chuang[2], James T Rutka[3], and O. Carter Snead III[1*]
Divisions of Neurology[1], Neuroraidology[2], and Neurosurgery[3], The Hospital for Sick Children, University of Toronto and Bloorview Epilepsy Research Program*. Toronto, Ontario, Canada

Introduction

Many children with epilepsy and epileptic syndrome may benefit from surgical treatment when disabling seizures and epiphenomenal disorders remain refractory to antiepileptic medications.
Magenetoencephalography (MEG) and magnetic source imaging (MSI) have changed imaging technology allowing clinicians to localize epileptic regions, functional cortex and lesions on MRI. The combined functional and anatomical information on MSI promises to enhance diagnostic and therapeutic approaches, to epilepsy surgery in pediatric patients. We evaluated the diagnostic value of MEG for possible epilepsy surgery in pediatric refractory epilepsies and Landau-Kleffner syndrome (LKS).

Methods:

The patients were admitted to the epilepsy monitoring unit and were monitored for up to 5 days. The International 10-20 scalp electrode placement system was used and closely spaced electrodes based on the 10-10 system were placed to cover the suspected epileptic regions. MR images were obtained in a multi sequence sagittal, axial and coronal volume acquisition study with T1-weighted thin slice MR images using 1.5 tesla MRI signa (Siemens, Germany). Gadlinium was injected for the patients with suspected tumors.
MEG studies were performed at Scripps Clinic and Research Foundation in San Diego, CA or the Veterans Administration Medical Center in Albuquerque, NM, using a single-probe Magnes I® (37-channel), dual-probe Magnes II (74-channel) or whole-head Magnes 2500 WH (148-channel) biomagnetometer system (Biomagnetic Technologies, Inc., San Diego, CA). The probe positions selected for each patient were selected based on clinical information such as the patient's EEG and VEEG. For most patients, multiple probe recording positions were used to insure full coverage. Concurrent with the magnetic recording, surface EEG was recorded using conventional scalp EEG electrodes and collodion application. (Neurofax 440A, Nihon Kohden, Tokyo, Japan). The simultaneous EEG was used to assist in spike identification and avoid collection and analysis of data contaminated by either artifact or sleep patterns. A physician or technician identified interictal spike in the MEG and EEG recordings and triggered the collection of 6 second epochs of data (5 seconds pre-trigger).
Patients were generally requested to deprive themselves of 2 hours of sleep or, for younger children, stay up to midnight the night before the exam. During the study, patients were drowsy and most fell asleep. For uncooperative children, intravenous Propofol was infused during the study. Propofol induces beta activity upon injection, but it subsequently disappears, allowing detection of epileptogenic activity. Prior to analysis, the MEG and EEG waveforms were digitally filtered with a bandpass of 3 to 70 Hz.
A single equivalent current dipole model was used to localize the source of interictal epileptic spikes. The model assumed the head to be a sphere, with the diameter and center location chosen to best fit the actual shape of the region of the head being monitored, as derived from the head digitization data. This equivalent current dipole model used an iterative algorithm to determine the location, orientation, and strength of the current dipole that best accounted for the measured magnetic field pattern. Only those dipoles that accounted for at least 98% of the recorded field pattern, had physiologically realistic current magnitude ($Q < 400$ nAm), and resulted from data for which the root mean square average of the magnetic field detected in all signal channels ($\sqrt{\Sigma B^2}$) was at least 400 femto Tesla, assuring an adequate signal-to-noise ratio, were regarded as a valid application of the model. For patients with a very large number of dipoles so selected, a clustering algorithm was applied to concentrate the data in regions with the most frequent epileptic activity. These constraints on the equivalent current dipole model limited the analysis of the very large time series of epileptic activity recorded for each patient to only those brain events that produced fields with a highly focal source.
A multiplanar T1- and T2-weighted MRI set was collected at the MEG site, using a 1.5 T scanner (Signa; General Electric Medical Systems, Milwaukee, WI). Generally, the images were produced as 5-mm slices, skip 1 mm. Three lipid markers were placed at fiducial points on the patient's head during the magnetic

©1999, Tohoku University Press
Recent Advances in Biomagnetism
T. Yoshimoto et al. (Eds)

resonance recording. The coordinates of the MEG dipoles were then transformed into the MRI frame.

A 4x5 surface electrode array (Ad-Tech, Racine, WI) was used for intraoperative electrocorticography (ECoG) to localize interictal epileptiform discharges and somatosensory evoked response after median nerve stimulation on the cortex. An ISG viewing wand was used to navigate the lesion and to direct the epileptic zone base upon the MEG spike field (ISG, Mississauga, ON).

Bilateral subdural strips were used to lateralize seizure onset using 4-electrode contact strips in two patients, in one of which a subdural grid was placed after lateralization was decided. Subdural grids with up to 128 contacts were shaped to cover the interictal MEG spike field and functional cortex based on the three dimensional MRI using 1.5 mm thin slice on T1 MR images. Split screen and time locked EEG was utilized to review clinical behavior of seizures (System 5000, Nicolet. Madison, WI). EEG data were digitized at a sampling rate of 200 samples / sec / channel. The digitized EEG data were stored by the automatic seizure detection, automatic spike detection and manual event alarm button.

Results:

A total of fifty-three patients were examined in this study. With prolonged video scalp recorded EEG monitoring, thirty-two patients were diagnosed with extra-temporal lobe epilepsy, nine with temporal lobe epilepsy, five with LKS and 7 possible LKS. Eight patients formerly had undergone epilepsy surgery which did not result in seizure control.

MRI showed lesion in all nine temporal lobe patients and in 19 extratemporal patients.

MEG spike sources were obtained in 48 of 53 patients (sensitivity 0.91). The remaining five patients were not cooperative (1) or under Propofol anesthesia which possibly induced beta activity (2) and no ECD (2).

Twenty-five patients had surgeries consisting of invasive intracranial video EEG monitoring prior to surgical excision (11), cortical excision with intraoperative ECoG (13), and corpus callosotomy (1).

Among 32 patients with extra-temporal lobe epilepsy, 19 patients presented with lesion on MRI, including 10 cortical dysplasias, 5 tumors, 1 each of Sturge-Weber syndrome, cyst (Fig 1, 2 and 3), Rasmussen syndrome and infarction. The 10 cortical dysplasias were in the frontal lobe in 4, in the parietal lobe in 4 and in the occipital lobe in 2.

In the total of 14 patients who underwent epilepsy surgery (8 guided by ECoG, 6 guided by IVEEG), all of the MEG spike fields correlated with the epileptic region (specificity 1.0). In 6 patients the MEG spike fields corresponded to the epileptogenic zone, which was recorded by IVEEG. In 6 patients, the MEG spike field corresponded with the ECoG field with a seizure free follow-up. In 2 patients the MEG spike field corresponded to the ictal symptomatogenic zone.

Scalp, zygomatic and sphenoidal electrodes revealed temporal lobe epilepsy in 9 patients in whom five patients underwent surgery, direct ECoG in 3 and IVEEEG in 2. MEG depicted spike sources in mesial temporal discharges in none of 4 patients in whom pathology confirmed mesial temporal sclerosis. In One patient with recurrent seizures secondary to residual cortical dysplasia in right posterior temporal region, MEG spike sources matched intraoperative ECoG spikes and follow-up seizure outcome was moderate improvement.

Five of 12 with LKS demonstrated MEG spike foci around bilateral Rolandic-Sylvian fissure. One patient with continuous spike and slow waves during sleep and acquired aphasia that was improved by initial steroid therapy underwent surgery guided with intraoperative ECoG. Multiple subpial transection and temporal lobectomy were performed after active epileptiform discharges over the left inferior frontal and posterior temporal region where MEG spike sources were localized with improvement of speech and behavior under valproic acid. In the other two patients, IVEEG resulted in epileptogenic zone in the interictal MEG spike zone. Following massive multiple subpial transection around Rolandic-Sylvivan fissures, both patients had improvement language and minimal seizures for several months compared to daily frequent seizures.

Discussion

In order to surgically treat seizure disorders, the epileptogenic zone, defined as the region that initiates seizures and has to be removed totally or disconnected for cessation of seizures [1], should be precisely delineated. Epileptogenic zones can be located in anywhere in pediatric epilepsy and epileptic syndrome, extratemporal lobe epilepsy which has been reported more frequently than those in adults [2, 3]. Conventional non-invasive video EEG recordings using scalp electrodes are not able to adequately differentiate the epileptogenic zone and the irritative zone. Epileptic MEG equivalent current dipole spike sources have been reported correlating with conventional noninvasive and invasive localizing modalities in adults, with refractory seizures who are candidates for epilepsy surgery, to localize the epileptogenic zone [4, 5, 6].

The extra-temporal lobe epilepsies have varied patterns of electrographical and clinical findings and the epileptic regions are much more difficult to localize than the patterns in temporal lobe epilepsy. In order to surgically treat seizure disorders secondary to a lesion, the epileptogenic zone may be located anywhere around the margin of, and / or distant from, a lesion [7]. In addition, the extra temporal epileptic regions are often located adjacent to the eloquent areas, making accurate localization essential for surgical planning. If the preoperative information provided by MEG about the relationship between the lesion and the epileptic irritative zone is accurate, the practice of ECoG guided surgical approach would be less invasive when compared to tailoring procedures which seek irritative spikes on ECoG without prior knowledge of the sources. The successful outcomes of seizure surgery in lesional extratemporal lobe epilepsy reported here, in which MEG spike sources were correlated with ECoG spikes and surgical site, supports the further concept that clusters of MEG spikes predict the epileptogenic zone within the irritative zone around the lesion.

In non-lesional extratemporal lobe epilepsy diagnosed by clinical features and scalp EEG recording, intracranial monitoring is often required, since prolonged scalp recorded video EEG telemetry has been reported to have a discrepancy between clinical and electrographical onset [8, 9]. Therefore, the IVEEG is the gold standard to define the epileptogenic zone. The agreement of the interictal MEG spike sources with the ictal onset zone from IVEEG in this study suggests that non-invasive MEG study can be efficiently used to guide subdural grid placement to cover the epileptic region and eloquent cortex in children with extratemporal lobe epilepsies.

Compared to the results from adult temporal lobe epilepsy series [5], MEG spikes sources have not been accurate in pediatric temporal lob epilepsy. This may be explained since our nine patients clinically presented with complex partial seizures originated from either temporal or extratemporal lobe foci in video scalp recorded EEG monitoring. Conventional sphenoidal electrodes did not succeed to distinguish mesial temporal onset, thus, MEG study was requested and possibly showed irritative extratemporal discharges. In adult populations, MEG study has differentiated among lateral, mesial and posterior temporal discharges in certain temporal lobe onset epilepsy, which was confirmed with intracranial EEG studies [10].

Landau-Kleffner syndrome has been studied by MEG to localize epileptiform discharges which occurred continuously during sleep, for possible multiple subpial transection (MST). The epiphenomenal discharges on EEG have hardly proved to produce language dysfunction in children with acquired aphasia. There are reports that significant improvement of speech and behavior after MST over the epileptic cortex where MEG spike sources were located [11]. MEG may be a diagnostic tool for LKS to localize epileptic discharges over the auditory cortex and preplanning for surgery.

Conclusions: MEG is an important and valuable adjunct to the non-invasive diagnostic arsenal in localizing the epileptic focus in children. This technology can contribute information about the relationship between the seizure focus and lesion, and the localization of the epileptogenic zone in patients with non-lesional epilepsy. For LKS, the MEG spike fields around auditory cortex support diagnosis, and possible surgical treatment of this disorder.

FIG. 1

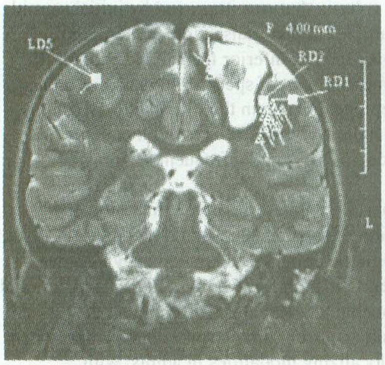

FIG. 2

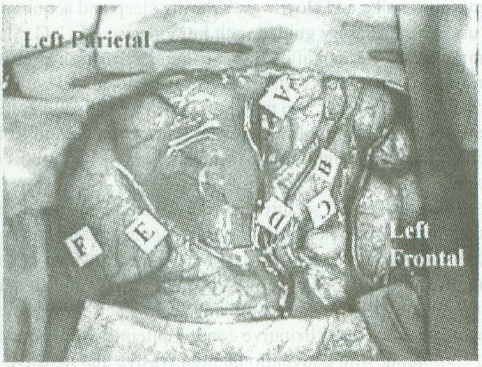

FIG. 3

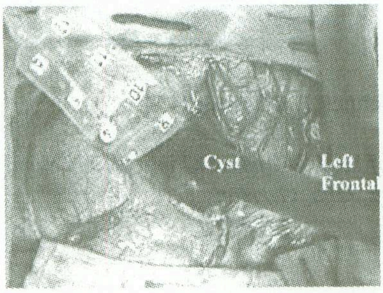

Fig. 1, A seven year old boy presented with refractory seizure disorders secondary to a left parietal cyst. MSI showed clusters of interictal spike sources (open triangles) in the inferior, mesial and posterior to the cyst, and somatosensory stimulation response (closed square) of right thumb (RD1), index finger (RD2) in the inferior cluster of spike sources, below the cyst. Fig. 2, Intraoperative right median nerve stimulation delineated sensory cortex on letter "A, E and F" and motor cortex on "B, C, and D" which located superior and anterior to the cyst. Fig. 3, Intraoperative ECoG, using a 2x6 electrode array, demonstrated active epileptiform discharges over the inferior wall of the cyst and the marginal cortex. MEG spike sources corresponded to this irritative zone. Multiple subpial transection was performed over the inferior, mesial and posterior margin of the cyst following lesionectomy. The patient has been seizure free for 6 month after the surgery.

Reference

[1] Luders HO and Awad I: Conceptual considerations, Luders HO (ed): In Epilepsy Surgery. New York: Raven Press, 1991, pp 51-62.

[2] Gilliam F, Wyllie E, Kashden J, et al: Epilepsy surgery outcome: comprehensive assessment in children. Neurology 48(5): 1368-1374, 1997

[3] Otsubo H, Steinlin M, Hwang PA, et al: Positive epileptiform discharges in children with neuronal migration disorders. Pediatr Neurol 16(1): 23-31, 1997

[4] Smith JR, Schwartz BJ, Gallen C, et al: Utilization of multichannel magnetoencephalography in the guidance of ablative seizure surgery. Journal of Epilepsy 8: 119-130, 1995

[5] Knowlton RC, Laxer KD, Aminoff MJ, et al: Magnetoencephalography in partial epilepsy: clinical yield and localization accuracy. Ann Neurol 42(4): 622-631, 1997

[6] Ko DY, Kufta C, Scaffidi D et al: Source localization determined by magnetoencephalography and electroencephalography in temporal lobe epilepsy: comparison with electrocorticography: technical case report. Neurosurgery 42(2): 414-421, 1998

[7] Awad IA, Rosenfeld J, Ahl J, et al: Intractable epilepsy and structural lesions of the brain: mapping, resection strategies, and seizure outcome. Epilepsia 32(2): 179-186, 1991

[8] Salanova V, Quesney LF, Rasmussen T, et al: Reevaluation of surgical failures and the role of reoperations in 39 patients with frontal lobe epilepsy. Epilepsia 35:70-80, 1989

[9] Salanova V, Andermann F, Rasmussen T, et al: Parietal lobe epilepsy. Clinical manifestations and outcome in 82 patients treated surgically between 1929 and 1988. Brain 118(3): 607-627, 1995

[10] Ebersole JS: Magnetoencephalography/magnetic source imaging in the assessment of patients with epilepsy. Epilepsia 38(Suppl 4): SI-S5, 1997

[11] Morrell F, Whisler WW, Smith MC, et al: Landau-Kleffner syndrome. Treatment with subpial intracortical transection. Brain 118(6): 1529-1546, 1995

Early Magnetic Field Changes Preceding Penicillin Induced Epileptiform Spikes

Eiselt M [1], Zwiener U [1], Gießler F[2], Schack B[3], Nowak H[2]

Inst. of Pathophysiology[1], Biomagnetic Center[2], Inst. of Med. Statistics, Comp. Science and Doc.[3], Friedrich Schiller University, Jena, Germany

Introduction

The concepts concerning the mechanisms responsible for the generation of epileptiform activity comprise two zones. The most important one is the primary epileptogenic zone with pacemaker structures [7, 12, 14]. In the secondary epileptogenic zone or irritative zone interictal epileptiform discharges can be detected. Its activity is dependent on the primary epileptogenic zone. According to this concept the primary epileptogenic zone has to be active before epileptiform activity is generated by the irritative zone

In most of the recent investigations interictal spikes were induced by artificial stimulation. The latencies of interictal spikes occurrence after stimulation vary between 60-80 ms [4, 11]. Similar latencies of about 35 ms were described by Traub and Wong [10] using simulations.

Concerning our knowledge no investigation has been performed describing the early processes related to the initiation of spontaneously occurring spikes after penicillin-application. The location of the initial process is not known and may vary from spike to spike. The detection of initial processes favor the use of magnetic field because activity generated at varying point in an extended cortical area can be measured.

The aim of the presented investigation was to determine early changes within the magnetic field related to the occurrence of interictal spike activity after focal penicillin application.

Methods

Preparation and penicillin application:

In 15 anaesthetized, nonrelaxed adult rabbits (White New Zealand, Halothan 0.5 - 1.0 Vol. %, $O_2/N_2O = 1/3$) the centroparietal cortical surface (ca. $100\ mm^2$) was exposed. Spike activity was induced in 10 animals by stereotactic application of 100 I. U. penicillin (0.2 μM) 400-600 μm subpially in the medial cortex (Regio retrosplenialis granularis) 5 mm posterior to the Bregma. We investigated interictal discharges only. In all experiments, callosotomias were performed.

Recording of magnetic and electric field:

The magnetic field was detected using a 7-channel 1st order gradiometer system (sensitivity $20fT/\sqrt{Hz}$; pick-up coil diameter 9.5mm, 30mm baseline). ECoG was recorded simultaneously (unipolar derivation; one electrode at the region of penicillin application, reference at nasal bone).

Data processing:

The MEG and ECoG signals were sampled at a rate of 1 kHz. High pass filter (< 3 Hz) and notch filter (47-53 Hz) were used. To improve the signal to noise ratio (> 30:1) 150 spikes detected by MEG and ECoG were averaged (trigger point: negative maximum in the ECoG). Recordings were used only if less than 5% of all interspike intervals were shorter than 500 ms.

Four different recording conditions were defined:

I.) without any animal, II.) spontaneous neuronal background activity without application of penicillin (n=5), III.) neuronal background activity after the application of penicillin ending 1 second before the following spike and IV.) during the occurrence of penicillin-induced epileptiform spike activity.

Calculation of parameters and statistics:

The magnetic global field power (GFP) was calculated according to Lehmann et al. [6]. Additionally, the z-parameter [2] was calculated. This parameter describes the topographic similarity of the MEG for two subsequent time intervals both with a duration of 5 milliseconds. Increasing z-parameter corresponds to increasing similarity (maximum value = 1). For summary statistics the z-parameter has been z-transformed.

Results

The main result was an increase of the mean z-parameter calculated from the MEG starting about 1 second before the negative maximum of the interictal penicillin-induced spike appeared.

The magnetic signal measured contained different parts. One part was caused by noise of the equipment and magnetic field from the surrounding. To assess the amount caused by these sources, the magnetic field was

©1999, Tohoku University Press
Recent Advances in Biomagnetism
T. Yoshimoto et al. (Eds)

detected without any animal. The z-parameter calculated from this magnetic field was about 0.010 ± 0.002 (z-transformed parameter; mean ± standard error of the mean (SEM)) and was not significantly different from zero.

It can be assumed that neuronal background activity may influence the z-parameter. The z-parameter calculated from spontaneous MEG in rabbits without penicillin application was 0.392 ± 0.103 (z-transformed parameter; mean ± SEM) and significantly different from zero ($p<0.001$). This indicates that the magnetic field measured is changed by the presence of an animal.

After penicillin-application but during periods without epileptiform spike occurrence the z-parameter reached a value of 0.380 ± 0.077 (z-transformed parameter; mean ± SEM). If z-parameters compared between animals treated with penicillin and those without penicillin no significant differences could be observed.

Because of the low signal to noise ratio averaging of spikes was performed. About 600 ms before the negative spike maximum the z-parameter changed and exceeded the 90th quantil of an empirical distribution calculated from spontaneous neuronal background activity about 500 ms before the negative maximum.

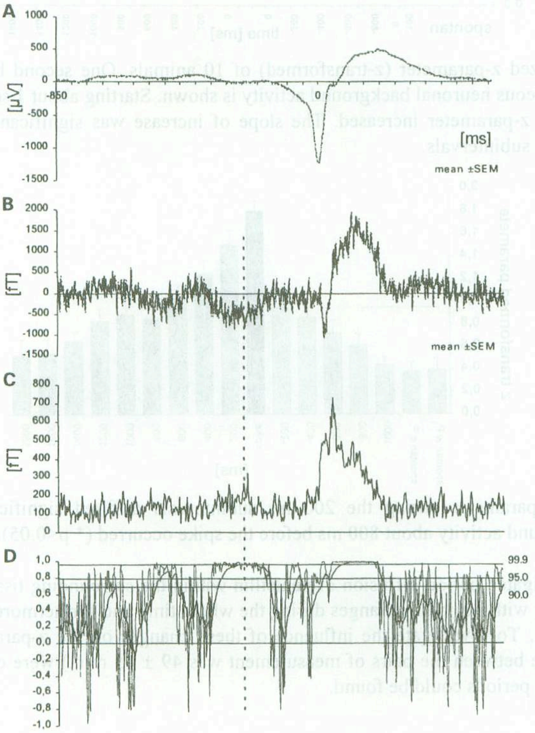

Fig. 1: MEG and ECoG from one rabbit after averaging the signal 150 times. A.) Averaged spike detected by the ECoG. Time scale was adjusted to the negative maximum (= 0 ms). B.) MEG: Before the spike occurred changes within the magnetic field could be observed. C.) The instantaneous square root (SQR) of GFP increased during spike appearance. Small increase of this parameter occurred also earlier (dashed line). Because of noise this increase is difficult to observe in the MEG as well as in the SQR GFP. D.) Increase of the z-parameter started early before the spike.

Taken the mean z-parameter of 10 animals into consideration, z-parameter changes about 1 s before the spike reached its negative maximum.

Comparing the mean z-parameter 1 second before the spike with that of MEG without penicillin, the differences do not reach the level of significance (fig. 2). During the next period (800-600 ms before the spike) the mean z-parameters differed significantly ($p<0.05$) from spontaneous neuronal activity without penicillin (fig. 3).

The z-parameter decreased in some cases just before the spike appeared (fig. 1). In fig. 2 this corresponds to a reduction of the slope of regression during the period 400 ms before the spike.

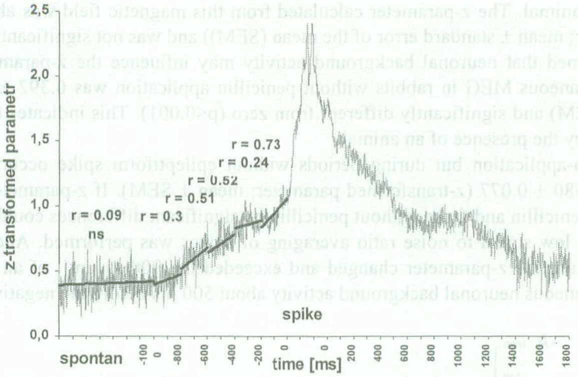

Fig. 2: Summarized z-parameter (z-transformed) of 10 animals. One second before the negative spike appeared spontaneous neuronal background activity is shown. Starting about 1 second before the negative spike maximum, z-parameter increased. The slope of increase was significant (p<0.001) and differed within successive subintervals.

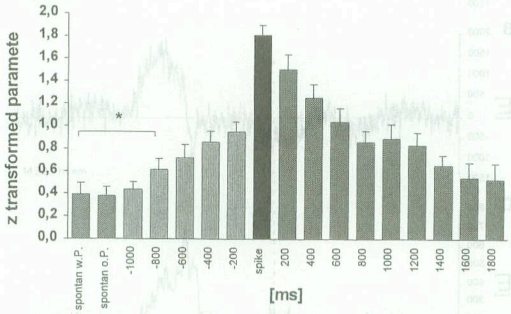

Fig. 3: Mean z-parameter during the 200 ms subintervals differed significantly from spontaneous neuronal background activity about 800 ms before the spike occurred (* p<0.05).

During the investigated period diffusion of penicillin within the surrounding tissue takes place. Thus the tissue which is in contact with penicillin changes during the whole time and furthermore the concentration at the neurons changes as well. To investigate the influence of these changes on the z-parameter, measurements at different time (difference between the pairs of measurement was 49 ± 15 min.) were compared. No significant differences between both periods could be found.

Discussion

The most important result was a significant increase of the z-parameter 800 ms before the negative maximum of the epileptiform spike. This increase may correspond to an intracortical pattern of functional organization, which persists for hundreds of milliseconds and may be related to the generation of epileptiform spikes. The very early changes of functional organization are confirmed by findings in human cortical slices. Here, changes of inhibitory potentials have been described by Avoli et al [1] in Mg^{2+}-free medium up to 2 seconds before epileptiform spikes appeared. From investigations of synchrony between cortical neurons in normal penicillin-treated cortex of monkeys, Wyler [13] concluded that interictal burst firing could be the result of intrinsic mechanisms triggered by normally synchronous events. Possible origin of these spontaneous activity may be the pyramidal cells of layer V [9]. Part of these cells have intrinsic membrane properties with sodium conductance essential for rhythmicity and calcium-dependent conductance strongly modify this rhythmicity. Action potentials generated by these cell can not be detected by the magnetic field. However, postsynaptic potentials caused by the synaptic transmission may cause intracortical current and magnetic fields.

While some cells may have extensive connections allowing them to trigger a population burst, most cells may have restricted projections with their influence confined to immediate neighbors. This variation in connectivity pattern would also provide an explanation for the long latency required for triggering synchronized bursting [3].

We assume that neurons with restricted connections are first activated by a weak stimulus and the excitation is conducted to a follower subpopulation. Such excitatory transmission persist for some times until a single neuron or set of neurons with extensive connections is stimulated to burst. This in turn leads to a population burst of the type of interictal discharge.

Penicillin is a $GABA_A$ channel blocker. Thus the effect of $GABA_A$ mediated inhibition is reduced. The focal application of penicillin changes the functional connections in a limited region. Diffusion of penicillin within the surrounding tissue and the focal concentration necessary to cause epileptic spikes has to be considered for the investigation near the region of penicillin application [5, 8]. Such a concentration was reached 20 minutes after the injection of 50 I.U. penicillin in a cortical area of 2-3 mm diameter.

The z-parameter calculated from spontaneous MEG is different from zero. That means, already physiological spontaneous background activity causes a magnetic fields which were similar at least over 10 ms.

It can be concluded that functional intracortical organization changes up to 800 ms before the negative maximum of epileptiform spike appears.

References

[1] Avoli M, Louvel J, Drapeau C et al: $GABA_A$ -Mediated Inhibition and in vitro epileptogenesis in the human neocortex. J Neurophysiol 73: 468-484, 1995

[2] Desmedt JE, Chalkin V: New method for titrating differences in scalp topographic patterns in brain evoked potential mapping. Electroencephalogr Clin Neurophysiol 74: 359-366, 1989

[3] Dichter M, Spencer WA: Penicillin-induced interictal discharges from the cat hippocampus. I. Characteristics and topographical features. J Neurophysiol 32: 649-662, 1969

[4] Ebersole JS, Chatt AB: Spread and arrest of seizures: The importance of layer 4 in laminar interactions during neocortical eleptogenesis, Delgado-Escueta AV, Ward AA, Woodbury DM et al (eds.), Advances of Neurology. 44. New York, Raven Press, 1986, pp 515 - 558

[5] Goldensohn ES, Salazar AM: Temporal andsSpatial distribution of intracellular potentials during generation and spread of epileptogenic discharges. New York, Raven Press 1986,

[6] Lehmann D, Ozaki H, Pal I: EEG alpha map series: brain micro-states by space-oriented adaptive segmentation. Electroencephalogr Clin Neurophysiol 67: 271-288, 1987

[7] Lüders HO, Awad I: Conceptual considerations. Lüders HO (ed) Epilepsy surgery. Raven Press, New York, pp 51-62, 1991

[8] Noebels J, Pedley TA: Anatomic localization of topically applied (1+C) penicillin during experimental focal epilepsy in cat neocortex. Brain Res 125: 293-303, 1977

[9] Silva LR, Amitai Y, Connors BW: Intrinsic oscillations of neocortex generated by layer 5 pyramidal neurons. Science 251: 432-435, 1991

[10] Traub RD, Wong RK: Cellular mechanism of neuronal synchronization in epilepsy. Science 216: 745-747, 1982

[11] Wadman WJ, Gutnick MJ: Non-uniform propagation of epileptiform discharge in brain slices of rat neocortex. Neuroscience 52: 255-262, 1993

[12] Wieser HG, Siegel AM: Indications for surgical treatment of epilepsies. Schweiz Rundsch Med Prax 81: 632-639, 1992

[13] Wyler AR: Synchrony between cortical neurons in normal and epileptogenic cortex of monkey. Epilepsia 27: 171-176, 1986

[14] Wyler AR, Ward AA: Epileptic neurons. Lockard JS, Ward AA (eds) Epilepsy, a window to brain mechanisms. Raven Press, New York, pp 51-68, 1980

Acknowledgment

This investigation was supported by BMBF project ZZ 00 9602 and TMWFK project B301 96051

Equivalent current dipole estimation of diffuse spike or spike and wave discharges in the interictal electroencephalogram of epileptic patients

Hattori H[1], Tsuyuguchi N[2], Tsutada T[3], Matsuoka O[1], Shimogawara M[4], Kuramoto T[5], Higuchi M[6], Haruta Y[7], Kado H[4], Isshiki G[1], and Murata R[8]

Department of Pediatrics[1], Neurosurgery[2], and Neurology[3], Osaka City University School of Medicine, Osaka, Japan; Applied Electronics Laboratory, Kanazawa Institute of Technology[4], Kanazawa, Japan; GE Yokogawa Medical Systems Ltd.[5], Osaka, Japan; Department of Linguistics and Philosophy, Massachusetts Institute of Technology[6], Boston, USA; Aerospace and Marine Products Business Div., Yokogawa Electric Corporation[7], Tokyo, Japan; Osaka City General Hospital[8], Osaka, Japan

Introduction

Diffuse spike (DS) or spike and wave discharges (DSW) including diffuse high voltage slow burst appear in the interictal electroencephalogram (EEG) both for the patients with generalized epilepsy (GE) and those with localization-related epilepsy (LRE). The purpose of this study was to determine whether recording of the magnetoencephalogram (MEG) is useful for differentiating GE from LRE. We also discuss the mechanisms responsible for the characteristic MEG findings of GE.

Methods

MEGs were recorded in a magnetically shielded room using a newly developed laying type whole-head MEG system with a 160-channel first-order gradiometer. Twelve-channel EEG and one-channel ECG were simultaneously recorded with a portable electroencephalography apparatus (Nihon Koden). MEG data were filtered with a bandpass of 3 to 100 Hz and digitized to 250Hz. The EEG data were also filtered with a bandpass of 0.5 or 1.5 to 60 Hz and digitized to 250 Hz. Five marker coils were attached on the patient's head including three on the forehead and two bilaterally on the preauricular points to obtain position information. One set of examination included three minutes of marker signals and ten minutes of MEG measurement. We changed head position in the dewar for children performed three to four sets of mesurements because their head sizes were too small for our dewar, which had been made to fit adult head sizes. We estimated equivalent current dipole (ECD) at the point of DS/DSW on the EEG. We use a sphere model and least-squares method for the estimation.

Vitamin E capsules were attached at the same positions as the marker coils when MRIs were obtained. The slice width was seven mm with no gap, and axial, coronal and sagittal scans were performed. We transferred the MRI data to our MEG system off-line, and superimposed the MEG data.

Patients

The patients were one to twenty-six years old. We obtained informed consent from the patients and their parents after explaining the purpose and safety of MEG.

Case one was a twenty-three-year old man with Lennox-Gastaut syndrome who had suffered daily tonic seizures and atypical absences. His EEG exhibited diffuse slow spike and wave bursts. Cortical dysplasia bilaterally in the parietotemporal area was found on MRI, suggesting a variant of bilateral perisyruvian syndrome (Fig.1) [1]. Case two was a six-year-old boy with secondary generalized epilepsy which had developed from West syndrome who had daily periodic tonic seizures. He has agenesis of the corpus callosum and porencephaly with severe developmental retardation. Case three was a thirteen-year-old girl with tonic seizures which were initially controlled with valproic acid and clonazepam. She relapsed later

©1999, Tohoku University Press
Recent Advances in Biomagnetism
T. Yoshimoto et al. (Eds)

Case	Age/ Sex	Diagnosis	Epileptc syndrome	Seizure type	EEG	MEG
1	23/M	perisyruvian syndrome	LGS	tonic seizure atypical absence	diffuse slow spike and wave(DSSW)	two dipole pattern
2	6/M	agenesis of corpus callosum, porencephaly	West→SGE	tonic spasms	diffuse apike and wave burst, hypsarrhythmia	no significant focus
3	13/F		FLE s/o	tonic seizure CPS (focal motor seizure)	Lt F dominant diffuse sharp wave	two dipole pattern
4	26/M	post encephalitis	LRE	GTC	diffuse spike and wave	3 foci
5	1/F	tuberous sclerosis	SGE	GTC status epileptics	diffuse spike and wave	3 foci
6	5/F		FLE	advesive seizure	diffuse spike and wave, diffuse sharp burst	1 focus
7	9/M		FLE	focal motor seizure	diffuse sharp wave	1 focus

Table1: The summary of patients' data LGS: Lennox-Gastaut syndrome, SGE: secondary generalized epilepsy, LRE: localization related epilepsy, FLE: frontal libe epilepsy

with complex partial seizures which gradually increased in severity. Her EEG revealed left frontal dominant DSW. Case four had generalized tonic clonic seizures (GTC) once every two or three days and mild mental retardation, which were residua of acute encephalopathy suffered at six years of age. Case five was a slightly retarded one-year-old girl with tuberous sclerosis. She had suffered GTC twice, one episode of which had developed to status epilepticus. Her MRI

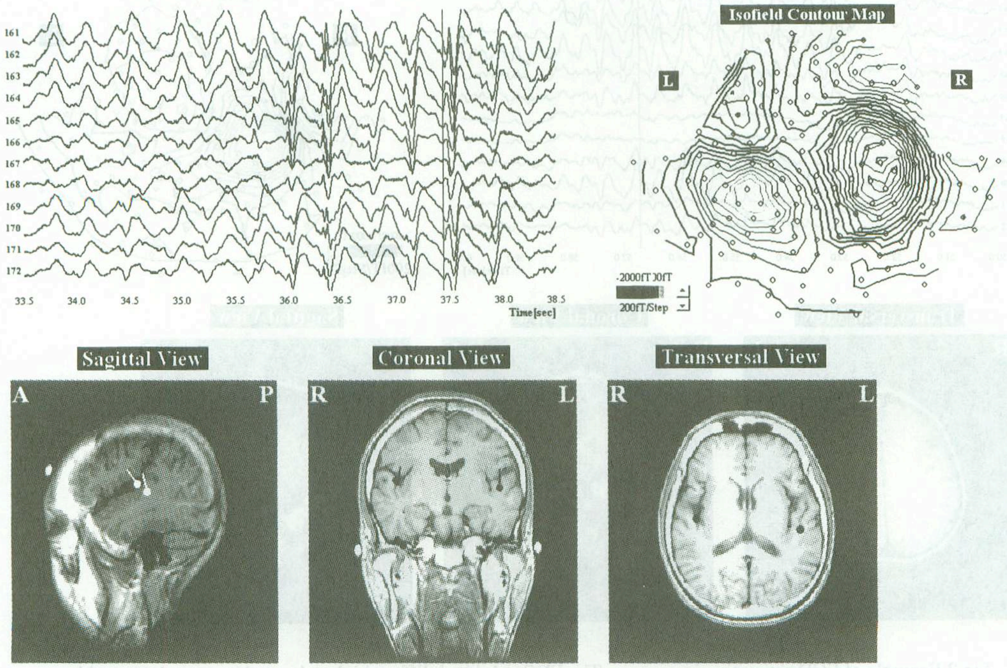

Figure 1: Example of ECD estimation in case one. The EEG exhibited diffuse slow spike and wave bursts (upper left). At 37 sec and 442 msec in the iso-contour map a two dipole patten appeared (upper right), and its ECDs were estimated to originate in the region of cortical dysplasia resion (lower).

revealed both subcortical tuber and severe white matter lesions. Frequent adversive seizures were observed in case six, in which frontal lobe epilepsy was suspected. Case seven was a nine-year-old boy with focal motor seizures and diffuse sharp waves on the EEG. Patient data are summarized in Table 1.

Results

We drew time step iso-contour maps continuously around the point of DS/DSW and estimated the ECDs at the point of dipole pattern in the iso-contour maps. Data for which goodness of fit (GOF) was over 90% in the selected channels was considered evidence of significant ECD. We were able to estimate one to three ECDs for six patients and no significant focus for one.

In case one, two dipole pattern was observed on the iso-contour map at the point of DSW in the EEG, and ECDs were superimposed onto the area of cortical dysplasia (Fig.1). The dipole pattern on the left side preceded that on the right side by about 16 msec. The median nerve somatosensory-evoked field exhibited the prolonged N20m with left-side stimulation, and there was no response on the right. We observed scattered ECD around the porencephalic ventricles on both side in case two, and found no significant focus. Most of the DSW on the EEG accompanied no significant dipole pattern in case three. However, a two dipole pattern observed in a few spike and waves and the ECDs were estimated to originate bilaterally from the parietal region. Case four revealed the ECDs in three local regions which were not detected by MRI. In case five, the ECD was estimated to originate mainly in the right parieto-occipital region but also in the left occipital and right frontal regions. The later two foci were located on the cortical tuber in MRI, but the parieto-occipital region didin't fit the cotical tuber of tuberous sclerosis. The ECDs were estimated to be in the frontal region in cases six and seven. The ECDs of case six were located in the right premotor area which agreed her advesive seizure.

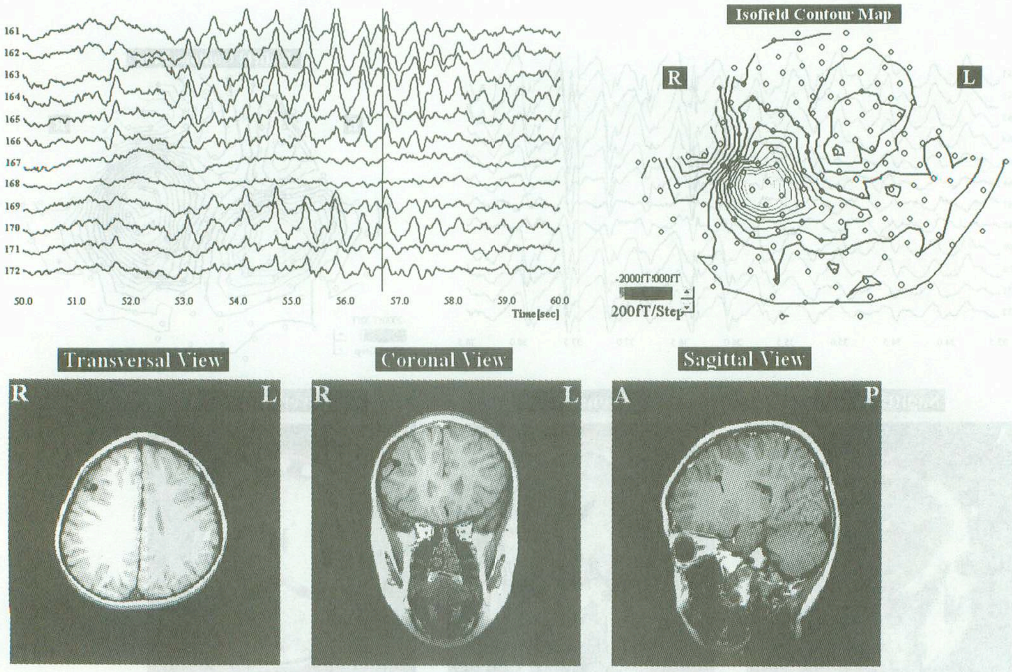

Fig.2 Example of ECD estimation in case six. The EEG exhibited diffuse high voltage slow wave bursts with small spike. (upper left). At 56 sec and 680 msec in the iso-contour map a dipole patten appeared on the right side (upper right), and its ECDs were estimated to originate in the right frontal premotor area (lower). Frequent adversive seizure observed in case six. The ECDs location seems to agree her clinical seizure.

Discussion

The decision whether GE or LRE is present is important for the treatment of epilepsy, since it determines the choice of antiepileptic drugs and prognosis. However, observation of clinical seizures alone is insufficient to differentiate the GE from LRE when seizures rapidly develop secondary generalization. The EEG is useful in these cases, but sometimes its findings are unclear. In fact, patients with frontal lobe epilepsy often exhibit bilateral synchronous discharges and resemble in this respect those with GE [2]. MEG can clearly differentiate GE from LRE by estimation of ECDs.

In the present study, there were three cases of GE and four of LRE. Between one and three ECDs were estimated by MEG for each of the four LRE patients. In the two frontal epilepsy patients MEG could exhibit the frontal focus which could not be detected by EEG and MRI. On the other hand, two of three GE exhibited a two dipole pattern. Actually, the ECDs in the LGS patient were estimated to originate in the region of cortical dysplasia detected on MRI providing evidence of the reliability of this estimation. LGS is classified as a form of GE. Our case is an example of induction by focal cortical lesions of GE. Cortical dysplasia is intrinsically epileptogenic [3]. However, 16 msec is too long a delay the left lesion to have induced the right cortex firing. We propose that a centrocephalic epileptic focus activated both cortical lesions and more rapidly transferred to the left. The SEF findings support this hypothesis. The underlying mechanism of absence seizure which is typical primary GE appears to involve thalamocortical circuitry [4]. The thalamo-cotical system is involved in spike and wave discharge generation [5][6]. In GE, the signal from thalamus may initially reach the bilateral somatosensory area and form a dipole pattern. We suspect that two dipole pattern is characteristic some types of general epilepsy.

Our results thus suggest that MEG findings will make the diagnosis of epilepsy more accurate and improve the prognosis of epilepsy patients.

Referrences

[1] Kuzniecky R, Andermann F, Guerrini R, et al: The epileptic spectrum in the congenital bilateral perisylvian syndrome. Neurology 44:379-385, 1994

[2] Roger J, Bereau M: Distinctive characteristics of frontal lobe epilepsy versus idiopathic generalized epilepsy. Chauvel P, Delgado-Escuta AV, Halgren E, et al (eds.): Advances in Neurology Vol.57, Frontal Lobe Seizures and Epilepsies. New York: Raven Press, 1992, pp399-410

[3] Palmani A, Gambardella A, Andermann F, et al: The human dysplastic cortex is intrinsically epileptogenic. Guerrini R, Andermann F, Canapicchi R, et al (eds.): Dysplasias of Cerebral Cortex and Epilepsy. Philadelphia/New York: Lippincott-Raven,1966, pp 43-52

[4] Snead III OC: Basic mechanism of generalized absence seizures. Ann Neurol 37:146-157, 1995

[5] de Curtis M, Avanzini G: Thalamic regulation of epileptic spike and wave discharges. Functional Neurology 9: 307-326, 1995

[6] Niedermeyer E: Primary generalized epilepsy and underlying mechanism. Clinical Electroencephalography 27: 1-21, 1996

Magnetoencephalographic study of epileptic foci in patients with tuberous sclerosis.

Kubota M, Ichiseki H, Takeshita K, Atsumi S, Sakakihara Y, Yanagisawa M

Department of Pediatrics, The University of Tokyo, 7-3-1, Hongo, Bunkyo-ku Tokyo 113-8655, Japan

Introduction

Tuberous sclerosis (TS) is an autosomal dominant hamartomatosis characterized by intractable epilepsy, mental retardation and other systemic lesions such as skin, renal and cardiac involvement. Intractable epilepsy includes infantile spasms, complex partial seizures and generalized seizures. Although neuropathological studies show abnormal findings such as cortical tubers, preventricular calcifications or cortical dysplasia [1,2], the relationship between these abnormalities and epileptogenesis is unclear.

The correlation between paroxysms in the EEG and cortical tubers on magnetic resonance imaging (MRI) or hypometabolism in positron emission tomography (PET) study has been reported [3,4,5,6,7]. However, it has been difficult to delineate the precise spatial relationship between them, because of the poor resolution of these methods.

The aim of this study is to analyze the spatial relation between spike foci and cortical tubers detected by magnetoencephalography (MEG) and MRI in patients with TS.

Patients report

Patient 1. This 25-year-old man was diagnosed as tuberous sclerosis when he was 3 months old, because he presented with infantile spasms, typical skin lesion such as multiple facial angiofibromas and the hypopigmented " ash leaf" spots, and periventricular calcification on the brain CT. Following successful ACTH (adrenocoticotropic hormone) treatment for infantile spasms, he had been seizure-free for 12 years. However, at the age of 13, antiepileptic medication was started again, since he exhibited complex partial seizure. The seizure was characterized by fear or anxiety as an aura, screaming and frenetic automatisms with violent thrashing, which lasted for several minutes. His consciousness was not always impaired. The seizure was occasionally induced by sound stimuli such as a bird song or an echo sound in the bathroom. Tonic clonic manifestations were not observed. Seizure frequency decreased to several times per week on the addition of phenytoin.

Patient 2. This 2-year-old boy developed myoclonic seizures of left-sided extremities when he was 2 months of age. He was diagnosed as tuberous sclerosis because of multiple tubers on the brain CT and typical skin changes. At 5 monts of age, clinically infantile spasms were noted and he gradually deteriorated. The EEG showed hypsarrhythmia. Following ACTH therapy the spasms reduced and general condition improved. MEG study of the paroxysmal discharges was performed at 10 months of age. Then the hypsarrhythmia disappeared and focal sharp waves were found in the right hemisphere, despite nodding spasms remained clinically.

Methods of MEG measurement

MEG was performed in a magnetically shielded room with a 37-channel neuromagnetometer (Biomagnetic Technologies Inc, San Diego, CA) with a simultaneous EEG recording. A spherical model was fitted to the digitized head shape of the patient, and the location (x, y, z position), orientation and amplitude of a best-fitting single equivalent current dipole (ECD) were calculated at 2 ms intervals from trough to negative peak of the spike. The correlation coefficient between the theoretical field generated by the model and the obtained field were used to estimate a localization error. To minimize a localization error, we analyzed the dipole fitting data with a correlation efficient above 0.985. The ECD with maximum correlation coefficient in selected duration was regarded as the representative ECD of the spike. The obtained ECDs were superimposed on the brain MRI to analyze the spatial relationship to cortical tubers.

MEG, MRI and PET findings

Simultaneous records of MEG and EEG were shown in Fig.1. The 37-channel-magnetometer was placed on the

©1999, Tohoku University Press
Recent Advances in Biomagnetism
T. Yoshimoto et al. (Eds)

left frontocentral portion and the right central portion in patients 1 and 2, respectively. The definite magnetic

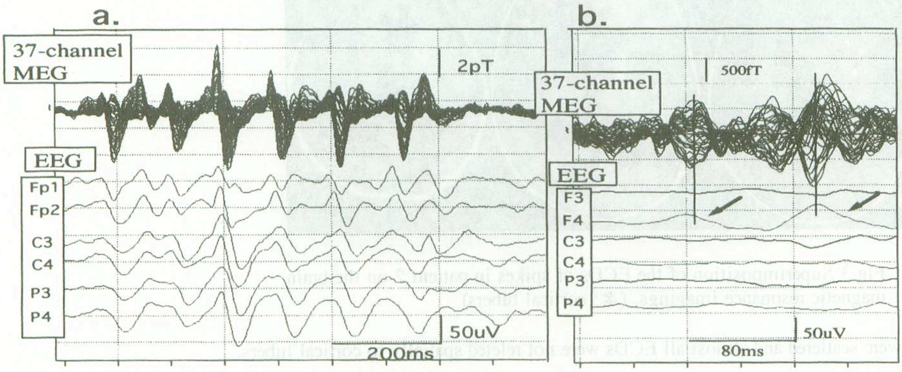

Fig.1 Simultaneous records of EEG and MEG. **a:** patient 1, **b:** patient 2.

changes corresponding with the EEG spikes were recorded.

As shown in Fig.2 , in patient 1,the ECDs of interictal spikes were localized in the left lower frontal area including the insula cortex and were mainly oriented posteroanteriorly. Although multiple cortical tubers were detected on brain MRI with fluid attenuated inversion recovery (FLAIR) pulse sequence, none of them was concordant spatially with the ECDs of the spikes. Brain CT showed periventricular calcifications, which were also not related spatially to spike localization. Interictal positron emission tomography with 2-deoxy-2 [^{18}F] fluoro-D-glucose (^{18}FDG) disclosed multiple areas of decreased glucose utilization (hypometabolism) in the left lower frontal, right middle medial frontal and right temporoparietal region (Fig. 2). As shown in Fig. 3, in patient 2, the ECDs of focal sharp

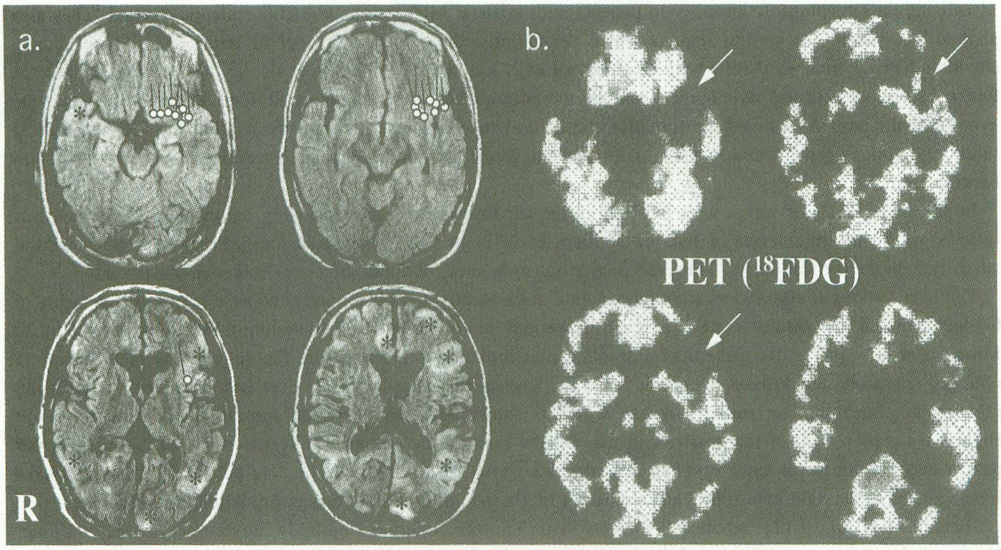

Fig.2 **a.** Superimposition of the ECDs of spikes in patient 1 on the brain magnetic resonance imagings with FLAIR (fluid attenuated inversion recovery) pulse sequence. They were localized in the left frontal area including the insula. (✱: cortical tubers) **b.** Interictal positron emission tomography (^{18}FDG-PET) showing multiple hypometabolic areas. The largest hypometabolic area (arrows) corresponded to the area of the ECDs localization detected by MEG.

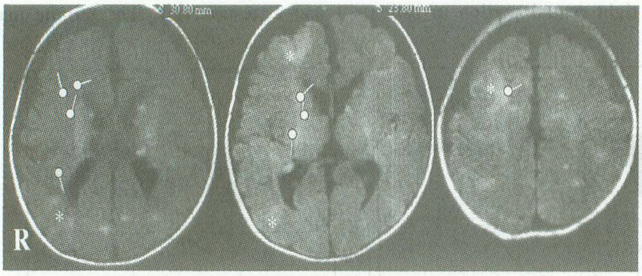

Fig.3 Superimposition of the ECDs of spikes in patient 2 on the brain magnetic resonance imagings. (✱: cortical tubers)

waves were scattered and almost all ECDs were not releted spatially to cortical tubers.

Discussion

A precise spatial relationship between EEG foci and CNS lesions such as cortical tubers, subependymal nodules and white matter heterotopia in patients with TS was not clearly demonstrated.

According to Cusmai et al. [3], who investigated the topographic relationship between cortical tubers on MRI and EEG foci in 34 TS patients, a topographic MRI/EEG correspondence was observed for at least one tuber in 25 of 26 patients, and correspondence was complete in 10 patients. In their definition, when one EEG focus and one tuber were located in the same lobe, they were topographically correlated. They also pointed out that large cortical tubers *without* corresponding EEG foci were observed in 11 patients, and these tubers mainly involved the frontal regions and were found before the patients were 2 years old. They concluded that cortical tubers are epileptogenic and that their expression may be influenced by regional cortical maturation. Tamaki et al. [6] demonstrated that MRI lesions in the occipital lobes showed the best correlation with the EEG epileptic foci, while the worst correlation was seen in the frontal lobes, and that single photon emission computed tomography (SPECT) was useful for visualizing the epileptogenic laterality in patients with bilateral MRI lesions and EEG epileptic changes. They also showed that among the cortical regions which consistently showed epileptic foci in serial EEGs, none showed abnormal SPECT findings if there were no abnormal MRI lesions [7]. Szelies et al. [5] demonstrated that large tubers disorganized cortical development and are the anatomic basis of epileptogenic foci. They assumed that the hypometabolic areas represented the epileptogenic cortical tubers. Thus, although the relationship between cortical tubers and epileptogenic foci has previously been suggested, no precise spatial correlation has been established between them.

In patient 1, ECDs of spikes were localized in the left lower frontal area including the insula cortex which was included in the maximum area of hypometabolism in PET. In MEG, the spike localization was not concordant spatially with the cortical tubers. Thus, the cortical tubers are not the direct sources of spikes in our patient.

The insula cortex is regarded as a complex region anatomically and functionally, because it includes elements of frontal, temporal and parietal cortex and controls various motor, sensory and autonomic functions. According to Mesulam et al. [8], the pattern of insulothalamic connection indicated that the anterior insula is related to olfactory, gustatory, and viscero-autonomic behavior, whereas the posterior insula is related to auditory-somesthetic-skeletomotor function. Our patient's seizure which is sometimes induced by the specific sound stimulus might suggest the involvement of the posterior insula. On the basis of the seizure manifestation and MEG findings, our patient may belong to the category of frontal complex partial seizure [9,10,11]. In patient 2, ECDs of spikes were scattered in the right hemisphere and almost all ECDs were not spatially concordant with cortical tubers.

Bebin-EM et al. [12] reported 9 patients with TS who underwent epilepsy surgery at the Mayo Clinic. Neuropathologic diagnoses of resected tissues were cortical tubers (n = 7) and glioneural hamartomas (n = 2). They showed postoperative complete or partial seizure reduction. Three of 9 patients had multifocal interictal scalp epileptiform EEG activity, however, ictal recordings identified a single focus of seizure activity, which in all cases corresponded to the neuroimaging (MRI and CT) abnormality. The surgical results suggested that despite the multiple cerebral involvement and multifocal EEG abnormalities, resection of a single cortical epileptogenic lesion might be possible.

From the fact that the seizures were controlled by surgical resection of the abnormal portion including the cortical tuber and surrounding tissues, it seems possible that the cortical tuber plays an important role in the development of epileptogenesis in patients with TS. According to Short et al. [2], on neuropathological examination, the cortical tuber stands out dramatically from the normal, orderly lamination of the cerebral cortex. The borders of the tuber are indistinct with an increase in glial fibrillarity and a decrease in the density of the myelinated fibers. Palmini et al. [13] reported that neuropathological examination of the lesion in patients with neuronal migration disorders including forme fruste of TS was characterized by the presence of giant, aberrent neurons and glial cells, and disorganized cortical architecture. They showed the epileptogenic area was usually more extensive than the imaged lesion. Recently MRI with FLAIR pulse sequence is reported to be more imformative on brain abnormality in patients with partial epilepsy as compared with the conventional T2-weighted imaging [14]. There was no previous comparative study as shown here concerning cortical tubers and EEG foci in patients with TS using MRI with FLAIR pulse sequence and MEG, both of which have a better spatial resolution than the conventional EEG and MRI.

In conclusion, based on MEG and MRI findings in our patient and studies of surgically-treated patients with TS, it can be speculated as follows: (1) cortical tubers in these patients are not a direct source of epileptogenic activity, although they are shown to be closely related to the formation of an epileptogenic neuronal circuit in the developing brain, and (2) the epileptogenic foci in our patients appear to be associated with the cortical hypometabolism rather than the cortical tuber itself as a structural abnormality.

Further longitudinal investigation using MEG and MRI (FLAIR) is needed to clarify the dynamic nature of the epileptogenic focus in the patient with TS.

References

[1] Raymond AA, Fish DR, Sisodiya SM, et al: Abnormalities of gyration, heterotopias, tuberous sclerosis, focal cortical dysplasia, microdysgenesis, dysembryoplastic neuroepitherial tumour and dysgenesis of the archicortex in epilepsy: clinical, EEG and neuroimaging features in 100 adult patients. Brain 118: 629-660,1995

[2] Short MP, Richardson EP Jr, Haines JL, et al: Clinical, neuropathological and genetic aspects of the tuberous sclerosis complex. Brain Pathology 5:173-179,1995

[3] Cusmai R, Chiron C, Curatolo P, et al: Topographic comparative study of magnetic resonance imaging and electroencephalography in 34 children with tuberous sclerosis. Epilepsia 31:747-755,1990

[4] Shepherd CW, Houser OW, Gomez MR: MR findings in tuberous sclerosis complex and correlation with seizure development and mental impairment. AJNR 16:149-155,1995

[5] Szelies B, Herholz K, Heiss W-D, et al: Hypometabolic cortical lesions in tuberous sclerosis with epilepsy: demonstration by positron emission tomography. J Comput Assist Tomogr 7: 946-953,1983

[6] Tamaki K, Okuno T, Itoh M, et al: Magnetic resonance imaging in relation to EEG epileptic foci in tuberous sclerosis. Brain Dev 12:316-320,1990

[7] Tamaki K, Okuno T, Iwasaki Y, et al: Regional cerebral blood flow in relation to MRI and EEG findings in tuberous sclerosis. Brain Dev 13:420-424,1991

[8] Mesulam MM, Mufson EJ: Insula of the old world monkey. III: Efferent cortical output and comments on function. J Comp Neurol 212:38-52,1982

[9] Stores G, Zaiwalla Z, Bergel N: Frontal lobe complex partial seizures in children: a form of epilepsy particular risk of misdiagnosis. Dev Med Child Neurol 33:998-1009,1991

[10] Waterman K, Purves SJ, Kosaka B, et al: An epileptic syndrome caused by mesial frontal lobe seizure foci. Neurology 37:577-582,1987

[11] Williamson PD, Spencer DD, Spencer SS, et al: Complex partial seizures of frontal lobe origin Ann Neurol 18:497-504,1985

[12] Bebin EM, Kelly PJ Gomez MR: Surgical treatment for epilepsy in cerebral tuberous sclerosis Epilepsia 34: 651-657,1993

[13] Palmini A, Andermann F, Olivier A, et al: Focal neuronal migration disorders and intractable partial epilepsy: a study of 30 patients. Ann Neurol 30:741-749,1991

[14] Bergin PS, Fish DR, Shorvon SD, et al: Magnetic resonance imaging in partial epilepsy: additional abnormalities shown with the fluid attenuated inversion recovery (FLAIR) pulse sequence. J Neurol Neurosurg Psychiatry 58:439-443,1995

Mesial Temporal Origin of Spike Bursts in a Patient with Complex Partial Seizures

Kanno, A.[1], Nakasato, N.[2], Hatanaka, K.[3], Ohtomo, S.[2],
Ohtsuki, T.[1], Fujiwara, S.[1], Yoshimoto, T[2].

Kohnan Hospital Ryogo Center[1], Sendai, Japan;
Department of Neurosurgery, Tohoku University School of Medicine[2], Sendai, Japan;
ELEKTA K.K.[3], Tokyo, Japan

Introduction

Magnetoencephalography (MEG) can be used for the presurgical evaluation of epileptogenic zones in patients suffering from partial seizures [1,2]. Interictal spike discharges are commonly employed for the source localization analysis using the equivalent current dipole (ECD) model. However, the time course of source localization in interictal spike bursts or trains is little understood. Whether mesial temporal localization of interictal discharge indicates "real" deep localization of the mesial activity or "false" deep localization of superficially spread activity is also controversial [3,4]. The present study investigated ECD localization over the time course of spike bursts using MEG.

Materials and Methods

A 24-year-old female suffered intractable complex partial seizures, often triggered by absence of light stimulation. MRI indicated no structural lesion. Interictal EEG showed spike bursts over the left parieto-occipital area. Ictal EEG indicated no localization or lateralization.

MEG was performed in a magnetically shielded room using a helmet-shaped MEG system (Neuromag-122, Neuromag Ltd.) with simultaneous EEG. The data were band pass filtered through 0.03-100 Hz and digitized at 0.4 kHz. Ten spike bursts were analyzed using the single or double ECD models sequentially from -300 ms before to 600 ms after the onset for each spike burst. ECDs with goodness-of-fit higher than 70% for all channel detectors were superimposed on the anatomical MRI.

Results

Interictal spike discharges were recorded as "trains." The amplitude dominance of the left hemispheric activity was clearer by MEG than EEG (Fig. 1). Isofield maps of most of the trains indicated left hemispheric single dipole patterns in the early part of the bursts and bilateral double dipole patterns over the bilateral hemispheres in the later part (Fig. 2). The ECDs of the left hemispheric single dipole patterns were located mainly in the mesial temporal area whereas the ECDs of the bilateral double dipole patterns in the left hemisphere were located in the lateral temporal areas or extratemporal cortices. Such mesial temporal localizations were frequently found in the early part of the spike trains followed by the lateral temporal or extratemporal localizations (Fig. 3). The ECDs of the bilateral dipole patterns in the right hemisphere were also located in the lateral or extratemporal areas.

©1999, Tohoku University Press
Recent Advances in Biomagnetism
T. Yoshimoto et al. (Eds)

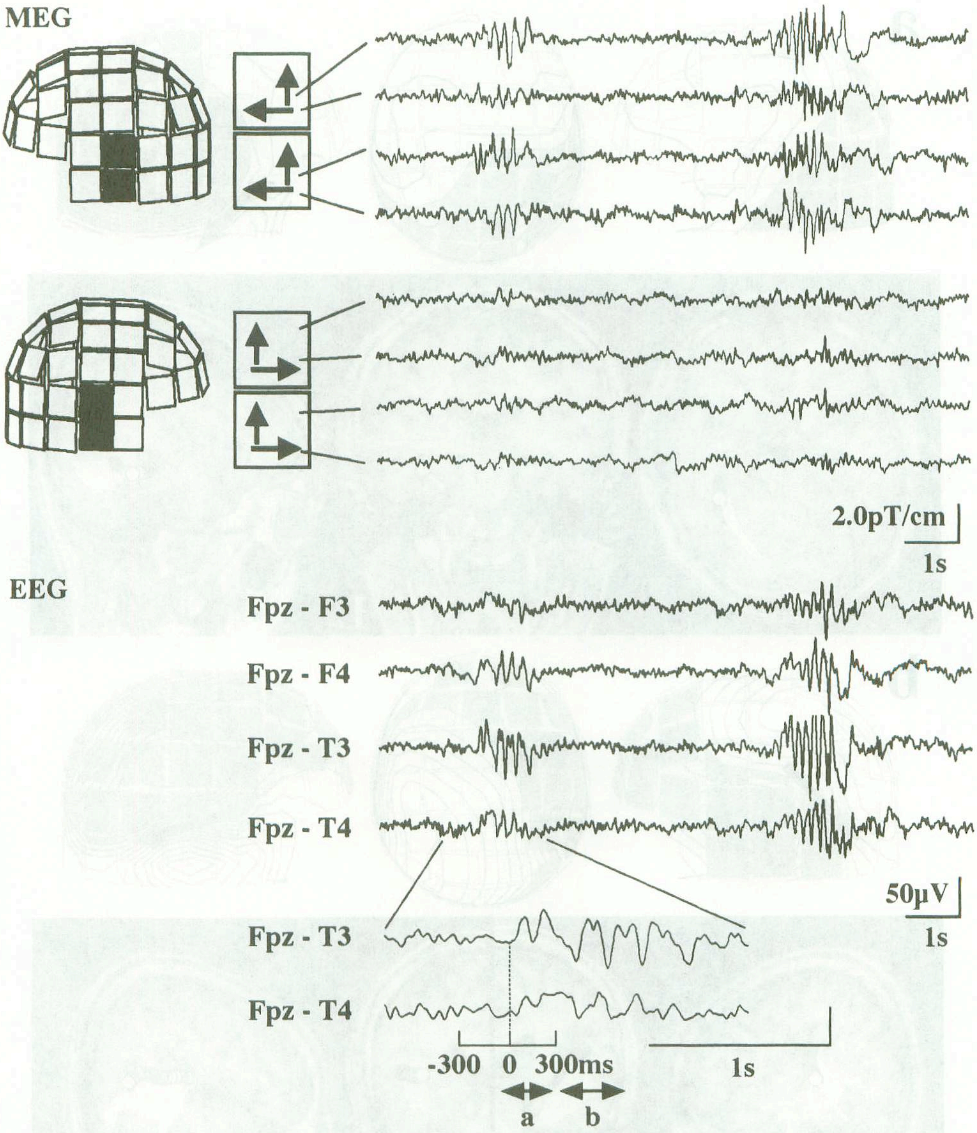

Fig. 1 Spike burst recording by simultaneous MEG and EEG. Left hemispheric dominance of the bursts is clearer by MEG than EEG. Early components of the bursts, from -300 ms to +600 ms of the approximate onset timing, were used for the following analysis (Fig. 3). Times "a" and "b" correspond to those in Fig. 2.

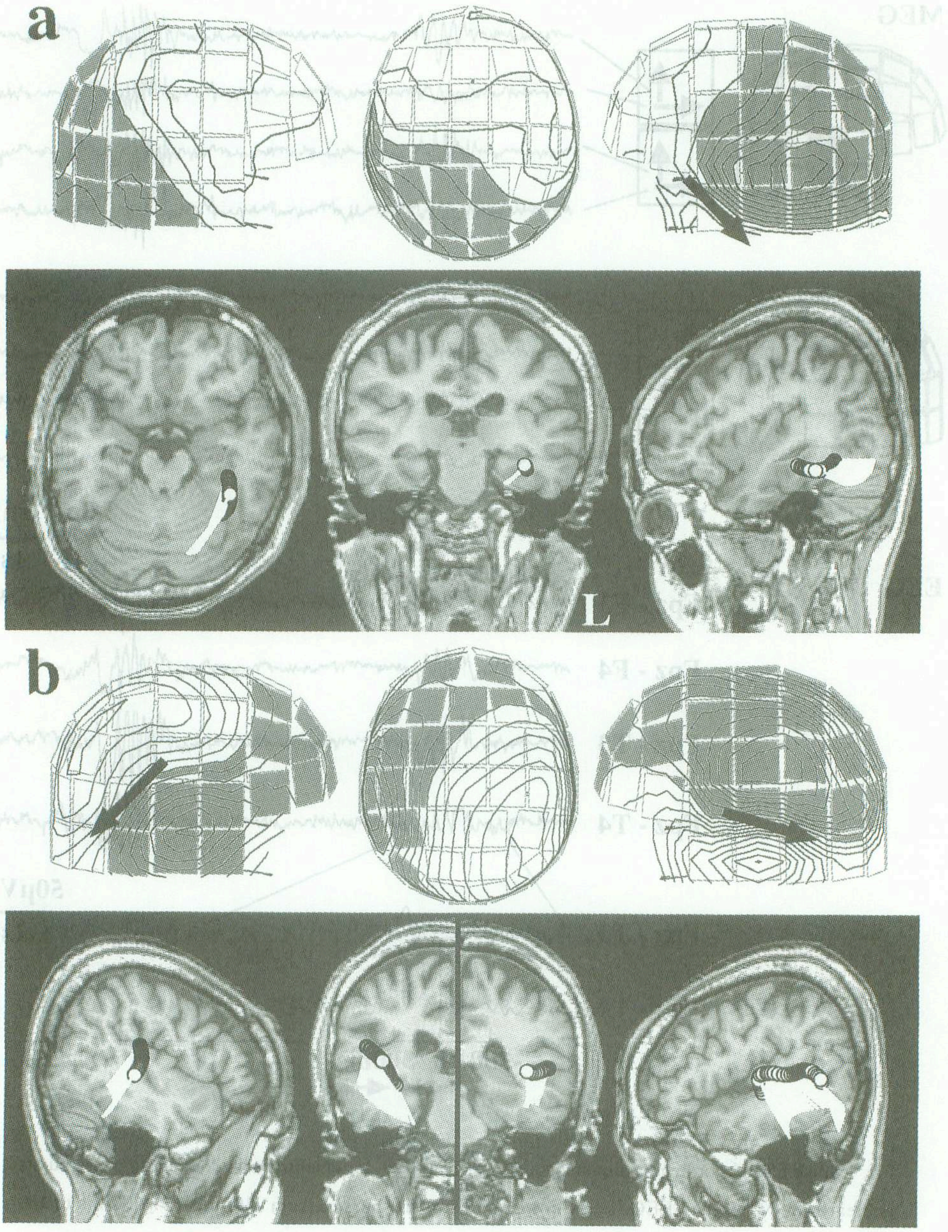

Fig. 2 Isofield maps and equivalent current dipoles of the spikedischarge in Fig. 1. (a) During the time window "a," the isofield maps indicate a single-dipole pattern over the left temporal area (top). Equivalent current dipoles (ECDs) are located in the mesial temporal structures (bottom). (b) During the time window "b," the isofield maps indicate a double-dipole pattern (top). The ECDs are located in the bilateral lateral and superior temporal areas (bottom).

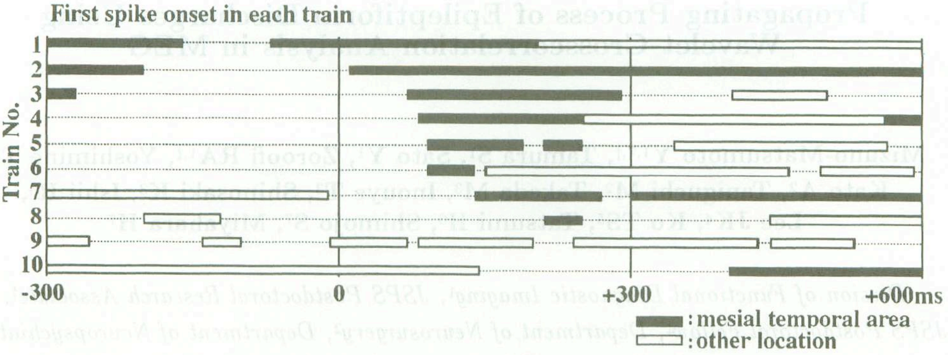

Fig. 3 Summary of left hemispheric ECD localization in the early part of 10 spike bursts (from -300 ms to +600 ms of the approximate onset). Most typical ECD localization starts from the mesial temporal structures (filled bars) followed by lateral ECD localization (open bars), such as the lateral temporal, frontal, parietal or occipital areas.

Discussion

Mesial temporal localization of ECDs can result from either "real" deep sources, or "false" deep localization of the superficial extended sources of epileptic discharges. In the present study, mesial temporal localization was frequently found in the early part of spike bursts followed by lateral temporal or extratemporal localization. We believe these recordings represent "real" deep activity because the spike zones usually spread along the positive time axis, and the mesial and posterior dipole localization corresponded to the seizure semiology of the patient in which complex partial seizures were often triggered by visual stimuli. This study emphasizes the importance of sequential time course analysis of the epileptic discharges, especially when discharge propagation is indicated.

References

[1] Nakasato N, Seki K, Kawamura T, et al: Whole head magnetoencephalography: detection of epileptic discharges on bilateral hemispheres. J Jpn Epil Soc 12: 213-220, 1994

[2] Nakasato N, Levesque MF, Barth DS, et al: Comparisons of MEG, EEG and ECoG source localization in neocortical partial epilepsy in human. Electroenceh Clin Neurophysiol 91: 171- 178, 1994

[3] Jukka S: Basic mathematical and electromagnetic concepts of the biomagnetic inverse problem. Phys Med Biol 37: 11-22, 1987

[4] Sutherling WW, Barth DS: Neurocortical propagation in temporal lobe spike foci on magnetoencephalography and electroencephalography. Annals of Neurology 25: 373-381, 1989

Propagating Process of Epileptiform Discharges Using Wavelet-Crosscorrelation Analysis in MEG

Mizuno-Matsumoto Y[1,7,†], Tamura S[1], Sato Y[1], Zoroofi RA[1,‡], Yoshimine T[2], Kato A[2], Taniguchi M[2], Takeda M[3], Inouye T[3], Shinosaki K[3], Ishii R[3], Lee JK[4], Ko TS[5], Tatsumi H[6], Shimojo S[7], Miyahara H[7]

Divsion of Functional Diagnostic Imaging[1], JSPS Postdoctoral Research Associate[†],
JSPS Postdoctoral Fellow[‡], Department of Neurosurgery[2], Department of Neuropsychiatry[3],
Osaka University Medical School, Osaka, JAPAN;
Departments of Neurological Surgery[4], Department of Pediatrics[5],
University of Ulsan College of Medicine, Asan Medical Center, Seoul, KOREA;
Department of Anatomy, Sapporo Medical College[6], Sapporo, JAPAN;
Department of Information and Computer Sciences, Faculty of Engineering Science,
Osaka University[7], Osaka, JAPAN

Introduction

Magnetoencephalography (MEG) is being investigated in the hope that it will provide accurate localization of cerebral current sources non-invasively, which in turn will improve our understanding of the generators of cerebral activity [1]. Non-invasive magnetoencephalographical localization of spikes, in contrast to the use of electrocorticography (ECoG), is useful because it avoids the need for surgical implantation with its consequent additional risks to the patient. Spherical single dipole models are often used for focus localization in MEG [2], although modeling the activity generated by multiple brain regions with a single dipole can lead to erroneous conclusions [3]. Therefore, the development of mathematical methods for the extraction of localization-relevant information is inevitable. In this study we report on a new technique, wavelet-crosscorrelation analysis, that we have developed to investigate the propagation of epileptiform discharges in Landau-Kleffner syndrome (LKS).

Methods

1. Data acquisition

A child with LKS were studied. MEG recordings were performed in a magnetically shielded room using a 64-channel whole-cortex MEG system. The recordings were digitized at 250 Hz and bandpass filtered at 2–25 Hz. MEG data mainly consisted of the spike wave and the following sharp-and-wave complexes except for the background activity.

2. Nonstationary Analysis

Wavelet-crosscorrelation analysis was developed as a means of nonstationary analysis for MEG data. This method provides a quantitative measure of the relatedness and time delay of two time-varying signals. The propagation of epileptiform discharges was also investigated.

Crosscorrelation analysis enables the degree of similarity in waveforms between two different time series to be determined. Fourier transformation of the crosscorrelation function, which yields the cross-spectra, has been often employed [4]. However, it has been pointed out that data segments analyzed using crosscorrelation functions should not include non-stationarities. Therefore, this method is not suitable for analyzing the dynamics of epileptiform discharges.

On the other hand, since wavelet analysis has a good spatio-temporal resolution, it has been more used as a non-stationary method to analyze physiological phenomena [5] [6] [7]. To utilize the features of both

©1999, Tohoku University Press
Recent Advances in Biomagnetism
T. Yoshimoto et al. (Eds)

procedures, we have proposed that crosscorrelation and wavelet analysis be combined. Wavelet-crosscorrelation analysis provides a quantitative measure of the similarity and time delay of two time-varying signals [8].

The crosscorrelation function of two time series is expressed by the equation

$$C_{k,i}(\tau) = \int_{t}^{t+w} f_k(\lambda) f_i(\lambda + \tau) d\lambda \tag{1}$$

where $f_i(t)$ and $f_k(t)$ are the filtered values of the MEG data from electrodes i and k at time t, τ is the time-shift (lag) of $f_k(t)$ with respect to $f_i(t)$, and w is the window size. $f_i(t)$ is the signal which should be evaluated and $f_k(t)$ is the reference for the crosscorrelation.

The wavelet transform of a signal can be computed by projecting the signal onto a wavelet basis [9] [10] [11]. A given basic wavelet $g(t)$ is scaled by a in the time domain and is shifted by b in order to generate a basic family $g_{a,b}(t)$. The wavelet transform $S(a,b)$ of a signal $s(t)$ is as follows:

$$S(a,b) = \frac{1}{\sqrt{c}} \int_{-\infty}^{\infty} g^*_{a,b}(t) s(t) dt, \tag{2}$$

$$g_{a,b}(t) = \frac{1}{\sqrt{a}} g\left(\frac{t-b}{a}\right). \tag{3}$$

According to equations (1)–(3), the wavelet crosscorrelation function can be written as

$$WC_{k,i}(a,b) = \frac{1}{\sqrt{c}} \int_{-\infty}^{\infty} \frac{1}{\sqrt{a}} g\left(\frac{\tau - b}{a}\right) C_{k,j}(\tau) d\tau. \tag{4}$$

The Gaussian wavelet (eq. 5) was employed as a basic wavelet.

$$g(n) = e^{-n^2/2}(e^{j\Omega n} - e^{-\Omega^2/2}) \tag{5}$$

where the constant Ω is given by 2π.

Wavelet-crosscorrelation values, which show the time-lag of non-stationary data, were calculated between every set of neighboring electrodes. In this case the spike wave was shown in the β band, the sharp wave in the α band and the slow wave in the θ band. From the time shift, the propagation speed between two sensors were calculated. The propagation mean speed values and the propagation directions in each frequency band were then derived from the time shift value. The propagation mean speed and directions figured as the vector in the map.

Results

The spike wave was generated from the antero-temporal area, the sharp wave from the superior temporal gyrus, and the slow wave from the antero-frontal area. The waves were propagated from the antero-temporal area to the superior temporal gyrus and antero-frontal area.

Discussion

In this study, the term "origin" does not indicate the origin where the current source is but where the magnetic field appears. However, using wavelet-crosscorrelation analysis MEG data can be precisely estimated in terms of time and frequency resolution. The results show the different origins and speed of spread in each frequency band corresponding to each wave component.

The Landau-Kleffner syndrome (LKS) of acquired aphasia, with convulsive disorder in childhood, was first reported in 1957 [12]. The dominant disorder is verbal auditory agnosia. In spite of many published cases, the etiology and pathogenesis of LKS remain unclear [13]. Although an encephalitic etiology is frequently postulated, no definite cause has been found. Cole et al. reported two patients with LKS who were treated surgically [14]. In both cases, neuropathologic studies revealed mild gliosis but not encephalitis. Furthermore, CT and MRI have failed to show consistent structural lesions. Therefore it is suggested that LKS is probably more a disorder of function than of structure [15].

In EEG findings, high- voltage focal or multifocal spikes and/or spike-and-wave complexes are typically shown. EEG discharges are generalized, bilateral, multifocal, or have shifting predominance, but are mainly shown in the temporal area. On the other hand, regional cerebral blood-flow measured by HMPAO and SPECT in LKS demonstrated relatively low-flow areas in the left-middle frontal gyrus and the right mesiotemporal/hippocampal region [15]. Rodriguez and Niedermeyer reported the presence of single spikes, sharp waves, and slow spike-wave complexes (1.5–2.5 Hz) [16]. They summarized the typical EEG characteristics of LKS as a combination of midtemporal spiking mainly on the left and bilateral-synchronous almost generalized bursts of spikes and slow spike-waves with a midtemporal maximum.

Paetau et al. recorded magnetoencephalographic (MEG) spikes in a patient with LKS [13]. In their study, 3 Hz spike-and-wave discharges, single spikes, and bursts of 3-Hz slow activities were shown in not only the left auditory cortex but the right hemisphere. They suggest that once discharges occur in the auditory cortex, the maturing interhemispheric pathways begin to transfer epileptic activity instead of verbal information.

In our study, the spike wave appeared from the antero-temporal area and the sharp-and-wave complexes were generated from the superior temporal gyrus and the frontal area. Furthermore, the wave propagation was from the antero-temporal area to the superior temporal gyrus. These results indicate that the preceding spike wave might influence the generation of sharp-and-wave complexes, and that not only the sharp waves from the temporal area but also the spike waves from the frontal area could be important in creating the symptoms. Additionally these findings suggest that the proposed method can be useful for analyzing MEG.

Acknowledgments

This work was supported in part by Research for the Future Program of Japan Society for the Promotion of Science (JSPS) under the Project "Integrated Network Architecture for Advanced Multimedia Application Systems" (JSPS-RFTF97R16301).

The authors would like to thank Mr. T. Kihara in Aloka Co., Ltd. for giving assistance.

References

[1] E. Niedermeyer and F. Lopes da Silva, *Electroencephalography.* Baltimore: Williams & Wikins, 1993.

[2] C. Baumgartner, A. Doppelbauer, W. Sutherling, G. Lindinger, M. Levesque, S. Aull, J. Zeitlhofer, and L. Deecke, "Somatotopy of human hand somatosensory cortex as studied in scalp EEG," *Electroencephalogr. Clin. Neurophysiol.*, vol. 88, no. 4, pp. 271–279, 1993.

[3] A. Gevins, "The future of electroencephalography in assessing neurocognitive functioning," *Electroencephalogr. Clin. Neurophysiol.*, vol. 106, no. 2, pp. 165–172, 1998.

[4] J. Gotman, "Interhemispheric relations during bilateral spike-and-wave activity," *Epilepsia*, vol. 22, pp. 453–466, 1981.

[5] Y. Mizuno-Matsumoto, K. Okazaki, A. Kato, T. Yoshimine, Y. Sato, S. Tamura, and T. Hayakawa, "Visualization of epileptogenic phenomena using crosscorrelation analysis: Localization of epileptic foci and propagation of epileptiform discharges," *IEEE Trans. Biomed. Eng.*, 1998. in press.

[6] Y. Mizuno-Matsumoto, K. Okazaki, A. Kato, T. Yoshimine, Y. Sato, S. Tamura, K. Yamashita, and T. Hayakawa, "Localization of epileptogenic foci and the visualizaion of its propagating process," in *Brain Topography Today* (Y. Koga, K. Nagata, and H.Hirata, eds.), pp. 512–516, Amsterdam: Elsevier, 1998.

[7] Y. Mizuno-Matsumoto, T. Inouye, and S. Tamura, "Occurrences of electroencephalographic (EEG) patterns that resemble epileptiform discharges in background EEG in epileptic patients," *Intern. J. Neurosci.*, vol. 91, no. 1-2, pp. 69–84, 1997.

[8] H. Li and T. Nozaki, "Wavelet cross-correlation analysis to a plane turbulent jet," *JSME Int. J., Ser. B*, vol. 40, no. 1, pp. 58–66, 1997.

[9] J. Benedetto and M. Frazier, *Wavelets: Mathematics & applications*. Boca Raton: CRC press, 1994.

[10] O. Rioul and M. Vetterli, "Wavelets and signal processing," *IEEE Signal Proc. Magazine*, vol. 8, no. 4, pp. 14–38, 1991.

[11] H. Kikuchi, M. Nakashizuka, H. Watanabe, S. Watanabe, and N. Tomisawa, "Fast wavelet transform and its application to detecting detonation," *IEICE Trans. Fundamentals.*, vol. E75-A, no. 8, pp. 980–987, 1992.

[12] W. Landau and F. Kleffner, "Syndrome of aquired aphasia with convulsive disorder in children," *Neurology*, vol. 7, no. 8, pp. 523–530, 1957.

[13] R. Paetau, M. Kajola, M. Korkman, M. Hamalainen, M. Granstrom, and R. Hari, "Landau-kleffner syndrome: epileptic activity in the auditory cortex," *Neuro Report*, vol. 2, pp. 201–204, 1991.

[14] A. Cole, F. Andermann, L. Taylor, A. Olivier, T. Rasmussen, Y. Robitaille, and J. Spire, "The landau-kleffner syndrome of acquired epileptic aphasia," *Neurology*, vol. 38, pp. 31–38, 1988.

[15] S. Mouridsen, C. Videbak, H. Sogaard, and A. Anderden, "Regional cerebral blood-flow measured by HMPAO and SPECT in a 5-year-old boy with landau-kleffner syndrome," *Neuropediatrics*, vol. 24, pp. 47–50, 1993.

[16] I. Rodriguez and E. Niedermeyer, "The aphasia-epilepsy syndrome in children: electroencephalographic aspects," *Clin. Electroencephalogr.*, vol. 13, pp. 23–35, 1982.

Correspondence to:
Yuko Mizuno-Matsumoto, M.D., Ph.D.,
Division of Functional Diagnostic Imaging, D11, Osaka University Medical School,
2-2 Yamadaoka, Suita, Osaka, 565-0871, JAPAN
Tel: +81-6-879-3564
Fax: +81-6-879-3569
E-mail: mizuno@image.med.osaka-u.ac.jp

MEG study of temporal epilepsy
- dipole analysis and synthetic aperture magnetometry (SAM) -

Ninomiya H[1], Yoshimine T[1], Nii Y[2], Kato A[1], Taniguchi M[1], Hirata M[1], Maruno M[1], Kihara T[3], Cheyne D[4], Robinson SE[4], Imai K[5], Hirabuki N[6], Nakamura H[6], and Hayakawa T[1]

Departments of Neurosurgery[1], Pediatrics[5], and Radiology[6], Osaka University Medical School, Osaka, Japan; Department of Neurosurgery, Iseikai Hospital[2], Osaka, Japan; Aloka Co.[3], Tokyo, Japan; CTF Systems Inc.[4], B. C., Canada

Introduction

Epileptiform discharges measured with magnetoencephalography (MEG) are analyzed with equivalent current dipole (ECD) model, which demonstrates the center of the abnormal electric activity [1]. However, accumulated evidence suggests that a certain volume of the brain is involved in the generation of epileptiform discharges [2, 3]. Since ECD analysis does not demonstrate this volume of abnormal brain activity, we applied a spatial filtering technique (synthetic aperture magnetometry, SAM [4]) to disclose the origin of epileptiform discharges. The spatial and temporal profiles of abnormal discharges were analyzed in patients with two different types of temporal lobe epilepsy (TLE).

Materials and Methods

Patients with mesial temporal lobe epilepsy (MTLE) and lateral neocortex temporal lobe epilepsy (LTLE) were studied using 64-channel whole head SQUID system (CTF Systems Inc.). The diagnosis was supported by symptomatology as well as scalp EEG. MEG data segments of 5-second duration including epileptiform discharges were collected at a sampling rate of 625 Hz. ECD for epileptiform discharges with a fitting error below 20% were superimposed on the MRI images of the patient [1, 5]. The same data were also analyzed with SAM by setting virtual channels on the sagittal plane of medial temporal lobe or lateral temporal lobe (Fig. 1). Intensity of electrical activity was displayed in a color-scaled topographical map using Quick Time™ Movie to analyze the temporospatial distribution of the epielptiform discharges (Fig. 2).

Results

A total of 29 epileptiform discharges were analyzed in a patient with right MTLE. The ECDs were distributed in the right medial temporal structure (n= 24), and in the left temporal structure (n= 5) (Fig.3a). SAM Movie demonstrated all the discharges began from the right medial temporal lobe and expanded to three different directions; parietotemporal, lower

©1999, Tohoku University Press
Recent Advances in Biomagnetism
T. Yoshimoto et al. (Eds)

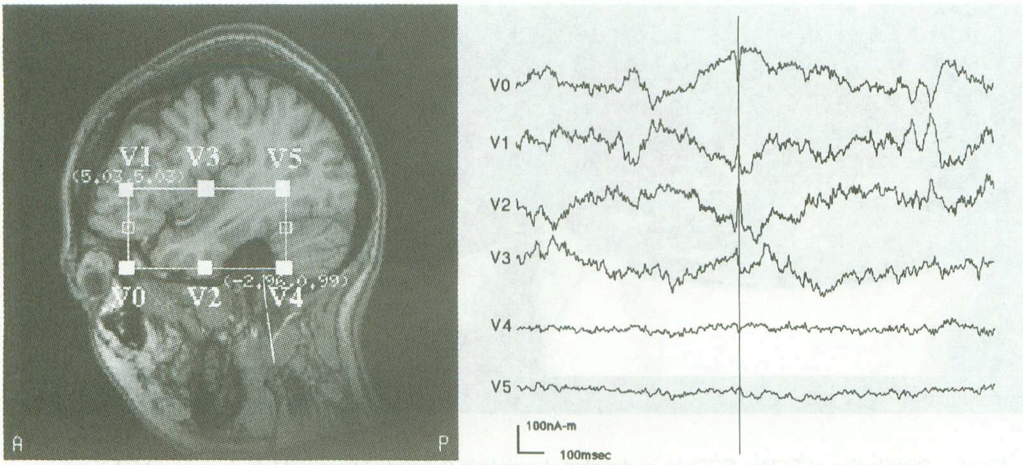

Fig. 1 An example of SAM virtual channel. Six virtual channels were shown as white squares (a). The abnormal epileptic discharge was observed at the cursole (b).

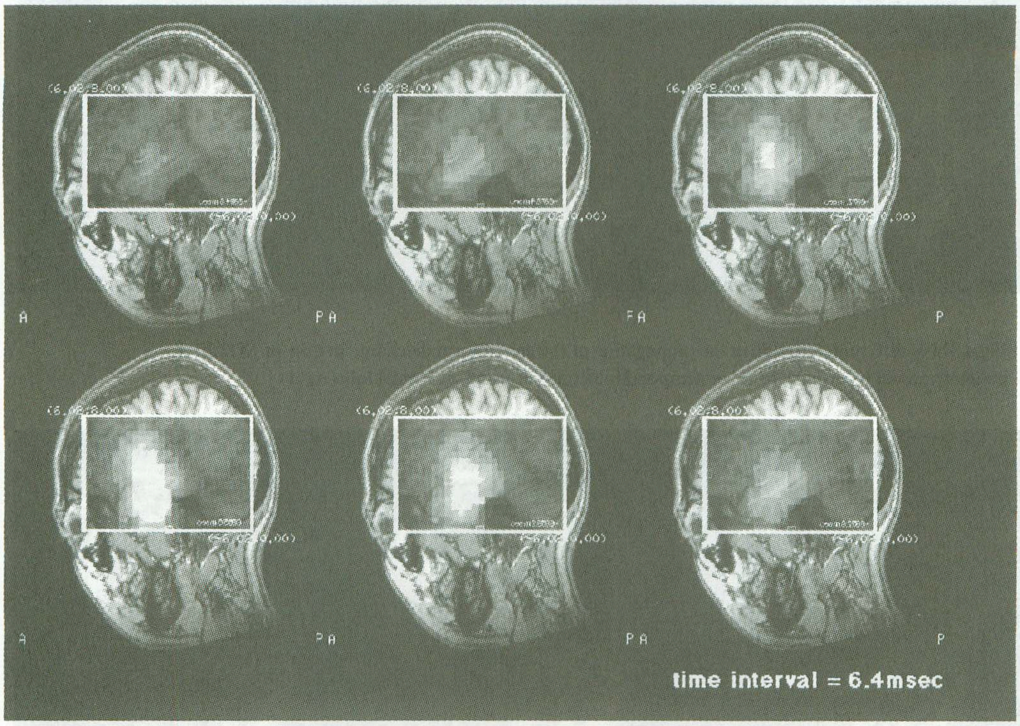

Fig. 2 The propagation of the abnormal activity was shown as the white desity area in about 40msec.

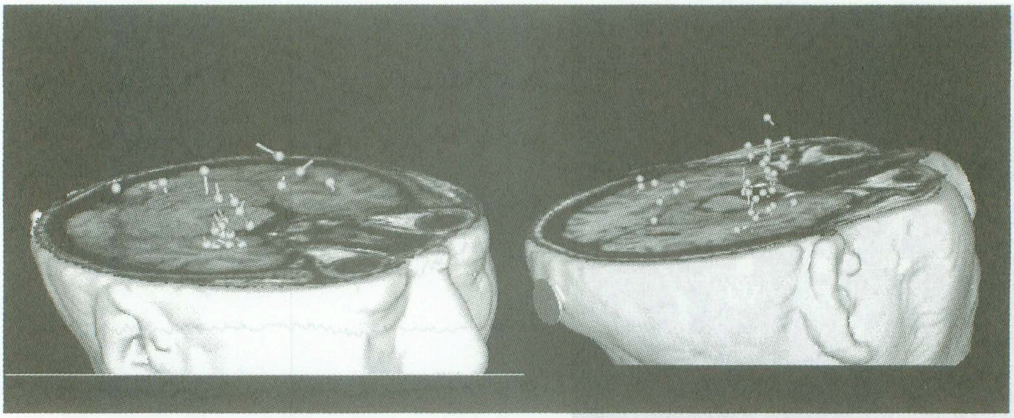

Fig. 3 Distribution of ECDs; ECDs were distributed mainly in the medial temporal lobe in case of MTLE (a) and on the posterior temporal lobe in case of LTLE.

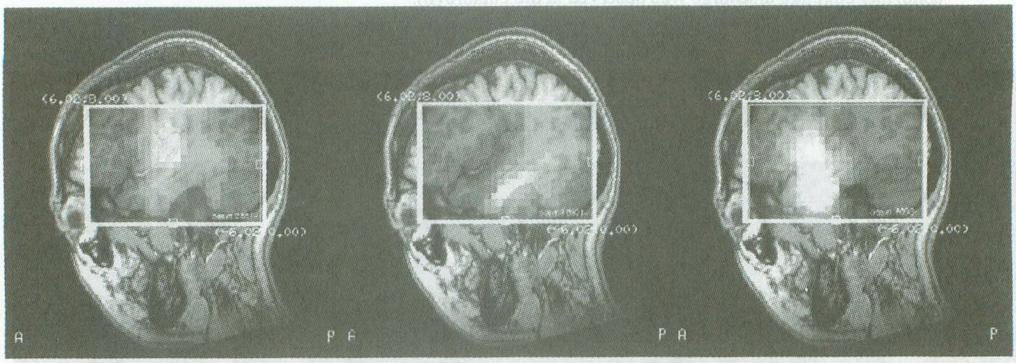

Fig.4 Three different direction in the propagation of the epieptiform discharge in case of MTLE; to parietotemporal lobe (left), to lower temporal lobe (middle), and to frontal lobe(right).

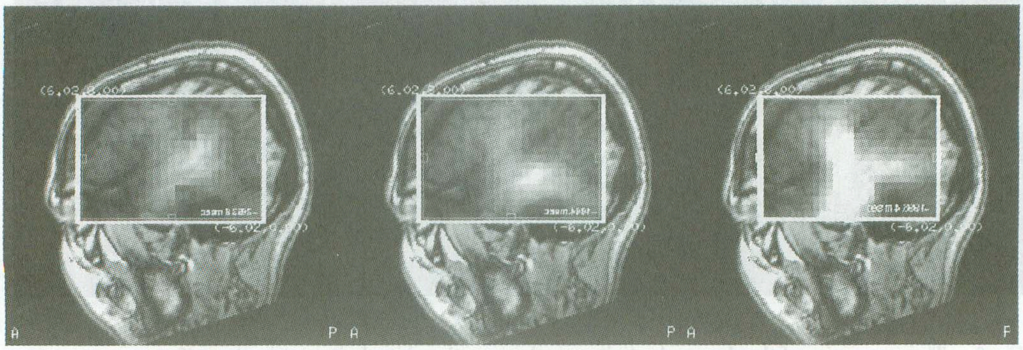

Fig. 5 Three direction in the propagation of the epileptiform discharge in case of LTLE; to posterior temporoparietal lobe (left), to temporal lobe (middle), and to lower posteriotemporal and frontal lobs (right).

temporal, and frontal within about 40 msec (Fig.4). In a patient with right LTLE, 32 abnormal discharges were analyzed. The ECDs were distributed in the posterior temporal lobe (n= 25) and in the occipital lobe (n= 7) (Fig.3b). SAM Movie demonstrated that the activities usually started from the lateral posterior temporal region and spreaded to the posterior temporoparietal lobe, temporal lobe (b), or lower-posteriortemporal and frontal lobes within about 40 msec (Fig.5).

Discussion

The SAM analysis demonstrated not only the origin of interictal epileptiform discharges, but also its propagation to the adjacent structures. The temporospatial profiles of these abnormal electric activity were quite different between MTLE and LTLE patients. These differences seem to be related to explain the different symptomatology and scalp EEG findings in those two types of TLE. The present study suggests that SAM analysis of epileptiform discharges could be a powerful tool to elucidate the complex neuropathophysiology of epileptic patients.

Reference

[1] Taniguchi M, Yoshimine T, Kato A, et al: Dysembryoplastic neuroepithelial tumor in the insular cortex.Three dimensional magnetoencephalographic localization of epileptic discharges. Neurol Res 20: 433-438, 1998

[2] Nakasato N, Levesque MF, Barth DS, et al: Comparisons of MEG, EEG, and ECoG source localization in neocortical partial epilepsy in humans. Electroenceph Clin Neurophysiol 171: 171-178, 1994

[3] Baumgartner C: MEG, EEG and ECoG: discussion. Acta Neurol Scand Suppl. 152: 91-92, 1994

[4] Robinson SE, Rose DF: Current source image estimation by spatially filterd MEG, Hoke M, et al (eds): Biomagnetism: Clinical aspects. Munster: Elsevier science publishers B. V., 1992, pp761-765

[5] Yoshimine T, Kato A, Taniguchi M, et al: Translucence stereoscopy of interictal magnetoencephalographic epileptiform discharge distribution. Neurol Res (in press)

Quick Time^{TM} is a trade mark of Apple Computor Inc..

©1999, Tohoku University Press
Recent Advances in Biomagnetism
T. Yoshimoto et al. (Eds)

Malignant Rolandic-Sylvian Spikes (MRSS) in childhood with refractory epilepsies: Magnetoencephalography, invasive intracranial EEG monitoring and surgical treatment

Hiroshi Otsubo[1*], Ayako Ochi[1*], Irene Elliott[1*], Venita Jay[2*], James T. Rutka[3], Mary-Lou Smith[4], and O. Carter Snead III[1*]
Divisions of Neurology[1], Neuropathology[2], Neurosurgery[3], and Neuropsychology[4].
The Hospital for Sick Children, Bloorview Epilepsy Research Program[*] and
University of Toronto, Toronto, Ontario, Canada

Introduction

Benign Rolandic Epilepsy (BRE), or benign epilepsy of childhood with centrotempoal spikes (BECCT)[1], consists of infrequent nocturnal seizures, normal intelligence, and centrotemporal spikes on EEG. Among BRE, there have been reported patients with atypical seizures, neurological deficits and a variety of centrotemporal spikes [2]. We present six non-lesional patients with intractable epilepsies, frontal-central-temporal spikes and malignant Rolandic-sylvian spikes (MRSS), on EEG and MEG who underwent invasive intracranial EEG (IVEEG) monitoring and surgery.

Methods

The patients were admitted to the epilepsy monitoring unit for up to 5 days. The International 10-20 scalp electrode placement system was used and closely spaced electrodes based on the 10-10 system were placed to cover the suspected epileptic regions. MR images were obtained in a multi sequence sagittal, axial and coronal volume acquisition study with T1-weighted thin slice MR images using 1.5 tesla MRI (Siemens, Germany).

MEG studies were performed at Scripps Clinic and Research Foundation (SCRF) in San Diego, CA, using dual-probe Magnes II (74-channel) or whole-head Magnes 2500 WH (148-channel) biomagnetometer system (Biomagnetic Technologies, Inc., San Diego, CA). The probe positions selected for each patient were selected based on clinical information such as the patient's EEG and VEEG. For most patients, multiple probe recording positions were used to insure full coverage. Concurrent with the magnetic recording, surface EEG was recorded using conventional scalp EEG electrodes and collodion application. (Neurofax 440A, Nihon Kohden, Tokyo, Japan). The simultaneous EEG was used to assist in spike identification and avoid collection and analysis of data contaminated by either artifact or sleep patterns. Patients were generally requested to deprive themselves of 2 hours of sleep the night before the exam. During the study, patients were drowsy and most fell asleep. For uncooperative children, intravenous Propofol was infused during the study. Propofol induces beta activity upon injection, but it subsequently disappears, allowing detection of epileptogenic activity. A physician or technician identified interictal spike in the MEG and EEG recording and triggered the collection of 6 second epochs of data (5 seconds pre-trigger). Prior to analysis, the MEG and EEG waveforms were digitally filtered with a bandpass of 3 to 70 Hz. A single equivalent current dipole model was used to localize the sources of interictal epileptic spikes. The model assumed the head to be a sphere, with the diameter and center location chosen to best fit the actual shape of the region of the head being monitored, as derived from the head digitization data. This equivalent current dipole model used an iterative algorithm to determine the location, orientation, and strength of the current dipole that best accounted for the measured magnetic field pattern. Only those dipoles that accounted for at least 98% of the recorded field pattern, had physiologically realistic current magnitude ($Q < 400$ nAm), and resulted from data for which the root mean square average of the magnetic field detected in all signal channels ($\sqrt{\Sigma B^2}$) was at least 400 femto Tesla, assuring an adequate signal-to-noise ratio, were regarded as a valid application of the model. For patients with a very large number of dipoles so selected, a clustering algorithm was applied to concentrate the data in regions with the most frequent epileptic activity. These constraints on the equivalent current dipole model

©1999, Tohoku University Press
Recent Advances in Biomagnetism
T. Yoshimoto et al. (Eds)

limited the analysis of the very large time series of epileptic activity recorded for each patient to only those brain events that produced fields with a highly focal source.

A multiplanar T1- and T2-weighted MRI set was collected, using a 1.5 T scanner (Signa; General Electric Medical Systems, Milwaukee, WI). Generally, the images were produced as 5-mm slices, skip 1 mm. Three lipid markers were placed at fiducial points on the patient's head during the magnetic resonance recording. The coordinates of the MEG dipoles were then transformed into the MRI frame.

Bilateral subdural strips were used to lateralize seizure onset using 4-electrode contact strips in three patients. Subdural grids with up to 128 contacts were shaped to cover the interictal MEG spike field and functional cortex based on the three dimensional MRI using 1.5 mm thin slice on T1 MR images (ISG viewing wand system, ISG, Mississauga, ON). Split screen and time locked EEG was utilized to review clinical behavior of seizures (System 5000, Nicolet. Madison, WI). EEG data were digitized at a sampling rate of 200 samples / sec / channel. The digitized EEG data were stored by the automatic seizure detection, automatic spike detection and manual event alarm button.

Results

Six children (age 5 - 16 years) presented with frontal, central and temporal spike discharges on prolonged scalp video EEG telemetry. Seizure onset varied between the age of 1 and 9 years. Semiology consisted of generalized epilepsy with preceding sensory aura, arm posturing, facial twitching in two each. Two patients had been diagnosed and treated as BRE because of initially controlled seizures and tangential dipoles over central temporal regions. MRI initially reported normal in all six children at the seizure onset, then subtle cortical dysplasia was delineated 2 years later in one patient. Interictal EEG defined tangential spikes (4). MEG showed interictal spike sources on planum temporale (1), superior sylvian (1), pre-Rolandic (2), and peri-Rolandic fissure (2). In 3 patients, interictal MEG spike sources are depicted on bilateral frontal and temporal regions, therefore bilateral subdural strips were placed. IVEEG was performed in all six patients, revealed ictal spikes around sylvian (2) and Rolandic fissure (4) using subdural grid electrodes. After cortical excision and multiple subpial transection (MST), three children were seizure free, two showed significant improvement and the other one mild improvement follow up period between 3 month and 2 years. Pathological findings were cortical dysplasia in two, cortical tuber and gliosis in one each. Two patients underwent only MST over Rolandic fissure. MEG spike sources corresponded to precise epileptogenic zone in three. One of MEG spike sources in bilateral discharges localized in the epileptogenic zone in the other three.

Discussion

BRE has been well known as age related epilepsy which appeared between age 3- 10 years, and controlled seizure with or without antiepileptic drugs [1]. Interictal EEG showed central and temporal spikes which more accentuated during sleep. Most spike have horizontal dipole sources which consisted of positive discharges on frontal and negative discharges on central or temporal region [2]. Dipole source localization study demonstrated two parts of pre-Rolandic area, inferior and superior parts corresponding to clinical findings of facial and hand motor seizures [3]. Among those patients, atypical BRE were also described in the patients with generalized seizures refractory to medications and inconsistent frontal, central and temporal spikes [2]. In recent more detailed cognitive study, Rolandic spikes were reported not as benign in terms of neuropsychological, intellectual, and behavioral findings compared to age matched controls [4]. Children with right-sided BRE showed cognitive disturbance, compared to children with left-sided BRE as well as the control subjects [5]. Central-temporal spikes are therefore considered as epiphenomena of cerebral dysfunction in a wide range of clinical and electroencephalographic expressions [6].

Cortical dysplasia has been reported often locating around the Rolandic cortex and causing intractable seizures in children [7, 8]. In three of our six children with initial MRI reported as normal, pathology from surgical tissue proved cortical dysplasia, as some lesions in focal cortical dysplasia have been reported not diagnosed on MRI [8]. In cases with central-temporal spikes, the seizures becoming refractory to antiepileptic drugs and cognitive deterioration noticed for years, MRSS would be considered. They need further evaluation of MRI, PET and the prolonged video EEG telemetry to capture seizure manifestation, ictal and interictal EEG abnormalities. The patients in whom interictal MEG spike sources localize around Rolandic and sylvian fissures, concordant to clinical and the other non-invasive studies, surgical treatment would be recommended for seizure control.

MSI combined with image-guided frameless stereotaxical approach has been reported to allow surgical treatment around motor strip in adult cases with the lesion [9, 10]. Complete resection or possible cessation of epileptogenic zone is a most important goal of epilepsy surgery. At this time, in the patients with MRSS, interictal MEG spike sources and sensory motor evoked response guide preplanning of subdural grid placement, to localize epileptogenic zone and functional mapping for maximum resection and improvement of seizure control.

Conclusion

Patients with MRSS should be considered for epilepsy surgery. Compared to BRE, MRSS represents intractable seizures originated from epileptogenic zone over the Rolandic and sylvian fissures, and is surgically treatable. Surgery of possible cortical excision and MST requires IVEEG to delineate functional cortex and epileptogenic zone to control seizures. MEG is a very valuable diagnostic method to localize MEG spike field and functional cortex for MRSS to remove maximum epileptogenic zone, furthermore with combination of frameless stereotaxic guided surgery may reduce that need for invasive studies in the certain patients with this MRSS.

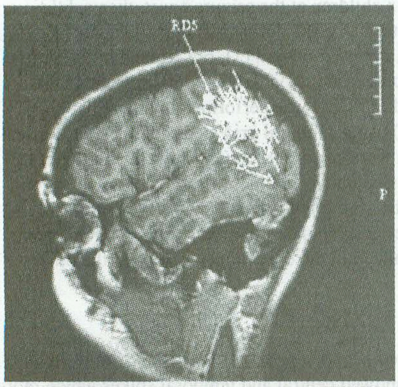

Fig. 1, A thirteen year old right handed girl initially presented with infrequent seizures consisting of right hand simple partial motor seizures with Todd's paresis since age of 2 years. After age of 12 years, frequent nocturnal seizures of both arms extensions and vocalization, with secondary generalization appeared and became refractory to multiple medications. MRI was reported as normal until 13 year old when subtle cortical dysplasia was noticed on the left parietal region. MSI showed clusters of spike sources (open triangle) on the left central parietal region, and somatosensory stimulation response (closed square) of little finger (RD5) in front of the spike fields.

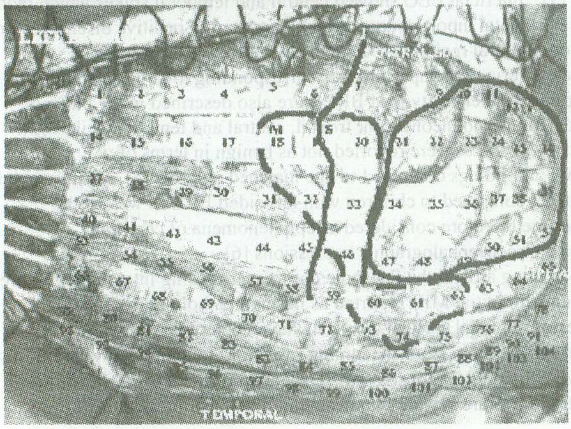

Fig. 2, Intraoperative view showed area of cortical excision over the epileptogenic zone (circle) behind the central sulcus (curved line), and MST (dotted circle) over the ictal symptomatogenic zone. These areas were confirmed using intracranial invasive video monitoring using 104 channel subdural grid electrodes implanted 3 days to capture 15 seizures. The epileptogenic zone and somatosensory mapping were concordant to the MSI spike sources and somatosensory stimulation responses (Fig 1). The patient has been seizure free for three month after the surgery.

References

[1] Gibbs EL and Gibbs FA: Good prognosis of mid-temporal epilepsy. Epilepsia 1: 448-453, 1959

[2] Gregory DL and Wong PKH: Clinical relevance of a dipole field in rolandic spikes. Epilepsia 33(1): 36-44, 1992

[3] Legarda S, Jayakar P, Duchowny M, et al: Benign rolandic epilepsy: high central and low central subgroups. Epilepsia 35(6): 1125-1129, 1994

[4] Weglage J, Demsky A, Pietsch M, et al: Neuropsychological, intellectual, and behavioral findings in patients with centrotemporal spikes with and without seizures. Dev Med Child Neurol 39(10): 646-651, 1997

[5] Piccirilli M, D'Alessandro P, Sciarma T, et al: Attention problems in epilepsy: possible significance of the epileptogenic focus. Epilepsia 35(5): 1091-1096, 1994

[6] de WA and Arts WF: Significance of centro-temporal spikes on the EEG. Acta Neurol Scand 87(6): 429-433, 1993

[7] Otsubo H, Steinlin M, Hwang PA, et al: Positive epileptiform discharges in children with neuronal migration disorders. Pediatr Neurol 16(1): 23-31, 1997

[8] Palmini A, Gambardella A, Andermann F, et al: Operative strategies for patients with cortical dysplastic lesions and intractable epilepsy. Epilepsia 35 Suppl 6: S57-S71, 1994

[9] Ganslandt O, Steinmeier R, Kober H, et al: Magnetic source imaging combined with image-guided frameless stereotaxy: a new method in surgery around the motor strip. Neurosurgery 41(3): 621-628, 1997

[10] Rezai AR, Hund M, Kronberg E, et al: The interactive use of magnetoencephalography in stereotactic image-guided neurosurgery. Neurosurgery 39(1): 92-102, 1996

Measurement and Quantification of Interictal and Postictal DC Magnetic Field Shifts in Unilateral Temporal Lobe Epilepsy

Saligram U.[1,2], Burdette DE.[1], Barkley GL.[1] Moran JE.[1], Tepley N.[1,2]

[1]*Department of Neurology, Henry Ford Hospital, Detroit, Michigan, U.S.A.;*
[2]*Department of Physics, Oakland University, Rochester, Michigan, U.S.A.*

Introduction

Unilateral low frequency activity in the region of the ictal onset is commonly found in patients with focal seizures arising from the temporal lobe (temporal lobe epilepsy or TLE) and may be best observed in the postictal period [1,2]. We hypothesized that magnetic field shifts should be present in TLE patients, particularly when DC recordings are used, and might provide information that could be used to support the diagnosis of epilepsy. Traditional DC magnetic field recordings are very time consuming, making it difficult to obtain DC-MEG data free of artifacts due to the subject becoming restless and changes in the state of awareness of the subject. Hence, there is a need for techniques which can be used to record DC field changes quickly. One such technique which we developed is presented here. Nine control subjects were studied on three consecutive days and 9 subjects with unilateral TLE were studied between (interictal MEG) and within 24 hours (postictal MEG) of a seizure. In each session, 7 channel DC-MEG recordings were obtained from both temporal lobes. We hypothesized that the post-ictal to interictal difference in the DC field shifts occuring in the epileptic temporal lobe of TLE patients would be greater than the difference for the "normal" temporal lobe and also greater than the day-to-day changes in DC field shifts occurring in control subjects. This hypothesis was based on the fact that epileptic brain tissue exhibits large depolarizations and hyperactivity during seizure and these in turn would change ionic concentrations leading to changes in DC potentials. These studies were aimed at determining whether this technique can be used to accurately detect the DC field changes due to seizure activity and to determine if the DC field changes occurring in TLE patients are different from the day-to-day changes occurring in control subjects.

Methods

Nine control subjects and 9 TLE subjects were used in this study. DC-MEG recordings were performed on these subjects using a seven channel BTi 607 neuromagnetometer in a shielded room. The technique used for these recordings consisted of raising and lowering the subject with respect to the probe. Polystyrene head holders were custom made for each subject and these were used as positioning devices. Fig. 1 is a schematic representation of the head holder. The head holder was placed on a non-magnetic platform in the shielded room. The position of the head holder on the platform was kept the same in all the runs for each subject. This was done by placing the head holder on a wooden base with wooden pins on the bottom. The wooden base was placed on a non-magnetic base plate with holes in it for the pins. This set up helped to position the subject in the same position in each run. The neuromagnetometer probe and the non-magnetic platform were also set in the same position with respect to the room and each subject in each run. Fig. 2 shows the experimental setup. The subject was degaussed using a video tape eraser and the subject's head was wet with water and sprayed with Anti-static spray (STATX brand, manufactured by RTW Int. Corp). The subject was asked to lie on the non-magnetic platform with head in the head holder.

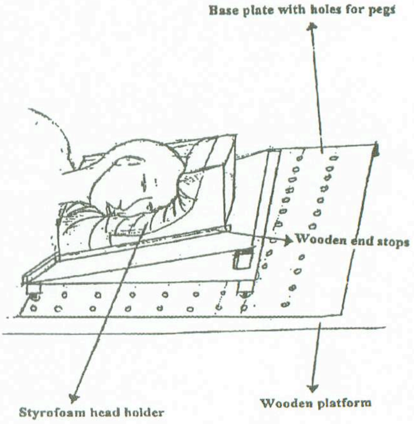

Fig.1. Schematic representation of polystyrene headholder

The platform was then raised until the probe was close to the head without touching it. This raising operation was done using a brass crank. The distance of the head from the probe was noted and this was designated the 'up' position. The subject was then lowered using an air driven piston, which moved the subject's head a distance of 2.5 cm from the probe. This position was noted and designated the 'down position. The above procedure of fixing the 'up' and 'down' position was done for each

©1999, Tohoku University Press
Recent Advances in Biomagnetism
T. Yoshimoto et al. (Eds)

subject during the first run. The 'up' and 'down' positions were kept the same for every run for each subject. Once the 'up' and 'down' positions were fixed the raising and lowering operations were performed by the air-driven piston during the subsequent runs.

The orientation of the neuromagnetometer probe over the subject's head was such that the center channel (channel 1) was directly over the T3 or T4 position, depending on the temporal lobe being studied. A total of 120 seconds of DC-MEG data was collected during each run, this was done as follows, with the subject in the 'down' position 12 seconds of DC data were collected, then the platform was raised to the 'up' position and 12 seconds of data were collected in this position, and 5 such epochs of 12 seconds were collected in each position. The entire procedure described above was repeated on three consecutive days for each control subject and on two different days for TLE subjects. The time points for the TLE measurements were interictally and within 24 hours of a seizure. Both temporal lobes were studied for subjects from both groups (control and TLE).

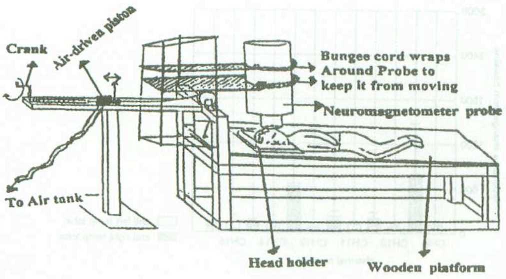

Fig.2. Experimental setup showing non-magnetic platform head holder, apparatus to lock probe in position, crank, air driven piston and probe.

Data Analysis

All DC-MEG data were analyzed using HP 694A multiprogrammer. Data were sampled at 130 Hz and the high and low pass filters were set at 0 and 50 Hz respectively. The DC magnetic field shift for each run, for each temporal lobe, for each subject was calculated by taking the difference between the DC-MEG data collected in the 'up' and the 'down' positions. The five differences thus calculated for each run for each temporal lobe were averaged to get a value DC shift for each channel. These average values per channel were in turn averaged to get a DC shift value for the temporal lobe. These values were further subjected to the following comparisons:

- The difference between the interictally and post-ictally measured DC magnetic field shift was expressed as a percentage of the field shift measured interictally (baseline). For control subjects the difference between field shift measured on day 1 and day 3 was expressed as a percentage of day 1 (baseline) measurement.
- The difference between the DC field shifts measured interictally and post-ictally in TLE patients from the epileptic temporal lobe and the difference measured from the normal temporal lobe was expressed as a ratio with the larger difference being the denominator. The difference between DC field shifts measured on day 1 and day 3 in control subjects from left temporal lobe and the difference measured from the right temporal lobe was expressed as a ratio. Thirty six different ratios were calculated for control subjects. This was done by taking the left temporal lobe difference as the denominator in seven subjects and right temporal lobe difference as the denominator in two subjects. This was done because in the TLE subject group seven subjects had left temporal lobe focus and 2 had right temporal lobe focus. Each of the 36 ratios was compared to the average TLE ratio.
- The magnitude of the DC field shift calculated interictally and post-ictally in TLE subjects from both temporal lobes was compared to measurements from control subjects.
- Comparison of the AC activity from the 2 subject groups were made by comparing the power in 5 frequency bands (1-4 Hz, 4-8 Hz, 8-12 Hz, 12-19 Hz, 19-30 Hz).

Results

- The percentage change from the baseline in the DC magnetic field shift in TLE subjects was higher on the epileptic temporal lobe than on the normal temporal lobe (See Fig. 3a). It was also higher than the change measured in controls. Both these differences were statistically significant (Wilcoxon test)
- The percentage change from baseline (day 1) in the DC magnetic field shift in control subjects was higher in the right temporal lobe; however, this difference was not statistically significant (See Fig. 3b).
- The ratio of the interictal and postictal DC field shift differences measured from the normal temporal lobe and that from the epileptic temporal lobe in TLE subject was less than 1 (See Table 1).
- The ratio of the day 1 and day 3 DC field shift difference measured in controls from one temporal lobe and the difference measured from the other temporal lobe was greater than 1 (See Table 1).

- **The magnitude of the DC field shifts measured in TLE subjects did not differ from those measured in control subjects (See Table 2).**
- **The comparison of the power in the five frequency bands shows that the power in the 1-4 Hz band postictally in TLE subjects on the epileptic side is higher than the postictal 1-4 Hz power on the normal side (See Fig. 4a).**
- **The comparison of the power in control subjects in the five frequency bands measured from one temporal lobe did not differ from that measured from the other temporal lobe (See Fig. 4b).**

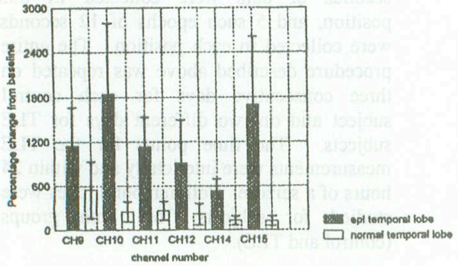

Fig. 3a. The percentage change from baseline in TLE subjects. Epileptic temporal lobe compared to normal lobe.

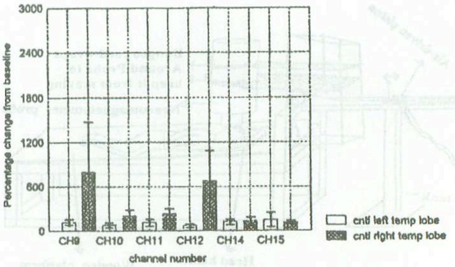

Fig. 3b. Percentage change from baseline in control subjects, right temporal lobe compared to left lobe

Descriptive Statistics for the Ratio in TLE subjects and Range of Ratios for the Control Subjects

Statistics	TLE subjects	Range for Controls
Mean	0.518	1.046-2.756
Std Dev	0.364	1.034-2.438
Median	0.593	0.759-1.944
Min	0.023	0.141-0.759
Max	0.994	3.362-7.068

Table 1. Comparison of the ratios of day-to-day difference in DC shift for one temporal lobe and the difference for the other lobe. TLE ratios compared to control ratios. TLE ratios are all less than 1 and do not lie within the range of ratios for control subjects.

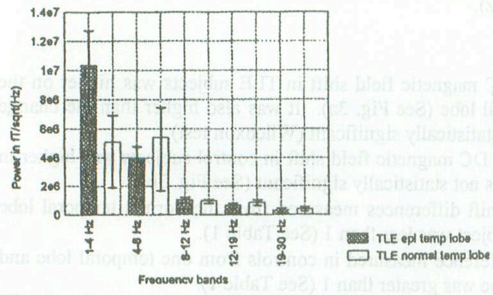

Fig. 4a. Comparison of the epileptic temporal lobe and normal temporal lobe, interictal to post-ictal difference in power in the five bands.

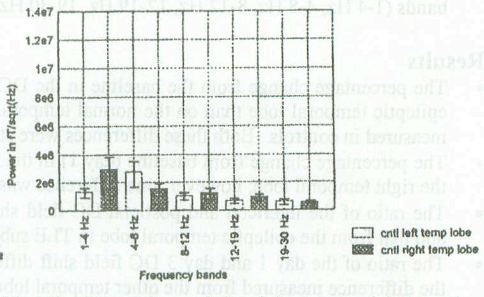

Fig. 4b. Comparison of the right temporal lobe and left temporal lobe, day 1 to day 3 difference in power in the five bands.

Epileptic Lobe DC shift amplitude (in fTesla)—post-ictal of TLE subjects vs

DC shift amplitude from day3 of Control subjects

Descriptive statistics	TLE subjects epileptic Lobe	Control Left Lobe	Control Right Lobe	Control Average
N	9	9	9	9
Mean	4066.8	812.5	1437.3	1124.9
Std Dev	5600.3	402.9	1298.7	692.7
Median	1667.2	712.3	1078.7	973.8
Range	348.2-17010.1	250.3-1528.0	179.1-3689.4	214.7-2234.0
p- value for TLE Vs control		0.0521	0.2893	0.1853

Table 2. Comparison of magnitude of DC field shift in Control subjects and TLE subjects.

Discussion

This pilot study shows that focal DC magnetic field shifts occur as a result of focal seizures and the technique developed here can be used to measure these field changes. If these findings are confirmed by further studies using large array magnetometers, this technique may have a clinical utility in the assessment of patients following presumed epileptic seizures. The day-to-day variability in the DC field shift measurement in control subjects was found to be larger than was expected based on previous data [3]. This variability in control subjects was larger on the right temporal lobe. The reason for this has yet to be determined. The DC field shift changes signs from one day to the next in measurements from both subject groups, though this sign change was seen more often in TLE subjects, mainly on the epileptic temporal lobe. Since, these sign changes occur in control subjects, it may be due to dynamic changes in neurophysiology which may in some way be amplified in TLE subjects.

References

[1] Kaibara M, and Blume WT: The postictal electroencephalogram. Electroencephalography and clinical Neurophysiology 70: 99-104, 1988.

[2] Ikeda A, Terada K, et al: Subdural Recording of Ictal DC Shifts in Neocortical Seizures in Humans. Epilepsia 37: 662-674, 1996.

[3] Saligram U, Moran JE, and Tepley N: DC-MEG Studies: Development of Techniques for Resolving DC fields. Advances in Biomagnetism Biomag96, Springer Verlag, New York. (in press)

Acknowledgments

This research supported by NIH/NINDS grant RO1-NS30914.

Magnetoencephalography of a Patient with Pure Photosensitive Epilepsy

Takahashi T[1], Hatanaka K[2], Kanno A[3], Nakasato N[4], Yoshimoto T[4]

Yaotome Clinic[1], Sendai, Japan; ELEKTA KK[2], Tokyo, Japan; Ryogo Center[3], Kohnan Hospital, Sendai, Japan; Department of Neurosurgery[4], Tohoku University School of Medicine, Sendai, Japan

Objective

We sought to better understand magnetoencephalography (MEG) changes in response to red flicker and flickering geometric pattern stimuli in a pure photosensitive epilepsy patient [1] whose photoparoxysmal response (PPR) was elicited by those stimuli.

Patient

A 16-year-old male pure photosensitive epilepsy patient had suffered a total of three generalized tonic clonic seizures since age13 [2]. The first seizure was induced by an electronic screen game; the second by television images; the third by electronic screen game images. Repeated electroencephalography (EEG) examinations using low luminance visual stimuli always showed positive findings: 18 Hz 20 c/m^2 red flicker and 18 Hz flickering 2 c/deg black and white geometric pattern (dot pattern and grating) to 25°×25°visual field [2,3] elicited generalized PPR (Fig. 1).

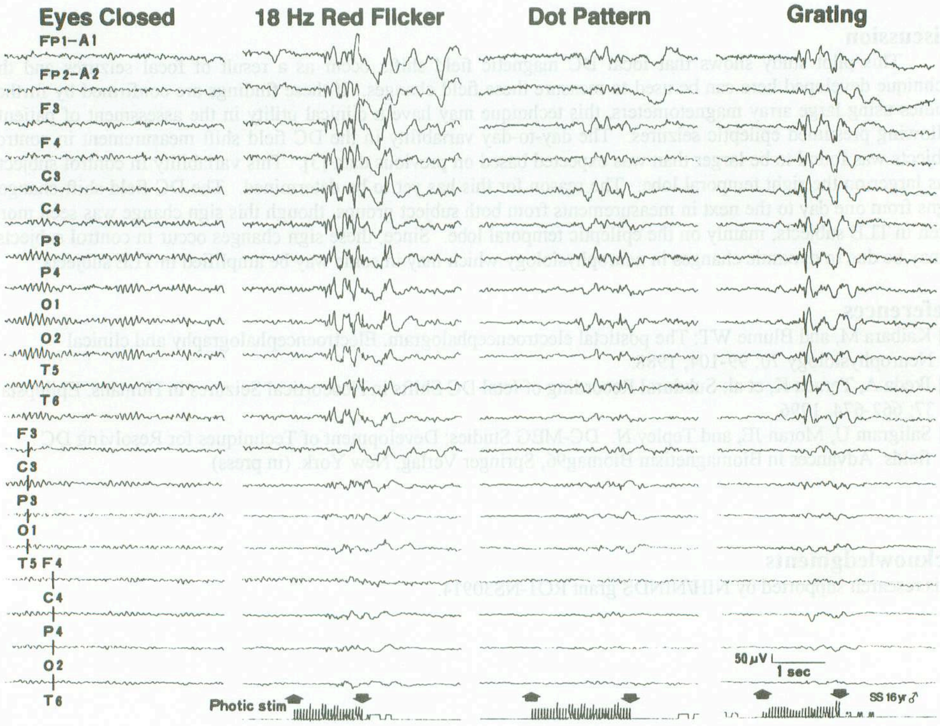

Fig. 1 Generalized PPR elicited by visual stimuli

©1999, Tohoku University Press
Recent Advances in Biomagnetism
T. Yoshimoto et al. (Eds)

MEG findings and Conclusions

Triphsic wave responses (N75-P100-N145) were shown by visual evoked magnetic field (VEF) using 2 Hz green-black checkerboard pattern reversal stimulation; VEF souces were located at the bottom of the calcarine fissure. Visual stimuli elicited no PPR; they only elicited photic driving response.

Fig.2 (a)-(b) illustrates MEG recordings over occipital areas in response to 18 Hz red flicker (a) and flickering dot pattern (b) stimuli. Lower tracing in each shows MEG power having strong peaks in the range of 9-11 Hz and small peaks in the range of 17-19 Hz. These findings indicate that the main photic driving response consists of 9-11 Hz subharmonic responses.

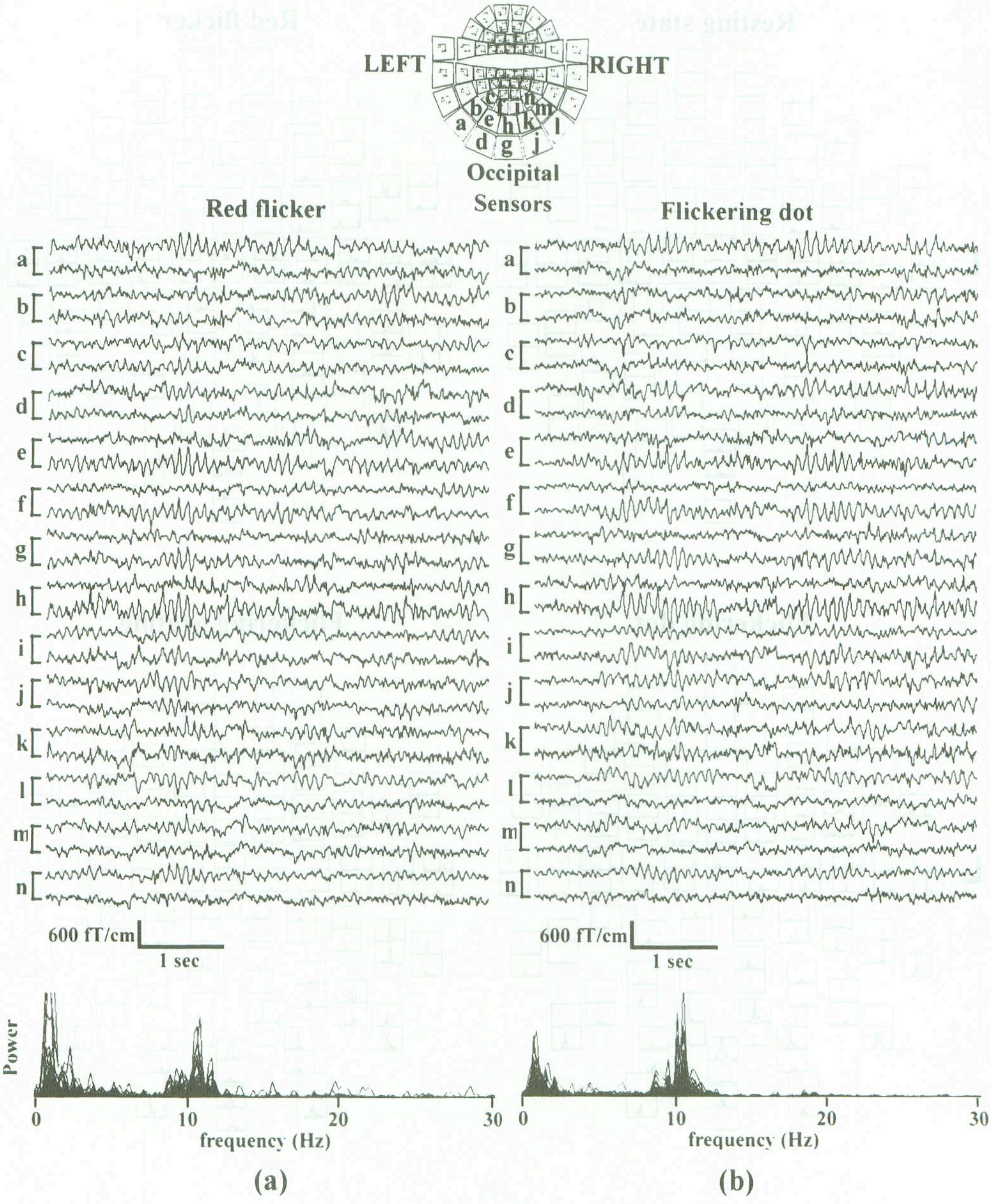

Fig. 2 MEG recordings over occipital areas and power spectrum over whole head in response to (a) 18 Hz red flicker and (b) flickering dot pattern stimuli. a~n indicate sensor position shown in the schematic head.

Fig. 3 illustrates topographic MEG power spectrum maps of resting state (upper left tracing) and those in response to red flicker (upper right tracing), flickering dot pattern (lower left tracing) and flickering grating pattern (lower right tracing) stimuli in the 5-15 Hz frequency range. All MEG powers reflecting subharmonic photic driving response were greatest over the mid-occipital areas (tracings of upper right, lower left and lower right); a red flicker stimulation elicited bitemporal responses (upper right tracing), whereas flickering geometric pattern stimuli induced subharmonic photic driving response, skewed to left temporal area (lower tracings).

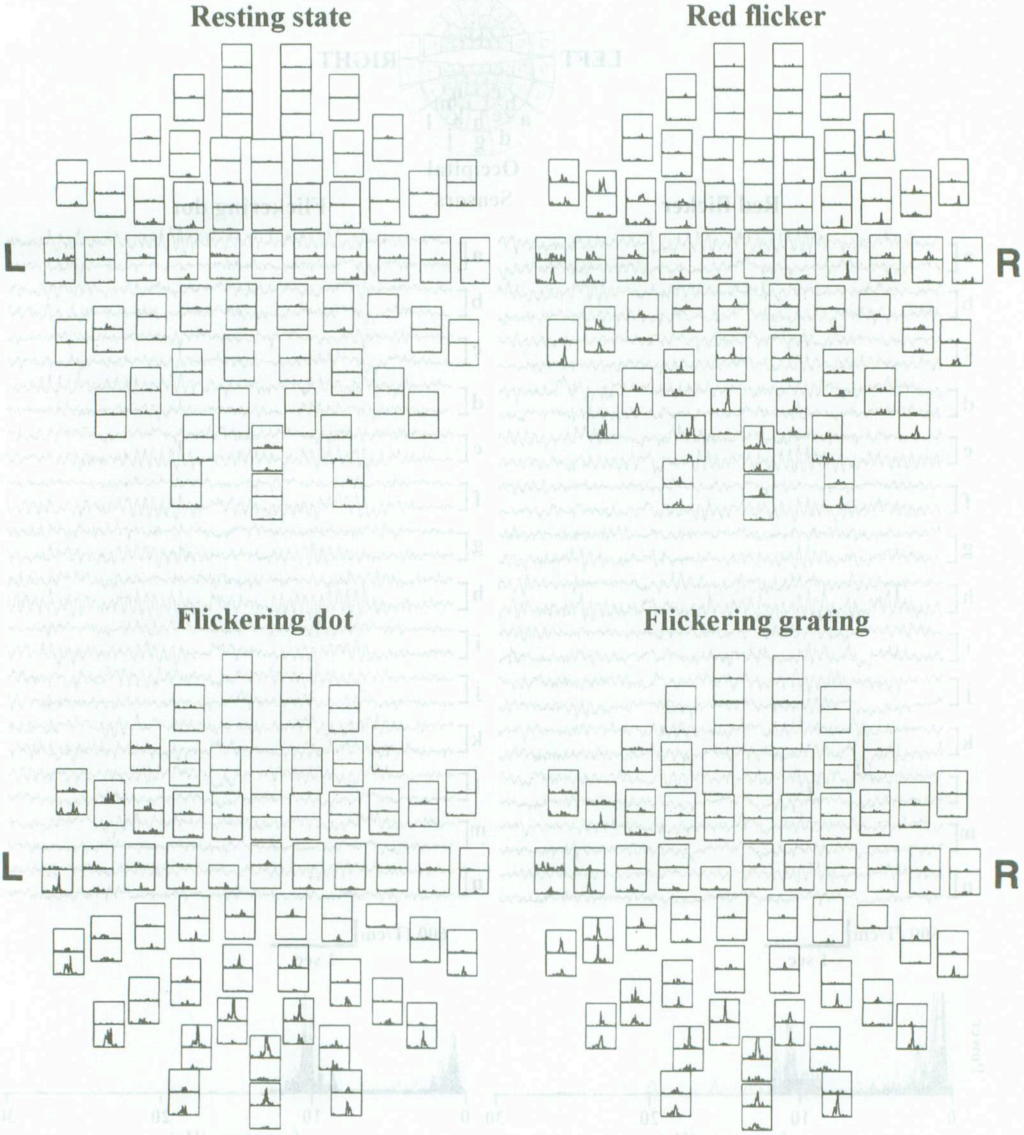

Fig. 3 Topographic MEG power spectrum maps of resting state (upper left) and those in response to visual stimuli (upper right, lower left and lower right). Frequency range: 5-15 Hz.

The above visual stimuli probably failed to induce PPR due to luminance reduction in MEG settings. Those, however, mainly elicited subharmonic photic driving response. Topographic MEG maps revealed that subharmonic photic driving response elicited by visual stimuli are different: 1. Some are elicited by a red flicker stimulus distributed symmetrically over the posterior and temporal areas. 2. Some are elicited by flickering geometric pattern stimuli also distributed over the posterior and temporal areas but with predominance over the left temporal area.

This study may suggest that neural networks for processing red flicker and flickering geometric pattern stimuli are different. Detailed studies including PPR analysis by MEG recording may provide further information.

References

[1] Binnie CD, Jeavons PM: Photosensitive epilepsies, Roger J, Bureau M, Dravet C, et al (eds): Epileptic Syndromes in Infancy, Childhood and Adolescence. London: John Libbey, 1992, pp 299-305

[2] Takahashi T: Activation methods, Niedermeyer E, Lopes da Silva F (eds): Electroencephalography: Basic Principles, Clinical Applications and Related Fields, 4th Edition. Baltimore: Williams & Wilkins, 1998, in press.

[3] Takahashi T, Tsukahara Y: Photoparoxysmal response elicited by flickering dot pattern stimulation and its optimal spatial frequency of provocation. Electroenceph clin Neurophysiol 106: 40-43, 1998

Magnetoencephalography of a Patient with Temporal Lobe Epilepsy Associated with Visual and Auditory Auras

Takahashi T[1], Hatanaka K[2], Kanno A[3], Nakasato N[4], Fujiwara S[3], Yoshimoto T[4]

Yaotome Clinic[1], Sendai, Japan; ELEKTA KK[2], Tokyo, Japan; Ryogo Center[3], Kohnan Hospital, Sendai, Japan; Department of Neurosurgery[4], Tohoku University School of Medicine, Sendai, Japan

Objective

To elucidate the precise focal cerebral disturbance from which partial seizures (visual and auditory auras) arise, we performed a magnetoencephalography (MEG) study of a temporal lobe epilepsy patient.

Patient

A 50-year-old female with temporal lobe epilepsy had suffered recurrent complex partial seizures since 17 years of age. She had an incident of head trauma at age 11 years. The first seizure manifested as visual and auditory auras; a flash appeared in her left upper visual field, followed by the sensation of diminished sound. At the age of 22 years, she lost consciousness and had a generalized tonic seizure following a visual aura (a flash and an effigy in her left visual field). Electroencephalography (EEG) showed focal paroxysmal discharges over the right temporal area. Since then she has had complex partial seizures several times per year.

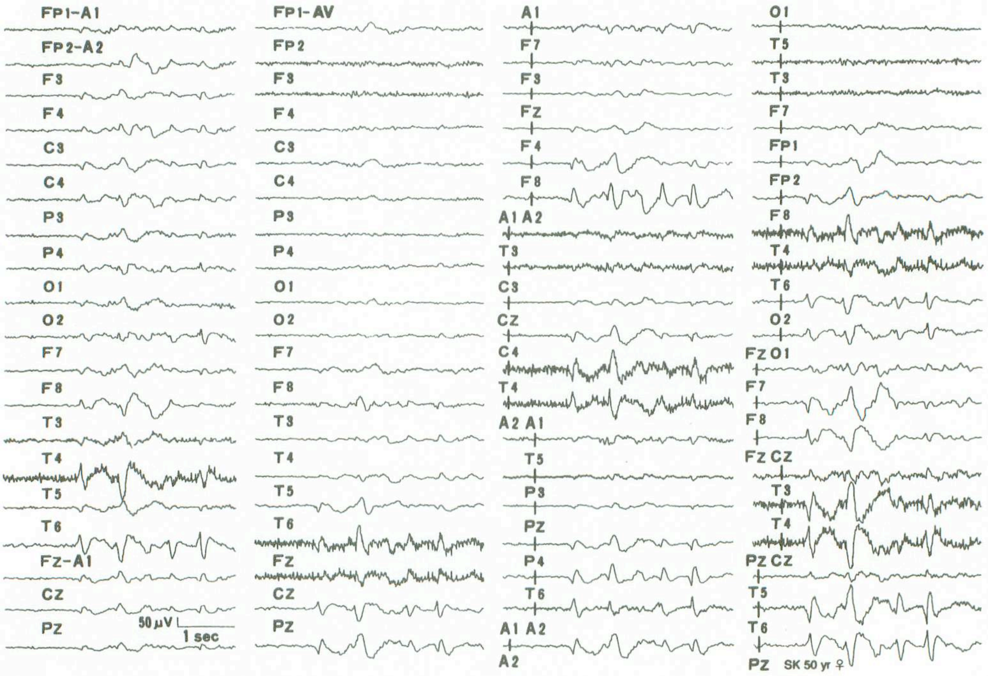

Fig. 1 EEGs recorded by different derivation montages.

©1999, Tohoku University Press
Recent Advances in Biomagnetism
T. Yoshimoto et al. (Eds)

On physical examination, she gave timid responses to questions and easily developed tachycardia, suggesting that she also had disturbance of the autonomic nervous system. Neurological examination found no particular abnormalities except for a slight finger tremor.

Fig. 1 illustrates EEG findings; the same EEG recorded by different derivation montages showed that paroxysmal discharges were maximal over the right posterior temporal (T6) to the right mid-temporal (T4) areas. Fig. 2 shows photic driving response (PDR) elicited by a 20 cd/m^2 5 Hz 0.5 c/deg dot pattern stimulation by use of strobo-filter method [1]; 5 Hz fundamental PDR over the occipital areas (see the right tracing) was skewed to the right side (see the right tracing).

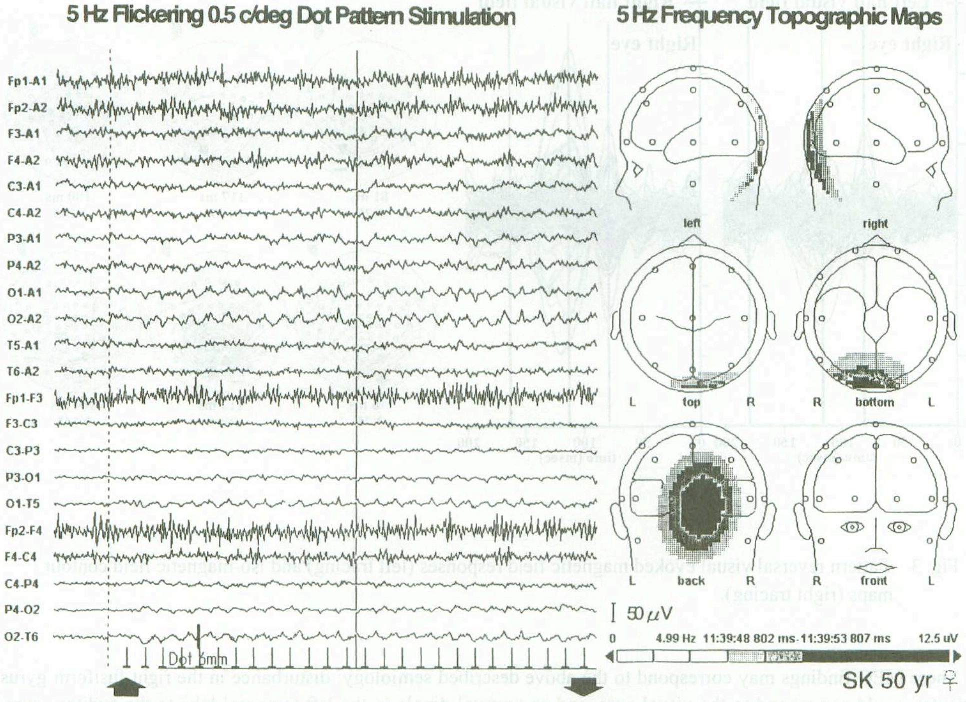

Fig. 2 EEG changes in response to 5 Hz flickering dot pattern stimulation (left tracing) and topographic maps of 5 Hz fundamental photic driving response (right tracing).

MEG findings and Conclusions

Fig. 3 demonstrates MEG findings obtained by using 2 Hz green-black checkerboard pattern reversal stimulation; MEG changes in response to a left-half visual field stimulation to each eye were smaller than those to the right-half, particularly with regard to N145. This finding indicates disturbance in the right visual cortex, particularly in the fusiform gyrus where the N145 component was supposed to go through [2]. As shown in Fig. 4 a, MEG study also revealed two unusual dipole patterns in the right fusiform gyrus and in the left temporal lobe (see Fig 4-b).

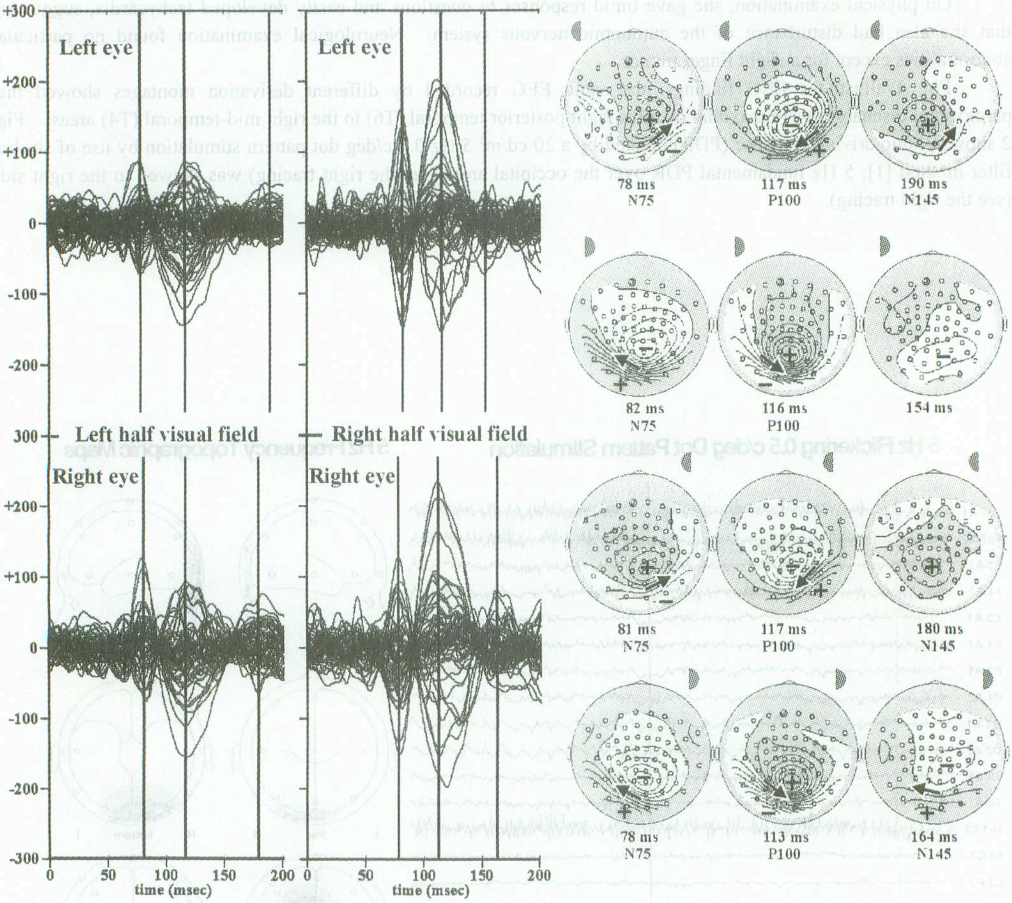

Fig. 3 Pattern reversal visual evoked magnetic field responses (left tracing) and iso-magnetic field contour maps (right tracing).

These MEG findings may correspond to the above described semiology: disturbance in the right fusiform gyrus in particular would correspond to the visual aura, and an unusual dipole in the left temporal lobe to the auditory aura. MEG is clinically very useful to elucidate correlative details of semiology of partial seizures and focal cerebral disturbance.

References

[1] Takahashi T, Tsukahara Y: Photoparoxysmal response elicited by flickering dot pattern stimulation and its optimal spatial frequency of provocation. Electroenceph clin Neurophysiol 106: 40-43, 1998

[2] Hatanaka K, Nakasato N, Kanno A, et al: Integration function of the primary visual cortex revealed by neuromagnetic analysis, Hashimoto I, Kakigi R (eds): Recent Advances in Human Neurophysiology: The 6th International Evoked Potentials Symposium in Okazaki. Amsterdam: Elsevier, 1998, in press

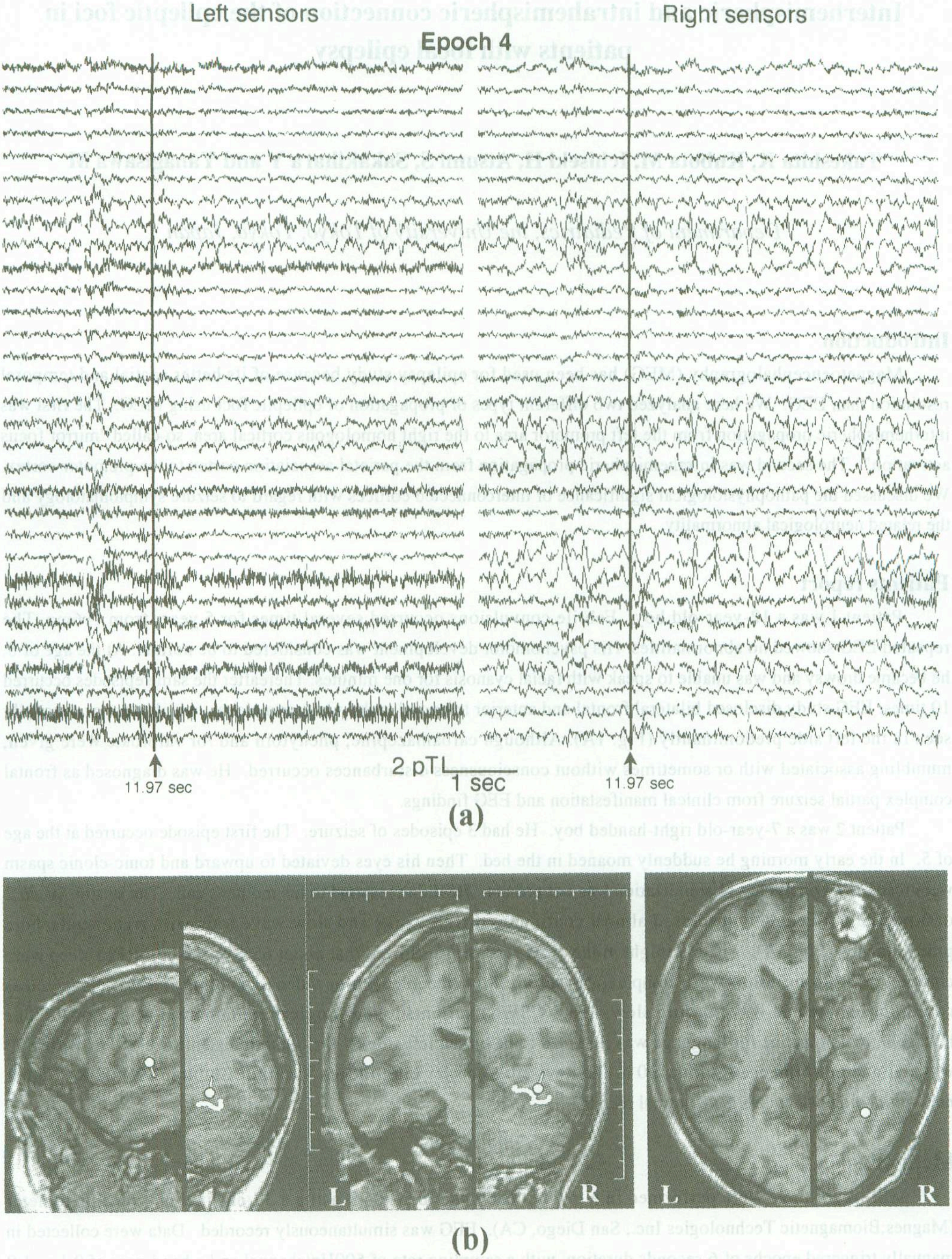

Fig. 4 (a) MEG recording on resting state; (b) dipole source localizations with MEG at the latency shown in (a). White lines indicate the fusiform gyrus.

Interhemispheric and intrahemispheric connection of the epileptic foci in patients with focal epilepsy

Takeshita K, Kubota M, Ichiseki H, Atsumi S, Sakakihara Y and Yanagisawa M

Department of Pediatrics, the University of Tokyo, Tokyo, Japan

Introduction

Magnetoencephalography (MEG) has been used for epilepsy study because of its better spatial and temporal resolution than EEG. We here analyzed two different types of propagation of epileptic foci using MEG. The first was interhemispheric propagation from the left premotor area to the right homologous cortical area, so-called "mirror focus activation". The second was intrahemispheric propagation from the parietal association cortex to the premotor cortex. We discussed the pathophysiological significance of interconnected cortices with regard to seizure symptomatology and the related neurological abnormality.

Patients report

Patient 1 was a 12-year-old boy. Febrile convulsions occurred several times for 5 years from 1y6mo. The repeated EEG showed no abnormalities. His psychomotor development was considered to be normal. At the age of 8, he became drowsy and was unable to speak with facial cyanosis for one minutes. Thereafter the same episodes occurred 10 times. EEG study disclosed bilateral frontal and anterior temporal spike-wave complexes, which were occasionally seen in the left side predominantly (Fig. 1A). Although carbamazepine, phenytoin and /or valproate were given, mumbling associated with or sometimes without consciousness disturbances occurred. He was diagnosed as frontal complex partial seizure from clinical manifestation and EEG findings.

Patient 2 was a 7-year-old right-handed boy. He had 3 episodes of seizure. The first episode occurred at the age of 5. In the early morning he suddenly moaned in the bed. Then his eyes deviated to upward and tonic-clonic spasm were recognized on the leg. Lateralization was not present. He didn't respond to his mother's call. The seizure lasted 2 or 3 minutes. EEG study disclosed almost continuous diffuse spike and slow wave train with right hemisphere predominancy (Fig. 3A). The overnight video-EEG recordings showed that about 65% of the non-REM sleep were consisted of spike and aslow wave complex. No seizures were recorded during video monitoring. He was diagnosed as continuous spike and wave during slow sleep (CSWS) variants. Neurological examination was normal. The hemispheric dominance for language was assumed to be on the left side by the dichotic listening test. His verbal IQ was 141 and performance IQ was 130 in the Revised Wechsler Intelligence Scale for Children (WISC-R). Other neuropsychological studies gave normal results.

Methods

MEG recordings were performed in a magnetically shielded room using a 37-channel neuromagnetometer (Magnes;Biomagnetic Technologies Inc., San Diego, CA). EEG was simultaneously recorded. Data were collected in manually triggered epochs of 6 seconds duration, with a sampling rate of 500Hz/channel and a band-pass of 0.1 or 1.0 Hz to 200Hz. After acquisition, the data were digitally filtered at 1.0 to 100Hz. To evaluate the whole head activity, several consecutive measurements from several locations were required, especially in Patient 2. When sensor was not covered 2 different epileptic foci, the peak latency was estimated with overlapping MEG waves based on a spike with the same configulation in simultaneously recorded EEG.

Somatosensory evoked magnetic fields (SEFs) were also measured with the same system to detect the primary sensoy cortex for landmark. The calculated equivalent current dipoles (ECDs) of spike foci and the N20m component

©1999, Tohoku University Press
Recent Advances in Biomagnetism
T. Yoshimoto et al. (Eds)

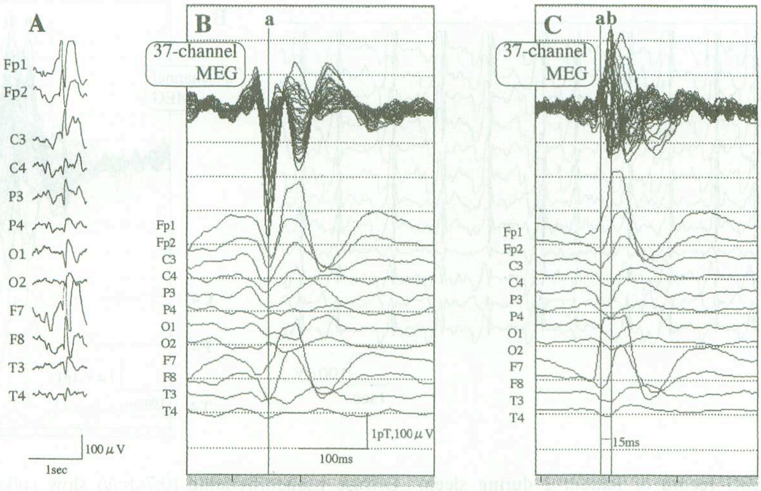

Fig. 1 A: EEG record of Patient 1 at rest. Electrodes are arranged according to the International 10/20 system, taking references at ipsilateral unlinked ear lobes. B: The 37 channel-MEG records on the left frontal lobe and EEG records of a representative spike. All MEG records are placed on the same line. C: The 37 channel-MEG records on the right frontal lobe and EEG records of the spike. The vertical lines show MEG peaks of left frontal cortex (a) and right frontal cortex (b).

of the SEF were superimposed on the patient's MRI, then the three-dimensional relationship between the location of the dipole of spikes and the SEF components was analyzed.

Results

In Patient 1, EEG showed frontal and anterior temporal spike-wave complexes. Almost all the spikes were recognized on both hemisphere, whereas some spikes were recognized only on the left hemisphere (Fig. 1A). The former made two different dipoles in bilateral frontal cortex in the MEG study. In superimposed imaging, the both were on the homologous area in the premotor cortex (Fig. 2). The large phase reversal activity in the right was appeared about 15ms later than the left one (Fig. 1B, C).

In Patient 2, spike and slow waves were distributed diffusely with the right predominancy (Fig. 3A). The MEG measurement on the right hemisphere detected two phase reversal peaks in each spike and wave complex formation (Fig. 3B). The time lag between the two peaks was 28.34ms (n=25). The ECDs of the two peaks were localized in the

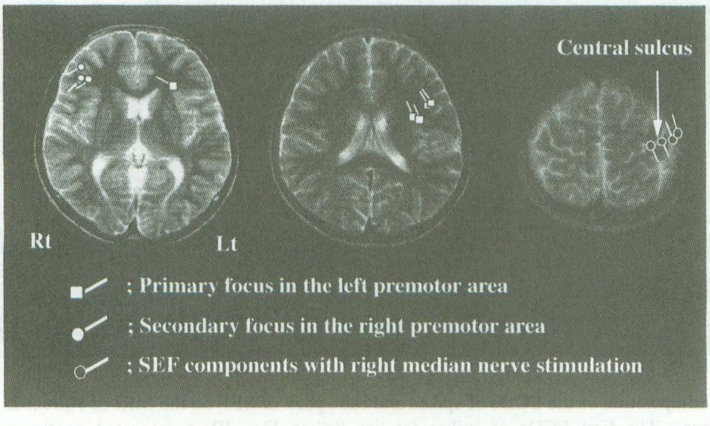
Central sulcus
Rt
Lt
; Primary focus in the left premotor area
; Secondary focus in the right premotor area
; SEF components with right median nerve stimulation

Fig. 2: Superimposition of the ECDs of spikes and each peak of SEF on the MRI of Patient 1. In the dipole plots, circles (squares) and bars indicate the dipole position and orientation, respectively.

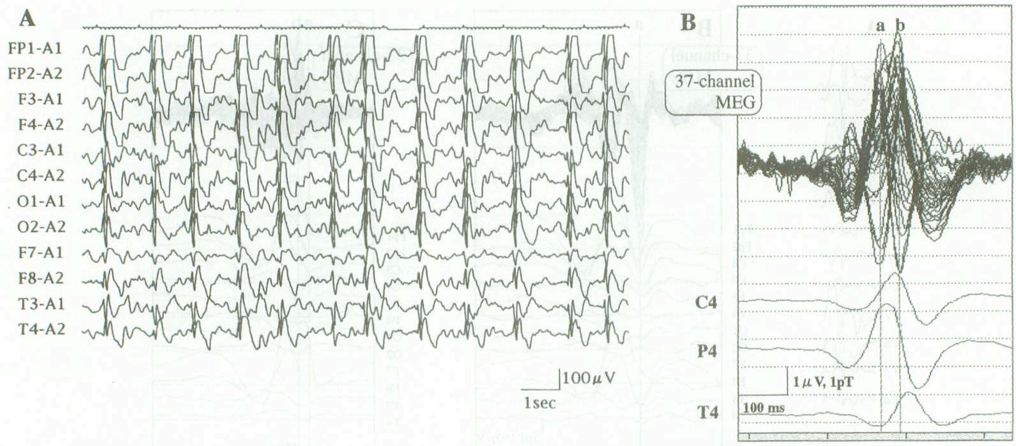

Fig. 3 A: EEG record of Patient 2 during sleep. Diffuse pseudorhythmic (0.7-1c/s) slow spike and wave complexes train are recognized. B: The 37 channel-MEG records on the right frontal-parietal lobe and EEG records of a representative spike. The vertical lines show two different MEG peaks.

right angular gyrus and the premotor cortex independently (Fig. 4). On the MEG measurement of the left hemisphere, spiky magnetic changes were recognized, but no reliable ECD were calculated.

Discussion

There have been no previous reports on the analysis of epileptic double foci using MEG except for Hari et al's paper [1], in which they showed interhemispheric parietal mirror focus using whole head type neuromagnetometer. We analyzed interhemispheric and intrahemispheric propagation of epileptic foci with a 37-channel neuromagnetometer. Because it covered only two thirds of the hemisphere, several measurements were required for the analysis of the whole head.

In Patient 1, spike discharges were recognized in the bilateral frontal lobe with left predominance. On MEG study, phase reversal peak occurred in the right frontal cortex which was delayed for about 15ms than that in the left frontal lobe when superimposed on a spike and wave complex with the same configulation in EEG. In this phenomenon, two independent cortical epileptic foci appeared in each hemisphere. The time differences were consistent with the transcallosal conduction time, which have already been reported [1, 2]. Each ECD superimposed on

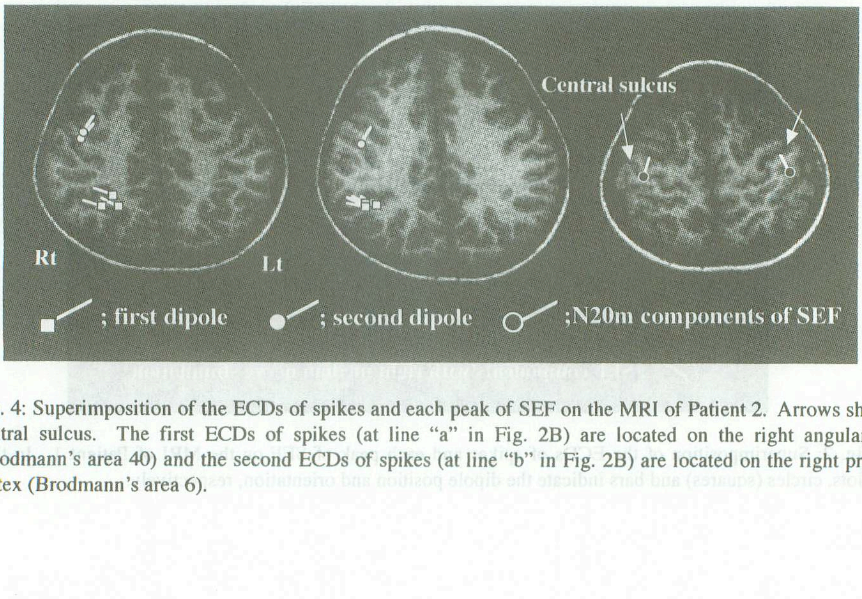

Fig. 4: Superimposition of the ECDs of spikes and each peak of SEF on the MRI of Patient 2. Arrows show the central sulcus. The first ECDs of spikes (at line "a" in Fig. 2B) are located on the right angular gyrus (Brodmann's area 40) and the second ECDs of spikes (at line "b" in Fig. 2B) are located on the right premotor cortex (Brodmann's area 6).

patient's MRI was distributed to premotor area just close to the oro-facial division of the primary motor area. We interpreted the transcallosal connection of the both premotor areas might be attributable to the enhanced physiological circuit rather than an abnormal projection. The premotor area is connected to the primary motor area and is also projected directory to the oro-facial motor neuron of the brainstem. We speculated that seizures in Patient 1 might be related to these connections.

The EEG of Patient 2 showed continuous diffuse spike and wave burst during sleep. The EEG's characteristics was considered to be a variant of epilepsy with electrical status epilepticus during slow sleep (ESES) or CSWS. MEG analysis of Patient 2 showed two remote current sources corresponded to single spike and wave complex of EEG. Each ECD were located on the right angular gyrus (Brodmann's area 40) and the right premotor area (Brodmann's area 6), respectively. Patients with CSWS are known to suffer from deterioration of cognitive function or behavioral disturbance with EEG abnormalities. Studies of CSWS with PET or SPECT showed regional metabolic abnormalities predominantly in the association cortex including the frontal, temporal or parietal regions [3, 4]. Secondary propagation was proposed as an important element for its pathophysiology [2, 5]. This patient had no mental deficits or behavioral problems like patients with CSWS or Landau-Kleffner syndrome. The absence of mental deterioration in our patient may be explained by non-involvement of the language-related cortex.

Time difference analysis between two dipoles represented 28.3ms on average. This was longer than that seen in Patient 1. Monkey data indicated that inferior premotor area had close connection with the rostral part of the inferior parietal lobule with both afferent and efferent projections [6]. Neurons in these area integrate motor signals with sensory signals to execute accurate reaching movement [7]. Two ECDs of Patient 2 may exist on the parietofrontal circuit and reflect the reinforced physiological connection of the two regions. The reason for the tight connection of the two remote regions remains to be clarified.

References

[1] Hari R, Antti A, Nina F, et al: Parietal epileptic mirror focus detected with a whole-head neuromagnetometer. Neuroreport 5: 45-48, 1993

[2] Kobayashi K, Nishibayashi N, Ohtsuka Y, et al: Epilepsy with electrical status epilepticus during slow sleep and secondary bilateral synchrony. Epilepsia 35(5): 1097-1103, 1994

[3] Maquet P, Hirsch E, Metz-Lutz MN, et al: Regional cerebral glucose metabolism in children with deterioration of one or more cognitive functions and continuous spike-and-wave discharges during sleep. Brain 118: 1497-1520, 1995

[4] Gaggero R, Caputo M, Fiorio P,et al: SPECT and epilepsy with continuous spike waves during slow-wave sleep. Childs Nerv Syst 11(3): 154-160, 1995

[5] Morrell F, Whisler WW, Smith MC,et al: Landau-Kleffner syndrome. Treatment with subpial intracortical transection. Brain 118: 1529-1546, 1995

[6] Matelli M, Camarda R, Glickstein M, et al: Afferent and efferent projections of the inferior area 6 in the macaque monkey. J Comp Neurol 251(3): 281-298, 1986

[7] Taira M: Neural mechanisms for visual controls of hand movement. Advances in neurological sciences (Japanese) 42(1): 86-97, 1998

Acknowledgments

We wish to thank Dr. A. Uno for neuropsychological examinations and Dr. M. Yumoto for his valuable help.

Magnetoencephalographic Study in Patients with Bilateral Focal Polymicrogyria

Tanaka M, Yamada K, Watanabe Y, Matsuda K, Inoue Y, Fujiwara T, Yagi K
National Epilepsy Center Shizuoka Higashi Hospital, Shizuoka City, Japan

Introduction

The advent of magnetic resonance imaging has allowed the recognition of neuronal migration disorders during life. Graff-Radford (1) described a set of identical twins whose MRI showed bilateral cortical dysplasia in the region of the sylvian fissure and failure of the opercular formation, and called it developmental Foix-Chavany-Marie syndrome. Kuzniecky, Barkovich, and Guerrini also described the patients having as the same cortical dysplasia in neuroimagings as Graff-Radford described (2). Later histological studies have verified that these cortical dysplasia observed in MRI were polymicrogyria. Most of these patients have either partial or generalized epilepsy in addition to pseudobulbar palsy and mental retardation of different severity. However, the question as to whether this type of cortical abnormality has epileptogenicity or not remains open. Magnetoencephalography(MEG) has the advantage of being influenced less by different conductivities in various brain tissues than electric fields and needless of reference. Multichannel recording system of MEG offers us single spike analysis and more accurate estimation. Its reliability for identifying epileptigenic location was verified by some institutions including our hospital (3,4). The dipole analysis of the epileptiform dischrges in EEG and/or MEG is expected to reveal the relationships between some brain lesions and their epileptogenicity. The aim of this study is to examine whether this type of structural lesion has epileptogenicity, using MEG combined with source modeling as a noninvasive ancillary method in addition to electroclinical analysis.

Methods

Three female patients and one male patient having bilateral focal cortical abnormalities in both perisylvian and perirolandic cortex observed in MRI were included in this study. All these patietns were treated for their epilepsy at our hospital, National Epilepsy Center, Shizuoka Higashi Hospital, at the time of this study. Age, sex, age at onset of epilepsy, results of neurological examination, full scale intelligence quotients, clinical seizure manifestation, and frequency of seizure were studied from their clinical records. All patients underwent EEG repetitively using the International 10-20 System of scalp electrode placement. In three patients (1, 2, 4), habitual seizures were recorded by the simultaneous video-EEG monitoring system. In patient 2, both ictal and interictal rCBF SPECT studies were performed, using a ring-type SPECT scanner, which provides 31 tomographic images simultaneously. In ictal SPECT, 222MBq of ^{123}I-IMP was injected soon after clinical seizure was observed and data acquisition was initiated 30minutes after injection. In the interictal SPECT, the same dose of ^{123}I-IMP was injected 24 hours after the last seizure and data acquisition was initiated in the same way.

Magnetoencephalography(MEG) was recorded in all patients using the Magnes system and Magnes II which has two sets of 37-channel SQUIDs (3.4). To ensure whole brain sampling, at least three overlapping sensor positions were recorded over each hemisphere. MEG was sampled in epoch modes which included some epileptiform discharges. A single equivalent-current dipole model was applied to the whole spike duration and best fitting dipole model in each spike was used as the dipole of its spike. These calculations were performed with Biomagnetic Technologies commercial software.

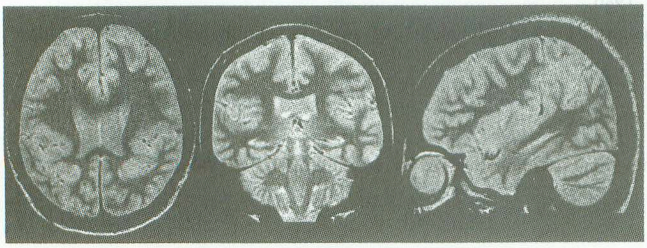

Fig.1 Proton density MRI of patient 1. Cortical thickening was observed in bilateral perisylvian, perirolandic, and insular regions.

Dipoles were accepted if all the following criteria were met (1) coefficient of 0.98 was achieved, (2) the dipole fit latency corresponded to an EEG or MEG event with a spike or sharp wave morphology, and (3) the current moment was rational. Calculated equivalent current dipoles were overlaid on individual MRI imaging.

©1999, Tohoku University Press
Recent Advances in Biomagnetism
T. Yoshimoto et al. (Eds)

Results

All patients had the same cortical abnormalities in MRI as shown in Fig. 1. These corticies showed irregular inner surfaces with increased interdigitaton between white and gray matter, suggesting polymicrogyria. Clinical features of patients are shown in table 1. All patients were born between healthy and unrelated parents. Age at the onset of epilepsy was from 8 and 20 years. There are no neurological traits except that patient 2 had an epileptic paternal uncle and an elder sister having had seizures associated with fever. No one had particular causative disorders in their histories. Two patients had neurological abnormalities which were considered to be pseudobulbar palsy. All patients except for patient 2 had severe mental retardation. Their seizures were resistant to various antiepileptic drugs. Three (patients 1, 2, and 3) had somatosensory manifestation in the initial phase of their seizures. In interictal EEG two of them (patients 1 and 3) had focal interictal discharges, one (patient 2) had multifocal interictal discharges, and one (patient 4) had generalized interictal discharges.

Patient No.	Age(yr) /Sex	Age at Onset of Epilepsy (yr)	Neurological Examination	I.Q.	Clinical Seizure Manifestation/ Frequency of Seizure	I.I.Ds.
1	31/F	18	No Abnormalities	66	Automatism with shaking of the arms occasionally preceded by the feeling as if her right arm had disappeared /Weekly	Spikes at T3T5
2	32/F	11	No Abnormalities	90	Flexion of the head and the chest rightward followed by salivation and at times jerks of jaw. She feels numbness in her hands before she lost consciousness/Weekly	Spike or spike activities at C3P3, T4T6, and T3T5 independently
3	26/M	20	Dysarthria, Dysphagia	27	Conscious head turning to the right followed by impairment of consciousness. He felt abnormal sensation in his left hand/Weekly	Spike activities at T4T6
4	34/F	8	Dysphagia	43	Slow or rapid forward dropping of the head and the upper trunk with loss of consciousness, Short duration of unresponsiveness/Daily	Bilateral synchronous, symmetrical and diffuse spike and wave or fast activities

Table 1 Clinical features of 4 patients

Abbreviations: I.Q.; intellectual quotient, I. I. Ds.; interictal discharges

Ictal EEG in patient 1 low voltage rhythmic fast activities appeared in the left hemisphere before her clinical seizure. In SPECT, there was an interictal hypoperfusion in left parietal lobe which changed to ictal hyperperfurion (Fig. 2). We considered this patient to have an epileptogenic zone in the left parietal lobe. Patient 2 had two types of ictal discharges. In one complex partial seizure, ictal discharges appeared at C4 and T4 (Fig. 3, Left), and in the other simple partial seizure, ictal discharges appeared at F3, C3, and P3 (Fig. 3, Right). It is considered that this patient has bilateral independent foci. In patient 3, ictal EEG was not recorded. He complained of sensory aura and his head turned to the ipsilateral side to that of IIDs. It is likely that he has parietal lobe epilepsy, although the side of epileptogenic zone remained uncertain. In patient 4, a short duration of unresponsiveness accompanied by bilateral synchronous and symmetrical spike with slow activities in the EEG (Fig. 4, Left) and tonic seizure were recorded (Fig. 4, Right). Final diagnosis of epilepsy on the basis of electroclinical analysis, and dipole localization using single equivalent-current dipole mode are shown in Fig.5.

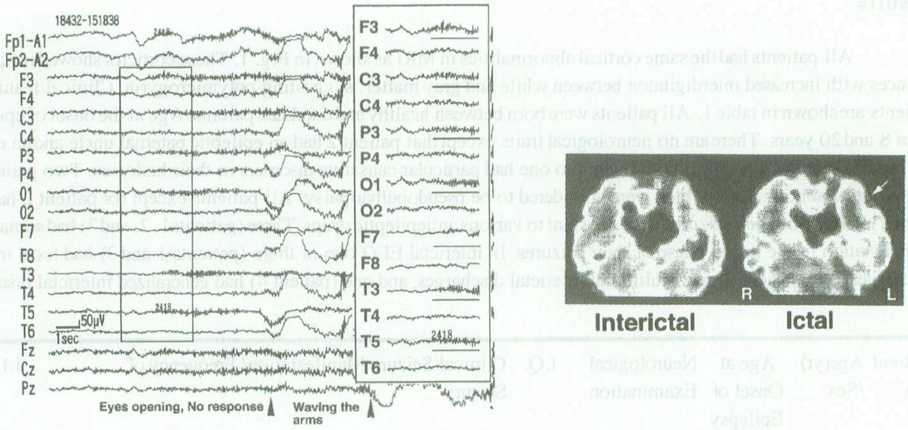

Fig. 2 Ictal EEG and interictal and ictal SPECT of patient 1

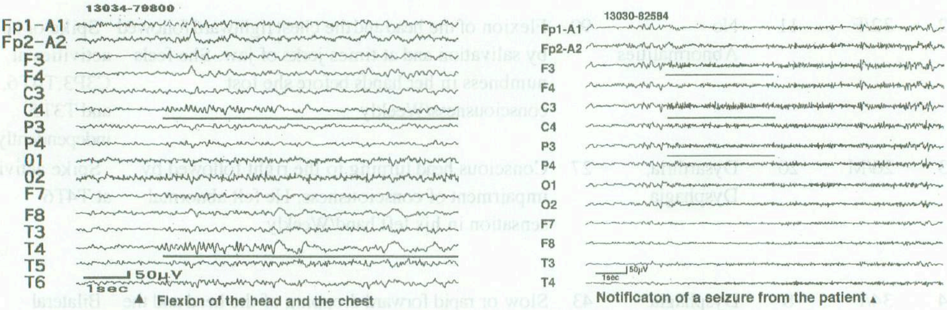
13034-79800
13030-82584
Fp1-A1
Fp2-A2
F3
F4
C3
C4
P3
P4
O1
O2
F7
F8
T3
T4
T5
T6
50μV
1sec
Flexion of the head and the chest
Notificaton of a seizure from the patient

Fig. 3 Ictal EEG of patient 2: Two types of ictal discharges were recorded.

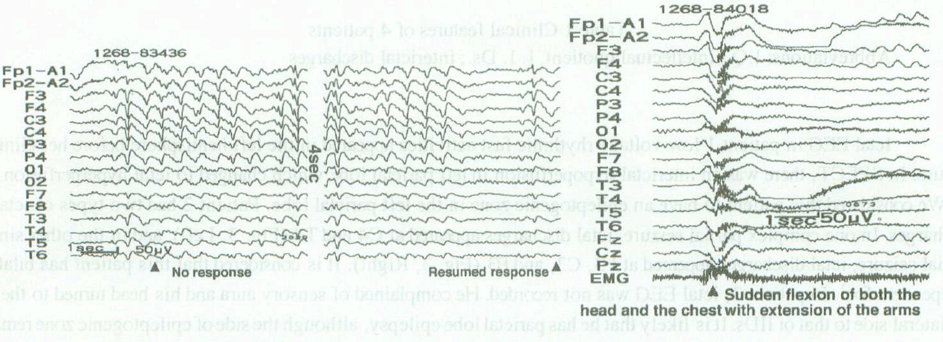

Fig. 4 Ictal EEG of patient 4. Left shows absence seizure and right tonic seizure.

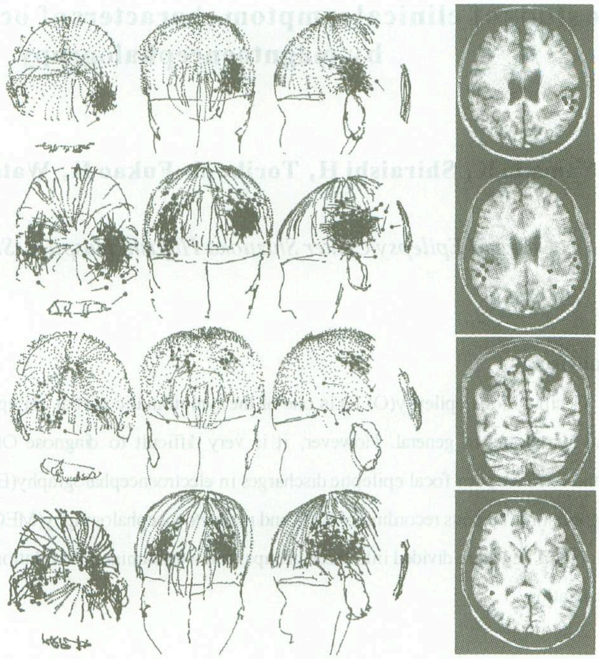

Patient 1:

Parietal lobe epilepsy,

Focus side is left.

Patient 2:

Parietal lobe epilepsy,

Bilateral independent foci.

Patient 3:

Parietal lobe epilepsy,

Focus side is unknown.

Patient 4:

Symptomatic generalized

epilepsy.

Fig. 5 Final diagnosis of epilepsy and dipole localization of 4 patients

In patient 1, most of the dipoles were clustered in and around the abnormal cortex of the left parietal lobe which is supposed to be epileptogenic electroclinically. In patients 2 and 3, most of them were clustered in and around the abnormal corticies bilaterally. In patient 4, dipoles scattered in both hemispheres, although some dipoles were clustered in and around the abnormal corticies.

Discussion

Recent MEG study of epilepsy has shown that the clustering of MEG spike dipoles represent rather reliable epileptogenic zones (3,4). In this study, we examined in four patients with bilateral focal cortical abnormalities in perislvian and perirolandic regions in MRI to determine whether this type of cortical abnormaly has epileptogenicity or not by the use of MEG. In three patients having seizure manifestations in the parietal lobe, MEG spike dipoles overlaid on MRI were clustered in and around the abnormal corticies in the temporo-parietal region. In the remaining one patient having generalized seizures, the MEG spike dipoles scattered diffusely in both hemispheres. Our results indicate that abnormal corticies showing polymicrogyria in MRI may be epileptogenic in patients having partial epilepsy. However, the relationship between the polymicrogyria and mechanism of generalized epilepsy remains uncertain.

The electroclinical manifestations and localization of dipoles of MEG in patients with bilateral focal cortical abnormalities differed. We therefore consider that each patient may have different epileptogenesis and epileptogenic zones relating to the bilateral focal cortical abnormalities suggesting polymicrogyria.

Reference

[1] Graff-Radford N, Bosch E., Stears J, et al: Developmental Foix-Chavany-Marie syndrome in identical twins. Ann Neurol 20: 632-635, 1986

[2]Kuzniecky R, Andermann F, Guerrini R: The epileptic spectrum in the congenital bilateral perisylvian syndrome. Neurology: 44;379-385, 1994

[3]Knowlton R, Laxer K, Aminoff M: Magnetoencephalography in Partial Epilepsy: Clinical Yield and Localization Accuracy. Ann Neurol 1997;42:622-631

[4]Watanabe Y, Fukao K, Watanabe M: Epileptic event observed by multichannel MEG, Visualization of Information Processing in the Human Brain. Elsevier, 383-392, 1996

The study of clinical symptom characters of occipital lobe epilepsy by magntoencephalograpy

Yamada K, Shiraishi H, Toribe Y, Fukao K, Watanabe Y, Yagi K

National Epilepsy Center Shizuoka Higashi Hospital, Shizuoka, Japan

Introduction

Occipital lobe epilepsy(OLE) is one of the symptomatic partial epilepsies(SPE), and is associated with ictal visual symptoms in general. However, it is very difficult to diagnose OLE when clinical symptoms are complex and there are poor focal epileptic discharges in electroencephalography(EEG). We studied 10 patients who had undergone simultaneous recording of EEG and magnetoencephalography(MEG), and whose dipoles localized in occipital lobes. They were divided into three groups, and we examined the relation between clinical symptoms and dipole localization.

Methods

We selected some patients of OLE at random who had undergone simultaneous recording of EEG and MEG at Shizuoka Higashi Hospital(National Epilepsy Center, Shizuoka Japan). MEGs were recorded using the 37-channel Magnes system and Magnes II, which have a pair of 37-channel SQUIDs(superconducting quantum interference devices). MEGs were sampled in epoch modes, and collected manually to capture epileptiform discharges whenever they were seen on the real-time EEG. A single equivalent-current dipole(ECD) model was used to estimate the location of the dipole source. An analysis was performed on selected data segments containing MEG-spikes. Calculation of the ECD location that best fit the measured magnetic fields was performed with Biomagnetic Technologies commercial software. Dipole fits were accepted if the following two criteria were met, (1) coefficient of 0.98 was achieved and (2) current moment must be between 100 and 350nAm. Ten patients were then selected who had well clustered ECD ; more than 10 dipoles clustered within a 3cm cube.

Results

1. The types of dipole localization These patients were divided into three groups according to location of dipoles: (1) the mesial type: dipoles were localized on the interhemispheric midline containing calcarine fissure, where the primary visual field is mainly located, (2) the lateral type: dipoles clustered in other area in occipital lobes, and (3) mixed type. There were 6 patients of the mesial type, 3 of the lateral type, and one patient of the mixed type. A classified list is showed in Table 1, and typical cases of each type are presented in Fig.1.

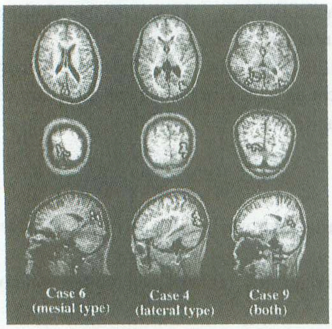

Fig. 1 MEG dipole localization

©1999, Tohoku University Press
Recent Advances in Biomagnetism
T. Yoshimoto et al. (Eds)

2. Diagnosis Eight of the patients had abnormal lesions in the occipital lobes, which was confirmed by magnetic resonance imaging(MRI), and in 6 of these patients, lateralities of lesions were in agreement with the side of the dipole localization, but the remaining 2 patients had bilateral dipole cluster. Except in one patients, lateralities of EEG findings were in agreement with dipoles localization. In two patients, lateralities of EEG findings were disagreement with lesions. One patient had a lesion in the left occipital lobe, but EEG showed bilateral diffuse spike and slow wave burst. Another had a lesion in the right occipital lobe contrary to the dominant side of interictal discharges(IIDs) in EEG. Regarding the areas where IIDs were recorded in EEG, 5 patients were seen to be limited to the occipital area, 2 to the temporal and 3 to multiple lobes(occipital-temporal-parietal). These results are shown in Table 2.

Table 1 Details of patients

patient NO.	sex	y.o	seizure	neuroimaging findings (MRI)
1	F	28	SCPS	atrophy in rt occipital lobe
2	F	17	SPS, CPS	cortical dysplasia in the rt occipital lobe, atrophy in rt occipital lobe
3	M	21	SCPS, pGTC	high-intensity spot in the rt occipital lobe with T2WI
4	M	12	SPS, CPS, pGTC	high-intensity spot in the lt occipital lobe with T2WI
5	F	16	SPS, CPS	atrophy in rt occipital lobe
6	M	14	SCPS	rt hemispheric diffuse atrophy
7	M	16	SPS, SCPS	
8	M	18	SPS, CPS	defect in lt parietooccipital(postoperation of AVM)
9	M	11	SCPS, pGTC	atrophy in lt occipital lobe
10	M	38	SCPS, pGTC	diffuse atrophy

*SPS; simple partial seizure, CPS; complex partial seizure, SCPS; simple-complex partial seizure,
*pGTC; secondary generalized tonic-clonic convulsion

Table 2 Lateralities of diagnosis

patient No.	Dipole laterality	Dipole localization mesial/lateral	Dipole upper/lower	EEG findings IID-side	EEG IID-area	Neuroimaging findings side of lesion in MRI
1	bilateral	mesial	lower	L	T	R
2	R	lateral	lower	R	T	R
3	R	lateral	both	R	O	R
4	L	lateral	both	L	O, P, mT	L
5	R	mesial	both	R	O, pT	R
6	R	mesial	upper	R	O	R
7	R	mesial	both	R	O	R
8	L	mesial	both	L	O, P, mT	L
9	bilateral	mixed	lower	bilateral	O	L
10	L	mesial	lower	L	O	bilateral diffuse

*R; right side, L; left side, upper (lower); upper (lower) side of calcarine fissure
*T; temporal, mT; mid-temporal, pT; posterior-temporal, O; occipital, P; parietal

3. Seizure manifestations Details of the seizure manifestations are shown in Table 3. All of them had visual signs preceding other epileptic symptoms: 3 patients had ictal blindness and 1 had blurred vision. Regarding hallucinations, 4 patients had phosphen, and 4 had other hallucinations, for example, 3 had elementary hallucinations and 1 had palinopsia. In regard to other visual signs, 1 had deja vu, 1 had metamorphopsia(loss of reality of view), and 1 had visual agnosia(disturbance of orientation in space). For symptoms other than visual signs, 1 had ictal deafness, 1 had alexia, 2 had blinking, 8 had another sensation(feeling of intracranial numbness, vague anxiety, feeling of the head being heavy, gastric ascending sensation, etc.). Eight patients had version of head and/or eyes(these cases mentioned above include some overlapping). Cases of the mesial type had a tendency to have phosphen or other elementary hallucination. In particular, all 4 patients who had phosphen were of mesial or mixed type. All of the 4 lateral and mixed type patients had the complex visual signs mentioned above, and two of them had symptoms that supposed simple partial seizures originated from other lobes close to occipital lobes. Further, 4 patients had moving visual signs: 2 had moving hallucination toward the opposite side to the dipole localization, 1 had hallucinations moving toward him, and another had hallucinations moving from the outskirts to center of view.

Table 3 Seizure manifestation

patient No.	dipole localization	details of visual signs	head version	eye version
1	bilateral-mesial	phosphen	L	
2	R-lateral	metamorphosia(loss of reality of view)	L	L
3	R-lateral	disturbance of orientation in space, deja vu, (alexia,)		
4	L-lateral	ictal blindness, hallucination(moving triangle), metamorphosia	R	R
5	R-mesial	ictal blindness, hallucination(white spot), phosphen		
6	R-mesial	bright spot(moving from R to L)	R	R
7	R-mesial	ictal blindness	L	L
8	L-mesial	elementary hallucination(black ball in the rt sight)	R	R
9	bilateral-mixed	palinopsia, blurred vision	R	R
10	L-mesial	phosphen	R	R

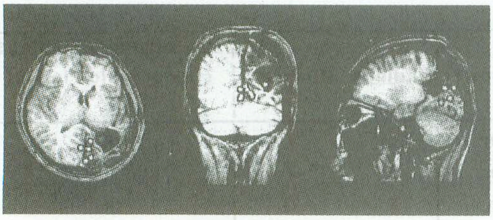

Fig. 2 Dipole localization in case 8

One interesting case(case 8, Fig. 2) had an elementary hallucination as a epileptic seizure manifestation at the time of this examination. He had arteriovenous malformation(AVM) in the left occipital lobe and he had an ictal complex visual hallucination, "a haunted house" before, but after resection of the cortex including the lesion, his ictal hallucination had changed to elementary hallucination, "a black ball moving in the right sight, then he lost the right-lower view". In addition, he had a homonymous quadrantanopsia in the right-lower view after the operation.

Lateralities of head/eye version were contralateral to the side of the dipole localization in 5 of the 8 patients, and 2 patients had a bilateral dipole cluster. Although another had ipsilateral version against the side of the dipole cluster and the lesion, he had no preceding visual signs and lost conscious at onset in this seizure.

Discussion

Recently, diagnosis of epilepsy has depended on seizure manifestations, EEG, and neuroimaging(CT, MRI, SPECT, PET etc.). The boundaries of occipital lobes are vague because they are not based on a functional map, so it is difficult to diagnose OLE without preceding visual signs. Moreover, it becomes more difficult, because epileptic discharges originated from occipital lobes spread into another lobes easily. In particular, in cases whose lesions are located near the midline of the brain, we have the risk of failing to decide laterality with EEG. In determing laterality, MEG has a big advantage because there is no influence from bone, muscle, and fluid between epileptogenesis and electrodes. Though there are some risks of false dipoles from spreading epileptic discharges, these may be prevented by accumulating experience and processing sufficient data. After due consideration of these merits of MEG, we investigated OLE due to a correlation between dipole localization and diagnosis or symptoms. We obtained a new understanding of the usefulness of neuroimaging (especially MRI) for clinical diagnosis. However, there are some cases which have no evidence of lesions provided by neuroimaging, even if there are any findings, these images can not reflect the electrophysiolosical-epileptic character of lesions. For these reasons, examinations of seizure manifestation and EEG findings are indispensable to diagnose epilepsies. Although EEG findings were very accurate in indicating lateralities, they were not sufficient to locate epileptogenic zone precisely.

In the case of versive seizure, with forced turning of head and eyes, which occurs most commonly in frontal lobe epilepsy, but may occur in parietal, temporal and occipital epilepsy. When the epilepsy involves the posterior brain regions, contraversive seizures generally occur, but both ipsi- and contraversion are features of more anteriorly placed lesions. Therefore, these symptoms have been considered an unreliable sign except eye deviation at the seizure onset in OLE.

As reported previously, it is important to investigate visual signs for diagnosis of OLE. In particular, we supposed that visual hallucination(elementary or complex) would be useful in determing both localization and extent of epileptogenesis. "Phosphen" named for the bright spot precipitated by stimulus from an electrode placed in occipital lobe by Brindley(1986), indicates a relationship with the primary visual field, and the results of our examination support this. We may obtain clues about the location of the epileptogenic focus in the transverse direction(mesial or lateral). Regarding case 8, it was supposed that his epileptogenic focus related to AVM located in the lateral occipital area, but after the operation another epileptogenesis appeared in the mesial area. Change of visual signs may reflect the change of the location of the epileptogenesis. As mentioned above, MEG dipole localization is related to the seizure manifestation, and it is probable that dipole localization reflect the location of the epileptogenic zone.

References

[1] Williamson PD, Spencer SS: Clinical and EEG features of complex partial seizures of extratemporal origin. Epilepsia 27: (Suppl 2): 46-63, 1986.

[2] Sveinbjornsdottir S, Duncan JS: Parietal and occipital lobe epilepsy: a review. Epilepsia 34(3):493-521, 1993

[3] Kuzniecky R: Symptomatic occipital lobe epilepsy. Epilepsia. 39 (Suppl 4): 24-31, 1998.

[4] Palmini A, Andermann F, Dubeau F, Gloor P, Olivier A, Quesney LF, Salanova V: Occipitotemporal epilepsies: evaluation of selected patients requiring depth electrodes studies and rationale for surgical approaches. Epilepsia. 34(1):84-96, 1993

[5] Watanabe Y, Fukao K, Watanabe M, Seino M: Epileptic events observed by multichannel MEG. Electroencephalography & Clinical Neurophysiology - Supplement. 47:383-91, 1996.

[6] Westmoreland BF: The EEG findings in extratemporal seizures. Epilepsia. 39 (Suppl) 4: 1-8, 1998

INTRAOPERATIVE CORTICAL AND SUBCORTICAL STIMULATION MAPPING TECHNIQUES IN NEURO-ONCOLOGY

Berger MS, Keles GE

Department of Neurological Surgery, University of California San Francisco, San Francisco, U.S.A.

Introduction

The effect of extent of tumor resection on outcome is one of the controversial topics in the management of patients with glial tumors, mainly due to the lack of prospective, randomized studies evaluating the issue. However, the efficacy of cytoreductive surgery to alleviate focal neurologic deficits secondary to mass effect and increased intracranial pressure, is generally accepted. In recent years, the trend in the literature has been to support the startegy of removing as much tumor as possible in both low and high grade glial tumors. Although this is not universally accepted, growing evidence suggests that patients will live significantly longer and have an improved fuctional status.

Hemispheric glial tumors are often located within or adjacent to functional areas, e.g., Rolandic cortex, supplementary motor ares, corona radiata, intemal capsule and uncinate fasciculus. As infiltrative gliomas always have a tendency to invade underlying white matter tracts, it is important to identify both cortical sites and their descending pathways for the motor and somatosensory systems. It has been shown by our group that functional cortex and subcortical white matter may be located within the tumor or the adjacent infiltrated brain, regardless of the degree of tumor infiltration, edema, apparent necrosis and mass effect [1].

Conventional neurosurgical teaching relying on standard landmarks restricts temporal lobe resections to within 4 centimeters of the temporal tip and to limit the removal of the superior temporal gyrus. However, even following these rules, there are several documented cases where dominant temporal lobe resections have been associated with permanent postoperative language deficits. In addition, it is well known that the anatomical location of essential language sites shows significant variability. In a series of 117 patients undergoing awake , dominant hemisphere surgery, it has been shown that language localization varies over the cortex and is distributed randomly from within the first few centimeters of the temporal lobe to within 4 cm of the midline in the posterior frontal - anterior parietal lobe [2]. In this study, no specific region of the temporal lobe cortex was found to be essential for language in more than 55% of the patients.

Cortical stimulation mapping for the identification of essential language sites in patients with tumors of the dominant hemisphere temporal lobe will maximize the extent of tumor resection while minimizing permanent language deficits. Therefore it is recommendable that any tumor involving the dominant temporal, mid to posterior frontal and mid to anterior parietal lobes should be operated on with the patient awake.

We here present intraoperative cortical and subcortical stimulation mapping techniques to maximize safe tumor removal.

Methods

The patient's neurological status should be preoperatively assessed in order to determine the extent of motor or language function impairment, if any. If the patient has severe hemiparesis, motor mapping will often not be useful. Similarly, those patients who will undergo intraoperative mapping for language sites should be preoperatively tested for language errors by being presented a series of slides with common objects to be named.

©1999, Tohoku University Press
Recent Advances in Biomagnetism
T. Yoshimoto et al. (Eds)

The craniotomy should be wide enough to expose the tumor and surrounding brain, including areas where language is likely to be located, to provide adequate cortical areas for language mapping. The tumor is localized with intraoperative ultrasound and its boundaries are marked by surface letters.

The stimulation mapping is performed by placing a bipolar electrode (5 mm spacing) on the surface for 2 to 3 seconds with a current amplitude between 2 and 16 mA. A constant current generator is used to produce biphasic square wave pulses at 60 Hz and a 1.25 ms single peak (pulse) duration. The current necessary to invoke motor movement will vary depending on the anesthetic condition of the patient, with lower currents used under awake conditions. The amplitude of the current is adjusted in 1 to 2 mA increments until motor movements are identified. If an intraoperative stimulation induced focal motor seizure develops, the best management is cortical application of cold Ringer's solution.

First, the inferior aspect of the Rolandic cortex is identified by eliciting responses in the face and hand. For identification of the leg motor cortex, a strip electrode may be inserted along the falx and stimulation using the same current applied to the lateral cortical surface may be delivered through it to evoke leg motor movements. Similarly, if the craniotomy is near but not overlying the Rolandic cortex, a subdural strip electrode may be inserted and stimulated to evoke the desired response.

Following identification of the motor cortex, the descending tracts may be found using similar stimulation parameters. Descending motor and sensory pathways may be followed into the internal capsule and inferiorly to the brain stem, and stimulation will be carried out throughout resection. Tumor resection should be followed by a final stimulation of cortical sites to confirm that the pathways are intact. This will also ensure that the underlying functional tracts have been preserved if subcortical responses have not been obtained. Even if the patient's neurological status is worse postoperatively, the presence of intact cortical and subcortical motor pathways will imply that the deficit will be transient and resolve in days to weeks.

For mapping of essential language sites, following the scalp opening and bone removal, the patient is kept awake during language mapping. After the motor pathways have been identified, the electrocorticography equipment is placed on the field and attached to the skull. While the electrocorticogram is in progress, the recording electrode-cortex contact point is stimulated with the bipolar electrode, which may result in afterdischarge potentials seen on the monitor. The presence of such afterdischarge potentials indicates that the stimulation current is too high and must be decreased by 1 to 2 mA until no afterdischarge potential is present following stimulation. Using this ideal stimulation current, object-naming slides are presented and changed every 4 seconds, and the patient is expected to correctly name the object during stimulation mapping. All cortical sites essential for naming are marked on the surface of the brain with sterile numbered tickets. A negative stimulation mapping may not provide the necessary security to proceed confidently with the resection. Therefore, it is essential to document where language is, as well as where it is not, located. This is also the reason for having a generous exposure, not only to maximize the extent of resection, but to minimize the possibility of obtaining negative data.

It has been shown that the distance of the resection margin from the nearest language site is the most important factor in determining the improvement in preoperative language deficits, the duration of postoperative language deficits, and whether the postoperative language deficits are permanent [3]. Significantly fewer permanent language deficits occur if the distance of the resection margin from the nearest language site is > 1 cm.

Conclusion

Surgical resection of tumors located in or near functional brain areas may not be safe even if the surgeon remains within the boundaries of the macroscopically obvious tumor. In addition to its use to determine functional cortical sites, stimulation mapping is the only available method that provides reliable identification of descending subcortical motor, sensory and language tracts [4,5]. For dominant hemisphere temporal lobe tumors, patients with normal preoperative language function who undergo cortical stimulation mapping for the identification of language sites will not have a permanent postoperative language deficit if the tumor resection margin is 1 cm or more distant to the essential language site.

Overall, intraoperative stimulation mapping of cortical and subcortical tissue in and around a tumor will identify functional tissue and its preservation will minimize the risk of permanent postoperative deficit.

References

[1] Skirboll SS, Ojemann GA, Berger MS, et al: Functional cortex and subcortical white matter located within gliomas. Neurosurgery 38:678-685, 1996

[2] Ojemann GA, Ojemann J, Lettich E et al: Cortical language localiation in left, dominant hemisphere. An electrical stimulation mapping investigation in 117 patients. J Neurosurg 71:316-326, 1989

[3] Haglund MM, Berger MS, Shamseldin M, et al: Cortical localization of temporal lobe language sites in patients with gliomas. Neurosurgery 34:567-576, 1994

[4] Berger MS, Ojemann GA, Lettich E: Neurophysiological monitoring to facilitate resection during astrocytoma surgery. In: Neurosurgery Clinics of North America, 1(1):65-80, 1990

[5] Berger MS: Functional mapping guided resection of low grade gliomas. In:Loftus C (ed), Clinical Neurosurgery, Vol 42, Williams & Wilkins, Baltimore, 1995, pp 437-452

Preoperative MEG, fMRI and Intraoperative Cortical Stimulation Methods for Neurosurgical Brain Mapping

Nakasato, N., Kanno, A.[1], Hatanaka, K.[2], Ohtomo, S., Inoue, T.,
Shimizu, H., Kumabe, T., Sato, K., Shirane, R. and Yoshimoto, T.

Department of Neurosurgery, Tohoku University School of Medicine, Sendai, Japan;
[1]Kohnan Hospital Ryogo Center, Sendai, Japan; [2]ELEKTA K.K., Tokyo, Japan

Introduction

Intraoperative functional brain mapping by direct cortical stimulation enables maximum tumor resection in glioma surgery with preservation of the eloquent cortical functions. Preoperative functional brain mapping is potentially possible using methods such as magnetoencephalography (MEG) and functional magnetic resonance imaging (fMRI). The present study assessed the accuracy of MEG and fMRI for the localization of the central sulcus in normal volunteers and patients with intracranial tumors in comparison with the results of intraoperative cortical stimulation.

Methods

The study included 12 normal volunteers and 17 patients with intracranial tumors adjacent to the central sulcus. MEG and fMRI studies were performed before surgery in 13 patients and after surgery in 5 patients.

Somatosensory evoked fields (SEFs) due to median, ulnar and tibial nerve stimulation were measured in a magnetically shielded room using a helmet-shaped MEG system (Neuromag-122 [1]). The first peak of the SEFs, i.e., N20m for the median and ulnar nerves and P38m for the posterior tibial nerve, was used for source estimation using an equivalent current dipole model. Three-dimensional MRIs were obtained in all subjects. The calculated dipole positions were superimposed on the MRIs using fiduciary markers as a guide.

fMRI was performed using a 1.5 T whole body clinical imager (Sigma Horizon, GE Medical Systems) and a standard head coil. Five to seven axial slices of 7 mm thickness were imaged including the anatomical sensorimotor area. Gradient-echo type echo planar imaging was used with repetition time of 2,000 or 3,000 ms, echo time of 40 to 60 ms, flip angle of 90 degrees, 64 by 64 matrix and 24 cm by 24 cm field of view. The activated area was delineated by post-procession of the images by the cross-correlation method. Sets of 70 images were obtained with the subject at rest and during unilateral hand grasping (Fig.1).

During surgery, the central sulcus was verified by cortical recording of somatosensory evoked potentials (all surgical cases) and intraoperative cortical stimulation during the awake condition (4 cases). A frameless stereotaxic system (Viewing Wand) was used for cortical stimulation in two cases (Fig.2).

©1999, Tohoku University Press
Recent Advances in Biomagnetism
T. Yoshimoto et al. (Eds)

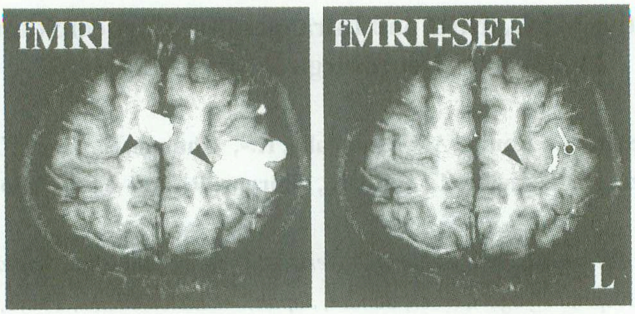

Fig. 1 Correspondence of fMRI for right hand grasping and SEFs for right median nerve stimulation in a normal volunteer. (Left) fMRI with correlation coefficient > 0.6 indicates multiple and extensive activation areas including the contralateral primary sensori-motor and bilateral supplementary motor cortices. (Right) fMRI with correlation coefficient > 0.8 indicates the highest activation area on the contralateral central sulcus, slightly medial to the location of the N20m dipole of the median nerve SEFs. (Arrowheads: central sulcus)

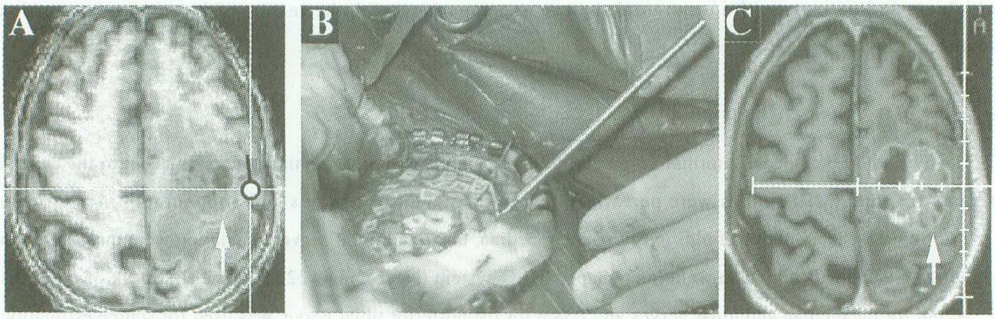

Fig. 2 (A) Localization of the N20m dipole of the median nerve SEFs in a patient with left frontal glioma. (B) Probe of the frameless stereotaxic system indicating the cortex of hand sensation evoked by intraoperative cortical stimulation. (C) Crossing bars indicate the probe tip in (B). Note the excellent correspondence between (A) and (C).

Results

The highest fMRI activation was located on the central sulcus, which was identified by SEFs in all hemispheres of the 12 normal subjects (Fig. 1) as well as all non-lesional and 13 lesional hemispheres of the 17 patients. However, fMRI and MEG disagreed in locating the central sulcus in 4 patients: Two patients with cortical motor weakness showed the highest fMRI activation in the bilateral supplementary motor cortices; one patient showed the highest fMRI activation in the sulcus furthest posterior to the central sulcus probably due to the inflow effect of a large vein (Fig. 3); and a patient with a right frontal tumor showed the N20m dipole of median nerve SEF localized one sulcus posterior to the central sulcus, whereas the P38m dipole of the tibial nerve SEFs was localized on the central sulcus (Fig. 4).

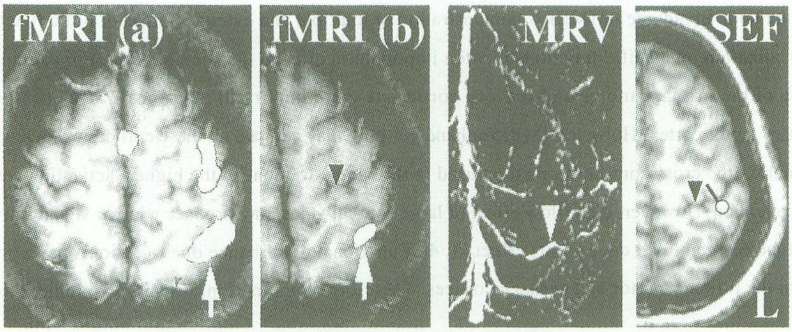

Fig. 3 fMRI for right hand grasping in a patient with left frontal glioma indicates multiple activation areas with correlation coefficient > 0.6 (A) but the highest activation area (arrow) with correlation coefficient > 0.8 (B) is located on the sulcus furthest posterior to the central sulcus (black arrowhead). MR venography (MRV) indicates a cortical vein (white arrowhead) in the same area as the highest fMRI activation (arrow). The central sulcus (black arrowheads) is confirmed by the localization of the N20m dipole of the median nerve SEFs.

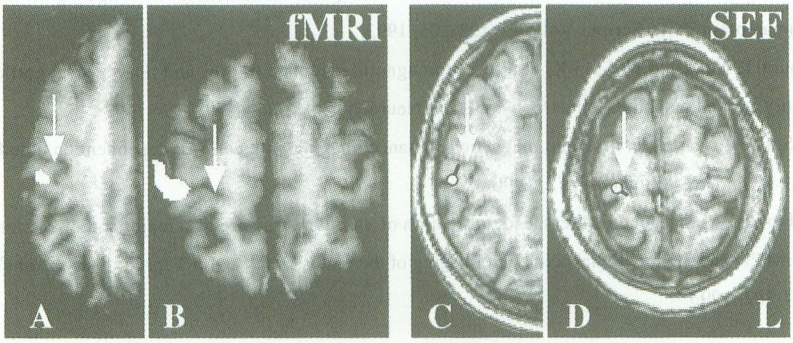

Fig. 4 Multimodal localization and confirmation of the central sulcus (arrows) in a patient with right frontal glioma. (A and B) fMRI for left hand grasping indicates the highest activation area on the right post-central gyrus (white arrows). (C) N20m dipole of the left median nerve SEFs is localized on the sulcus posterior to the central sulcus, suggesting a localization error. (D) P38m dipole of the tibial nerve SEFs is localized on the central sulcus. The position of the central sulcus is confirmed by intraoperative cortical SEP.

Discussion

The present study demonstrated the complementary usefulness of MEG and fMRI for noninvasive localization of the central sulcus. However, the use of only fMRI or MEG may result in misinterpretation of the functional localization, especially in lesional hemispheres.

Localization accuracy for SEFs was estimated at within 2 to 3 mm in our previous study [2]. However, clinical MEG users must always consider possible localization errors in SEFs. One practical way to avoid such misinterpretations is to compare SEFs for different nerve stimuli. The combination of median, ulnar and tibial nerve stimuli is useful for both somatotopic localization and verification of sulcus identification (Fig.4). Combination with other modalities such as anatomical landmarks, functional MRI and intraoperative mappings is also important.

The major advantage of fMRI is demonstration of multiple and extended areas of brain function. However, pinpoint localization of specific functions is often important in clinical decision making. For example, presurgical localization of the primary motor and sensory cortices is more important than localization of the pre-motor or supplementary motor cortex. However, fMRI for hand grasping may activate all these cortices at once. Using statistical methods, such as the cross correlation method used in this study, to identify the highest activation area may provide pinpoint localization. However, the inflow effect of large cortical veins may produce a larger signal activation than the primary (blood oxygen level dependent) effect [3, 4]. Functional disturbance due to lesions may also reduce fMRI *signals* from the primary motor and sensory cortices. Therefore, combination of fMRI with other modalities is also important.

Intraoperative cortical stimulation has been established as the "gold standard" for functional brain mapping. However, combination of multimodal magnetophysiological methods such as MEG and fMRI, together with anatomical landmarks, can provide similar information at the preoperative stage and may replace intraoperative cortical stimulation, at least in the central area.

References

[1] Ahonen A, Hämäläinen M, Kajola M, et al: A 122-channel SQUID instrument for investigating the magnetic signals from the human brain. Phys Scripta Vol T49: 198-205, 1993

[2] Kawamura T, Nakasato N, Seki K, et al: Neuromagnetic evidence of pre- and post-central cortical sources of somatosensory evoked responses. Electrophysiol Clin Neurophysiol 100: 44-50, 1996

[3] Ogawa S, Lee T, Kay A, et al: Brain magnetic resonance imaging with contrast dependent on blood oxygenation. Proc Natl Acad Sci USA 87: 9868-9872, 1990

[4] Lai S, Hopkins AL, Haacke EM, et al: Identification of vascular structure as a major source of signal contrast in high resolution 2D and 3D functional activation imaging of the motor cortex at 1.5 T: preliminary results" Magn Reson Med 30: 387-392, 1993

Frameless Stereotaxy with MEG

Ganslandt O, MD,[1]; Kober H, PhD[2]; Nimsky Ch, MD[1]; Möller M, MD,[2]; Fahlbusch R, MD[1]; Vieth J, MD[2]

(1) Dpt. of Neurosurgery, (2) Dpt. of Experimental Neuropsychiatry, University Erlangen-Nuremberg, Germany

Introduction:

It is often difficult to depict the relationship of a lesion adjacent to the motor cortex to the known anatomic structures since the neuroradiologic assessment of the central sulcus is sometimes ambiguous, especially in the presence of edema or mass lesions. Magnetoencephalography (MEG) with its capability to accurately localize intracranial currents is an interesting tool to be used in the field of neurosurgery. So it was an obvious step to utilize the MEG-based localizations of the somatosensory cortex with magnetic source imaging for the presurgical assessment of the motor cortex at risk during neurosurgical treatment [2,3]. This method introduced for the first time the possibility for the preoperative evaluation of the relation of a lesion to the sensorimotor cortex. However, a shortcoming of this method has been that the neurosurgeon could not transfer the information of these functional data directly to the operation field. Especially in surgery of low grade gliomas, where the differentiation of tumor tissue and boundary to normal brain parenchyma is often difficult, the surgeon must know the relation of the lesion to functional important brain areas. The advent of neuronavigation systems (frameless stereotaxy) finally offered the chance to combine anatomical and functional information about the brain for direct visualization in the OR [4,7,8]. Until now in our institution a large series of patients harboring tumors within the motor cortex have been operated with the aid of MEG and neuronavigation.

Material and Methods

Magnetic Source Imaging

All patients were examined with Somatosensory Evoked Fields (SEF) and in some patients additionally Motor Evoked Fields (MEF) were registered. We used a MAGNES II biomagnetometer (Biomagnetic Technologies, Inc. San Diego, CA) with 2 x 37 channels for the MEG-recording. The recording was performed within a magnetic shielded room. For SEF 200 tactile stimuli were applied to the lesions contralateral thumb, index finger and little finger (Interstimulus interval 1 sec.) and averaged, covering a 300-millisecond intervall (150 msec. pre- and 150 msec poststimulus), the sampling rate was 560 Hz. For MEF the patients were asked to perform repetitive finger tapping with the contralateral index finger with high frequency. The single finger movement was triggered with the surface electromyogram (EMG) of the flexor digitorum superficialis indicis muscle. For the average 60 runs were sampled, covering a 600 millisecond intervall. Special care was administerd to avoid motion artefacts. The patients arm was fixed and the head was embedded in a vacuum cushion. The somatosensory neuromagnetic peak components ranged from 20 to 100 msec representing activitiy in the primary sensory cortex (S1) [5]. The MEF showed marked activity with 100 msec latency after EMG onset. These latencies were investigated with the dipole fit, the equivalent current dipole (ECD) model and the sphere as the head model. The localization with the best correlation of measured and calculated magnetic fields was

©1999, Tohoku University Press
Recent Advances in Biomagnetism
T. Yoshimoto et al. (Eds)

used for image fusion with magnetic resonance imaging (SIEMENS Magnetom Open, Erlangen, Germany, 0.2 T; 3-D-FLASH (Fast Low Angle Shot) sequence with a slab thickness: 168mm, slice thickness: 1.5mm, TR: 16ms, TE: 7ms, FOV: 250mm). The image fusion was achieved with a self-developed contour fit program [6].

Neuronavigation

In 25 cases we used the StealthStation (Surgical Navigation Technologies, Inc., Bloomfield CO), a free hand stereotactic device where the position of a pointing device is registered via light emitting diods (LED). The position of the pointer tip in the surgical space is displayed on the workstations monitor with the corresponding location in the image space. In these cases the MEG marked gyrus was found by projection of the MEG dipole to the surface of the gyrus with the workstations software. In all other procedures the Zeiss MKM Neuronavigation system was used (Zeiss, Oberkochen, Germany). This system consists of a robotic microscope which uses the autofocus as the pointig device. All information, that is visible on the workstation can be displayed through the eyepiece of the microscope as well. This ability is comfortable for displaying tumor contours, as well as surgical pathways to the target, or for incorporation and visualization of functional data within the surgical space.

For referencing image space and patient we used a set of at least 8 –10 fiducial markers that were attached to the patients head. While the MEG measurement was conducted in general 2 days prior to surgery, the data transfer to the neuronavigator was done on the evening before operation. The image data were transfered via a local area network with the DICOM III protocol. During the image preperation the best surgical plan was depicted by the surgeon. Before draping, the tumor contour was superimposed onto the patients skin, allowing to mark an adequate skin incision and planning of the bone flap. After craniotomy four additional bone fudicials were applied around the trephination. These markers were used for new reference in case the initial reference is lost due to technical failure of the workstation, or in case of an update of the neuronavigation after scanning the patient intraoperatively in the open-MRI. However in these cases the functional data are no longer included.

After opening of the dura the motor cortex is identified either with the StealthStation´s pointer, or by direct visualization with the MKM microscope. Intraoperative recording of the somatosensory evoked potentials (SEP) phase reversal with median nerve stimulation was then performed to localize the central sulcus and to verify the MEG localization. For the SEP monitoring strip electrodes with 4 or 8 electrodes were used. A Nicolet Pathfinder I (Nicolet Instruments, Biomedical Division, Madison, WI) was used for all recordings. Stimulation parameter were: Intensity 10 to 25 mA, frequency 5.1 Hz, duration 100 µs, filter 30-3kHz.

Results

A total of 45 patients were operated with the help of MEG-derived SEF and MEF data of the sensorimotor cortex and neuronavigation (13 astrocytomas, 12 glioblastomas, 12 meningiomas, 6 metastasis, other). 18 of these tumors were located in the precentral area, 12 were located in the postcentral area and 15 lesions had infiltrated the motor cortex. A complete resection could be achieved in 30 patients (67%), partial resection in 11 patients (24%) and biopsy in 4 patients (9%). 14 (31%) patients with paresis of the contralateral side experienced amelioration after surgery. 29 patients (64.5%) remained unchanged and 2 patients (4.5%) had a neurological deterioration, which however was not related to the method (two elder patients with meningiomas had pulmonary embolism and bleeding from the sagittal sinus).

Discussion

The combination of magnetoencephalography and frameless stereotaxy is a new approach in surgery around eloquent brain areas. In our experience of patients with tumors around the motor cortex we could perform more radical surgery with less morbidity compared to other series, that were conducted with intraoperative SEP monitoring alone [1]. This method is a true clinical application of the MEG. Future applications in this field should incorporate MEG localization of spike and slow wave activity in epilepsy patients together with intraoperative electrocorticography and neuronavigation, as well as language MEG in patients with tumors adjacent to language related brain areas. The role of functional MRI in respect of localization accuracy is currently under investigation in our institution.

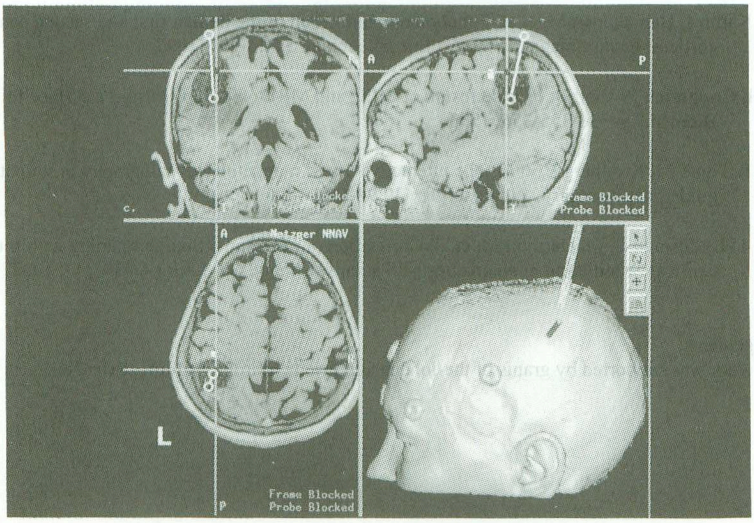

Figure 1: 53-year old female patient with a cystic metastasis in the left parietal cortex. The MEG localization of the SEF dipole indicated that the tumor is located posterior to the somatosensory cortex and could be removed without danger of inducing hemiparesis. The MEG results are used with frameless sterotaxy (Surgical Navigation Technologies, Inc., Bloomfield CO).

References

[1] Cedzich C, Taniguchi M, Schafer S, et al: Somatosensory evoked potential phase reversal and direct motor cortex stimulation during surgery in and around the central region. Neurosurgery 38:962-970, 1996

[2] Gallen CC, Sobel DF, Waltz T, et al: Noninvasive Presurgical Neuromagnetic Mapping of Somatosensory Cortex. Neurosurgery 33:260-268, 1993

[3] Ganslandt O, Kober H, Ulbricht D, et al: Presurgical Localization of Functional Brain Areas with Magnetoencephalography (MEG). Zentralblatt für Neurochirurgie 55 (Suppl.):611994

[4] Ganslandt O, Steinmeier R, Kober H, et al: Magnetic source imaging combined with image-guided, frameless stereotaxy: a new method in surgery around the motor strip. Neurosurgery 41:621-628, 1997

[5] Hari R, Karhu J, Hamalainen M, et al: Functional organization of the human first and second somatosensory cortices: a neuromagnetic study. Eur.J.Neurosci. 5:724-734, 1993

[6] Kober H, Grummich P, Vieth J: Precise fusion of MEG and MRI tomography using a surface fit. Biomed.Eng. 38:355-356, 1993

[7] Rezai AR, Hund M, Kronberg E, et al: The interactive use of magnetoencephalography in stereotactic image-guided neurosurgery. Neurosurgery 39:92-102, 1996

[8] Roberts TPL, Zusman E, McDermott M, et al: Correlation of Functional Source Imaging with Intraoperative Cortical Stimulation in Neurosurgical Patients. J Image Guid Surg 1:339-347, 1995

Acknowledgements:
Part of this work was supported by grants of the Johann and Frieda Marohn Stiftung, Erlangen.

Coregistration of MEG, anatomical MRI and MR-venography

Mäkelä JP

Brain Research Unit, Low Temperature Laboratory, Helsinki University of Technology; Dept. of Clinical Neurosciences, Helsinki University Central Hospital, Finland.

Introduction

Tumors, vascular malformations, and previous operations may deform brain anatomy so extensively that eloquent areas are not recognized from preoperative magnetic resonance images (MRIs), or from anatomic landmarks during surgery. Surgery of diffusely infiltrating gliomas requires a compromise between an extensive enough resection, and the risk of damage to adjacent eloquent cortices. Furthermore, somatosensory representations may be modified by the tumor [1], and functional cortex may reside inside gliomas [2]. Consequently, glioma surgery benefits from information about the functional brain anatomy in the tumor region.

Source locations of magnetoencephalographic (MEG) signals, displayed on three-dimensional MRIs, including the blood vessels on the brain surface, pinpoint functionally irretrievable areas [3–4]. Presurgical MEG studies may prevent involuntary damage of functional areas dislocated to unexpected directions, and may also encourage operations on tumors abutting eloquent brain areas. The sources of the somatosensory evoked fields (SEFs) to electric stimulation of peripheral nerves identify the somatosensory cortex in the posterior wall of the central sulcus [5]. Although sensory deficits due to lesion of the somatosensory cortex in the posterior wall may render a limb largely useless, the primary motor cortex in the anterior wall of the central sulcus needs to be specially protected during operations to prevent a severe paresis. Direct localization of the motor strip is feasible by using correlograms between cortical spontaneous activity and surface electromyograms (EMGs). The 15-30 Hz rhythmic activity of the motor cortex is coherent with the EMG of muscles contracting isometrically [6–7]. The generation sites of the cortical MEG signals that show the highest coherence with the simultaneously recorded EMG from activated muscles in arm and leg reveal the locations of the cortical arm and leg representations.

We identified somatomotor strip of neurosurgical patients by recording SEFs to electric stimulation of different body parts, and evaluated the value of the cortex-muscle coherence [7] for directly localizing the motor cortex. We also identified the central sulcus by anatomical MRI landmarks. The presurgical findings were compared with cortical stimulation and evoked potential data obtained during awake craniotomy. The data are described in more detail elsewhere [8].

Methods

Twelve patients (27–60 yrs) were studied; five had primary, and four recurrent GII or GIII gliomas, one a metastatic neurofibrosarcoma, one a hemangioma, and one an arteriovenous malformation in the vicinity of the somatomotor strip. Eleven patients were operated with awake craniotomy; one operation was postponed due to a stroke before the planned operation.

Recording and data analysis

MEG was recorded in a magnetically shielded room with a whole-scalp magnetometer (Neuromag 122^{TM} [9]. SEFs were elicited by electric stimulation of the median nerve (MN) at the wrist and the posterior tibial nerve (TN) at the ankle (0.2 ms pulses; interstimulus interval, ISI, 0.5 s), and by vibratory stimulation of the upper lip (LIP; 250 Hz, 4 ms, ISI 0.5 s). Auditory evoked fields (AEFs) were elicited by tones (1 kHz, 50 ms, ISI 1 s) delivered alternately to both ears. For cortex-muscle correlograms, a 4-min period of spontaneous MEG activity was collected during wrist and ankle extension; simultaneous surface EMG was recorded from extensor carpi radialis and tibialis anterior muscles. The highpass filter was at 0.03 Hz. The lowpass filter and sampling rates were 320 Hz and 987 Hz for MN and TN, 100 Hz and 397 Hz for LIPs, and 90 Hz and 297 Hz for AEFs. The 500-ms analysis period included a 100-ms pre-stimulus baseline. About 120 responses were averaged for MNs and AEFs, and about 500 for TNs and LIPs. The vertical electro-oculogram (EOG) was recorded simultaneously and epochs in which the EOG activity exceeded ±150 μV were rejected from the averages. Spontaneous MEG was recorded with 190-Hz lowpass and with 597-Hz sampling rate; EMG was collected with 100-Hz lowpass. SEFs were digitally low-pass filtered at 190 Hz and AEFs at 40 Hz. Spherical head model was matched to the local curvature of the inner skull. Sources of maximum deflections were modelled as equivalent current dipoles (ECDs) found by a least-squares fit to recordings from a subset of 18 to 24 channels surrounding the maximum signals over each hemisphere. Only ECDs explaining at least 80% of the field variance were accepted. The MN source was searched during 18–33 ms and the TN source during 39–59 ms after the stimulus onset; the corresponding ranges were 40–80 ms for LIPs and 80–130ms for AEFs. The exact location of the patient's head with respect to the sensors was determined by measuring the magnetic field produced by small currents

©1999, Tohoku University Press

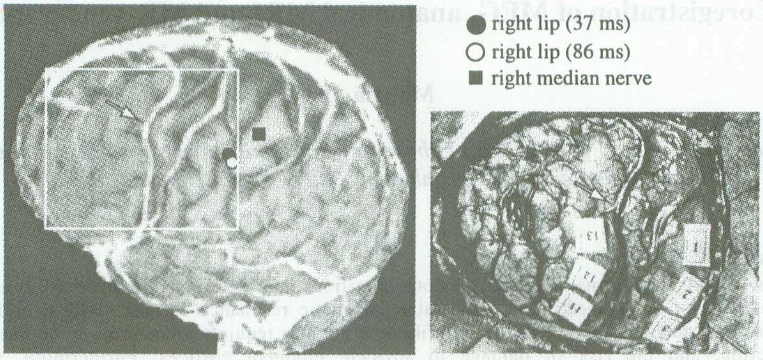

Fig. 1. Left: 3-D surface rendering including veins of a patient with a left frontal GII oligodendroglioma. The sources of responses to lip and median nerve stimulations are projected on the cortex. Right: Intraoperative photograph of the same subject. The veins in the tumor region are readily identifiable. The box in the 3-D MRI corresponds to the region depicted in the photograph. The arrow shows a vein bifurcation both in the surface rendering and in the photograph. Stimulation of site 1 elicited finger movements and sites 2-3 lip movements.

delivered to four coils attached to the scalp. The coil locations with respect to the nasion and periauricular points were determined with a 3-D digitizer; this information was used to align the MEG and MRI coordinate systems.

The MR images (1.5 T Siemens Magnetom Vision system) were acquired using regular T1-weighted MPRAGE sequence for reconstructing 3-D brain images and gadolinium-enhanced MPRAGE sequence for visualizing the venous system and tumor enhancement. To depict the veins on the brain surface, the contrast-enhanced MR images were manually segmented for the inner surface of the skull. The MEG source locations were visualized as colored dots on top of the images. The anatomical identification of the motor cortex was based on the omega-shaped knob in the hand area [10] and on broader precentral motor than postcentral somatosensory gyrus; the central sulcus was found on the basis of its continuation from the mesial surface, anterior to the posterior ramus of the cingulate sulcus [11].

Patients were operated by awake craniotomies, which were well-tolerated. Functional cortical areas around and over the tumor were identified by comparing the exposed cortex with the MEG data and cortical veins superimposed on 3-D MRIs (Fig.1). Cortical somatosensory evoked potentials (SEPs) to median nerve stimulation were recorded from 8 locations in five patients. The cortex around and over the tumor region was mapped by cortical electric stimulation for motor, sensory and speech function in seven patients. The cortical surface, location of stimulation sites, and the SEP grid position were photographed for comparisons with preoperative findings. Subsequently, the tumor was removed under the operating microscope.

To provide a rough estimate of the location accuracy of the SEF sources, the sensory sites identified by cortical stimulation, and sites of electrodes displaying maximum negative deflections in 20-25 ms range in the cortical SEPs were overlaid on the surface of the individual 3-D MRIs. The MEG sources were projected to the nearest brain surface. The distance between these points was then calculated.

Results

SEF recordings identified the postcentral gyrus correctly in all patients. The preoperative localizations generally agreed with cortical stimulation and SEP recordings. The mean distance between the SEF source and electrode producing maximum N20 was 9 mm (range 5–18 mm); the corresponding value for sensory response site in cortical stimulation and SEF source was 8 mm (range 6–12 mm). In four patients, the central sulcus was located in relation to recurrent glioma, and ferromagnetic dust from the previous operations produced noise to the signals. However, in all four subjects, central sulcus was identified reliably by the MN and TN stimulations. In eight of the 12 patients, the MEG-EMG coherence maxima could be localized with a satisfactory goodness of fit (Fig. 2). The results did not yield new information as compared with SEFs; however, they gave another independent confirmation of the central sulcus location.

The anatomical MRI landmarks were useful in all patients. The omega-shaped knob of the precentral gyrus in the hand region was identified in 11 of 12 affected hemispheres, and it agreed with the functional localization. The ramus posterior of cingulate sulcus was an useful landmark in 10 of 12 affected hemispheres. The wider precentral than postcentral gyrus was observed in in 10 of 12 affected hemispheres. The operating neurosurgeon considered vein overlay on 3-D MR images very practical.

Discussion

Successfull integration of MEG and MRI data for neurosurgery has been previously reported by several research groups [3–4;12–16], and MEG data can easily be incorporated into intraoperative stereotaxic navigation methods [13–14]. Preoperative MEG localization of the central sulcus agrees well with intraoperative one [3–4;12–16], as confirmed also in this study; the differences between preoperatively and intraoperatively evaluated cortical representations were well within the error limits of the methods. When available, the anatomical landmarks agreed with functional localization. The omega-shaped knob of the central sulcus in the hand region was especially useful; highlighting its localization in the 3-D MRIs (*e.g.*, [17]) would probably be useful in several patients, even without functional information.

Eight of our 12 patients showed reliable cortex-muscle correlograms. Consequently, the method cannot replace the SEF measurements but, when available, it confirms the central sulcus location, and may be especially useful in patients who do not produce SEFs due to polyneuropathy or a lesion limited to the somatosensory cortex. Illustration of veins on the 3-D MRIs clearly facilitated orientation to tumor and eloquent cortices in the limited operational field of view. This speeded up the selection of sites for intracortical stimulation and SEP grid positioning, particularly in operations for recurrent gliomas where anatomy was blurred and dural adhesions complicated the surgery. Furthermore, the 3-D MRIs including veins eased surface orientation to subcortical tumors in cases where functional landmarks, projected on the cortex, were in the vicinity of the tumor, and added information in deciding on how to approach tumors from the surface. The vein overlay on the 3-D MRIs can be recommended for all applications of functional localization. Such images probably also alleviate the inaccuracy caused by possible brain shifts, due to, *e.g.*, cyst evacuation, in conventional neuronavigation systems.

Preoperative localization of speech-related areas would be beneficial in planning and performing surgery in the speech-dominant hemisphere. The sources of the responses to tones are located bilaterally in the vicinity of the primary auditory cortex on supratemporal cortices [18–19]. Functional localization of the auditory cortex is useful for surgery, because the 100-ms AEF source in the dominant temporal lobe is surrounded by the language-related cortex [16]. At present, there is no adequate stimulus battery to identify all speech-related cortical areas directly by MEG. However, reading-related MEG activations have recently been described in the vicinity of the left auditory cortex at about 400 ms after the word onset [20]. The source modelling of these late signals is complex, but our preliminary results imply that they may be useful also as functional landmarks. Obviously, these approaches require further experimentation and rigorous intraoperative controls.

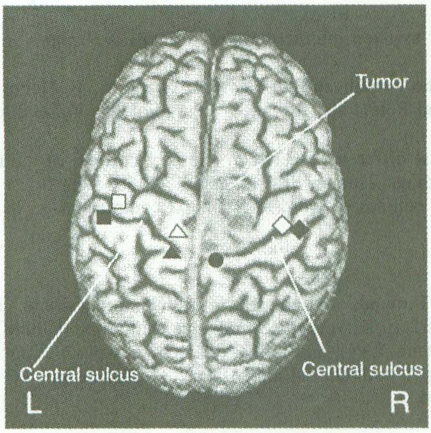

Fig. 2: Sources of SEFs to right and left median and tibial nerve stimulations, and locations of maximal coherence of MEG spontaneous activity with right (r.) and left (l.) arm and right leg EMG, overlaid on a 3-D MRI surface reconstruction of a patient with right mesial low-grade glioma. No coherence was observed between spontaneous MEG and left leg EMG.

▲ right tibial nerve
△ MEG-EMG-coherence (r. leg)
■ right median nerve
□ MEG-EMG-coherence (r. arm)
● left tibial nerve
◆ left median nerve
◇ MEG-EMG-coherence (l. arm)

Conclusions

In all our patients, SEF recordings identified the central sulcus, and use of MEG-EMG coherence for motor strip identification further confirmed its localization. Surface veins increase the usefulness of 3-D renderings, and ease the use of information about functional localization of eloquent cortical areas during operation. Anatomical landmarks, illustrated on the 3-D brain surface renderings, might provide information about the location of the motor cortex even when functional data are not available. Functional cortical localization, tailored individually for each patient, could be applied regularly before surgery of any cerebral pathology.

References

[1] Wunderlich, G, Knorr, U, Herzog, H, et al: Precentral glioma localization determines the displacement of cortical hand representation. Neurosurg 42: 18-27, 1998

[2] Skirboll, SS, Ojemann, GA, Berger, M, et al: Functional cortex and subcortical white matter located within gliomas. Neurosurg 38: 678-685, 1996

[3] Gallen, CC, Sobel, DF, Waltz, T, et al: Noninvasive presurgical mapping of somatosensory cortex. Neurosurg 33: 260-268, 1993

[4] Gallen, CC, Schwartz, BJ and Bucholz, RD: Presurgical localization of functional cortex using magnetic source imaging. J Neurosurg 82: 988-994, 1995

[5] Sutherling, WW, Crandall, PH, Darcey, TM, et al: The magnetic and electric fields agree with intracranial localizations of somatosensory cortex. Neurol 38: 1705-1714, 1988

[6] Conway, BA, Halliday, DM, Farmer, SF, et al: Synchronization between motor cortex and spinal motoneuronal pool during the performance of a maintained motor task in man. J Physiol 489.3: 917-924, 1995

[7] Salenius, S, Portin, K, Kajola, M, et al: Cortical control of human motoneuron firing during isometric contractions. J Neurophysiol 77: 3401-3405, 1997

[8] Mäkelä, JP, Seppä, M, Hämäläinen, M, et al: Three-dimensional imaging of functional brain anatomy to facilitate intraoperative navigation around the somatomotor strip. Submitted, 1998

[9] Ahonen, A, Hämäläinen, M, Kajola, M, et al: 122-channel SQUID instrument for investigating the magnetic signals from human brain. Physica Scripta T49: 198-205, 1993

[10] Yousry, TA, Schmid, UD, Alkadhi, H, et al: Localization of the motor hand area to a knob on the precentral gyrus. A new landmark. Brain 120: 141-157, 1997

[11] Berger, MS, Cohen, WA and Ojemann, GA: Correlation of motor cortex brain mapping data with magnetic resonance imaging. J Neurosurg 72: 383-387, 1990

[12] Kamada, K, Takeuchi, F, Kuriki, S, et al: Functional neurosurgical simulation with brain surface magnetic resonance images and magnetoencephalography. Neurosurg 33: 269-273, 1993

[13] Rezai, AR, Hund, M, Kronberg, E, et al: The interactive use of magnetoencephalography in stereotactic image-guided neurosurgery. Neurosurg 39: 92-102, 1996

[14] Ganslandt, O, Steinmeier, R, Kober, H, et al: Magnetic source imaging combined with image-guided frameless stereotaxy: a new method in surgery around the motor strip. Neurosurg 41: 621-628, 1997

[15] Hund, M, Rezai, AR, Kronberg, E, et al: Magnetoencephalographic mapping: basis of new functional risk profile in the selection of patients with cortical brain lesions. Neurosurg 40: 936-943, 1997.

[16] Nakasato, N, Kumabe, T, Kanno, A, et al: Neuromagnetic evaluation of cortical auditory function in patients with temporal lobe tumors. J Neurosurg 86: 610-618, 1997

[17] Kikinis, R, Gleason, PL, Moriarty, TM, et al: Computer-assisted interactive three-dimensional planning for neurosurgical procedures. Neurosurg 38: 640-651, 1996

[18] Hari, R: The neuromagnetic method in the study of the human auditory cortex, Grandori, F, Hoke, M, Romani, GL (Eds.), Auditory Evoked Magnetic Fields and Potentials. Advances in Audiology, Vol 6. Basel: Karger, 1990, pp 222 - 282

[19] Mäkelä, JP, Ahonen, A, Hämäläinen, M, et al: Functional differences between auditory cortices of the two hemispheres revealed by whole-head neuromagnetic recordings. Human Brain Mapp 1: 48-56, 1993

[20] Helenius, P, Salmelin, R, Service, E, et al: Distinct time courses of word and context comprehension in the left temporal cortex. Brain 112: 1133-1142, 1998

Acknowledgements

This study has been supported by the Academy of Finland, and the EU's Biotech programme. The collaboration of S. Avikainen, N. Forss, M. Hämäläinen, R. Hari, E. Kirveskari, S. Salenius, M. Seppä (CliniMEG group, Low Temperature Laboratory, Helsinki University of Technology), and J. Jääskeläinen, T. Kovala (Dept. of Clinical Neurosciences), T. Randell (Dept of Anesthesiology) and O. Salonen (Dept. of Radiology) of the Helsinki University Central Hospital is gratefully acknowledged.

3D-Localization of Conduction Blocks in Patients with S1 Root Compression by Magnetoneurography

Mackert BM [1], Curio G [1], Burghoff M [2], Trahms L [2], Marx P [1]

Neurophysics Group [1], Dept. of Neurology, Klinikum Benjamin Franklin, Freie Universität Berlin;
Physikalisch-Technische Bundesanstalt [2], Berlin, Germany.

Introduction:

Tibial nerve Somatosensory Evoked magnetic Fields (tSEFs) measured at the body surface over the lower back allow to visualize the propagation of compound action currents inside the body along fibers of plexus, nerve roots and cauda equina [1,2,3]. One clinical perspective for this *magnetoneurography* (MNG) is the non-invasive 3D-localization of focal slowings or blocks of conduction. Notably, based on electric surface recordings the localization of acute proximal nerve lesions, e.g. in case of nerve root compression, is often not possible [4]. Here, tSEF mappings in three patients with acute unilateral S1 nerve root compression are reported.

Methods:

Inside a magnetically shielded room (Vacuum-Schmelze AK 3b) three consecutive patients suffering from an acute unilateral S1 syndrome (loss of ankle jerk, paresis of S1 muscles, dermatomal hypaesthesia, without any further neuropathy) were carefully laid in a relaxed prone position with some pelvic support for offsetting the lumbar spine lordosis. Right and left tibial nerves (Fig. 1) were electrostimulated in alternation (9 Hz monophasic squarewave pulses, 0.1 ms width; bridge electrode, cathode proximal; constant current 6 mA - 13 mA, above motor threshold; 9000 epochs on each side; time delay 55 ms right/left). Signals were recorded using 49-channels of a dc-SQUID system (30 mm interchannel distance in a planar triangular grid, 7 mm diameter SQUID pick up area, covering an area of 210 mm diameter; white noise level 2.7 fT/√Hz; 1st order axial electronic gradiometer with 70 mm baseline [5]). The Dewar was centered over the spinous process of L4 coplanarly to the lower back (distance of body surface to Dewar bottom was between 1 cm and 3 cm).

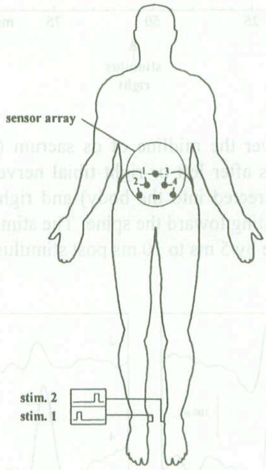

Figure 1:
Tibial nerves were electrostimulated at the ankle bilaterally in alternation. Magnetic signals were recorded with a multichannel SQUID system centered over the spinous process of L4. A singel channel record from one representative site (m) is shown in Fig. 2. Additionally, bipolar electrical surface SEPs were recorded from adjacent electrode pairs (filled dots) placed under the Dewar area (dashed circle). Recordings of electric channels 1-4 are shown in Fig. 3.

©1999, Tohoku University Press
Recent Advances in Biomagnetism
T. Yoshimoto et al. (Eds)

Data were acquired continuously with 6 Hz - 500 Hz analog bandpass filtering and 4 kHz AD conversion rate. Responses upon left and right nerve stimulation were averaged separately off-line using weighted averaging algorithms [6]. For improvement of the signal-to-noise ratio optionally a digital 360 Hz low-pass filter was applied off-line. A least squares fit of an equivalent current dipole was performed. For each dipole position a confidence interval of 95% is given. The propagation pathway of the moving dipole was superimposed on conventional X-ray of the lumbar spine or on myelography. For comparison, electric Somatosensory Evoked Potentials (SEP) were recorded simultaneously with the tSEFs using bipolar electrode pairs (interelectrode distance 5 cm) placed over the proximal sciatic nerve and nerve roots (i.e. under the Dewar pick-up area). Additionally, conventional cortical SEPs, F-wave and H-reflex tests were performed.

Results:

Given the present experimental noise level (3 fT - 4 fT peak-to-peak in the averaged data) spinal magnetic fields of about 10 fT evoked upon tibial nerve stimulation were detected at the lower lumbar level in all three patients (Fig. 2: representative single channel record over the midline of os sacrum). It was possible to monitor the propagation of the tSEFs triggered on the left and right nerve stimulus, respectively, simultaneously and free of mutual interference. Hence, an intraindividual side-to-side comparison of spinal tSEF mappings and tSEF propagation in patients was obtained. In all three patients tSEF maps on the non-affected side showed a basically dipolar field configuration between 17 ms and 20 ms (Fig. 4: representative tSEF maps). tSEF propagation was monitored along plexus, nerve roots and cauda equina. On the affected side, however, propagating dipolar field patterns were detected only distal to the spinal transforaminal root entrance (Fig. 5); this was probably due to a partial block of conduction in nerve root fibers as indicated by SEPs, F-wave and H-reflex tests: simultaneously recorded lumbar SEPs (Fig. 3) showed similar amplitudes and latencies at the distal bipolar montage, whereas at the proximal recording site amplitudes in all three patients showed a decrement on the affected side. Cortical SEPs showed no latency differences, but a significant amplitude-decrement for the affected side. On the affected side H-reflex was either absent or showed pathological amplitude/latency values and tibial F-waves were pathologically delayed by 1.6 ms - 2 ms.

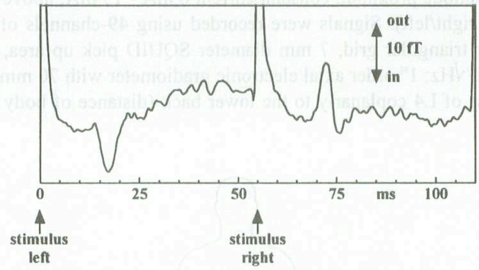

Figure 2:
One representative MNG channel over the midline of os sacrum (marked as m in Fig. 1). The peak latency of the tSEF was about 18 ms after left or right tibial nerve stimulation, respectively. Note the different field direction upon left (directed into the body) and right (outward) tibial nerve stimulation corresponding to the tSEF dipole pointing toward the spine. The stimulus artifact, caused by the electrical nerve stimulation, returned to baseline by 5 ms to 10 ms post stimulus and did not contaminate the signal.

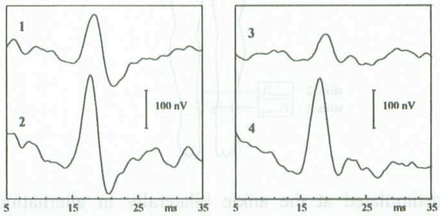

Figure 3:
Bipolar electrical surface recordings are shown from sequential electrode pairs (filled dots in Fig 1: 1, 2 left; 3, 4 right) placed at the lower back under the Dewar pick up area (patient 1 with rightsided S1 nerve root compression).

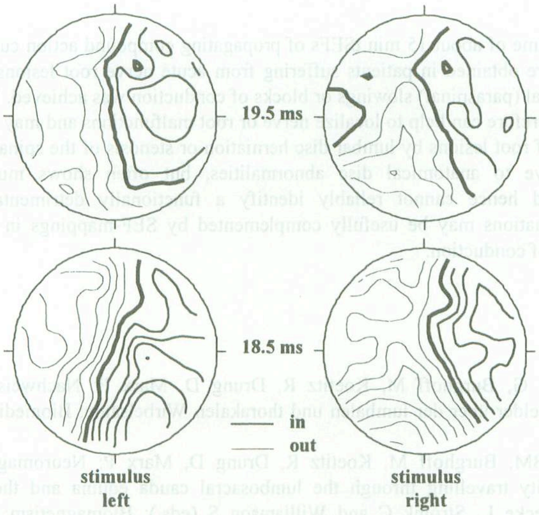

Figure 4:
Isofield maps of somatosensory magnetic fields recorded over the lower lumbar spine in patient 1 with a unilateral S1 root compression on the right side (isofield step 1 fT). tSEFs evoked upon left and right tibial nerve stimulation at the ankle are shown at two representative time points. Note that tSEF maps upon stimulation on the left (non-affected) side show a basically dipolar field configuration when propagating caudocranially. On the affected side, however, tSEFs could be interpreted in terms of a dipolar source only distal to the spinal transforaminal root entrance.

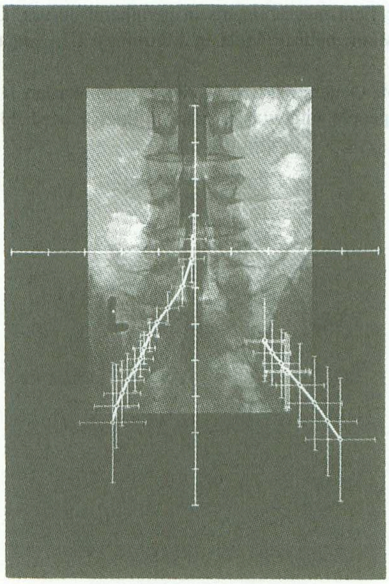

Figure 5:
Sequential positions of the moving dipole (X/Y-coordinates ± 95% confidence interval) in patient 1 with a S1 nerve root compression on the right side. Upon tibial nerve stimulation on the left side the propagation of the dipole (16.25 ms - 19.50 ms; time step 0.25 ms) could be localized up to the spinous process of L4, wheras on the right side (17.00 ms - 19.75 ms) the dipole propagation could be monitored only distal to the spinal transforaminal root entrance. XY-coordinates are superimposed on a lumbar myelography centered at the spinous process of L4. The depth of the dipole (Z) along the propagation pathway was calculated 9.5 cm - 12.7 cm under the sensor area.

Discussion:

With a registration time of about 15 min tSEFs of propagating compound action currents evoked upon bilateral tibial nerve stimulation were obtained in patients suffering from acute nerve root lesions. Using these tSEFs, a 3D-localization of focal proximal (paraspinal) slowings or blocks of conduction was achieved. This non-invasive tracing of neuromagnetic activities therefore can help to localize nerve or root malfunctions and may assist in guiding therapeutic interventions, e.g. in case of root lesions by lumbar disc herniation or stenosis of the spinal canal. Magnetic resonance imaging is highly sensitive to anatomical disc abnormalities, but often shows multiple protrusions even in asymptomatic subjects and hence cannot reliably identify a functionally detrimental bulging disc [7]. Thus electrophysiological examinations may be usefully complemented by SEF-mappings in such cases of circumscript proximal slowing or block of conduction.

References:

[1] Mackert BM, Curio G, Burghoff M, Koetitz R, Drung D, Marx P: Nachweis somatosensibel evozierter neuromagnetischer Felder über der lumbalen und thorakalen Wirbelsäule. Biomedial Engineering 38 suppl. 1: 201-202, 1993

[2] Curio G, Mackert BM, Burghoff M, Koetitz R, Drung D, Marx P: Neuromagnetic correlates of evoked somatosensory activity travelling through the lumbosacral cauda equina and thoracic spinal cord in man, Baumgartner G, Deecke L, Stroink C and Williamson S (eds.): Biomagnetism: Fundamental research and clinical applications, Amsterdam: Elsevier Science/IOS Press, 1995, pp 723-726

[3] Mackert BM, Curio G, Burghoff M, Marx P: Mapping of tibial nerve evoked magnetic fields over the lower spine. Electroenceph. clin. Neurophysiol. 104: 322-327, 1997

[4] Eisen A: The utility of proximal nerve conduction in radiculopathies: the cons. Electroenceph. clin. Neurophysiol. 78: 171-172, 1991

[5] Drung D: The PTB 83-SQUID system for biomagnetic applications in a clinic. IEEE Trans. Appl. Supercond. 5: 2112-2117, 1995

[6] Graebe T, Burghoff M, Steinhoff U, Mackert BM, Curio G: Identification of signal components by stochastic modelling in evoked magnetic field measurements in peripheral nerves, Ciarlini P, Cox MG, Pavese F and Richter D (eds.): Advanced Mathematical Tools in Metrology III, Singapore: World Scientific Publishing Comp., 1997, pp 178-185

[7] Jensen MC, Brant-Zawadzki M, Obuchowski N, Modic MT, Malkasian D and Ross JS: Magnetic resonance imaging of the lumbar spine in people without back pain. N. Engl. J. Med. 331: 69-73, 1994

Integration of Multimodality Pre-Operative Functional Mapping Data with Stereotactic Image-Guided Neurosurgery: A Correlative and Cost-effectiveness Study

Chong BW[1], McDonald JD[2], Lewine JD[1], Davis JT[1], Jones GM[1], Funke M[1], Burr R[2], McDonald P[2], Tsuruda J[1], Heilbrun MP[2], Orrison WW[1]

The Departments of Radiology[1] and Neurosurgery[2], University of Utah, Salt Lake City, Utah, USA

Introduction

The goal of complete surgical resection of brain tumors is often compromised by the potential for damage to eloquent cortex which is either involved by tumor or which resides in close proximity to the tumor margin. Discerning whether a tumor involves essential brain areas using standard anatomical criteria is fraught with potential for error either due to local variations in anatomical landmarks between subjects [1] or secondary to distortion of the anatomy by the tumor and associated mass effect [2-4]. The gold standard, intraoperative electrocorticography (ECoG), requires a craniotomy and therefore a commitment to a particular surgical approach. If there were a readily available method of determining if indeed eloquent cortex was involved before surgery was undertaken, then the risks and benefits of the treatment could be ascertained beforehand.

Non-invasive neurofunctional mapping techniques such as functional MRI (fMRI) and magnetoencephalography (MEG) have been employed for presurgical assessment of eloquent cortex in brain tumor patients both independently and together as multimodality neurofunctional mapping [5,6]. Various groups have reported integrating MEG brain mapping data into an image guided stereotactic neurosurgical device in order to facilitate neuronavigation at the time of surgical resection [7-8]. However, to our knowledge this is the first report of integration of multimodality functional brain mapping data into an image-guided stereotactic neurosurgical device.

Our objectives were: (1) To assess the utility of multimodality preoperative neurofunctional analysis with respect to presurgical planning, accuracy of gyral localization, and intraoperative resection, and (2) to assess the cost-effectiveness of preoperative neurofunctional analysis.

Methods:

MEG, and fMRI were used to preoperatively identify the central sulcus in five patients with brain tumors. Intraoperative stimulation was used to determine the validity of the noninvasive MEG and fMRI inferences.

For MEG, the magnetic signal evoked by median nerve stimulation was used to identify somatosensory cortex. In a single patient tongue somatosensory localization was achieved with tongue stimulation. Motor cortex was identified using a visually-cued finger movement paradigm. Responses were recorded with a 122-channel biomagnetometer. Data were analyzed using a multiple-dipole, spatio-temporal model. In fMRI, somatosensory stimulation was achieved by rubbing a toothbrush across the hand, and motor activation was achieved via alternating clenching of right and left hands while imaging with an echo-planar sequence at 1.5T. In a single patient tongue motor cortex was localized using a task involving sub-vocalizing the word "lollypop". The MEG and fMRI data were digitally registered within a stereotactic image-guided surgical device and correlated with intraoperative mapping results (also digitally registered).

Costs were defined as the charges related to the preoperative investigations (neurofunctional mapping, conventional anatomical imaging), the surgery (hospital, surgical and anesthesia charges), and the postoperative admission period (postoperative imaging, rehabilitation).

©1999, Tohoku University Press
Recent Advances in Biomagnetism
T. Yoshimoto et al. (Eds)

Results:

Tumor types included 4 oligodendrogliomas (low grade) and 1 glioblastoma multiforme. In all cases, the pre- and post-central gyri as identified by MEG agreed with the intraoperative identification. Disturbingly, data from fMRI were sometimes discordant. Specifically, motor function on fMRI was discrepant with intraoperative data by as much as one gyrus in one case (figure 1). This seems to indicate that for some subjects, despite employing a "motor" task, the main fMRI activation was in the somatosensory cortex.

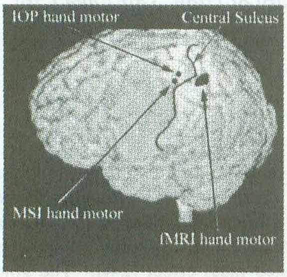

Figure 1: 25 year old male with a benign oligodendroglioma. The tumor is manifest by the distorted surface of the brain anterior to the central sulcus. Pre-operative mapping with fMRI indicated that the motor cortex was one gyrus posterior to the location mapped with MSI. ECoG mapped motor cortex to the same location as MSI (apparent separation of points is due the parallax effect of projecting a deep MSI point to the cortical surface).

In 2 patients presurgical neurofunctional mapping indicated that the motor cortex was involved by tumor. Subsequently, management of the 2 patients was altered and they underwent stereotactic biopsy only. Accuracy of localization in one patient was confirmed by the fact that the patient suffered a transient motor deficit after biopsy. The second patient has had new onset focal motor seizures confirming clinically that the tumor involves motor cortex.

The patient (SM) in whom there was discordant localization of the motor cortex with MEG and fMRI, underwent a craniotomy with ECoG confirming that motor cortex was involved by tumor as indicated by MEG. Therefore, the lesion was biopsied and not resected.

There were two patients where mapping excluded involvement of the primary motor or somatosensory cortex. Preoperative neurofunctional mapping confirmed that the tumor was anterior to the primary motor cortex in one patient and posterior to the post-central gyrus (somatosensory cortex) in another. Both patients underwent gross total resection of their benign oligodendrogliomas.

Pre-operative functional mapping decreased costs by as much as 35% (Table 1). Cost savings were realized when a patient's functional mapping data indicated that biopsy rather than resection should be performed (because the tumor invaded motor cortex). We compared the cost savings between one patient (CC) in whom neurofunctional mapping indicated that motor cortex was involved (sterotactic biopsy only) with the patient (SM) who had discrepant mapping results (open craniotomy with ECoG followed by biopsy only) (Table 1). Our rationale was that each patient had an identical tumor (oligodendroglioma) but one had successful neurofunctional mapping which indicated that stereotactic biopsy through a burr hole was appropriate. Cost savings were predominantly due to reduced hospital stay in the patient who underwent stereotactic biopsy only.

Discussion:

The impetus for this work originated from the variable experiences of mapping brain function with multiple modalities and the desire to compare the results of the different mapping techniques in an objective fashion. We also believed that our preoperative mapping efforts were making a difference in the management of patients with brain tumors and therefore wanted to document the treatment decisions that were effected by the mapping results as well as the impact on the cost of care.

Integration of MEG and fMRI neurofunctional mapping data into an image-guided stereotactic neurosurgical device in which the ECoG data is similarly registered, provides a method for objective assessment of the accuracy of localization of our mapping techniques. On a practical level, integration of the mapping data allowed the surgeon to manipulate the plane of viewing the data so as to determine the location of the surgical wand relative to fMRI and MEG localized sources on a single image (Figure 2).

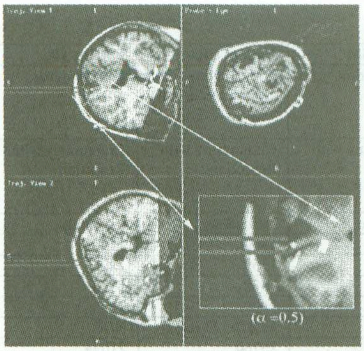

Figure 2: *42 y/o female with a benign oligodendroglioma. The mapped points have been digitally registered into a neuronavigational system. White dot = intraoperative finger contraction. White bar = MEG hand somatosensory. White ovoid = fMRI hand motor.*

The neuronavigational capability provided by having the neurofunctional mapping data as digitalized coordinates in the stereotactic image-guided system, allows the surgeon to pursue an aggressive resection with a view to total resection and potential cure. The two patients who did not have involvement of primary sensory or motor cortex by neurofunctional mapping and then went on to total resection, demonstrated postoperative deficits that resolved in 4-6 weeks. The deficits were attributed to aggressive resection in the supplementary motor cortex and the sensorimotor association cortex in each of the respective patients. One patient has returned to her preoperative deficit baseline, while the other patient has residual mild decreased sensation in his right hand and foot but has returned to work. Neither patient has demonstrated evidence of tumor recurrence at 3 months follow-up. We anticipate that the incidence of postoperative deficits in this population of patients will be high relative to a patient with a similar tumor and location who does not have neurofunctional mapping. Resection of brain tumors without the benefit of mapping is less aggressive and therefore less likely to yield a postoperative deficit. We are presently reviewing our data obtained prior to having neurofunctional mapping capability in order to confirm our hypothesis.

Neurofunctional mapping provided the surgeon and the patient with the essential data required for planning treatment options. That is, the patient no longer had to commit to an open craniotomy without knowing whether resection of the tumor was possible. Mapping indicated in 2 patients that the tumor involved eloquent cortex and therefore surgical resection was contraindicated and the patients underwent stereotactic biopsy through a burr hole. The resulting reduction in costs was due predominantly to a reduction in length of hospitalization. Prior to the availability of preoperative neurofunctional mapping, such patients would have undergone an open craniotomy and ECoG at greater cost to the health care system. Further reduction in costs could be realized when functional mapping helped surgeons to avoid induction of hemiparalysis by re-direction of the surgical approach away from motor cortex.

The mis-mapped localization of motor cortex with fMRI is disturbing. Similar results have been reported by others [9]. Interestingly, in the MEG motor task, the post-movement response from somatosensory cortex was usually of greater magnitude than the pre-movement activity from motor cortex. But, in MEG, the temporal information clearly allowed for distinction between the motor and somatosensory components. It is plausible that with fMRI, the somatomotor response predominates and therefore localizes the motor task to the post-central gyrus. This is supported by PET measurements of regional cerebral blood flow where greater changes in rCBF are seen with sensorimotor activation paradigms than with passive sensory-only paradigms [10,11]. The finding that fMRI may yield ambiguous results requires awareness and caution when interpreting preoperative localization data and emphasizes the importance of multimodality correlation.

Conclusions:

1. Preoperative neurofunctional mapping changes management (eg biospy vs. resection)
2. Integration of MEG and fMRI mapping data into an image-guided stereotactic neurosurgical system allows objective correlation of the localization points with ECoG.
3. Integration allows more aggressive resection and therefore may result in a higher incidence of short-term deficits. It is anticipated that the more aggressive resections of benign tumors may result in greater short term costs (rehabilitation therapy for deficits) but increased long-term survival.
4. Reduction in costs may be seen with preoperative neurofunctional mapping primarily due to a shift from open craniotomy and ECoG to stereotactic biospy with a resultant reduction in hospital stay.

Table 1

	Patient CC	**Patient GH**	**Patient SM**	**Patient PR**	**Patient JB**
Tumor	Oligodendro-glioma	Glioblastoma	Oligodendro-glioma	Oligodendro-glioma (recurrent)	Oligodendro-glioma
Surgical Procedure	Stereotactic Biopsy	Stereotactic Biopsy	Craniotomy with Biopsy	Craniotomy with Resection	Craniotomy with Resection
fMRI	none	none	No charge	No charge	No charge
MEG	1500	1500	1500	1500	1500
MRI	1182	1228	1228	1359	1228
Surgery	5302	5302	5912	7538	7538
Anesthesia	980	1015	1820	2100	2205
Rehabilitation	N/A	N/A	N/A	**34,070 (23 days)**	N/A
Hospital	10,563	9268	19530	25764	21694
Length of stay	**1 day**	1 day	**2 days**	5 days + 23 days	4 days
Post-op MRI scan	N/A	N/A	N/A	1760	1760
TOTAL CHARGES	**$19,527***	**$18,313**	**$29,990****	**$69,091**	**$34,925**

Hospital charges: The difference in charges between patients SM** and CC* total $10,463 (35%). This difference is due mainly to the additional hospital stay (1 day) and slightly prolonged anesthesia charge associated with a craniotomy for biopsy. Also note that Patient PR underwent aggressive resection of a recurrent oligodendroglioma and subsequently had a post-operative deficit requiring prolonged rehabilitation. At 2 months follow-up she has returned to her pre-operative baseline with minor left arm and leg weakness and no evidence for recurrence of her oligodendroglioma.

References:

1. Sobel DF, Gallen CC, Schwartz BJ, et al. Locating the central sulcus: comparison of MR anatomic and magnetoencephalographic functional methods. Am J Neuroradiol 14:915-925,1993
2. Gallen CC, Sobel DF, Waltz T, et al. Non-invasive presurgical neuromagnetic mapping of somatosensory cortex. Neurosurgery 33:260-268,1993
3. Orrison WW. Non-invasive preoperative cortical localization by magnetic source imaging. Am J Neuroradiol 13:1124-1128,1992
4. Orrison WW, Davis LE, Sullivan GW, et al. Anatomic localization of cerebral cortical function by magnetoencephalography combined with MR imaging and CT. Am J Neuroradiol 11:713-716,1990
5. Jack CR Jr.,Twomey CK, Zinsmeister AR, et al. Sensory motor cortex: correlation of presurgical mapping with functional MR imaging and invasive cortical mapping. Radiology 190:85-92,1994
6. Pujol J, Conesa G, Deus J, et al. Presurgical identification of the primary somatosensory cortex by functional magnetic resonance imaging. J Neurosurg 84:7-13,1996
7. Rezai AR, Mogilner AY, Cappell J, Hund M, Llinas RR, Kelly PJ. Integration of functional brain mapping in image-guided neurosurgery. Acta Neurochir Suppl (Wein) 68:85-89,1997
8. Ganslandt O, Steinmeier R, Kober H, et al. Magnetic source imaging combined with image-guided frameless sterotaxy: a new method in surgery around the motor strip. Neurosurgery 41:621-627,1997
9. Lee CC, Jack CR, Reiderer SJ. Mapping of the central sulcus with functional MR: active vs. passive activation tasks. Am J Neuroradiol 19:847-852,1998
10. Gelmers HJ. Cortical organization of voluntary motor activity as revealed by measurement of regional cerebral blood flow. J Neurol Sci 52:149-161,1981
11. Fox PT, Raichle ME. Focal physiological uncoupling of cerebral blood flow and oxidative metabolism during somatosensory stimulation in human subjects. Proc Natl Acad Sci USA 83:1140-1144,1986

Magnetoencephalography (MEG) Reveals Focal Pathology in Patients with Cerebral Ischemia

Fuchs O[1], Wildermuth S[1], Ille N[1], Stippich C[2], Scherg M[1]

Dept. of Neurology, Sect. of Biomagnetism[1], University of Heidelberg, Heidelberg, Germany;
Dept. of Neuroradiology[2], University of Heidelberg, Heidelberg, Germany

Introduction

Pathologic brain activity in patients with cerebral ischemia is a widely discussed topic in electroencephalography [1] and magnetoencephalography (MEG) [2,3,4,5]. In the MEG literature, mostly case reports with abnormal focal slow wave activity have been described. Analysis methods have been mainly concerned with identifying epochs of increased oscillatory activity in the δ and ϑ frequency bands [2,3,4,5,6]. Dipoles were fitted in the selected epochs and then subjected to cluster [4,5,6] or dipole density analysis [2,3] if exceeding specific thresholds.

The aim of our study was to develop a procedure for the reliable detection of focal abnormal MEG activity in patients with cerebral ischemia. The procedure was to have a minimum degree of observer bias. It should be easy to handle and not too time consuming to be feasible in a clinical routine setting. Our basic approach was to detect the slow wave activity emerging from an ischemic focus directly over the involved brain region at the sensor plane of a whole-head planar gradiometer system (Neuromag-122™) using a measure of spectral power for each sensor chip. For this, we developed a quantitative technique, spectral power distribution analysis (SPDA) to assess focal abnormalities in MEG spectral power in patients with circumscribed ischemic brain lesions and patients with transient ischemic attacks (TIA) in comparison to a control group.

Methods

We examined a control group of 25 subjects (15 males and 10 females, mean age 41.2, range 22-82) without pre-existing neurological disease. The patient group included 25 subjects (10 males and 15 females, mean age 48.8, range 22-79). 18 patients had manifest stroke and seven transient ischemic attacks (TIA). All patients had cranial computed tomography (CCT) or magnetic resonance imaging (MRI) that were read by staff neuroradiologists. The patients with manifest strokes had lesions in the territory of the middle cerebral artery, eleven in the left, seven in the right hemisphere. Morphological changes in all patients with manifest stroke were concordant with their clinical symptoms. CCT/MRI scans of all patients with TIA were considered normal. Of the seven patients with TIA, four showed definite left hemispheric signs, while three did not reveal any definite hemispheric signs (Tab. 1). All subjects gave their written informed consent to the examinations.

MEG measurements were performed within ten days after the onset of neurological symptoms with a Neuromag-122™ whole-head MEG system (Neuromag Ltd., Picker International Inc.). This planar gradiometer system has maximum sensitivity for tangential currents in the brain region directly below each sensor chip [7]. Signals were sampled at 320 Hz and filtered from 0.1 Hz to 80 Hz. Subjects were seated in a magnetically shielded room with head fixation by a custom-made pneumatic device. Electrocardiogram (Einthoven II) and the vertical and horizontal electro-oculograms were recorded simultaneously. Brain activity was recorded in two conditions, with eyes opened and closed, over a period of ten minutes each. During the measurement with open eyes, subjects had to watch a silent movie for control of attention. In the later analysis, only the data of the eyes closed condition were used, since they were less contaminated by artifacts.

Prior to spectral power distribution analysis (SPDA), MEG recordings were visually scanned using the MEGFOCUS program (MEGIS Software GmbH) to mark epochs with artifacts. Power spectra were calculated using the fast Fourier transformation over $\cos^2$-windowed epochs (duration 1.6 seconds) and averaged over each condition in overlapping steps of 0.8 seconds excluding epochs with artifacts. Mean power was summed over six predefined frequency bands (δ: 0.5-4 Hz, ϑ_1: 4-6 Hz, ϑ_2: 6-8 Hz, α: 8-14 Hz, β_1: 14-20 Hz, β_2: 20-35 Hz) and across the sensors of seven regions of interest (ROIs) over each hemisphere. These seven ROIs covered all supratentorial vascular territories: frontal (anterior cerebral artery), fronto-temporal, centro-temporal, lateral-temporal, centro-parietal (predominantly medial cerebral artery), temporo-occipital, occipital (posterior cerebral artery). For visualization (Figs. 1, 2), power was normalized relative to the mean over the corresponding hemisphere. Power differences between homologous ROIs were displayed as positive values on the side of greater power. Thus, decrease in power on one side, e.g. in the β band, will appear as an increase at the opposite ROIs.

©1999, Tohoku University Press
Recent Advances in Biomagnetism
T. Yoshimoto et al. (Eds)

For quantitative analysis, consideration of mean and relative power in bands as well as hemispheric differences was achieved by calculating the following logarithmic parameters:

(1) $A = \ln[(|\delta_R - \delta_L| + \delta_{mean}) / (|\beta_R - \beta_L| + \beta_{mean})]$

(2) $B = \ln[(|\delta_R + \vartheta_{1\,R} - \delta_L - \vartheta_{1\,L}| + \delta_{mean} + \vartheta_{1\,mean}) / (|\beta_R - \beta_L| + \beta_{mean})]$

(ln = natural logarithm , R / L = power values of ROIs in right / left hemispheres)

Parameter A reflects the relative power in the δ band alone, while parameter B includes frequencies up to 6 Hz (lower ϑ band) normalized by the total power in the β band. Both parameters A and B reflect hemispheric differences and are symmetric in the right and left hemisphere. Thus, they were obtained for each ROI over the right hemisphere only, and the maximum value over the seven ROIs was selected for each subject and displayed in a scatterplot to analyze group differences and to determine a threshold of abnormality (Fig. 3). The abnormal side was defined by the greater slow wave power in the 0.5-6 Hz range.

Results

Using visual evaluation of the SPDA diagrams, we found the spectral power distribution to be symmetric between corresponding brain regions in 24 healthy control subjects. An increase in power across all frequency bands was found at the left lateral-temporal ROI in an 82-year old control subject. This increase was caused by heart cycle related magnetic field artifacts.

In 22 of 25 patients a focal increase in power at one to three ROIs was detected in the δ and/or ϑ bands by visual inspection (Figs. 1, 2). The locations of the ROIs were consistent with neurological and radiological findings in all 18 patients with manifest stroke. Of the seven patients with TIA, all four patients with definite hemispheric signs showed a focal increase in the SPDA diagrams. In contrast, the three patients with TIA and missing definite hemispheric signs had normal power distributions. In all patients, the increase in δ and ϑ spectral power appeared to be accompanied by a decrease in β power. Because heart cycle related activity caused concurrent increase over all frequency bands, left temporal foci in patients with cerebral ischemia could be separated from these artifacts by considering the ratio of δ and/or ϑ versus β power.

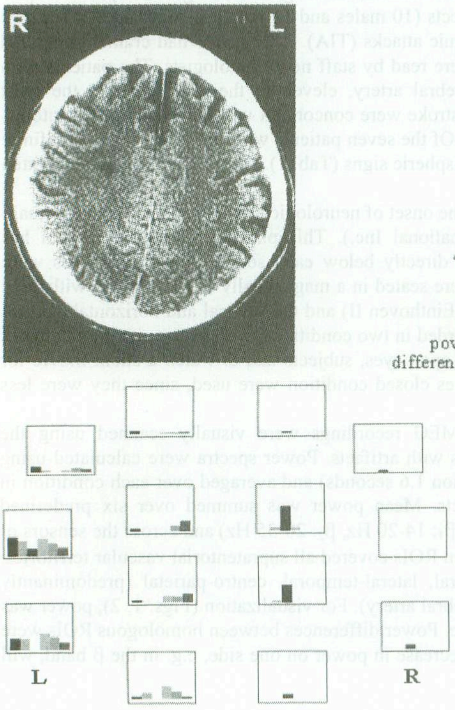

Fig. 1. CCT scan and SPDA diagram of a patient with a right high parietal ischemic infarction

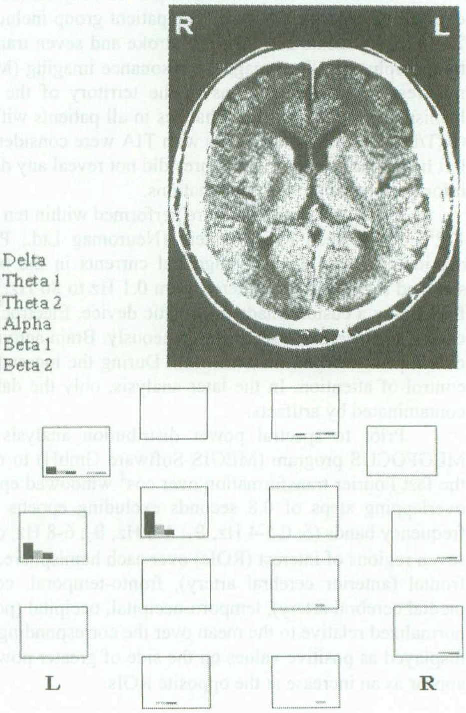

Fig. 2. CCT scan and SPDA diagram of a patient with transient aphasia

Fig. 1 displays a circumscribed lesion visible in the CCT scan of a patient with a right hemispheric stroke. The spectral power distribution diagram shows a prominent ϑ focus over the corresponding high parietal brain region. The concurrent decrease in β power appears as an increase at the contralateral ROIs due to the plotting of positive hemispheric differences. Heart cycle related artifacts are visible as an increase in power in all frequency bands over the left temporal ROIs. Fig. 2 presents the SPDA data of a patient with TIA who had transient aphasia and a normal CCT scan. The SPDA diagram of this patient shows a prominent increase in δ and ϑ power over the left temporal (central and lateral) ROIs accompanied by a weak decrease in β power (visible as an increase at the contralateral ROIs). MEG was recorded in both patients four days after the onset of symptoms.

Quantitative evaluation of the maximum parametric values A and B (equations 1 and 2) over the right in comparison to the left hemispheric ROIs revealed clear-cut differences between the patient and control groups (Tab. 1, Fig. 3). Parameter B separated the 25 controls from all 18 patients with manifest stroke. Also, the four patients with TIA and definite hemispheric signs had B values above the threshold of 17.8 ln (fT/cm)^2. The three patients with TIA with missing hemispheric signs had normal B values (Fig. 3). The relative power in the δ frequency band alone (parameter A) did not fully separate the groups, but was highly correlated with parameter B. Parameter B evaluated power in an extended frequency range of 0.5-6 Hz (r=0.92). The healthy subject with the left temporal increase in power over all frequency bands due to cardiac artifacts had normal parameters A and B.

Tab. 1. Number of subjects in each group and SPDA results

group	Control	Stroke	TIA	
		with focal CCT or MRI lesion	with definite hemispheric signs	without definite hemispheric signs
number	25	18	4	3
normal SPDA	25	0	0	3
abnormal focal SPDA	0	18	4	0

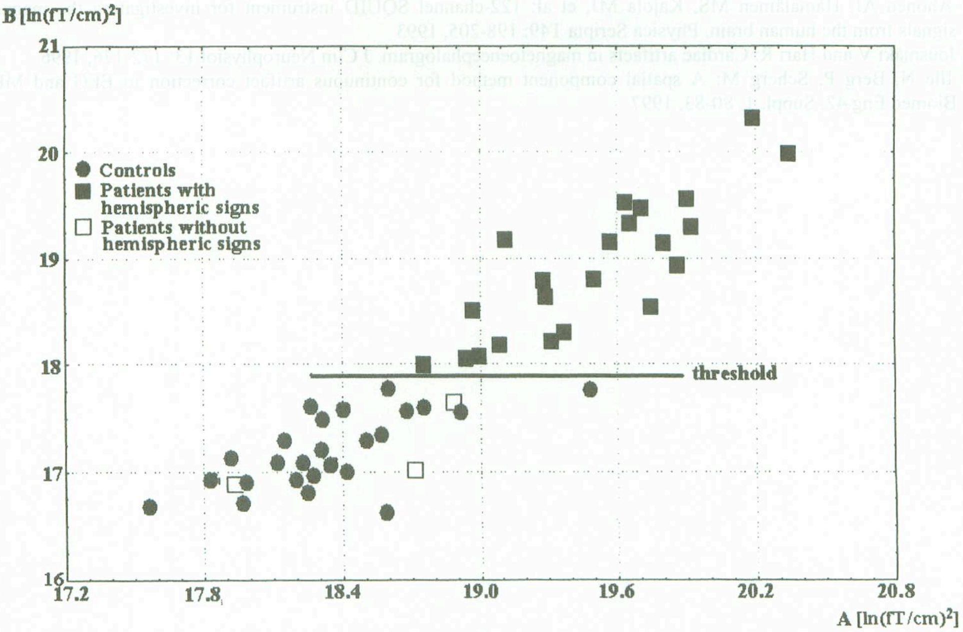

Fig. 3. Scatterplot of transformed relative δ power (parameter A) versus $\delta+\vartheta_1$ power (parameter B)

Discussion

Spectral power distribution analysis detects abnormal brain activity in patients with cerebral ischemia with a sensitivity comparable to or higher than other more time consuming MEG analyzing techniques [2,3,4,5,6]. MEG acquisition and analysis takes approximately two hours and thus proves feasible in a routine clinical setting. The derived parameter B presents a possible objective criterion for the definition of abnormal focal MEG power in patients with cerebral ischemia. Furthermore, it can confirm the presence of hemispheric brain pathology in patients with TIA having normal CCT/MRI scans. The patients without clear hemispheric signs and normal SPDA could possibly have suffered from transient brainstem ischemia which may not be detectable by MEG.

The presented new quantitative analysis technique can be interpreted to have both a high sensitivity (>95%) and an excellent specificity (>96%) for the separation of patients with definite hemispheric signs on one side and control subjects and patients without hemispheric signs on the other. In the present study, the number of patients with TIA is still too small to establish this technique as a diagnostic tool for the objective verification of transient hemispheric signs.

Heart cycle related magnetic fields are a limiting factor in the interpretation of MEG data [8]. The effect of these cardiac artifacts has been reduced in SPDA by considering power ratios rather than absolute power values in the parameter equations. Further improvements could be expected when applying artifact correction techniques recently developed in our laboratory [9] to the continuous MEG data prior to SPDA.

Spectral power distribution analysis of whole-head MEG data could become a quick and reliable procedure for the assessment of abnormal brain activity in patients with transient ischemic attacks. Thus, MEG could help to identify patients who will benefit from therapeutic interventions aimed at preventing infarction.

References

[1] Faught E: Current role of electroencephalography in cerebral ischemia. Stroke 24: 609-613, 1993

[2] Vieth JB: Magnetoencephalography in the study of stroke (cerebrovascular accident). Sato S (ed): Advances in Neurology, Vol.54: Magnetoencephalography. New York: Raven Press, 1990, pp 261-269

[3] Vieth JB, Sack G, Kober H, et al: Magnetoencephalography, a method to localize clinically silent transient ischemic attacks (TIA) using an improved dipole-density-plot. Biomed Eng 36, Suppl. 1: 155-156, 1991

[4] Vieth JB, Kober H and Grummich P: Sources of spontaneous slow waves associated with brain lesions, localized by using the MEG. Brain Topogr 8: 215-221, 1996

[5] Lewine JD, Orrison WW Jr, Astur RS, et al: Explorations of pathophysiological spontaneous activity by magnetic source imaging. Baumgartner C et al (eds): Biomagnetism: Fundamental research and clinical applications. Amsterdam: Elsevier/IOS Press, 1995, pp 55-59

[6] Rieke K, Gallen CC, Sobel DF, et al: Magnetic source imaging in cerebrovascular diseases. Baumgartner C et al (eds): Biomagnetism: Fundamental research and clinical applications. Amsterdam: Elsevier/IOS Press, 1995, pp 46-49

[7] Ahonen AI, Hämäläinen MS, Kajola MJ, et al: 122-channel SQUID instrument for investigating the magnetic signals from the human brain. Physica Scripta T49: 198-205, 1993

[8] Jousmäki V and Hari R: Cardiac artifacts in magnetoencephalogram. J Clin Neurophysiol 13: 172-176, 1996

[9] Ille N, Berg P, Scherg M: A spatial component method for continuous artifact correction in EEG and MEG. Biomed Eng 42, Suppl. 1: 80-83, 1997

SURGERY IN AND AROUND ELOQUENT AREAS USING PRECISE FUNCTIONAL MAPPING WITH MEG AND INTRAOPERATIVE MONITORINGS, ESPECIALLY FOR GLIOMAS

Kayama T, Sakurada K, Sato S, Kuroki A and Saito S

Department of Neurosurgery, Yamagata University School of Medicine, Yamagata, Japan

INTRODUCTION

Classical anatomical functional mapping is insufficient to perform precise and safe resection of lesions adjacent to the cerebral eloquent areas. We have made use of magnetoencephalography (MEG) to detect sensorimotor, auditory and visual cortices and the intraoperative monitorings such as motor evoked potential (MEP) and somatosensory evoked potential (SEP) to prevent morbidity. We would like to focus this time about the usefulness of the MEG for the surgical resection of cerebral gliomas in and around the eloquent areas.

METHOD

Subjects are 62 patients with cerebral gliomas experienced during 4 years since May, 1994. Seventeen patients with gliomas those were diffuse and uncircumscribed on magnetic resonance (MR) imaging and advanced on admission were subjected to only stereotactic biopsy or no surgery. Thus, 45 patients underwent open surgical removal.

We have defined the eloquent cortices as the motor, sensory, speech and visual cortices excluding the thalamus or the brainstem. Patients with gliomas in and around the eloquent cortices underwent the MEG and the intraoperative monitoring such as SEP and MEP [2]. Functional brain mapping was obtained with MRI-linked whole head MEG system [4].

With the results of the SEP and MEP and in some cases with the wake-up surgery using Propofol, we could confirm the central sulcus, the primary sensori-motor cortex and the speech areas. With these results and the MEG information, we could design the area to be resected. The amplitude of the MEP was monitored during the removal of the lesions adjacent to the motor cortex, especially when dividing the precentral sulcus and the subcortical area.

Especially for those patients with gliomas, the results of the MEG, the classical anatomical measurements of the central sulcus and the operative results were compared to find out the preciseness and the usefulness of the MEG for lesions adjacent to but not involving the eloquent cortices.

RESULT

Gliomas in and around the eloquent cortices were 28 in those 62 gliomas (45 %) and were 24 in the 45 cases underwent surgical removal (53 %). Thus, the operated rate of the lesions in and around eloquent cortices was 86 % (=24/28). Total or subtotal removal of the tumor, that is defined as the removal over 95 % of the tumor bulk, were achieved in 18 out of the 24 cases with gliomas in and around the eloquent areas.

MEG were examined in 15 patients with gliomas, while 36 patients underwent the MEG during these four years. Total or subtotal removal was performed in 13 (86.7 %) among 15 cases with lesions in and around the eloquent areas and with the MEG examination.

Motor function deficit did not occur or the morbidity was mild and transient when the MEP amplitude was unchanged or 50% and larger of the baseline amplitude. The amplitude decreased less than 50 % in 1 patients among 15 patients with gliomas adjacent to the eloquent areas and with the MEG examination. The glioma was quite invasive at the subcortex. The patient needed a rehabilitation to walk.

In 10 of 15 patients with gliomas adjacent to the eloquent areas and with the MEG examination, the MRIs and

©1999, Tohoku University Press
Recent Advances in Biomagnetism
T. Yoshimoto et al. (Eds)

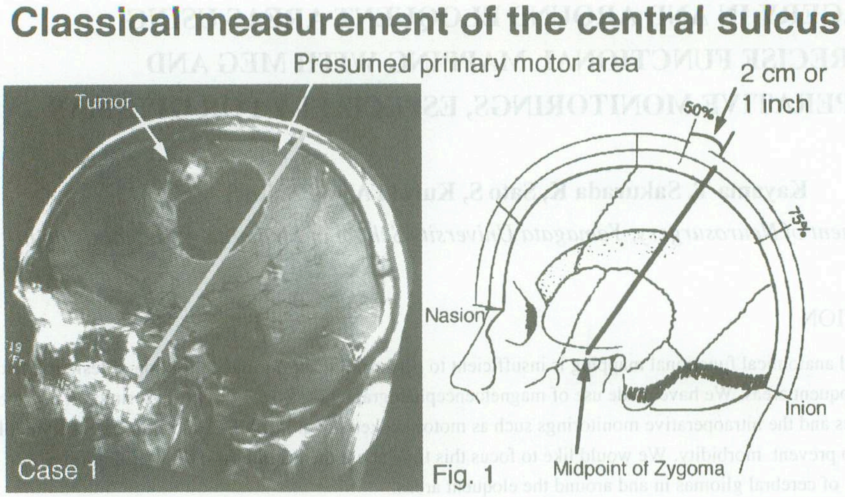
Classical measurement of the central sulcus
Presumed primary motor area
2 cm or
1 inch
50%
75%
Tumor
Nasion
Inion
Case 1
Fig. 1
Midpoint of Zygoma

Fig.1 Sagittal T1 weighted MRI with Gd was superimposed with the lateral view of right cerebral angiography. The gray line is the presumed central sulcus according to the method shown in the right figure.

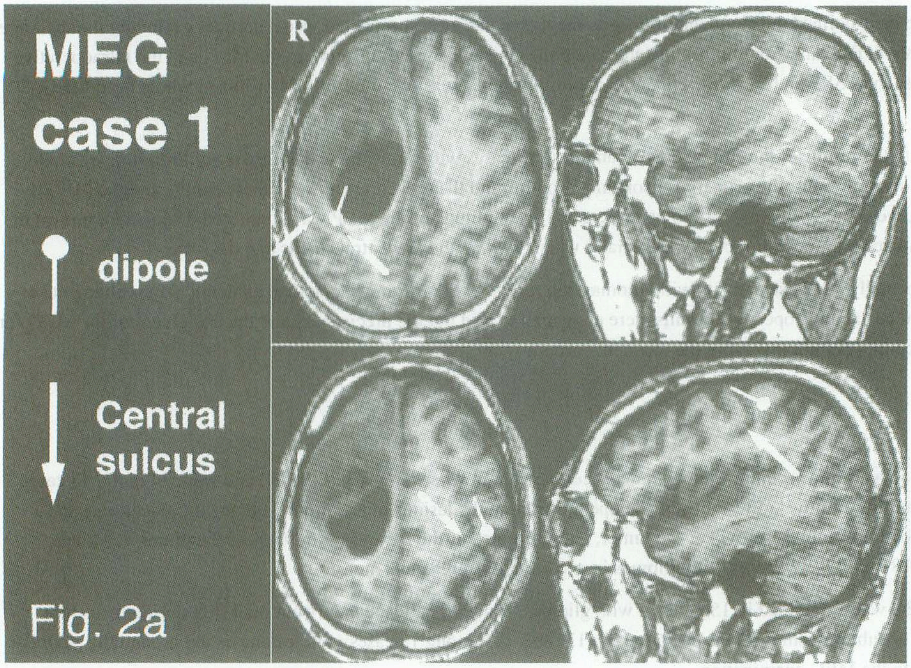

Fig. 2a MRI-linked MEG system showed that the posterior border of the glioma situated just anterior to the motor cortex, compressing it posteriorly.

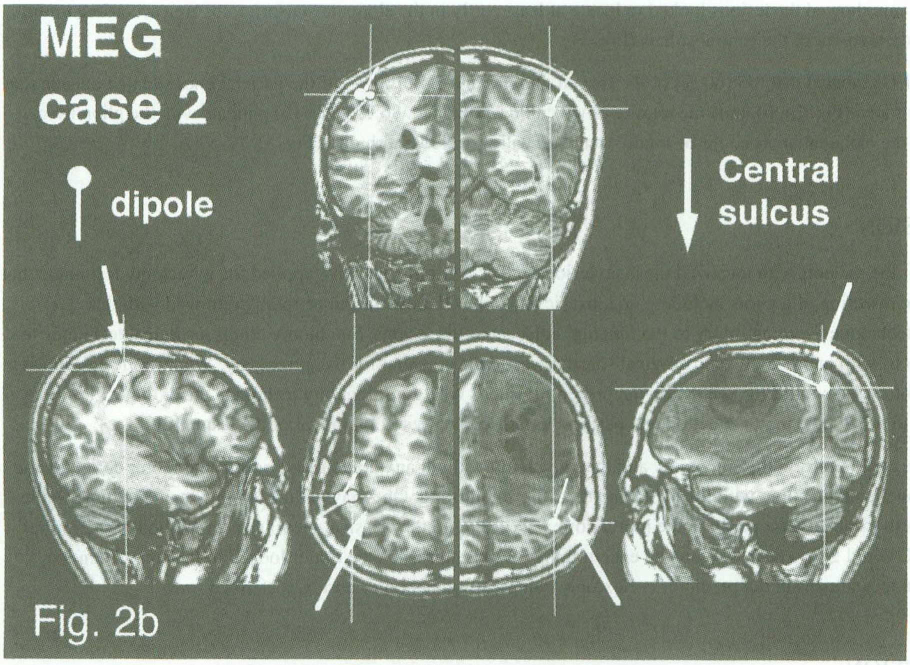

Fig. 2b

Fig. 2b MRI-linked MEG system showed that the glioma extended to posterior part of the premotor cortex, compressing the motor cortex posteriorly.

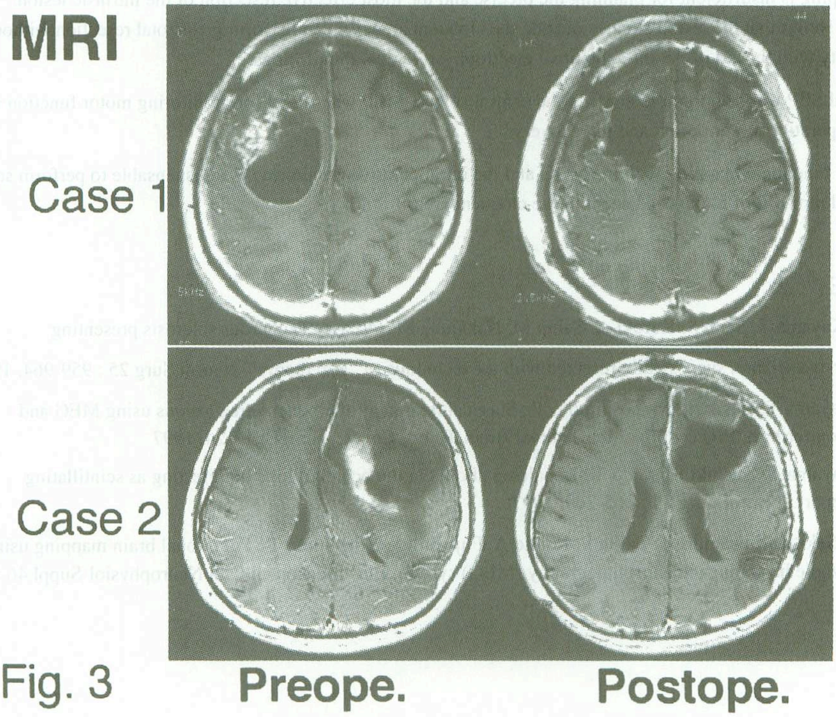

Fig. 3

Fig. 3 The pre- & postoperative MRIs showed the total removal of the tumor sparing the motor cortex.

the angiograms showed the lesions looked to locate at least partly in the eloquent sensorimotor area according to the classical measurement of the central sulcus (Fig. 1).

MEG revealed that 3/5 (60 %) of the frontal gliomas and 5/5 (100 %) of the parietal ones situated outside the sensorimotor area (Fig. 2a, b), thus the total removal could be planned. 86.7 % (13/15) patients with the gliomas in and around the eloquent areas could be totally removed with very low morbidity (Fig. 3).

DISCUSSION

For the patients with localized intrinsic lesion such as a glioma, we have applied the gyrectomy technique that is an en bloc resection of a gyrus including an intrinsic lesion [1, 3]. Glioma can be totally removed with this gyrectomy technique avoiding injury to the function adjacent to the lesions. Sulcotomy that is a surgical technique to divide a sulcus with meticulous microsurgical sharp dissection is essential for the gyrectomy. When the lesion situates in the premotor area or anterior, we divide the precentral sulcus with the sulcotomy technique under the MEP monitoring to protect the motor function and perform macroscopically total removal of the lesion [2].

We could perform the sulcotomy and the gyrectomy without anxiety to cause permanent motor deficit by the results of functional mapping with the MEG and the MEP monitoring. One may not try to remove all the tumor bulk which looks to locate at least partly in the motor cortex according to the classical measurement method of the central sulcus. MEG could give a neurosurgeon an encouraging information when the tumor looked to locate in the motor cortex but in fact situates in the premotor cortex only compressing the motor cortex posteriorly.

CONCLUSION

MEG can provide us important information of the cerebral eloquent areas for planning surgery. Classical anatomical mapping is insufficient for planning the precise and the most effective resection of the intrinsic lesion. When the MEG shows that the lesion situates outside the eloquent area, we can perform gross total resection without causing morbidity with the aid of the intraoperative electrophysiological monitorings.

Cortical SEP was important to confirm the central sulcus. MEP was useful for monitoring motor function and predicting postoperative motor deficit and its recovery.

Precise functional mapping with the MEG and the intraoperative monitoring is indispensable to perform safe and sure surgical removal of gliomas adjacent to the eloquent areas.

REFERENCE

[1] Kokubo Y, Kayama T, Saito S, Kuroki A, Saino M, Nakajima M : A case of tuberous sclerosis presenting intractable adversive seizure, successfully resected with the technique of "gyrectomy". Neurol Surg 25 : 959-964, 1997

[2] Kuroki A, Kayama T, Nakasato N, Yoshimoto T : Surgical treatment of eloquent area lesions using MEG and intraoperative monitorings. Proceeding of the Tohoku Brain Tumor Conference 31 : 17-24, 1997

[3] Maruya J, Kayama T, Kuchiki H, Ando T : Localized glioma in the occipital lobe manifesting as scintillating scotoma : case report. Neurol Surg 25 : 265-269, 1997

[4] Nakasato N, Seki K, Kawamura T, Fujita S, Kanno A, Fujiwara S, Yoshimoto T : Functional brain mapping using an MRI-linked whole head magnetoencephalography (MEG) system. Electroencephal Clin Neurophysiol-Suppl 46 :119-126, 1996

Recordings of SEF and AEF in Patients of Cerebrovascular Diseases using a 61-channel MEG System Cooled by a Cryocooler

Kubo T[1], Suzuki A[1], Yoshioka K[1], Nishimura H[1], Nagata K[1], Yoshida T[2], Kang YM[2]

Research Institute for Brain and Blood Vessels-Akita[1], Akita, Japan
MEC Laboratory[2], Daikin Industries, Ltd., Tsukuba, Japan

Introduction

We recorded SEF and AEF in patients of cerebrovascular diseases using a 61-channel MEG system cooled by a cryocooler, which was developed by the technology of MEC Laboratory in Daikin Industries[1-4]. In this system, the superconducting coils are cooled by a cryocooler without using liquid helium. The electromagnetic noise generated from the cryocooler can be reduced by using a digital noise subtraction process[4]. The sound noise generated by the twitching of helium gas and movement of the displacer cannot be suppressed. Before applying our MEG system for patients, we evaluated the effect of sound noise by estimating the accuracy of source localization, and confirmed that the effect of sound noise was small.

Clinical Material and Methods

We recorded SEF and AEF in ten patients of cerebrovascular diseases. However, both of SEF and AEF were not recorded in four patients due to direct damage of somatosensory and auditory areas by the cerebrovascular accident. Thus, those four patients were excluded from the study. The patient population consisted of two males and four females aged between 43 and 86 years (average 68 ± 14 years). All patients were attacked by cerebral infarction without direct damage of the somatosensory and auditory areas. SEF and AEF were recorded in the subacute stage. Table 1 shows clinical signs in patients.

Case	Age	Sex	Side of Infarction	Level of Consciousness	Motor Disturbance	Sensory Disturbance	Others
1	72	F	Lt	Alert	None	None	Aphasia, mild
2	86	M	Rt	Alert	Mild	None	
3	67	F	Rt	Alert	None	None	TIA
4	66	F	Lt	Alert	None	Mild	
5	43	M	Rt	Alert	Moderate	Moderate	
6	74	F	Lt	Alert	None	Unknown	Aphasia, severe

Table 1 Clinical signs in patients.

SEF was recorded by the random stimulation of the median nerve. The electrical stimuli (intensity; thumb twitch, duration; 0.2 msec., constant-current) were delivered to the unilateral median nerve. From the contralateral hemisphere to the stimulation side, SEF was recorded by averaging 450 responses. The estimation of the location of generator source of N1m and P1m was carried out, and the dipole moment was calculated.

AEF was recorded by the random stimulation of the unilateral ear. The tone burst (intensity; 90 dB, raise; 10 msec., plateau; 50 msec., fall 10 msec.) was applied as the auditory stimulation. From the contralateral cerebral hemisphere to the stimulation side, AEF was recorded by averaging 450 responses. AEF could be recorded in three patients. AEF recordings of other three patients were poor and impossible to analyze. The estimation of the location of generator source of N1m was carried out, and the dipole moment was calculated in three patients.

The quasi-Newton method was applied for the estimation of the location of generator source.

Cerebral blood flow (CBF) was measured by SPECT (HMPAO), and the existence of focal hypoperfusion was detected qualitatively.

Illustrative cases

Case 3 was 67 year-old female who was attacked by symptoms of transient ischemia in the right cerebral hemisphere. She was free clinically during recordings of SEF and AEF. The estimated dipole moment was shown

©1999, Tohoku University Press

in Table 2, 3 and 4. Fig.1 shows the estimated location of generator source and CBF images. SPECT shows no focal hypoperfusion, however the estimated dipole moment of N1m in AEF and SEF was lower in the affected side to compare with that of the non-affected side. The subclinical hypofunction may be considered.

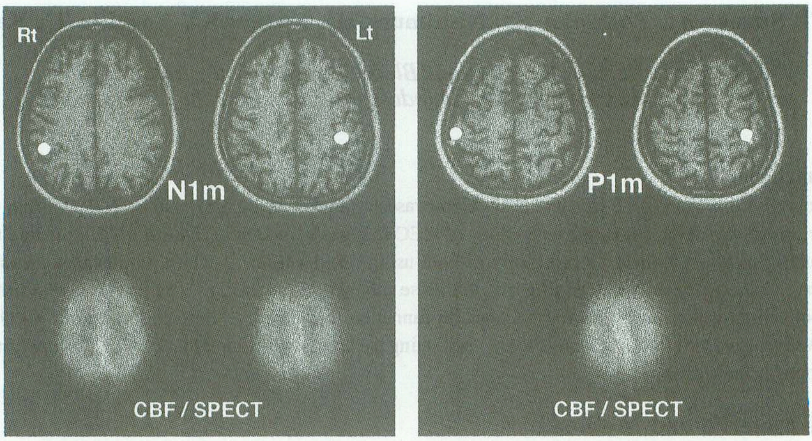

Fig. 1 Estimated location of generator source of N1m and P1m of SEF (white point) in case 3.

Case 4 was 66 year-old female who was attacked by cerebral infarction in the leftt occipital lobe. She showed mild sensory disturbance clinically during recordings of SEF and AEF. The auditory function was difficult to evaluate clinically. The estimated dipole moment was shown in Table 2, 3 and 4. Fig.2 shows the estimated location of generator source and CBF images. SPECT shows no focal reduction of CBF in the somatosensory and auditory areas. CBF was reduced in the affected occipital lobe. The estimated dipole moment of N1m in AEF and SEF was lower in the affected side to compare with that of the non-affected side. However, the goodness of fit (GOF) was poor in the estimation of SEF of the affected side, and the estimated location of generator source was considered to be unreliable.

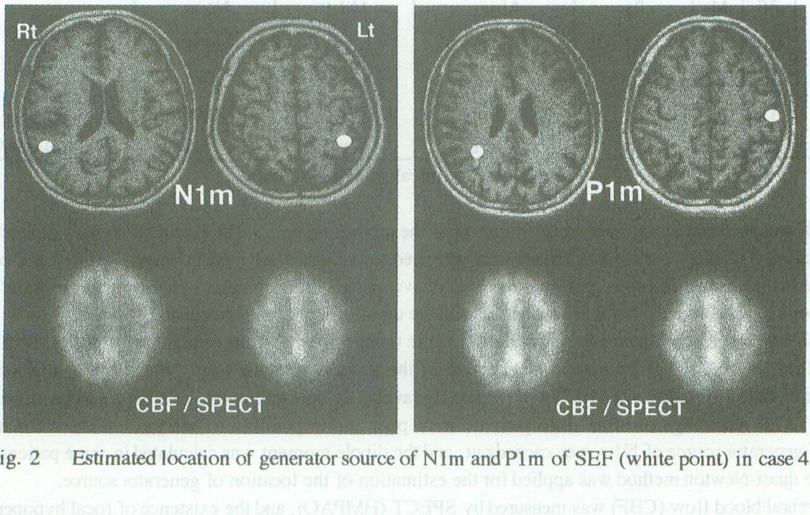

Fig. 2 Estimated location of generator source of N1m and P1m of SEF (white point) in case 4.

Results

1. Results of AEF

AEF was analyzed in cases 1, 3 and 4. Table 2 shows the estimated dipole moment of N1m and the goodness of fit (GOF) in these 3 patients.

Case	Affected side	Goodness of Fit	Non-affected side	Goodness of Fit	Ratio
1	15.17	0.933	28.7	0.868	0.52
3	16.57	0.919	25.23	0.909	0.65
4	18.58	0.906	22.62	0.902	0.82

Table 2 The estimated dipole moment (nAm) and the goodness of fit (GOF) of N1m of AEF in three patients. Ratio; dipole moment of the affected side / dipole moment of the non-affected side

The GOF was over 0.9 except for the non-affected side of case 1. In these 3 patients, the estimated dipole moment of the affected side was low to compare with that of the non-affected side. The ratio (affected side / non-affected side) was below 1.0. The degree of auditory dysfunction was difficult to evaluate clinically in these patients. Therefore, the relationship between the intensity of dipole moment and the auditory function could not be studied.

2. Results of SEF

Table 3 shows the estimated dipole moment of N1m and the goodness of fit (GOF). The estimated dipole moment and the ratio (affected side / non-affected side) of N1m were variable. The significant relationship between the intensity of dipole moment of N1m and the degree of sensory disturbance (shown in Table 1) could not be found in these 6 patients. The GOF was over 0.9 bilaterally only in cases 3 and 6. The ratio was below 1.0 in case 3, and over 1.0 in case 6. Case 3 was presented in the illustrative cases. Case 6 showed severe aphasia, and the clinical evaluation of sensory disturbance was impossible.

Case	Affected side	Goodness of Fit	Non-affected side	Goodness of Fit	Ratio
1	13.8	0.894	28.68	0.951	0.48
2	19.06	0.813	31.45	0.859	0.6
3	20.97	0.963	30.53	0.954	0.68
4	10.37	0.87	9.17	0.815	1.13
5	25.2	0.962	19.2	0.894	1.31
6	79.84	0.972	50.8	0.939	1.57

Table 3 The estimated dipole moment (nAm) and the goodness of fit (GOF) of N1m of SEF. Ratio; dipole moment of the affected side / dipole moment of the non-affected side

Table 4 shows the estimated dipole moment of P1m and the goodness of fit (GOF).

Case	Affected side	Goodness of Fit	Non-affected side	Goodness of Fit	Ratio
1	26.57	0.9	16.73	0.895	1.59
2	14.23	0.842	23.9	0.783	0.6
3	39.09	0.991	39.9	0.968	0.98
4	8.01	0.763	25.3	0.902	0.32
5	32.41	0.901	19.81	0.937	1.63
6	139.4	0.994	95.8	0.982	1.45

Table 4 The estimated dipole moment (nAm) and the goodness of fit (GOF) of P1m of SEF. Ratio; dipole moment of the affected side / dipole moment of the non-affected side

The estimated dipole moment and the ratio (affected side / non-affected side) of P1m were also variable. The significant relationship between the intensity of dipole moment of P1m and the degree of sensory disturbance (shown in Table 1) could not be found in these 6 patients. The GOF was over 0.9 bilaterally in cases 3, 5 and 6. The ratio was below 1.0 in case 3, and over 1.0 in cases 5 and 6.

3. Results of CBF

In six patients, the focal hypoperfusion was not detected except for infarcted areas. The somatosensory and auditory areas were preserved from the focal hypoperfusion.

Discussion

In our patients of cerebral infarction, the estimated dipole moment of SEF and AEF was variable, and showed no significant relationship with clinical signs. In case 3, the subclinical hypofunction of somatosensory and auditory systems was considered. In these patients, the somatosensory and auditory areas were not affected directly by the cerebral infarction, and the focal hypoperfusion was not observed in these areas. SEF could be analyzed in all patients and AEF could be analyzed in three patients. Our previous experience revealed that the intensity of dipole moment of N1m of AEF was lower than that of SEF in normal subjects. Thus, the analysis of N1m of AEF may be difficult in patients of brain diseases. The variability of dipole moment may be due to the valiable pathophysiology in the central nervous system of our patients. However, the goodness of fit (GOF) was poor especially in the estimation of SEF. The poor GOF may be due to the low intensity of the generator source, however the practical problem should be considered.

Some practical problems were considered as described in our study of normal subjects. Some patients were not co-operative sufficiently, and motion artifacts were mixed in the recordings. Furthermore, some patients moved their head during the recording, and we resetted the head position. The co-operation of patients is necessary for precise recordings and analysis of MEG. The position of the head under the surface of cryostat is also important. We recorded MEGs by attaching the head to the surface of cryostat. For the precise estimation of the location of generator source, the generator source should be positioned under the center of cryostat. However, it was difficult to know the location of generator source precisely before analyzing the recording of MEG. In some patients, the auditory area nor the somatosensory area of the cerebral hemisphere was not centered during recordings of AEF or SEF.

Therefore, the practical problem and the low intensity of generator source due to a pathologic process should be considered for the clinical application of MEG.

References

[1] Kang Y M, Ogura T, Uosaki K, et al: 4 K GM/JT cryocooler for cryogenic sensor, Prc. 6th Int. Cryocoolers Conf. vol. 1, 1990, pp17

[2] Sata K, Fujimoto S, Fukui N, et al: Development of SQUID based systems cooled by GM/JT cryocooler, Proc. ISEC16/ICMC, Elsevier Science, 1997, pp1173

[3] Sata K, Fujimoto S, Fukui N, et al: A 61-channel SQUID system for MEG measurement cooled by a GM/JT cryocooler. IEEE Trans. Appl. Superconductivity 7: 2526, 1997

[4] Yoshida T, Sata K, Yoshii K, et al: A cryocooled 61-channel MEG system, Applied Superconductivity, Elsevier Science, (in press).

Acknowledgment

The authors thank staffs of Department of Strokology, Department of Surgical Neurology and Department of Neurology in Research Institute for Brain and Blood Vessels-Akita for their co-operation of MEG recordings.

This study was supported by Japan Science and Technology Corporation.

Temporal Resolution and Spatial Resolution, and Clinical Utility of fMRI

Peter A. Bandettini

Biophysics Research Institute, Medical College of Wisconsin, Milwaukee, Wisconsin, USA

fMRI Contrast Mechanism Review

Several types of physiologic information can be mapped using fMRI, including baseline cerebral blood volume[1, 2], changes in blood volume [3], baseline and changes in cerebral perfusion[4, 5], and changes in blood oxygenation[6-10]. Recently, quantitative measures of $CMRO_2$ changes with activation have been derived from fMRI data[11, 12].

Because of its sensitivity and ease of implementation, the contrast used to observe susceptibility changes with changes in blood oxygenation, coined blood oxygenation level dependent (BOLD) contrast by Ogawa et al.[6] is the most commonly used functional brain imaging contrast used, and is the technique that will be primarily discussed in this chapter.

With each of the above-mentioned techniques, the precise type of observable cerebrovascular information can be more finely delineated. Regarding susceptibility contrast imaging, spin-echo sequences are more sensitive to small susceptibility compartments (capillaries and red blood cells) and gradient-echo sequences are sensitive to susceptibility compartments of all sizes[13, 14]. Outer volume RF saturation removes inflowing spins [15], therefore reducing non-susceptibility related inflow changes when using short TR sequences. Diffusion weighting or "velocity nulling," involving the use of $b > 50$ s^2/mm, reduces the intravascular signal [16] therefore reducing, but not eliminating, large vessel effects (intravascular effects are removed but extravascular effects remain) in gradient-echo fMRI and all large vessel effects in spin-echo fMRI. Going to higher field strengths has the same effect as diffusion weighting in the context of susceptibility - based contrast because the T2* and T2 of venous blood becomes increasingly shorter than the T2* and T2 of gray matter as field strength increases, therefore less signal will arise from venous blood, at higher field strengths, in sequences having TE = T2 and T2* of gray matter.

Regarding arterial spin labeling techniques that image perfusion, the time between the inversion "tag" and the image acquisition, the inversion time, (TI), roughly determines the predominant vasculature being imaged. A short TI selects rapidly flowing spins (protons in arteries). A long TI selects spins that take longer to reach the imaging plane (protons that are either in capillaries or have exchanged with tissue). Again, as with susceptibility contrast, diffusion weighting gradients reduce or remove intravascular signal in perfusion imaging, allowing the creation of maps that exclusively delineate intravascular capillary and exchanged protons[17].

Temporal Resolution Issues

The temporal resolution of fMRI has been variably defined in the literature. These definitions include the image acquisition rate, the time it takes for the activation - induced response to rise or fall a given amount - otherwise phrased as the time constant of the measured changes, the maximum rate at which activation can be turned on and off and still generate a detectable response, the smallest detectable activation duration, the smallest detectable difference in latency (between two identical activations that have different onset times) in an individual voxel or region of interest (ROI), and the smallest detectable difference in latency across separate voxels or ROI's. Each of these aspects of fMRI temporal resolution will be discussed.

With neuronal activation, the time for the BOLD response to first significantly increase from baseline is approximately 2. The time to plateau in the "on" state is approximately 6 to 9. With cessation of activation, the time to return to baseline is longer than the rise time by about one or two. Several groups have reported a "pre-undershoot " or initial dip during the first 500 ms [18] to 2 seconds of the signal [19]. More commonly observed is a post-undershoot, which is observed more in the visual cortex than motor cortex, and has an amplitude which is dependent on stimulus duration [20]. On cessation of activation, the post-undershoot signal can take up to a minute to return to baseline[21, 22].

©1999, Tohoku University Press
Recent Advances in Biomagnetism
T. Yoshimoto et al. (Eds)

Event – related fMRI: The first “event-related” fMRI experiments were performed using primary visual and motor activation [23-25], demonstrating the critical fact that a single transient activation (2 seconds or less) can induce a measurable hemodynamic response. The general response was shown to peak at about 4 to 6 seconds following activation, then return to baseline at about 10 seconds following activation.

Figure 1 shows these early results of varying brief stimuli durations - obtained from a region in motor cortex.[25]. The time series consist of two finger tapping durations of 5 seconds, 3 seconds, 2 seconds, 1 seconds, and 500 ms. The responses are able to be clearly delineated from each other based on the finger tapping duration. Savoy et al [24] reduced the stimulus duration further, performing a study in which the fMRI response to stimulus durations of 1000 ms, 100 ms, and 34 ms were compared. A measurable response was obtained using all stimulus durations. The responses to the 100 ms and 34 ms stimuli were considerably smaller than the response to the 1000 ms stimulus, and were similar in shape and amplitude to each other. These results suggest that the minimum stimulus duration has not yet been determined, but that below a specific stimulus duration, now thought to be about 500 ms, the hemodynamic response remains constant.

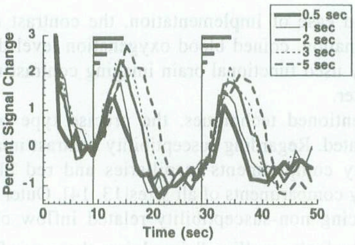

Figure 1: Signal from a ROI in motor cortex across five separate runs during which the subject was cued to perform finger tapping for 0.5, 1, 2, 3, and 5 sec twice during the time series. The time between the two finger tapping periods was 20 sec. TR = 1 sec.

The advantages of event-related activation strategies are many[26]. These include the ability to more completely randomize task types in a time series, the ability to selectively analyze fMRI response data based on measured behavioral responses to individual trials, and the option to incorporate overt responses into a time series. Separation of motion artifact from BOLD changes is possible by the use of the temporal response differences between motion effects and the BOLD contrast-based changes.

Several recently published studies have demonstrated the ability to create functional maps and to derive useful information using only a single response to a single inputs. Richter and colleagues have been able to derive the relative onset of activation of supplementary motor cortex relative to primary motor cortex using a delayed motor task following a readiness cue [27, 28]. Also, Richter et al [29] have demonstrated the ability to correlate individual response widths to the duration of a mental rotation task

Latency estimation within imaging voxels: Savoy and colleagues [24] have begun to address the issue of latency estimation accuracy. Variability of several temporal components of an activation-induced response function were determined. Six subjects were studied, and for each subject, ten activation - induced response curves were analyzed. The relative onsets were determined by finding the latency with which each of the temporal “compents” was maximized with each of three reference functions, representing three “components” of the response curve: the entire curve, the rising section, and the falling section. The standard deviations of the entire curve, rising phase, and falling phase were found to be 650 ms, 450 ms, and 1250 ms respectively.

Latency estimation across voxels or regions of interest: Can inferences of the spatial - temporal cascade characteristics of networked brain activation be made on this time scale from fMRI data? Without controlling for the intrinsic temporal variability of the BOLD signal over space, such inferences cannot be easily made for temporal latency differences below about 4 seconds. Lee et al [30] were the first to observe that the fMRI signal change onset within the visual cortex during simple visual stimulation varied from 6 seconds to 12 seconds. These latencies were also shown to correlate with the underlying vascular structure. The earliest onset of the signal change appeared to be in gray matter and the latest onset appeared to occur in the largest draining veins. To obtain information about relative onsets of cascaded neuronal activity from latency maps, it is important to characterize the underlying vasculature-related latency distribution at which one is looking. Savoy et al. [31, 32] demonstrated that activation onset latencies of 500 ms were discernible.

1. Fastest image acquisition rate: ≈ 64 images / sec.
2. Minimum time for signal to significantly deviate from baseline: ≈ 3 sec.
3. Fastest on off rate in which amplitude is not compromised: ≈ 8 sec on, 8 sec off.
4. Fastest on off rate in which hemodynamic response keeps up: ≈ 2 sec on, 2 sec off.
5. Minimum activation duration: ≈ 30 (the response characteristics unchanged below 500 ms)
6. Standard deviation of baseline signal: ≈ 1% (less if filtering is used)
7. Standard deviation of onset time estimation: ≈ 450 ms.
8. Standard deviation of return to baseline time estimation: ≈ 1250 ms.
9. Standard deviation of entire on-off response time estimation: ≈ 650 ms.
10. Range of latencies over space: ± 2.5 sec.

Table 1: Functional fMRI temporal resolution factors.

Spatial Resolution Issues

The upper limit on functional spatial resolution, similar to the limit on temporal resolution, is likely determined not by MRI resolution limits but by the hemodynamics through which neuronal activation is transduced. Evidence from *in vivo* high resolution optical imaging of the activation of ocular dominance columns suggests that neuronal control of blood oxygenation occurs on a spatial scale of less than 0.5 mm. MR evidence suggests that the blood oxygenation increases that occur on brain activation are be more extensive than the actual activated regions. In other words, it is possible that, while the local oxygenation may be regulated on a submillimeter scale, the subsequent changes in oxygenation may occur on a larger scale due to a "spill-over" effect

In general, to achieve the goal of high spatial resolution fMRI a high functional contrast to noise and reduced signal contribution from draining veins is necessary. Greater hemodynamic specificity, accomplished by proper pulse sequence choice (selective to capillary effects), innovative activation protocol design (phase-tagging), or proper interpretation of signal change latency (latency mapping), may allow for greater functional spatial resolution. If the contribution to activation-induced signal changes from larger collecting veins or arteries can be easily identified and/or eliminated, then, not only will the confidence in brain activation localization increase, but also the upper limits of spatial resolution will be determined by scanner resolution and functional contrast to noise rather than variations in vessel architecture.

Voxel volumes as low as 1.2 microliters have been obtained by functional FLASH techniques at 4T , and experiments specifically devoted to probing the upper limits of functional spatial resolution, using spiral scan techniques, have shown that fMRI can reveal activity localized to patches of cortex having a size of about 1.35 mm. These studies and others have observed a close tracking of MR
signal change along the calcarine fissure as the location of visual stimuli was varied.

The voxel dimensions typically used in single - shot EPI studies are in the range of 3 to 4 mm, in plane, and having 4 to 10 mm slice thicknesses. These dimensions are determined by practical limitations such as readout window length, sampling bandwidth, limits of dB/dt, SNR, and data storage capacity. Other ways to bypass the practical scanner limits in spatial resolution include partial k-space acquisition and multi - shot mosaic or interleaved EPI. In many fMRI situations, multishot EPI may be the optimum compromise between spatial resolution, SNR, and temporal resolution for fMRI .

Clinical Applications

Currently, the clinical uses of fMRI include presurgical mapping, seizure foci identification, and mapping of blood volume, perfusion, and transit time. One drawback in clinical applications is that the fMRI signal is extremely complicated. The utility of fMRI is directly related to how precisely the fMRI signal characteristics can be characterized.

Potential clinical applications of fMRI are many. Characterization of vascular reserve is possible with the use of a hypercapnic stress. Noninvasive mapping of mechanisms of drug addiction holds considerable promise for treatment and monitoring. Research is also being carried out in correlating the spatial and temporal characteristics of the activation – induced signal changes and baseline fluctuation with disease states, neurological deficits, and cognitive disorders, including Tourettes syndrome, obsessive compulsive disorder, visual deficits, dyslexia, chronic pain, tinnitus, stroke, and attention deficit disorder.

References:

1. Rosen, B.R., J.W. Belliveau, and D. Chien, *Perfusion imaging by nuclear magnetic resonance*. Magn. Reson. Quart, 1989. **5**: p. 263-281.
2. Moonen, C.T.W., *et al.*, *Functional Magnetic Resonance Imaging in Medicine and Physiology*. Science, 1990. **250**: p. 53-61.
3. Belliveau, J.W., *et al.*, *Functional mapping of the human visual cortex by magnetic resonance imaging*. Science, 1991. **254**: p. 716-719.
4. Edelman, R., P. Wielopolski, and F. Schmitt, *Echo-planar MR imaging*. Radiology, 1994. **192**: p. 600-612.
5. Kim, S.-G., *Quantification of relative cerebral blood flow change by flow-sensitive alternating inversion recovery (FAIR) technique: application to functional mapping*. Magn. Reson. Med., 1995. **34**: p. 293-301.
6. Ogawa, S., *et al.*, *Brain magnetic resonance imaging with contrast dependent on blood oxygenation*. Proc. Natl. Acad. Sci. USA, 1990. **87**: p. 9868-9872.
7. Turner, R., *et al.*, *Echo-planar time course MRI of cat brain oxygenation changes*. Magn. Reson. Med., 1991. **22**: p. 159-166.
8. Kwong, K.K., *et al.*, *Dynamic magnetic resonance imaging of human brain activity during primary sensory stimulation*. Proc. Natl. Acad. Sci. USA., 1992. **89**: p. 5675-5679.
9. Ogawa, S. and T.M. Lee, *Functional brain imaging with physiologically sensitive image signals*. JMRI, 1992. **2(P)-WIP suppliment, [Abstr.]**: p. S22.
10. Bandettini, P.A., *et al.*, *Time course EPI of human brain function during task activation*. Magn. Reson. Med., 1992. **25**: p. 390-397.
11. Davis, T.L., *et al.*, *Calibrated functional MRI: Mapping the dynamics of oxidative metabolism*. Proc. Natl. Acad. Sci. USA, 1998. **95**: p. 1834-1839.
12. vanZijl, P.C.M., *et al.*, *Quantitative assessment of blood flow, blood volume, and blood oxygenatoin effects in functional magnetic resonance imaging*. Nature Medicine, 1998. **4**(2): p. 159-16.
13. Ogawa, S., *et al.*, *Functional brain mapping by blood oxygenation level - dependent contrast magnetic resonance imaging: a comparison of signal characteristics with a biophysical model*. Biophysical J, 1993. **64**: p. 803-812.
14. Boxerman, J.L., *et al.*, *MR contrast due to intravascular magnetic susceptibility perturbations*. Magn. Reson. Med., 1995. **34**: p. 555-566.
15. Duyn, J.H., *et al.*, *Inflow versus deoxyhemoglobin effects in BOLD functional MRI using gradient-echoes at 1.5 T*. NMR in Biomedicine, 1994. **7**: p. 83-88.
16. Boxerman, J.L., *et al.*, *The intravascular contribution to fMRI signal change: Monte Carlo modeling and diffusion-weighted studies in vivo*. Magn. Reson. Med., 1995. **34**: p. 4-10.
17. Wong, E.C., R.B. Buxton, and L.R. Frank, *Implementation of quantitative perfusion imaging techniques for functional brain mapping using pulsed arterial spin labeling*. NMR in Biomedicine, 1997. **10**: p. 237-249.
18. Hennig, J., *et al.*, *Functional spectroscopy of brain activation following a single light pulse:examinations of the mechanism of the fast initial response*. Int. J.ournal of Imag. Syst. and Tech., 1995. **6**: p. 203-208.
19. Menon, R.S., *et al. Cerebral oxy/deoxy hemoglobin changes during neural activation: MRI timecourse correlates to optical reflectance measurements*. in *Proc., SMR, 2nd Annual Meeting*. 1994. San Francisco.
20. Davis, T.L., *et al. Susceptibility contrast undershoot is not matched by inflow contrast undershoot*. in *Proc., SMR, 2nd Annual Meeting*. 1994. San Francisco.
21. Fransson, P., *et al.*, *Temporal characteristics of oxygenation-sensitive responses to visual activation in humans*. Magn. Reson. Med., 1998. **39**: p. 912-919.
22. Bandettini, P.A., *et al.*, *Characterization of cerebral blood oxygenation and flow changes during prolonged brain activation*. Human Brain Mapping, 1997. **5**: p. 93-109.
23. Blamire, A.M., *et al.*, *Dynamic mapping of the human visual cortex by high-speed magnetic resonance imaging*. Proc. Natl. Acad. Sci. USA, 1992. **89**: p. 11069-11073.
24. Savoy, R.L., *et al. Pushing the temporal resolution of fMRI: studies of very brief visual stimuli, onset variablity and asynchrony, and stimulus-correlated changes in noise*. in *Proc., SMR 3rd Annual Meeting*. 1995. Nice.
25. Bandettini, P.A., *et al.*, *Functional MRI using the BOLD approach: dynamic characteristics and data analysis methods*, in *Diffusion and Perfusion: Magnetic Resonance Imaging*, D. LeBihan, Editor. 1995, Raven Press: New York. p. 335-349.
26. Zarahn, E., G. Aguirre, and M. D'Esposito, *A trial - based experimental design for fMRI*. Neuroimage, 1997. **6**: p. 122-138.
27. Richter, W., *et al.*, *Sequential activity in human motor areas during a delayed cued finger movement task studied by time-resolved fMRI*. NeuroReport, 1997. **8**: p. 1257-1261.
28. Kim, S.-G., W. Richter, and K. Ugurbil, *Limitations of temporal resolution in fucntional MRI*. Magn. Reson. Med., 1997. **37**: p. 631-636.
29. Richter, W., *et al.*, *Time-resolved fMRI of mental rotation*. NeuroReport, 1997. **8**: p. 3697-3702.
30. Lee, A.T., G.H. Glover, and C.H. Meyer, *Discrimination of large venous vessels in time-course spiral blood-oxygen-level-dependent magntic-resonance functional neuroimaging*. Magn. Reson. Med., 1995. **33**: p. 745 -754.
31. Savoy, R.L., *et al. Exploring the temporal bourdaries of fMRI: measuring responses to very brief visual stimuli*. in *Book of Abstracts, Soc. for Neuroscience 24'th Annual Meeting*. 1994. Miami.
32. Rosen, B.R., R.L. Buckner, and A.M. Dale, *Event-related functional MRI: past, present, future*. Proc. Natl. Acad. Sci. USA, 1998. **95**: p. 773-780.

Non-Invasive Localization of Hand Primary Motor and Somatosensory Areas using MEG, fMRI, and Anisotropic Diffusion Weighted MR Imaging.

Jones, G.M.[1], Tsuruda, J.S.[1], Alexander, A.L.[1] Chong, B.W.[1], Burr, R.B.[2], McDonald, J.D.[2], Davis, J.T.[1], Paulson, K. M.[1], Jones, J.E.[1], Andelin, C.O.[1], Buswell, H.R.[1], Funke, M.E.[1], and Lewine, J.D.[1],
University of Utah, [1]Department of Radiology, [2]Department of Neurosurgery, Salt Lake City, Utah, USA.

Introduction

In recent years pre-surgical planning has been greatly enhanced by a variety of brain imaging modalities able to non-invasively map eloquent cortex. To further the utility of the various imaging modalities, studies defining relative strengths and weaknesses of each modality are required. In this report, magnetoencephalography (MEG), functional MRI (fMRI), and anisotropic diffusion weighted imaging (ADWI) were compared in their ability to identify primary motor and somatosensory areas for the hand for 6 normal control subjects. MEG data were obtained on a 122 channel biomagnetometer using a visually cued motor task and stimulation of the median nerve. fMRI data were collected on a GE 1.5T MRI using a hand movement task.

MEG and fMRI have been used in several studies to localize pre and post-central gyri (1). In this report a relatively new method of MR imaging, ADWI is also studied. ADWI relying on signals associated with proton motion was performed on a GE 1.5T MR scanner. ADWI provides information on the structural organization of white matter tracks projecting to cortical regions.

Methods

MEG MEG was performed on a Neuromag 122 channel biomagnetometer and structural MR imaging was done using a Picker Eclipse 1.5T imager. Somatosensory cortex was activated using electrical median nerve stimulation. The electrical stimulation of left and right median nerves was done in an alternating fashion, with a pulse length of 250 µs. Activation of the motor cortex was achieved using a visually cued index finger lift. Data collection was triggered using the finger lift.

Analysis of the MEG data was done using software supplied by Neuromag. The analysis uses a single dipole model for the current dipole and a spherical head model. The somatosensory data was filtered using a highpass filter of 6 Hz, 12 Hz FWHM and a lowpass filter of 100 Hz, 200 Hz FWHM. The motor data was filtered using a highpass filter of 2 Hz, 4 Hz, FWHM and a lowpass filter of 20 Hz, 40 Hz, FWHM. The combining of MEG and MRI data was done using a protocol where three anatomical points (nasion, left periaricular, right periaricular) were digitized and incorporated in the MEG data and subsequently aligned with their respective positions on the anatomical MRI volume.

Functional Magnetic Resonance Imaging (fMRI) Functional MR data were collected in a GE Signa 1.5T imager, using an EPI sequence. 6 slices were collected in an axial orientation with an image resolution of 64x64 pixels. The data were collected using a 7 mm slice thickness in a 5 mm skip 2 mm configuration. The input function or task paradigm was an alternating left/right hand flexion. The rate of hand flexion was between 1

©1999, Tohoku University Press
Recent Advances in Biomagnetism
T. Yoshimoto et al. (Eds)

and 2 hz, as the subjects were instructed to keep pace with the sound intrinsic to the EPI scan sequence.

Data processing consisted of pixel-by-pixel statistical analysis using the MedX software package. Statistical analysis was accomplished using a reference waveform to separate images of the "task" group from images defined as the control group. Task and control images were statistically compared using an unpaired student t-test. The reference waveform was a boxcar with a delay of 4 seconds. Analysis was performed on the 64 X 64 pixel EPI images and the statistical threshold was set using z-scores generated from the unpaired student t-test analysis. In this report all fMRI images were viewed with a statistical threshold of $z = 4$. Statistical maps were rendered via a spatial transform into an anatomical volume.

Anisotropic Diffusion Weighted Imaging The diffusivity of water in tissues can be measured by applying strong magnetic field gradients during the imaging sequence (2,3). The diffusivity in a particular direction is evaluated by applying the gradient field in that direction. The full diffusion tensor is mapped out by obtaining independent diffusivity measurements in at least six directions (4,5). Estimates of the directional diffusivity are made using measurements from a pair of images with and without diffusion gradients. The same reference image obtained without diffusion gradients is used for the diffusion calculation in all directions. Consequently, a minimum of seven images must be obtained to measure the diffusion tensor.

Fibrous tissues such as the white matter tracts have preferential diffusivity along the long axis of the fiber, whereas other tissues in the brain such as gray matter and CSF demonstrate isotropic diffusion. By measuring the degree of diffusion anisotropy, the position of the white matter fibers can be determined (see Fig.1).

Diffusion measurements in six directions were obtained using a diffusion-weighted echo-planar imaging technique described previously (6). A diffusion weighting factor of ~900 sec/mm^2 was used.

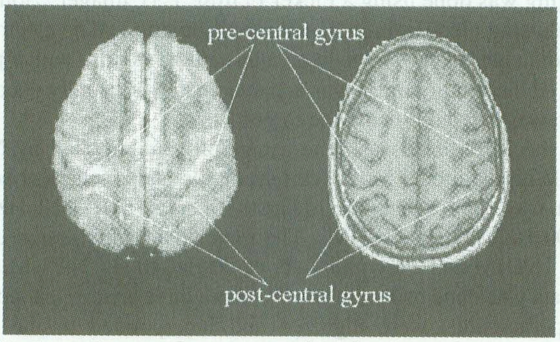

Figure 1. Localization of pre and post-central gyri using anisotropic diffusion weighted MR imaging (ADWI). The images should be viewed as if the viewer is at the subject's feet. The subject is a right handed male.

Results

MSI, fMRI, and ADWI were compared with one another in the ability of the modalities to map pre and post-central gyrus. The results appear as a ratio where 6 volunteers produced 12 chances to map motor or somatosensory cortex.

MEG – Using electrical median nerve stimulation allowed for functional localization of the somatosensory cortex in every case examined. In general, localization of the somatosensory area was found to be lateral to the anatomical landmark known as the handknob on the pre-central gyrus. The visually cued motor task presented substantially less robust signal, especially when compared to the very reliable somatosensory task. The localization of motor cortex with the motor task was successful in 6 of 12 cases. When localization of motor cortex using MSI failed it was due to a lack of signal in the –60 to –70 ms region of the response, rather than a mis-mapping of a strong response.

fMRI - The fMRI data typically imaged combinations of both pre and post-central gyri (see Fig. 2). In some cases, either post or pre-central gyrus was imaged using the hand flexion task. A rough tabulation of the data showed fMRI able to image the motor strip with a efficiency of 75%. Imaging of the somatosensory strip was done with an efficiency of 83%. A closer examination of the data showed that in 7 images fMRI saw activation in both pre and post-central gyrus, while 3 images showed only post-central activation and 2 images showed only pre-central activation. The challenge is without clean anatomical markers, fMRI does not distinguish between pre and post-central gyri.

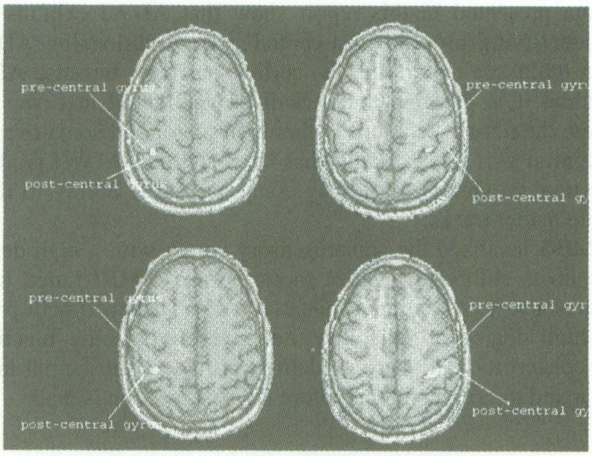

Figure 2. Functional imaging of motor cortex and somatosensory cortex using functional MR imaging. All four slices pictured are from the same subject and orientation is as if the viewer were at the subject's feet. The left side slices show activation in response to left hand flexion (see gray shaded area) and right side slices show activation in response to right hand flexion

ADWI – Both pre and post-central gyri were dependably localized with anisotropic diffusion weighted imaging (see Fig. 1). Using ADWI images to localize the gyri involved side-by-side comparison of the anatomical images with the ADWI images. In all cases, the area with the highest intensity correlated with the handknob in the dominant hemisphere, as judged by handedness. It is important to note that only one left handed subject was involved in the study. The ADWI images visualized white matter tracks throughout the 2 –3 slices (equivalent to 14-21 mm) inferior to and including the slices in which activation was seen in either MSI or fMRI images.

Discussion Using MSI for the localization of somatosensory cortex in normal subjects is quite robust. Additionally, it is our experience that in cases where the patient's ability to comply with the exam is limited, electrical stimulation of the median nerve continues to be reliable.

When MSI is used to map motor function in normal subjects, the reliability seen in somatosensory function is lost. In our study, with a limited number of subjects, we saw only a 50% success rate using a visually cued, finger lift task. This suggests that this paradigm may be of only limited utility with clinical patients.

The results from the fMRI experiments are mixed, while the percentage of successful mapping of either motor or somatosensory appears relatively high, 75% and 83% respectively, the precision of the method is suspect. The fMRI results generally mapped to the central sulcus, with instants mapping to either pre or post-central gyri. The difficulty that arises is that it is not certain to which gyrus fMRI will map a motor task. With fMRI mapping to either central sulcus, pre-central gyrus, or post-central gyrus and no means to predict which area will be visualized, fMRI is not reliable as singular modality.

The data presented in this report show that ADWI exhibits a high degree of reliability in identifying pre and post-central gyri. Additionally, ADWI also provides information on the tissue underlying the cortical surface. Because ADWI is not truly a functional method it is possible that it will prove limited in cases of severe cortical pathology where the normal relationship between motor and somatosensory function and pre and post-central gyri (respectively) has been altered. ADWI is also under-tested in cases of large tumors where edema may compromise the ability to distinguish sensory and motor white matter tracks.

Conclusion MEG localized the somatosensory cortex with a high degree of reliability, but was weak in its ability to localize motor cortex. fMRI failed to reliably localize motor or somatosensory cortex independently. ADWI mapped both pre and post-central gyrus with a high degree of reliability, but gives no specific functional information. When used in concert though, these modalities provide a substantial information set that has the ability to aid the surgeon long before the first incision is made.

References

1)Stippich C, Freitag P, Kassubek J, et al., Motor, somatosensory and auditory cortex localization by fMRI and MEG. Neuroreport, 9:1953-1957 (1998)

2) Stejskal E.O., Tanner J.E., Spin diffusion measurements: spin echoes in the presence of a time dependent field gradient. J. Chem. Phys. 42:288-292 (1965)

3) LeBihan D, Breton E, Lallemand D, et al., MR imaging of intravoxel incoherent motion: application to diffusion and perfusion in neurologic disorders. Radiology 161:401-407 (1986)

4) Pierpaoli C, Jezzard P, Basser PJ, et al., Diffusion tensor MR imaging of the human brain. Radiology 201:637-648 (1996)

5) Basser PJ, Pierpaoli C., A simplified method to measure the diffusion tensor from seven MR images. Magn. Reson. Med. 39:928-934 (1998)

6) Alexander AL, Tsuruda JS, Parker DL, Elimination of eddy current artifacts in diffusion-weighted echo-planar images: the use of bipolar gradients. Magn. Reson. Med. 38:1016-1021 (1997)

Combination Study of Cerebral Ischemia using Magnetoencephalography and Proton MR Spectroscopic Imaging

Kamada K[1], Saguer M[2], Möller M[2], Wicklow K[3], Kaltenhäuser M[2], Kober H[2], Vieth J[2]

[1] *Department of Neurosurgery, Hokkaido University, Sapporo, Japan;* [2] *Dept of exp Neuropsychiatry, Erlangen-Nürnberg University, Erlangen, Germany;* [3] *Siemens AG, Medical Engineering Group, Erlangen, Germany*

Introduction

It is of clinical importance to identify and preserve the residual brain tissue which is surviving and functioning in ischemic lesions. Magnetoencephalography (MEG) reflects intracellular electric current flow in brain, providing direct information of neural activitiy. We have previously reported the abnormal magnetic brain activities in the areas adjacent to the lesions of cerebral infarction [1].

The purpose of this study is to investigate the abnormal brain activities and pathological metabolism in ischemic brain using spontaneous MEG and proton magnetic resonance spectroscopic imaging (^{1}H MRSI) for analyzing the relationship between brain function and metabolism, respectivey.

Subjects and Methods

Patients

Studies were performed on patients with nonhemorrhagic cerebral infarcts (n = 11). An age-matched control group consisted of 10 subjects.

Proton Magnetic Resonance Imaging (^{1}H MRI) and Spectroscopic Imaging (^{1}H MRSI)

MR experiments were performed using a 1.5 T Magnetom Vision (Siemens AG, Germany). Spectroscopic SE signals were collected using a combination of localized excitation and phase-encoded acquisition (16 increments). A rectangular region within the brain was selected which contained the infarcted lesions and the surrounding cortex. Control data of normal volunteers were obtained from the left parietal lobe. The echo signals were obtained using standard parameters (echo time (TE) = 270 msec) and shorter TE parameter (TE = 135 msec). After ^{1}H MRSI experiments, three-dimensional images were acquired of the entire head to process the MEG data.

Four peaks were assigned; NAA, creatine and phosphocreatine (Cr), choline-containing compounds (Cho) and lactate (Lac) and then the signal intensity was measured by integrating each peak in the complete stack of spectra as described in previous reports [2]. In each MRSI data set the internal standard was calculated from the peak integral of NAA, averaged over 4 voxels in the uninvolved occipital lobe.

Spontaneous MEG

Spontaneous magnetic brain activity was recorded using a 2x37-channel biomagnetic system (Bti, USA). Each patients' head was fixed between the two MEG dewars. The collected 600 sec digital data were filtered at 2 to 6 Hz or 14 to 30 Hz for the analysis of slow and fast wave activities, respectively. Principle Component Analysis (PCA) was used in order to select the time sections with one component dominating the measured signal by a contribution of at least 90% (slow) or 85% (beta). Equivalent current dipoles were calculated using the single equivalent current dipole model amd the Dipole Density Plot (DDP) was applied on the results to show density of brain activity (the minimum

©1999, Tohoku University Press
Recent Advances in Biomagnetism
T. Yoshimoto et al. (Eds)

correlation was more than 0.8) [3]. The quantified DDP result was demonstrated as isocontour lines. The line spacing was standardized in each measurement by the equation as follows;

$$\text{Line spacing} = \frac{D_{Total} \times 12}{100 \times T_{Total}}$$

where D_{Total} t = Total number of calculated dipoles, T_{Total} = total time of selected component, the mean value of normal T_{Total} was approximately 12 (Table 1). The highest density of the dipoles (D_{Max}) was divided by the line spacing to give a normalized value in an each measurement ($D_{Standard}$).

Combination of Spontaneous MEG and ^{1}H MRI

During the MEG measurement, the accessible parts of the head surface of a subject were scanned by an electromagnetic digitizer (Isotrak™ 3D Digitizer, Polhemus Navigation Sciences Inc., USA). In order to superimpose the MEG results on 3D MRI and ^{1}H MRSI data, the scanned head surface data set was fitted to the reconstructed MRI headshape using our surface-fit program.

Results

^{1}H MRSI: Peaks corresponding to NAA, Cr, Cho and Lac were readily assigned in normal and ischemic brain (Fig. 1).

Fig 1. (A)T2-weighted image. Four voxels "N" are used as internal reference. 1 = infarction, 2 = a region adjacent to the infarction. **(B) Proton MR spectrum from the voxel.**

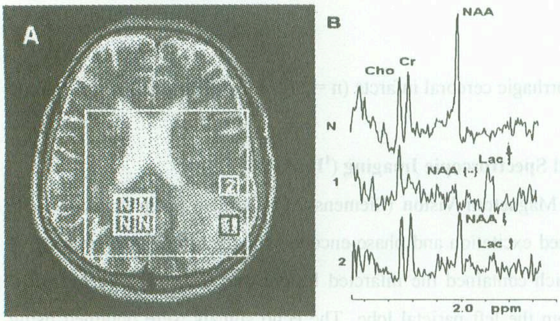

Spontaneous MEG

In 20 hemispheres of 10 normal volunteers, there was no significant differences in slow wave and fast wave between both hemispheres. DDP projected little focal abnormal activity on the MRI of all the normal hemispheres. Infarcted hemispheres revealed conspicuous concentration of slow wave dipoles in the DDP results and significant higher $D_{Standard}$ of slow wave magnetic activity in comparison to the unaffected hemispheres ($p = 0.0414 < 0.05$) and normal brains of the volunteers ($p = 0.001 < 0.05$). Fast wave activity was not frequently observed in the infarcted brain. $D_{Standard}$ of the fast wave activity was 1.71 ± 0.81 and not statistically significant ($p = 0.5529 > 0.05$) (Table 1).

Table 1. Results of DDP * $p < 0.05$ compared with healthy volunteers.

	Slow wave activity				Fast wave activity			
Subjects	Time (sec)	Total(D_{Total}) Dipoles	Max(D_{Max}) Dipoles	$D_{Standard}$	Time (sec)	Total(D_{Total}) Dipoles	Max(D_{Max}) Dipoles	$D_{Standard}$
Healthy (n=10) Mean ± S.D.	12,45 ± 1,39	2252,15 ± 363,14	43,29 ± 7,33	2,25 ± 0,33	12,05 ± 1,85	1996,40 ± 496,65	33,40 ± 10,64	2,09 ± 0,78
Patients								
RHC	15	3573	99,88	2,80	11	1705	20,55	1.64
GWE	11	2346	50,46	2,93	10	1809	17,65	1,64
HLC	10	3074	61,09	2,98	11	1695	12,49	1,00
ALR	11	2212	52,55	3,24	12	1579	35,82	2,84
KHE	11	2244	53,85	3,27	13	2954	6,97	0,20
IRA	10	1663	36,48	3,29	14	3072	34,22	1.19
ASI	10	2330	58,57	3,78	12	2025	16,35	1,01
EDA	11	1629	45,34	3,80	10	1638	26,18	2,40
KFA	15	3452	154,6	4,48	13	859	14,1	1.89
GPB	10	1803	73,17	6,09	14	1634	35,07	2.30
AAA	10	2476	143,67	8,70	11	1716	33,44	2.66
Mean ± S.D.	11,27 ± 1,90	2436,56 ± 670,04	75,42* ± 40,07	4,12* ± 1,79	11,91 ± 1,45	1880,55 ± 628,03	22,99 ± 10,39	1,71 ± 0,81

Combination of ^{1}H MRSI and Spontaneous MEG: In Fig.2, combined images of patient KFA with ^{1}H MRS and spontaneous MEG found markedly increasing slow wave magnetic activity in the cortical region adjacent to the infarction, where mild reduction of NAA and slightly elevated Lac were observed

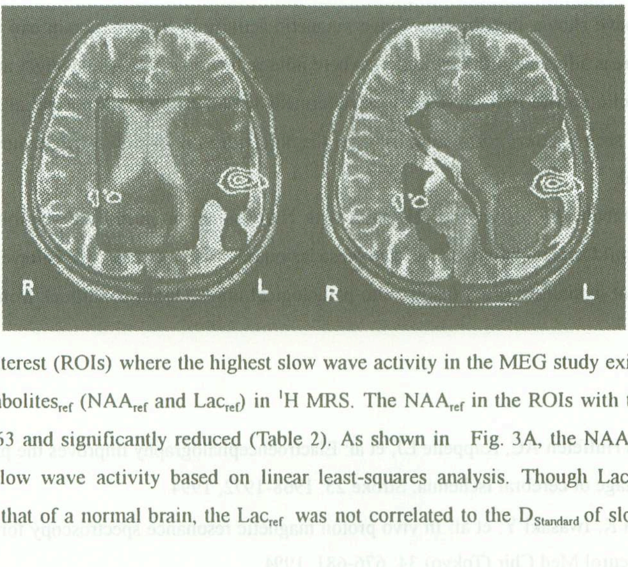

Fig 2. Combined images of patient KFA. (A) NAA image and slow wave activity, (B) Lac image and slow wave activity. (A) (B)

The regions of interest (ROIs) where the highest slow wave activity in the MEG study existed were selected for comparison with metabolites$_{ref}$ (NAA$_{ref}$ and Lac$_{ref}$) in ^{1}H MRS. The NAA$_{ref}$ in the ROIs with the highest slow wave dipole density was 0.63 and significantly reduced (Table 2). As shown in Fig. 3A, the NAA$_{ref}$ was well correlated with $D_{Standard}$ of the slow wave activity based on linear least-squares analysis. Though Lac$_{ref}$ of the lesions was markedly higher than that of a normal brain, the Lac$_{ref}$ was not correlated to the $D_{Standard}$ of slow wave activity (Fig. 3B).

Table 2. Spectroscopic Data from Eleven Patients

Subjects	NAAref	Lacref	Crref	Choref
Healthy (n=10) Mean ± S.D	1,03 ± 0,09	not detected	0,55 ± 0,10	0,45 ± 0,07
Patients				
RHC	0,29	0,09	0,39	0,45
GWE	0,54	0,13	0,37	0,48
HLC	0,54	0,22	0,38	0,64
ALR	0,53	0,13	0,32	0,62
KHE	0,59	0,14	0,62	0,59
IRA	0,53	0,08	0,30	0,32
ASI	0,50	0,12	0,61	0,40
EDA	0,73	0,12	0,60	0,42
KFA	0,63	0,10	0,40	0,45
GPB	1,15	0,14	0,67	0,58
AAA	0,92	0,27	0,58	0,61
Mean ± S.D.	0,63* ± 0,23	0,14* ± 0,06	0,48 ± 0,14	0,51 ± 0,11

* $p < 0.05$ compared with healthy volunteers.

Fig 3. Plots of DDP of slow wave activity vs NAA (A) and lac (B).

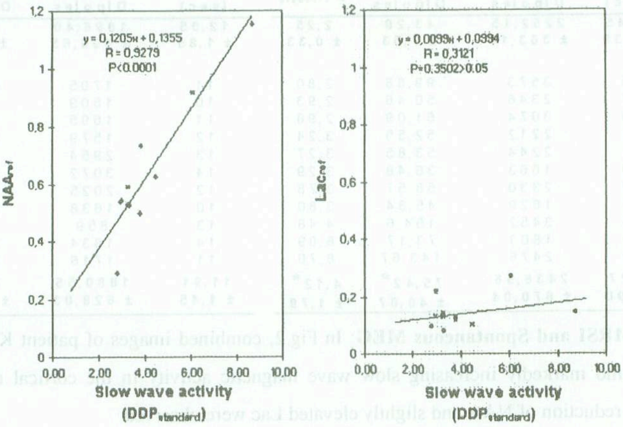

Discussion

In this study we have shown that the slow wave magnetic activity in ischemic brain can be readily localized by MEG in the cortical areas adjacent to the infarction, where mild reduction of NAA and slight accumulation of Lac are observed. This metabolic profile is interpreted as an intermediate pattern between normal and infarcted brain in ^{1}H MRSI study. We have seen a strong correlation between the dipole density of slow wave component and the intensity of residual NAA signal.

Preserved and metabolically active cortical tissue with NAA signal produced the abnormal slow wave activity under lactic acidosis (mild accumulation of Lac) and these lesions should be treated. We believe that a combined study with these two different modalities gives insight into pathological human brain conditions from functional as well as metabolic aspects.

References

[1] Cillessen JPM, van Huffelen AC, Kappelle LJ, et al: Electroencephalography improves the prediction of functional outcome in the acute stage of cerebral ischemia. Stroke 25: 1968-1972, 1994

[2] Kamada K, Houkin K, Iwasaki Y, et al: In vivo proton magnetic resonance spectroscopy for metabolic changes of human brain edema. Neurol Med Chir (Tokyo) 34; 676-681, 1994

[3] Kober H, Vieth J, Grummich P, et al: The factor analysis used to improve the dipole-density-plot (DDP) to localize focal concentrations of spontaneous magnetic brain activity. Biomedical Engineering 37 (Suppl 2): 164-165, 1992

Acknowledgments

This study was financially and partly supported by Alexander-von-Humboldt Foundation.

Stereotactic Transcranial Magnetic Stimulation Combined with EEG

Ilmoniemi RJ[1], Karhu J[1,3], Ruohonen J[1], Tiitinen H[4], Virtanen J[1,4], Kamppuri J[1], Ollikainen M[1], Ylöstalo J[1], Aronen HJ[2], Katila T[1,5], and Näätänen R[1,4]

BioMag Laboratory, Medical Engineering Centre[1] and Dept. of Radiology[2], Helsinki Univ. Central Hospital, Helsinki, Finland; Dept. of Clinical Neurophysiology[3], Kuopio Univ. Hospital, Kuopio, Finland; Cognitive Brain Research Unit, Dept. of Psychology[4], University of Helsinki, Helsinki, Finland; Laboratory of Biomedical Engineering[5], Helsinki University of Technology, Espoo, Finland

Introduction

In Transcranial Magnetic Stimulation (TMS [1,2]), cortical neurons are stimulated by the electric field induced by externally applied quickly changing magnetic field. The induced field required for neuronal stimulation is on the order of 100 V/m. The magnetic field of up to 2–3 tesla is generated by discharging a large capacitor from several kilovolts through a coil placed over the scalp. TMS can be used 1) to artificially activate cortical areas, 2) to influence ongoing neuronal processing, or 3) to treat, e.g., severely depressed patients. Until recently, the stimulator coils have been positioned manually and only behavioral or peripheral-muscle responses have been recorded.

An evaluation of the feasibility of a magnetic stimulator for the brain was presented by David Cohen at the Vancouver Biomagnetism Conference in 1984 [3]. The practical demonstration of the technique was reported in 1985, when Barker *et al.* [4] found that magnetic stimulation of the motor cortex produced contralateral muscle movements. Initially, TMS was used to study neural conduction from the brain to the periphery. A new paradigm was introduced by Amassian *et al.* [5], who showed that a subject's performance in a visual task was impaired when TMS pulses were delivered between 60 and 140 ms after the stimulus; a temporary functional lesion had been created. Many successful studies using this technique have been performed since then (see, e.g., [6–8]). In electrophysiological studies, functional lesions can be used as probes to determine the role of different cortical areas on evoked responses.

Significant benefits are expected from the combination of TMS with other functional imaging methods such as MEG, EEG, fMRI, or PET. While these methods reflect changes in electrophysiological activity, blood flow, or metabolism, TMS can be used to either induce, modulate or block cortical activity. Anatomical structures seen in MRI and activation sites determined by PET, fMRI or MEG/EEG can be used for the selection of TMS target areas in the brain. EEG [9–11], PET [12–13], and fMRI [14] can be used to measure the cerebral response to TMS.

In most TMS studies, the stimulator coil is positioned manually until, e.g., a thumb twitch is generated. For the accurate targeting of the stimulation pulses and for the proper combination of the coordinate systems in different imaging modalities, we have developed a stereotactic system for TMS. By determining the stimulator coil location with respect to the head and by aligning the head and MRI coordinates, cortical targets can be selected from the subject's individual MRI slices [15–16]. We have also developed a 60-channel EEG system capable of operating in the harsh electromagnetic conditions of TMS. For the first time, we can electrically map cortical reactivity as well as functional connectivity in the brain. We have observed transcallosal transfer of signals [11], a strong nonlinearity of the EEG response as a function of TMS magnitude [17], and modulation of the early sensory evoked responses even contralaterally, indicating interhemispheric transfer.

Methods

TMS is the converse of MEG. The electric field induced in the tissue by TMS can be calculated using the formulae that give the magnetic flux produced by a current dipole in the brain. The macroscopic electromagnetic theory for TMS can be summarized in a compact way: If $\mathbf{L}(\mathbf{r})$ is the lead field of a coil with area A and current $I = I(t)$ is fed into the coil, then the total electric field, induced directly and caused by charges at conductivity boundaries, is

$$\mathbf{E}(\mathbf{r}) = -A \, \mathrm{d}I/\mathrm{d}t \, \mathbf{L}(\mathbf{r}) \, .$$

The reciprocity between MEG and TMS [18–19] permits several results obtained for MEG to be used in magnetic stimulation, and vice versa.

The magnetic field itself has practically no effect on the tissue; it is the electric field $\mathbf{E}$ induced by the changing magnetic field $\mathbf{B}$ (from Maxwell's equation $\nabla \times \mathbf{E} = -\partial \mathbf{B}/\partial t$) that causes ion flow in the brain. In the cellular scale, the current tends to follow low-resistance pathways within the cellular matrix. When the electric current induced by a TMS pulse meets a cell membrane, the membrane potential is altered and the probability of firing of the cell is changed. It has been shown that in a homogeneous medium, a straight axon is activated at places where $\partial E_x/\partial x$ is maximum, E_x being the component of the electric field along the axon [20]. However, there are no straight axons in the cortex. Instead of the electric field gradient, the important quantity for cortical excitation is the amplitude of the field. Excitation probably takes place best at bends of axons, at constrictions in the extracellular space or at synaptic terminals [21].

Because of the strong dependence of the magnetic field on the distance from the coil, even millimeter-level changes in its position or small changes in its orientation may change the locally induced field considerably. Therefore, stimulation amplitudes are typically selected on the basis of muscle response thresholds, which is not directly possible when other than motor areas are studied. Computer-assisted stereotactic TMS, when made sufficiently precise, will allow one to select the level of the induced field instead of selecting the stimulus amplitude as a percentage of the maximum stimulator output or on the basis of the individual motor threshold.

The focality of stimulation depends also on the type of coil and on its distance from the head. Small coils which are pressed against the scalp generally produce the most focal stimulation. With the figure-of-eight coil one can obtain a

©1999, Tohoku University Press
Recent Advances in Biomagnetism
T. Yoshimoto et al. (Eds)

better focus than with a simple loop [22]; it has been shown that further improvement is possible by using arrays of small coils [15]. While focusing is possible in the directions tangential to the skull, it is not possible to focus in depth even with combined magnetic and electric fields [23]. In other words, the maximum induced field is always at the most superficial part of the brain near the coil.

We are developing the use of EEG mapping and source localization in conjunction with stereotactic computer-assisted TMS. Our EEG system comprises a 60-electrode cap and electronics designed to function in the presence of the strong TMS pulses. The electrodes are 0.5-mm-thick Ag/AgCl rings, each interrupted by a 3-mm-wide slit to reduce the eddy currents that might otherwise cause excessive heating. In addition to heating, the TMS pulse produces a force on metallic objects; this force appears to cause an EEG artefact, which is dramatically reduced when a slit is introduced.

A key feature in avoiding the stimulus artefact is a sample-and-hold circuit that keeps the amplifier output at a constant level during the pulse. Although the stimulus artefact can be dealt with by a hold period of just 1 ms, one often observes artefacts from muscles activated by the TMS pulse, in particular when the lateral aspect of the head is stimulated. These can often be handled with a longer hold period, although at the expense of losing data.

The following observation can be made concerning the EEG response evoked by TMS. Since the lead fields of EEG and TMS are orthogonal in the spherically symmetric conductor geometry, EEG is blind to the part of the TMS-evoked primary current distribution that has the same pattern as the induced electric field. The induced field, of course, is registered by EEG unless compensated for or blocked from the amplifier input during the stimulus pulse.

Results

By recording the cortical response just milliseconds after a TMS pulse, we can obtain an index of the local reactivity of the cortex. Subsequent activity reflects corticocortical and transcallosal connectivity. Although the TMS-evoked responses are quite strong, averaging of perhaps 50–100 responses is required to obtain a good signal-to-noise ratio. In one set of experiments, we stimulated motor and visual cortices of volunteers [11]. The stimulation of the left sensorimotor hand area elicited an immediate strong response at the stimulated site. The activation spread to adjacent ipsilateral motor areas within 5–10 ms and to homologous regions in the opposite hemisphere within 20 ms. Similar activation patterns were generated by magnetic stimulation of the visual cortex: after the immediate ipsilateral response, the contralateral response was observed at about 20 ms. Fig. 1 shows the time evolution of the potential distribution in one subject after magnetic stimulation of the left motor cortex. A shift in the pattern from left to right is clearly seen between 11 and 17 ms.

When only one area of the cortex is active, dipole modeling may be appropriate in locating activity elicited by TMS. For more often encountered multiple or distributed sources, continuous current estimates are more reliable in indicating the active areas. We have used minimum-norm estimation [24] when observing the evolution of TMS-evoked brain activity.

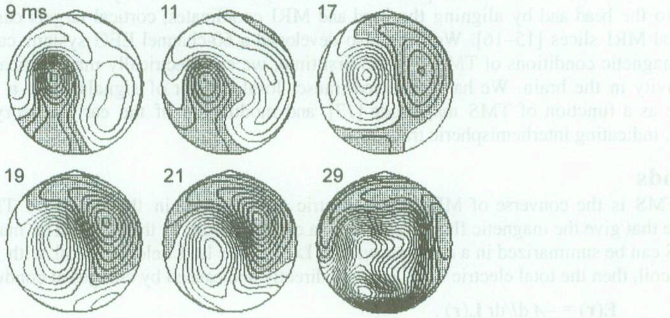

Fig. 1. Contour maps of scalp potentials recorded with 60-channel EEG after left motor cortex TMS. Activity is drawn at latencies from 9 to 29 ms. The contour spacing is 0.4 μV; negative potentials are shaded. The inter-stimulus interval was 2 s; 150 EEG responses to TMS at an intensity slightly below motor threshold (90% MT) were averaged. The head is seen from above, the nose pointing up in the figure.

Discussion

We have demonstrated that TMS can provide maps of reactivity and connectivity. In addition, TMS can be used to map areas that are important for the performance of a given task or areas that influence the activation of a muscle. One advantage of simultaneous use of EEG and TMS is that one can obtain direct information about the timing of signals transmitted from the stimulated site to other areas. We expect that the combination of TMS and EEG will offer a powerful tool for basic neuroscience and for clinical diagnosis, for example in the assessment of brain connectivity in patients suffering from neurodegenerative diseases or head injuries.

The combination of TMS with EEG provides direct information about the timing of signals transmitted from the stimulated site to other areas. It is also possible to combine sensory evoked potential and TMS studies [17]. A potentially useful application of EEG might be the early detection of approaching seizures during rapid-rate TMS treatment.

The combination of theoretical understanding in MEG and TMS as well as the combination of TMS with other methods in functional imaging will offer unprecedented possibilities for learning how the brain is functionally organized on the macroscopic level.

TMS is not completely noninvasive [25]. Risks from TMS include the possibility of an epileptic seizure when rapid-rate TMS (rTMS; stimulus rate 5 Hz or more) is used or when low-rate stimulation is applied to stroke patients. Magnetic stimulation may disturb nearby electronic devices such as hearing aids, cardiac pacemakers, or any other implanted electrical devices.

In the future, the brain can be stimulated by means of superposed fields from an array of dozens of separate coils in a helmet-like arrangement [15]. The current amplitude in the coils will be individually controlled, which makes it possible to move the stimulated spot electronically to any desired location without moving the coils themselves. Electronic targeting can give a dramatically improved accuracy and specificity of stimulation. The activating field can be focused on a smaller volume of critical tissue with an array of coils than with the traditional single-coil equipment.

References

[1] Nilsson J, Panizza M, and Grandori F (eds): Advances in Magnetic Stimulation: Mathematical Modeling and Clinical Applications. Advances in Occupational Medicine & Rehabilitation 2. Pavia: Maugeri Foundation, 1996

[2] Walsh V and Cowey A: Magnetic stimulation studies of visual cognition. Trends Cogn Sci 2: 103–110, 1998

[3] Cohen D: Feasibility of a magnetic stimulator for the brain, Weinberg H, Stroink G, and Katila T (eds): Biomagnetism: Applications & Theory. New York: Pergamon Press, 1985, pp 466–470

[4] Barker AT, Jalinous R, and Freeston IL: Non-invasive magnetic stimulation of human motor cortex. Lancet 1: 1106–1107, 1985

[5] Amassian VE, Cracco RQ, Maccabee PJ, Cracco JB, Rudell A, and Eberle L: Suppression of visual perception by magnetic coil stimulation of human occipital cortex. Electroenceph Clin Neurophysiol 74: 458–462, 1989

[6] Pascual-Leone A, Gates JR, and Dhuna A: Induction of speech arrest and counting errors with rapid-rate transcranial magnetic stimulation. Neurol 41: 697–702, 1991

[7] Jennum P, Friberg L, Fuglsang-Frederiksen A, and Dam M: Speech localization using repetitive transcranial magnetic stimulation. Neurol 44: 269–273, 1994

[8] Cohen LG, Celnik P, Pascual-Leone A, Corwell B, Faiz L, Dambrosia J, Honda M, Sadato N, Gerloff C, Catala MD, and Hallett M: Functional relevance of cross-modal plasticity in blind humans. Nature 389: 180–183, 1997

[9] Cracco RQ, Amassian VE, Maccabee PJ, and Cracco JB: Comparison of human transcallosal responses evoked by magnetic coil and electrical stimulation. Electroenceph Clin Neurophysiol 74: 417–424, 1989

[10] Amassian VE, Cracco RQ, Maccabee PJ, and Cracco JB: Cerebello-frontal cortical projections in humans studied with the magnetic coil. Electroenceph Clin Neurophysiol 85: 265–272, 1992

[11] Ilmoniemi RJ, Virtanen J, Ruohonen J, Karhu J, Aronen HJ, Näätänen R, and Katila T: Neuronal responses to magnetic stimulation reveal cortical reactivity and connectivity. NeuroReport 8: 3537–3540, 1997

[12] Paus T, Jech R, Thompson CJ, Comeau R, Peters T, and Evans AC: Transcranial magnetic stimulation during positron emission tomography: a new method for studying connectivity of the human cerebral cortex. J Neurosci 17: 3178–3184, 1997

[13] Fox P, Ingham R, George MS, Mayberg H, Ingham J, Roby J, Martin C, and Jerabek P: Imaging human intra-cerebral connectivity by PET during TMS. NeuroReport 8: 2787–2791, 1997

[14] Bohning DE, Shastri A, Nahas Z, Lorberbaum JP, Andersen SW, Dannels WR, Haxthausen EU, Vincent DJ, and George MS: Echoplanar BOLD fMRI of brain activation induced by concurrent transcranial magnetic stimulation. Invest Radiol 33: 336–340, 1998

[15] Ruohonen J and Ilmoniemi RJ: Focusing and targeting of magnetic brain stimulation using multiple coils. Med & Biol Eng & Comput 36: 297–301, 1998.

[16] Krings T, Buchbinder BR, Butler WE, Chiappa KH, Jiang HJ, Rosen BR, and Cosgrove GR: Stereotactic transcranial magnetic stimulation: correlation with direct electrical cortical stimulation. Neurosurg 41: 1319–1325, 1997

[17] Tiitinen H, Virtanen J, Ilmoniemi RJ, Kamppuri J, Ollikainen M, Ruohonen J, and Näätänen R: Separation of contamination caused by coil click from responses elicited by transcranial stimulation. Submitted, 1998

[18] Plonsey R: Capability and limitations of electrocardiography and magnetocardiography. IEEE Trans Biomed Eng BME-19: 239–244, 1972

[19] Ilmoniemi RJ, Ruohonen J, and Virtanen J: Relationships between magnetic stimulation and MEG/EEG, Nilsson J, Panizza M, and Grandori F (eds): Advances in Magnetic stimulation: Mathematical Modeling and Clinical Applications. Advances in Occupational Medicine & Rehabilitation 2. Pavia: Maugeri Foundation, 1996, pp 65–72

[20] Roth BJ: Mechanisms for electrical stimulation of excitable tissue. Crit Rev Biomed Eng 22: 253–305, 1994

[21] Maccabee PJ, Amassian VE, Eberle L, and Cracco RQ: Magnetic coil stimulation of straight and bent amphibian and mammalian peripheral nerves in vitro: locus of excitation. J Physiol 460: 201–219, 1993

[22] Ueno S, Tashiro T, and Harada K: Localized stimulation of neural tissues in the brain by means of paired configuration of time-varying magnetic fields. J Appl Phys 64: 5862–5864, 1988

[23] Heller L and van Hulsteyn DB: Brain stimulation using electromagnetic sources: theoretical aspects. Biophys J 63: 129–138, 1992

[24] Hämäläinen MS and Ilmoniemi RJ: Interpreting magnetic fields of the brain: minimum-norm estimates. Med & Biol Eng & Comput 32: 35–42, 1994

[25] Wassermann EM, Grafman J, Berry C, Hollnagel C, Wild K, Clark K, and Hallett M: Use and safety of a new repetitive transcranial magnetic stimulator. Electroenceph Clin Neurophysiol 101: 412–417, 1996

Acknowledgements

This work was supported by TEKES, the Foundation for Finnish Inventions, the Runar Bäckström Foundation, the Instrumentarium Science Foundation and the Academy of Finland.

Clinical application of functional MRI

Tanaka C, Fukunaga M, Ebisu T, Umeda M, Aoki I
Department of Neurosurgery and MR Center, Meiji University of Oriental Medicine
Hiyoshi-cho, Funai-gun, Kyoto, 629-0392, Japan

Introduction

Functional magnetic resonance imaging (fMRI) is a useful tool for functional mapping and analysis of the activated brain [1], [2]. However, some problems exist concerning the clinical application of fMRI. In clinical examination for neurosurgery, presurgical evaluation of the relationship between brain tumors or AVM and the eloquent cortex is important [3]. Recently, Mueller et al. used fMRI in patients with >2 cm between the margin of the tumor and the activated area and no decline in motor function occurred from surgical resection [4]. Another presurgical studies determined the central sulcus and lateralization of the dominant hemisphere [5], [6]. To evaluate the laterality of the dominant hemisphere, the lateralization index is sometimes useful. However, motion artifacts may cause serious errors for the clinical application of fMRI. As it is difficult for patients with neurological deficits to keep their head still during motor tasks, sensory stimulation was useful for determination of the sensoriomotor cortex using fMRI. In this study, we investigated the usefulness of sensory stimulation in clinical fMRI.

Materials and Method

The subjects were 10 normal volunteers and 20 patients with neurological disorders who examined by an activation study using clinical 1.5 T MRI (Signa Horizon; GE-YMS). During 120 images per slice using gradient echo echo planar imaging, fMRI were consecutively obtained using following parameters; Tr/Te/FA/slices=2000ms/50ms/90°/5-7, 24cm FOV, and 96 x 96 matrix. The slice thickness was 5mm. Brain activation was performed using sensory stimulations, including somatosensory stimulation, visual stimulation with a checkerboard pattern using a projector, and auditory stimulation with earphones. Patients with lesions near the motor cortex are examined by 2 activation tasks, finger opposition and somatosensory stimulation. For somatosensory stimulation, the patient's hand or foot was rubbed with a sponge every 20 seconds. Anatomical images were also obtained using a conventional 2D and 3D imaging sequence. The parameters of the spin echo T1w image was Tr/Te/FOV = 500ms/9ms/24cm and that of the 3D gradient echo image were Tr/Te/FA//thickness = 11.4ms/2.1ms/15°/1mm. Statistical analysis was performed by a cross correlation method using MRVision software (MRVision company) and analysis of motion artifact was performed using SPM (Statistical Parametric Mapping: free software; Neurological Institute, London) or MEDx software (Sensory Systems Inc.).

Results

In all patients, using somatosensory stimulation of the palm and foot, an activated area in the sensoriomotor cortex was detected at one examination using fMRI. No activated area using the motor task was detected in 2 cases. Moreover, using the motor task, we examined the activation study 2 or 3 times in several cases. In many cases, the activated area using sensory stimulation was almost the same intensity as that of the motor task. Futhermore, in several cases (Fig. 1), the activation area using sensory stimulation showed a slightly lower signal intensity and smaller area compared to that with the motor task. In a 19 years old female with right frontoparietal arteriovenous malformation (AVM), the activation area in both right and left motor cortecies was detected by the left finger opposition task. However, the activated area was only detected in the left sensoriomotor cortex with right finger opposition task. In this case, the activated area using left finger opposition was also located in the AVM (Fig. 2) [7]. In a case of left temporal malignant glioma, the right-handed patient did not complain of speech disturbance. Using both word and sound listening tasks, neither the Wernicke's area nor the dominant hemisphere was marked using fMR images. Using listening stimulation with words, fMRI showed activated areas in the bilateral temporal lobe (Fig. 3). The central sulcus was also detected by three dimensional images using the anatomical method (Fig. 4) [8]. Futhermore, functional mapping on 3 D images was very useful to evaluate the relationship between the activated area of sensoriomotor cortex and the central sulcus.

©1999, Tohoku University Press
Recent Advances in Biomagnetism
T. Yoshimoto et al. (Eds)

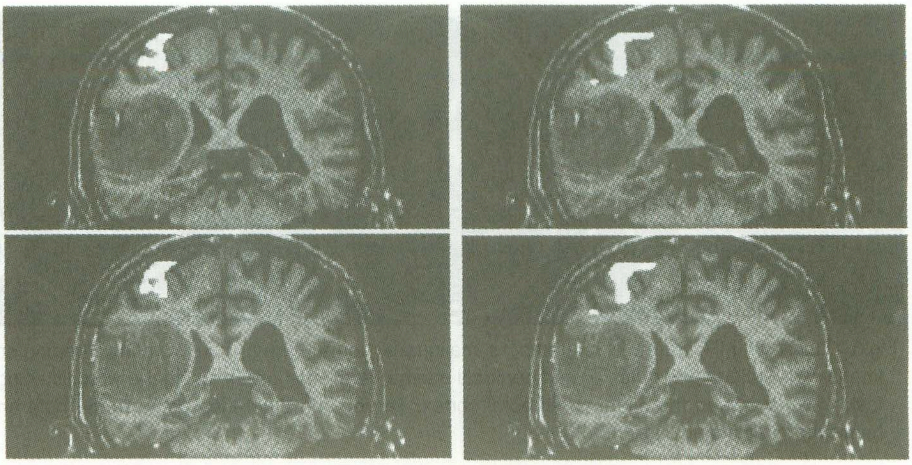

Fig. 1 Functional MR images of right frontal glioblastoma
Left images; fMR images using somatosensory stimulation of the left palm using a sponge.
Right images; fMR images using motor task, left finger opposition.
Activation area using both stimulations is almost the same.

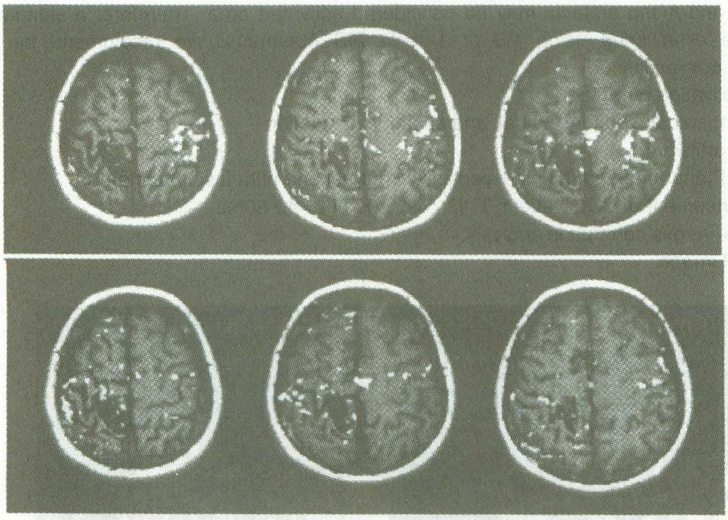

Fig. 2 Functional MR images of right frontoparietal AVM
upper images: Left motor cortex was activated by right finger opposition.
lower images: Right and left motor cortices are activated by left finger opposition.
Using this task, activation areas are also shown in the AVM.

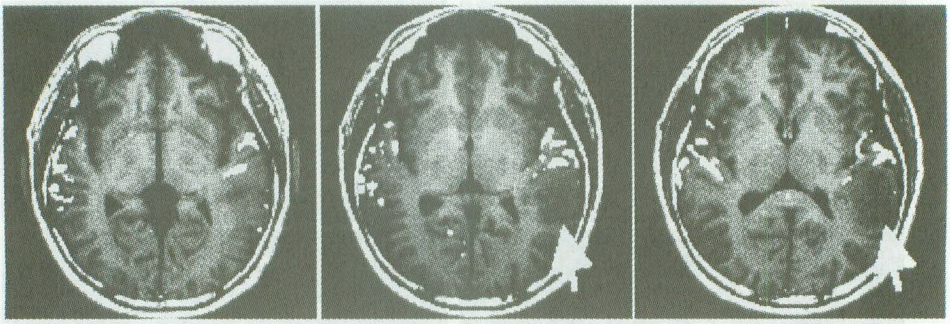

Fig.3 Functional MR images of left temporal malignant glioma (arrow): The low density region on T1w image was including both tumor and perifocal edema. Activation areas, using the word listening task, was shown in the bilateral temporal cortex. There is no difference between the right and left hemispheric activated regions.

Conclusion and Discussion

Functional mapping using sensory stimulation on 3 D images was very useful to determine the relationship between the sensoriomotor cortex and brain tumor or vascular lesions. Three dimensional anatomical images were also useful to confirm the central sulcus using anatomical method (Fig.4). These images were helpful for presurgical evaluation of brain tumors and AVM. However, in many previous studies on clinical fMRI, the main activation task was the motor task. The motor task caused many motion artifacts in functional images and these artifacts may be considered activated area. Therefore, a standard clinical fMRI study must be established using 1.5 or 1 tesla MR apparatus. We recommend the following parameters based on our results.

(1) Recommended activation paradigm:
Sensory stimulation; somatosensory, visual, and auditory stimulation
(minimal motion artifacts)
(2) Sequence---Echo Planar Imaging (high susceptibility contrast and ultra fast imaging).
(3) Parameters; enhancement of BOLD effect; Tr (2 - 4s) > 1s, Te =40-60ms.
(4) Statistical analysis---cross correlation analysis.
(5) Overlay on 3D MR image.

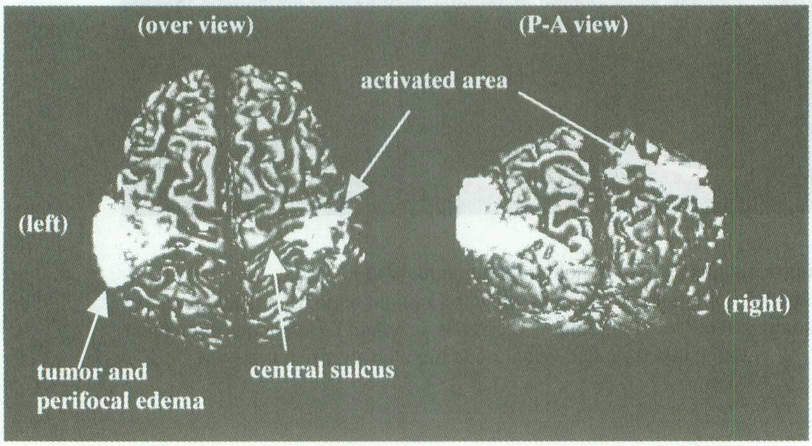

Fig.4Functional MR images of left temporal malignant glioma (arrow): fMR images on 3 D anatomical images. The high intensity region included both tumor and perifocal brain edema.
Activation areas, using the sensory stimulation of palm, are shown in the post central gyrus. The central sulcus was determined by anatomical method.

Acknowledgment

The study was performed supported by Special Coordination Funds for Promoting Science and Technology of the STA of the Japanese Government.

References

[1] Belliveau JW, Kennedy DNJr, Mckinstry RC, et al: Functional mapping of the humanvisual cortex by magnetic resonance imaging. Science 254: 716-719, 1991

[2] Ogawa S, Tank DW, Menon R, et al: Intrinsic signal changes accompanying sensory stimulation: functional brain mapping with magnetic resonance imaging. Proc Natl Acad Sci USA 89: 5951-5955, 1992

[3] Hammeke TA, Yetkin FZ, Mueller WM, et al: Functional magnetic resonance imaging of somatosensory stimulation. Neurosurgery 35: 677-681, 1994

[4] Mueller WM, Zetkin FY, Hammeke TA, et al: Functional magnetic resonance imaging mapping of the motor cortex in patients with cerebral tumors. Neurosurgery 39: 515-520, 1996

[5] Yetkin FZ, Mueller WM, Morris GL, et al: Functional MR activation correlated with intraoperative cortical mapping. AJNR 18: 1311-1315, 1997

[6] Binder JR, Swanson S, Hammecke T, et al: Determination of language dominance using functional MRI: a comparison with the Wada test. Neurology 46: 978-984, 1996

[7] Maldjian J, Atlas SW, Howard RS, et al: Functional magnetic resonance imaging of regional brain activity in patients with intraverebral arteriovenous malformations before surgical or endovascular therapy. J Neurosurg 84: 477-483, 1996

[8] Sobel DF, Gallen CC, Schwartz BJ, et al: Locating the central sulcus: comparison of MR anatomic and magnetoencephalographic functional methods. AJNR 14: 915-926, 1993

How do data analysis techniques influence neuronal localization with fMRI? A comparison of Fuzzy Cluster and Correlation Analysis regarding Hand Motor Somatotopy

Beisteiner R[1], Windischberger C[2], Edward V[1], Kaindl T[1], Erdler M[1], Moser E[1,3]

Neurology Department[1] - General Hospital of Vienna, Austria; NMR Group - Institute for Medical Physics[2], Vienna, Austria; MR unit[3], University of Vienna, Austria

Introduction

The purpose of the present study was to compare the model free fuzzy clustering technique with the widely used correlation analysis method in a finger flexion task designed to localize finger specific sensorimotor activity.

Methods

Paradigm

Right handed subjects were asked to perform regular tapping of either the 2nd or the 5th finger of the right hand. Different conditions were used: 1.) rest-2nd-rest-2nd-rest-2nd-rest, 2.) rest-5th-rest-5th-rest-5th-rest, 3.) rest-5th-rest-2nd-rest-5th-rest-2nd-rest-5th-rest-2nd-rest. Subjects were instructed to perform movements regularly, with about the same speed and to keep non moving fingers relaxed.

Data acquisition

Measurements were done on a BRUKER Medspec 3080 3T MR unit using a phase corrected blipped gradient echo EPI sequence. TR = 4 sec, TE = 84 msec, FA = Ernst angle, FOV = 256 mm, matrix 128*128, slice thickness 3 mm, acquisition time per image 160 ms. 10 adjacent transversal slices covering the cortical hand motor area were measured. For each resting/activation phase, 5 images were recorded per slice (about 20 sec per phase).

Data analysis

To minimize time dependent artifacts, only condition 3 was analyzed using the Fuzzy Clustering technique (Scarth et al. [4]) and a Correlation technique provided by the EVIDENT software (Inst. for Biodiagnostics, Winnipeg, Canada). Clustering was performed to yield clearly defined signal fluctuations corresponding to the stimulation paradigm and located predominantly within the primary sensorimotor area. The latter criterium allowed to separate movement artifacts. Correlation analysis was done by using a step function as reference. Subjects showing visible head movement artifacts were excluded. 2 evaluation procedures were used: A) Subjective: the primary contralateral sensorimotor area was individually defined according to anatomical and functional markers on the MR images and only pixels within this area were accepted for localization calculations. B) Objective: every pixel within the contralateral hemisphere but outside the interhemispheric fissure was accepted for localization calculations. Where possible, a separation in large and small amplitude results was used with the fuzzy cluster technique [1]. After thresholding (cluster membership > 0.8, correlation coefficient > 0.6), the center of gravities of the resulting pixel corresponding to the 2nd and the 5th finger were compared with regard to the cranio-caudal and the medio-lateral differences.

Results

Artifact free data of 6 subjects allowed analysis of 9 runs of condition 3. Evaluation procedure A. (exclusion of pixels outside the sensorimotor area on a subjective basis) is presented for low amplitude clusters and the correlation analysis. Procedure B. (no exclusion of "mislocalized" pixels) is presented for high amplitude clusters (separable in 5 runs), low amplitude clusters and the correlation analysis. Center of gravity differences between digit V and digit II as found with the various procedures are shown in table 1, 2 and figure 1.

©1999, Tohoku University Press
Recent Advances in Biomagnetism
T. Yoshimoto et al. (Eds)

TABLE 1: Cranial displacement of 5th finger motor activity localization relative to 2nd finger in mm.

RUN #	Low amplitude cluster analysis:		High amplitude cluster analysis:	Correlation Analysis:	
	Subjective	Objective	Objective	Subjective	Objective
Run 1	+1.20	+1.08	-	+3.27	+3.45
Run 2	+3.78	+3.09	-	+1.50	+1.17
Run 3	+3.45	+3.45	+2.64	+1.41	+0.54
Run 4	+1.71	+3.75	+2.46	-0.36	-0.12
Run 5	+0.63	+0.93	+3.00	+1.38	+1.38
Run 6	+2.31	-0.30	+1.08	+1.74	+1.74
Run 7	+3.06	-0.66	+2.28	+0.75	+0.75
Run 8	+1.32	+1.32	-	+2.49	+2.34
Run 9	+0.69	+4.89	-	+2.52	+3.42
MEAN	+2.01	2.18	2.29	1.60	1.65

TABLE 2: Lateral displacement of 5th finger motor activity localization relative to 2nd finger in mm.

RUN #	Low amplitude cluster analysis:		High amplitude cluster analysis:	Correlation Analysis:	
	Subjective	Objective	Objective	Subjective	Objective
Run 1	-2.08	-1.62	-	-0.32	+0.56
Run 2	-3.64	-2.42	-	+0.94	+1.74
Run 3	-2.92	-2.92	-2.76	-1.56	-0.52
Run 4	-2.48	-1.84	-2.40	+0.70	-1.58
Run 5	+0.14	+0.42	-2.20	-0.64	+0.94
Run 6	-1.10	+1.42	-6.00	-2.34	-2.34
Run 7	-2.78	+1.68	-7.44	-2.18	-2.20
Run 8	-0.09	-0.90	-	-2.50	-2.40
Run 9	-1.28	-1.06	-	-0.62	-2.20
MEAN	-1.80	-0.84	-2.31	-0.95	-0.89

Fig. 1. Graphic illustration of the data of table 1 & 2.

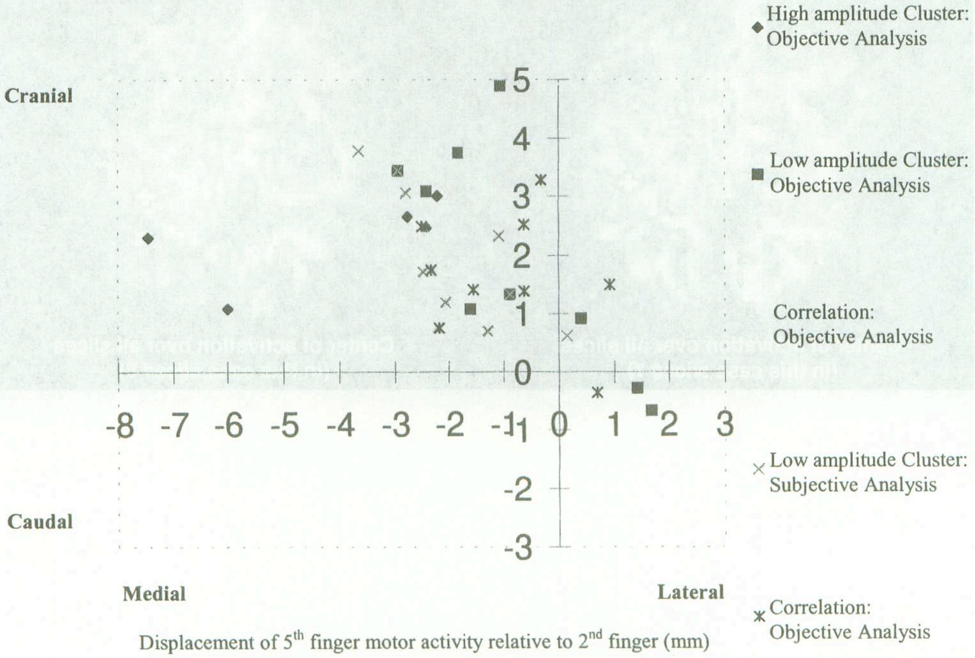

Fig. 2. 2nd finger low amplitude fuzzy cluster, objective analysis.

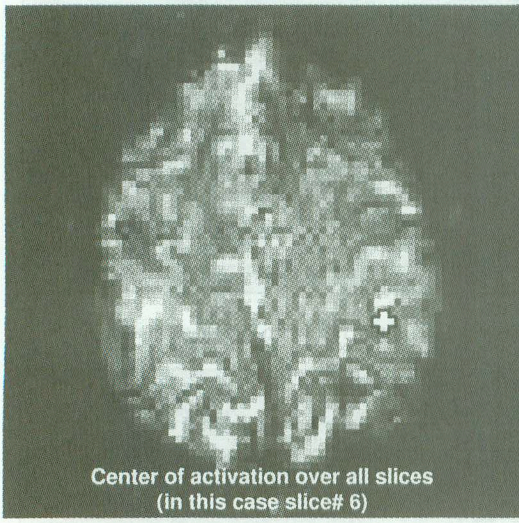

Fig. 3. 5th finger low amplitude fuzzy cluster, objective analysis. Same subject as Fig. 2. Slice 7 is superior to slice 6.

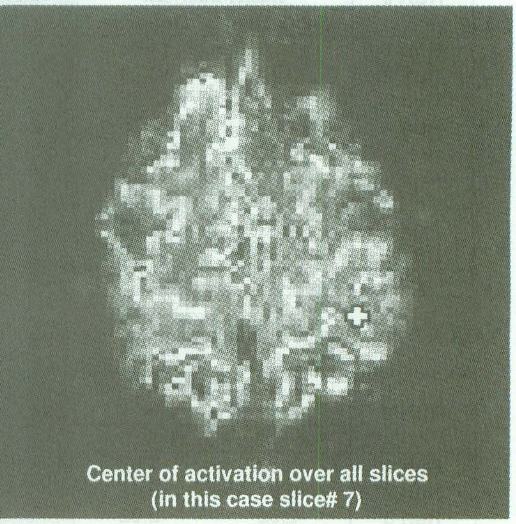

Fig. 4. 2nd finger low amplitude fuzzy cluster, subjective analysis. Same subject as Fig. 2.

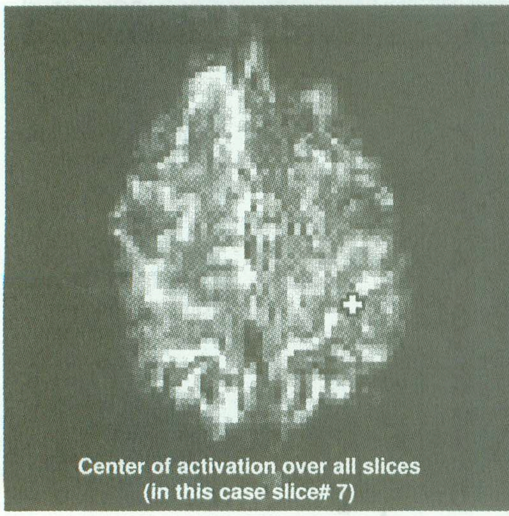

Fig. 5. 5th finger low amplitude fuzzy cluster, subjective analysis. Same subject as Fig. 2. Slice 8 is superior to slice 7.

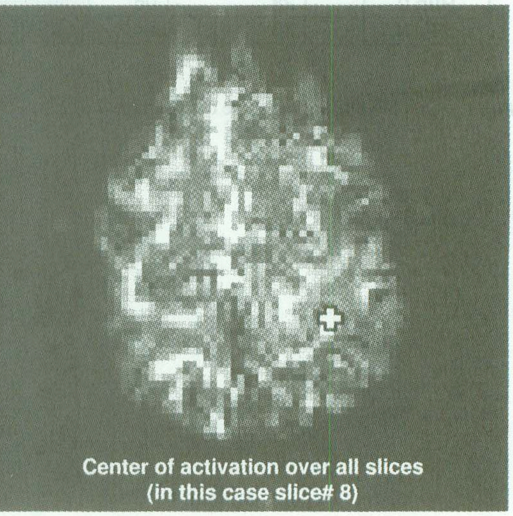

Discussion

When comparing the early data of Vogt [5], Foerster [2] or Penfield [3] on the motor homunculus in man, center to center distances of motor activity of finger II and V may be expected to lie around 15 mm. The comparison between the widely used correlation analysis and fuzzy cluster analysis showed that the largest differences in the expected direction were found when using only low signal amplitudes and fuzzy clustering (FCA) for analysis [1].

References

[1] Beisteiner et al. Magnetoencephalography (MEG) may help to improve Functional MRI brain mapping. Eur J Neurosc 1997, 9: 1072-1077.

[2] Foerster O. Motorische Felder und Bahnen. In: Bumke O., Grosshirn O, eds. Handbook of Neurology, vol. 6., Berlin: Springer Verlag 1936.

[3] Penfield W, Boldrey E. Somatic motor and sensory representation in the cerebral cortex of man as studied by electrical stimulation. Brain 1937, 60: 389-443.

[4] Scarth et al. Detection of novelty in functional images using fuzzy clustering. Proceedings ISMRM 1: 238; 1995

[5] Vogt C., Vogt O. Allgemeinere Ergebnisse Unserer Hirnfoschung. J Psychol Neurol 1919, 25: 279-439.

Magnetic Stimulation Effects of Eddy Current Orientation on Energy Metabolism in Frog Muscle

Chiba, A. and Chichibu, S.

Dept. Physiol., Kinki Univ. Sch. Med., Osaka-Sayama, Osaka 589-8511, Japan

Introduction

Magnetic stimulation has several advantages over the conventional electric stimulation method currently available; it is pain-free, non-invasive, and stimulates relatively deep tissues in the body.[1] Barker et al. found that the brain can be stimulated by a magnetic field change caused by a 1 Tesla pulse from a circular coil placed on the head.[2] Stimulation of muscles induced somatosensory evoked potentials confirming the usefulness of magnetic stimulation.[3] However, this method has several intrinsic problems: excitation does not occur at the highest current density, and there are difficulties in localizing the precise sites of excitation.[4,5] The difference in muscle responses to magnetic and electric stimulation led us to the idea that magnetic stimuli activate horizontally oriented neural elements and cortical cells trans-synaptically, whereas electrical stimuli excite cortical cell bodies and axons directly. An important parameter of magnetic stimulation is the direction in which the induced electric current flows within the tissue. The purpose of this study is to find the relationship between the cell orientation of muscle and nerve to magnetic stimulation. We examined the locus of initiation of muscular contraction along the eddy current generated by local magnetic stimulation using a figure-eight magnetic coil. To clarify whether the eddy current initially acted on nerve bundles and then propagated the excitation to the muscle or if it directly stimulated muscle cells, we performed magnetic stimulation after blocking neuromuscular transmission in the terminal and plates. In addition, metabolism of high energy phosphate during muscular contraction due to electrical and magnetic stimulation was examined by ^{31}P nuclear magnetic resonance (^{31}P-NMR).

Methods

Bullfrogs (Rana catesbeiana) of either sex, weighing between 350 and 450 g, were cooled to immobilization in an ice bath, in order to avoid the use of anesthetic agents, which might have influenced the results. The experiments were conducted in accordance with the protocol approved by the Animal Care and Use Committee at the Kinki University School of Medicine.

After the frogs were immobilized by immersion in ice water for about 10 min, the gastrocnemius muscles in the hind legs were excised. The isolated gastrocnemius muscles were immersed in Ringer's solution at 19 °C for 10 min, and then magnetic stimulation was applied. As the control, electric stimulation of a 0.05 msec width pulse at strengths from 0.09 V to 0.014 V was applied to the sciatic nerve with the innervated muscle. A magnetic stimulation system (Magstim M200, Magstim Inc., UK) equipped with a figure-eight coil 70 mm in diameter was used. Local magnetic stimulation with fairly precise localization is possible with the use of a figure-eight coil; the eddy current is induced in the opposite direction in 2 crossed loops, and the coil current is the strongest immediately below the coil junction. Therefore, the direction of the eddy current can be controlled by changing the direction of the coil. Each isolated gastrocnemius was transversely placed in Ringer's solution in an acrylic chamber measuring 8 x 12 x 5 cm, which was aerated with a mixture of 95% O_2 and 5% CO_2. The femur was fixed, and the Achilles tendon was connected to a strain gauge using a piece of string. Displacement was monitored with a carrier amplifier to an oscilloscope (VC-11, Nihon Kohden, Japan). A figure-eight coil was set at 1 cm above the center of the gastrocnemius muscle center. The eddy current was induced by currents at opposite directions at the locus of the junction in the figure-eight coil.[6] The angle between the figure-eight coil and the longitudinal axis of the gastrocnemius muscle was defined as 0° when the distal-proximal line of the muscle was parallel to the direction of the eddy current, 90° when it was perpendicular to the eddy current, and 180° when it was in the opposite direction to the eddy current. Tension changes caused by muscular contraction at magnetic stimulation with intensities of 0 - 100% of 2.2 Tesla were measured at 0°, when the distal proximal line of the muscle was parallel to the eddy current, 90° and 360°. Muscular contraction caused by supermaximal electric stimulation of the sciatic nerve was considered 100%. Thirty minutes after application of TTX (1 x 10^{-7} mol/l) and *d*-tubocurarine chloride (1 x 10^{-6} mol/l), which block neurotransmission in terminal end plates of frogs, the changes in muscular contraction due to magnetic stimulation were studied.

The metabolism of high energy phosphates during muscular contraction (M. sartorius) due to electrical and magnetic stimuli was evaluated with ^{31}P-NMR. Muscles were stimulated directly by passing current down the central glass

©1999, Tohoku University Press

Recent Advances in Biomagnetism
T. Yoshimoto et al. (Eds)

tube, which contained 3 mol KCl in D_2O, returning through the outer Ringer-filled annulus via short Pt electrodes at the bottom.[6] For indirect muscle contraction, muscle was set in the chamber and the sciatic nerve stimulated. For muscle contraction by magnetic stimulation, the muscle was set in the chamber and a figure-eight coil was positioned over the muscle so that the magnetic field passed through the muscle in opposite directions around the target. Twitch amplitudes elicited by magnetic and electrical stimuli were measured alternately at every 10s. ^{31}P-NMR spectroscopy was performed using a high-resolution NMR system (JEOL, GX-400, Japan), and ^{31}P was determined at the observation frequency of 161.7 MHz. The pulse angle was 60°, and the pulse repetition time was 2 sec, with an iteration of 60 repetitions. The creatine phosphate (PCr) level was set to equal 0 ppm, and all chemical determinations were performed at 20°C. The concentration of each compound was obtained from the area under the resonance curve of each signal. Peak areas were determined by computer integration and were used to assess the relative concentrations of various phosphorus metabolites. The intracellular pH of the muscle was determined from the chemical shift difference between the PCr and inorganic phosphate (Pi).

Results

Figure 1 shows the twitch and muscular contraction curves induced by electrical stimulation of nerves and magnetic stimulation of muscles. With increasing electric stimulation intensity, an S-shaped increase in muscular contraction was observed (Figs. 1 A and D). The panels B, C and E in Fig. 1 show the twitch and muscular contraction curves induced by eddy currents at 0° and 90° caused by magnetic stimulation. The twitch curves induced by magnetic stimulation at 10 - 90% output were not sharp, even at 0° and 90° eddy current. Magnetic stimulation induced muscular contraction when the eddy current was parallel to the muscle cell fiber axis (0° and 180°), and weaker contraction when the eddy current was perpendicular to the muscle fiber axis (90° and 270°). To clarify whether magnetic stimulation induced muscular contraction by direct stimulation of muscle cells or by excitation of muscles via nerve excitation, responses to magnetic stimulation after administration of tetrodotoxin (TTX) and d-tubocurarine were examined. The amplitude of muscular contraction gradually decreased after administration of neurotransmitter blocking agents. Muscular contraction by magnetic stimulation did not occur 30 min after application of TTX and d-tubocurarine.

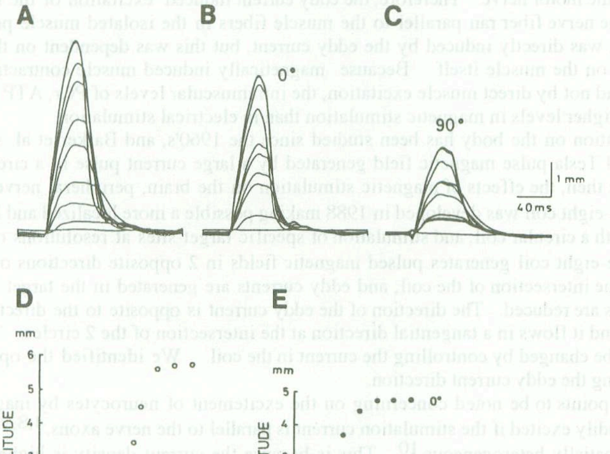

Fig.1 The evoked tension in the gastrocnemius muscle by electric and magnetic stimuli.

Figure 2 shows the changes of PCr/Pi and pH of 20 g weight loading after direct electrical muscle stimuli, electrical nerve stimuli and magnetic stimuli. The muscles contained 28.0 ± 2.1 mmol PCr and 1.8 ± 0.2 mmol. The PCr/Pi and pH changed only slightly following magnetic stimulation. When the nerve was stimulated, the pH shifted more distinctly toward acidic and reduced from 7.4 to 6.7 by the last contraction. With direct stimulation of the muscle, the pH rapidly reduced from about the second contraction to 6.53 by the last train. Both PCr and pH changes were more marked after direct electrical stimulation than after magnetic stimulation.

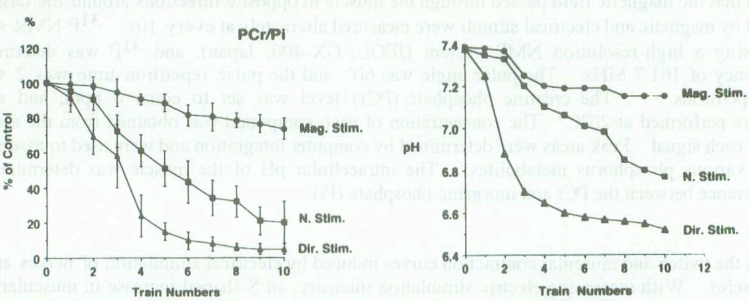

Fig. 2 Changes of PCr/Pi and pH in the muscle under various stimuli.

Discussion

In the present study, the optimum locus of magnetic stimulation on the muscular surface for inducing muscular contraction was determined, and the metabolism of high energy phosphate during muscular contraction due to electrical and magnetic stimuli were examined with ^{31}P-NMR. If the eddy current induced was parallel to the muscle cells, muscular contraction was large, while no muscular contraction was observed if the eddy current occurred perpendicular to the muscle cells. Since inhibition of the neurotransmission in the terminal endplate by TTX or d-tubocurarine suppresses muscular contraction induced by magnetic stimulation, the eddy current must have been acting on the terminal endplate of the motor nerve. Therefore, the eddy current induced excitation of the nerve, if it was parallel to the nerves. Since the nerve fiber ran parallel to the muscle fibers in the isolated muscle preparation, it is likely that muscular contraction was directly induced by the eddy current, but this was dependent on the orientation of the nerve distribution and not on the muscle itself. Because magnetically induced muscle contraction was caused via motor nerve stimulation, and not by direct muscle excitation, the intramuscular levels of PCr, ATP and pH during contraction were maintained at higher levels in magnetic stimulation than in electrical stimulation.

Magnetic stimulation on the body has been studied since the 1960's, and Barker et al. succeeded in stimulating a human brain with a 1 Tesla pulse magnetic field generated by a large current pulse in a circular coil placed above the head in 1985. Since then, the effects of magnetic stimulation on the brain, peripheral nerves, and muscles have been studied.[1] The figure-eight coil was developed in 1988 making possible a more localized and higher current density than could be obtained with a circular coil, and stimulation of specific target sites at resolutions of less than 5 mm became possible.[7] A figure-eight coil generates pulsed magnetic fields in 2 opposite directions on both sides of the target immediately below the intersection of the coil, and eddy currents are generated in the target region in the directions in which magnetic fields are reduced. The direction of the eddy current is opposite to the direction of the induced current flowing in the coil, and it flows in a tangential direction at the intersection of the 2 circles. Therefore, the direction of the eddy current can be changed by controlling the current in the coil. We identified the optimum stimulation site of the muscle by changing the eddy current direction.

There are several points to be noted concerning on the excitement of neurocytes by magnetic stimulation. First, neurocytes can be readily excited if the stimulation current is parallel to the nerve axons.[4,8,9] Secondly, the density of the eddy current is spatially heterogeneous.[10] This is because the current density is highest immediately below the figure-eight coil, and the membrane potential becomes depolarized at the front and hyperpolarized at the back.[11,12] Thirdly, unidirectional stimulation can be obtained by tilting the coil relative to the nerve fiber. We believed that muscular contraction by magnetic stimulation was induced by excitement of the nerve fiber. From experiments using neurotransmission blockers at the terminal endplates, we concluded that magnetic stimulation did not directly induce excitation of muscle cells but induced excitation of the synapses of motor nerve endplates distributed on muscles, resulting in muscular contraction.[13,14] Therefore, to induce excitation of the muscle by magnetic stimulation, a coil must be placed in a position in which the eddy current is generated parallel to the motor nerve innervating the muscle cells.

The immediate source of energy for muscle contraction is ATP, whose hydrolysis yields energy, adenosine diphosphate (ADP) and Pi. ATP levels are maintained by enzymatic transfer of phosphate from PCr. PCr serves as an important reservoir of high energy phosphate groups for regeneration and synthesis of ATP.[6] The concentration of PCr relative to ATP can be an index of energy storage.[6] ATP use could be calculated by measuring for ATP derived from the creatine kinase reaction (measured from the decrease in PCr) and from glycolysis (estimated from decreases of intracellular pH).[15,16] In the present experiment, muscle contraction induced by electrical stimulation showed nearly a 20% decrease in PCr/Pi compared to muscle contraction by magnetic stimulation during 5 trials, but the mean value of the relative concentration in the indirectly stimulated muscles was lower than that in the muscle contraction by magnetic stimulation. This difference seems to be largely due to differences in stimulation among species. The metabolism of frog muscle contraction by magnetic stimulation is assumed to be smaller than that of muscle contraction induced by electrical stimulation, although the contraction shows the same working load. During direct electrical stimulation of muscles and indirect stimulation via muscle nerves, the muscle contraction is so intense that the intracellular pH value is greatly decreased. Compared with muscle contraction by magnetic stimulation, electrical stimulation showed lower intracellular pH and a slight change in PCr consumption, despite having the same working load. Muscle contraction by direct stimulation acts on the sarcoplasmic reticulum with membrane potential changes to release calcium ions for the induction of contraction.[6] Little is known about the phosphate metabolism of muscle contraction induced by magnetic stimulation.[17] Energy metabolism during contraction shows a difference between magnetic and electrical stimulation. [15,16] We belive that this muscle contraction arising independent of metabolites was due to impaired activation beyond the neuromuscular junction.

In summary, we examined the effect of the orientation of the figure-eight coil with respect to the muscle, and the tension evoked in the gastrocnemius muscle by magnetic stimulation. The maximum responses were obtained at a position where the longitudinal axis of the figure-eight loop was positioned perpendicular to the nerve fiber. After *d*-tubocurarine chloride application, muscular contraction gradually decreased, and finally disappeared. Magnetically induced muscle contraction was caused by motor nerve stimulation, not by direct muscle excitation. The metabolism of high energy phosphates during muscular contraction due to electrical and magnetic stimuli was evaluated with ^{31}P-NMR. The intramuscular levels of PCr, ATP and pH during contraction were maintained at higher levels in magnetic stimulation than that in electrical stimulation.

References

[1] Rossini PM, Barkar AT, Berardelli A, et al: Non-invasive electrical and magnetic stimulation of the brain, spinal cord and roots: basic principles and procedures for routine clinical application. Report of an IFCN committee. Electroenceph clin Neurophysiol 91: 79-92, 1994

[2] Barker AT, Jalinous R, Freeston IL.: Non-invasive magnetic stimulation of the human motor cortex. Lancet i: 1106-1107, 1985

[3] Zhu Y, Star A.: Magnetic stimulation of muscle evokes cerebral potentials. Muscle Nerve 14: 721-732, 1991

[4] Mills KR, Boniface SJ, Schubert M.: Magnetic brain stimulation with a double coil: the importance of coil orientation. Electroenceph clin Neurophysiol 85: 17-21, 1992

[5] Maccabec PJ, Amassian VE, Eberle LP at al: Magnetic coil stimulation of straight and bent amphibian and mammalian peripheral nerve in vitro: locus of excitation. J Physiol 460: 201-219, 1993

[6] Dawson MJ, Gadian DG, Wilkie DR.: Contraction and recovery of living muscles studied by ^{31}P nuclear magnetic resonance. J Physiol 267: 703-735, 1977

[7] Ueno S, Tashiro T, Harada K.: Localized stimulation of neural tissues in the brain by means of a paired configuration of time-varying magnetic fields. J Appl Phys 64:5862-5864, 1988

[8]Ueno S, Matsuda T, Fujiki M.: Functional mapping of the human motor cortex obtained by focal and vectorial magnetic stimulation of the brain. IEEE Trans Mag 26: 1539-1544, 1990

[9] Werhahn KJ, Frong JK, Meyer BU et al: The effect of magnetic coil orientation on the latency of surface EMG and single motor unit responses in the first dorsal interosseous muscle. Electroenceph clin Neurophysiol 93: 138-146, 1994

[10] Abdeen MA, Stuchly MA.: Modeling of magnetic field stimulation of bent neurons. IEEE Trans Biomed Eng 41: 1092-1095, 1994

[11] Weidmann S.: Magnetic stimulation of ferret papillary muscle. J Physiol 475: 169-173, 1994

[12] Nagarajan SS, Durand DM.: A generalized cable equation for magnetic stimulation of axons. IEEE Trans Biomed Eng 43: 304-312, 1996

[13]Machetanz J, Bischoff C, Pichlmeier R et al: Magnetically induced muscle contraction is caused by motor nerve stimulation and not by direct muscle activation. Muscle Nerve 17: 1170-1175, 1994

[14]Ellaway PH, Rawlinson SR, Lewis HH et al: Magnetic stimulation excites skeletal muscle via motor nerve axons in the cat. Muscle Nerve 20: 1108-1114, 1997

[15] Kemp GJ, Sanderson AL, Thompson GH et al: Regulation of oxidative and glycogenolytic ATP synthesis in exercising rat skeletal muscle studied by ^{31}P magnetic resonance spectroscopy. NMR Biomed 9: 261-270, 1996

[16]Barker AJ, Carson PJ, Miller RG et al: Metabolic and nonmetabolic components of fatigue monitored with ^{31}P-NMR. Muscle Nerve 17: 1002-1009, 1994

[17] Matheson GO, Dunlop RJ, Mckenzie DC et al: Force output and energy metabolism during neuromuscular electrical stimulation: a ^{31}P-NMR study. Scand J Rehabil Med 29: 175-180, 1997

Analysis of Visual Stimulation Data Obtained During High Resolution Functional MR Imaging (HIFI) Using Fuzzy Clustering Analysis (FCA) and a nonlinear Motion-Artifact Reduction Algorithm

Edward V[1], Beisteiner R[1], Langenberger W[2], Barth M[3,2], Windischberger C[2], Kaindl T[1], Erdler M[1], Moser E[1,3]

Department of Neurology[1] - General Hospital of Vienna, Austria; NMR Group - Institute for Medical Physics[2], Vienna, Austria; MR unit[3], University of Vienna, Austria

Introduction

The high temporal resolution of Echo Planar Imaging (EPI) facilitates single event fMRI [6,9]. A common method for evaluating fMRI data is correlation analysis. However, there are some drawbacks when using EPI in combination with correlation analysis: The high temporal resolutions are achieved at the expense of spatial resolution. Considerable image distortion occurs along susceptibility boundaries, which introduces large uncertainties in relating function to anatomy. When using short stimuli, difficulties arise in modeling an appropriate reference function for correlation analysis due to the variability of the signal time course. Furthermore, additional hardware usually not present on routine clinical imagers is required.

In the present study, we used a modified FLASH sequence (HIFI) first suggested by Beisteiner et al. [2] to achieve simultaneous high spatiotemporal resolution without image distortion and additional hardware requirements. We expanded this methodology which is analogous to electrophysiological ERP recording methods to include movement artifact reduction (k-space correction scheme, Langenberger et al. 1997 [11]) and reliable detection of activations having unpredictable response functions with fuzzy cluster data analysis [13].

Methods

Paradigm

2 subjects were recorded during repetitive tonic visual stimulation with 7.5s of red light followed by 24.5s of darkness.

Data acquisition

In HIFI, the sequential recording of the fourier lines of each image is replaced by sequential recording of corresponding fourier lines of consecutive images, thereby achieving a time resolution equal to TR [2, 12]. Stimuli are repetitively presented timelocked to the running image numbers. This methodology is analogous to electrophysiological ERP recording methods. A FLASH sequence (flow compensated, spoiled, TE = 42 ms, TR = 90 -500 ms, FA = 30°, FOV = 230 mm, 128*128 matrix, d = 3 mm, 128 consecutive images equaling a TR dependant time window of 11.5 -32 sec, 2-4 posteriorly tilted transversal slices, running through the calcarine sulcus) was used.

Data analysis

A major challenge in HIFI is it's susceptibility to motion artifacts. We used a nonlinear k-space correction scheme [11] in combination with Fuzzy Cluster Analysis (FCA) [13] to overcome this problem. In FCA, pixel are divided into clusters on the basis of the similarity of their time courses and are assigned a membership value to the clusters. Motion corrected, as well as uncorrected data were evaluated with FCA. In addition, correlation analysis with a box-car reference function was performed for comparison (activation threshholds; FCA cluster membership > 0.8, correlation coefficient > 0.6). FCA and correlation analysis was done with the EVIDENT software package (Inst. for Biodiagnostics, Winnipeg, Canada).

Results

After elimination of motion and other global artifacts using the k-space correction scheme and FCA, highly localized activation can be seen in the left calcarine sulcus. When omitting the correction scheme, artifacts become visible (fig. 1.)

©1999, Tohoku University Press

Recent Advances in Biomagnetism
T. Yoshimoto et al. (Eds)

Fig. 1. (a.) FCA activations of slice 1 and 2 overlayed onto slice 2.

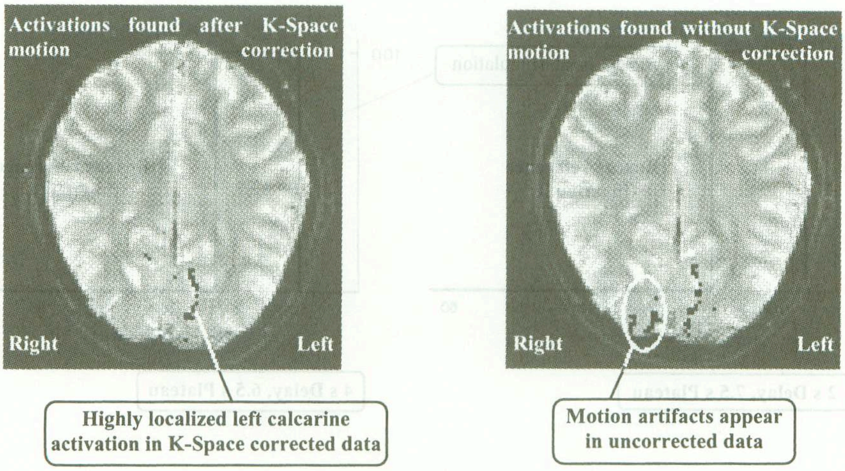
Activations found after K-Space motion correction
Right
Left
Highly localized left calcarine activation in K-Space corrected data
Activations found without K-Space motion correction
Right
Left
Motion artifacts appear in uncorrected data

(b.) Average time courses of active pixel in slice 1 and 2.

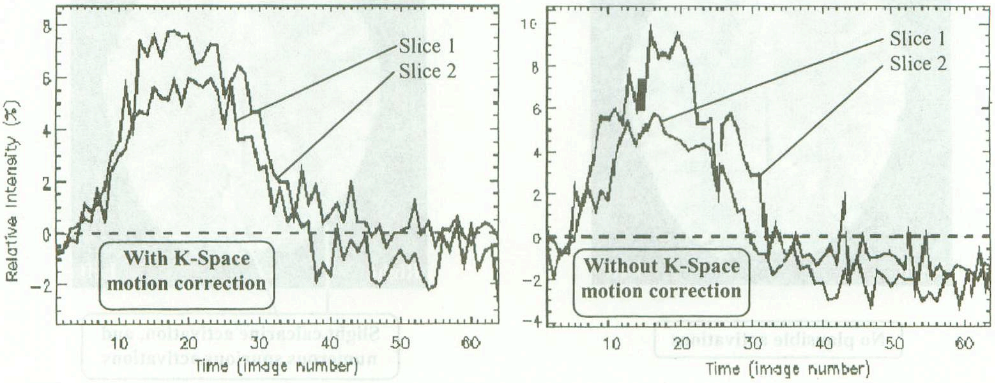

Discussion

The challenges of using correlation analysis are twofold. Firstly, the onset latency of the box car reference function is unknown. In fig. 2., although a "plausible" boxcar reference function with a latency of 2s and plateau of 7.5 s was used in correlation analysis, no "plausible" activation appeared. This lack of activated pixel may be due to a different onset latency of the physiological response. Secondly, the precise shape of the physiological response curve is unknown. For a stimulation period of 7.5 s, a physiologically plausible reference function might have a plateau phase onset latency of about 4s (including ascent) with a plateau phase shorter than the actual stimulation (due to the ascent), egs. 6.5 s. Using a boxcar reference function with a latency of 5 s, and a plateau of 6.5 s, only a small portion of the calcarine sulcus shows activations, and there are numerous spurious activations due to the discrepancy between the actual physiological response and the boxcar reference function used (fig. 2.).

In conclusion, by facilitating event related fMRI with high spatio-temporal resolution, good artifact reduction and model independent signal extraction, the suggested methodology holds much promise for improved crossvalidative experimentation with electrophysiological techniques [1, 3, 4, 5, 7, 8, 10, 14].

Fig. 2. (a.) 2 "plausible" boxcar reference functions used in the correlation analysis:

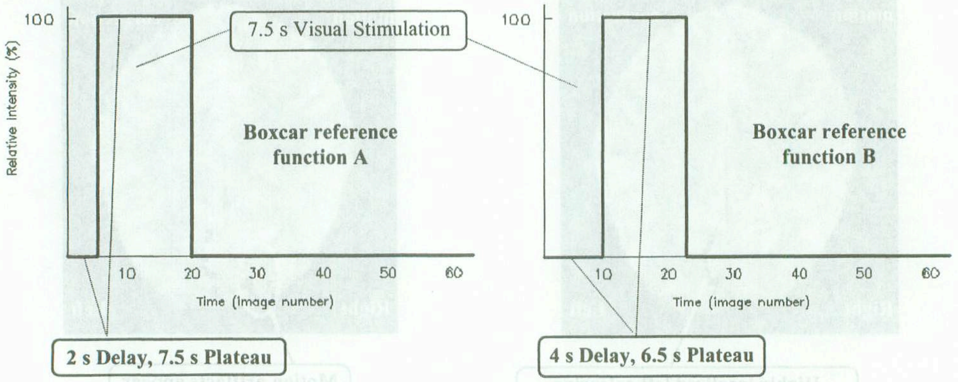

(b.) Correlation analysis activations of slice 1 and 2 with K-Space correction over-layed onto slice 2

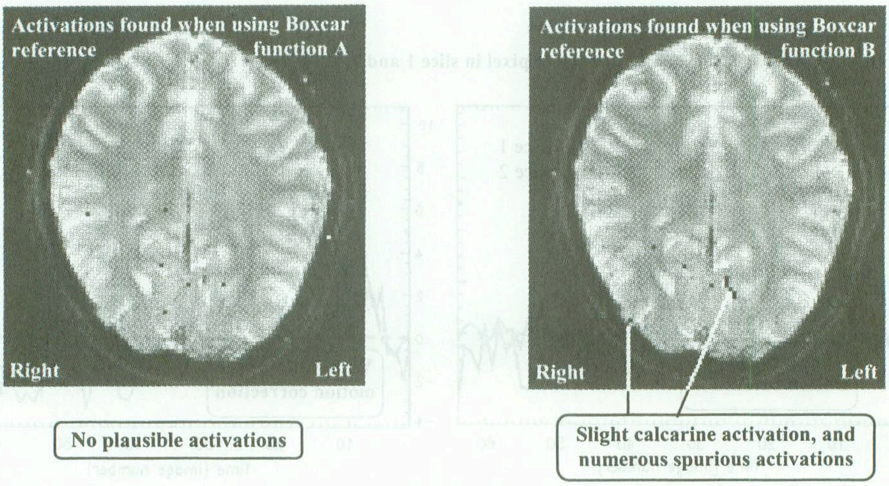
Activations found when using Boxcar reference function A
Right
Left
No plausible activations
Activations found when using Boxcar reference function B
Right
Left
Slight calcarine activation, and numerous spurious activations

(c.) Average time courses of active pixel in slice 1 and 2.

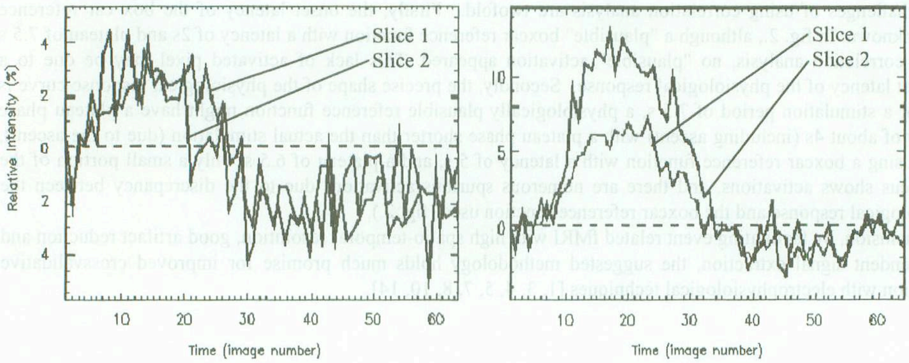

References

[1] Baumann et al. Comparison of functional magnetic resonance imaging with positron emission tomography and magnetoencephalography to identify the motor cortex in a patient with an arteriovenous malformation. J-Image-Guid-Surg. 1995; 1(4): 191-7

[2] Beisteiner et al. In: Book of Abstracts: The European Society for Magnetic Resonance in Medicine and Biology, 11th annual meeting, April 20-24: 226, 1994

[3] Beisteiner et al. [Correlation of results of localization by functional magnetic resonance tomography with magnetoencephalography] Radiologe. 1995 Apr; 35(4): 290-3

[4] Beisteiner et al. Comparing localization of conventional functional magnetic resonance imaging and magnetoencephalography. Eur-J-Neurosci. 1995 May 1; 7(5): 1121-4

[5] Beisteiner et al. Magnetoencephalography (MEG) may help to improve Functional MRI brain mapping. Eur J Neurosc 1997, 9: 1072-1077

[6] Buckner et al. Selective averaging of rapidly presented individual trials using fMRI. HUMAN-BRAIN-MAPPING. 1997; 5 (4) : 243-248

[7] George et al. Mapping function in the human brain with magnetoencephalography, anatomical magnetic resonance imaging, and functional magnetic resonance imaging. J-Clin-Neurophysiol. 1995 Sep; 12(5): 406-31

[8] Gerloff et al. Coregistration of EEG and fMRI in a simple motor task. HUMAN-BRAIN-MAPPING. 1996; 4 (3) : 199-209

[9] Josephs et al. Event-related fMRI. HUMAN-BRAIN-MAPPING. 1997; 5 (4) : 243-248

[10] Kwong. Functional magnetic resonance imaging with echo planar imaging. Magn-Reson-Q. 1995 Mar; 11(1): 1-20

[11] Langenberger et al. Nonlinear motion artifact reduction in event-triggered gradient-echo FMRI. Magn-Reson-Imaging. 1997. 15(2): 163-7

[12] Moser et al. In: The Bio-Clinical Interface - Bio-clinical Psychiatry Mapping Brain Function, J.P. Macher, M.A. Croq, JF Nedelec (eds), J. Libbey-Eurotext: 385-390, 1995.

[13] Scarth et al. Detection of novelty in functional images using fuzzy clustering. Proceedings ISMRM 1: 238; 1995

[14] Stippich et al. Motor, somatosensory and auditory cortex localization by fMRI and MEG. NEUROREPORT-. JUN 22 1998; 9 (9) : 1953-1957

Direct Activation of Pyramidal Tract Neurons Evoked by Transcranial Magnetic Stimulation with a Medio-laterally Oriented Figure-eight Coil

Hyodo, A.[1,*], Kobayashi, M.[1,2], Ueno, S.[1]

Department of Biomedical Engineering[1], and Department of Orthopedics[2],
Graduate School of Medicine, University of Tokyo, Tokyo, Japan.

Introduction

Magnetic stimulation is a non-invasive method to stimulate both the central and peripheral nervous systems [1]. A method to stimulate localized areas of the cortex by a figure-eight coil was developed [2]. In transcranial magnetic stimulation (TMS), multiple descending volleys are produced. These volleys contain D-wave generated by the direct activation of pyramidal tract neurons (PTNs), and I-waves generated by transsynaptically indirect activation of PTNs [3][4][5]. It is argued that TMS preferentially produces I-waves rather than D-wave, although transcranial electrical stimulation easily generates corticospinal D-wave [4][5]. However, it was shown that D-wave was evoked when the coil current at the intersection of the figure-eight coil flows medio-laterally (ML stimulation) rather than Antero-Posterior (AP) stimulation [6][7]. It was also shown that motor evoked potentials (MEPs) recorded at the first dorsal interosseous muscle (FDI muscle) evoked by ML stimulation were resistant to suppressive effects with paired-TMS (pTMS) [6], which are composed of subthreshold condition and suprathreshold test stimuli at the short interstimulus intervals (ISIs)[8][9][10][11].

Wilson et al. reported that ML stimulation generates discretely polyphasic surface MEPs from the FDI muscle during voluntary contraction [12]. Using the technique of pTMS, we verified the hypothesis that the early component of polyphasic MEPs reflects corticospinal D-wave, which is resistant to suppressive effects with pTMS, rather than I-waves.

Methods

10 normal subjects (8 males and 2 females) aged 24-33 years who gave informed consent were examined. MEPs were recorded from the left-FDI muscle with surface disk-electrodes placed on it in belly-tendon profile and amplified by electromyograph (MEB-5504, Nihon Kohden Co., Bandwidth 50-3000 Hz). The FDI muscle was voluntarily contracted at approximately 10 % of maximum contraction and the contraction level was monitored by audio-visual feedback throughout the experiment. Even the MEPs from contracted FDI muscle are suppressed by pTMS at the short intervals [13][14], though less compared to the relaxed FDI muscle [15].

The condition stimulus (SMN-1100, Nihon Kohden Co.) was delivered via a round coil centered at vertex , the coil's inner and outer diameters are 100 mm and 122 mm, respectively. The coil current direction was clockwise viewing

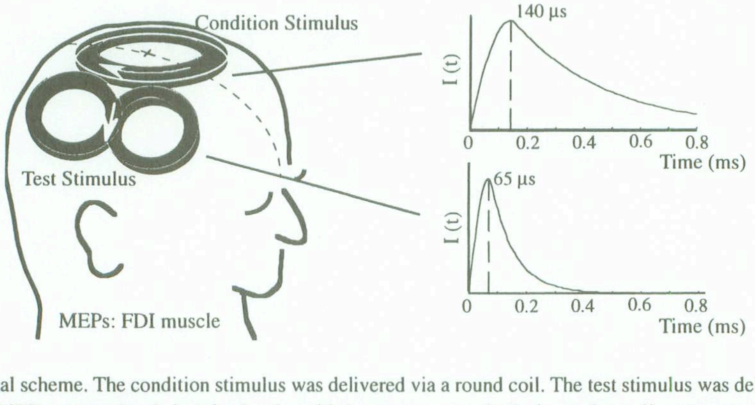

Fig. 1. Experimental scheme. The condition stimulus was delivered via a round coil. The test stimulus was delivered via a figure-eight coil. MEPs were recorded at the 1st dorsal interosseous muscle during voluntarily contracted at 10 % of maximum contraction. Arrows indicate coil current directions. The right side of this figure shows the coil current waveforms of both condition and test stimuli. They are both monophasic waveforms.

** Present address: Nihon Kohden Corporation, Tokyo, Japan.*

©1999, Tohoku University Press
Recent Advances in Biomagnetism
T. Yoshimoto et al. (Eds)

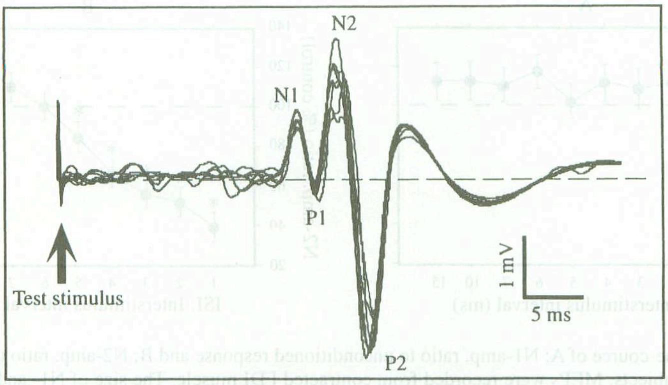

Fig. 2. Control MEPs recorded from FDI muscle of 1 subject evoked by unconditioned stimulus. Polypasic MEPs were recorded. Early and late negative (positive) peaks of MEPs are termed as N1 (P1) and N2 (P2), respectively. Each trace was the average of 2 trials and 8 waveforms are superimposed.We measured the amplitudes of N1 and N2 components. The N1-amp. was defined as baseline-N1 amplitude. The N2-amp. was defined as the mean value of P1-N2 and P2-N2 amplitudes.

from the top. The test stimulus (a prototype AAA-10687, Nihon Kohden Co.) was delivered via a figure-eight coil placed over the right motor cortex area. The figure-eight coil (inner diameter: 53 mm, outer diameter : 73 mm.) was bent at the intersection (140 degrees) in order to fit the scalp. The coil current direction at the intersection of the figure-eight coil was medio-lateral. The waveforms of both condition and test stimuli were monophase, and their rise-time were 140 μs and 65 μs, respectively. The intensities of condition and test stimuli were 80 % and 130-140 % of the threshold intensity, respectively. The threshold intensity was determined as the minimum intensity of evoking the MEPs at the contracted FDI in 50 % of the trials. The figure-eight coil was positioned at the optimal site for eliciting the polyphasic surface MEPs. ISIs were 1, 2, 3, 4, 5, 6, 7, 10 and 15 ms (Fig. 1). After recording the unconditioned test responses, the conditioned responses at different ISIs were recorded in a randomized order. Every 2 trials were averaged, and 8 waveforms were recorded. The N1- and N2-amplitudes at different ISIs of each subject were compared to those of the unconditioned responses by the Wilcoxon signed-ranks test with Holm correction for multiple comparison [16]. The N1- and N2-amplitudes at each ISI were expressed as the ratio to the mean values of the unconditioned (control) responses.

Results

The control MEPs evoked by only the test stimulus from 1 subject are shown in Fig. 2. Each trace was the average of 2 trials and 8 waveforms were superimposed. The N1-amp. was defined as the baseline-N1 peak amplitude. The N2-amp. was defined as the mean value of P1-N2 and P2-N2 amplitudes. The representative MEPs evoked by pTMS at the ISIs of 1, 5, 10 ms from the same subject are shown in Fig. 3. The late components were affected by changing the ISIs, however, the early components were stable at any ISIs. Fig. 4 shows the mean (± 2S.E.) time course of N1-amp. ratio and N2-amp. ratio.

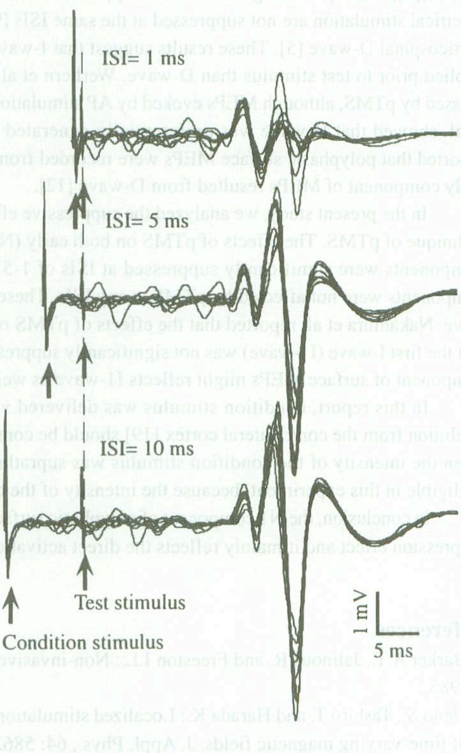

Fig. 3. Responses to pTMS at different ISIs (1, 5, 10 ms) recorded from same subject in Fig.2. The 2nd negative phase is suppressed at the ISI of 1 ms, whereas the 1st negative phase is stable at any ISIs.

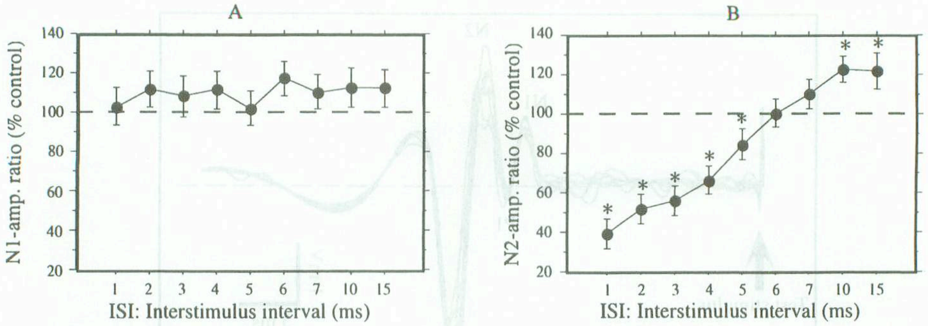

Fig. 4. Mean ± 2S.E. time-cource of A: N1-amp. ratio to unconditioned response and B: N2-amp. ratio to unconditioned response in 10 normal subjects. MEPs were recorded from contracted FDI muscle. The size of N1- and N2- amp. were expressed as the percentage of the size of control MEPs (100 %). N2-amp. were suppressed at ISIs of 1, 2, 3, 4, 5 ms and facilitated at ISIs of 10 and 15 ms (*: $p < 0.05$, Wilcoxon-signed ranks test with Holm correction). However, N1-amp. were not suppressed nor facilitated at any ISIs.

There was no significant difference in N1-amp. ratio between conditioned and unconditioned responses at any ISIs. The N2-amp. were significantly suppressed at ISIs of 1, 2, 3, 4, 5 ms and facilitated at ISIs of 10 and 15 ms ($p < 0.05$, Wilcoxon signed-ranks test with Holm Correction), although the N1-amp. were not significantly affected by condition stimulus.

Discussion

In pTMS composed of subthreshold condition and suprathreshold test stimuli, the MEPs were suppressed at short ISIs [8][9][10][11]. It is argued that this suppressive effect occurs at cortical level [9][17]. MEPs evoked by the anodal electrical stimulation are not suppressed at the same ISIs [9][11]. Anodal transcranial stimulation preferentially generates corticospinal D-wave [5]. These results suggest that I-waves are more easily affected by subthreshold condition stimulus applied prior to test stimulus than D-wave. Werhern et al. showed that MEPs evoked by ML stimulation were not suppressed by pTMS, although MEPs evoked by AP stimulation were suppressed at short ISIs [6]. Kaneko et al. and Nakamura et al. showed that D-wave was preferentially generated by ML stimulation [7][18]. On the other hand, Wilson et al. reported that polyphasic surface MEPs were recorded from contracted FDI muscle in ML stimulation and argued that the early component of MEPs resulted from D-wave [12].

In the present study, we analyzed the suppressive effects on polyphasic MEPs evoked by ML stimulation, using the technique of pTMS. The effects of pTMS on both early (N1) and late (N2) components were observed severally. The N2 components were significantly suppressed at ISIs of 1-5 ms and facilitated at ISIs of 10 and 15 ms. However, the N1 components were not affected by pTMS at any ISIs. These results suggest that the N1 component results mainly from D-wave. Nakamura et al. reported that the effects of pTMS on evoked spinal cord potentials in conscious human and found that the first I-wave (I1-wave) was not significantly suppressed at ISIs of 2 and 5 ms [18]. These results suggest that the N1 component of surface MEPs might reflects I1-wave as well as D-wave.

In this report, condition stimulus was delivered via a round coil centered at vertex, therefor, interhemispheric inhibition from the contralateral cortex [19] should be considered. Inhibition effects from contralateral cortex is observed when the intensity of the condition stimulus was suprathreshold [19]. Thus, the effects from contralateral cortex were negligible in this experiment, because the intensity of the condition stimulus was subthreshold.

In conclusion, the N1 component of polyphasic surface MEPs evoked by ML stimulation is resistant to corticocortical suppression effect and it mainly reflects the direct activation of PTNs.

References

[1]Barker A.T., Jalinous R. and Freeston I.L.: Non-invasive stimulation of the human motor cortex. Lancet, 1: 1106-1107, 1985

[2]Ueno S., Tashiro T. and Harada K.: Localized stimulation of neural tissues in the brain by means of paired configuration of time-varying magnetic fields. J. Appl. Phys., 64: 5862-5864, 1988

[3]Patton H.D. and Amassian V.E.: Single- and multiple-unit analysis of cortical stage of pyramidal tract activation. J. Neurophysiol., 17: 345-363, 1954

[4]Amassian V.E., Cracco R.Q. and Maccabee P.J.: Focal stimulation of human cerebral cortex with the magnetic coil: a comparison with electrical stimulation. Electroenceph. clin. Neurophysiol. 74: 401-416, 1989

[5]Day B.L., Dressler D., Maertens de Noordhout A. et al.: Electric and Magnetic stimulation of human motor cortex: surface EMG and single motor unit responses. J. Physiol. (Lond.), 412: 449-473, 1989

[6]Werhern K.J., Fong J.K.Y., Meyer B.U. et al.: The effect of magnetic coil orientation on the latency of surface *EMG and* single motor unit responses in the first dorsal interosseous muscle. Electroenceph. clin. Neurophysiol. 93: 138-146, 1994

[7]Kaneko K., Kawai S., Fuchigami Y. et al.: The effect of current direction induced by transcranial magnetic stimulation on the corticospinal excitability in human brain. Electroenceph. clin. Neurophysiol. 101: 478-482, 1996

[8]Claus D., Weis M., Jahnke U. et al: Corticospinal conduction studied with magnetic double stimulation in the intact human. J. Neurol. Sci. 111: 180-188, 1992

[9]Kujirai T., Caramia M.D., Rothwell J.C. et al.: Corticocortical inhibition in human motor cortex. J. Physiol. (Lond.), 471: 501-519, 1993

[10]Ziemann U., Rothwell J.C. and Ridding M.C.: Interaction between intracortical inhibition and facilitation in human motor cortex. J. Physiol. (Lond.), 496: 873-881, 1996

[11]Yokota T., Yoshino A., Inaba A. and Saito Y.: Double cortical stimulation in amyotrophic lateral sclerosis. J. Neurol. Neurosurg. Psychiat., 61: 596-600, 1996

[12]Wilson S.A., Day B.L., Thickbroom G.W. and Mastaglia F.L.: Spatial differences in the sites of direct and indirect activation of corticospinal neurons by magnetic stimulation. Electroenceph. clin. Neurophysiol. 101: 255-261, 1996

[13]Ridding M.C., Sheean G., Rothwell J.C. et al.: Changes in the balance between motor cortical excitation and inhibition in focal, task specific dystonia. J. Neurol. Neurosurg. Psychiat., 59: 493-498, 1995

[14]Kobayashi M., Hyodo A., Kurokawa T. and Ueno S.,: The 1st component of polyphasic motor evoked potentials is resistant to suppression by paired transcranial magnetic stimulation in humans. J. Neurol. Sci., 1998 (in press.)

[15]Ridding M.C., Taylor J.L. and Rothwell J.C.: The effect of voluntary contraction on cortico-cortical inhibition in human motor cortex. J. Physiol. (Lond.), 487: 541-558. 1995

[16]Aickin M. and Gensler H.: Adjusting for multiple testing when reporting research results: the Bonferroni vs Holm methods. Am. J. Public Health, 81: 726-728, 1996

[17]Di Lazzaro V., Restuccia D., Oliviero A. et al.: Magnetic transcranial stimulation at intensities below active motor threshold activates intracortical inhibitory circuits. J. Phyisiol. (Lond.), 119 (2): 265-268, 1998

[18]Nakamura H., Kitagawa H., Kawaguchi Y. and Tsuji H.: Intracortical facilitation and inhibition after transcranial magnetic stimulation in conscious humans. J. Physiol. (Lond.), 498: 817-823, 1997

[19]Ferbert A., Priori A., Rothwell J.C. et al.: Interhemispheric inhibition of the human motor cortex. J. Physiol. (Lond.), 453: 525-546, 1992

Functional MR mapping of the cortical hand and lip areas

Inoue T[1], Shimizu H[2], Nakasato N[1],
Kanno A[3], Fujiwara S[2], Yoshimoto T[1]
Department of Neurosurgery, Tohoku University School of Medicine[1];
Department of Neurosurgery, Kohnan Hospital[2];
MEG lab, Kohnan Hospital Ryogo Center[3], Sendai, Japan

Introduction

Surgical treatment of brain tumors near the eloquent areas requires appreciation of individual topographic brain function. Distinct localization of hand and oro-facial sensorimotor cotices is critically important for preoperative decision of resection area.

Recently, functional magnetic resonance imaging (fMRI) has been attractive to determine extension of brain function before surgery [1]. Functional localization can be also achieved by using magnetoencephalography (MEG) for the distinct localization of primary sensorimotor area [2]. In this study, we performed hand- and lip-movement fMRI for localizing functional somatotopy in the sensorimotor area. The results were compared with MEG with median nerve stimualtion.

Methods

Eight normal volunteers (two females and six males, age 23-66 years) and two patients with glioma (one female and one male, age 38-46) underwent fMRI and MEG. The study protocol was approved by the ethical commitee of Kohnan Hospital. All subjects understood the aim and the procedures of the functional paradigm and task performance was visually monitored.

fMRI was performed with a commercial 1.5 Tesla whole body scaner (GE SIGNA, Milwaukee, WI) and the standard head coil. The head was fixed with Velcro tape, airmat and neck collar. Five oblique-axial slices, parallel to the bicommissural line, were obtained for anatomical reference images using T1 weighted inversion recovery echo planar imaging (EPI) sequence: repetition time (TR); 20 msec, field of view (FOV); 24 x 24 cm, matrix; 128 x 128, slice thickness; 10 mm. fMRI was performed on the same slices using a gradient echo type EPI sequence: TR 3000 msec, TE; 60 msec, slice thickness; 10 mm. fMRI consisted of six 30-second epochs alternating between rest and activation. The specific task was repetitive opening and closing of the hand and the lip protrusion per second.

Functional images were analyzed with an image analysis software (FuncToolTM, GE Medical Systems, Buc, France). The images during the first nine seconds of each rest and task period were not included for the analysis because of the delay for the increase in fMRI signal. The time intensity curve of each pixel was stataistically analyzed by a cross correlation method (correlation coefficient>0.6).

MEG was performed using an MRI-linked whole head 122-channel MEG system (Neuromag, Helsinki, Finland) in a magnetically shielded room. The relative position of the subject's head and the MEG sensors were determined using reference coils attached to the scalp fiduciary points. SEFs were measured during median nerve stimulus. The MEG signals were filtered from 0.03 Hz to 400 Hz and digitized at 1280 Hz. The resulting data were averaged for 200 stimulus presentations. The first peak of the SEFs, i.e. N20m was employed for source estimation using an equivalent current dipole model at the peak latency. To place the dipole position on the individual anatomical images, three-dimensional spoiled gradient recalled acquisition in the steady-state sequences were obtaiend by following acquisition parameters: TR; 40 msec, TE; 2 msec, flip angle; 45 degree, section thickness 1.5 mm, FOV; 24 cm, matrix 256 x 160. The fiduciary points used in MEG were marked with small oil-containing capsules. The calculated dipole positions were superimposed on the MRI using by a graphic worksation linked to the MEG system. In the present MEG study, the central sulcus was defined as the nearest sulcus to the dipole position of N20m.

Results

In all subjects, focal functional activity was demonstrated by fMRI. The hand area on fMRI was detected around the contra-lateral central sulcus defined by MEG. The lip area on fMRI was demonstrated bilateraly, and was localized inferoanterior to the hand area. In addition, fMRI demonstrated activation in other areas such as the supplementary motor area.

The dipole position of MEG successfully indicated the central sulcus in all subjects.

fMRI and MEG were coincidental in defining the central sulcus in all subjects.

©1999, Tohoku University Press
Recent Advances in Biomagnetism
T. Yoshimoto et al. (Eds)

Discussion

The primary finding of this study is that the fMRI-defined central sulcus and the MEG-defined central sulcus coincided with each other, and functional somatotopy in the sensorimotor area could be discribed by fMRI.

fMRI signal activation was detected not only in the primary motor cortex but also in wider regions such as the supplementary motor area. Because the principle of fMRI is the visulalization of T2* shortning due to the blood oxygen level-dependent effect [3], fMRI may provide somatotopic extension of functional activity. The capability of fMRI to demonstrate spatial extension of activation area may be an advantage of fMRI, however, to determine the central sulcus in patients it may also be a disadvantage obscuring the exact position of the sulcus. On the other hand, MEG detects the central sulcus in a pinpoint fushion with very small variation [2]. In the present study, it was possible to detect the central sulcus objectively in all subjects.

Combination of fMRI and MEG would be ideal for precise functional assessment.

References

[1] Mueller WM, Yetkin FZ, Hammeke TA, et al: Functional magnetic resonance imaging mapping of the motor cortex in patients with cerebral tumors. Neurosurgery 39: 515-520, 1996

[2] Kawamura T, Nakasato N, Seki K, et al: Neuromagnetic evidence of pre- and post-central cortical sources of somatosensory evoked responses. Electroencephalogr Clin Neurophysiol 100: 44-50, 1996

[3] Belliveau JW, Kennedy DNJr, McKinstry RC, et al: Functional mapping of the human visual cortex by magnetic resonance imaging. Science 254: 716-719, 1991

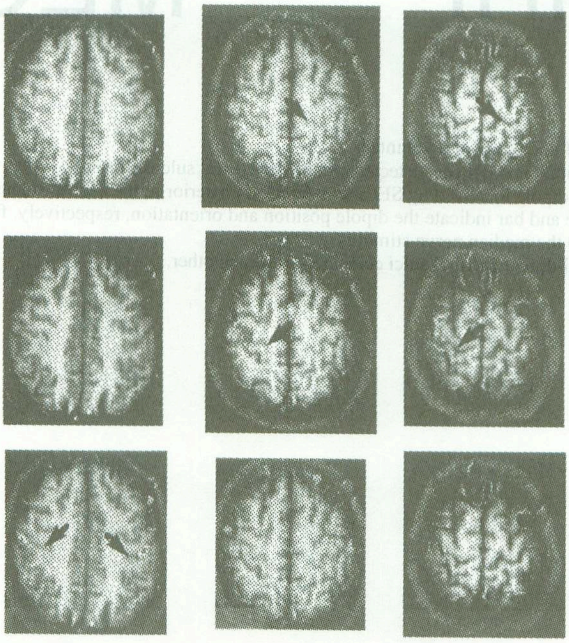

Figure 1

Representative fMRI of a volunteer during right hand grasping (upper), left hand grasping (middle) and lip protrusion (lower).

The hand areas were detected around the contralateral central sulci defined by MEG (arrows). The lip areas on fMRI were inferolateral to the hand motor areas bilateraly. In addition, fMRI demonstrated activation in other areas such as the supplementary motor area.

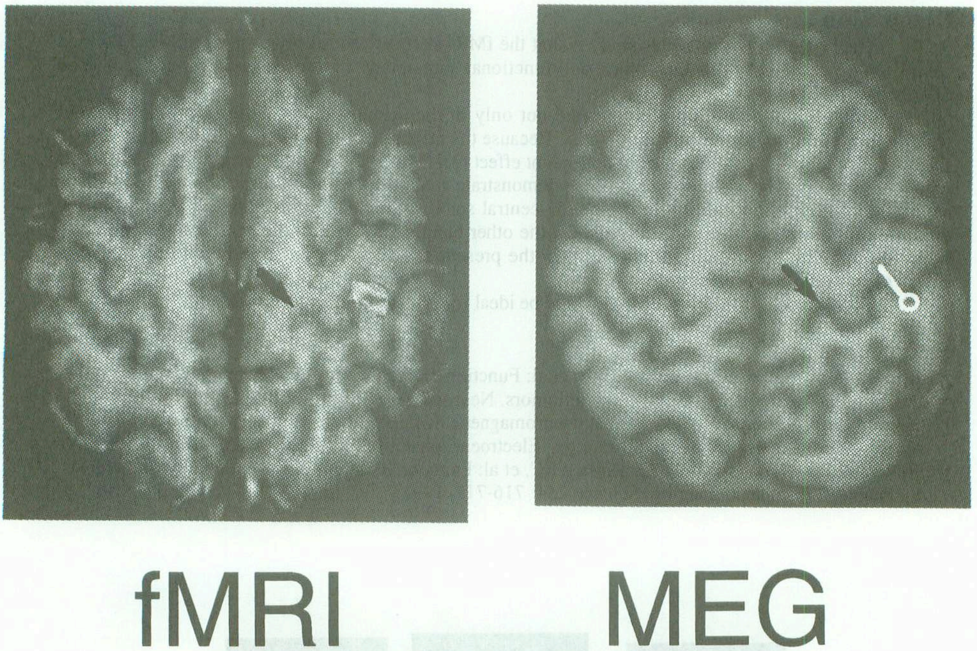

Figure 2
Representative fMRI and MEG of a volunteer.
Left: The activation on fMRI was detected around the central sulcus (arrow).
Right: The N20m dipole localized by SEFs was detected posterior to the central sulcus (arrow). The white circle and bar indicate the dipole position and orientation, respectively, for the N20m response to the median nerve stimulus.
The fMRI- and MEG-defined central sulci coincided with each other.

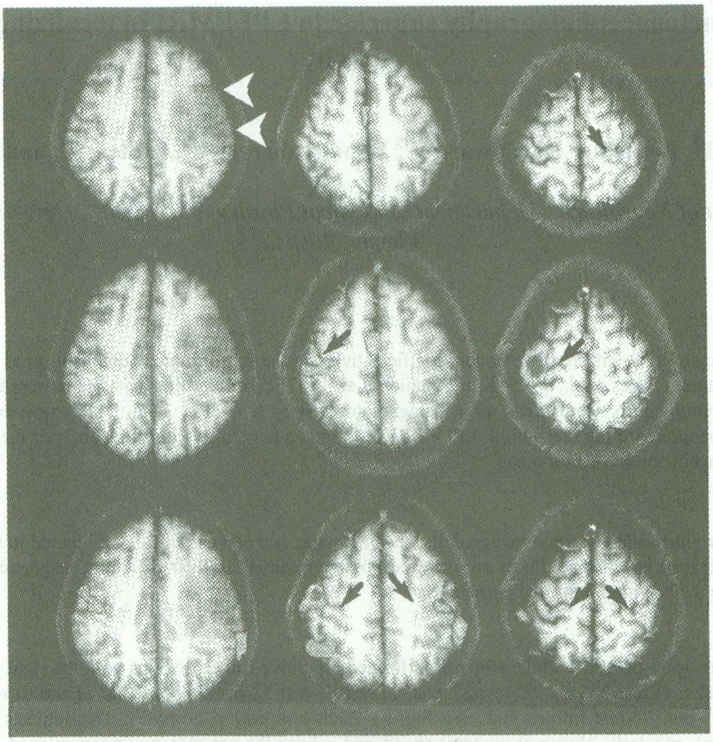

Figure 3
Representative fMRI of a patient with left frontal glioma (arrow heads) during right hand grasping (upper), left hand grasping (middle) and lip protrusion (lower).
The hand areas were detected around the contralateral central sulci defined by MEG (arrows). The lip areas on fMRI were demonstarated inferolaterally bilateraly.

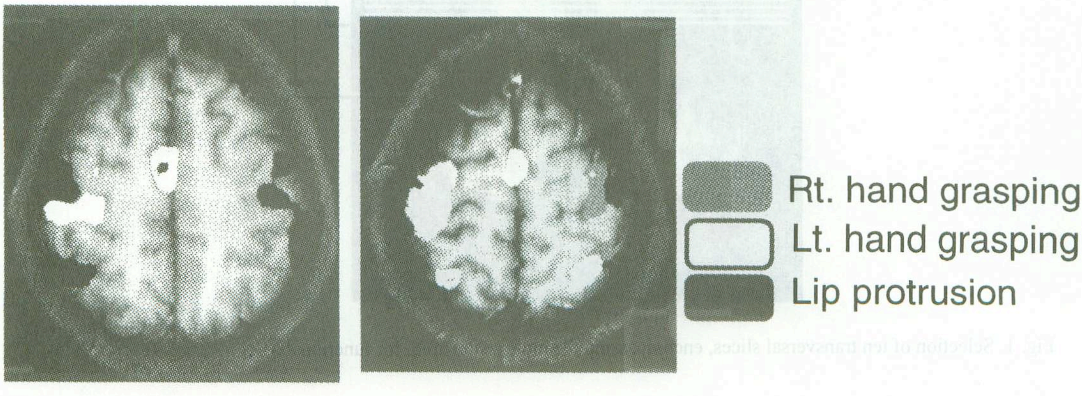

Figure 4
fMRI activation areas by right hand grasping (gray), left hand grasping (white) and lip protrusion (block) were overlaid on the same anatomical images.

Is Magnetoencephalography superior to EPI FMRI in localizing neuronal activity?

Kaindl T[1], Beisteiner R[1], Edward V[1], Windischberger C[2], Erdler M[1], and Moser E[2,3]

Department of Neurology [1], Department of Medical Physics [2], MR Unit [3], University of Vienna, Vienna, Austria

Introduction

MEG's capability to differentiate finger specific activity on the sensorimotor homunculus has been demonstrated. Former fMRI studies (Sanes et al., 1995; Kleinschmidt et al. 1997) could not find separate representations for different fingers in the motor cortex hand area, when using motor rest as a control state. This study examines the spatial sensitivity and specificity of high resolution EPI FMRI at 3 T and a new fuzzy clustering analysis method to separate the activation of adjacent cortical motor areas.

Methods

Eighteen right-handed healthy young adults, seven females and eleven males, participated in this study. All were free of neurological or psychiatric illness and showed no abnormalities in their structural magnetic resonance images. All subjects gave their written informed consent.

Task design

fMRI scans were obtained while subjects performed repetitive finger flexions with the right hand (2^{nd} or 5^{th}) in three different tasks: 1) rest-2^{nd}-rest-2^{nd}-rest-2^{nd}-rest, 2) rest-5^{th}-rest-5^{th}-rest-5^{th}-rest (Fig. 2) and 3) rest-5^{th}-rest-2^{nd}-rest-5^{th}-rest-2^{nd}-rest-5^{th}-rest-2^{nd}-rest (mixed task, see Fig. 3). Each task was done twice. The subjects were instructed to perform movements regularly, always at the same speed, and to keep the non moving fingers relaxed.

Image procedure

All MRI studies were conducted on a 3 T whole body imaging system (BRUKER Medspec 3080) with a birdcage coil. Before fMRI, frontal images were acquired with conventional FLASH techniques. From these images, ten transversal slices for functional imaging were selected in the upper half, between the lateral sulcus and vertex (Fig. 1), encompassing the motor cortex hand area.

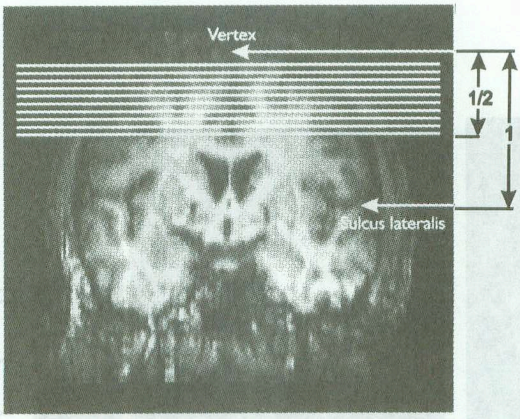

Fig. 1. Selection of ten transversal slices, encompassing the motor hand area, for functional MRI

For functional imaging studies, a phase corrected blipped gradient echo EPI sequence (TR = 4 sec, TE = 80 msec, FA = Ernst angle, FOV = 256 mm2, matrix 128*128, slice thickness 3 mm, 10 transversal slices, acquisition time per image 160 ms, 5 images per resting/activation phase) was used.

©1999, Tohoku University Press
Recent Advances in Biomagnetism
T. Yoshimoto et al. (Eds)

Data analysis

Data were evaluated with Fuzzy Clustering Analysis (EVIDENT software, Inst. for Biodiagnostics, Winnipeg, Canada). The contralateral hemisphere was defined as a region of interest (ROI), and a step-wise cluster analysis was performed. Pixel-clusters with a time course clearly not related to the paradigm were excluded from the next cluster analysis. By repeating this process in a standardized way, we obtained two clusters with a signal fluctuation corresponding to the stimulation paradigm, located predominantly within the primary sensorimotor area, but with differing amplitudes. The lower amplitude cluster reflected activation mainly in the small vessels, and was therefore used for a center of gravity (COG) calculation, after excluding pixels obviously outside the sensorimotor area, especially in the SMA. The timecourse in task 3 (mixed task) was split into two, according to the active finger (see Fig. 3), and each timecourse was than analyzed separately as described above. This interlocked task design reduces the influence of motion on the results. Because each task was performed twice, up to four COG values for each finger (2nd and 5th) were obtained for each subject. Subjects showing visible head movement artifacts were excluded.

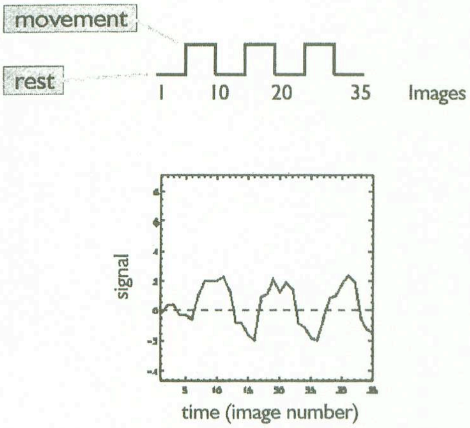

Fig. 2. Design for task 1 (movement of the 2nd finger only) and task 2 (5th finger). 35 images (= 140s). The lower figure shows a typical time course in a resulting pixel cluster. A threshold of 0.8 was chosen for cluster membership. For each trial a COG calculation was done as a measure of the localization of neuronal activity. Different positioning of the head due to motion between two trials for different fingers may therefore simulate different centers of activation in the sensorimotor cortex.

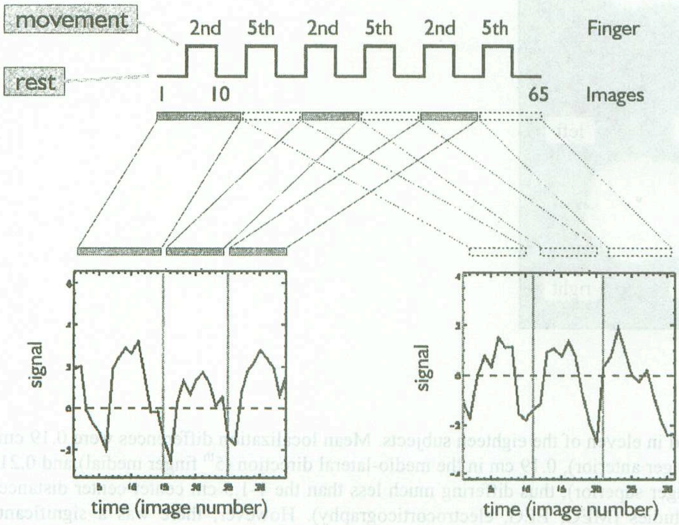

Fig. 3. Task 3 (mixed task), in which the 2nd and the 5th finger were moved alternately. This task design is less susceptible to motion, because activity for both fingers can be located within the same trial. Motion during the trial will be detected by the fuzzy cluster analysis, and the trial will then be excluded. Trial duration 260s (65 images).
The lower figures show resulting time courses of clusters for the 2nd and 5th finger after combining corresponding time windows.

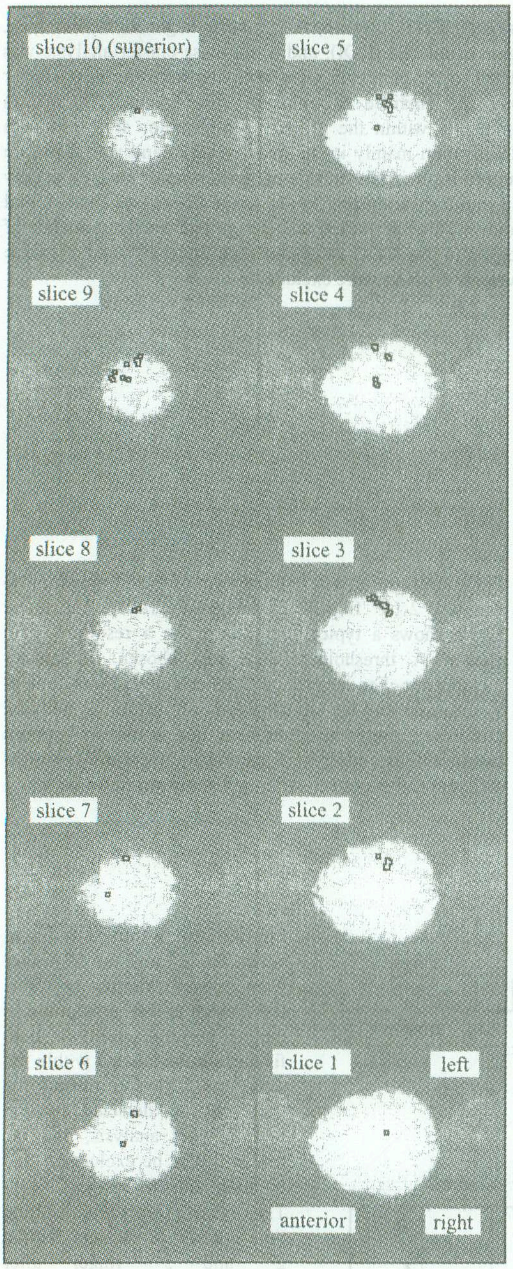

Fig. 4. Resulting low amplitude pixel cluster of the 5th finger for the same subject as in Fig.3. Activated pixels are shown in white, surrounded with a black border, for better visualization. Resulting pixels are predominantly located around the central sulcus, but with some pixels in the midline, expected to reflect activity in the SMA.

Results

Artifact free results were obtained in eleven of the eighteen subjects. Mean localization differences were 0.19 cm in the anterior-posterior direction (5th finger anterior), 0.19 cm in the medio-lateral direction (5th finger medial) and 0.21 cm in superior-inferior direction (5th finger superior), thus differing much less than the 1-1.5 cm center-center distance expected from neuronal localization studies (MEG, EEG, electrocorticography). However, there was a significant tendency for the 5th finger to lie more superior (10:1 subjects, Wilcoxon $p = 0.004$) and medial (10:1, $p = 0.008$) compared with the 2nd finger.

subject		number of pixels		x		y		z	
	fing.	mean	s	mean	s	mean	s	mean	s
S1	II	46,00	20,25	77,79	0,50	63,31	1,10	4,53	0,14
	V	39,75	22,04	77,26	0,41	62,49	1,00	5,03	0,89
S2	II	33,00		75,36		52,00		3,88	
	V	12,50	4,95	74,40	2,45	50,20	1,85	3,97	1,37
S3	II	42,00	11,27	80,82	0,17	51,17	0,18	2,70	0,43
	V	83,25	18,89	79,28	0,74	51,20	0,50	3,84	0,21
S4	II	26,33	13,80	73,07	0,81	60,47	2,90	4,29	0,51
	V	43,75	39,13	72,59	1,07	60,89	1,62	4,94	1,55
S5	II	47,00		77,11		58,02		3,68	
	V	20,50	9,75	76,05	2,52	58,39	1,28	4,07	1,12
S6	II	12,00		79,42		51,83		3,00	
	V	76,50	74,25	79,23	0,61	51,96	0,76	3,90	0,39
S7	II	39,50	7,78	78,35	0,83	52,14	0,01	4,81	0,19
	V	17,00		77,53		56,47		6,59	
S8	II	42,00	17,69	76,48	0,89	76,77	0,46	2,70	0,34
	V	51,50	16,74	73,65	1,45	76,69	1,63	3,85	0,75
S9	II	47,00	24,04	81,50	0,90	60,13	0,14	4,81	1,10
	V	28,75	14,41	81,69	1,84	58,99	3,93	5,33	0,43
S10	II	31,00		83,61		51,42		3,58	
	V	39,67	24,01	81,95	0,81	52,23	0,56	4,00	0,32
S11	II	37,00	10,17	77,31	0,44	58,41	0,88	6,51	0,56
	V	27,75	14,82	77,28	0,90	58,02	0,78	6,48	1,38

Table 1. Localization of center of gravity in 11 subjects for the 2nd (II) and 5th (V) finger. Values given in voxels (voxel size 2 x 2 x 3 mm). Interval of axes: X: 1 (right) - 128 (left), Y: 1 (anterior) - 128 (posterior), Z: 1 (inferior) - 10 (superior). Mean of four trials for each finger and standard deviation (s).

Discussion

The results indicate relatively small distances between the COGs of activated areas associated with movements of the 5th and 2nd fingers, however there are some shortcomings with the method used in this study. First of all there is the influence of intertrial motion, which could be compensated by registration of all trials, thereby improving the accuracy of comparisons of localizations over different trials. Exclusive use of the paradigm of task 3 (mixed task) would also help to improve the consistency of results. The subjective influence of excluding of pixels outside the sensorimotor area could be avoided by employing the median instead of the mean in the center of gravity calculation. Looking at the results a possible explanation for the significant but small distance between COGs for each finger, could be that there is a greater overlap in functional blood flow response compared with the neuronal response. However, blood flow responses may still be, albeit to a lesser extent than the neuronal response, distributed in a homuncular manner.

References

[1] Kleinschmidt A, Nitschke MF, Frahm J: Somatotopy in the human motor cortex hand area. A high-resolution functional mri study. European J Neuroscience 9: 2178-2186, 1997

[2] Sanes JN, Donoghue JP, Thangaraj V, Edelman RR and Warach S: Shared neural substrates controlling hand movements in human motor cortex. Science 268: 1775-1777, 1995

Acknowledgments

I would like to thank Ross Cunnington for helpful suggestions on the manuscript.

CORTICAL EXCITATORY AND INHIBITORY FUNCTIONS DEPEND ON THE DIRECTION OF INDUCED CURRENT BY TRANSCORTICAL MAGNETIC STIMULATION

Kujirai, T.[1], Kurimura, M.[1], Kurokawa, K.[1], Kujirai, K.[2], and Kato, T.[1]

3rd Department of Internal Medicine[1] *; Laboratory Medicine*[2]*, Yamagata University School of Medicine, Yamagata, Japan*

Introduction

The double magnetic stimulation technique has provided a great insight into the investigation of cortical inhibitory or excitatory functions so far. The method is applied by the conditioning-test shock design. We have reported the unique methods for rest and activated states using the double stimulation technique (1,2,3). Conditioning shocks can affect the following MEPs in size. In activation, motor evoked potentials (MEPs) and the following silent periods are greatly modulated by preceding conditioning stimuli. The degree of the cortical excitation or inhibition here may be associated with the silent period. Regarding motor cortical modulation, it is intriguing to verify whether the direction of magnetic stimulation can affect the silent period. The purpose of our study is to investigate the relationship between the direction of induced eddy current, cortical modulation and/or silent period, using the double magnetic stimulation technique.

Methods

We studied seven control subjects who gave written informed consents. They were seated in a comfortable chair and were required to perform sustained activation of their first dorsal interosseous muscles (FDIs) during each study. Surface electromyography was recorded from the FDIs using the belly-tendon method. The double magnetic stimulation technique was applied with one figure-of-8 coil placed over the contralateral motor hand area. A conditioning-test design was used for cortical stimulation. The intensity of the first conditioning shock was adjusted so that it would fail to evoke any motor response (MEP). It was virtually below the threshold in the activated muscle. In the following test shock, the intensity was adjusted so that the MEP was around 1 mV in peak-to-peak amplitude. At this intensity, the silent period can be detected following the MEP. Conditioning-test intervals were varied from - 10 ms to + 20 ms. Excitation or inhibition was evaluated as the ratio of the fraction of a conditioned test response in peak-to-peak. All of the subjects were also studied at rest with the same intensity as that of the conditioning shock in the active situation. These test shocks were needed to induce almost the same test size at rest as in activation. In addition, the test magnetic coil was rotated for the evaluation of the effect on the excitation, inhibition or silent period.

In some subjects, an anodal stimulation over the hand motor area was delivered for the test shock. In order to verify whether cortical excitation or inhibition occurs by the double magnetic stimulation technique, a single motor unit monitoring from the FDI muscle was applied for the evaluation of I-wave production by reconstructing a peristimulus time histogram.

Results

The averages of the test stimulation responses and of the conditioned test responses in activation are shown in Figure 1. Motor evoked response (MEPs) here are followed by silent periods (SPs). The test response consists of the two different components in terms of their peak latencies, especially in a posterior-anterior direction of 45 degrees. The earlier

©1999, Tohoku University Press
Recent Advances in Biomagnetism
T. Yoshimoto et al. (Eds)

component holds at around 23 ms. In contrast, the later component holds at 24 ms or so, which is compatible with the latency for I-wave production. The inhibition ratio was calculated by a formula as $|(C+T) - C| / T$. The excitation as well as inhibition occurs just around the peak latency of the later component of the test response. Conditioning-test intervals (CTIs) were varied from -10 to +20 ms. The inhibition curves consists of three phases in terms of the inhibition ratio. There is a statistical difference ($p < 0.05$) between rest and active situations across at -4 ms and -1 ms, showing a greater facilitation in activation than at rest (Figure 2). In contrast, the facilitation effect remained poor in the plus phase in an active state compared with that when at rest. As for an anodal test response, however, any change such as excitation or inhibition disappeared.

The peri-stimulus time histogram (PSTH) was created after reconstructing motor-unit counts by a single motor unit recording study. One peak corresponding to I_3-wave was greatly increased in count number by conditioning magnetic shocks. At +3 ms of the CTI, conversely, the peaks for I-waves were preferentially inhibited. The increment and decrement of the peaks were statistically significant ($p < 0.05$) for the double magnetic stimulation technique.

When a magnetic coil was rotated, the wave shape of a test response and the inhibition degree were gradually changed (Figure 4). In addition, the duration of the SP following a motor response was influenced by the direction. In the anterior-posterior direction, the shape of MEP was quite similar to the later component only, remaining a great modulation such as facilitation and inhibition. The duration of the SP showed no change. In contrast, in a posterior-anterior direction, especially of 45 degrees, the duration is prominently prolonged ($T= 34 \pm 2.7$ ms, $C+T=46 \pm 3.6$ ms, $p < 0.05$) at -1 ms of the CTI, but not at +3 ms (Figure 1).

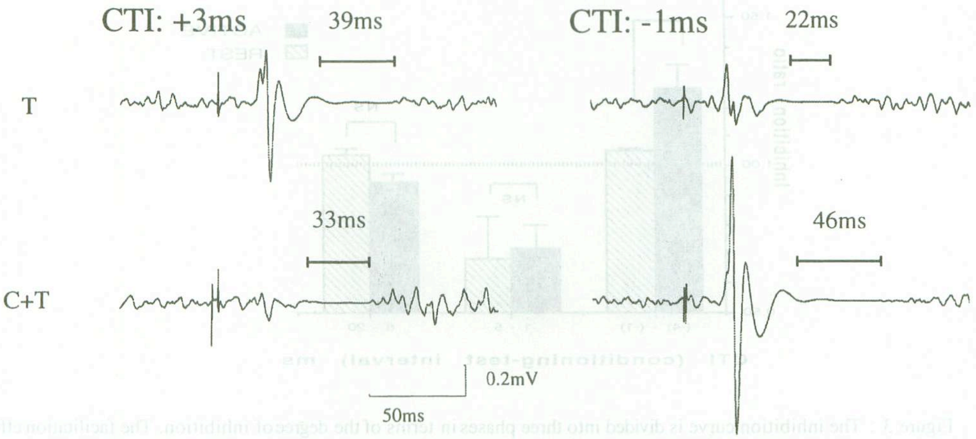

Figure 1 : Comparison of surface EMG responses from FDI muscles at different interstimulus intervals. A test response (T) in activation consists of two components in terms of their latencies. Note that the conditioned test response at +3 ms of the CTI is greatly inhibited. In contrast, even with the same intensity of a conditioning shock, it is facilitated at -1 ms. The modulation of test responses takes place on the later component. With regard to the silent period following the MEP, the duration of this holds virtually different values depending on the evaluation method. In a posterior-anterior direction of 45 degrees, the duration is prominently prolonged by the preceding subthreshold conditioning shock as shown in this figure. There is a significant difference ($p<0.05$) between the durations induced by test alone and conditioned test responses.

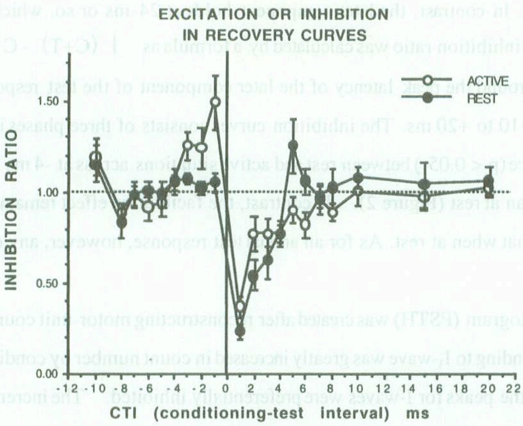

Figure 2 : The graph shows superimposed curves in the studies at rest and in an active situation from -10 to + 20 ms of the CTI. Note that the difference between the two curves holds from -4 to -1 ms ($p < 0.05$) in terms of the degree of the inhibition.

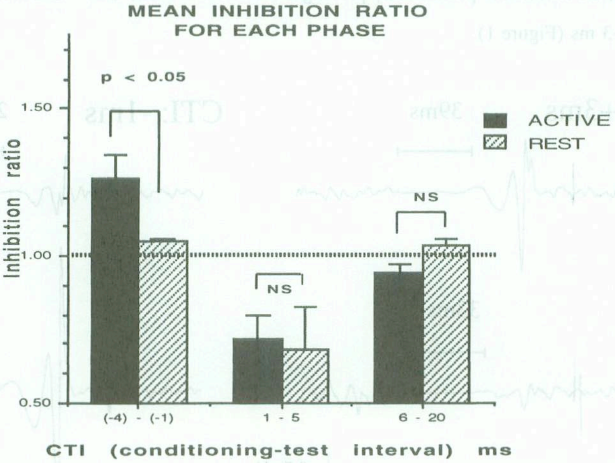

Figure 3 : The inhibition curve is divided into three phases in terms of the degree of inhibition. The facilitation effect from 6 to 20 ms at rest is not significant.

Discussion

We reported the double magnetic stimulation technique at rest evaluating motor cortical inhibition before 〔1〕. We also demonstrated that magnetic shocks can affect some facilitation and inhibition in the sensorimotor cortex at the same time 〔2〕. We have applied this method to the active situation here particularly for motor cortical functions. Although the intensity of a conditioning shock was far below the motor threshold even in the active target muscles, the inhibition still remained in the almost same degree as that at rest. This technique is quite applicable because the cortical facilitation is also detectable at the minus phase of the conditioning-test interval, lasting for about 4 ms. The peri-stimulus time histogram study and the anodal test stimulation study also support that the modulation of MEPs is of cortical origin. The facilitation and inhibition occur on the later component coincidentally. The coil-rotation study revealed that the later component of the MEP is tightly associated with I_3-wave. The later component favors the anterior-posterior direction of induced eddy current. The silent period following the MEP, however, is prominently prolonged in a posterior-anterior direction of 45 degrees. These results indicate that motor cortical network inducing facilitation and/or inhibition probably is under the influence of the direction of induced current.

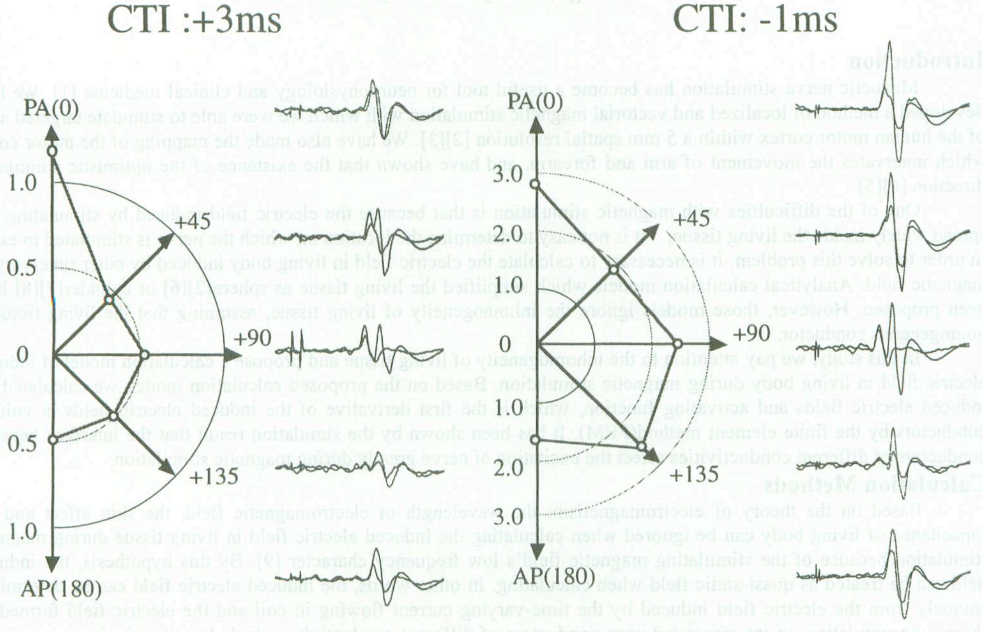

Figure 4 : This illustrates the effect of the direction of induced current on the excitation as well as on the inhibition. The inhibition ratio and the raw data at +3 ms are shown on the left side, and those at -1 ms on the right. The responses for the test and the conditioned test for each direction are superimposed. The test coil here was placed over the left motor hand area. The change in size and in the degree of the modulation are also subject to the direction. When the coil is rotated in a clockwise direction, the earlier component is gradually reduced in size at +3 ms of the CTI. The degree of the inhibition at +3 ms is vice versa. In contrast, the excitation at -1 ms holds in all directions, irrespective of the existence of the earlier component.

References

(1) Kujirai T, Caramia M , Rothwell JC, et al: Corticocortical inhibition in human motor cortex. J Physiology 471: 501-519, 1993

(2) Kujirai T, Cohen L and Rothwell JC: The effect of transcranial magnetic stimulation on median nerve somatosensory evoked potentials. Electroencephalography and Clinical Neurophysiology 89: 227-234,1993

(3) Kujirai T, Kurimura. Kujirai K, et al: Investigation of cortical excitation and inhibition in active target muscles using double magnetic stimulation technique. Electroencephalography and Clinical Neurophysiology 106: 66p,1998

Determination of the Induced Electric Fields and the Activating Function in an Inhomogeneous Volume Conductor during Magnetic Stimulation

Liu R, Ueno S

Dept. of Biomedical Eng., Graduate School of Medicine, University of Tokyo,
7-3-1 Hongo, Bunkyo-ku, Tokyo 113-0033

Introduction

Magnetic nerve stimulation has become a useful tool for neurophysiology and clinical medicine [1]. We have developed a method of localized and vectorial magnetic stimulation with which we were able to stimulate targeted areas of the human motor cortex within a 5 mm spatial resolution [2][3]. We have also made the mapping of the motor cortex which innervates the movement of arm and forearm, and have shown that the existence of the optimistic stimulation direction [4][5].

One of the difficulties with magnetic stimulation is that because the electric field induced by stimulating coil spread widely inside the living tissue, it is not easy to determine the location on which the nerve is stimulated to excite. In order to solve this problem, it is necessary to calculate the electric field in living body induced by outer time-varying magnetic field. Analytical calculation models which simplified the living tissue as sphere[2][6] or cylinder[7][8] have been proposed. However, those models ignore the inhomogeneity of living tissue, assuming that the living tissue is homogeneous conductor.

In this study, we pay attention to the inhomogeneity of living tissue and propose a calculation model of induced electric field in living body during magnetic stimulation. Based on the proposed calculation model, we calculated the induced electric fields and activating function, which is the first derivative of the induced electric fields in volume conductors by the finite element method(FEM). It has been shown by the simulation result that the interface between conductors of different conductivities affect the excitation of nerve greatly during magnetic stimulation.

Calculation Methods

Based on the theory of electromagnetism, the wavelength of electromagnetic field, the skin effect and the capacitance of living body can be ignored when calculating the induced electric field in living tissue during magnetic stimulation because of the stimulating magnetic field's low frequency character [9]. By this hypothesis, the induced field can be treated as quasi-static field when calculating. In other words, the induced electric field can be determined uniquely from the electric field induced by the time-varying current flowing in coil and the electric field formed by charges accumulating on interfaces between conductors of different conductivities, including the air-tissue interfaces. This fact can be expressed by the following equation.

$$\mathbf{E} = -\frac{\partial \mathbf{A}}{\partial t} - \nabla\Phi \tag{1}$$

here $\mathbf{A}$ is the vector potential induced by the current flowing in the coil, Φ is the scalar potential formed by charges on interfaces. If we assume

$$\mathbf{E}_{\mathbf{A}} = -\partial\mathbf{A}/\partial t\,,\ \mathbf{E}_{\Phi} = -\nabla\Phi \tag{2}$$

then the total induced electric fields can be considered as composing of two components $\mathbf{E}_{\mathbf{A}}$ and $\mathbf{E}_{\Phi}$. By summing these two components up, we then have the final electric field.

The electric field $\mathbf{E}_{\mathbf{A}}$ can be calculated as

$$\mathbf{E}_{\mathbf{A}} = -\frac{\partial \mathbf{A}}{\partial t} = -\frac{\mu_0 N}{4\pi}\frac{\partial I}{\partial t}\int\frac{d\mathbf{l}'}{\mathbf{R}} \tag{3}$$

here N is the number of turns of the coil, I is the current flowing in the coil, $d\mathbf{l}'$ is a segment of the coil, $\mathbf{R}$ is the distance between $d\mathbf{l}'$ and the point where the electric field is calculated. Usually, numerical integration is used to calculate $\mathbf{E}_{\mathbf{A}}$. The coil is usually approximated by polygons.

It is necessary to find out the scalar potential Φ in order to calculate $\mathbf{E}_{\Phi}$. When the living tissue is treated as homogeneous conductor, due to the above mentioned quasi-static hypothesis, charges exist only on the tissue-air interfaces, thus $\operatorname{div} E_{\Phi} = 0$ is satisfied everywhere inside the conductor. From this we know that the scalar potential Φ which is defined as $\mathbf{E}_{\Phi} = -\nabla\Phi$ satisfies

$$\nabla^2\Phi = 0 \tag{4}$$

We can also know that on the boundary the normal component of the induced current $\mathrm{I} = \sigma\,\mathrm{E}$ (E is the total

©1999, Tohoku University Press
Recent Advances in Biomagnetism
T. Yoshimoto et al. (Eds)

electric field according to equation (1), σ is the conductivity of living tissue) is zero, thus we know that electric field $\mathbf{E}_A$ cancels electric field $\mathbf{E}_\Phi$ on the normal direction at the boundary. Therefore the boundary condition becomes

$$\frac{\partial \Phi}{\partial n} = \mathbf{n} \cdot \mathbf{E}_A \tag{5}$$

then the scalar potential can be found out by solving the Laplace equation (4) with the boundary condition (5).

The above-mentioned equations are the calculation model for induced electric field in homogeneous volume conductor during magnetic simulation. Before we propose the calculation model for inhomogeneous volume conductor, the definition of inhomogeneous volume conductor should be given here. As shown in figure 1, the inhomogeneous conductor is made up of homogeneous conductors of different conductivities, that is, volume conductor which is homogenous inside every subregions. Because the living tissue is made up of tissues such as muscles or fats which are of different conductivities, the authors think this definition is reasonable.

In order to calculate the induced electric field in inhomogeneous conductor, because the above-mentioned quasi-static hypothesis is still applicable, the equation

$$\mathbf{E} = \mathbf{E}_A + \mathbf{E}_\Phi \tag{6}$$

still holds. Because $\mathbf{A}$ is irrelevant to the conductivity of conductor the equation (3) is still applicable when calculating $\mathbf{E}_A$ in the inhomogeneous case. However, because $\mathbf{E}_\Phi$ is affected by the charges accumulating on the interface besides charges on the air-tissue boundary, we have to consider the continuous conditions on the interface besides the boundary condition (5) when calculating the scalar potential Φ.

In the case of electric stimulation, in order to calculate quasi-static electric field in inhomogeneous volume conductor, continuous condition

$$\Phi_1 = \Phi_2 \tag{7}$$

$$\mathbf{n} \cdot \sigma_1 \cdot \nabla \Phi_1 = \mathbf{n} \cdot \sigma_2 \nabla \Phi_2 \tag{8}$$

should be satisfied on the interface between conductor 1 with conductivity σ_1 and conductor 2 with conductivity σ_2 as shown in figure 2 [10]. Φ_1 and Φ_2 are scalar potentials in conductor 1and conductor 2 respectively, $\mathbf{n}$ is the unit normal vector on the interface. The continuous condition (8) can be deduced from the fact that because $\operatorname{div} i = 0$ holds inside a quasi-static electric field, the normal direction component of current is continuous on the interface.

In the case of magnetic stimulation, as mentioned above the induced electric field can be approximated as quasi-static field, $\operatorname{div} i = 0$ holds inside the conductor, thus we can lead to the conclusion that on the interface between conductors of different conductivities the normal direction component of electric current continuous. Therefore the continuous condition (8) and (9) should be satisfied. But in the case of magnetic stimulation, electric field $\mathbf{E}_A$ could cause currents flowing through the interface, it is necessary to take $\mathbf{E}_A$ into consideration. Therefore equation (8) becomes:

$$\sigma_1 (\mathbf{n} \cdot \mathbf{E}_A - \frac{\partial \Phi_1}{\partial \mathbf{n}}) = \sigma_2 (\mathbf{n} \cdot \mathbf{E}_A - \frac{\partial \Phi_2}{\partial \mathbf{n}}) \tag{9}$$

As mentioned above, when calculating the induced electric fields in inhomogeneous volume conductors during magnetic stimulation, the induced fields can be considered as composing of two sources as shown by (6). $\mathbf{E}_A$ can be calculated by equation (3). It is necessary to find out scalar potential Φ in order to calculate $\mathbf{E}_\Phi$. Φ satisfies the Laplace equation (4) inside the conductor. The boundary condition (5) has to been held on the boundary between air and conductor, and the continuous conditions (7) and (9) should be satisfied on the interface between conductors.

Simulation model

Based on the calculation model proposed above, we carried out simulation on a model as shown in figure 2. Here we assume that the unit cubic volume conductor 1 with conductivity σ_1 contacts with the unit volume conductor 2 with conductivity σ_2, a figure 8 coil is placed just above the interface between the two conductors. The size of unit cubic is 1cm, the radius of figure 8 coil is 0.25cm. The figure 8 coil is placed on the plane z=1.1cm, the turns of coil is set to 30. The current flowing in coil is assumed to be $dI / dt = 1\,\mathrm{A}/\mu\mathrm{s}$, the coil is approximated by a 64 segments polygon when calculating $\mathbf{E}_A$. Numerical integration is carried out to find out $\mathbf{E}_A$. Finite element method is applied to compute scalar potential Φ. In order to utilize finite element method, we have to take advantage of the simulation model's symmetry about the plane x=0 to get the equation

$$\frac{\partial \Phi_1}{\partial \mathbf{n}} = -\frac{\partial \Phi_2}{\partial \mathbf{n}}$$

which simplified equation (9) to the boundary condition as shown below.

$$\frac{\partial \Phi}{\partial \mathbf{n}} = \frac{\sigma_2 - \sigma_1}{\sigma_2 + \sigma_1} \cdot \mathbf{E}_A \tag{10}$$

In order to compare with the electric field induced in homogeneous volume conductor, we calculated the spatial distribution of electric field in conductor in the case $\sigma_1 = \sigma_2$ and $\sigma_1 = 10\sigma_2$. Furthermore, in order to investigate the effects of inhomogeneous conductor to nerve excitation during magnetic stimulation we calculated the partial differentiation of the electric field's x direction component to x direction and the electric field's y direction component to y direction. The current in coil flows in the direction as shown in figure 2.

Result

In the case $\sigma_1 = \sigma_2$, the distribution of electric field, $\partial E_x / \partial x$ and $\partial E_y / \partial y$ on plane z=0.9cm is given in figure 3,4 and 5. The results is almost the same as analytical calculation result in the case when the conductor is assumed to be a half-plane except near the boundary. It is been considered that the validity of the calculation model is proved partially.

In the case $\sigma_1 = 10\sigma_2$, the distribution of electric field, $\partial E_x / \partial x$ and $\partial E_y / \partial y$ on plane z=0.9cm is shown as figure 6,7 and 8. It had been observed that near the interface the strength of the electric field in conductor 1 is small while the strength of the electric field in conductor 2 is large. Furthermore, there is a large negative peak appeared near the interface in the spatial distribution of $\partial E_x / \partial x$, the region of negative value in the spatial distribution of $\partial E_y / \partial y$ is shifted to be on the interface comparing to the homogeneous case.

Discussion

First let us discuss how the interface between conductors with different conductivities affects the nerve excitation during magnetic stimulation. From the theory of Roth and Basser [11], we know that when applying magnetic stimulation to long straight nerve, it is the first derivative of the nerve running direction component of electric field, so called activating function, decides whether the nerve is excited or inhibited. In other words, the nerve is depolarized to be excited easier at where the activating function is negative, on the contrary, the nerve is hyperpolarized to be inhibited at where the activating function is positive. Therefore, when determining where the nerve is excited, the nerve will fire first at the place where the maximum value of its negative value is reached. As for the simulation model in this study, when the long straight nerve fiber runs perpendicular to the interface between conductor 1 and conductor 2, the activating function becomes $\partial E_x / \partial x$; when it runs parallel to the interface, the activating function becomes $\partial E_y / \partial y$. Therefore, the effects of interface to nerve excitation can be investigated by calculating the spatial distribution of activating function.

When the nerve runs perpendicular to the interface, from figure 4 and 7 we can see that comparing to homogeneous case a huge negative peak of activating function $\partial E_x / \partial x$ appear just under the figure 8 coil on the interface. As described above, if the nerve pass through the interface here, the nerve is very possibly to be excited. Furthermore, if the nerve runs parallel to the interface, by comparing figure 5 and 8 we can see that in the case of inhomogeneous conductor the negative peak of activating function $\partial E_y / \partial y$ shifts to the interface. Therefore if a nerve placed nearby the interface it will be depolarized by the negative peak and becomes easier to be excited.

In conclusion, we have proposed a calculation model on the electric field induced in inhomogeneous volume conductors during magnetic stimulation. We calculated the activating function based on the proposed calculation model to investigate the effects of the interface between conductors of different conductivities to nerve excitation during magnetic stimulation. As the result, we know that the interface affect the nerve excitation greatly.

References

[1] A.T.Barker, R.Jalinous, et al: Noninvasive magnetic stimulation of human motor cortex. Lancet ii: 1106-1107, 1985

[2] S.Ueno, T.Tashiro, et al: Localized stimulation of neural tissues in the brain by means of paired configuration of time-varying magnetic fields. J.Appl.Phys, Vol 64, No.10: 5862-5864, 1988

[3] S. Ueno, T. Tashiro, et al: Functional mapping of the human motor cortex obtained by focal and vectorial magnetic stimulation of the brain. IEEE Trans. Magn., vol. 26, no. 5: 1539-1544, Sept. 1990

[4] S.Ueno, T.Matsuda et al: Estimation of structures of neural fibers in the human brain by vectorial magnetic stimulation. IEEE Trans on Magnetics, vol 27, no.5: 5387-5389, Sept. 1991

[5] A.Hyodo, S.Ueno: Nerve excitation model for localized magnetic stimulation of finite neuronal structures. IEEE Trans on Magnetics, vol 32, no.5: 5112-5114, Sept. 1996

[6] F.Grandori, P.Ravazzani: Magnetic stimulation of the motor cortex--- theoretical considerations. IEEE Trans. Biomed. Eng., vol 38, no.2:180-191, 1991

[7] K.P.Esselle, M.A.Stuchly: Quasi-static electric field in a cylindrical volume conductor induced by external coils. IEEE Trans.Biomed. Eng., vol 41, no.2: 151-158, 1994

[8] P.J.Basser, B.J.Roth: Stimulation of a myelinated nerve axon by electromagnetic induction . Med. & Bio. Eng. & Comp.: 261-268, May, 1991

[9] B.J.Roth, L.G.Cohen, et al: The electric field induced during magnetic stimulation: Magnetic motor stimulation: basic principles and clinical experience (EEG Suppl. 43), W.J.Levy, R.Q.Cracco, A.T.Barker, et al (eds): Elsevier Science Publishers, 1991

[10]C.E. Miller, C. S. Henriquez: Biomedical Engineering, Finite Element Analysis of Bioelectric Phenomena .IEEE Trans.Biomed.

Eng., vol 18: 207-233, 1990

[11]B.J. Roth and P.J. Basser: A model of the stimulation of a nerve fiber by electromagnetic induction. IEEE Trans. Biomed. Eng., vol. 37: 588-597, Jun. 1990

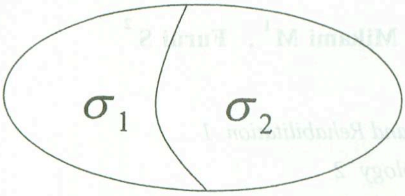

Fig. 1 Inhomogeneities of piecewise-homogeneous conductors. An inhomogeneous volume conductor formed by two piecewise-homogeneous conductors with conductivities σ_1 and σ_2.

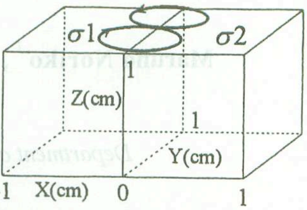

Fig. 2 Simulation model. A figure of eight coil with radius 0.25 cm is put on the plane $Z=1.1$ cm. Regions 1 and 2 are cubic volume conductors with conductivities σ_1 and σ_2, respectively. The number of turns of the coil is 30. The current flows as shown in the figure.

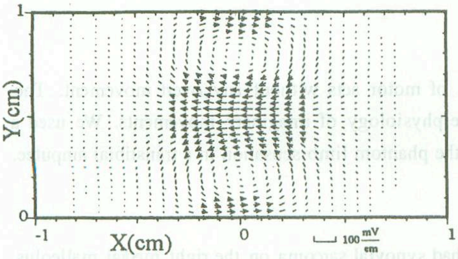

Fig. 3 Induced electric fields in the plane $Z=0.9$ cm for the case where $\sigma_1=\sigma_2$. The arrows show the directions and strengths of the induced electric fields. Calibration of the induced fields is also given.

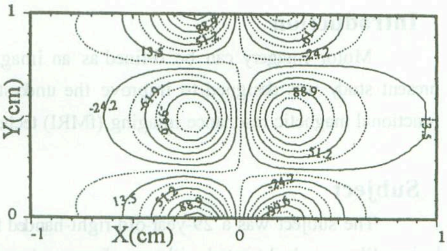

Fig. 4 Spatial distribution of $\partial E_x/\partial x$ in the plane $Z=0.9$ cm for the case where $\sigma_1=\sigma_2$. The solid lines and dotted lines are contour lines of function $\partial E_x/\partial x$. The values of solid contour lines are given on the contour plot.

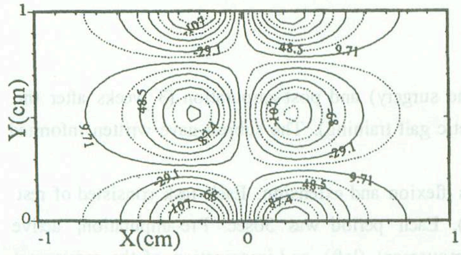

Fig. 5 Spatial distribution of $\partial E_y/\partial y$ in the plane $Z=0.9$ cm for the case where $\sigma_1=\sigma_2$. The solid lines and dotted lines are contour lines of function $\partial E_y/\partial y$. The values of solid contour lines are given on the contour plot.

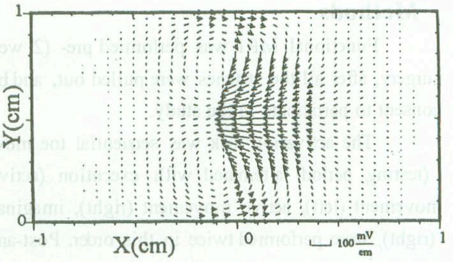

Fig. 6 Induced electric fields in the plane $Z=0.9$ cm for the case where $\sigma_1=10\sigma_2$. The arrows show the directions and strengths of the induced electric fields. Calibration of the induced fields is also given.

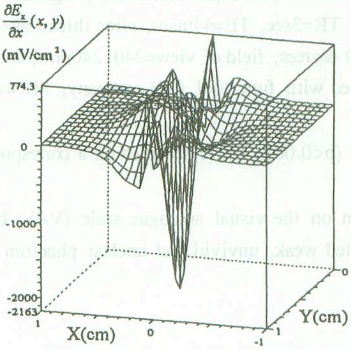

Fig. 7 Spatial distribution of $\partial E_x/\partial x$ in the plane $Z=0.9$ cm for the case where $\sigma_1=10\sigma_2$.

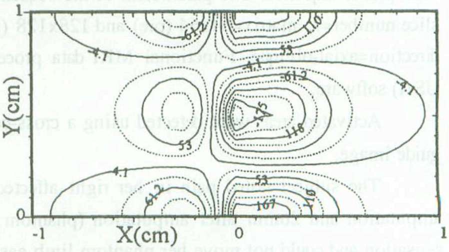

Fig. 8 Spatial distribution of $\partial E_y/\partial y$ in the plane $Z=0.9$ cm for the case where $\sigma_1=10\sigma_2$. The solid lines and dotted lines are contour lines of function $\partial E_y/\partial y$. The values of solid contour lines are given on the contour plot.

An fMRI study on Pre- and Post-Transtibial Amputation

Maruno Noriko[1], Kaminaga T[2], Mikami M[1], Furui S[2]

Department of Physical Medicine and Rehabilitation 1
Department of Radiology 2
Teikyo University, School of Medicine, Tokyo, JAPAN

Introduction

Motor imagery can be defined as an imagined rehearsal of motor acts without any overt movement. The present study was designed to improve the understanding of the physiology of imaginary movements. We used a functional magnetic resonance imaging (fMRI) technique to map the phantom limb sensation in a transtibial amputee.

Subject

The subject was a 29-year-old right-handed female, who had synovial sarcoma on the right medial malleolus lesion. She was had treated with neoadjuvant chemotherapy, but the response was incomplete. Dynamic MRI study showed increased vascularity in an early phase. After resection of the bilateral lung metastases, transtibial amputation was performed for local tumor control .

Methods

Functional MRI was performed pre- (2 weeks before the surgery) and post-amputation (3 weeks after the surgery, after all the stitches were pulled out, and before prosthetic gait training). The subject gave written informed consent to participate in the study.

The activation task was sequential toe movement; mass flexion and extension. Each task consisted of rest (resting period) alternated with execution (activation period). Each period was 30sec. Pre-amputation, active movement (left), active movement (right), imagination of the movement (left), and imagination of the movement (right), were performed twice in this order. Post-amputation, active movement (left), imagination of the movement (right=phantom), and imagination of the movement (left), were performed twice in this order. Toe movement was visually observed by a physician standing.

Functional MRI was performed with a 1.5 T super conducting machine (GE Signa Horizon) by a gradient-echo echo-planar sequence. The parameters of the sequence were as follows: TR=3sec, TE=44msec, slice thickness=8mm, slice number=7, matrix=64x64 (pre) and 128x128 (post), flip angle=90 degrees, field of view=240x240mm, and slice direction=axial-oblique. Functional MRI data processing was performed with func tool (GE company, Milwaukee, USA) software.

Activated areas were detected using a cross-correlation technique ($p<0.001$) and represented on a corresponding guide image.

The subject noted pain in her right affected leg. It was 68mm on the visual analogue scale (VAS) before amputation and 26mm after amputation (phantom pain). She exhibited weak, unvivid and unclear phantom limb sensation and could not move her phantom limb easily.

©1999, Tohoku University Press
Recent Advances in Biomagnetism
T. Yoshimoto et al. (Eds)

Results

The first activated areas were superimposed on the second ones.

The activation areas appeared on the top slice in the axial-oblique section (Fig. 1).

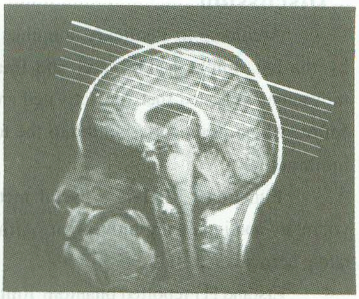

Fig. 1 Slice direction (axial-oblique)

(1) Pre-amputation

In the actual movement, left toe movements (normal side) activated the contralateral supplementaly motor area (SMA) alongwith the sensorimotor cortex (SMC). Right toe movements (affected side) activated the contralateral SMA and SMC, and both were reduced compared to the left toe movement (Fig. 2).

During imaginary movement, both left and right toe movements activated the contralateral SMA, which was smaller than the actual movement.

(2) Post-amputation

The left side actual movement activated the bilateral SMA and contralateral SMC, was shown before amputation. The right side (phantom toe imaginary movement) activated the bilateral SMA and ipsilateral SMC. Imaginary movement of the left side activated the bilateral SMA and contralateral SMC; and was very similar to phantom movement. Left SMC was not activated duling these 3 tasks (Fig. 3).

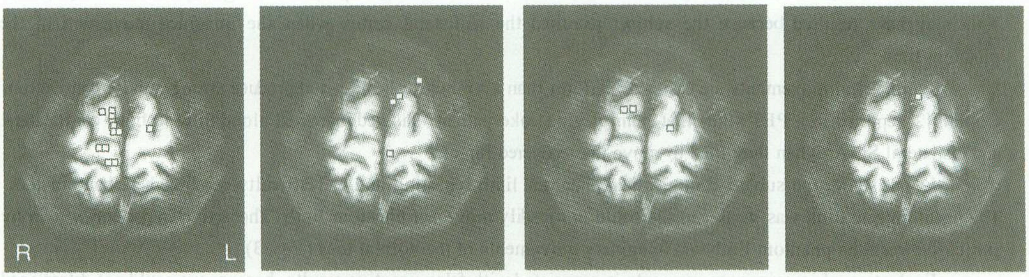

Lt. active Rt. active Lt. imaginary Rt. imaginary

Fig. 2 Pre-amputation

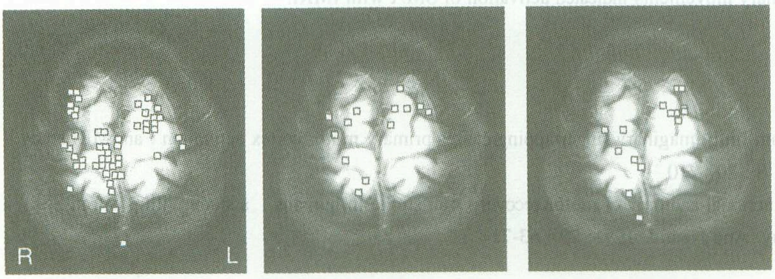

Lt. active Rt. imaginary(phantom) Lt. imaginary

Fig. 3 Post-amputation

Discussion

According to Penfield's homunculus, the toe and foot areas are located in the most medial positions, followed by the leg, trunk, hands, face, and finally, most laterally, the swallowing system. Based on our results, active movement indicated that the activated areas were located around the central sulcus, and medial portion of the caudal cortex, which were corresponded to the foot area in his homunculus. Functional MRI data yielded excellent localizing information.

Functional MRI is a useful method for analyzing neurophysiological roles of the SMA and SMC during voluntary and imaginary movement. Although many studies have examined this theme, phantom limb movement has rarely been studied.

Ersland [1] reported phantom limb imaginary finger tapping with transhumeral amputation. In his study, both actual and imaginary finger tapping resulted in activation of the contralateral precentral area (primary motor cortex ; M1), but not the SMA. His subject exhibited severe phantom pain.

In our case, the SMA was activated during all tasks (Fig. 2, 3). Phantom imaginary movements readily activated the SMA. Our subject exhibited slight phantom pain after amputation, but she was required no treatment. Pain was reduced compared to the pre-amputation state (68 to 26, measured by VAS). Activation of the SMA in phantom imaginary movement may be suppressed by pain.

We could not compare pre- and post-amputation states accurately, because the recording conditions were different. The matrix size was different in our study; pre was 64x64 and post was 128x128. Moreover, we And could not distinguish between SMA and the premotor cortex, because they were close together and and premotor the top slice was evaluated.

Furthermore, our case indicated activation of the bilateral SMA in phantom imaginary movement (Fig. 3). This may have resulted because the subject recruited the ipsilateral cortex when she imagined movement of the phantom limb.

Symmetrical movements are easier to perform than asymmetrical ones, and produce strong muscle contraction. Chollet [2] reported in a PET study that hemiplegic stroke patients showed increased blood flow in both contralateral and ipsilateral SMA, when they tried to move the recovered fingers.

In our study, the subject demonstrated phantom limb sensation and had difficulty moving her phantom toes. The phantom sensation was weak and she could not readily move her phantom limb. The activated patterns were very similar between the phantom limb and imaginary movements of the normal toes (Fig. 3).

Evaluation of imaginary movements is associated with false negative results, because we could not determined whether or not the subject performed the task earnestly. In our study, SMA was activated in all tasks, indicating that closely followed our instructions.

Conclusion

Phantom toe imaginary movements indicated activation of SMA with fMRI.

References

[1] Ersland et al. Phantom limb imaginary fingertapping causes primary motor cortex activation : an fMRI study. NeueoReport 1996 ; 8 : 207-210

[2] Chollet et al. The functional anatomy of motor recovery after stroke in humans : a study with positron emission tomography. Ann Neurol 1991; 29 : 63-71

Magnetic stimulation of the spinal cord in the rat

Matsumiya Y[1, 2], Kling J.W.[1], Yarita M.[2], Yanagihara K.[1, 2],
Imashioya H.[1, 3]

Brown University[1], Providence, RI, USA; Nihon Kohden
Corporation[2], Tokyo, Japan; Hyogo University of Teacher
Education[3], Hyogo, Japan

Introduction

Transdermal magnetic stimulation over the spinal cord easily stimulates the roots, but spinal cord stimulation is not easy. In a previous study [1], we demonstrated that when the magnetic coil was moved over the spinal cord, the onset latency of the compound muscle action potentials (CMAP) was shortened as the coil shifted in the rostral to caudal direction. This experiment was performed under ketamine anesthesia, but when it was changed to barbiturate (Nembutal), all responses above the lower thoracic level were abolished.

These results seem to demonstrate successful spinal cord stimulation, but the referees of a journal which received our paper based on these results thought that we had not excluded possibilities that the observed phenomena were the results of either brainstem or lumbar root stimulation (both structures are known to be sensitive to the magnetic stimulation) and not by cord stimulation.

To clarify the situation, we added two more experiments. This paper reports the results.

Method

Seventeen fully grown male albino rats (>400 grams) were used. Under ketamine anesthesia, the cervical area was stimulated (Nihon Kohden Model

©1999, Tohoku University Press
Recent Advances in Biomagnetism
T. Yoshimoto et al. (Eds)

SMG0101 stimulator) using a transverse method [1] and the CMAP was recorded from the left femoral muscles (PREsurgery record). Then a hole was made in the vertebra(e) in the lower cervical/upper thoracic area (C_4 - T_2). The size of the hole ranged from 7.16 -29.26 mm^2. Immediately after the surgery, the muscle and the skin were put back and the stimulation was given (POST surgery record). In these recordings, the stimulus was delivered at 300 V (no animal responded), and the intensity was raised in 100 V steps to 900 V. The lowest stimulus intensity which produced a minimum response, as well as the size of the response measured by the area covered by the CMAP waveform (1 to 20 msec) at each intensity was determined for each animal. During the POST session, a few animals also received electric stimulation through the burr hole and the recorded CMAP onset latency was compared with its counter part evoked by the magnetic stimulation.

Results

Figure 1 shows that the POST CMAP was larger than PRE CMAP. Despite of the large SDs, the difference was statistically significant ($p<0.05$). Figure 2

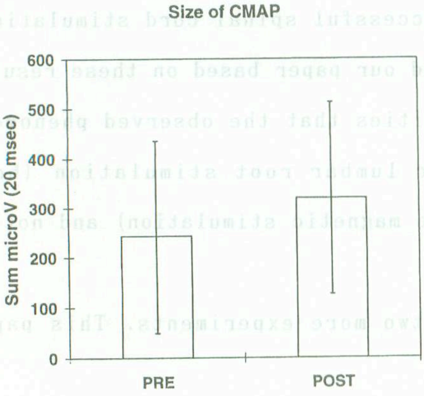

Figure 1. Enhancment of CMAP after the surgery. The stimulus intensity is 800V).

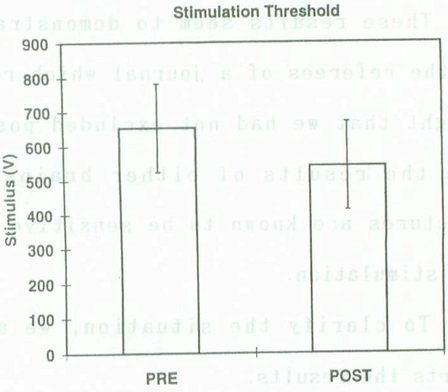

Figure 2. Lowered threshold of CMAP after the surgery.

shows that the stimulus intensity at which the minimum CMAP was observed was lower in POST than in PRE recordings ($p<0.01$). The magnetic and the electric stimulations had comparable onset latencies of approximately 6 msec. No apparent effects of the size of the hole were observed on either size or threshold of the CMAP

Discussion

From the evidence collected from this and the previous experiments, what can we say about the spinal cord stimulation?

① Findings: The latency becomes shorter as the coil moves from rostral to caudal.

Comments: Although this finding is consistent with spinal cord stimulation, there is a possibility that in the upper cord section, the current elicited by the magnetic flux stimulates the brainstem, and in the lower cord section, it stimulates the roots.

② Findings: The above results were obtained under ketamine anesthesia. Under Nembutal anesthesia, all CMAPs above mid-thoracic were abolished.

Comments: If the brainstem alone is responsible for the CMAP, all responses should be abolished. The stimulation above mid-thoracic does not stimulate the roots.

③ Findings: A hole made in the lower cervical/upper thoracic area enhances CMAP when the same area is stimulated.

Comments: If the brainstem or lumbar roots are responsible for the CMAP, a hole should not influence CMAP.

④ Findings: Electrical stimulation through the hole produced similar onset latency comparable to that produced by the magnetic stimulation.

Comments: We know that the electrical stimulation stimulates the cord. The similar onset latencies by the magnetic stimulation suggests that the latter also stimulates the cord.

From these findings, we think that the magnetic stimulation over the lower cervical/upper thoracic area did produce CMAP of the femoral muscles through spinal cord stimulation and not by either brainstem or lumber root stimulation.

Finally, we would like to discuss possible reasons why the hole made in the vertebrae enhances the CMAP (see ③). The vertebra is transparent to the magnetic field but is a good electric insulator. When a magnetic stimulation is applied, it produces currents within the vertebral foramen, but it appears to be just strong enough to stimulate the spinal cord. On the other hand, the stimulation also produces a much larger current through the entire neck, but this current can enter the vertebral foramen only through small holes around the nerve entries and exits. Making an artificial burr hole let some fraction of this much larger current enter the vertebral foramen, thus enhancing the CMAP. This is our hypothesis at present, but should be verified using a technique similar to [2] experimentally in the future.

Reference

[1] Matsumiya Y. et al: Compound muscle action potentials from the lower extremity elicited by pulsed magnetic stimulation of the upper spinal cord (in preparation).

[2] Yunokuchi K and Ueno S: Measurements of induced currents near the boundary of simulated vertebra in magnetic nerve stimulation. Iyodenshi to Kougaku, 31: 47-52, 1993

Toward Research-Promotion Infrastructure for Multi-Modal Imaging

Matsuura K, Imai H

Institute of Industrial Science, the University of Tokyo, Tokyo, Japan

Introduction

Biomagnetic imaging usually works well when combined with other measurements. Currently common way is MRI superposition; estimated biomagnetic signal sources are superposed on magnetic-resonance images which provide anatomical information of the subject. Future directions, however, will very probably include multi-modal imaging [1]–[3]; wide variety of different measurements or estimated results will get together onto the same platform aiming at revealing more and more complicated neural activities as a whole. Looking ahead at such a situation, we consider how to provide a "research-promotion" infrastructure in the following two senses. First, we wish to encourage researchers with different scientific or technological backgrounds to cooperate together as openly as possible. Second, we wish to protect privacy of subjects.

Basically, the infrastructure should

- ensure data integrity hopefully even over an open and insecure network,
- control access structure and data linkage, and
- be efficient enough to be applied to medical data of a large size.

Conforming to these points, our framework is both at the level or layer of cryptographic primitives and at protocol design and integration. In this paper, we are devoted to the first issue and propose an extended use of "signcryption" which provides both the functions of public-key encryption and digital signature [4].

In writing a letter with ensured confidentiality and no forgery, for centuries it has been a common practice for the originator of the letter to sign his/her name on it and then seal it in an envelope. This two-step "signature-then-seal" process is not inconvenient to most originators since the time and cost involved is usually regarded as being marginal. Likewise, electronic message-delivery services often use digital signature and encryption technologies consecutively. Although the sum of the cost for signature and the cost for encryption are computationally expensive, this two-step "signature-then-encryption" process has been a standard method for a secure and authenticated delivery. Originating from questioning whether it is absolutely necessary for one to spend the sum of the costs to achieve both confidentiality and authenticity, the author of [4] proposes a new cryptographic primitive called signcryption.

Intuitively, a digital signcryption is a cryptographic method that fulfills both the functions of secure encryption and digital signature, but with a cost smaller than that required by signature-then-encryption. For details, the readers can consult [4]. We here note that three important properties can be efficiently adopted: confidentiality of contents, unforgeability, and non-repudiation. In the following, we show how to extend this primitive for digitized multi-modal data $(M_1, M_2, \cdots, M_n; m_1, m_2, \cdots, m_{n'})$ where $M_1, M_2, \cdots, M_n$ are materials which require both secrecy and integrity while $m_1, m_2, \cdots, m_{n'}$ need only integrity.

Methods

We use system parameters and functions as follows:

p:	a large prime (1024bit, for example)
q:	a large prime factor of $p-1$
g:	an integer with order q modulo p
$hash()$:	a one-way hash function whose output has at least 128bit
$KH()$:	a keyed one-way hash function
(E, D):	encryption and decryption algorithms of a private-key cipher
$\|\|$:	concatenation
x_a:	sender's private key chosen from $[1, 2, \cdots, q-1]$
y_a:	sender's public key such that $y_a = g^{x_a} \bmod p$
x_b:	recipient's private key chosen from $[1, 2, \cdots, q-1]$
y_b:	recipient's public key such that $y_b = g^{x_b} \bmod p$.

©1999, Tohoku University Press

Recent Advances in Biomagnetism
T. Yoshimoto et al. (Eds)

At the first step, the sender (say, Alice) chooses an integer u randomly from $[1, 2, \cdots, q-1]$. She then computes

$$\begin{aligned} (k_1, k_2) &= hash\,(y_b^u \bmod p) & (1)\\ r &= KH_{k_2}(M_1\|M_2\|\cdots\|M_n\|m_1\|m_2\|\cdots\|m_{n'}) & (2)\\ s &= (u + r\cdot x_a) \bmod q & (3)\\ c &= E_{k_1}(M_1\|M_2\|\cdots\|M_n) & (4)\end{aligned}$$

and sends r, s, c, m_1, m_2, $\cdots$, m_n to the recipient (say, Bob). On receiving this message set, Bob first recovers (k_1, k_2) as

$$(k_1, k_2) = hash\left((g^s \cdot y_a^{-r})^{x_b} \bmod p\right). \tag{5}$$

He then decrypts the secret materials by

$$(M_1\|M_2\|\cdots\|M_n) = D_{k_1}(c). \tag{6}$$

Finally, the data integrity and the linkage between the encrypted and the plain materials are verified by the following criterion:

$$\begin{array}{ll} \text{Valid} & \text{if } r = KH_{k_2}(M_1\|M_2\|\cdots\|M_n\|m_1\|m_2\|\cdots\|m_{n'})\\ \text{Invalid} & \text{otherwise.}\end{array}$$

If an attacker modifies some of the plain materials, the keyed hash value is changed and no longer equivalent to r. The attacker cannot adjust r to the message set with modified materials since he has no knowledge of the recipients secret key x_b and thus can get neither k_1 nor k_2. The concept of the proposed scheme is outlined in Fig. 1 We call this scheme "multi-modal signcryption".

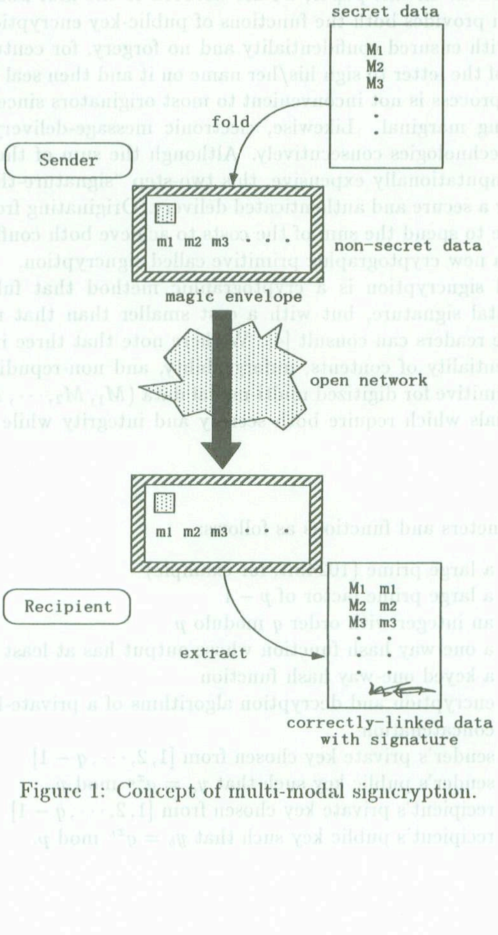

Figure 1: Concept of multi-modal signcryption.

We evaluate the performance of multi-modal signcryption by comparing computational cost and communication overhead with those of conventional signature-then-encryption approach based on RSA scheme, where the sender Alice

1. computes the authenticator S by using her secret key with the input of $(M_1\|M_2\|\cdots\|M_n\| m_1\| m_2\| \cdots \|m_{n'})$,
2. encrypts $(M_1\|M_2\|\cdots\|M_n\|S)$ with the public key of the recipient, and
3. sends the encrypted result together with $(m_1, m_2, \cdots, m_n)$

and the recipient Bob

1. decrypts the encrypted materials with his secret key, and
2. verifies the sender's authenticator S is valid by using her public key.

The RSA encryption/decryption considered is a version designed for inputs of arbitrary length.

Specific numeric comparison requires the knowledge of up-to-date implementation technique. Regarding conventional schemes, a high-quality survey of cryptographic software implementation in [5] is helpful. We follow [6] regarding the techniques and the assumptions for estimating the performance of multi-modal signcryption.

Results

The performance analysis was carried out for different levels of security including the currently standard one. The result is summarized in Table 1 where the size of the RSA composite determines the level of security. The larger the composite gets, the more secure the system is. The security level currently recommended by research community of information security is about 1024 bits. At this level, multi-modal signcryption saves computational cost and communication overhead by 32.3[%] and by 88.3[%], respectively.

Table 1 also shows that these advantages will get more significant in the future; larger sizes of RSA composite bring larger cost reduction both in computation and in communication. Although not included in this paper, a comparison with ElGamal scheme [7] gives similar characteristics.

Discussion

This paper shows how to adapt a relatively new cryptographic primitive called signcryption to multi-modal imaging data. The proposed scheme, called multi-modal signcryption, maintains three important security properties of the original signcryption: confidentiality of contents, unforgeability, and non-repudiation. In addition, we can verify the linkage between different imaging data, especially between encrypted materials and non-encrypted materials.

Table 1: Advantage of multi-modal signcryption in comparison with signature-then-encryption based on RSA. The larger the size of RSA composite, the higher the security level. Currently recommended level is 1024 bits or so.

size of RSA composite in bits	Reduction in computational cost [%]	Reduction in communication overhead [%]
768	14.2	84.9
1024	32.3	88.3
1280	43.1	90.0
1536	50.3	91.4
2048	59.4	93.0
2560	64.8	94.0
3072	68.4	94.5
4096	72.9	95.0
5120	75.6	96.0
10240	86.5	98.0

A cost evaluation tells that the computational cost is reduced by at least 32.3[%]. This reduction gets more significant if we consider future situation with higher level of security. Likewise, the communication overhead is reduced by at least 88.3[%]. This reduction also becomes more significant in future situation. Since biomedical imaging data are in general of a large size, the efficiency of multi-modal signcryption will contribute a lot to a practical system.

We can find an approach to use a global network for medical imaging [8] and expect that networked research-promotion infrastructure would enhance the progress of brain science with higher speed. One feasible scenario is a commitment of the inverse analysis.

Non-invasive measurements play an important role in biomedical research. A very common research flow is composed of setup, data acquisition, inverse analysis, interpretation of the inverse solutions, and update of the setup and the inverse-analysis algorithm. In an advanced research such that physiologists and signal-processing engineers work separately, the research tends to make a progress very slowly. Two main reasons for this slow progress are (i) slow experiments and (ii) slow data-circulation. That is, (i) we have to be careful in dealing with the subjects (very probably human beings) and (ii) it takes quite a long time to make contracts between the researchers. It is difficult to solve the first problem. By contrast, the second problem could be solved by using information-security technologies to build research-promotion infrastructure which allows the commitment of inverse analysis over an open and global network.

In search of faster flows in biomedical researches based on non-invasive measurements, our framework should cover not only signal processing but also information security technologies.

References

[1] Garnero L, Baillet S, Lachaux J-P, Renault B: Data operating in a PET/EEG/MRI fusion experience. Human Brain Mapping Suppl. 1: 84, 1995

[2] Hochman DW, Whitaker HA, Haglund M, Ojemann GA: Is there concordance between functional brain mapping techniques? Human Brain Mapping Suppl. 1: 85, 1995

[3] Takanashi Y, Yoshikawa K, Iwamoto K, et al: Comparison of functional localization in human visual cortices using MEG and fMRI: a preliminary report, Hashimoto I, Okada YC, Ogawa S (eds): Visualization of Information Processing in the Human Brain: Recent Advances in MEG and Functional MRI (EEG Suppl. 47). Amsterdam: Elsevier, 1996, pp. 59–63

[4] Zheng Y: Digital signcryption or how to achieve cost(signature & encryption) << cost(signature) + cost(encryption), Advances in Cryptology — Crypto'97, Lecture Notes in Computer Science 1294, Berlin: Springer-Verlag, 1997, pp. 165–179

[5] Menezes A, van Oorschot P, Vanstone S: Handbook of Applied Cryptography. Boca Raton, Florida: CRC Press, Inc., 1996

[6] Matsuura K, Zheng Y, Imai H: Compact and flexible resolution of CBT multicast key-distribution, Proc. of Worldwide Computing and Its Applications '98 (WWCA'98), Lecture Notes in Computer Science 1368, Berlin: Springer-Verlag, 1998, pp. 190–205

[7] ElGamal T: A public key cryptosystem and a signature scheme based on discrete logarithms. IEEE Trans. Information Theory: IT-31, 4, 469–472, 1985

[8] Wong STC, Huang HK: Networked multimedia for medical imaging. IEEE Multimedia: 4, 2, 24–35, 1997

Acknowledgments

The authors would like to thank Prof. Zheng at Monash University for his motivating us to extend signcryption for next-generation applications.

The Effect of Magnetic Fields on The Heart

O. Okai and H. Mitani
Department of Clinical Physiology, Kyorin University of Health Sciences
Miyashita 476, Hachioji, Tokyo 192-8508

1. Introduction

The physiological function of the heart is indicated as to make heart rate, blood pressure and so on. There is an effect of magnetic fields on the heart. Heart rate increases or decreases according to direction of static magnetic field to the heart. It is seen in many cases that blood pressure increases or decreases according as heart rate increases or decreases, respectively.

Here, we investigated the effect of magnetic fields on pathological function of the heart. When the myocardial infarction took place, there are much examples of decrease in the chest pain by applying the magnetic fields to the heart. We clarified the mechanism of the pain decrease.

2. Method

Six mongrel dogs weighing 8-12 kg were used for the experiments. Each dog was anaesthetised with intravenous pentobarbital sodium (30 mg / kg) and placed on respirator after the trachea was intubated. A catheter-tip pressure transducer was advanced from the femoral artery to the root of the ascending aorta. Simultaneous recordings of the ascending-aorta pressure and ECG of the lead II were obtained at a chart speed of 10 mm/sec. A dog was placed in a static magnetic field (DC field) or an alternative magnetic field (AC field). Here we stop the breath of a dog. The responses of a dog was compared with these of the dog in a magnetic field until ST elevation of ECG took place.

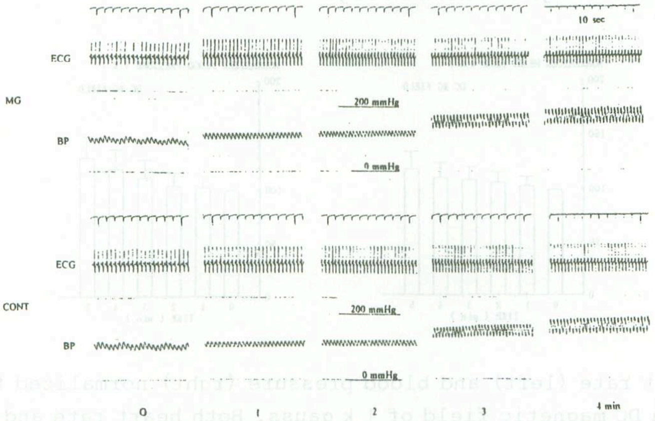

Fig. 1. ECG and blood pressure (BP) from a dog for control (CONT) and for a DC magnetic field of 1 k gauss (MG).

©1999, Tohoku University Press
Recent Advances in Biomagnetism
T. Yoshimoto et al. (Eds)

3. Results and Discussion

ECG and blood pressure of a dog with a magnetic field and without were recorded as shown in Fig. 1. When we stopped the respiration of a dog, heart rate and blood pressure were increased with time elapsed until the ST elevation of ECG as shown in Fig. 2. The time from the choke until ST elevation take place, is named as CT time. All running data were normalized to the first data.

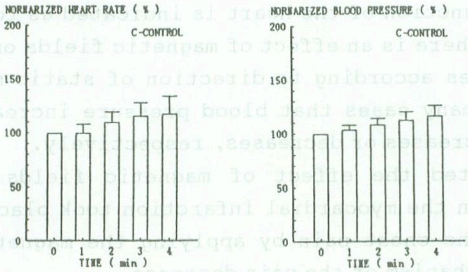

Fig. 2. Heart rate (left) and blood pressure (right) nomalized to control data for control from a dog. Both heart rate and blood pressure increased with increasing carbon dioxide in the blood.

Data for control

We investigated ECG, heart rate and blood pressure from a dog without magnetic field as shown in Fig. 2. After the choke of a dog, the average of heart rate was 100 % for 0 min, 100 % for 1 min, 110 % for 2 min, 116 % for 3 min, and 118 % for 4 min; the average of blood pressure was 100 % for 0 min, 104 % for 1 min, 109 % for 2 min, 113 % for 3 min, and 117 % for 4 min as shown in Fig. 2.

The elevation of ST tracing of ECG took place in the average of 4.03 min after the choke of 6 dogs as shown in Fig. 3.

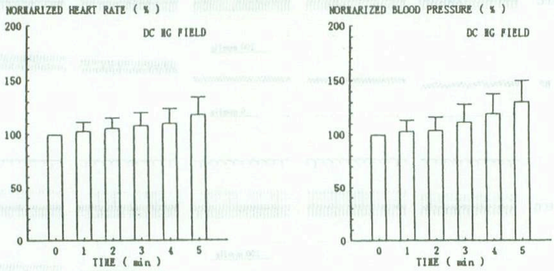

Fig. 3. Heaart rate (left) and blood pressure (rght) normalized to control data from a dog in a DC magnetic field of 1 k gauss. Both heart rate and blood pressure increased with increasing carbon dioxide in the blood.

Data for DC magnetic field

In a DC magnetic field of 1 k gauss the same experiment was carried out The average of heart rate was 100 % for 0 min, 103 % for 1 min, 106 % for 2 min, 109 % for 3 min, 111 % for 4 min, and 119 % for 5 min; the average of blood pressure was 100 % for 0 min, 103 % for 1 min, 104 % for 2, 112 % for 3 min, 120 % for 4 min, and 131 % for 5 min.

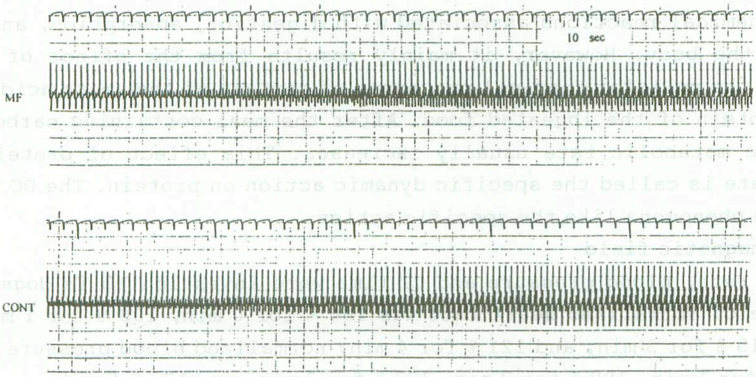

Fig. 4. ECG changes after the choke of a dog; MF for DC magnetic field and CONT for control.

Heart rate, blood pressure, and CT time for control were compared with data for a DC magnetic field; the ratio of heart rate for control to that for a DC magnetic field is 101 % ; the ratio of blood pressure 112 %, and the ratio of CT time 150 % as shown in Fig. 3.

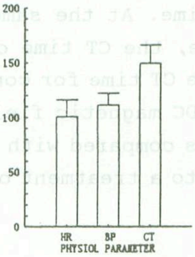

Fig. 5. Ratio of control data to that for a DC magnetic field; HR is the ratio for heart rate; BP for blood pressure; CT for a time from the choke until ST elevation of ECG of a dog.

The avarage time from the choke until the ST elevation of ECG took place, was 4.03 min in a dog without the magnetic field and 6.04 min with a DC magnetic field of 1 k gauss. It may be explained that since the a DC magnetic field exerts a cooling effect on a dog, oxygen consumption decreased. In other words mouse rectal temperature decreased by 0.7° C during and immediately after exposure to 4 k gauss. Then it considered that the DC magnetic field decreased the metabolic rate and oxygen consumption. Therefore, the avarage CT time of the dog using a DC magnet was significantly longer than the CT time for control ($p < 0.01$).

There is another consideration for the result. After a meal is ingested, the metabolic rate increases. This believed to result to very slight extent from different chemical reactions associated with digestion, absorption, and storage of food in the body. However, it mainly results from the effect of directly stimulating the cellular chemical processes of certain of the amino acids derived from the protein of the ingested food. After the meal containing carbohydrates and fats the metabolic rate usually increases. This effect of protein on the metabolic rate is called the specific dynamic action on protein. The DC field may decrease the phenomena like the specific action.

Data for AC magnetic field

Heart rate, blood pressure and CT time were investigated in dogs in an AC magnetic field. Normalized heart rate was 100 % for 0 min, 108 % for 1 min, 110 % for 2 min, 115 % for 3 min, and 121 % for 4 min; normalized blood pressure 100 % for 0 min, 104 % for 1 min, 109 % for 2 min, 123 % for 3 min, and 133 % for 4.

Comparison of heart rate, blood pressure and CT time for control with these for an AC magnetic field was made; ratio of heart rate for control to that for an AC magnetic field is 103 ± 19 %; the ratio of blood pressure 114 ± 11 %; the ratio of the CT time 106 ± 11 %. The heart rate and the CT time did not changed significantly but blood pressure increased significantly.

4. Conclusion

When we stopped the respiration of a dog, bicarbonate content in the blood increased with increasing CT time. At the same time both heart rate and blood pressure increased. Furthermore, the CT time of dogs for the DC magnetic field significantly prolonged than the CT time for control ($p < 0.01$). From the results yielded it is concluded that a DC magnetic field retarded the time point of the elevation of ST segment of ECG as compared with a case of control. Therefore, the DC magnetic field may be useful to a treatment of the myocardial ischemia or like this.

5. Acknowledgements

We wish to thank Mr. S. kanaumi and Mr. M. Doi (U-medic Inc.) for various supports about the effect of magnetic field on man.

6. References

1) J.F.Barnothy et al: Magnetobiology. In Slonim, N.B., editor: Environmental physiology, Saint Louis, 1974, The C.V. Mosky company, p 313-349.

2) A.C. Guyton: Metabolism and temperature reguration, In Texstbook of medical physiology, Philadelphia, 1981, W.B. Saunders company, p 807-871.

Preoperative and Intraoperative Identification of Sensorimotor Function

Okumura A, Takenaka K, Kawaguchi M, Nishimura Y, Sakai N

Department of Neurosurgery, Gifu University School of Medicine, Gifu, Japan

Introduction

Human brain functional mapping has been widely performed with several kinds of modalities used to explore the spatial and temporal organization of the neural systems supporting human behavior. These modalities are being developed to provide the neurosurgeon with brain functional information prior to the surgical procedure [1]. The neurosurgeon now has a selection of the techniques for brain functional mapping. For preoperative brain mapping, functional magnetic resonance imaging (fMRI) and radionuclide method, which reflect the hemodynamic changes that presumably follow neuronal activation have been reported to be the same useful as electrophysiological method such as magnetic source imaging, which can almost directly rely on neuronal activity [1, 2]. On the other hand, it is urgently important and necessary for surgeons to identify the real-time functional localization during surgery. For localization of sensorimotor area during surgery under general anesthesia, intraoperative method detecting hemodynamic changes following activated neuronal function has been a little reported in clinical setting previously, while cortical recording of somatosensory evoked potentials (SEPs) has been performed. The purpose of this study is to evaluate the applicability of hemodynamic studies, such as fMRI and SPECT for preoperative functional mapping and cortical thermomapping during surgery in combination with cortical recording of SEPs.

Methods

Fifteen patients who had brain tumor located around the primary sensorimotor area were studied by using both fMRI and activation study with SPECT. Patients were operated and cortical recording of SEPs was performed. Pathological study revealed 10 glioblastomas and 5 metastatic brain tumors. The MR examinations were performed on a 1.5 T system, using a standard head coil. The sequence consisted of obtaining 375 consecutive single shot echo planner sequence with multislice. The functional image was generated from 75 images in 5 selected planes from the vertex to the corpus callosum with the following parameters: repetition time (TR) 2000 msec; echo time (TE) 40 msec; flip angle 60 degree; field of view (FOV) 22~38 cm; section thickness 5 mm; one signal averaged; a 128 x 128 matrix. During this 375-image acquisition, the patients alternated between rest (30 second) and a voluntary activation task (30 second), which consisted of repetitive opening and closing of the fist at a frequency of approximately two times per second. Patients performed motor task with the contralateral hand of involving by the tumor. Statistical fMRI was superimposed onto 3D anatomical image with venography. Activation study with SPECT was performed in modification of previous study [2], so-called split dose and subtraction method with ^{99m}Tc-ethyl cysteinate dimer. The motor task was performed with the same task as that of fMRI. The activation area obtained from SPECT was superimposed onto anatomical detail 3D MRI by means of the image analysis software. Based on the localized sensorimotor area on the 3D image, cortical recording of SEPs was performed intraoperatively to validate the location of the central sulcus by the stimulation of median nerve. This was accomplished using a single strip 4-electrode array placed on the surface of the brain, attached via cables to a standard evoked potential machine. In 2 patients, cortical thermomapping was also performed during median nerve stimulation.

©1999, Tohoku University Press
Recent Advances in Biomagnetism
T. Yoshimoto et al. (Eds)

Results

In fMRI, the significant activation area of sensorimotor where the change in signal intensity coincided with the beginning and end of the motor task, could be observed in 14 patients of 15. In activation study with SPECT, the sensorimotor area was observed as the most increased area in regional cerebral blood flow (rCBF) during motor task in 12 patients of 15. The sensorimotor area from fMRI was consistent with that from SPECT in all cases. Based on the functional mapping obtained from fMRI and SPECT, intraoperative cortical recording of SEPs was performed. In 11 patients of 15, the polarity reversal of N20 and P20 was observed and the validity of the sensorimotor area obtained from fMRI and SPECT was established. Thermomapping could demonstrate the localized area, where cortical temperature during the stimulation was increased during the stimulation. The changed area in temperature was consistent with the N20 area in SEPs.

Discussion

Each technique such as fMRI, radionuclide method or electrophysiological method gives its own view of some aspect of brain function, and each technique has its own set of strengths and weakness. In this study, the sensorimotor area in fMRI is consistent with that in radionuclide method and intraoperative SEPs. In pathophysiological condition involved in brain tumor, our study demonstrated that fMRI was considered to be more sensitive and reliable method to localize the sensorimotor area. This advantage of fMRI may be based on the different process of activation from electrophysiological method. Namely, while the electrophysiological method reflects neuronal activity, fMRI reflects oxygen consumption in addition to the change in CBF, which radionuclide method reflects. Moreover, brain functional mapping which reflects the changes in rCBF might yield quantitative physiological information as presentation of image form. These modalities have the potential utility to measure brain function and display quantitatively while it is difficult for electrophysiological method to evaluate the degree of brain function [3]. On the other hand, in our study, thermomapping for functional localization during surgery was preliminarily used. Thermomapping could display the localized area with excellent spatial sensitivity in the operative field of view. In conclusion, the demonstration of convergence in brain functional mapping using various techniques not only increased the confidence of functional mapping in clinical setting, but also can be possibly useful for characterizing pathophysiological conditions.

References

[1] Okumura A, Takenaka K, Nishimura Y, et al: Functional MR imaging with venography for neurosurgical identification of the central sulcus. Neurol Res (in press)

[2] Okumura A, Kuwata K, Nishimura Y, et al: Clinical applicability of functional magnetic resonance imaging and activation study with single photon emission computerized tomography for functional mapping. Neurol Res 20: 191-197, 1998

[3] Okumura A, Kawaguchi M, Takenaka K, et al: The activation study with combination of fMRI and SPECT in stroke patients with hemiparesis. Eur J Neurol 5 Suuppl: 32-33, 1998

Evaluation of the Pyramidal Tract by Diffusion-weighted Magnetic Resonance Imaging

Shimizu H[1], Inoue T[2], Yoshimoto T[2]

Department of Neurosurgery, Kohnan Hospital [1];
Department of Neurosurgery, Tohoku University School of Medicine[2], Sendai, Japan

Introduction

Recently, magnetoencephalography and functional magnetic resonance imaging povide noninvasive preoperative evaluation of cortical functional topography [1, 2]. However, all currently available functional mappings investigate only the cortical function. Although it is eaqually important to recognize functional distribution of subcortical nerve fibers, few studies have been attempted.

Diffusion-weighted magnetic resonance imaging (DWI) has been well acknowledged as a powerful tool for the early diagnosis of acute stroke. In addition, DWI has a capability to distinguish nerve fibers or axons, because diffusion perpendicular to the fiber orientation is more restricted than that of parallel direction. This anisotropy can be imaged by applying different diffusion gradients relative to the fiber orientation; when they are parallel, the fiber appears as hypointense and when they are perpendicular, hyperintense. Although axonography, named 3DAC, has been reported in the rat spinal cord [3], their clinical implication has not been clarified.

In the present study, we have introduced a method to visualize the entire pyramidal tract on a single image and compared the pyramidal tract integrity with motor function of patients with brain lesions.

Methods

Three normal volunteers (23-25 years old), two patients with intracerebral hemorrhage (58 and 63 years old), one patient with cerebral infarction (62 years old) and three patietns with brain tumors (19-62 years old) underwent the current imaging protocol, approved by the ethical committee of Kohnan hospital, after receiving informed concent. All imagings were performed with a commercial 1.5 Tesla whole body scanner and the standard head coil. The imaging protocol included single-shot echo planar DWI and fast spin echo T2-weighted image (T2WI). Two oblique-coronal slices were obtained; one through the presumed primary motor cortex, the corona radiata and the internal capsule (slice A), the other through the internal capsule, the cerebral pedancle and the ventral brain stem (slice B) (Fig. 1). Acquisition parameters for the DWIs were as follows; repetition time 3000 msec, echo time 100 msec, matrix 128*128, field of view 24 cm, and b value 1000 sec/mm^2.

After the acquisition, the DWIs were transfered to a Machintosh computer (Apple Japan Inc., Tokyo, Japan) and analyzed with Photoshop software (Adobe Systems Japan, Tokyo, Japan). The greyscale image with superior-inferior, left-right or anterior-posterior diffusion gradient was first turned over in gradation, and then color-cordinated with red, green or blue gradation, respectively. These colored images were piled into a single RGB color image. Thus, a nerve fiber running superior-inferior, left-right or anterior-posterior direction resulted in red, green or blue, respectively. Mixed colors were indicative of oblique orientation of nerve fibers. The superior half of the slice A and the inferior half of the slice B were cut and combined to generate a compound image. For convenience, this is refered to a fiber mapping image in the present study.

Results

Representative fiber mapping image of a normal volunteer was shown in Fig. 1. Due to limitation of publication policy, greyscale image was presented. In the superior half of the fiber mapping image, the pyramidal tracts were seen bilaterally as several bands coming from the presumed primary motor cortex gathering into the corona radiata. From the corona radiata, the pyramidal tracts run in anterior-inferior-medial direction until the internal capsule. In the inferior half of the image, the pyramidal tracts between the internal capsule and the brain stem were shown as black bands. In all volunteers fiber mapping image demonstrated the pyramidal tracts continuously from the presumed motor cortex to the brain stem.

In patients, depending on the lesion locations, variable disturvances of the pyramidal tract were demonstrated with the present fiber mapping images. In the patient with right thalamic hemorrhage, who had slight left hemiparesis, the pyramidal tract was slightly compressed but not severely damaged (Fig. 2). In the patient with right cerebral infarction, who had severe left hemiparesis, the pyramidal tract was severely damaged and discontinued (Fig. 3). In the patient with left frontal meningioma, who had slight

©1999, Tohoku University Press
Recent Advances in Biomagnetism
T. Yoshimoto et al. (Eds)

left lower limb monoparesis, the pyramidal tract was obscure and probably compressed laterally on the preoperative image. On the right postoperative image, the entire pyramidal tract appeared normal (Fig. 4).

Discussion

The present study provided a simple method to visualize the entire pyramidal tract from the primary motor cortex to the brain stem on a single compound image. The advantage of using single-shot echo planar DWI is motion-free and short imaging time, whereas the disadvantage is poor spacial resolution and image distortion due to susceptibility artifact.

In the patients with intaracerebral hemorrhage and infarction, appearance of the pyramidal tract on the fiber mapping image showed good correlation with motor function. Obvious dyscontinuity indicated motor dysfunction more sensitively than compression only. Postoperatively, delineation of the pyramidal tract improved in association of improvement of patient's motor function.

In the patients with brain tumors, investigation of the neuronal pathway in the white matter is important to decide the area of resection.

The fiber mapping may make a predictor of postoperative motor function and influence the surgical strategy.

References

[1] Nakasato N, Seki K, Kawamura T, et al: Cortical mapping using an MRI-linked whole head MEG system and presurgical decision making. Electroencephalogr Clin Neurophysiol Suppl 47: 333-41, 1996

[2] Yetkin FZ, Mueller WM, Morris GL: Functional MR activation correlated with intraoperaive cortical mapping. AJNR 18: 1311-1315, 1997

[3] Nakada T, Matsuzawa H, Kwee IL: Magnetic resonance axonography of the rat spinal cord. NeuroReport 5: 2053-2056, 1994

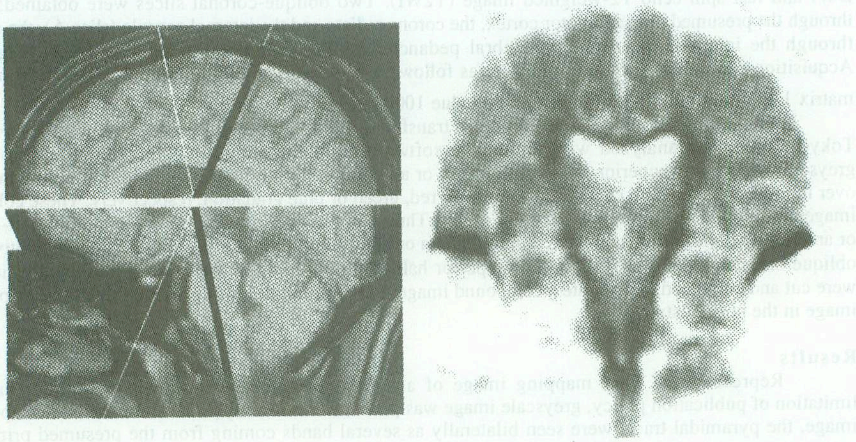

Fig. 1

Left: Two oblique-coronal slices, A and B, were shown. Slice A: From the presumed primary sensorimotor area, through the corona radiata, to the internal capsule. Slice B: From the internal capsule, throught the cerebral peduncle, to the ventral brain stem. Combined image: The superior half of the slice A and the inferior half of the slice B were cut and combined.

Right: The superior half of the image showed the bilateral pyramidal tracts as several bands coming from the presumed primary motor cortex and gathering into the corona radiata. The inferior half of the image showed the pyramidal tracts between the internal capsule and the brainstem. Due to limitation of publication, this has been made of gray scale so that only the direction of superior-inferior was demonstrated as the black band.

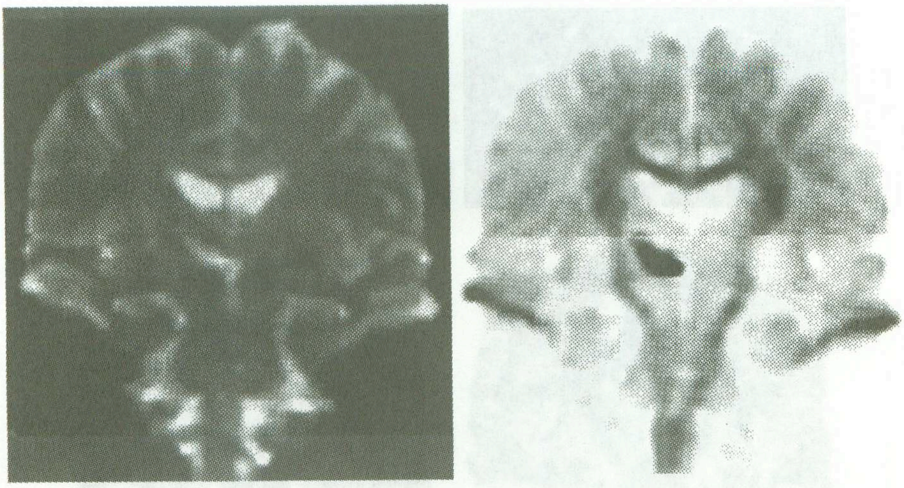

Fig. 2
A patient with right thalamic hemorrhage manifesting slight left hemiparesis.
Left: T2 weighted MRI demonstrated the hematoma as high intensity area surrounded by a low intensity limb.
Right: DWI demonstrated that the right pyramidal tract was slightly compressed but not severely damaged.

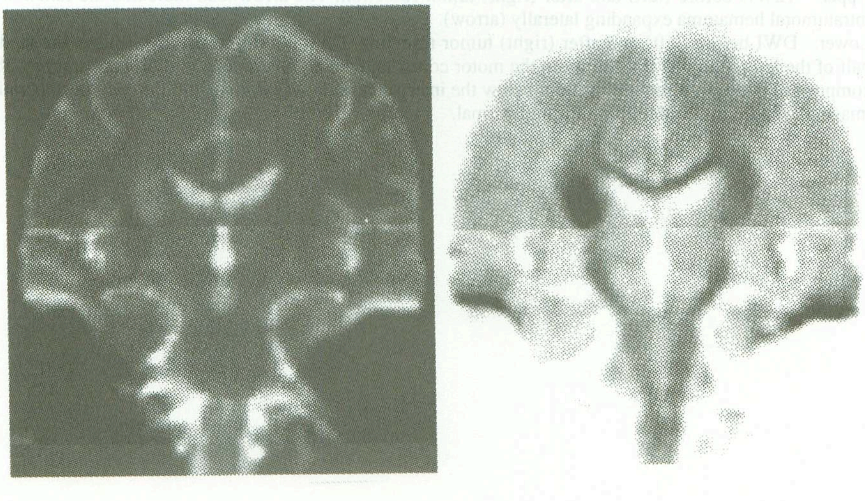

Fig. 3
A patient with right cerebral infarction manifesting severe left hemiparesis.
Left: T2WI demonstrated the infarction as high intensity area in the right corona radiata.
Right: DWI demonstrated that the right pyramidal tract was severely damaged and discontinued.

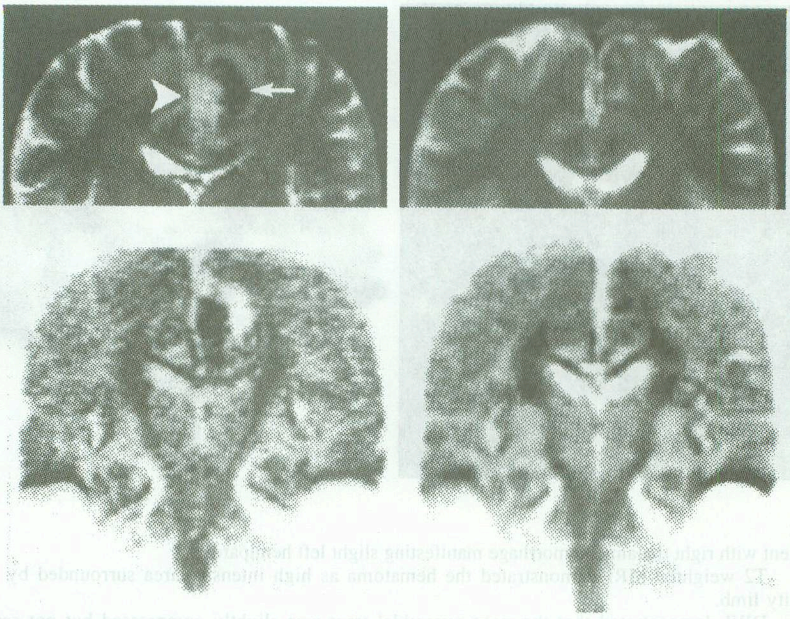

Fig. 4
Pre- (left) and post- (right) operative findings of a patient with left frontal menigioma, preoperatively manifesting slight right lower limb monoparesis.
Upper: T2WIs before (left) and after (right) tumor resection. The arrowhead indicated the tumor with intratumoral hematoma expanding laterally (arrow).
Lower: DWI before (left) and after (right) tumor resection. On the left preoperative image, the medial half of the left pyramidal tract between the motor cortex and the corona radiata was obscure and probably compressed laterally, although the tract below the internal capsule was normal. On the right postoperative image, the entire pyramidal tract appeared normal.

Estimation of a Developed Focal Magnetic Stimulator

Tamari Y[1], Yunokuchi K[2], Yoshida H[2]

Kagoshima National College of Technology[1], Aira-gun Kagoshima, Japan
Kagoshima University[2], Kagoshima, Japan

Introduction

In recent years, magnetic stimulation has emerged as an useful method for stimulating nerves in clinical site. It is mainly used a figure-of-8 coil as focal stimulator, because magnetic stimulation is noninvasive and less painful than electric stimulation. It is, however, difficult to predict distributions of induced electric field or induced eddy current in an inhomogeneous medium like as the human. Thus, we have predicted the spatial distributions of electric field induced in a tank model filled with saline solution, when the tank was exposed to pulsed magnetic fields.

We have developed several coils which enable stimulation to focus in a small volume under the coil due to change geometry of it. The circular coil, figure-of-8 coil and slinky coil[1] have been manufactured for an experiment. The properties of these coils with respect to focal stimulation were estimated by measuring electric field directly in the model. These results showed that the induced eddy current density by using slinky coil was more localized than that of other coils. We found that focality of induced eddy current at the arbitrary distance from coil depended on the radius of slinky coil's vertical. And using each Slinky coils, we recorded from bipolar surface electrodes of EMG over abductor pollicis brevis in response to a single magnetic stimulus applied at the forearm. These result was reported.

Methods

To estimate the localization of eddy current induced by pulse magnetic field, we calculated the electric field in an infinite volume conductor exposed to magnetic fields. The types of magnetic coil used the simulation were figure of 8 coil and Slinky coil. We compared the focality of figure of 8 coil with that of Slinky coil.

To enable to focus in a small volume under the coil, we changed geometry of the coil. The circular coil, figure-of-8 coil and Slinky coil have been manufactured for an experiment. Fig.1 shows the shape of these coils. The Slinky coil in shape adds vertically one circular coil as shown in Fig.1(c) to the figure of 8 coil. The diameter of each coils is 67[mm]. The diameter of perpendicular coil to the figure of 8 coil was varied the following three types; 4.5[cm], 6.7[cm], 9.5[cm]. The number of turns of each coils (circular coil, figure of 8 coil and Slinky coil) was 10, 10 ×2, and 5×3 turns. The each coils were wound by a coated copper wire.

The electric field induced by pulsed magnetic field was measured for estimating the focality of these coils. The induced eddy current is measured with a probe composed of extremely thin coaxial cable[2]. An end-part of cable

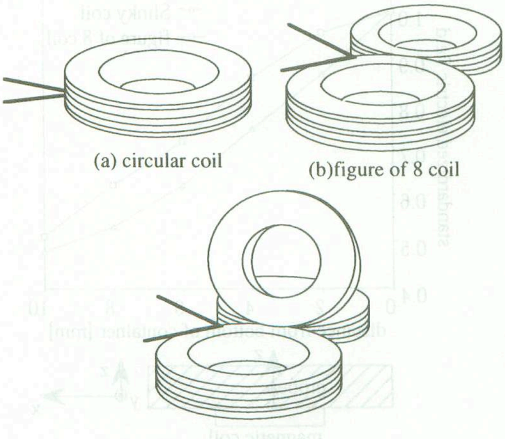
(a) circular coil
(b)figure of 8 coil
(c) Slinky coil

Fig.1 Shape of the each coils.

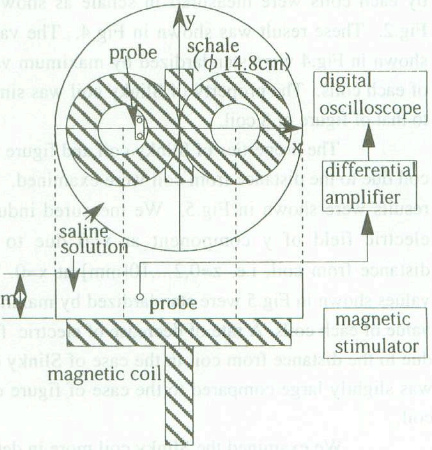

Fig.2 Measuring system.

©1999, Tohoku University Press
Recent Advances in Biomagnetism
T. Yoshimoto et al. (Eds)

is used as the electrodes. The outer conductor of the cable is connected to the ground. The electrode parts of cable are both plated by platinum black in order to reduce the electrode impedance. The cable is connected to the differential amplifier. We used a magnetic stimulator made by our laboratory. Fig.2 shows the measuring system of the induced electric field in schale filled saline solution. We measured electric field of y component on x axis as shown in Fig.2.

Using Slinky coils, we recorded of EMG over abductor pollicis brevis by using bipolar surface electrodes in response to a single magnetic stimulus applied at the forearm. The EMGs were recorded and displayed by computer. When the diameter of perpendicular coil to the figure of 8 coil in Slinky coil was varied the three types, each EMG's amplitudes were compared.

Results

To simulate the localization of induced eddy current by pulsed magnetic field, we calculated the electric field in an *infinite* volume conductor induced by magnetic stimulation. The types of magnetic coil for the simulation are figure of 8 coil and Slinky coil. We compared the focality of figure of 8 coil with that of Slinky coil. These results were shown in Fig.3. The value of electric field induced by Slinky coil at the center is larger than that induced by figure of 8 coil. We found that magnetic stimulation by Slinky coil is better focality than that by figure of 8 coil.

We manufactured the circular coil, figure of 8 coil and Slinky coil for an experiment. To examine the properties of these coils, the induced electric field by each coils were measured in schale as shown in Fig.2. These result was shown in Fig.4. The values shown in Fig.4 were standardized by maximum value of each coils. The property of Slinky coil was similar to that of figure of 8 coil.

The properties of Slinky coil and figure of 8 coil due to the distance from coil were examined. The results were shown in Fig.5. We measured induced electric field of y component at x=0 due to the distance from coil, i.e. z=0,2,...10[mm] at x=0. The values shown in Fig.5 were standardized by maximum value of each coils. A rate of decrease of electric field due to the distance from coil in the case of Slinky coil was slightly large compared to the case of figure of 8 coil.

We examined the Slinky coil more in detail. When the radius of perpendicular coil in Slinky was

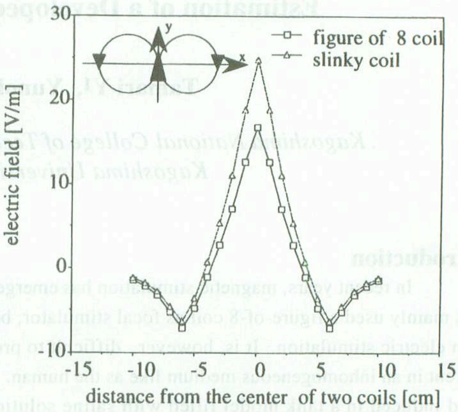

Fig.3 Calculated electric field induced by Slinky coil and figure of 8 coil.

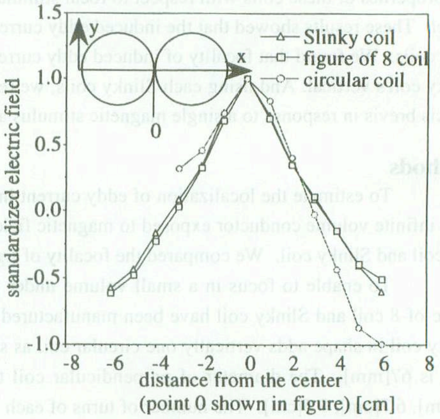

Fig.4 Measured electric field by the each coils.

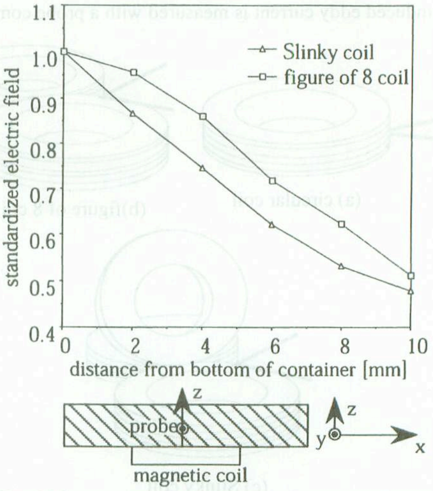

Fig.5 Measured electric field due to distance from coil.

changed , the induced electric field was measured in schale as shown in Fig.2. Each coils are defined as follows: the diameter perpendicular coil ϕ=4.5[cm] is small Slinky coil, ϕ=6.7[cm] is normal Slinky coil, ϕ=9.5[cm] is big Slinky coil. We measured induced electric field of y component at x=0 due to the distance from coil, when the vertical coil's diameter in Slinky coil was changed. The values shown in Fig.6 were standardized by maximum value of each coils. The result was that the rate of decrease of induced electric field by magnetic stimulation using small Slinky coil (ϕ=4.5) due to the distance from coil was largest compared to the others.

We recorded EMG from APB, when left forearm was applied to pulsed magnetic stimulation. The induced current was flowed as shown in Fig.7. EMGs were recorded and displayed. The results were shown in Fig.7. The amplitude of EMG evoked by magnetic stimulation using the normal Slinky coil was larger than that of EMGs using other coils.

We compared between induced electric field and evoked EMG's amplitude by magnetic stimulation. The result was shown in Fig.8. We found that the results of measurements did not suggest a correlation between induced electric field and evoked EMG's amplitude.

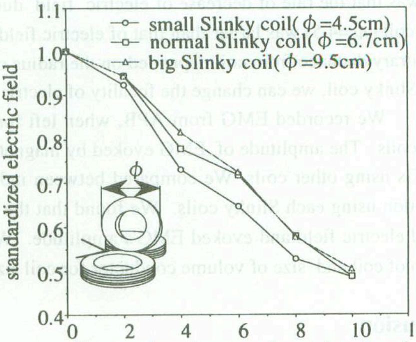

Fig.6 Measured electric field due to the distance from coil when diameter of vertical coil changed.

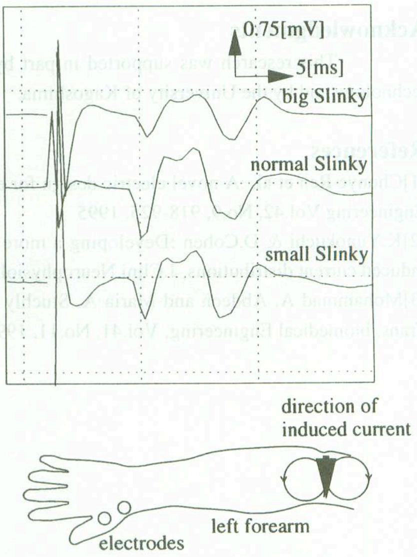

Fig.7 EMGs from APB when the each coils were used.

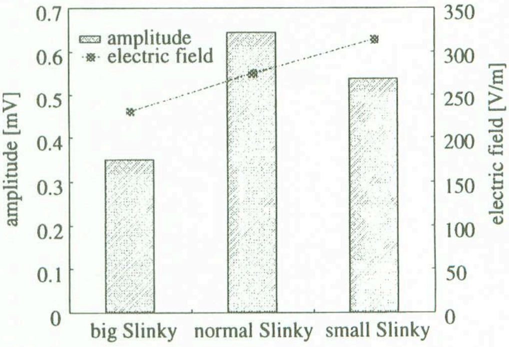

Fig.8 Comparison between amplitude of EMG and electric field.

Discussion

To estimate the localization of induced eddy current by pulsed magnetic field, we calculated the induced electric field in an infinite volume conductor by magnetic stimulation. We found that stimulation using Slinky coil can good focalize compared to the stimulation using figure of 8 coil.

We manufactured the circular coil, figure of 8 coil and Slinky coil for an experiment. To compare the properties of these coils, induced electric field by each coils were measured directly in schale. The properties of Slinky coil was similar to that of figure of 8 coil.

The properties of Slinky coil and figure of 8 coil due to the distance from coil (z direction) were examined. The rate of decrease of electric field due to the distance from coil (z direction) was compared. The result was the rate of decrease of electric field due to the distance from coil using Slinky coil was larger than that using figure of 8 coil. The magnetic stimulation using Slinky coil is better focal than that using figure of 8 coil due to the distance from coil (z direction).

Therefore, we examined the Slinky coil more in detail. To get a good focality of electric field, the radius of vertical coil in Slinky coil was changed. The result was that the rate of decrease of electric field due to the distance from coil by magnetic stimulation using small Slinky coil (ϕ=4.5) was larger than that of electric field using others. We found that focality of induced eddy current at the arbitrary distance from coil depended on the radius of vertical coil in Slinky. By the change of the radius of vertical coil in Slinky coil, we can change the focality of electric field due to the distance from coil.

We recorded EMG from APB, when left forearm was applied to pulsed magnetic stimulation using these Slinky coils. The amplitude of EMG evoked by magnetic stimulation using the normal Slinky coil was larger than that of EMGs using other coils. We compared between induced electric field and evoked EMG's amplitude by magnetic stimulation using each Slinky coils. We found that the results of measurements did not suggest a correlation between induced electric field and evoked EMG's amplitude. We suggest that the location and shape of median nerve[3], the location of coil and size of volume conductor for coil size affect to the focality of magnetic stimulation.

Conclusion

Slinky coil is better focal coil than others. We could control induced current in volume conductor using Slinky coil by changing the radius of vertical coil. The relationship between the size of coil and the size of volume conductor of stimulus target.

Acknowledgments

This research was supported in part by a grant from the principal of the Kagoshima National College of technology and by the University of Kagoshima.

References

[1]Chunye Ren et al. :A novel electric design for electromagnetic stimulation-The slinky coil, IEEE Trans. Biomedical Engineering Vol.42, No.9, 918-925, 1995

[2]K.Yunokuchi & D.Cohen :Developing a more focal magnetic stimulator. Part II : Fabricating coils and measuring induced current distributions, J.Clini.Neurophysiol. 8, 112-120, 1991

[3]Mohammad A. Abdeen and Maria A. Stuchly : Modeling of Magnetic Field Stimulation of Bent Neurons, IEEE, Trans. biomedical Engineering, Vol.41, No.11, 1994

Measurement of Auditory Evoked Electric and Magnetic Fields of Rats Before and After Transcranial Magnetic Stimulation with High-Frequency Repetitive Train Pluses

Ueno, S.[1], Uchida, S.[1], Kaga, K.[2], Shen W. D.[2], Nonaka, Y[3]., Ishikawa, S. [3] and Yarita, M[3]

Department of Biomedical Engineering[1], and Department of Otolaryngology[2], Graduate School of Medicine, University of Tokyo, Tokyo, Japan; Nihon Kohden Corporation[3], Tokyo, Japan.

Introduction

Recently, rapid rate magnetic stimulation and repetitive transcranial magnetic stimulation (rTMS) have been applied to medical diagnosis and treatment. Safty aspests of the rTMS have been reported [1-9].

In spite of these studies, the safety of repetitive magnetic stimulation has not yet been clarified. The studies have focused the effects of the repetitive magnetic stimulation on mood, hormones, the immune system, the kindling effect, and the auditory nervous system. The aim of this study is to investigate the safety of rTMS. We observed the influence of rTMS on the auditory brainstem responses (ABR), the middle latency responses (MLR) and the auditory evoked magnetic fields (AEMF).

Method

We evaluated the influence of rTMS by the latency and the amplitude of ABR, MLR and AEMF. The measurements of MLR and AEMF were carried out in pre stimulation and post stimulation, respectively. The measurements of ABR were carried out in pre stimulation, post stimulation and one week, respectively.

In the measuring of ABR and MLR, we made three holes in the skull and put three electrodes on the dura. Electrodes were fixed with dental cement. The electric potential between the parietal electrode and the frontal electrode was measured, and the temporal electrode was earthed (Fig.1).

When the ABR, the rat heard the click sound, at 1 msec duration and 70dB amplitude. The stimuli were presented with 10Hz to both ears through a speaker. The measured electric potentials were filtered from 20 Hz to 2000Hz and averaged 1000 times. With the MLR, the rat heard the click sound, at 0.1msec duration and 70dB amplitude. The stimuli were presented with 2Hz to both ears through the a speaker. The measured electric potentials were filtered from 10 Hz to 1000Hz and averaged 1000 times.

When the measuring of the AEMF, we used a 12ch high spatial resolution DC-SQUID magnetometer [10]. In the left ear, the rats heard tone bursts of 3KHz, at 10msec duration and 105dB amplitude. The stimuli were presented with 2 Hz through two meters of a plastic tubing. The sound was the same amplitude as the ABR and the MLR in the rat's ear because the amplitude of the sound was decreased through the tube. The measured magnetic fields were filtered from 1 Hz to 100Hz and averaged 3000 times. The center of the base of the dewar was placed on the right ear of the rat. Fig.2 shows the positions and sizes of the pickup coils in magnetometer

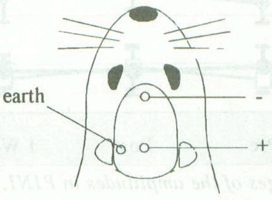

Fig. 1 Electrodes of ABR and MLR.

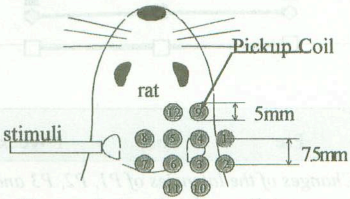

Fig.2 Positions and size of pickup coils in magnetometer

©1999, Tohoku University Press
Recent Advances in Biomagnetism
T. Yoshimoto et al. (Eds)

Subjects

Six female rats whose average weight is 238.3.g (STD=62.7) ranging from 200g to 360g were used in ABR. Eight female rats whose average weight were 285.6g (STD=113.4) from ranging 200g to 480g were used in MLR. Eight male rats whose average weight were 206.7g (STD=20) ranging from 200g to 260g were used in AEMF. All rats were anesthetized intraperitoneally with Nembutal (40 mg / 1kg)

Magnetic Stimulation

We carried out rTMS using a magnetic stimulator (Nihon Kohden Corporation). The unit of the bursts of train pulses was composed of 30 pulses with 25 Hz (25 pulses per second). The stimuli carried out by 67 burst with an interval of 50 seconds. The total pulses applied to the rats brain were 2010. Rats were stimulated by intensities of 43 percent. The intensity of the motor threshold in rats was observed at 23.3 ± 2 (average ± STD). The intensity of TMS produced muscular contraction in rat. The stimulating coil was a the circle type which was 22.2mm in inside diameter and 71.0mm in outside diameter (Fig.3). A coil was placed 5mm over the rat's head as in Fig.3 and a current was induced in the auditory cortex.

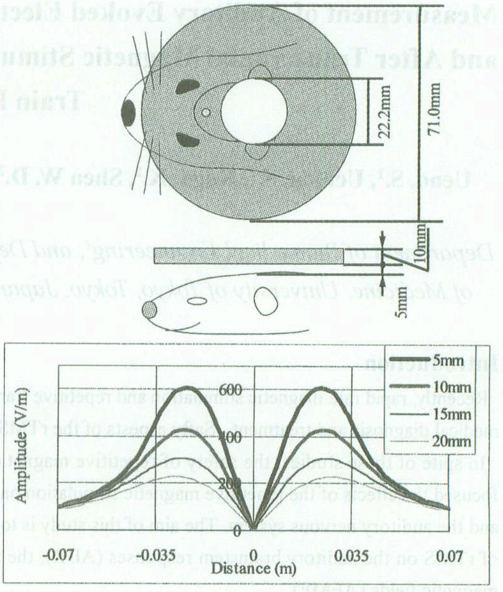

Fig. 3 The position and the sizeof the stimulating coil and the distribution of Electric fields of the coil for the distance from the coil . Upper is a top view. middle is a lateral view.

Result and Discussion

Fig.4 shows waveforms of ABR pre, post and post one week stimulation in a rat. Peaks of ABR were defined as P1,P2,P3,P4 N1,N2 and N3. Latencies of P1, P2, P3 and P4, amplitudes from N1 to P1, form N2 to P2 and from N3 to P3 were observed, respectively. In this case, the latency of P1 decreased at one week. The latency of P2 shoed no change. The latency of P3 increased at post. The latency of P4 decreased at one week. Fig. 5 shows changes of the latencise in four positive peaks. Fig.6 shows changes in the

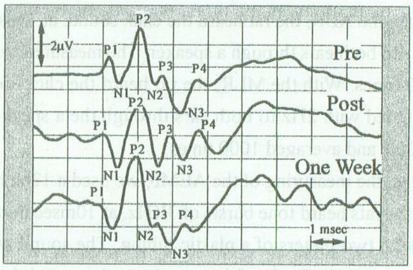

Fig.4 Waveforms of ABR pre, post and post one week stimulation in a rat.

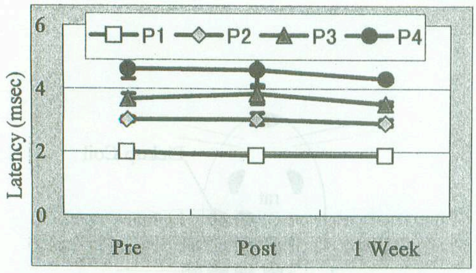

Fig. 5 Changes of the latencies of P1, P2, P3 and P4.

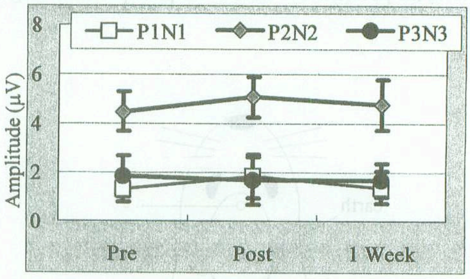

Fig. 6 Changes of the amplitudes in P1N1, P2N2 and P3N3.

amplitudes of three peaks. The individual change of the amplitude and latency was observed, but the changes in the latencies and the amplitudes by rTMS were statistically insignificant.

Fig.7 shows waveforms of MLR pre and post stimulation in a rat. Peaks of MLR were defined as Na, Pa and Pb. Latency of Na, Pa and Nb, Amplitude from Na to Pa and from Nb to Pa were observed, respectively. In this case, the latencies of Na, Pa and Nb slightly changed. Fig. 8 shows the changes of the latencies of three positive peaks. Fig.9 shows the changes of the amplitude in two peaks. The changes of the latency and the amplitude by rTMS were statistically insignificant.

Fig. 10 shows waveforms of the magnetic fields in both pre and post stimulation in a rat. The upper figure indicates pre stimulation and the bottom figure indicates post stimulation. The right indicates highlighted waveforms. In this case, the responses of mono phase waveforms were observed. Especially, the source appeared at 10ch and the sink appeared at 9ch. However, 4ch and 12ch of magnetic fields in pre stimulation and 12ch in the post stimulation were not measurable. The latencies of pre and post stimulation observed were 51msec and 59msec. The delay between pre and post was 8msec. Fig. 11 shows the changes of the latencies of magnetic fields in the eight rats. Although individual changes of the latencies were observed, but the changes of the latency and the amplitude by rTMS were statistically insignificant.

George et al [1] applied rTMS to six depressed patients. They stimulated the left frontal cortex of the patients with rTMS daily for several minutes. Their depression scores improved significantly. Also, Kirkcaldie et al [2] also applied rTMS to electroconvulsive therapy (ECT).

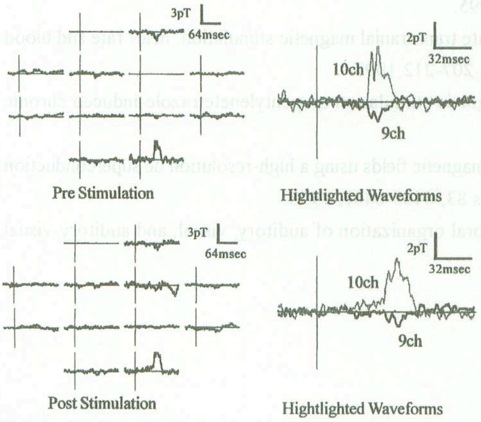

Fig. 10 Waveforms of magnetic fields pre and post stimulation in a rat. The upper indicates pre stimulation and the bottom indicates post stimulation. The right indicates highlighted waveforms. 4ch and 12ch of magnetic fields in pre stimulation and 12ch in the post stimulation were not measurable.

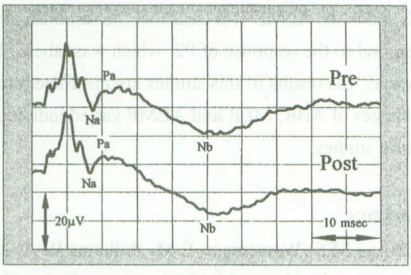

Fig.7 Waveforms of MLR pre and post stimulation in a rat.

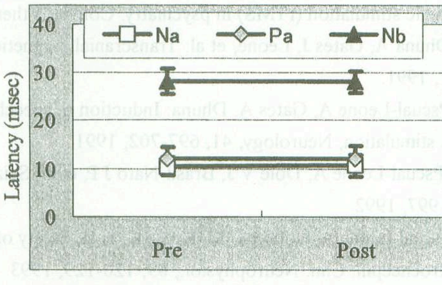

Fig. 8 Changes of the latencies of Na, Pa and Nb.

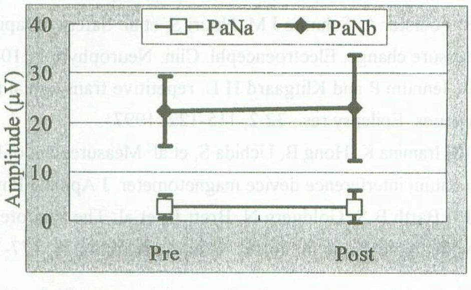

Fig. 9 Changes of the amplitudes in PaNa and PaNb.

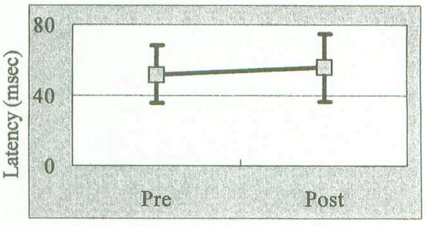

Fig. 11 Changes of the latencies of magnetic fields in the eight rats.

The safety aspects of repetitive magnetic stimulation have been investigated. Several papers reported that the rTMS induced epilepsy and speech arrest in normal volunteer[3-6]. Yamada et al [7] concluded that TMS did not influence epilepsy nor the spatial short memories of monkeys. Foerster et al [8] investigated the change in heart rate and blood pressure by rTMS in 13 normal volunteers. P Jennum et al [9] investigated the induction of convulsions in a acute stimulation group and the chronic stimulation group of rTMS in rats, which were administered penthleneterazole. In the group of rats receiving chronic RTMS some rats showed facial contractions, chewing or head movements during or immediately after the stimulations. None of the rats developed tonic or clonic seizures in relation to RTMS.

We observed that there were no change in the ABR and MLR parameters such as peak amplitudes and latencies by rTMS and in the AEMF. It is clear that the response of the AEMF appeared later then Nb of MLR. We suggest that these correspond to the response of P2, which was labeled by barth[12].

However, the results of this studies are insufficient to prove the safety of rTMS to the auditory nerve of rats, because the changes of ABR, MLR and AEMF varied individually, and widely. We will investigate these matters in more detail in future studies.

Reference

[1] George M S, Wassemann E M, Williams W A, et al: Daily repetitive transcranial magnetic stimulation (rTMS) improves mood in depression. Neuroreport, 23 2, 1853-1856, 1995.

[2] Kirkcaldie M, Pridmore S and Reid P: Bridging the skull: electroconvulsive therapy and repetitive transcranial magnetic stimulation (rTMS) in psychiatry. Convuuls ther. 13 2, 83-91, 1997.

[3] Dhuna A, Gates J, Leone, et al: Transcranial magnetic stimulation in patients with epilepsy. Neurology, 41, 1069-1071, 1991.

[4] Pscual-Leone A, Gates A, Dhuna: Induction of speech arrest and counting errors with rapid-rate transcranial magnetic stimulation, Neurology, 41, 697-702, 1991.

[5] Pscual-Leone A, Dole V J, Brasil-Nato J P, et al: Seizure induction and transcranial magnetic stimulation, Lancet, 339, 997, 1992.

[6] Pscual-Leone A, Houser C M, Reese K, et al: Safety of rapid transcranial magnetic stimulation in normal volunteers. Electroencephl. Clin. Neurophysiol., 89, 120-129, 1993.

[7] Yamada H, Tamaki T, Wakano, et al: Effect of transcranial magnetic stimulation on cerebral function in a monkey model, Electroencephl. Clin. Neurophysiol., 97, 140-144, 1995.

[8] Foerster A, Schmitz J M, Nouri S, et al: Safety of rapid rate transcranial magnetic stimulation: heart rate and blood pressure change, Electroencephl. Clin. Neurophysiol., 104 3, 207-212,1997.

[9] Jennum P and Klitgaard H L: repetitive transcranial magnetic stimulation on pentylenetetrazole-induced chronic seizures. Epilepsy res., 32 2, 115-122, 1997.

[10] Iramina K, Hong B, Uchida S, et al: Measurement of biomagnetic fields using a high-resolution dc superconduction quantum interference device magnetometer. J Applied Physics 83, 6465-6467, 1998.

[11] Barth B S, Goldgerg N, Brett B, et al: The spatiotemporal organization of auditory, visual, and auditory-visual evoked potential in rat cortex. Brain Research, 678, 177-190.

Combined Analysis of MEG and fMRI Using Minimum l1-norm Estimates

Uutela K.[1] and Ryymin, P.[2]
Brain Research Unit[1], Low Temperature Laboratory, Helsinki University of Technology, Finland;
Tampere University Hospital[2], Finland

Introduction

Magnetoencephalography (MEG) provides excellent temporal resolution to functional brain imagining. However, because the exact source locations can be obtained from MEG unambiguously only if the number of distinct sources or other constraints are known in advance, the interpretation of the results and combination with other functional imaging methods has been difficult.

Functional magnetic resonance images (fMRIs) provide good spatial resolution. However, because the hemodynamic response times that the method measures are of the order of several seconds, the estimation of the order and timing of the activations has been difficult.

In this article we present a method for combining the results of these two modalities to produce both spatially and temporally accurate estimates of the brain activity.

Methods

Sensitivity differences

Activity recorded with MEG and the hemodynamic responses measured with fMRI seem to be correlated with the synaptic activity [1],[2]. In this sense, the two methods are closer to each other than, for example, MEG and single cell recordings: the latter is mainly used to detect firing neurons while MEG and fMRI also detect subthreshold activity.

However, some other differences make the methods sensitive to different activations. The activation detected with MEG has to be spatially and temporally coherent, which is not required in fMRI recordings. Evoked response measurements are typical to MEG, and transient activity can be easily detected, while typical fMRI measurements involve sustained activation.

The sensitivity differences have to be taken into account in any combination method. Our method explains almost all the MEG results, but some active areas detected with fMRI are often missing from the results. Besides, strong MEG results can in some cases generate estimates with activity in areas that are not detected with fMRI.

Minimum l1-norm Estimate

The minimum norm estimates (MNEs) in general place no explicit constraints to the current distribution. Instead, the most plausible source distribution among the ones compatible with measurements is selected. Thus no parametric model is needed, but without external *a priori* information, the accuracy of the result is worse than with dipole models. The general format of the estimate is

$$\hat{\mathbf{q}} = \arg\min \|\mathbf{q}\|$$

subject to

$$\mathbf{G}\,\mathbf{q} \approx \mathbf{B}\,,$$

where **q**, **G**, and **B** are the primary current vector, gain matrix of the magnetometer, and measured results, respectively.

There are different versions of this type of approach depending on how the current vector is being minimized (the selection of the norm and possible weighting matrix) and what kind of errors are tolerated (the selection of the regularization method).

In the minimum *l1* norm estimate [3] the sum of the absolute currents is minimized. This leads to more focal source estimates than with the estimates using Euclidean (*l2*) norm, and the method can represent well the relatively small discrete source areas that are activated in typical sensory experiments.

With suitable regularization the minimum *l2*-norm estimate can be thought as a Bayesian estimate for the sources with Gaussian *a priori* distribution of the current [4]. Accordingly, the minimum *l1*-norm estimate is a Bayesian estimate with an exponential *a priori* distribution (Fig. 1).

©1999, Tohoku University Press
Recent Advances in Biomagnetism
T. Yoshimoto et al. (Eds)

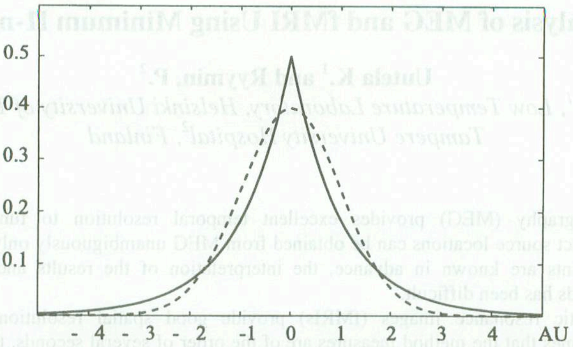

Fig. 1 *A priori* probability of minimum *l1*- (solid) and *l2*-norm (dashed) estimates.

Because different current distributions may produce similar magnetic fields, the inverse problem is ill-posed and sensitive to measurement errors. The singular value truncation is computationally efficient with *l1*-MNE. The idea of the method is to use only the most significant parts of the system matrix **G** as constraints. If the singular value decomposition of **G** is $\mathbf{U}\,\Lambda\,\mathbf{V}^t$, , the regularized version of constraints are

$$\Lambda_n \mathbf{V}^t = \mathbf{U}_n{}^t \mathbf{B},$$

where Λ_n includes the first *n* rows of Λ and $\mathbf{U}_n$ includes the first *n* columns of **U**. The optimal value for regularization parameter *n* depends on the signal-to-noise ratio of the measurements.

We compensated for the bias for too superficial sources by using a weighted norm [5],[6] where the weight of each element of **q** in minimization is proportional to the Euclidean norm of the corresponding row of matrix **G**.

The minimization problem can be efficiently solved using linear programming, if the current orientation is constrained in advance. An efficient way is to select for each source location the current orientation in a minimum *l2*-norm estimate.

Combination

The fMRI information was incorporated by using a weighted norm where the weighting factor was inversely proportional to the average fMRI activation near the source area [7]. The fMRI values were averaged using a bell-shaped weighting function (Fig. 2). The scaling of the norm (Fig. 3) allowed sources to exist also in places which were not active in fMRI and, on the other hand, assigned a minimum cost also to areas that were very active in fMRI.

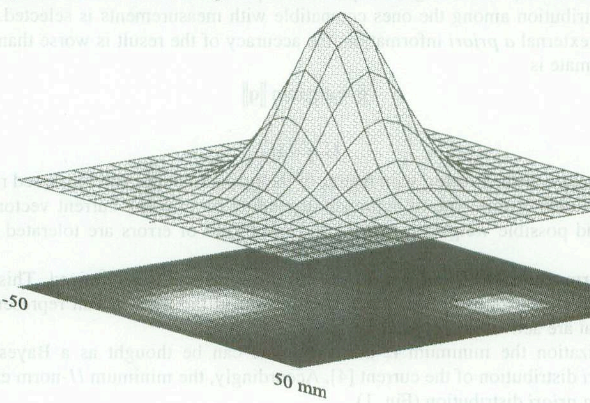

Fig. 2 Bell-shaped weighting function used in the calculation of average fMRI activity

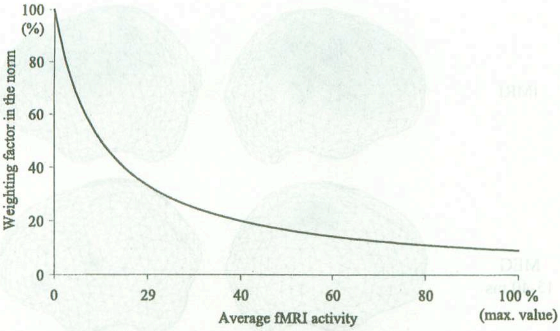

Fig. 3 Scaling of the weighting factor

Visualization

In order to visualize the results calculated in the 3-dimensional point set, the results are shown on a triangle mesh representing the surface of the brain The mesh was calculated from segmented anatomical MRIs [8]. Each 3-dimensional source location is projected along the radius of the sphere model to a triangle. The source strength at the 3-dimensional location is added to the activity of the vertices by weighting inversely proportionally to the distance to the vertices. The results are shown with interpolated color-coding on the triangle net.

Measurements

The method was applied to analysis of somatosensory MEG and fMRI measurements. In the fMRI measurement, the right palm of the subject was physically stimulated during two 30 s periods with 30 s rest before, after, and between the stimulation periods. The MRI data was measured with a 1.5 T GE Signa Horizon Echospeed every third second on 10 planes with 5 mm separation (Fig. 4).

In the MEG measurement, the right median nerve of the same subject was stimulated electrically with ISI 1,5 s [9]. The evoked response data was acquired using Neuromag-122™ and averaged.

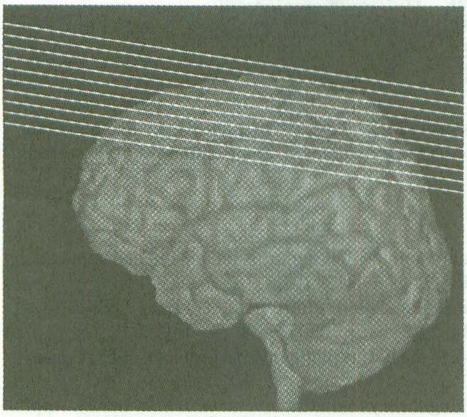

Fig. 4 fMR imaging planes

Table 1 fMR imaging parameters

Pulse sequence	Spin Echo EPI
TR/TE/NEX	3000ms/50ms/1
FOV	28 x 21 cm
Matrix	96 x 64
Slice thickness	5 mm

Results

The fMRI results (Fig. 5) show activation especially along the left central sulcus. The MEG results show activity mainly in the primary sensory cortex in the beginning, and later also bilaterally near secondary sensory cortices. The combination results show activity mainly in the vicinity of the areas detected by MEG alone, but especially in the period 100-150 ms the activity is focused closer to the secondary sensory cortices.

Discussion

If the combination results are compared with plain fMRI results, it is evident that the MEG information not only adds temporal information to the estimate, but also constrains the estimate to areas where the activity is temporally coherent. The images are simple and easier to interpret, but some areas are neglected. Compared with plain MEG results, the combination is rather similar, but the activity is more concentrated to the known sensory areas, because of the spatial information provided by fMRI.

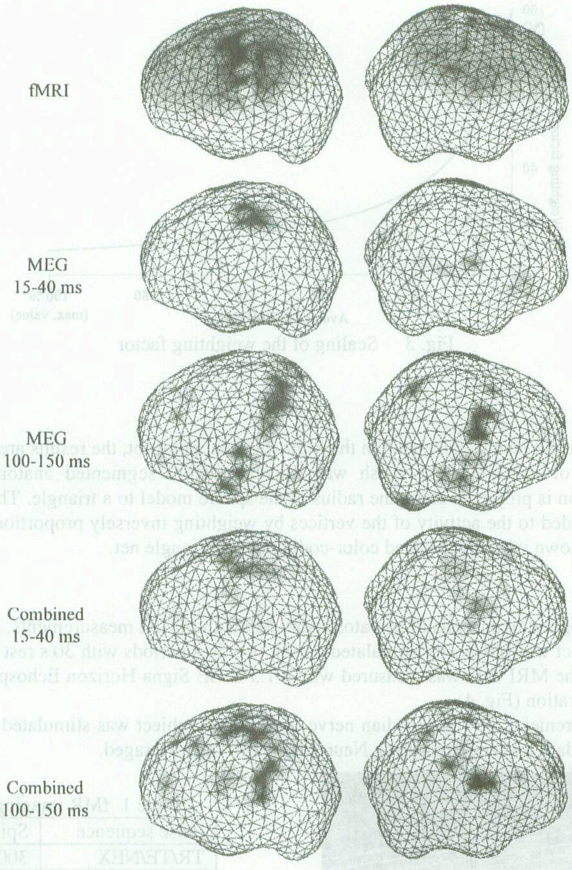

Fig. 5 fMRI *a priori* information (top row), estimates using MEG alone (rows 2 and 3), and combination results (rows 4 and 5). Activity is shown with darker color on the triangle mesh representing the brain surface.

References

[1] Hämäläinen M, Hari R, Ilmoniemi R, et al: Magnetoencephalography — theory, instrumentation, and applications to non-invasive studies of the working human brain. Rev. Mod. Phys.65:413–497, 1993

[2] Roland P and Widen L: Brain metabolism during physiological stimulation, Pfurtscheller G,Lopes da Silva F (eds.): Functional Brain Imaging. Hans Huber, 1988, pp 213–229

[3] Matsuura K and Okabe U: Selective minimum-norm solution of the biomagnetic inverse problem. IEEE Trans. Biomed. Eng. 42:608–615, 1995

[4] Foster M: An application of the Wiener-Kolmogorov smoothing theory to matrix inversion. J. Soc. Indust. Appl. Math. 9:387–392, 1961

[5] Clarke C, Ioannides A, and Bolton J: Localised and distributed source solutions for the biomagnetic inverse problem I, Williamson S, Hoke M, Stroink G, et al (eds.): Advances in biomagnetism. Plenum, 1989, pp. 587–590

[6] Köhler T, Wagner M, Fuchs M, et al: Depth normalization in MEG/EEG current density imaging, Conference Proceedings of the 18th Annual International Conference of the Engineering in Medicine and Biology Society of the IEEE, Amsterdam, 1996.

[7] Dale A, Halgren E, Lewine J:Spatio-temporal localization of cortical word repatition effects in a size judgement task using combined fMRI/MEG. NeuroImage 5:S592, 1997

[8] Seppä M and Hämäläinen M: Use of 3D MRI data for advanced modelling and visualization in MEG studies, NeuroImage 3:142, 1996

[9] Salenius S, Schnitzler A, Salmelin R, et al: Modulation of human rolandic rhythms during natural sensorimotor task. NeuroImage 5:221–228, 1997.

Localization of Somatosensory Cortex - MSI versus fMRI -

Wienbruch C[1], Scholz V H[2], Hauk O[1], Elbert T[1]

[1]*Fachgruppe Psychologie, Klinische Psychologie, Universität Konstanz, Germany*
[2]*Institut für Radiologische Diagnostik, Klinikum Großhadern, Ludwig-Maximilian University, München, Germany*

Introduction

The localization of the somatosensory cortex and in particular the Brodmann area (BA) 3b beneath other activated brain structures during sensory stimulation was compared using Magnetic Source Imaging (MSI) and functional Magnetic Resonance Imaging (fMRI). MSI is the localization of neuronal activity based on the magnetoencephalogram (MEG), fMRI uses the blood oxygenation level dependent (BOLD) method to detect hemodynamic changes due to neuronal activity. Depending on the underlying brain activity both methods can provide similar spatial resolution.

Methods

After informed written consent, three right-handed healthy volunteers (ages 24-26, mean age 25.3 ± 1.2; 3 M) participated in 12 activation studies performed during one imaging MR session and one MEG session. All subjects were drug-free and had no evidence of nervous system disease or injury.

MSI: Somatosensory stimulation was delivered separately to the second, third and fourth digit of both hands. The stimulation was a short, nonpainful superficial pressure stimulus delivered through a pneumatic device. 256 stimuli were applied with a repetition rate of 1 Hz. The interstimulus interval was randomly changed between 950 and 1050 ms. Magnes® 2500 WH was used to record somatosensory evoked magnetic fields. The signals were filtered between 1 and 200 Hz and digitized with a sampling frequency of 678 Hz. External noise was removed using online and offline noise reduction methods. After epochs with eye-artefacts had been removed the data were averaged and filtered with a 30 Hz lowpass Butterworth, filter (second order). For five channel-groups (left, left-central, central, right-central and right) equivalent current dipoles (ECD) were estimated. In a first step all dipole solutions were excluded if their goodness-of-fit (GOF) was smaller than 97%. The location medians of all remaining dipole solutions within 16 ms around RMS maximum of SI-activation were taken to be the best fitting dipole solution. Localization results were averaged across subjects.

fMRI: We conducted functional studies by applying noxious cold or warm stimuli to the fingertips of subjects. A Peltier thermode integrated in a thermal stimulation system (TSA) was used for noxious thermal stimulation. The Peltier thermode was regulated and controlled by a PC (Pentium). For heat stimulation, the thermode warmed up from 22ºC to 49ºC in 2 s and provided stimulation for a period of 20 s. For cold stimulation, the thermode cooled down from 22ºC to 8ºC in 2 s and provided stimulation for a period lasting 20 s. To define each subject's level of pain sensation, each volunteer was individually tested before the functional sessions outside the magnet room. The final functional noxious thermal stimulation used in data analysis was performed 1ºC below the noxious level in order to avoid dermal injuries. This is equivalent to 8 on a pain scale of 12. We used a visual pain scale to determine the level of the applied pain. In all studies a permanent thermal sensory stimulation of 22ºC was used as baseline. The noxious cold or warm stimuli were applied to the fingertips of digits D2, D3, and D4 of either the right or left hand in each study. Each noxious cold or hot stimulation was repeated at least three times in one session. In all subjects the noxious warm stimulus was applied first to the right hand, then to the left hand followed by the noxious cold stimulus which was applied in the same manner.

All MRI measurements were performed on a 1.5 Tesla MR whole body scanner (MAGNETOM Vision, Siemens). The MR scanner was equipped with a three-axis standard gradient coil with a maximum gradient field strength of 25 mT/m and with an additional resonance system (EPI–Booster), which can sinusoidally switch the gradients from 0 to 25mT/m in 300 µs.

After a localization measurement, a MAP shim [1] was performed over the entire brain. The shim procedure was repeated until a field homogeneity less than 15 full-width half maximum (FWHM) was reached. For the functional studies, an EPI sequence was used based on the FID principle. The parameters for the FID sequence using the EPI booster were as follows: TR=0.8 s, TE=54 ms, FL=90º, slice thickness=5 mm, FOV=280 mm, matrix=128x128, pixel bandwidth=1450 Hz. The 10 to 14 slices were collected in a pseudo-oblique axial orientation including the somatosensory cortex down to the thalamus and parallel to the anterior commissure - posterior commissure line (ACPC coordinate system). For all studies, a circular polarized head coil with a diameter of 25 cm was used (Siemens standard head coil). Twenty-eight images of each slice were collected over a 70-s period, which included one thermal

©1999, Tohoku University Press
Recent Advances in Biomagnetism
T. Yoshimoto et al. (Eds)

stimulation epoch of 20 s alternated with a baseline of 20 s before and after the stimulation. Four dummy scans were acquired before the first baseline period in order to reach an equilibrium.

For exact anatomical localization, high resolution T1-weighted images were acquired in all volunteers. An MPRAGE sequence was used with the following parameters: TR = 11.4 ms, TE = 4.4 ms, FL = 8°, slice thickness = 160 mm, eff. thickness = 2.5 mm, FOV = 270 mm, Matrix = 256x256 and a sagittal orientation. This three-dimensional data set was reconstructed according to the orientation of the slices of the functional data. By localizing the magnetic field axis, an exact overlay of the functional and anatomical data was possible.

The fMRI studies were postprocessed on a Sun sparc20 workstation using the acquired functional neuroimaging (AFNI) software written at the Medical College of Wisconsin [2]. All functional data were corrected for motion using the additional motion correction plug-in program of two-dimensional motion correction [3]. Activation maps were generated by pixelwise cross-correlation calculation between the time series data and an ideal reference function corresponding to the paradigm timing of the study. The first four images were excluded from further statistical analyses to account for system equilibration. Each data set from corresponding studies of one subject were first postprocessed separately, then compared in terms of location and volume of functional activation. If there was a match between functional activity, then the functional data were averaged. The paradigm timing of the stimulus was cross-correlated with the acquired slices of the specific brain regions using the $p < 0.001$ level of significance. Then, all activated pixels within a particular region were counted and compared to other brain regions, both inter- and intrahemispherically. The color-coded maps of the statistically significant pixels were localized by the position parameters in the magnetic field and matched to the MPRAGE-based anatomical data set. The MPRAGE-data were corrected in size and shape to fit the functional EPI data. Talairach coordinates and ACPC coordinates were used to determine the exact anatomical position of the activated areas.

The quality of the noxious thermal stimulation was estimated by the volume of functional activation of the contralateral somatosensory cortex. If there was no corresponding functional activation, then this measurement was excluded from further analyses. The activated areas were analyzed according to location based on the Talairach coordinates and Brodmann's areas, volumes of activated pixels, mean of signal changes, standard deviation, and time course. The ACPC coordinates of the main functional activity gain from fMRI was compared to the location of the ECD estimated for the main activity of the MEG data.

Results

For comparison all locations were estimated in the ACPC coordinate system. MSI source localization results for subject NW (left hand's digit 3 (LD3) and right hand's digit 3 (RD3)) are shown in Fig.1. The estimated ECD locations for all subjects were found within the postcentral gyrus (BA 3b).

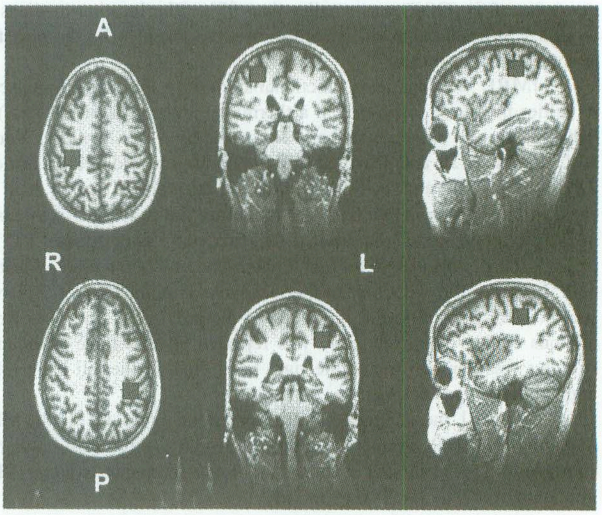

Fig 1: MSI – location of left and right digit 3 (LD3, RD3) of subject NW (in ACPC-coordinates L=36, P=36, S=38, R=36, P=33, S=45). The GOF was 98,6% for LD3 and 98,3% for RD3. Single equivalent current dipoles have been estimated for different channel groups separately (left; left-central; central; right-central; right). The best fitting ECD, indicated by the filled square, has been projected onto the corresponding MRI sagittal, coronal, and axial slices.

FMRI for subject NW left hand thermal stimulation (Fig. 2) demonstrates that after applying a sensory warm stimulation to the fingertips, positive functional activity was observed in the contralateral somatosensory cortex. Functional activity was detected in the ipsilateral hemisphere as well.

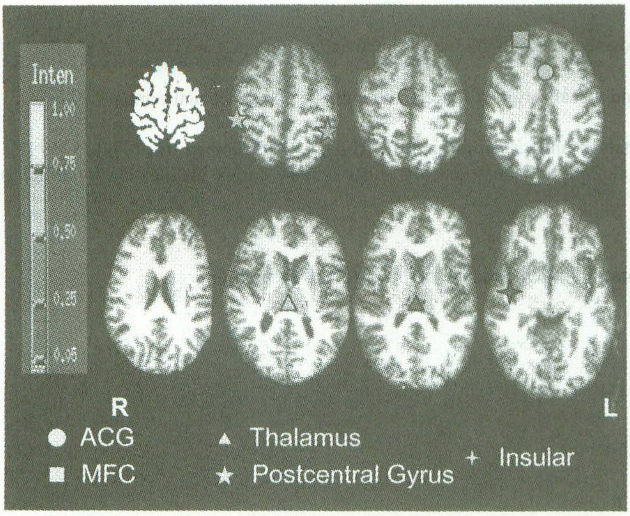

Fig 2: After applying a noxious warm stimulation to the left hand fingertips of D2-D4, positive functional activity was observed in the contralateral and ipsilateral somatosensory cortex (SI,),the anterior cingulate gyrus (acg) (BA24 and BA32), the insular cortex (in the anterior and posterior part), in the medial frontal gyrus, mfg, (BA 46). Thalamic functional activation in the dorsal medial nuclei was observed bilaterally. As a general rule, noxious heat or cold stimulation of the left-hand fingertips in right-handed subjects caused significant functional activation not only in the contralateral right hemisphere but also in the ipsilateral left hemisphere.

In addition in the fMRI studies the anterior cingulate gyrus, acg, (BA24 and BA32) showed mainly bilateral functional activation.. The insular cortex showed consistently bilateral activation. There was no significant difference between the amount of functionally activated pixels for the contra- or ipsilateral hemispheres. Functional activation was primarily located in the anterior and posterior part of the insula. Functional activation in the frontal cortex was mostly observed in the medial frontal gyrus, mfg, (BA46), which showed bilateral activation.

MSI localization revealed similar results for the localization of SI. Between the fMRI based location and the MSI-based location an euklidean distance of 13,4mm (left hand) and 16,8mm (right hand) was found (Tab.1) with the main difference in posterior direction (L:10.2mm, R:16.7mm; Mean 13.5 mm).

Method – Stim. Hand	Left/Right [mm]	Posterior [mm]	Superior [mm]
MSI; right	L=37,8 ± 4,2	P=24,8 ± 6,2	S=48,5 ± 3,4
fMRI; right	L=41,7 ± 6,0	P=35,0 ± 3,6	S=56,3 ± 3,1
MSI – fMRI	-3,9	-10,2	-7,8
MSI; left	R=36,0 ± 3,8	P=25,3 ± 9,3	S=53,5 ± 6,2
fMRI; left	R=35,7 ± 3,8	P=42,0 ± 5,6	S=55,0 ± 3,5
MSI – fMRI	0,3	-16,7	-1,5

Tab1: Grand Average accross subjects (and fingers D2-D4 in case of MSI). Euklidean distance between MSI and fMRI locations of SI: L=13,4mm R=16,8 mm

Conclusion

Within the somatosensory cortex Stippich et al. [3] found mean distances between MSI and fMRI of 10.1mm in 6 subjects. This is in the order of magnitude of our results (13.5mm). The euklidean distance can be explained mainly by the posterior differences. Due to the type of stimulation MSI localizations are based mainly on the afferent input into the wall of the central sulcus (BA3b). With fMRI the afferent input to area BA3b is localized as well but the texture and shape of the thermode may lead to afferent input into area BA1 and BA2, which are posterior to BA3b. This could be the reason for the observed differences in posterior direction.

Our study demonstrates that both, fMRI and MSI, can be used to localize the postcentral gyrus with the same accuracy. The question if activity in areas BA1 and BA2 lead to the observed difference in posterior coordinates remains open.

References

[1] Shen J, Rycyna RE, Rothman DL, Improvements on an in vivo automatic shimming method [FASTERMAP]. *Magn Reson Med* **38**, 834-839 (1997).

[2] Cox RW, AFNI: software for analysis and visualization of functional magnetic resonance neuroimages. *Comput Biomed Res* **29**, 162-173 (1996).

[3] Cox RW, Hyde JS, Software tools for analysis and visualization of fMRI data. *NMR Biomed* **10**, 171-178 (1997).

[4] Stippich C, Freitag P, Kassubek J, et al: Motor, Somatosensory and Auditory cortex localization by fMRI and MEG. *NeuroReport* **9**, 1953-1957, 1998

Research was supported by the Deutsche Forschungsgemeinschaft and the Volkswagenstiftung

Resolution Enhanced Echo Planar Imaging at 3 Tesla

Windischberger C.[1], Beisteiner R.[2], Edward V.[2],
Kaindl T.[2], Erdler M.[2], Moser E.[1,3]

AG NMR[1], Institute for Medical Physics, University of Vienna, Austria
Department of Neurology[2], University of Vienna, Austria
MR-Einrichtung[3], General Hospital, University of Vienna, Austria

Introduction

Exact localization of activated areas in the human cortex is essential for functional brain studies. Common pulse sequences allow either a short repetition time with low spatial resolution or high matrix sizes with poor temporal resolution. Single shot EPI with a matrix size over 128 by 128 pixel could be a feasible method to combine both requirements. Additionally, increase of matrix size can significantly reduce image distortions resulting from B_0 inhomogeneites [1]. However, special care has to be taken to minimize loss of spatial resolution due to T_2^*-relaxation processes during the acquisition period.

Materials and Methods

Test objects with grid distances of 1 pixel have been set up for 128^2, 192^2, 256^2 matrices (fig. 1). Computational simulations for matrix sizes of 128^2, 192^2 and 256^2 describing the acquisition of k-space with decaying signal, programmed in IDL (Research Systems, Inc., USA), were used to study the behavior of spatial resolution with varying imaging parameters. T_2^* for white and gray matter have been obtained from [2]. Two different acquisition schemes have been examined: Either "classic" k-space sampling or, in order to increase signal/noise, central k-space line acquisition shifted 25% to shorter echo time. Calculations have been performed for 100kHz as well as 200kHz readout bandwidth.

Five healthy subjects (age: 18-30 yrs.) were studied. All experiments have been performed at 3 Tesla on a BRUKER Medspec DBX 30/80 (Ettlingen, Germany) equipped with an actively-shielded whole body gradient coil (BG-A55: 20mT/m in less than 300µs) and a bird cage head resonator. For this study a (zero and first order) phase-corrected blipped single-shot EPI sequence with the following parameters has been used:

Matrix size:	128^2, 192^2, 256^2
Readout bandwidth (RBW):	100-200kHz
Repetition time:	3s
Echo time (effective):	43-163ms
Flip angle:	Ernst angle
Slice thickness:	4mm

Linear and second order shimming has been performed. For reduction of motion artifacts a head shaped pillow and a belt around the front head were used to comfortably fix the subject's head.

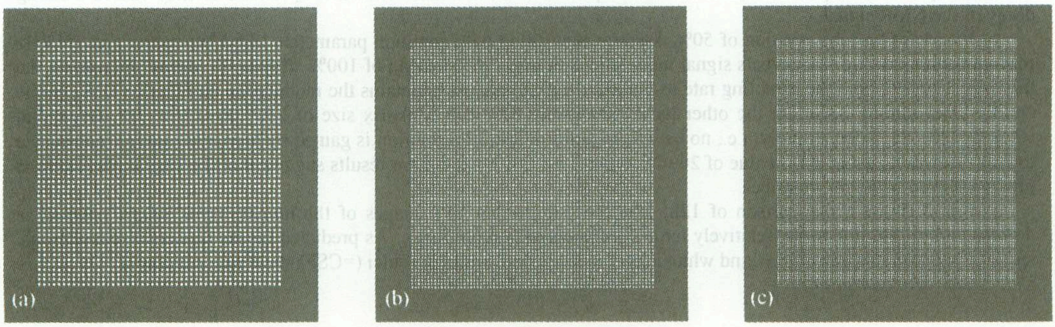

Fig. 1: Test objects used for simulation. Matrix sizes are (a) 128^2, (b) 192^2 and (c) 256^2

©1999, Tohoku University Press
Recent Advances in Biomagnetism
T. Yoshimoto et al. (Eds)

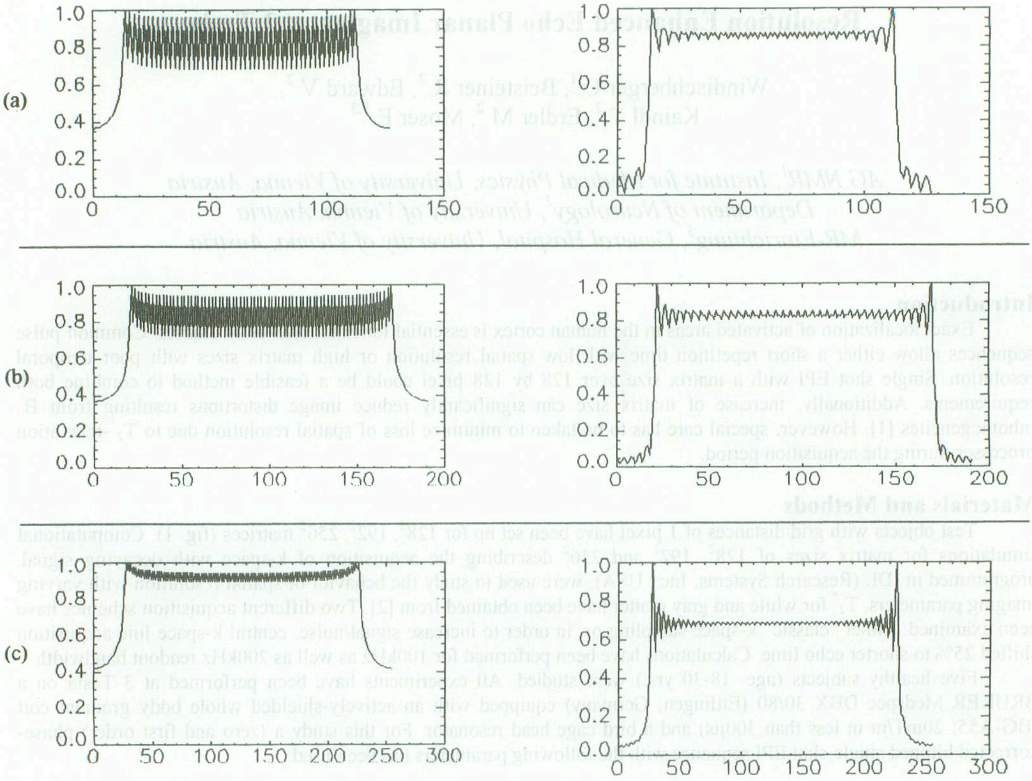

Fig. 2: Line profiles of simulation results. (a) 128^2-matrix, RBW=100kHz, (b) 192^2-matrix, RBW=200kHz and (c) 256^2-matrix, RBW=200kHz. Echo position 50% (left) and 25% (right).

Results and Discussion

Fig. 2 shows the results of the computational simulations. All calculations have been performed using a T_2^*-value of 42ms which is typical for gray and white matter [2]. In general, echo shifting to 25% results in a loss of resolution by a factor of 2. This is due to the fact that the highest spatial frequencies, which are represented in the outer areas of k-space, are acquired at the end of the acquisition, i.e., at a time when the T_2^* effects already caused a strong decay of the NMR signal.

In case of an echo position of 50%, k-space acquisition with common parameters like 128^2-matrix and 100kHz readout bandwidth (fig. 2a) reveals signal modulations of only 26% instead of 100% without T_2^* decay. Increasing the matrix size to 192^2 and the sampling rate to 200kHz (fig. 2b) almost maintains the modulation amplitude (21%), while cutting pixel size by 33%. On the other hand, single-shot EPI with a matrix size of 256^2 pixel (fig. 2c) shows that resolution has degraded strongly, i.e., no benefit in terms of spatial resolution is gained by increasing image matrix size to 256^2. However, using a T_2^*-value of 200ms (typical for CSF), simulation results suggest that the spatial resolution is preserved even with 256^2-matrices.

Fig. 3 shows a comparison of 128^2 and 256^2 single-shot EPI images of the human brain. Image contrast is dominated by CSF, due to the relatively long T_2^* compared to brain tissue. As predicted by the numerical simulations, spatial resolution in areas of gray and white matter is decreased, while the sulci (=CSF) show fine structures.

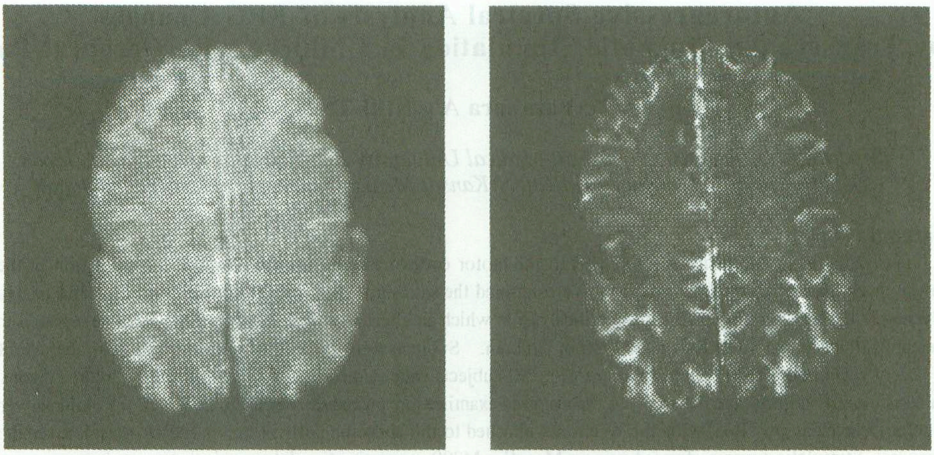

Fig. 3: Transversal single-shot gradient-echo EPI-images of the human brain. (a) 128^2-matrix, RBW=100kHz, 163ms acquisition time, (b) 256^2-matrix, RBW=200kHz, 327ms acquisition time. Note the contrast change due to prolonged imaging time. In areas of CSF ($T_2^* > 200$ms, bright) spatial resolution is conserved, while brain tissue resolution ($T_2^* = 42$ms) suffers from strong signal decay

Conclusion

In this work we demonstrate that increasing spatial resolution in single-shot EPI has some advantages when local field inhomogenities are present, which are even more significant at higher field strengths (e.g., 3 T). There is also the advantage of reduced geometric distortions. By adjusting the RBW proportionally to the matrix size, one is left with the same modulation amplitude, but with decreased SNR. However, high resolution single-shot EPI provides a powerful tool to gain maximum spatial resolution in a minimum amount of time. Our results suggest an optimum matrix size of 192^2 for functional MRI measurements. Higher matrix sizes do not increase "real" spatial resolution, due to T_2^* signal decay in gray and white matter. Nevertheless, 256^2 single-shot EPI may be used as a reference for functional activation maps, because it shows decreased but similar geometric distortions as the functional images and improves anatomical localization.

References

[1] Reichenbach J. et al: JMRI 1997, 266
[2] Wansapura JP et al: Proceedings ISMRM 1997, p. 685

Acknowledgements

This work has been supported by the „Fonds zur Förderung der wissenschaftlichen Forschung" (FWF grant P12451-Med) and the „Ludwig-Boltzmann-Institut für radiologische Tumordiagnostik".

Autoregressive Spectral Analysis of EEG Changes by Transcranial Magnetic Stimulation in Children with Cerebral Palsy

Yasuhara A[1], Niki T[2]

Department of Pediatrics[1], Kansai Medical University Kori Hospital, Neyagawa, Japan;
Department of Laboratory Medicine[2], Kansai Medical University, Moriguchi, Japan

Abstract

Transcranial magnetic stimulation (TMS) to the motor cortex has been used to examine the function of the motor pathway in children with cerebral palsy. We examined the safety of TMS using autoregressive spectral analysis (AR analysis). In this study, we clarified the critical age at which an effect was recognized by TMS, and we assessed the range of cerebral influence that TMS had on the EEG in children. Subjects were 20 children with cerebral palsy, between the ages of 6 and 14 years, and 10 adults used as a control. All subjects were studied in a fully awake state. Informed consent was obtained from all subjects and parents. A standardized examination procedure was used, in which the children were lying supine, as relaxed as possible, with the electrodes attached to the abductor pollicis brevis (APB) muscle over the thenar eminence. Stimulation was performed using a Magstim M200 magnetic stimulator producing a maximum magnetic field of 2.0 tesla with an 8-shaped stimulator coil. We recorded the EEG before and after TMS, and analyzed EEG data using AR analysis. Magnetic stimulation motor-evoked potential (MEP) was recorded from APB. Damping Frequency (FD) of AR analysis increased temporarily after TMS ($p<0.05$). The change in FD did not continue more than 5 minutes. This change was seen on the lesion only under stimulation by topographical analysis. No change was found in other parameters on AR analysis. Changes of FD after TMS were observed only in children under 12. Because TMS only influences the FD of the EEG temporarily, TMS can be safely performed on children with cerebral palsy.

Introduction

Muscle discharges recorded by transcranial magnetic stimulation (TMS) of the motor cortex have been used to examine the motor function of adults with motor disorders. Previous publications have addressed the safety of TMS by studying changes in the EEG, the vascular system, and the neural morphology [1-7]. Previous studies have described the motor responses evoked by TMS in normal children and those evoked in children with motor disturbances [8-12]. We studied the safety of TMS on children, and observed temporary changes in the EEG frequency in subjects placed under TMS [13].

In this study, we clarified the critical age at which this effect of TMS was recognized, and we assessed the range of cerebral influence of TMS on the EEG in children.

Subjects and Methods

Subjects were 20 children with cerebral palsy, between the ages of 6 and 14 years, and 10 adults used as a control. All patients who had spastic diplegia showed normal EEG and normal response of upper extremities to TMS. All subjects were studied in a fully awake state. Informed consent was obtained from all subjects and parents.

We used a standardized examination procedure, in which the children were lying supine, as relaxed as possible, with the electrodes attached bilaterally to the abductor pollicis brevis (APB) muscle over the thenar eminence.

We stimulated the cerebral cortex by single-pulse using the Magstim (M200) magnetic stimulator, producing a maximum magnetic field of 2.0 tesla with an 8-shaped stimulator coil. Stimulation was performed over the scalp according to the Nihon standard technique, applying 50~90% output capacity of the Magstim. We limited the number of stimuli above the motor threshold to fewer than 20.

We recorded 19 channels EEG according to the international 10-20 electrode standard, before and just after TMS, and again at 5 and 15 minutes after TMS. All channels were digitized at 200 Hz and stored on magnetic disk backup. EEGs were reviewed and artifact-free segments 10 seconds long were selected for autoregressive (AR) power spectral analysis [14]. We evaluated EEG changes before and after TMS by visual assessment.

We also analyzed the EEG by autoregressive (AR) power spectral analysis [14]. The AR power spectral analyses were decomposed into first and second order elementary processes. The EEG characteristics of these rhythms were assessed in terms of the damping frequency (FD), the resonance frequency (FR), the percent power of AR power spectrum (P%), the mutual information amount (I), and the damping coefficient (ZETA) [14].

Results

MEP was recorded from APB in all patients with spastic diplegia. The mean latency of MEP was 20.6 ± 1.86msec, n=20.

©1999, Tohoku University Press
Recent Advances in Biomagnetism
T. Yoshimoto et al. (Eds)

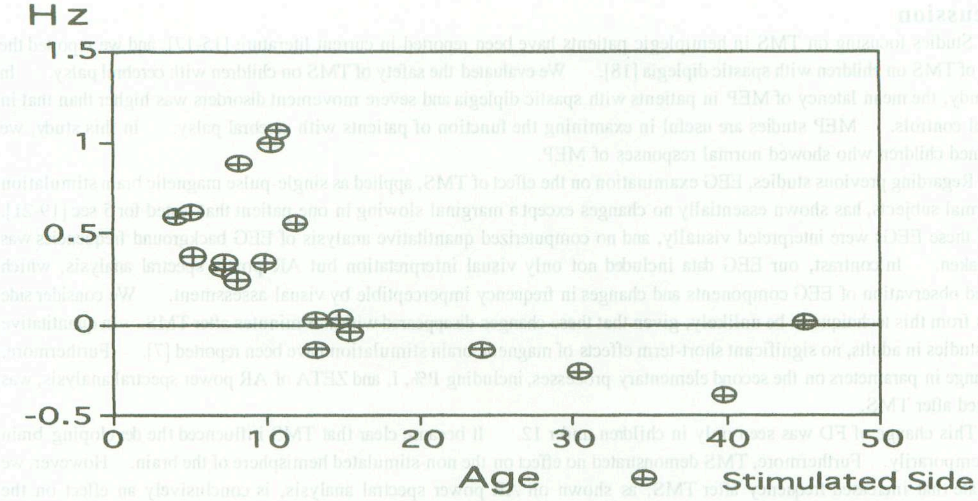

Fig. 1 Comparison of changes of FD and age. FD after TMS were observed only in children under 12.

Visual assessment of all EEGs obtained during the 4 experimental periods was performed blinded, without knowledge of clinical history. There were no changes observed by visual assessment in the EEG before and after TMS.

The results of AR power spectral analysis showed that the peak power frequency is increased after TMS. The second order elementary processes, damping frequency (FD), increased significantly in the stimulated hemisphere after TMS. Changes of FD after TMS were observed in children under 12 (Fig. 1). These changes had disappeared at 5 minutes after TMS. This change was only seen on the region under stimulation by topographical analysis of FD, and no change after TMS was seen on the contralateral side, in the non-stimulated hemisphere (Fig. 2).

There was no change of P%, I, or ZETA of AR power spectrum after TMS.

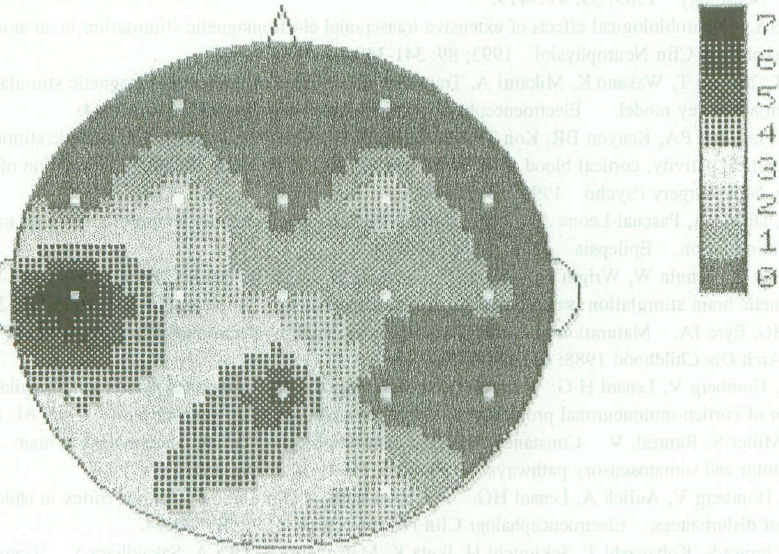

Fig. 2 The topographical analysis of FD changes. Red indicates quickness, and blue indicates slowness. This change was seen only under the stimulation of topographical analysis, and no change after TMS was seen on the contralateral side, in the non-stimulated hemisphere.

Discussion

Studies focusing on TMS in hemiplegic patients have been reported in current literature [15-17], and we reported the effect of TMS on children with spastic diplegia [18]. We evaluated the safety of TMS on children with cerebral palsy. In our study, the mean latency of MEP in patients with spastic diplegia and severe movement disorders was higher than that in normal controls. MEP studies are useful in examining the function of patients with cerebral palsy. In this study, we examined children who showed normal responses of MEP.

Regarding previous studies, EEG examination on the effect of TMS, applied as single-pulse magnetic brain stimulation in normal subjects, has shown essentially no changes except a marginal slowing in one patient that lasted for 5 sec [19-21]. All of these EEGs were interpreted visually, and no computerized quantitative analysis of EEG background frequencies was undertaken. In contrast, our EEG data included not only visual interpretation but AR power spectral analysis, which allowed observation of EEG components and changes in frequency imperceptible by visual assessment. We consider side effects from this technique to be unlikely, given that these changes disappeared within 5 minutes after TMS. In quantitative EEG studies in adults, no significant short-term effects of magnetic brain stimulation have been reported [7]. Furthermore, no change in parameters on the second elementary processes, including P%, I, and ZETA of AR power spectral analysis, was observed after TMS.

This change of FD was seen only in children under 12. It became clear that TMS influenced the developing brain only temporarily. Furthermore, TMS demonstrated no effect on the non-stimulated hemisphere of the brain. However, we speculate that increased frequency after TMS, as shown on AR power spectral analysis, is conclusively an effect on the developing brain by TMS, given its direct temporal association, and its rapid declension following cessation. The effect of single-pulse TMS on the developmental brain is transient and thus poses no danger with use in children.

Acknowledgment

This study was supported by a Grant-in-Aid for Scientific Research (06670841) from the Ministry of Education, Science and Culture of Japan, the Research Grant (9B-4) for Nervous and Mental Disorders from the Ministry of Health and Welfare, and the Mami Mizutani Foundation

References

[1] Agnew WF, McCreery DB. Considerations for safety in the use of extracranial stimulation for motor evoked potentials. Neurosurgery 1987; 20: 143-147.

[2] Bridgers SL, Delaney RC. Transcranial magnetic stimulation: An assessment of cognitive and other cerebral effects. Neurology 1989; 39: 417-419.

[3] Counter SA. Neurobiological effects of extensive transcranial electromagnetic stimulation in an animal model. Electroencephalogr Clin Neurophysiol 1993; 89: 341-348.

[4] Yamada T, Tamaki T, Wakano K, Mikami A, Transfeldt EE. Effect of transcranial magnetic stimulation on cerebral function in a monkey model. Electroencephalogr Clin Neurophisiol 1995; 97: 140-144.

[5] Eyre JA, Flecknell PA, Kenyon BR, Koh THHG, Miller S. Acute effects of electromagnetic stimulation of the brain on cortical activity, cortical blood flow, blood pressure and heart rate in the cat: an evaluation of safety. J Neurology Neurosurgery Psycho 1990; 53: 507-513.

[6] Gates JR, Dhuna A, Pascual-Leone A. Lack of pathologic changes in human temporal lobes after transcranial magnetic stimulation. Epilepsia 33; 504-508: 1992.

[7] Chokroverty S, Hennin W, Wrigth D, Walczak T, Goldberg J, Burger R, Belsh J, Patel B, Flynn D, Shah S, Mero R. Magnetic brain stimulation: safety studies. Electroencephalogr Clin Neurophisiol 1995; 97: 36-42.

[8] Koh THHG, Eyre JA. Maturation of corticospinal tracts assessed by electromagnetic stimulation of the motor cortex. Arch Dis Childhood 1988; 63: 1347-1352.

[9] Muller K, Homberg V, Lenard H-G. Magnetic stimulation of motor cortex and nerve roots in children: maturation of cortico-motoneuronal projections. Electroencephalogr Clin Neurophysiol 1991; 81: 63-70.

[10] Eyre JA, Miller S, Ramesh V. Constancy of central conduction delays during development in man: investigation of motor and somatosensory pathways. J Physiol 1991; 434: 441-452.

[11] Muller K, Homberg V, Aulich A, Lenard HG. Magnetoelectrical stimulation of motor cortex in children with motor disturbances. Electroencephalogr Clin Neurophysiol 1992; 85: 86-94.

[12] Nezu A, Kimura S, Kobayashi T, Sekiguchi H, Ikuta K, Matsuyama S, Oka A, Sakakihara Y. Transcranial magnetic stimulation in an adrenoleukodystrophy patient. Brain Dev 1996;18: 327-329.

[13] Yasuhara A, Niki T, Ochi A. Developmental Changes of Motor Evoked Potentials and Changes in Electroencephalography by Transcranial Magnetic Stimulation in Children. Jpn J EEG EMG 1998; 26: in press.

[14] Sato K, Ono K, Chiba G, Fukata K. Component activities in the autoregressive activity of physiological systems.

Intern J Neuroscience 1977; 7: 239-249.

[15] Carr, LJ, Harrison LM, Evans AL, Stephens JA. Patterns of central motor reorganization in hemiplegic cerebral palsy. Brain 1993; 116: 1223-1247.

[16] Farmer SF, Harrison LM, Ingram DA, Stephens JA. Plasticity of central motor pathways in children with hemiplegic cerebral palsy. Neurology 1991; 41: 1505-1510.

[17] Maegaki Y, Maeoka Y, Ishii S, Shiota M, Takeuchi A, Yoshino K, Takeshita K. Mechanisms of central motor reorganization in pediatric hemiplegic patients. Neuropediatrics 1997; 28: 168-174.

[18] Yasuhara A, Niki T, Ochi A. Changes in EEG after Transcranial Magnetic Stimulation in Children with Cerebral Palsy. IEPS Proceeding 1998.

[19] Bridgers SL, Delaney RC. Transcranial magnetic stimulation: An assessment of cognitive and other cerebral effects. Neurology 1989; 39: 417-419.

[20] Krain L, Kimura J, Yamada T, Cadwell J, Sakamaki S. Consequences of cortical magnetoelectric stimulation. In: S. Chokroverty (Ed.), Magnetic Stimulation in Clinical Neurophysiology. Butterworth, Boston, MA, 1990, 157-163.

[21] Levy WJ, Oro J, Tucker D, Haghighi S. Safety studies of electrical and magnetic stimulation for the production of motor evoked potentials. In: S. Chokroverty (Ed.), Magnetic Stimulation in Clinical Neurophysiology. Butterworth, Boston, MA, 1990, 165-172.

Dependence on an orientation of magnetic coil for the distributions of induced electric field in an inhomogeneous medium

Yunokuchi, K[1], Kato, R[1], Yoshida, H[1], Tamari, Y[2], Saito, M[3]

[1]The University of Kagoshima, Kagoshima, Japan
[2]Kagoshima National College of Technology, Kagoshima, Japan
[3]Tokyo Denki University, Tokyo, Japan

Introduction

Many researchers are now interested in the transcranial magnetic stimulation[2],[3],[4],[5]. It is non-invasive and free from pain in the treatment method, compared to the conventional therapy[1]. Recent studies shows that the transcranial magnetic stimulation tends to be applied to the clinical diagnosis, such as the examination of the brain nerve diseases. The figure-of-8 coil and double cone coil are widely used to achieve the focal stimulation. Some reports say that the two dimentional spatial resolution in magnetic stimulation improves[6],[7],[8].

It is difficult to locate the point of stimulation in an inhomogeneous medium accurately [2],[4],[11]. Focality of stimulation and mechanism of nerve excitation have not been clear in spite of the great efforts of many medical researchers. The induced eddy current distributes in the living tissue, according to the inhomogeneous tissue and complexes structure of the body[9],[11]. In displaying the induced currents, we use a flow arrows[2],[9],[10]. When the display is in the form of arrows, the arrows are always equally spaced, and the current density is indicated by the length of each arrow[2]. In this paper, we measured spatial distributions of currents induced in an inhomogeneous medium model. We also measured the distributions of induced eddy currents by the boundary between media with different conductivity.

Methods

A. *An experimental set-up*

The induced eddy current or induced electric field is measured with a probe composed of extremely thin coaxial cable[6]. An end-part of the cable is used as the electrode. The outer conductor of the cable is connected to the ground. The electrode parts of cable are both plated by platinum black in order to reduce the electrode impedance. The cable is connected to the differential amplifier. We used a magnetic stimulator, Magstim Model 200, which is widely used in clinical fields.

B. *Experimental procedure*

1)*Distributions of induced electric field in a cranial model*

A human head is a inhomogeneous conductor, which consists of skull, dura matter, brain, and liquor cerebrospinal. When magnetic stimulation is performed to the brain, induced currents flows spread over the brain and its distribution may be complicated by many holes at the skull. It is known that a property of nerve excitation depends on the orientation of induced current[11],[12]. Fig.1 shows the measuring system of the induced eddy current in the cranial model. We use the figure-of-8 coil or the double cone coil. Both the skull and the cover are made of plastic and the conductor are filled with saline solution(0.9%). We placed the center of intersection at the coil wings to an inion of the head model. Fig.2 shows the location of measuring points. An amplitude and direction of induced electric field were measured at each measuring point.

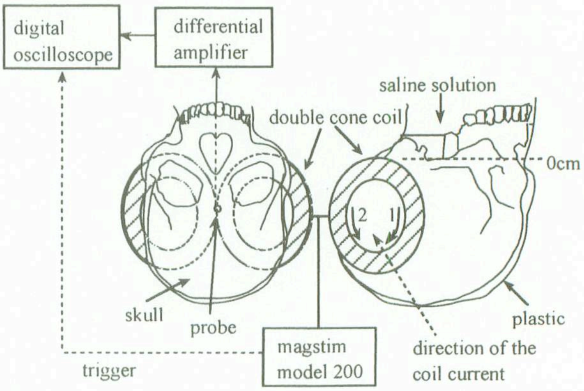

Fig.1 The measuring system of induced electric field.

2)*Distributions of induced electric field in an inhomogeneous conductor*

©1999, Tohoku University Press
Recent Advances in Biomagnetism
T. Yoshimoto et al. (Eds)

A rectangular prism conductor with a base (7 cm x 27 cm) and height of 7 cm made of plastic are filled with saline solution in height of 6 cm. Two types of agar-agars with different concentration are prepared and each of them is placed in the saline tank. We measured the distributions of induced electric field on the two sides of agar-agar and their extension lines shown in Fig.3. One line is perpendicular to the surface of the coils, above the intersection of the two coils. The other is a top horizontal line of agar-agar. Fig.3 shows the experimentary system of the inhomogeneous tank model.We defined the coil location as (I) or (ii).

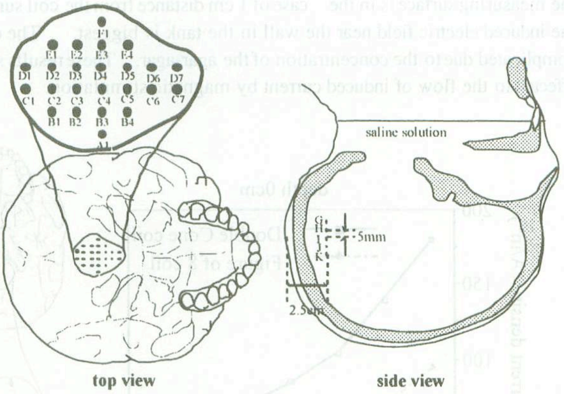

Fig.2 The measuring points of induced electric field.

Results

1)*Distributions of induced electric field in a cranial model*

When the cranial model is exposed the pulsed magnetic field, a high induced eddy current is confirmed in the foramen magnum. Fig.4 shows the current distributions in the cranial model using the double cone coil. The current density at opstion is approximately 2.2 times higher than that of the point o in Fig.4. The hole which exists at the lower part of the skull, that is foramen magnum, affects to the current distribution in the model. Therefore, we conclude that the distributions of induced eddy current density is significantly affected the hole of the skull or the shape of the hole. In this case, the density of induced current at opstion, center of margo posterior foramen magnum, is the largest. This suggests that nerves lying near the hole or the bone will be stimulated more strongly.

The change of induced eddy current depending on the depth and the types of coil is shown in Fig.5. When the orientation of the coil is changed, there is no significant difference of the current density between 1 and 2 direction. Using the double cone coil, the density of induced current at all measuring points is larger than the results by figure-of-8 coil.

2)*Distributions of induced electric field in an inhomogeneous conductor*

The results of induced electric field is shown in Fig.6. In the case of 0.3% concentration of agar-agar and the location (i), the highest current density was measured above the intersection of the coil as we had expected. The same results was gained on the same location (I), using 1.5 % concentration of agar-agar. In the case of 0.3 % concentration of agar-agar and the location(ii), the highest current density was measured not above the intersection but near above the intersections on the agar-agar. On the contrary, 1.5 % concentration of agar-agar shows the different results. The highest rrent density was indicated not on the agar-agar but on the extention line in the saline solution. Fig.7 shows the arrow of induced electric field in the inhomogeneous volume conductor, using 1.5% concentration of agar-agar. This result shows that

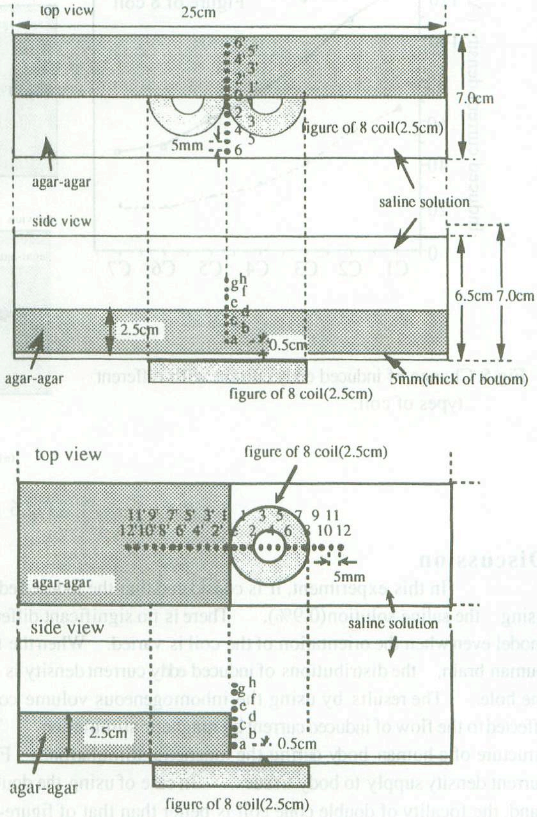

Fig.3 Experimentary system of the inhomogeneous tank.

the measuring surface is in the case of 1 cm distance from the coil surface. As the coil radius is larger than the tank width, the induced electric field near the wall in the tank is biggest. The distributions of induced eddy current is very complicated due to the concentration of the agar-agar. These results suggest that the conductivity of the human tissue is affected to the flow of induced current by magnetic stimulation.

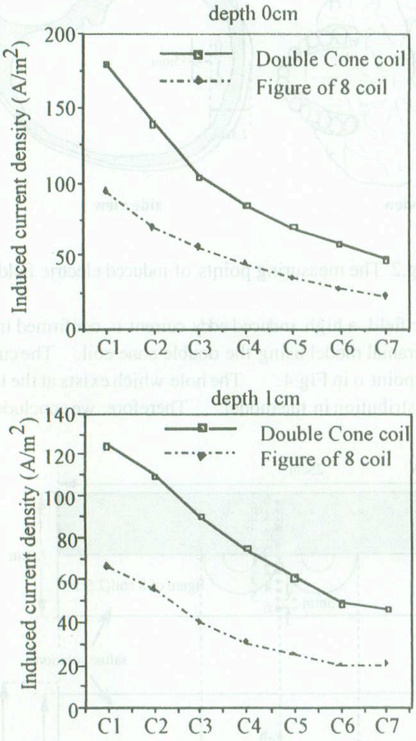

Fig.5 Change of induced eddy current with different types of coil.

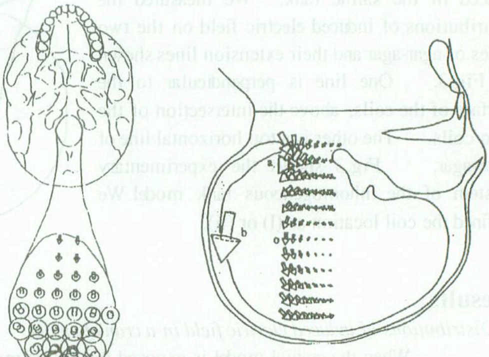

Fig.4 The distributions of induced eddy current near the foramen magnum.

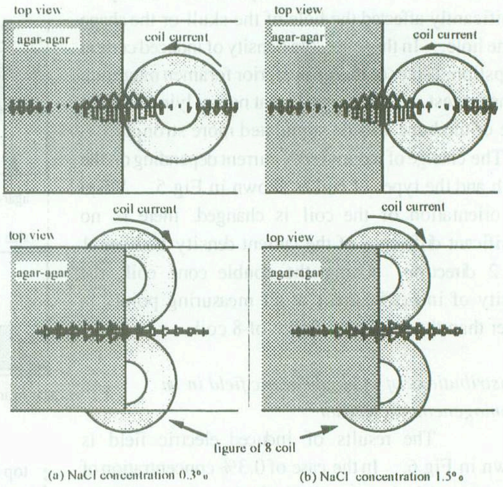

(a) NaCl concentration 0.3%

(b) NaCl concentration 1.5%

Fig.6 Distributions of induced electric field near the boundary of different medium.

Discussion

In this experiment, it is considered that the induced eddy current is proportional to the induced electric field for using the saline solution(0.9%). There is no significant difference of the distributions of induced current in the cranial model even when the orientation of the coil is varied. When the transcranial magnetic stimulation has been applied to the human brain, the distributions of induced eddy current density is significantly affected the hole of the skull or the shape of the hole. The results by using the inhomogeneous volume conductor suggest that the conductivity of the medium is affected to the flow of induced current by magnetic stimulation. Therefore, we must pay special attention to an anatomical structure of a human body during the magnetic stimulation. Furthermore, we must take precautions to avoid an extra current density supply to body tissues. In case of using the double cone coil, this affect is more serious. On the other hand, the focality of double cone coil is better than that of figure-of-8 coil.

To sum up, the results of this study suggest that this measuring method is useful to estimate the distributions of induced eddy current in the human body applying the magnetic stimulation. It is evident that more studies relating to the focality of magnetic stimulation is necessary.

Conclusions

This paper investigates the distributions of induced eddy current or induced electric field by magnetic stimulation. The results of these experiments suggested that the distributions of current or field depends on the volume or the conductivity of conductor, or the coil structure. This measuring method enables to estimate the focality of magnetic stimulation.

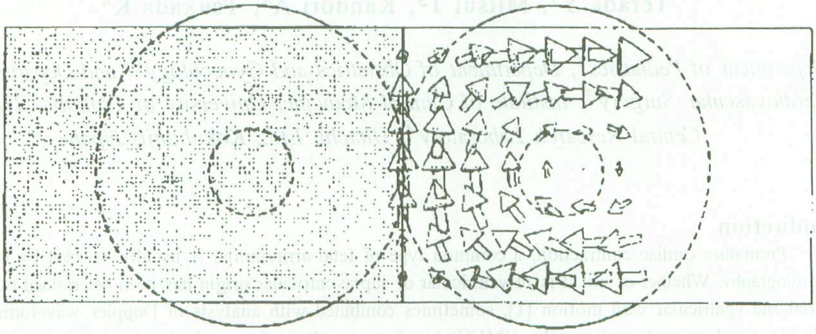

Fig.7 The arrows of induced electric field in the inhomogeneous tank model.

References

[1] A.T.Barker, R.Jalinous, I.L.Freeston : Non-invasive magnetic stimulation of human motor cortex. Lancet, 2, 1106/1107(1985)

[2] D.Cohen and B.N.Cuffin : Developing a more focal magnetic stimulator. Part I: Some basic principles. 8(1), 102/111(1991)

[3] A.T.Barker, I.L.Freeston, R.Jalinous & J.A.Jarrat : Magnetic stimulation of the human brain and peripheral nervous system:An introduction and the results of clinical evalution. Neurosurgery, 20,100/109(1987)

[4] S.Chokeoverty : Magnetic stimulation in clinical neurophysiology, Butterworths, Boston, (1990)

[5] N.M.F.Murray : The clinical usefulness of magnetic cortical stimulation,Electroenceph.clin. Neurophysiol., 85, 81/85 (1992)

[6] S.Ueno,T.Tashiro & K.Harada : Localized stimulation of neural tissues in the brain by means of paired configulation of time-varying magnetic fields. J.Appl.Phys.,64, 5862/5864(1988)

[7] S.Ueno, T.Matsuda & M.Fujiki : Functional mapping of the human motor cortex obtained by focal and vectorial magnetic stimulation of the brain. IEEE Trans.on Magnetics, 26, 5, 1539/1544(1990)

[8] T.Krings, B.R.Buchbinder, W.E.Butler, K.H.Chappa, H.J.Jiang, B.R.Rosen & G.R.Cosgrove : Stereotactic transcranial magnetic stimulation: Correlation with direct electrical cortical stimulation. Neurosurgery, 41, 6, 1319/1325(1997)

[9] K.Yunokuchi & D.Cohen : Developing a more focal magnetic stimulator. Part II: Fabricating coils and measuring induced current distributions. J.Clin.Neurophysiol., 8, 1, 112/120(1991)

[10] K.Yunokuchi : A method of measuring the induced current in saline conductor by magnetic stimulator. T.IEE Japan, 111-A, 9, 828/834(1991)

[11] K.Yunokuchi, H.Yoshida, K.Mamitsuka & T.Asakura : Characteristics of nerve excitation by the pulsed magnetic stimulation. BME'96, F2-3, 303/306(1996)

[12] V.E.Amassian, L.Eberle, P.J.Maccabee & R.Q.Cracco : Modelling magnetic coil excitation of human cerebral cortex with a peripheral nerve immersed in a brain-shaped volume conductor:the significance of fiber bending in excitation. Electroenceph. clin. Neurophysiol., 85, 291/301(1992)

Investigation of fetal premature cardiac contractions by magnetocardiography

Horigome H[1], Takahashi MI[1], Asaka M[2], Shigemitsu S[2], Matsui A[1], Terada Y[3], Mitsui T[3], Kandori A[4], Tsukada K[4]

Department of Pediatrics[1], Department of Obstetrics and Gynecology[2], and Department of Cardiovascular Surgery[3], Institute of Clinical Medicine, University of Tsukuba, Tsukuba; Central Research Laboratory[4], Hitachi, Ltd., Kokubunji, Japan

Introduction

Premature cardiac contraction, a common type of fetal arrhythmia, is usually detected by routine fetal echocardiography. Whether or not it is of ventricular or supraventricular origin has been determined by analyzing the atrial and ventricular wall motion [1], sometimes combined with analysis of Doppler waveforms of major vessels [2]. Fetal magnetocardiography (fMCG) has been an alternative method to diagnose fetal arrhythmias since the introduction of a superconducting quantum interference device (SQUID) for prenatal diagnosis [3]. Although fetal electrocardiography (fECG) obtained through the maternal abdominal wall is another method to directly diagnose fetal dysrhythmias from the waveform, fMCG is advantageous because magnetic fields generated by a fetal heart remain mostly unaffected not only due to the electrical conduction properties of materials around the fetus but also the mother's distant heart [4,5]. We measured premature cardiac contractions in fetuses using a newly-developed SQUID system to determine whether MCG is useful in the differentiation between premature ventricular contractions (PVC) and premature supraventricular contractions (PSVC).

Methods

Study Population

Fetal MCG (fMCG) was measured in 13 fetuses who were diagnosed as having premature cardiac contractions by routine fetal echocardiography. The gestational age ranged from 27 to 39 weeks (median 37 weeks) as shown in Table 1. No structural abnormalities of the heart were noted on echocardiography. The study protocol was approved by the ethics committee of the University Hospital of Tsukuba. Informed consent was obtained from each parent before participation in the study.

Instrumentation & Measurements

FMCG was recorded using a 9-channel SQUID system, which was originally developed by our group [6] and housed in a magnetically shielded room in the University Hospital of Tsukuba. Nine bobbin-type gradiometers were distributed at 3×3 points on a sensor array at a constant interval of 30 mm, providing a measurement area of 60×60 mm^2. The coils were circular and 20 mm in diameter, and the baseline distance was 60 mm. The signals, acquired at a sampling rate of 1,000 Hz, were passed through a 0.1-100 Hz band-pass filter and power-line noise filters (50 and 100 Hz).

Immediately before the measurement, the fetal heart position was determined by 2-dimensional echocardiography to direct the sensor array as close as possible to what was determined to be the center of the fetal heart. We initially investigated the waveforms on beat-to-beat tracings to determine the origin of the premature contractions. Then, time-averaging of the data triggered by the peak of the QRS complex of the fetus was applied individually to more than 50 sinus beats and to as many premature beats as possible to improve the signal-to-noise (S/N) ratio. After birth, we recorded a standard ECG in each subject and compared it with the fMCG waveforms.

Results

Recording and time-averaging of QRS waveforms in both sinus beats and premature beats were successful in all subjects. The origin of the premature contractions was determined by fMCG as ventricular in 7

©1999, Tohoku University Press
Recent Advances in Biomagnetism
T. Yoshimoto et al. (Eds)

cases, supraventricular in 6 and both in 1 (Table 1). In 2 of the cases which were estimated to be PSVC, aberrantly conducted PSVC were also diagnosed (Fig. 1), as we recognized a preceding p wave, prolonged PQ interval and following wide QRS complex. Configuration of the PVC waveform was constant on beat-to-beat tracing, indicating monofocal ectopy and reduced fetal movement (Fig. 2). Two cases revealed a bigeminy or trigeminy pattern. ECG obtained after birth confirmed the diagnosis except in 4 cases. One of the 4 cases showed aberrantly conducted PSVC, which had been estimated to be of ventricular origin (case 12), and in the other 3 cases no premature beat was observed on ECG recordings after birth (case 1, 7, 8), so the prenatal diagnosis could not be confirmed. The QRS duration of PVC ranged from 61 to 100 msec (mean, 83 msec), and those of sinus rhythm were 40 to 65 msec (mean, 49 msec). The QRS duration of PVC was similar to that determined by electrocardiography after birth (Table 1).

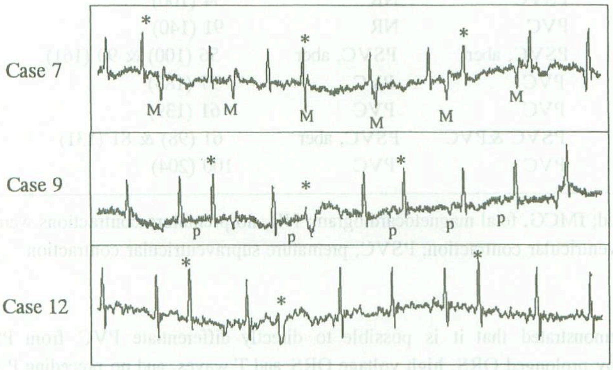

Fig. 1 Unaveraged fetal magnetocardiographic waveforms of cases 7, 9 and 12.
Note that premature beats (*) in each case show similar QRS durations as those of sinus beats. The fifth QRS complex on the tracing of case 9 and case 12 are wide, but the former was determined to be an aberrantly conducted ectopy of supraventricular origin because it follows a premature p wave with a prolonged PQ interval. Mark "M" represents interference of the maternal magnetic fields in the waveform of fetal magnetocardiography.

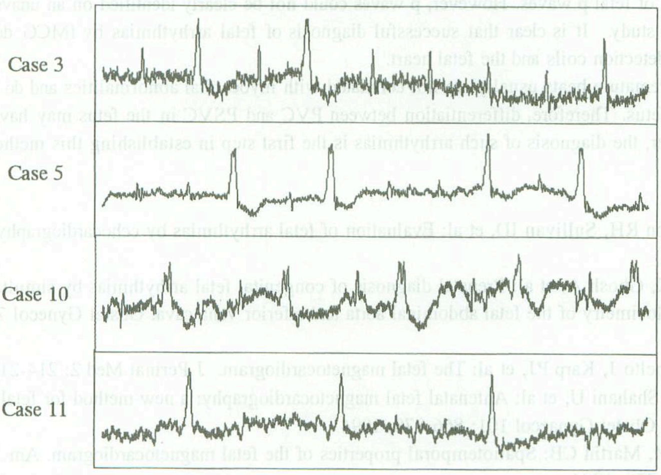

Fig. 2 Unaveraged fetal magnetocardiographic waveforms of cases 3, 5, 10 and 11.
Note that the premature beats in each case show a wide and highly amplified QRS complex and T wave, indicating ventricular origin. These ectopies can be clearly differentiated from sinus beats with narrow QRS.

Table 1 Results of subjects

Case	Gestational	fMCG	ECG diagnosis	QRS duration (msec)	
	Age(w, d)	diagnosis	after birth	fMCG (% of sinus beat)	ECG after birth
1	27w 2d	PSVC	NR	40 (100)	NR
2	29w 2d	PVC	PVC	69 (173)	70
3	32w 0d	PVC	PVC	83 (166)	85
4	35w 1d	PSVC	PSVC	62 (116)	60
5	35w 3d	PVC	PVC	81 (184)	85
6	35w 4d	PSVC, aber	PSVC, aber	43 (110)	50 & 80
7	36w 5d	PSVC	NR	54 (100)	NR
8	37w 5d	PVC	NR	91 (140)	NR
9	38w 0d	PSVC, aber	PSVC, aber	56 (100) & 90 (161)	60 & 90
10	38w 0d	PVC	PVC	97 (183)	95
11	38w 2d	PVC	PVC	61 (139)	80
12	38w 3d	PSVC &PVC	PSVC, aber	61 (98) & 81 (131)	60 & 90
13	39w 0d	PVC	PVC	100 (204)	100

aber, aberrantly conducted; fMCG, fetal magnetocardiogram; NR, no premature contractions were recorded after birth; PVC, premature ventricular contraction; PSVC, premature supraventricular contraction

Discussion

Our results demonstrated that it is possible to directly differentiate PVC from PSVC from their waveform characterized by prolonged QRS, high voltage QRS and T waves, and no preceding P wave. The QRS duration of PVC in each case was similar to that recorded after birth. The diagnosis of PSVC with aberrant conduction was also possible except 1 case in which P waves were not clearly detected on the beat-to-beat tracing due to the deep location of the fetus. With the conventional method, in which atrial and ventricular wall motions were analyzed on an M-mode echocardiogram [1], it is not necessarily easy, in some cases, to distinguish PVC from PSVC. For example, the amplitude of the atrial wall motion may be too small to analyze during early gestation. FMCG theoretically reflects regional myocardial current sources with fewer insulation effects by vernix caseosa than fECG [3,4]. Therefore, fMCG is more effective than fECG obtained through the maternal abdomen for detection of fetal p waves. However, p waves could not be clearly identified on an unaveraged tracing in some cases in this study. It is clear that successful diagnosis of fetal arrhythmias by fMCG depends on the distance between the detection coils and the fetal heart.

Most fetal premature beats usually are not correlated with myocardial abnormalities and do not influence the prognosis of the fetus. Therefore, differentiation between PVC and PSVC in the fetus may have less impact on clinicians. However, the diagnosis of such arrhythmias is the first step in establishing this methodology.

References

[1] Allan LD, Anderson RH, Sullivan ID, et al: Evaluation of fetal arrhythmias by echocardiography. Br Heart J 50: 240-245, 1981

[2] Chan FY, Woo SK, Ghosh A, et al: Prenatal diagnosis of congenital fetal arrhythmias by simultaneous pulsed Doppler velocimetry of the fetal abdominal aorta and inferior vena cava. Obstet Gynecol 76: 200-205, 1990

[3] Kariniemi V, Ahopelto J, Karp PJ, et al: The fetal magnetocardiogram. J Perinat Med 2: 214-216, 1974

[4] Quinn A, Weir A, Shahani U, et al: Antenatal fetal magnetocardiography: a new method for fetal surveillance? Br J Obstet Gynaecol 101: 866-870, 1994

[5] Wakai RT, Wang M, Martin CB: Spatiotemporal properties of the fetal magnetocardiogram. Am J Obstet Gynecol 170: 770-776, 1994

[6] Tsukada K, Haruta Y, Adachi A, et al: Multichannel SQUID system detecting tangential components of the cardiac magnetic fields. Rev Sci Instruments 66: 5085-5091, 1995

Assessment of Fetal Development on the Basis of Fetal Magnetocardiography

P. Van Leeuwen,[1] S. Lange,[2] B. Hailer,[3] M. Hartmann,[1] L. Lajoie-Junge,[1] W. Hatzmann,[4] D. Grönemeyer,[1,2]

[1] *Dept. of Biomagnetism, EFMT, Bochum, Germany;*
[2] *Institut for Microtherapy, University of Witten/Herdecke, Bochum, Germany;*
[3] *Dept. of Cardiology and Angiology, Augusta Kranken Anstalt, Bochum, Germany;*
[4] *Dept. of Gynecology and Obstetrics, Marienhospital, Witten, Germany*

Introduction

Studies over the last number of years have shown that fetal magnetocardiography may be useful in describing fetal state and fetal development [1]. Compared to other methods such as fetal ECG or cardiotocography, the fetal magnetocardiogram (FMCG) can register fetal cardiac activity with a good to excellent signal to noise ratio as well as with high temporal resolution as of the second trimester. This allows the analysis of signal morphology, cardiac time intervals and heart rate variability. In the following we present the results obtained on a reasonable number of subjects demonstrating the potential of the FMCG in assessing fetal development.

Methods

We have investigated more than 60 pregnant women, registering over 190 FMCG between the 13th and 42st week of gestation. Between one and eleven measurements per fetus were performed (mean 3 ± 2). In over 92% of the registrations fetal R-waves could consistently be acquired, signal strength being too weak to permit evaluation in 16 cases (all before the 20th week). Roughly 3/4 of the FMCG recordings (155) were performed using a 37 channel biomagnetometer (Siemens Krenikon, Erlangen, Germany) consisting of first order gradiometers with a baseline of 7 cm with a probe diameter of 19 cm. System noise was less than 30 fT/Hz^{-1} for frequencies > 2 Hz and 10 fT/Hz^{-1} for frequencies > 10 Hz. The remaining measurements were performed with a 67 channel biomagnetometer (BTi 1300C, San Diego, USA) consisting of magnetometer sensing coils arranged on a curved surface with a diameter of 33 cm and including a configuration of 11 reference coils used to detect ambient noise. Intrinsic system noise was less than 10 fT/Hz^{-1} for frequencies > 5 Hz. To reduce the influence of electromagnetic artifacts the measurements were performed in a shielded room (Vakuumschmelze AK3b, Hanau, Germany). The position of the probe was placed over the maternal abdomen such that the fetal signal amplitude was optimized. Data was generally recorded for five minutes with a bandpass of 1-200 Hz at a sampling rate of 1 kHz.

In order to examine fetal activity uncorrupted by the maternal cardiac signal, maternal beats were identified and digitally subtracted in all channels. Fetal QRS complexes were identified using an appropriate signal template. Complexes not automatically recognized were visually identified and added manually; similarly, falsely marked artifacts were removed. For the determination of signal amplitude and cardiac time intervals, single beats of raw data were averaged and subsequently DC-offset in an interval prior to P wave onset. In order to assure maximum precision in the determination of time intervals, the deflections of the FMCG signal in the averaged beat were examined in all channels, thereby taking differences in signal polarity and intensity in individual channels into account. For the analysis of heart rate, the duration of single heart beats was determined with an accuracy of 1 ms as the time between consecutive QRS complexes. The time series of a complete set of fetal heart periods served as the basis for the calculation of heart rate variability parameters. In the time domain, the standard deviation (SD) and the root mean square of successive differences (RMSSD) were calculated. Spectral analysis was performed on the basis of the fast Fourier transform and the frequency spectrum was examined between 0-1 Hz. Furthermore complexity measures such as the approximate entropy (ApEn) and approximate dimension (ApD1) were calculated [2].

Results

In approximately one quarter of all registrations, preferentially in mid-pregnancy, short bradycardic episodes were found which could not be associated with any pathological condition. They are most likely due to the immaturity of the autonomic nervous system with respect to vagal innervation. Furthermore, in a number of the FMCG traces arrhyth-

©1999, Tohoku University Press
Recent Advances in Biomagnetism
T. Yoshimoto et al. (Eds)

mic activity could be found, including premature beats of ventricular and supraventricular origin (n=21), *sino*-atrial block (n=2) and tachycardia (n=2) (Fig.1). Most of this fetal arrhythmic activity was of no clinical significance and did not persist after birth. However tachycardia and AV-blocks may lead to heart failure and their identification aided in the determination of treatment regimes [3].

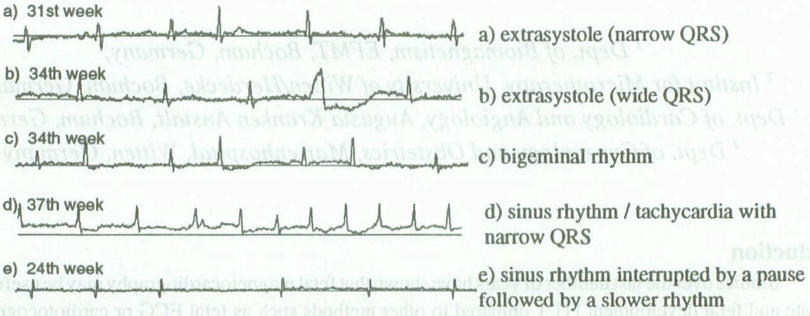

Fig. 1: Examples of various kinds of fetal arrhythmic activity.

Examination of the averaged PQRST waveform of healthy fetuses in the course of pregnancy showed that the P wave and the QRS complex may be easily identified whereas the unambiguous detection of the T wave was generally difficult. Signal amplitudes and interval durations increased over time as follows: P wave: 0.01 to 0.25 pT, 40 to 70 ms; QRS: <1 to 4 pT, 30 to 55 ms. Fig. 2A demonstrates such changes for a single fetus and Fig. 3 shows the results for 80 measurements in 19 healthy singleton pregnancies. The observed changes may be attributed to the increase in cardiac muscle mass as gestation progresses. Cardiac time intervals and wave amplitudes may be thus useful in the assessment of fetal growth, congenital defects and 0_2 saturation [4].

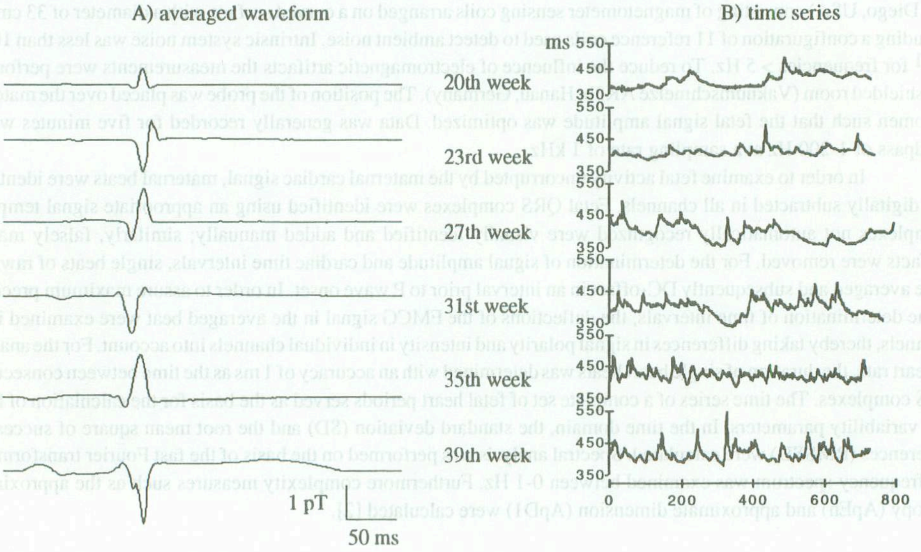

Fig 2: Healthy fetus between the 20th - 39th week of gestation: A) averaged beats showing increase in amplitude and cardiac intervals duration over time; B) time series of the beat duration showing increase in heart rate variability over time.

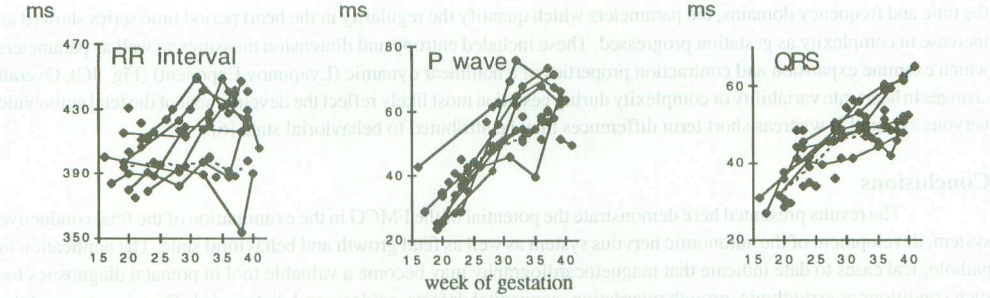

Fig 3: Changes in duration of RR interval, P-wave and QRS complex over gestation in 80 measurements. ◆—◆ courses of individual fetuses with ≥3 measurements.

Changes in heart rate variability could be observed as gestation progressed (see Fig. 2B) and were quantitatively confirmed by parameters from the time and frequency domain. In the time domain the standard deviation of the RR-interval increased from 10 to 20 ms, the RMS of successive differences from 2 to 6 ms (Fig. 4A). The frequency spectrum showed a clear increase in the low frequency band (LF = .05-.15 Hz) and a moderate change in the high frequency band (HF = .15-.4 Hz). As a measure for the redistribution in power over different frequency bands, the decrease in slope of the log-log spectrum indicated a shift away from very low to higher frequencies (Fig. 4B). Beyond

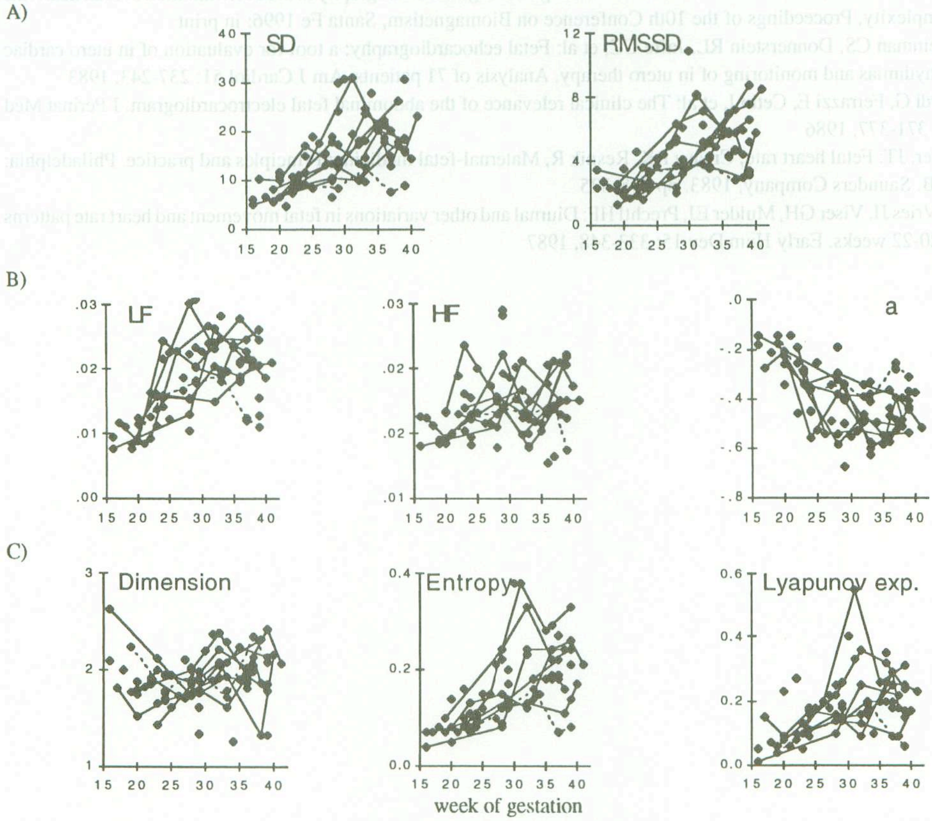

Fig. 4: Changes in heart rate variability during gestation in 80 measurements (5-min. time series): A) time domain: standard deviation (SD) and RMS of successive differences (RMSSD); B) frequency domain: low frequency (LF = .05-.15 Hz), high frequency (HF = .15-.4 Hz) and slope of the log-log spectrum (a); C) complexity: approximate Dimension, Entropy and Lyapunov exponent. ◆—◆ courses of individual fetuses with ≥3 measurements.

the time and frequency domains, the parameters which quantify the regularity in the heart period time series showed an increase in complexity as gestation progressed. These included entropy and dimension measures as well as parameters which examine expansion and contraction properties of a nonlinear dynamic (Lyapunov Exponent) (Fig. 4C). Overall changes in heart rate variability or complexity during gestation most likely reflect the development of the fetal autonomic nervous system [5] whereas short term differences may be attributed to behaviorial state [6].

Conclusions

The results presented here demonstrate the potential of the FMCG in the examination of the fetal conductive system, development of the autonomic nervous system as well as fetal growth and behavioral state. The application in pathological cases to date indicate that magnetocardiography may become a valuable tool in prenatal diagnostics for such conditions as arrhythmia, growth retardation, congenital defects, acidosis and distress [1]. The advantages of the method lie in its simple and noninvasive registration from the second trimester onwards and as well as in its high temporal resolution and good signal to noise ratio. Apart from improvements in instrumentation, investigations with large numbers of fetuses in healthy pregnancies are required to serve a reference database and to establish ranges of normal values for the various measures. Furthermore prospective multicenter studies with sufficient numbers of appropriate subjects with various forms of pathology are necessary to determine which conditions are most amenable to fetal surveillance and clinical use.

References

[1] Van Leeuwen P: Fetal magnetocardiography. Herzschr Elektrophys 8: 184-194, 1997

[2] Van Leeuwen P, Bettermann H, Schüßler M, Lange S: Magnetocardiography in the determination of fetal heart rate complexity, Proceedings of the 10th Conference on Biomagnetism, Santa Fe 1996: in print

[3] Kleinman CS, Donnerstein RL, Jaffe CC, et al: Fetal echocardiography: a tool for evaluation of in utero cardiac arrhythmias and monitoring of in utero therapy. Analysis of 71 patients. Am J Cardiol 51: 237-243, 1983

[4] Pardi G, Ferrazzi E, Cetin I, et al: The clinical relevance of the abdominal fetal electrocardiogram. J Perinat Med 14: 371-377, 1986

[5] Parer, JT: Fetal heart rate, Creasy RK, Resnik R, Maternal-fetal medicine: Principles and practice. Philadelphia: W.B. Saunders Company, 1983. pp 298-325

[6] de Vries JI, Viser GH, Mulder EJ, Prechtl HF: Diurnal and other variations in fetal movement and heart rate patterns at 20-22 weeks. Early Hum Dev 15: 333-348, 1987

RECORDING OF HUMAN FETAL AUDITORY EVOKED FIELDS

Eswaran H[2], Lowery CL[1], Robinson SE[3], Cheyne D[3], Haid V[3], McKenzie D[3], Vrba J[3], Wilson JD[2].
University of Arkansas for Medical Sciences, Dept. of Ob/Gyn, Little Rock, AR, USA[1];
Univeristy of Arkansas at Little Rock, Dept. of Applied Science, Little Rock, AR, USA[2];
CTF Systems, Inc., Port Coquitlam, B.C. Canada.[3]

Introduction

Antepartum knowledge of the fetal health helps in early prediction and prevention of any in utero fetal risk of death or damage. The recording of fetal heart sounds, fetal electrocortical activity, fetal breathing and fetal body movements help the obstetricians in assessing the well-being of the fetus. Currently, there are no reliable tests to assess the functional integrity of the fetal brain. Auditory evoked responses (AER) have been used as a sensitive test to determine the functional status of the adult and neonatal brain. In this study, we used the non-invasive magnetoencephalographic technique in an unshielded environment to elicit AERs from the fetuses in utero. This is the first reported fetal magnetoencephalography measurement made in an unshielded environment. We were able to detect N1 (100ms)-P2 (200ms) long latency peak in three out of the four fetuses studied. Based our preliminary recordings it was clear that to effectively apply this technique for clinical use, we need to use better signal processing methods in addition to the traditional averaging technique to improve the signal-to-noise ratio (SNR).

Methods

Prior to the recording session the research protocol was discussed with each patient and a written consent was obtained. Subjects in our study were low-risk pregnancies with fetuses whose gestation ages ranged from 33- 40+ weeks. The recordings were made using a seven-channel SQUID (a CTF test system, CTF Systems, Canada) in an unshielded environment. The noise level of the instrument was < 10 $fT/Hz^{1/2}$ per channel. The sensors were arranged in a hexagonal shape and the center to center spacing between each sensor was five cms. The diameter of the detection coil was two cms and the baseline of the gradiometer was five cms. Also, the system was equipped with an eight channel reference array for environmental noise cancellation. The auditory stimulus was a one kHz tone burst of 100 ms duration delivered at a randomly generated rate. The speaker driver was placed 6.09 m(20 ft) away from the mother to have minimal interference with the SQUID system. The sound was delivered to the maternal abdomen using a 6.09 m (20 ft) long plastic tube with a five cm diameter mask at the end (Figure 1). The sound intensity at the end of the tube was measured to be 120 dB (SPL - referenced to 20 μPascal). A portable Corometrics ultrasound instrument was used to determine the fetal presentation and the head position. All of the fetuses in this study were cephalic and the distance from the maternal skin surface to the fetal head was measured and found to be less than five cms. In all the cases, the fetal head was facing either to the right or to the left within the uterus, thus presenting either the right or left temporal areas to the sensor array. The experimental set-up is shown in Figure 1. The recordings were repeated at three different locations (L1, L2 and L3, see Figure 1) over the fetal head. The recordings were performed on four pregnant women with gestation ages of 37, 40+, 33 and 39 weeks. The data was collected at a rate of 1250 samples/sec before using an anti-aliasing lowpass filter of 350 Hz. Each recording set consisted of 600 trials. The duration of each trial was 800 ms (200 ms before the stimulus and 600 ms after the stimulus). Improvements in filtering and noise reduction were used to separate what appears to be a fetal auditory evoked response from other interfering signals. The signals were averaged and digitally filtered with bandpass filter (4-40 Hz). Attempts to bandpass filter the signals in order to remove artifacts resulted in additional artifacts, manifested by “ringing.” The “ringing” artifacts were traced to application of a digital filter to short data segments that contained high amplitude 60 Hz signals and harmonics. The solution to this was to remove the 60 Hz noise by decorrelation rather than notch filtering. Also, all evoked trials having a peak-to-peak low frequency noise of greater than 1.5 pT were rejected.

©1999, Tohoku University Press
Recent Advances in Biomagnetism
T. Yoshimoto et al. (Eds)

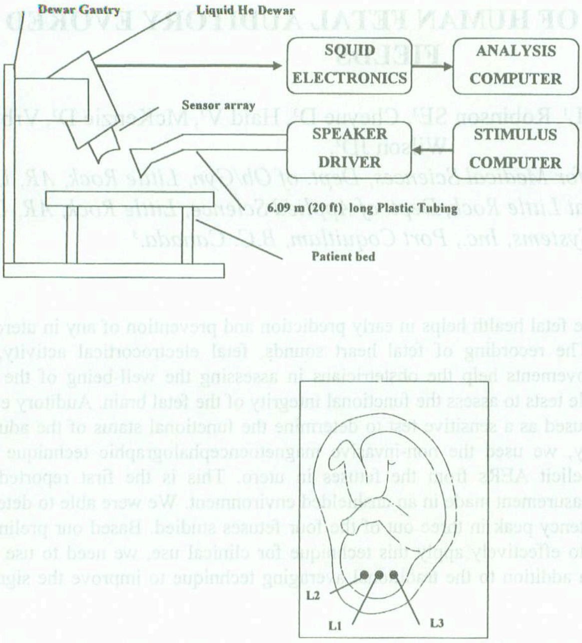

Fig 1. Overview of the experimental set-up. The figure at the bottom shows the three different recording sites L1, L2 and L3 used on a subject to obtain the evoked response data.

Results

Recordings on Subject I failed to show any obvious response. This subject did not consent to an ultrasound examination to locate the position of the fetal head and we positioned the sensor array over the fetal head by palpation. Fetal heart signals could be seen in all these recordings and we were unable to detect an evoked response. An ultrasound exam on Subject II showed the fetus in a cephalic position, facing to the right. In the initial recordings no obvious evoked responses were seen. The failure was attributed to the non-optimal positioning of the sensor array over the fetal head. The mother was repositioned using a foam wedge that elevated the maternal abdomen and allowed the hips to be adducted and dropped below the lower portion of the abdomen above the symphysis pubis. This provided a closer contact of the seven-channel SQUID array with the maternal abdomen. This positioning of the mother provided a better access to the pelvic area without having to tilt the dewar more that 15 degrees. We were successful in acquiring the evoked response with this new position on Subject II. This study was repeated on two more subjects. Table. 1 shows the amplitude and latency values recorded from all the subjects. Figure 2 shows evoked responses from Subject III (33 weeks) at position L3 over the fetal head. The sensor montage (Figure 2) indicates the averages of the six working SQUID sensors. Two types of signal averages were computed. The common signal average, in which all trials are summed constructively, indicates the averaged signal that is synchronous with the stimulus. So-called "plus-minus" averaging was also computed, for which alternating trials are either added or subtracted from the totals (Figure 2). The plus-minus average indicates the measurement noise level for signals that are not synchronous with the stimulus. In this data set, 35 trials were rejected, reducing the number averaged from 600 down to 565. The plus-minus average is denoted by a gray trace, while conventional signal averages are shown in black. The conventional signal average reveals what appears to be an N1(100 ms)-P2(200 ms) evoked response complex, most prominent in sensors S1, S2, S3and S4, with smaller signals seen in sensors SS6 and SS7. The observed response is well above the measurement noise level shown by the corresponding plus-minus averages. This demonstrates that the putative evoked response is not due to the summation of artifacts as seen by the sensors. As further evidence that we were able to record a true fetal transient auditory evoked response, we can also show replication of measurement results with the same patient. Figure 3 compares two sets of data recorded at positions L1 and L2 on the same patient. Though the Figure 3a has a poorer signal to noise compared to Figure 3b but has a strikingly similar morphology, thus clearly showing evidence of the N1(100 ms)-P2(200 ms) evoked waveforms. This is unlikely to be a chance occurrence due to artifacts such as the fetal MCG.

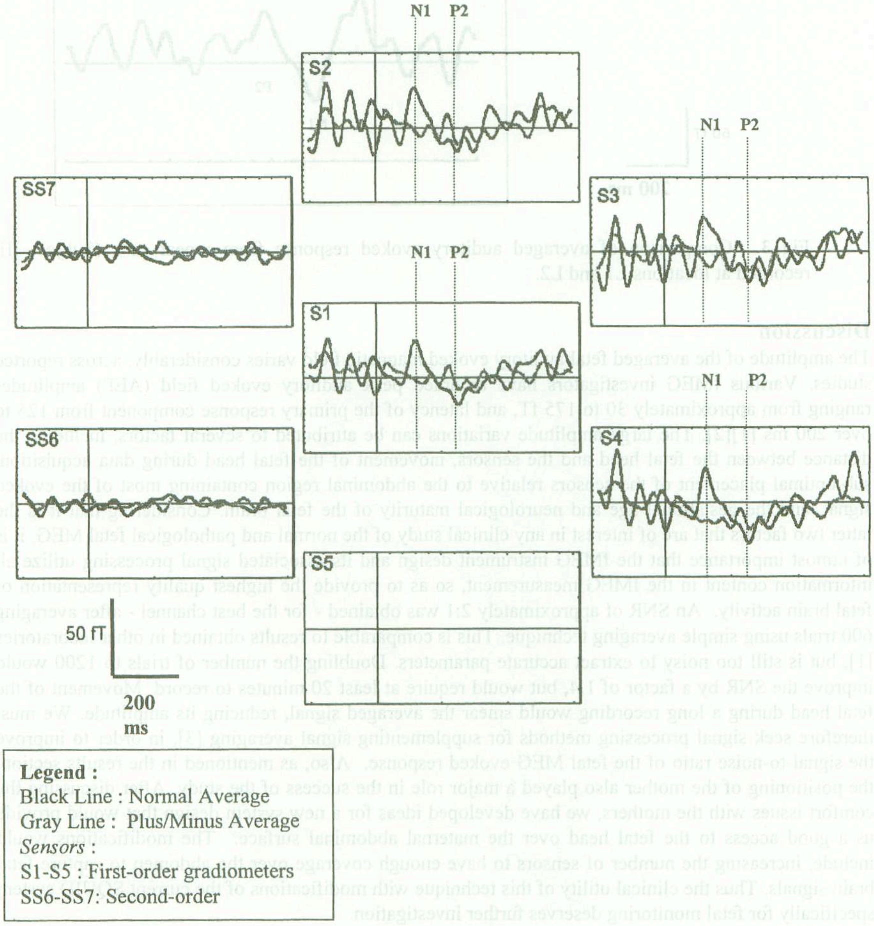

Fig 2. Auditory evoked response recorded at site L3, obtained by de-noised averaging (565/600 accepted trials) of the raw data. The de-noised averages are shown in black and the plus-minus averaging in gray (Subject III).

Table 1. N1 and P2 peak latency and amplitude values from four fetuses.

	N1 peak latency		P2 peak latency	
Subject	**Latency (ms)**	**Amplitude (fT)**	**Latency (ms)**	**Amplitude (fT)**
I	No response	-	No response	-
II	110	50	200	30
III	100	50	230	45
IV	100	30	180	45

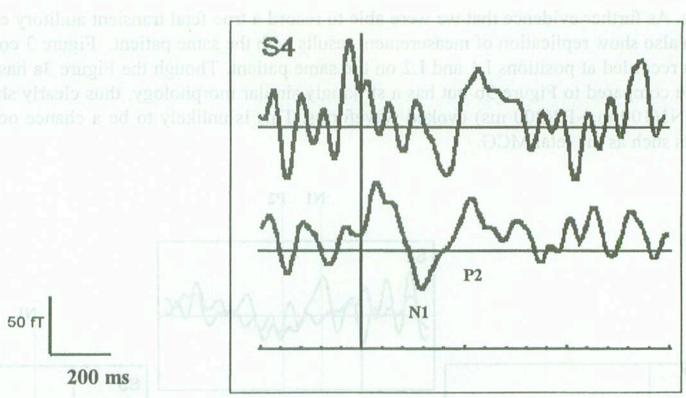

Fig 3. Comparison of averaged auditory evoked response from repeat runs (Subject III) recorded at locations L1 and L2.

Discussion

The amplitude of the averaged fetal auditory evoked magnetic field varies considerably, across reported studies. Various fMEG investigators have recorded peak auditory evoked field (AEF) amplitudes ranging from approximately 30 to 175 fT, and latency of the primary response component from 125 to over 200 ms [1][2]. The large amplitude variations can be attributed to several factors, including the distance between the fetal head and the sensors, movement of the fetal head during data acquisition, sub-optimal placement of the sensors relative to the abdominal region containing most of the evoked signal, and the gestational age and neurological maturity of the fetal brain. Considering that it is the latter two factors that are of interest in any clinical study of the normal and pathological fetal MEG, it is of utmost importance that the fMEG instrument design and its associated signal processing utilize all information content in the fMEG measurement, so as to provide the highest quality representation of fetal brain activity. An SNR of approximately 2:1 was obtained - for the best channel - after averaging 600 trials using simple averaging technique. This is comparable to results obtained in other laboratories [1], but is still too noisy to extract accurate parameters. Doubling the number of trials to 1200 would improve the SNR by a factor of 1.4, but would require at least 20 minutes to record. Movement of the fetal head during a long recording would smear the averaged signal, reducing its amplitude. We must therefore seek signal processing methods for supplementing signal averaging [3], in order to improve the signal-to-noise ratio of the fetal MEG evoked response. Also, as mentioned in the results section, the positioning of the mother also played a major role in the success of the study. After discussing the comfort issues with the mothers, we have developed ideas for a new system design that would provide us a good access to the fetal head over the maternal abdominal surface. The modifications would include, increasing the number of sensors to have enough coverage over the abdomen to capture fetal brain signals. Thus the clinical utility of this technique with modifications of the current SQUID system specifically for fetal monitoring deserves further investigation.

References

1. Blum T, Saling E, Bauer R. First magnetoencephalographic recordings of the brain activity of the human fetus. Br J Obstet Gynaecol 1985;92:1224-29.

2. Wakai RT, Leuthhold AC, Martin, Jr., CB. Fetal auditory evoked responses detected by magnetoencephalography. Am J Obstet Gynecol 1996;174(8):1484-86.

3. Lowery CL, Robinson SE et al. Detection of the Transient and Steady-state Auditory Evoked Responses in the Human Fetus. Poster Presentation - 11th International Conference on Biomagnetism, Sendai, Japan, 1998.

Detection of the Transient and Steady-State Auditory Evoked Responses in the Human Fetus

Lowery C[1], Robinson S[2], Eswaran H[1], Vrba J[2], Haid V[2], and Cheung T[2]
University of Arkansas[1], Little Rock, AR, USA; CTF Systems Inc.[2], Port Coquitlam, BC, Canada

Introduction

Measurement of fetal brain activity has potential clinical value in maintaining high-risk pregnancies, and is important to our understanding of basic developmental neuroscience [1]. Modern dc-SQUID sensors appear to have the necessary sensitivity for quantifying the fetal magnetoencephalogram (fMEG). However, the signal-to-noise ratio (SNR) of fMEG may be poor, due to interference from neighboring biological current sources such as the fetal heart (fetal MCG). Although signal averaging over a large number of stimulus trials should improve SNR, the likelihood that the fetus will move (thus reducing SNR) increases with longer recording duration. The use of selective signal averaging in which trials containing the fetal MCG QRS complex are discarded can only result in increasing artifacts due to other portions of the cardiac cycle (primarily the T-wave). In this study, we have applied two techniques to fMEG analysis – spatially selective noise reduction and frequency spectral analysis – in order to enhance the SNR of unshielded fMEG recordings.

The amplitude of the averaged fetal auditory evoked magnetic field varies considerably, across reported studies. The waveform component corresponding to the adult $N100_M$ also appears to be delayed significantly in the fetus and neonate. Various fMEG investigators have recorded peak auditory evoked field (AEF) amplitude ranging from approximately 30 to 175 fT. They reported the latency of the primary response component from 125 to over 200 ms [2] [3]. The large amplitude variations can be attributed to factors, including: 1) the distance between the fetal head and the sensors, 2) movement of the fetal head during data acquisition, 3) sub-optimal placement of the sensors relative to the abdominal region containing most of the evoked signal, and 4) the gestational age and neurological maturity of the fetal brain. The latter two factors are of interest in any clinical study of the normal and pathological fetal MEG. Hence, it is of utmost importance that the fMEG signal processing utilize all information content in the fMEG measurement.

Prior to engagement of the fetal head in the pelvic girdle, fetal movement during data acquisition can result in significant degradation of fMEG recordings. Since one cannot control fetal head movement, one must minimize the fMEG measurement time, since this reduces the likelihood of head movement during data acquisition. However, a reduction in total measurement time could also degrade the averaged fetal evoked response. One must therefore seek signal-processing methods for supplementing signal averaging, in order to improve the signal-to-noise ratio of the fetal MEG evoked response.

Assuming statistically random noise, signal averaging improves the signal-to-noise ratio of the evoked response by $N^{1/2}$, where N is the number of trials averaged. A quick calculation will show that reasonable dc-SQUID sensor noise, together with relatively few evoked response trials, should result in sufficiently low noise to accurately characterize the fetal evoked response. Assuming a sensor noise of 5 $\text{fT-Hz}^{-1/2}$ a bandwidth of dc to 30 Hz, and an average of 600 trials, the noise will be approximately 5.6 fT peak-to-peak. If the measurement noise is attributed entirely to the sensors, one expects an evoked response signal-to-noise ratio of from 4:1 to 23:1 (based on reported peak values). Even if the number of trials were reduced to 100 (which would significantly reduce examination time), characterization of the fMEG would not be limited by the dc-SQUID sensor noise. In actuality, the observed SNR is much lower than this, indicating the presence of excess noise, greater than can be accounted for by the sensor white noise level.

At present, we have a much clearer picture of the sources of excess noise in fetal MEG recordings. Biological sources, including maternal heart (magnetocardiogram - MCG), fetal heart (fMCG), uterine smooth muscle, and skeletal muscle, all contribute to the signal "clutter" in the near-field of the sensor array. These signals are not effectively attenuated by sensors placed near the fetal head. In this fMEG pilot study, we observed fetal MCG with peak amplitude of 1,500 fT (unaveraged) in sensor channels for which the fetal auditory evoked response was only 30 fT (averaged).

The body of MEG literature has focused primarily on source localization, rather than on characterization of the evoked response waveform. Localization, using the traditional non-linear equivalent current dipole solutions, requires low noise in individual sensor channels, and so far there has been only a limited need to apply methods deriving synthetic channels - other than for formation of synthetic high-order gradiometers. Nonetheless, very high SNR MEG measurements have been attained by processing the entire array of sensors as a single synthetic sensor, using techniques based on adaptive beamforming [4][5].

We recorded the fMEG response to transient tone bursts, and to steady-state clicks in human fetuses from 33 to 40 weeks gestational age, using an unshielded 7-channel dc-SQUID system. Sensor positions were selected based upon fetal ultrasound examination. Using spatially selective noise reduction and signal averaging, both N100 and P200 response to tone bursts were observed. Analysis of the steady-state fMEG data revealed a spectral line at twice the click frequency, which could not be accounted for by any environmental source. Either method provided good separation of the fMEG signal from the "clutter."

©1999, Tohoku University Press
Recent Advances in Biomagnetism
T. Yoshimoto et al. (Eds)

Methods

Instrumentation was a prototype dc-SQUID system with seven primary MEG sensors and eight reference sensors. The seven primary sensors were comprised of five hardware 1st-order gradiometers and two hardware 2nd-order gradiometers. The reference channels permitted synthesis of 2nd-order gradiometers response from the 1st-order sensors. The sensor dewar was supported by a wooden gantry that was adjustable for height and tilt angle. The volunteer subjects – mothers ranging from 33 to 40 weeks gestational age – reclined on a cushioned wooden platform. The platform was on rollers, and provided two additional degrees of movement for positioning the sensors relative to the mother. Only six of the seven primary MEG sensors were operational, due to insufficient RF shielding in the test dewar.

The auditory stimuli were generated using a computer sound card, and the signal connected to an amplified loudspeaker. The computer also provided triggers to the data acquisition system. Sound from the speaker was coupled to the mother's abdomen by a 7-m flexible plastic tube terminated by an anesthesia mask with a soft inflatable rim.

Diagnostic ultrasound was used to locate the head of the fetus, and the gantry and bed were adjusted to position the sensors near the fetal head. The anesthesia mask providing auditory stimulation was strapped to the mother's abdomen at a position near the fetal head.

Both transient and steady state auditory evoked responses were recorded. The transient evoked response stimulus consisted of 100 ms 1000 Hz tone bursts, with an interstimulus interval of 1.1 to 1.3 seconds. The tone level in the tubing was adjusted to a peak sound pressure level (SPL) of 120 dB, using a calibrated sound meter. The expansion of the anesthesia mask and interface with the mother's abdomen resulted in a path loss of greater than 40. Peak sound level at the fetal head was therefore less than 80 dB SPL. The steady state stimulus consisted of continuous clicks of 80 μsec duration and 15 Hz repetition rate. The peak click SPL was adjusted, using a microphone and oscilloscope, to the same peak SPL as the tone bursts.

The fetal response to the transient auditory stimulus was acquired at a 1250 Hz sample rate, with a bandwidth of dc to 300 Hz. Each trial had a total duration of 800 ms, with a pretrigger window of 200 ms. Tone bursts were repeated for 600 trials. MEG data were collected without signal averaging, and stored on disk for subsequent processing. The steady-state response data were acquired at the same sample rate and bandwidth. Data were recorded for one hundred 10-second segments. Thus, spectral peaks could be resolved with a frequency resolution of 0.1 Hz.

The signal-to-noise ratio of the fetal magnetoencephalogram was enhanced using adaptive beamforming. The signal recorded from each individual sensor is the linear superposition of the signals generated by all sources. These include the desired fetal brain signals and the undesired interfering sources (which may be either in the near field or far field of the sensors). The task, then, is to resolve this linear superposition such that one obtains a synthetic signal channel containing only the fetal brain signal.

The beamforming problem reduces to finding a solution for the linear weighting coefficients that define the synthetic channel. The spatiotemporal character of the noise may not be precisely known. Therefore, one must use an adaptive algorithm that adjusts the weights in response to the observed data. This problem, known as "adaptive beamforming" [6][7], is the subject of considerable literature. The requirement of fixed gain for a given location (that of the fetal brain) creates a problem of constrained adaptive beamforming [8]. The standard adaptation strategy, known as the "least mean squares" (LMS) algorithm, adjusts the weights by a small amount after each set of data samples from the array, to diminish the output due to interference. With this method, the weights gradually converge on a solution that cancels the interference, but can adjust to changes in source location. Adaptive beamforming has also been used successfully to improve the SNR of biomagnetic signals [4].

The averaged fetal auditory evoked response was extracted from the multi-channel data, by means of vector noise reduction. First, a covariance matrix **C** was computed from the unaveraged data, where each element is:

$$C_{ij} = \frac{1}{K}\sum_{k=1}^{K}\left[m_{ik} - \overline{m}_i\right]\left[m_{jk} - \overline{m}_j\right] \quad (i, j = 1,2,\cdots,M),$$

where M, is the number of sensors is (six channels, in this study), and k is the time sample index for a total of K samples. The signal was then averaged synchronous to the tone-burst trigger. The resulting average was bandpass filtered, and the mean pretrigger baseline subtracted from the signal. At each time latency k, a signal-space vector was extracted from the average:

$$\overline{\mathbf{M}}_k = \frac{1}{K}\sum_{e=1}^{N} m_{ke}$$

Signals arriving from directions in signal-space other than along the selected average vector were attenuated by computing an adaptive beamformer. A different synthetic time-series ${}^j\rho$ was thus generated, corresponding to the signal vector at latency j:

$${}^j\rho = \overline{\mathbf{M}}^{\mathrm{T}}\mathbf{C}^{-1}\overline{\mathbf{M}}_j \quad \left(j, k = 1,2,\cdots,K\right).$$

Each time-series can be seen to represent a projection of the multichannel signal for which signals arriving from vector directions other than the one selected are attenuated. If the signal-space vector at a specified latency happens to point in the direction of the fetal auditory evoked response, its signal-to-noise ratio will be enhanced. If, however, the signal-vector points away from that of the fetal brain response, the fMEG signal will be attenuated. Let us assume that the fMEG signal is contaminated by the fMCG signal (which is the case). Let us further assume that the ratio of the desired fMEG signal and the unwanted fMCG signal are not constant over time. Then the signal-space vector, by chance, may happen to point in the direction of the fMEG signal at some latency. This is most likely to occur during signal peaks in the averaged auditory evoked response – such as N100, P200, etc. Hence, vectors may be found by chance that improve the SNR of the fMEG. Inspection of each of the time-series was required to find those showing the fMEG auditory evoked response

The steady-state evoked response signal is recovered from the MEG measurements using spectral decomposition. Since synaptic connections may be represented as rectifiers, one expects to see even numbered harmonics of the stimulus signal appearing in the MEG. Since the fetal MEG measurements were conducted in an unshielded environment, the spectrum in the vicinity of 30 Hz (the expected 2^{nd}-harmonic of the 15 Hz stimulus) was badly contaminated by numerous spectral lines. Formation of the synthetic 2^{nd}-order gradiometer response required a linear combination of the reference array with each primary MEG sensor. That linear combination is frequency independent. However, the presence of eddy-current scatterers, such as RF shields, connectors, and other conducting bodies near the sensors, results in frequency-dependent terms. These terms become significant when measurements are conducted in the unshielded environment. The frequency-dependent noise can be removed by the process of adaptive coherence balancing.

Results

Without noise reduction, the transient evoked response to the tone bursts could be observed in a few individual averaged channels, with a signal-to-noise ratio as high as 1:1 (bandwidth dc – 30 Hz). The putative evoked response waveform had an amplitude of only 40 fT peak, in the best channel. The latency at the peak of the response could not be determined due to the noise. Following adaptive balancing, using the reference channels, the evoked response waveform could be seen clearly in all six primary sensors. This is shown in Fig. 1. The SNR of the evoked response increased to 2:1, in the best channel. The latency at the peak of the response was 125 ms. Thus, the transient evoked response waveform corresponded to be the adult N100 wave. We observed a peak-to-peak noise of approximately 20 fT in these denoised averages. This excess noise did not correlate with the reference sensors.

When the response was observed through the signal-space vector filter, signal-to-noise ratio improved dramatically at latencies around 200 ms. Three examples are shown in Fig. 2, for signal-space vectors at 180, 225, and 230 ms. The noise increased dramatically when using signal vectors at other latencies, including near the putative N100 peak. As can seen in Fig. 2, the filter emphasized a wave at a latency of about 200 ms, raising its SNR to about 4:1. The putative N100 wave – still visible – has been attenuated by the vector filter.

The steady-state evoked response appeared as the 2^{nd}-harmonic of the click frequency, which was slightly less than 15 Hz. A 30 Hz response appeared in all six sensor channels but was not seen in any of the reference channels. Additional spectral lines were seen close to the 30 Hz line. However, these were removed by a process of frequency dependent coherence balancing. An example of the spectrum before and after adaptive balancing is shown in Fig. 3. The response in this channel was 16 fT rms in a 0.1 Hz bandwidth. The sensor white noise level was 10 fT per root Hz in the vicinity of the 2^{nd}-harmonic peak. The click stimulus was recorded independently on an analog input channel and digitized at 1250 Hz (following a 300 Hz lowpass filter) with the SQUID data. The spectrum of this channel showed the 2^{nd}-harmonic at precisely the same frequency as was observed in the sensor channels.

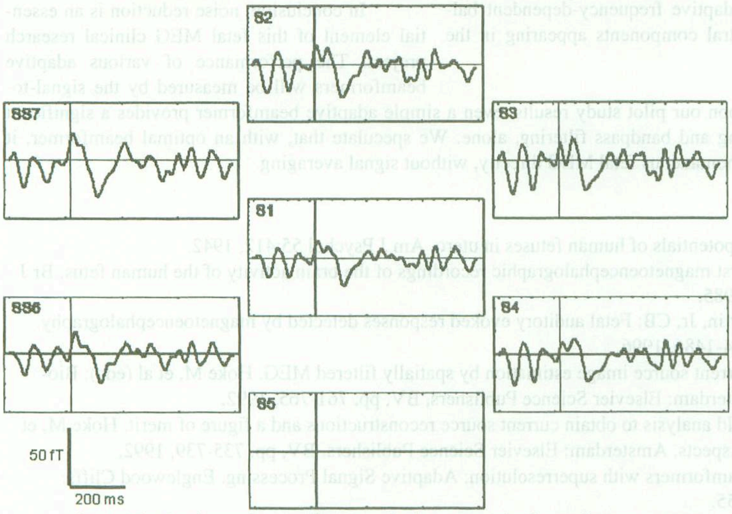

Fig. 1: The fetal transient auditory evoked response is shown here as a montage of sensor averages (dc – 30 Hz, N = 600). Adaptive linear noise reduction was used to attenuate environmental noise, using the reference sensor array. The residual noise seen here is, in part, due to interference from the fetal heart. The amplitude of the noise has the same spatial distribution as the fetal MCG, as seen in the spontaneous record.

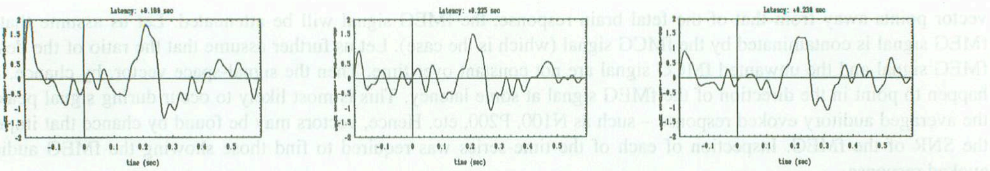

Fig. 2: Three synthetic averaged time series of the fetal transient auditory evoked response were derived using mean signal vectors at 180, 225, and 230 ms (Traces: dc – 30 Hz, N = 600). These examples represent the linear combination signals from the six primary SQUID sensors, derived by adaptive beamforming. The beamformer rejected correlated signal arriving from signal-space directions other than that of the selected vector. Time series derived at other latencies had much poorer signal-to-noise ratio.

Discussion

Signal-space filtering was extremely effective at increasing the signal-to-noise of the evoked response. This method suffered from there being too few channels available. This implies that there was not enough signal-space information to attenuate all the interfering sources. In addition, this technique requires that there be sufficient SNR, at some latency in the average, to properly characterize the signal vector of the fetal evoked response signal. A more powerful method is to apply a spatially selective filter to the data [4]. Since the precise position of the fetal head, relative to the sensors, is generally not known, the spatial filtering method would require an exhaustive search for the coordinate corresponding to (for example) the fetal auditory cortex.

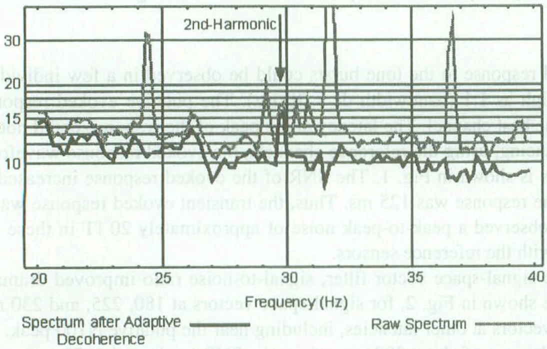

Fig. 3: The 2nd-harmonic of the steady-state fetal auditory evoked response appears as a spectral line at slightly below 30 Hz. This line was coherent with the click stimulus, and did not appear in any of the reference channels. Adaptive frequency-dependent balancing was used to remove spectral components appearing in the environment.

It is particularly disturbing that the signal-space vector filter that enhanced the putative P200 response did not greatly improve the N100. This suggests that the signal-space vectors corresponding to these two events were different, implying that the spatial location of the N100 and P200 generators must have been different.

In conclusion, noise reduction is an essential element of this fetal MEG clinical research project. The performance of various adaptive beamformers will be measured by the signal-to-noise ratio they provide. Based upon our pilot study results, even a simple adaptive beamformer provides a significant improvement over signal averaging and bandpass filtering, alone. We speculate that, with an optimal beamformer, it may even be possible to observe spontaneous fetal MEG directly, without signal averaging.

References

[1] Lindsley DB: Heart and Brain potentials of human fetuses in utero. Am J Psychol 55:412, 1942.

[2] Blum T, Saling E, Bauer R: First magnetoencephalographic recordings of the brain activity of the human fetus. Br J Obstet Gynaecol 95: 1224-1229, 1985.

[3] Wakai RT, Leuthhold AC, Martin, Jr, CB: Fetal auditory evoked responses detected by magnetoencephalography. Am J Obstet Gynecol 174 (8): 1484-1486, 1996.

[4] Robinson SE and Rose DF: Current source image estimation by spatially filtered MEG. Hoke M, et al (eds): Biomagnetism: Clinical Aspects, Amsterdam: Elsevier Science Publishers, BV, pp. 761-765, 1992.

[5] Tesche CD: Exploiting lead field analysis to obtain current source reconstructions and a figure of merit. Hoke M, et al (eds): Biomagnetism: Clinical Aspects, Amsterdam: Elsevier Science Publishers, BV, pp. 735-739, 1992.

[6] Widrow B and Stearns SD: Beamformers with superresolution: Adaptive Signal Processing. Englewood Cliffs: Prentice-Hall, Inc, 1985, pp 445-455.

[7] Widrow B, Mantey PE, et al: Adaptive antenna systems. Proc IEEE, 55: 2143-2159, 1967.

[8] Frost OL, An algorithm for linearly constrained adaptive array processing, Proc IEEE, 60: 926-935, 1972.

The classification of foetal cardiac conduction disorders by means of magnetocardiography

Huirne JAF[1], Krooshoop HJG[2], Quartero HWP[1], Peters MJ[2]

Department of Obstetrics and Gynaecology, Medisch Spectrum Twente[1], Enschede, The Netherlands; University of Twente[2], Low Temperature division, Graduate School iBME, Enschede The Netherlands.

Introduction

Currently, the diagnosis of foetal arrhythmias relies on an ultrasound evaluation of cardiac anatomy and M-mode analysis of atrial and ventricular contraction patterns. Foetal electrocardiography (fECG) has failed to provide a reliable tool in this respect mostly due to the large interference of the maternal electrocardiogram and the insulating effect of the surrounding tissues. Generally, the recording of an fECG using abdominal leads provides no information about the P- and T-waves in the unaveraged traces. Foetal magnetocardiography (fMCG) is a non-invasive technique to detect the magnetic field generated by the electrical activity of the foetal heart, using superconducting quantum interference devices (SQUIDs). The fMCG is less hampered by the problems of fECG; it is less influenced by the maternal cardiac electrical activity and by the insulating effects of the surrounding tissues, *e.g.* the vernix caseosa [1,2]. Consequently, the signal-to-noise ratio is higher than that of fECG. Hence in the second and third trimester of pregnancy, it can be used to obtain the foetal heart rate with a beat-to-beat accuracy. In this paper, the diagnostic use of fMCG in five pregnant women with foetal arrhythmias is discussed.

Methods

From five pregnant women referred with foetal arrhythmia, informed consent was obtained to perform fMCG, once standard ultrasound evaluation had been completed. The experimental nature of the fMCG technique was fully explained to the women. Ethical approval from the local ethical committee was received. The fMCG recordings were performed using a custom-made SQUID magnetometer, cooled with liquid helium. To reduce the influence of electromagnetic disturbances, the measurements were carried out in a magnetically shielded room. Measurements were performed with the woman in a supine position. An adjustable gantry allowed repositioning of the cryostat containing the sensors. Palpation and Doppler ultrasound were used to determine the position of the foetal heart, to optimise the sensor positions. During the fMCG measurements simultaneous recording of the maternal ECG took place to provide a trigger allowing elimination of the maternal cardiac signal from the MCG tracing. To enhance the signal-to-noise ratio the fMCG signals were averaged using the top of the R-peak as a trigger. For foetal R-peak detection a matched filter and a threshold were used [3].

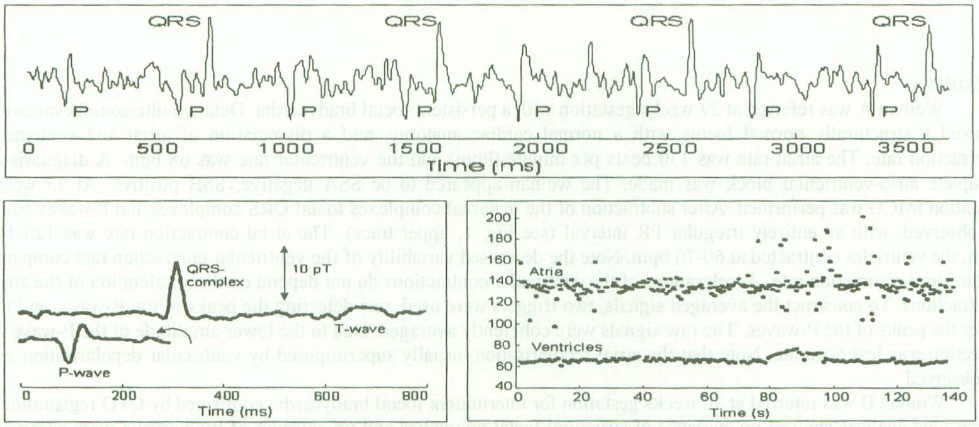

Fig. 1 Registrations of foetus A. The signals are averaged in two ways; using the R-peak (left, higher trace), and using the P-peak as a trigger (left, lower trace). The repolarisation of the atria is indicated by an arrow. The foetal heart rates are given in bpm for the atria (upper trace) and ventricles (lower trace).

©1999, Tohoku University Press
Recent Advances in Biomagnetism
T. Yoshimoto et al. (Eds)

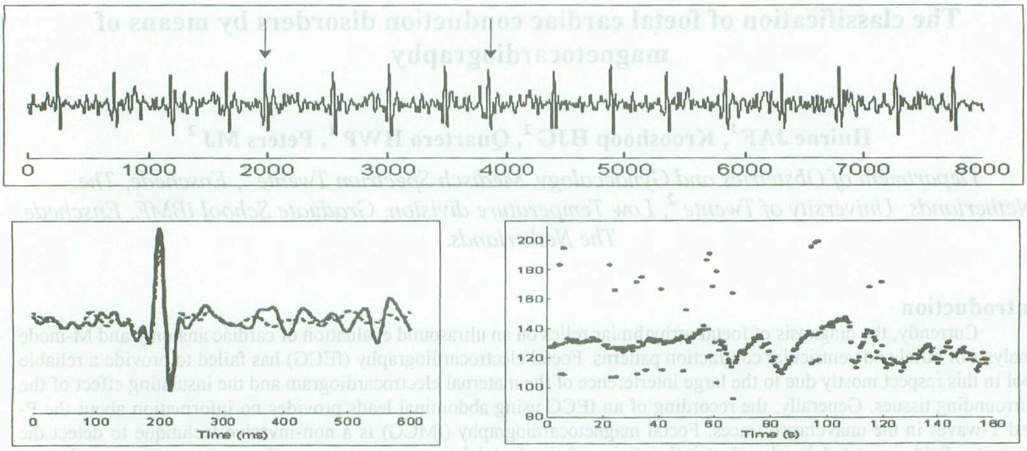

Fig.2 Registration of foetus B. Premature beats are indicated by arrows. The averages of the normal beats (closed line) are superimposed on the averages of the premature beats (dashed line).

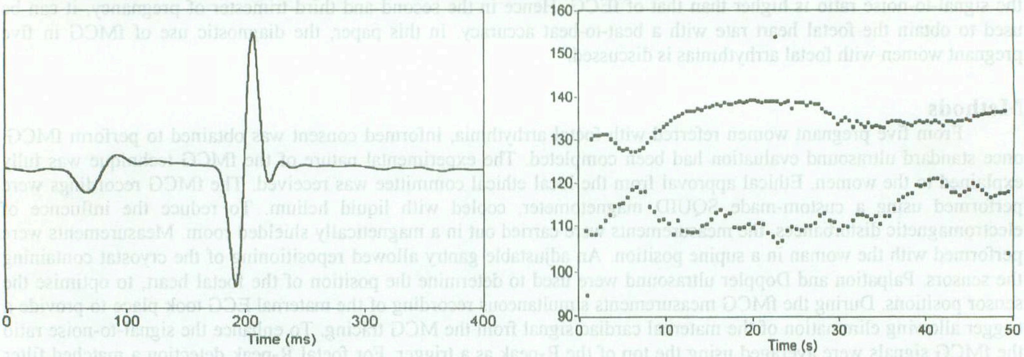

Fig. 3 Registrations of foetus C. The averaged signal shows a prolonged PR-interval of 126 ms. Both the heart rate of the foetus (upper trace) as well as that of the mother are depicted.

Results

Woman A was referred at 27 weeks gestation with a persistent foetal bradycardia. Detailed ultrasound evaluation showed a structurally normal foetus with a normal cardiac anatomy, and a dissociation of atrial and ventricular contraction rate. The atrial rate was 130 beats per minute (bpm) and the ventricular rate was 68 bpm. A diagnosis of complete atrio-ventricular block was made. The woman appeared to be SSA negative, SSB positive. At 35 weeks gestation fMCG was performed. After subtraction of the maternal complexes foetal QRS complexes and P-waves could be observed, with an entirely irregular PR interval (see Fig. 1, upper trace). The atrial contraction rate was 120-140 bpm, the ventricles contracted at 60-70 bpm. Note the decreased variability of the ventricular contraction rate compared to the atrial contraction rate. Accelerations of the ventricular contractions do not depend on the acceleration of the atrial contractions. To construct the averaged signals, two triggers were used, one detecting the peaks of the R-wave, and the other the peaks of the P-waves. The raw signals were coherently averaged. Due to the lower amplitude of the P-wave its detection was less accurate. Note that the atrial repolarisation, usually superimposed by ventricular depolarisation can be observed.

Woman B was referred at 30 weeks gestation for intermittent foetal bradycardia confirmed by CTG registrations. Ultrasound analysis showed no evidence of structural foetal anomalies and no episodes of bradycardia were observed. Some extrasystolic beats were seen. FMCG was performed at 31 weeks gestation. The traces show short cycles followed by a compensatory pause, alternated by a cardiac cycle of normal duration (see. Fig. 2). This can be ascribed to supraventricular extrasystoly. The pattern is normal except for the various premature beats appearing during the quieter stages. To differentiate between normal and extrasystolic beats, the average was calculated for each type of beat. Both normal and extrasystolic beats show the same morphology. The identical morphology of the QRS complexes assumes a supraventricular origin.

Woman C was referred with an intermittent bradycardia at 30 weeks gestation. Ultrasound evaluation showed no evidence of foetal structural anomalies. No arrhythmia was observed despite repeated examinations. At 33 weeks gestation fMCG was performed. All registrations showed a fixed PR interval. This PR interval, defined as the duration of the interval between the beginning of the P-wave and the onset of the QRS complex had a duration of 126 ms, see Fig. 3. This PR interval seems to be prolonged if we compare this PR interval to the PR interval of registrations performed for healthy foetuses at the same gestational age as found in the literature [4,5]. A diagnosis of a first degree AV conduction block was made.

Woman D was referred because of a foetal tachyarrhythmia at 30 weeks gestation. Ultrasound analysis showed no evidence of foetal structural anomalies and confirmed a foetal tachycardia of 220-240 bpm. The pregnancy had been uncomplicated otherwise and no evidence of infection could be found. Treatment with flecanide 80mg tds was installed, resulting in a foetal heart rate of approximately 114 bpm as established by ultraound. Unfortunately, episodes of tachyarrhythmia recurred intermittently. FMCG was performed at 32 weeks gestation and a 12 minute recording time

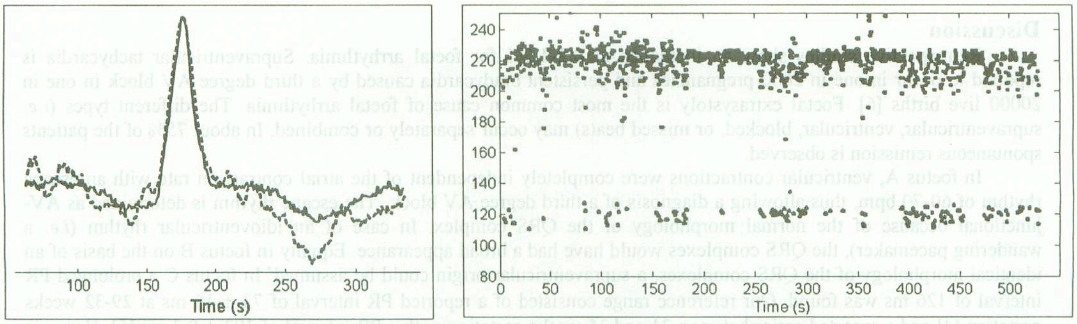

Fig.4 Registrations of foetus D. The foetal heart rate shifts between 120 bpm and 220 bpm in an irregular way. The signals are averaged in two different ways that are superimposed; first, taking the R-peak of the fast beats as a trigger (closed line) and second, taking the R-peak of the slower beats as a trigger (dashed line).

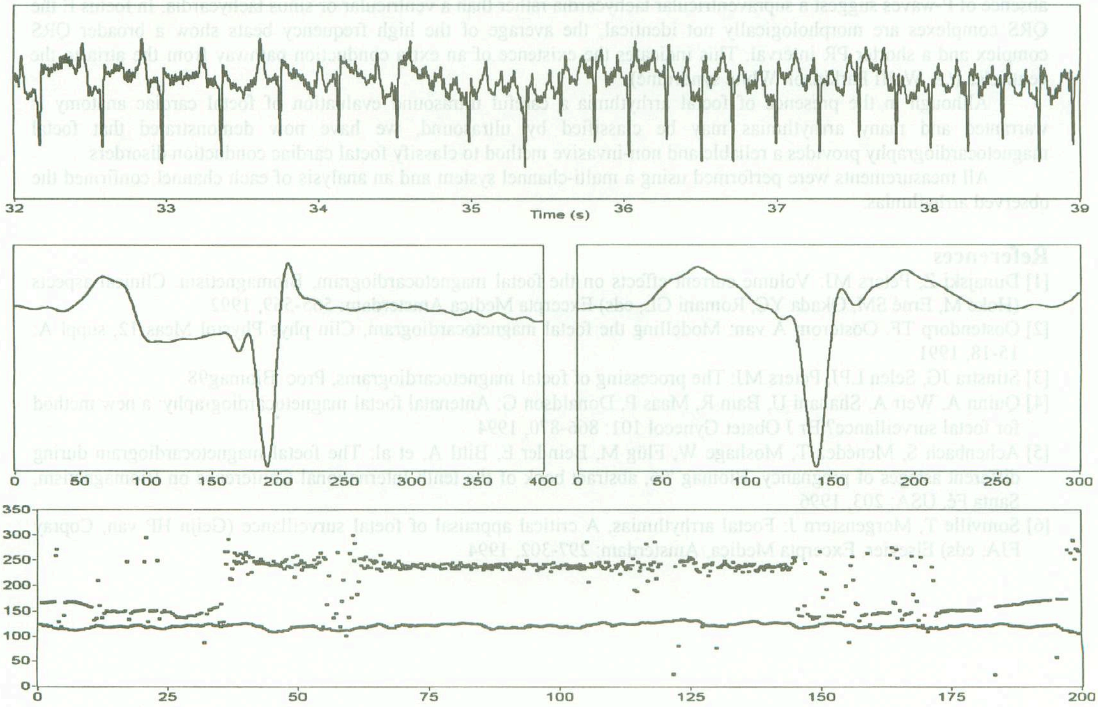

Fig. 5 Registration of foetus E. The foetal heart rate shifts between 150-170 bpm and 250 bpm. The signals are averaged in two different ways; taking the R-peaks of the fast beats as a trigger (middle right) and taking the R-peaks of the slower beats as a trigger (middle left). Both the heart rates of the foetus and the mother (± 130 bpm) are shown.

was used. Shifts between a foetal heart rate of 220 bpm and 120 bpm were observed, in an irregular way, see Fig.4. Compensation of the slower beats is not observed. The averaged signals during episodes of tachycardia and those during normal heart rate were identical morphologically with an absent P-wave and a distinct T-wave. A diagnosis of supraventricular tachycardia was made.

Woman E was referred with tachyarrhythmic episodes at 36 weeks gestation. The pregnancy had been uncomplicated otherwise. Ultrasound analysis assumed the existence of an atrial flutter, without evidence of structural foetal anomalies. FMCG registrations, performed at 36 weeks gestation, showed a foetal heart rate pattern with a basic contraction rate of 150-170 bpm and tachycardiac episodes of 240-250 bpm, as shown in Fig. 5. The records were averaged in two ways, first taking the R-peaks of the normal beats as a trigger (Fig. 5, left trace), second taking the R-peaks during episodes of tachycardia as a trigger (Fig. 5, right trace). These averages are not identical, the average of the PQRST complexes during episodes of tachycardia shows a shorter PR interval, the QRS complex has a broader aspect, and the T wave is more obvious.

Discussion

Retrospective studies show an incidence of 0.2-1.3% for foetal arrhythmia. Supraventricular tachycardia is reported to occur in one in 2000 pregnancies and persistent bradycardia caused by a third degree AV block in one in 20000 live births [6]. Foetal extrasystoly is the most common cause of foetal arrhythmia. The different types (*i.e.* supraventricular, ventricular, blocked, or missed beats) may occur separately or combined. In about 75% of the patients spontaneous remission is observed.

In foetus A, ventricular contractions were completely independent of the atrial contraction rate with an escape rhythm of 60-70 bpm, thus allowing a diagnosis of a third degree AV block. The escape rhythm is determined as AV-junctional because of the normal morphology of the QRS complex. In case of an idioventricular rhythm (*i.e.* a wandering pacemaker), the QRS complexes would have had a broad appearance. Equally in foetus B on the basis of an identical morphology of the QRS complexes, a supraventricular origin could be assumed. In foetus C a prolonged PR interval of 126 ms was found. Our reference range consisted of a reported PR interval of 73 ± 16 ms at 29-32 weeks gestation [4] and a reported series between 31 and 35 weeks gestation with a PR interval of 103 ± 9.3 ms [5]. Hence, a diagnosis of a first degree AV block was made. To our knowledge, no PR intervals obtained from fECG using abdominal leads have been reported, most likely because the P-wave is not detected due to the insulating effect of the vernix caseosa during that period of gestation. In foetus D, the identical morphology of the QRS complexes and the absence of P-waves suggest a supraventricular tachycardia rather than a ventricular or sinus tachycardia. In foetus E the QRS complexes are morphologically not identical, the average of the high frequency beats show a broader QRS complex and a shorter PR interval. This indicates the existence of an extra conduction pathway from the atria to the ventricles (*i.e.* Wolff Parkinson White syndrome).

Although in the presence of foetal arrhythmia a careful ultrasound evaluation of foetal cardiac anatomy is warranted and many arrhythmias may be classified by ultrasound, we have now demonstrated that foetal magnetocardiography provides a reliable and non-invasive method to classify foetal cardiac conduction disorders.

All measurements were performed using a multi-channel system and an analysis of each channel confirmed the observed arrhythmias.

References

[1] Dunajski Z, Peters MJ: Volume current effects on the foetal magnetocardiogram, Biomagnetism: Clinical aspects (Hoke M, Erné SM, Okada YC, Romani GL, eds) Excerpta Medica Amsterdam: 565-569, 1992

[2] Oostendorp TF. Oosterom A van: Modelling the foetal magnetocardiogram, Clin phys Physiol Meas 12, suppl A: 15-18, 1991

[3] Stinstra JG, Selen LPJ, Peters MJ: The processing of foetal magnetocardiograms, Proc. Biomag98

[4] Quinn A, Weir A, Shahani U, Bain R, Maas P, Donaldson G: Antenatal foetal magnetocardiography: a new method for foetal surveillance? Br J Obstet Gynecol 101: 866-870, 1994

[5] Achenbach S, Menédez T, Moshage W, Flüg M, Beinder E, Bittl A, et al: The foetal magnetocardiogram during different astages of pregnancy, Biomag '96, abstract book of the tenth International Conference on Biomagnetism, Santa Fé, USA: 203, 1996

[6] Somville T, Morgenstern J: Foetal arrhythmias, A critical appraisal of foetal surveillance (Geijn HP van, Copray FJA, eds) Elsevier, Excerpta Medica, Amsterdam: 297-302, 1994

The Processing of foetal Magnetocardiograms

Stinstra JG, Selen LPJ, Peters MJ

University of Twente, Low Temperature Division, Graduate School iBME, Enschede, The Netherlands

Introduction

Foetal magnetocardiograms (fMCGs) can be used to diagnose and classify cardiac arrhythmias [1]. Usually, the duration of the RR-interval can be reliably deduced from the measurements. However, the diagnostic applicability of fMCG is still limited, because the onset and strengths of the P- and T-waves cannot be determined reliably. Noise sources, such as baseline wandering, powerline interference, muscle activity, instrumental noise, or disturbances from traffic affect the measurements. Due to the presence of noise, the typical PQRST-waveform of a heart signal is hardly recognisable in the raw data. In order to obtain a useful recording the raw data is filtered and an average PQRST-waveform is calculated. However, the P- and T-wave are often indistinguishable in the averaged signal. This may have various reasons.

1) The vernix caseosa may act as a highpass filter, filtering out the low frequency components of the P- and T-wave. This could deform the shape of both waves, making it hard to recognise them [2].

2) It may be due to the signal processing (*i.e.* filtering and coherent averaging). The choice of the sample frequency and the lowpass filters is based on the frequency content of the signal. This knowledge is based on cardiograms of neonates and adults and may be not correct. For adults the maximum frequencies that can be assessed from an ECG are f_{max} = 55 Hz for the P-wave; f_{max} = 65 Hz for the QRS-complex, and f_{max} = 25 Hz for the T-wave [3]. The averaging procedure is based on the assumptions that the signal does not change in time and that the noise is uncorrelated with respect to the detected triggers (R-peaks). The former assumption is violated when the foetus moves with respect to the pick-up coil. Also breathing of the mother will affect the signal. In practise the duration of the PR-interval and that of the RT-interval are irregular. Fluctuations in these intervals may be of physiological origin. For instance, the fluctuations in the AV-conduction time may give rise to fluctuations in the duration of the PR-interval [4]. For healthy adults the standard deviation in both the PR- and the RT-interval is found to be about 1.5 ms. In addition, errors in the determination of the triggers increase these fluctuations. Consequently, the averaging procedure gives rise to a deformation of the signal that can be modelled as a lowpass filter. For fluctuations of about 1.5 ms the cut-off frequency is 73 Hz and for fluctuations of longer duration this frequency is lower [5].

3) The disappearance of the P- and T-waves may be partly due to the magnetometer system. For instance, the flux transformer acts as a spatial filter and may have a larger cancelling effect on the T-wave than on the other waves.

4) Because the foetal heart differs from that of an adult, the T-wave may not be present or may have a different morphology, that does not resemble the morphology of an adult T-wave.

5) The P-wave and T-wave may be observable in those measuring positions where the QRS-complex is not distinguishable or they may be observable in another component of the magnetic field.

Magnetometer systems that are presently used are very expensive and a skilled technician is necessary to perform the measurements. Therefore, we want to design a foetal magnetocardiograph that is user-friendly, transportable, needs nitrogen as a coolant, and can be used in a clinical (unshielded) environment [6]. A relatively simple magnetometer is a one-channel system. In the present paper, the signal processing performed on recordings using a one-channel system, is evaluated and illustrated for an fMCG measurement during the 34th week of gestation. The measurement is complicated, because the mother was pregnant of twins.

Method

Foetal MCGs are measured in a magnetically shielded room by means of a one-channel first-order gradiometer. The component of the field in the vertical direction is recorded with the mother in supine position underneath the system. In many measuring points over the maternal abdomen, the signal-to-noise ratio of a measured fMCG is too low to distinguish foetal QRS-complexes from the noise by eye. If so, the pickup coil is repositioned and the measurement is repeated. This procedure is time consuming. To avoid the measurement becoming a burden for the mother, the measurement time is not allowed to exceed

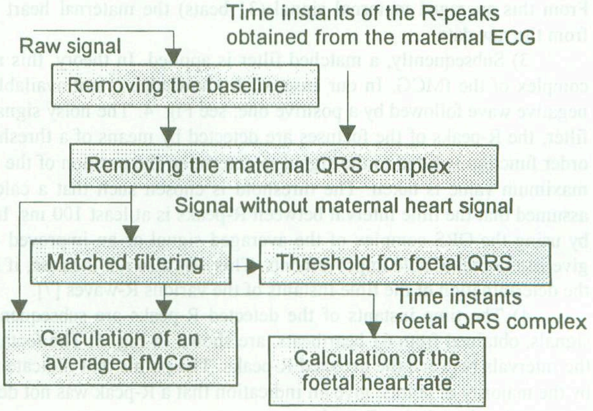

Fig. 1 The signal processing scheme

©1999, Tohoku University Press
Recent Advances in Biomagnetism
T. Yoshimoto et al. (Eds)

20 minutes. Consequently, an optimal position with a one-channel system is often not found. Hence, an fMCG signal is recorded under noisy conditions, even when measured in a magnetically shielded room. Therefore, it has to be thoroughly processed in order to acquire a signal, in which the different stages of the depolarisation and repolarisation of the heart are visible. Sometimes, the measured fMCG is severely contaminated by signals from the maternal heart. To be able to distinguish between maternal and foetal heart signals, an ECG of the mother is measured simultaneously. The mother's ECG is measured via electrodes attached to the right wrist and the left ankle.

In the next section, the signal processing procedure is illustrated for a rather poor fMCG measurement (the signal-to-noise ratio is low) that is complicated, because the mother is pregnant of twins. The foetuses were lying on top of each other in a transverse position. Both heads were at the left side. The magnetic field was measured at different positions.

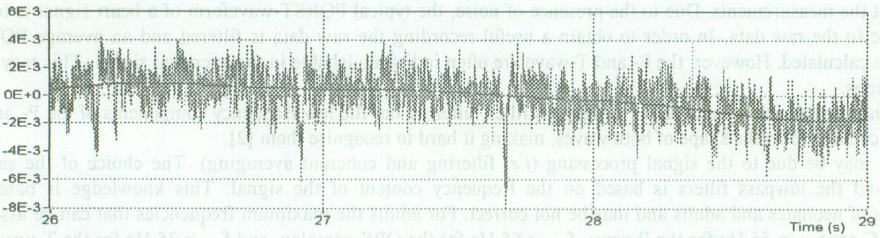

Fig. 2 Correction of the baseline wandering. Raw signal, with superimposed the output of the lowpass filter (1 Hz).

Signal Processing

In order to measure the foetal heart rate and to calculate an averaged signal, the individual heartbeats have to be detected and aligned. The algorithm to calculate the averaged signal and the foetal heart rate has four main stages: 1) removal of baseline wandering, 2) removal of the maternal heart contribution, 3) R-peak detection in the foetal fMCG, and 4) coherently averaging of the individual beats and calculation of the foetal heart rate. The signal processing is performed using LabView® and the scheme is pictured in Fig.1. This scheme will now be illustrated using a signal recorded above the right upper quadrant of the maternal abdomen.

1) Fig. 2 shows original (raw) data against time. The units in all our figures are volts (the output of our magnetometer system). In our case, the sensitivity of the magnetometer system is estimated at 4×10^{-10} T/V. The signal was sampled with a frequency of 1 kHz and was filtered between 0.1 Hz and 470 Hz. The first processing stage removes fluctuations in the baseline by using a lowpass FIR filter having 2001 coefficients and a cut-off frequency of 1 Hz. The resulting signal is then subtracted from the original signal.

2) The removal of the contribution of the maternal heart is depicted in Fig. 3. An averaged maternal MCG signal is calculated, using the time instants of the peaks of the R-waves obtained from the maternal ECG as a trigger for coherently averaging. After coherently averaging, there is still an offset present in the averaged signal. By assuming that the averaged signal is zero during the pre-P-wave and post-T-wave intervals, the offset can be calculated and subsequently removed. The averaged signal describes the contribution of the maternal heart at the position where the fMCG is measured. Usually, this averaged maternal signal shows a QRS-complex and a T-wave. From this averaged maternal signal (31 beats) the maternal heart signal is reconstructed, which is then subtracted from the raw data.

3) Subsequently, a matched filter is applied. In theory, this requires prior knowledge of the shape of the QRS complex of the fMCG. In our case, such knowledge is not available. Hence, a template is chosen that consists of a negative wave followed by a positive one, see Fig. 4. The noisy signal is correlated with this template. After using this filter, the R-peaks of the foetuses are detected by means of a threshold chosen by hand. In order to do so, a second-order function is fitted to the signal to determine the position of the peak. The time instant where this function has its maximum value is taken. The threshold is chosen such that a calculated heart rate displays a regular rhythm. We assumed that the time interval between R-peaks is at least 100 ms. It is possible to derive the matched filter iteratively by using the QRS-complex of the averaged signal as an improved matched filter. In practice, this next step did not give rise to remarkable improvements. This was also not the case, if instead of a matched filter, wavelets were used for the determination of the time instants of the various R-waves [7].

4) The time instants of the detected R-peaks are subsequently used for coherently averaging. The averaged signals, obtained from 61 heartbeats, are shown in Fig. 5. The foetal heart rate in beats per minute is calculated from the intervals between the detected R-peaks. The points that indicate that the foetal heart rate is half the rate expressed by the majority of points, give an indication that a R-peak was not detected. Changing the threshold (locally) may help to recognise the missing R-peaks.

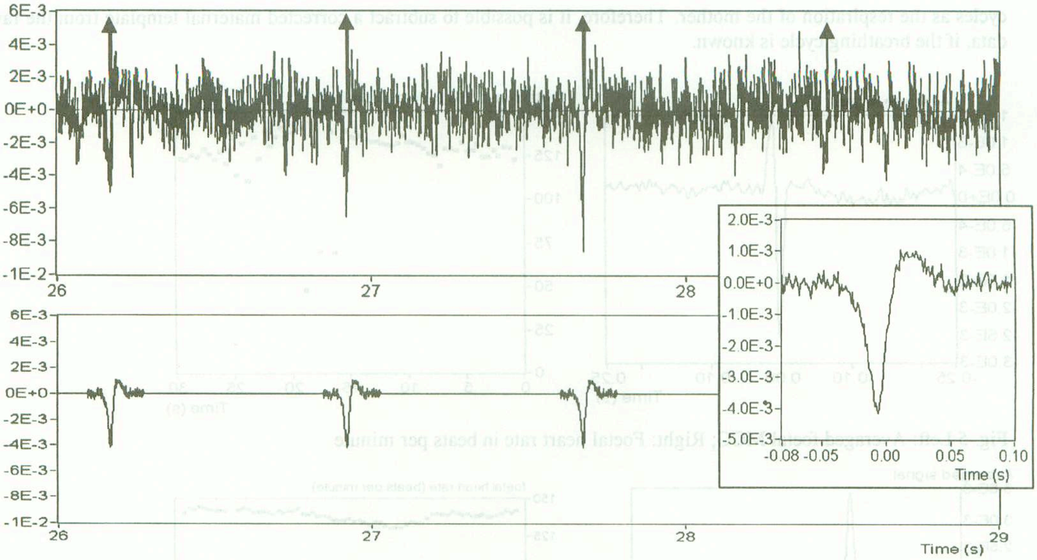

Fig. 3 Removal of the maternal heart contribution. Upper trace, the time instants of the R-peaks obtained from the maternal ECG are shown in the preprocessed data (Fig. 2 lower trace). Lower right, the averaged maternal contribution. Lower left: the template that will be subtracted from the preprocessed data.

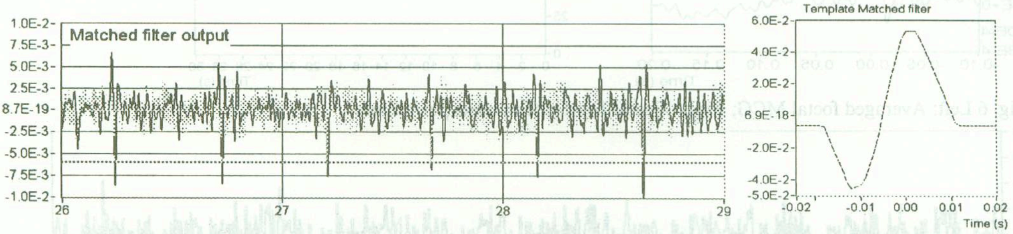

Fig. 4 Detection of the R-peaks of one foetus using the matched filter (right). In the trace showing the data after the application of the matched filter (left), the chosen threshold is indicated (at about -6×10^{-3}).

The results for a measurement above the right lower quadrant of the maternal abdomen are shown in Fig. 6. Presumably, the results of Figs. 5 and 6 are of different foetuses. In signals measured in positions between the measurement points of Figs. 5 and 6, foetal contributions were hardly recognisable, see Fig. 7. Although not with a beat-to-beat accuracy, some R-waves of the foetuses are observable.

Discussion

Foetal magnetocardiograms measured above the maternal abdomen can be used to diagnose and classify cardiac arrhythmias as the duration of cardiac time intervals can be reliably deduced from the measurements. Moreover, the analysis of spontaneous fluctuations in the foetal heart rate can be used for the investigation of the neurocardiovascular system.

As the simplest magnetometer is a one-channel system, the possibilities of such a system are evaluated. The signal processing is illustrated for noisy measurements of a twin pregnancy. With a one-channel system, it turns out to be impossible to find a position where both foetuses generate a signal with an adequate signal-to-noise ratio. Therefore, it is recommended to enhance the number of channels of the magnetometer system. Another reason in favour of using a multi-channel system is that more information will be available on signals, disturbances, and noise. This knowledge can be used to design a better signal processing procedure and to determine the reliability of the signals after signal processing. If more fMCGs are measured simultaneously, the results can be used to confirm the observed foetal heart rate, as the foetal heart signal should be observed in more channels. The time instants obtained from a channel with an adequate signal-to-noise ratio can be used also for coherently averaging of signals from a channel with a poor signal-to-noise ratio. Additional information may also be obtained by other means, like a Doppler ultrasound measurement to determine the maternal breathing cycle or the position of the foetal heart. For instance, the amplitudes of the maternal R-waves found in the raw data measured above the maternal abdomen show the same time

cycles as the respiration of the mother. Therefore, it is possible to subtract a corrected maternal template from the raw data, if the breathing cycle is known.

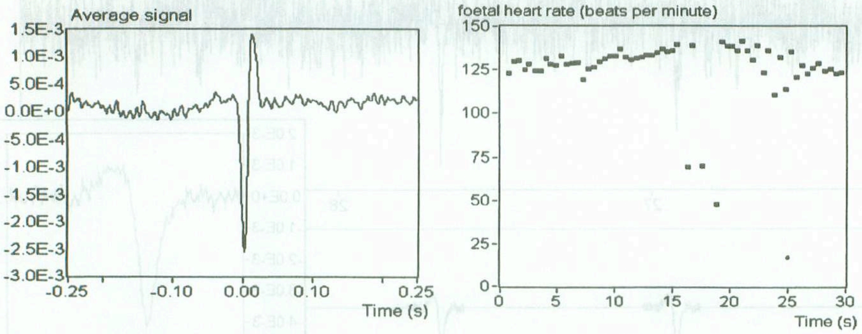

Fig. 5 Left: Averaged foetal MCG; Right: Foetal heart rate in beats per minute

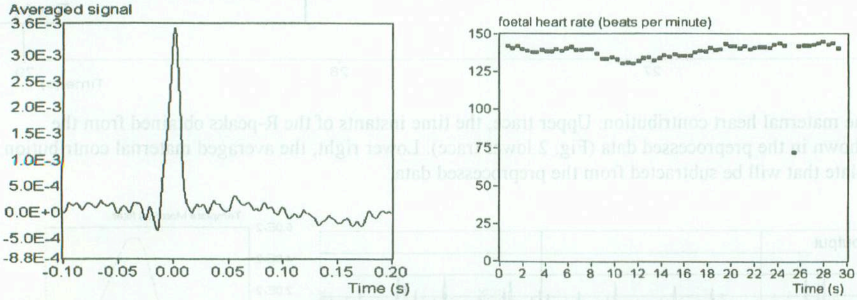

Fig. 6 Left: Averaged foetal MCG; Right: Foetal heart rate in beats per minute

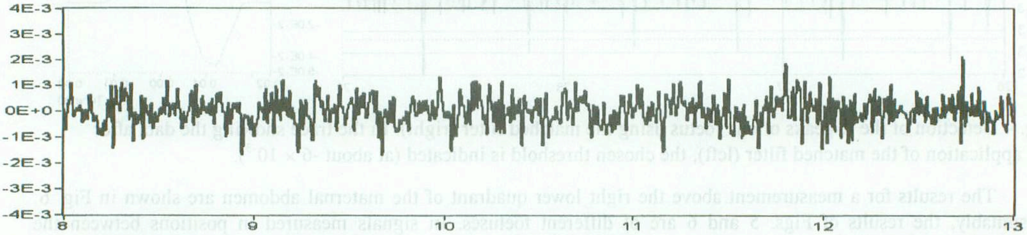

Fig. 7 fMCG recorded at a position in between those of Figs. 5 and 6 (band-pass filtered between 1 Hz and 60 Hz)

References

[1] Huirne JAF, Krooshoop HJG, Quartero HWP, Peters MJ: The classification of foetal cardiac conduction disorders by means of magnetocardiography, Proc. Biomag98

[2] Stinstra JG, Krooshoop HJG, Muis B, Peters MJ, Huirne JAF, Quartero HWP: The influence of the vernix caseosa on foetal cardiograms, Proc. Biomag98

[3] Rompelman O, Janssen RJ: Use of phase reversal information in assessment of frequency contents of ECG waveforms, IEE Proc. 129, Pt. A: 679-683, 1982

[4] Heethaar RM: A mathematical model of AV-conduction in the rat heart, PhD thesis, Utrecht, The Netherlands, 1972

[5] Rompelman O, Ros HH: Coherent averaging technique: A tutorial review, Part 1: Noise reduction and equivalent filter, Part 2: Trigger jitter, overlapping responses and non-periodic stimulation, J. Biomed. Eng. 8: 24-35, 1985

[6] Brake M ter, Peters M, Rogalla H: Application of SQUID magnetometers in foetal magnetocardiography, Rogalla H, (ed) Applied superconductivity, Instit of Physics Conf series, IOP, 1997, pp 771-774

[7] Li C, Zheng C, Tai C: Detection of ECG characteristic points using wavelet transforms, IEEE Trans on Biomed Eng, 42: 21-28, 1995

Assessment of the Fetal Neuronal Maturation using Auditory Evoked Fields in Fetal Magnetoencephalography

Schleussner E[1], Schneider U[1], Olbertz D[2], Kähler C[1], Huonker R[3], Michels W[1], Nowak H[3], Seewald H-J

Department of Gynaecology and Obstetrics [1]; Department of Paediatrics [2]; Biomagnetic Centre[3];
Friedrich-Schiller-University Jena, Germany

Introduction

Decisive stages of human neuronal maturation are passed through during the last month of gestation and the first 3 months of infant life. Currently there are no reliable tests to directly assess functional integrity of the fetal brain. Therefore a non-invasive method providing exact information about the state of cerebral maturation and malfunctional development could prove a highly valuable tool in preventing cerebral impairment and reduce the risk of later disability from a clinical point of view. Fetal magnetoencephalography (fMEG) is the only non-invasive method to detect such functional maturation processes and their possible disturbances.

While first magnetoencephalographic recordings of the brain activity of a human fetus were reported by Blum et al 1986 [1], until now the reproduction of evoked responses from the fetal brain is quite difficult. Methodical problems are particularly due to the registration of the very weak fetal biomagnetic fields.

Methods

We used a 31-channel-SQUID-magnetometer (Philips) [2] in a magnetically shielded room (AK 3b, Vacuumschmelze Hanau) to record auditory evoked fields (AEF) of fetuses in the third trimester of gestation and preterm delivered babies of the same age of conception (CA). At the beginning of each session the fetal head was localised by real time ultrasound (SDR 1200, Philips). The Dewar was then positioned as close to the abdominal wall above the fetal head as possible to minimise the distance to the fetal brain. Fetal well-being and a state of relative rest according the fetal 1F phase of Nijhuis [3] were controlled by cardiotocography (HP 8040A, Hewlett Packard).

During fetal or neonatal sleep phase we applied 500 auditory stimuli generated by a computerised sound generator outside of the shielded room via a 5 m long plastic tube with a shower head at the end on the maternal abdominal wall next to the fetal head. We used 500 Hz or 1000 Hz tone bursts respectively with a sound level of 100 dB (70 dB in preterm infants) and 50 ms tone length. The inter-stimulus interval was 1000 ms with a single trial length of 800 ms recording time. For signal processing and analysis we used the CURRY software by Philips on a SUN workstation. The wide-band responses were digitally filtered with passbands 2.7 - 20 Hz, using a Fourier filter. The signal analyses were performed by (1) a simple averaging of the 500 trials, (2) medianising the data at a rate of 1/ms and (3) the principle component analysis (PCA).

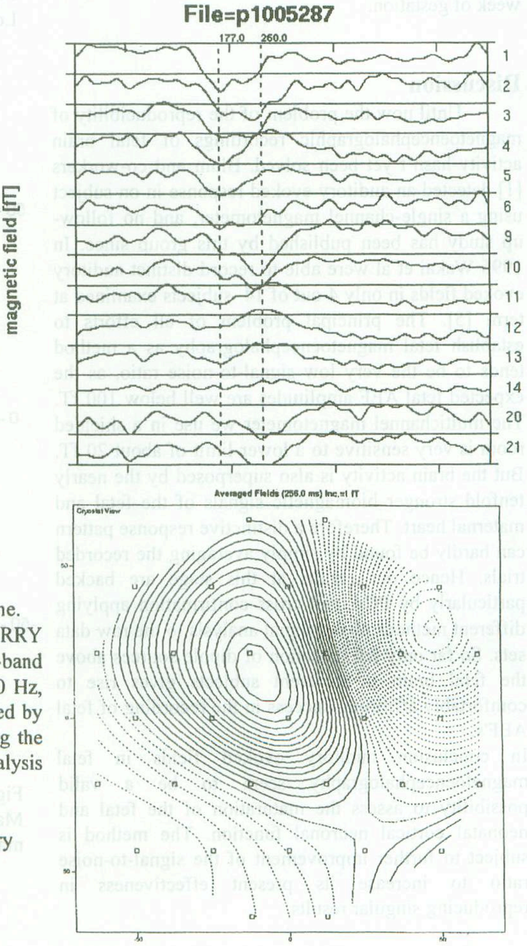

Figure 1. Averaged Signal and PCA revealing an auditory evoked response in an infant of 36 wks CA

©1999, Tohoku University Press
Recent Advances in Biomagnetism
T. Yoshimoto et al. (Eds)

Results

In collaboration with the Department of Paediatrics we performed studies in neonates from 34 weeks CA onwards who were all in stable condition and under permanent supervision. Written consent of the parents was obtained in advance. We were able to record auditory evoked responses in almost all subjects examined between 34 weeks and 41 weeks CA as shown in Figure 1. Lack of results could usually be attributed to movement of the infant during examination. Recordings at an early stage (34 - 36 weeks CA) show a long lasting deflection of the baseline rather than any particular pattern. Beyond the conceptional age of 36 weeks the evoked responses mature developing several peaks, higher amplitudes and a distinctive pattern almost comparable to those seen in older children by Paetau et al [4]. A representative example of a longitudinal study in a preterm born infant is given in Figure 2.

By using the results from neonates examined as a reference we recorded auditory evoked fields of fetuses during the third trimester of pregnancy. For the first time we are able to show a magnetic dipole source revealed by principal component analysis under the recording site above the fetal head in a pregnancy of 41 weeks proving an acoustic evoked response (Figure 3). The latency of it's occurrence is consistent with those measured in new-born of comparable CA. The earliest successful recording showing a singular magnetic source above a fetal head dates from the 34 week of gestation.

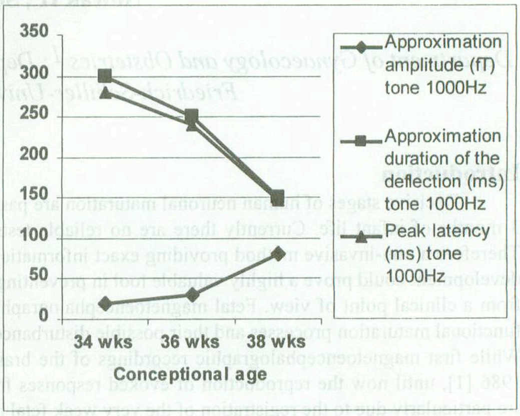

Figure 2
Longitudinal study in an infant at 34-38 wks CA

Discussion

Until now the problem of the reproducibility of magnetoencephalographic recordings of fetal brain activity hasn't yet been solved. Blum and co-workers [1] detected an auditory evoked response in on subject using a single-channel magnetometer, and no follow-up study has been published by this group since. In 1996 Wakai et al were able to record distinct auditory evoked fields in only 4 out of 14 subjects examined at term [5]. The principal problem of all efforts to establish fetal magnetoencephalography as a method tends to be the very low signal-to-noise ratio, as the expected fetal AEF amplitudes are well below 100 fT. The multichannel magnetometer we use in a shielded room is very sensitive to a lower limit of about 20 fT. But the brain activity is also superposed by the nearly tenfold stronger biomagnetic signals of the fetal and maternal heart. Therefore a distinctive response pattern can hardly be found by simply averaging the recorded trials. Hence our results at this stage are backed particularly by PCA and cross confirmation applying different methods of the signal analysis to the raw data sets. So far only the detection of dipole sources above the fetal brain in different subjects gives rise to comfortably affirming success in the recording of fetal AEF's.

In conclusion auditory evoked fields in fetal magnetoencephalography seem to be a valid possibility to assess the maturation of the fetal and neonatal cortical neuronal function. The method is subject to further improvement of the signal-to-noise ratio to increase its present effectiveness in reproducing singular results.

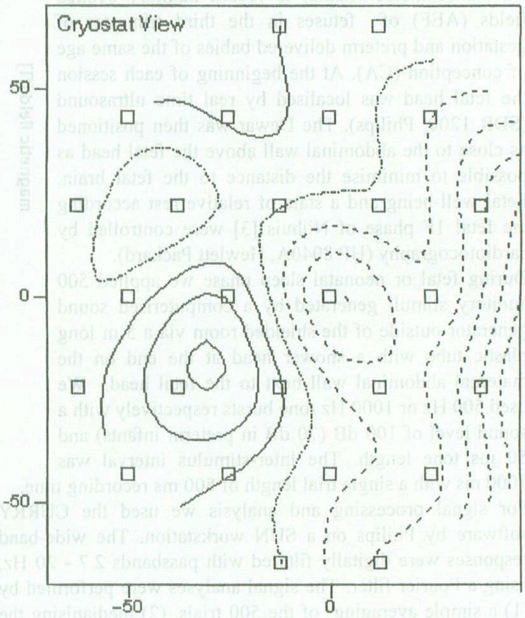

Figure 3
Magnetic dipole of the fetal brain recorded above the maternal abdominal wall in a pregnancy at term

References

[1] Blum T, Saling E, Bauer R: First magnetoencephalographic recordings of the brain activity of the human fetus. Br J Obstet Gynaecol 92: 1224-1229, 1985

[2] Dössel O, David B, Fuchs M, et al: A 31-channel SQUID system for biomagnetic imaging. Appl Supercond 1: 1813-1825, 1993

[3] Nijhuis JG, Prechtl HFR, Martin CB, et al: Are there behavioural states in the human fetus? Early Hum Dev 6: 177-195, 1982

[4] Paetau R, Ahonen A, Salonen O, et al: Auditory evoked magnetic fields to tones and pseudowords in healthy children and adults. J Clin Neurophys 12: 177-185, 1995

[5] Wakai RT, Leuthold AC, Martin CB: Fetal auditory evoked responses detected by magnetoencephalography. Am J Obstet Gynecol 174: 1484-1486, 1996

Acknowledgement

The authors thank Sylvia Kausch and Uwe Schulze for their excellent assistance in performing measurements and signal analysis.

This work was supported by the German BMBF grant 01 ZZ 9104.

MEG of the Neonate During Sleep

Wakai RT[1,2], **Leuthold AC**[1], **Weber SM**[2], **and Martin CB**[3]

Departments of Medical Physics[1]*, Neurology*[2] *and Obstetrics and Gynecology*[3]
University of Wisconsin-Madison, Madison, Wisconsin, USA

Introduction

The MEG has been studied extensively in adults, and recently there have been efforts to extend MEG measurement to the study of seizure and other neurological disorders in children [1] and even to fetal brain activity [2,3]. There remains, however, a paucity of MEG data from neonates. While there are practical difficulties associated with neonatal studies, the smallness of the neonatal head potentially is a significant advantage for MEG measurement. At birth the biparietal diameter is only about 10 cm, implying a significant reduction in source-to-sensor distance and a corresponding increase in signal-to-noise ratio, compared to measurements in adults. In addition, the smaller surface area allows a modest channel-count SQUID array to cover a substantial portion of the scalp with a single probe placement.

In a previous study we measured and compared auditory evoked responses in fetuses and neonates [3]. In this paper we report measurements of the spontaneous MEG from four healthy full-term infants during their first few weeks of life.

Methods

The subjects were four healthy neonates, whose conceptual ages ranged from 40-45 week'. They were changed into non-magnetic clothing and were placed on their side during the measurements.

The MEG recordings were made using a seven-channel SQUID array (Biomagnetic Technologies 607 Neuromagnetometer) with 1.8 cm diameter, 4.0 cm baseline second-order gradiometer coils. The center coil was surrounded by six others, spaced evenly on a circle, with 2.0 cm center-to-center coil spacing. Each channel had magnetic field resolution 20 $\mathrm{fT/(Hz)^{1/2}}$. Two of the subjects were studied in an eddy-current shielded room and two were studied in a room with both mu-metal and eddy-current shielding.

The probe was positioned approximately over an EEG electrode at International 10-20 location T3. Simultaneous recordings of the neonatal EEG were made from this electrode, referenced to the left ear. The EOG was also recorded from a pair of eye leads. The passband of the MEG and EEG channels was 0.1-50 Hz. The subjects could be observed directly through an aperture in the shielded room. The spontaneous MEG was recorded within a two-hour session during periods when the subject was asleep, drowsy, or was lying awake quietly.

Following acquisiton, the MEG and EEG signals were bandlimited using a digital filter with passband 0.5-30 Hz. The recordings were displayed, and conventional neonatal sleep stages were identified on the basis of the EEG, the EOG, and behavioral activity.

Results

Head movement was a continual problem, resulting in frequent artifact in the MEG. Another difficulty related to head movement was the maintenance of the integrity of the EEG electrode contacts throughout the study; thus some portions of the EEG record were not usable. In one subject, a healthy male at conceptual age 42 weeks, nearly an hour of excellent MEG/EEG recordings were obtained. Segments of these data are presented in the figures below.

In the absence of head movements the MEG appeared artifact-free, and was as large as six picotesla during some high amplitude sleep patterns. The neonatal MEG was similar in terms of waveform morphology, dynamic range, and frequency progression to the EEG simultaneously obtained from monopolar electrodes located in the same general scalp region (approximately T3, left temporal cortex). Fig. 1 shows the MEG and EEG simultaneously derived during a period of early quiet sleep, characterized by behavioral quiescence and regular respiration. Both signals exhibit a mixed frequency background without appreciable waveform phase correspondence. Fig. 2 was taken approximately 15 minutes later; the EEG has progressed to a high voltage slow rhythm with abundant delta activity and the MEG demonstrates similar changes in background frequencies and amplitudes. The *trace' alternant* rhythm of quiet sleep was also clearly represented in the MEG as shown in Fig. 3. Further, Fig. 4 exemplifies the rough morphological correspondence of the EEG and MEG during active sleep in this same infant. In most of our recordings, the EEG signal contained generally faster low amplitude components in both active sleep and quiet sleep and EEG transients such as vertex waves were not always discernible in the MEG derived from the left temporal region.

©1999, Tohoku University Press
Recent Advances in Biomagnetism
T. Yoshimoto et al. (Eds)

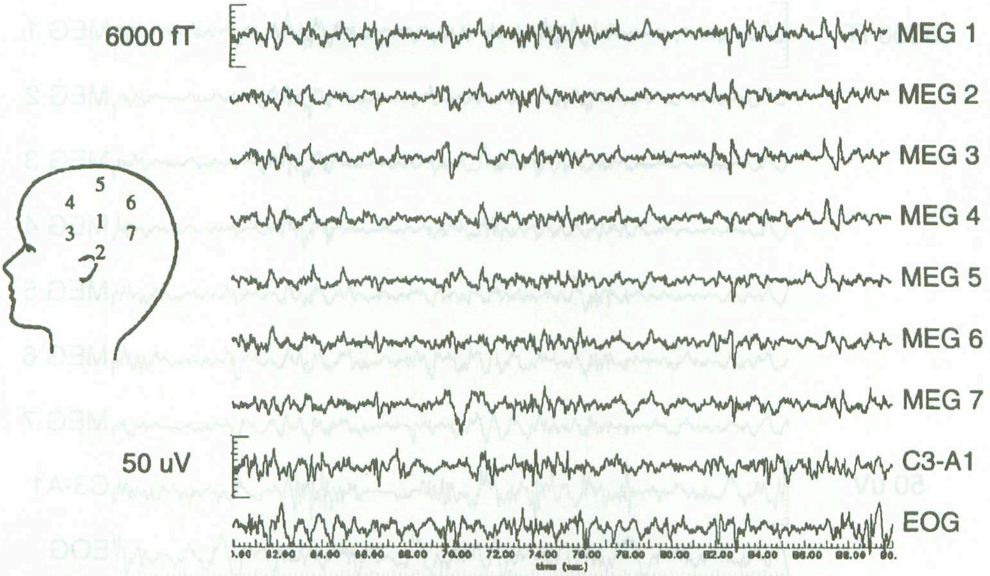

Fig. 1. Neonatal/EEG recording of duration 30 seconds showing mixed frequency pattern during quiet sleep. The inset at left shows the positions of the MEG channels for the recordings in Figs. 4-7. The center channel is approximately over International 10-20 position C3.

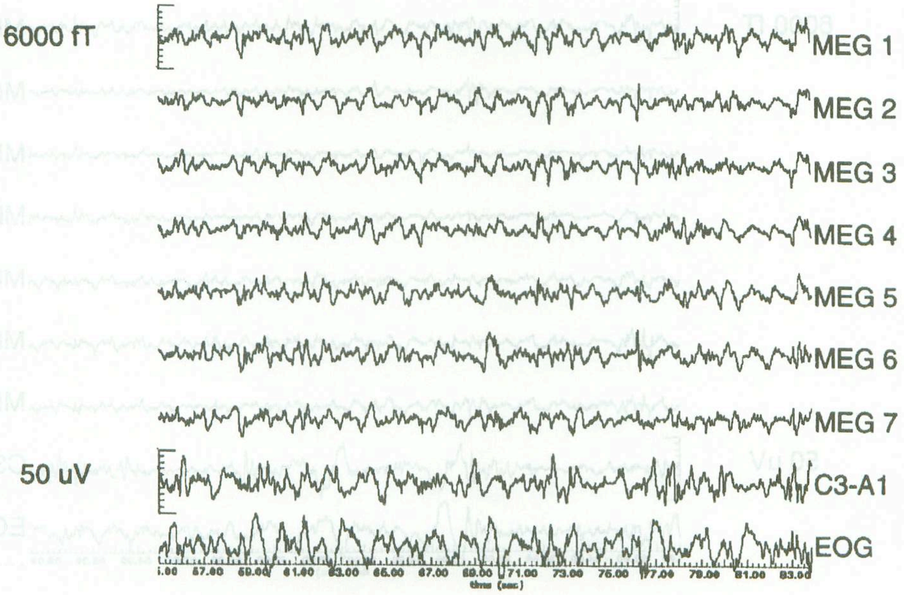

Fig. 2. Neonatal MEG/EEG recording showing progression from mixed frequency pattern to high amplitude, slow (delta) rhythms.

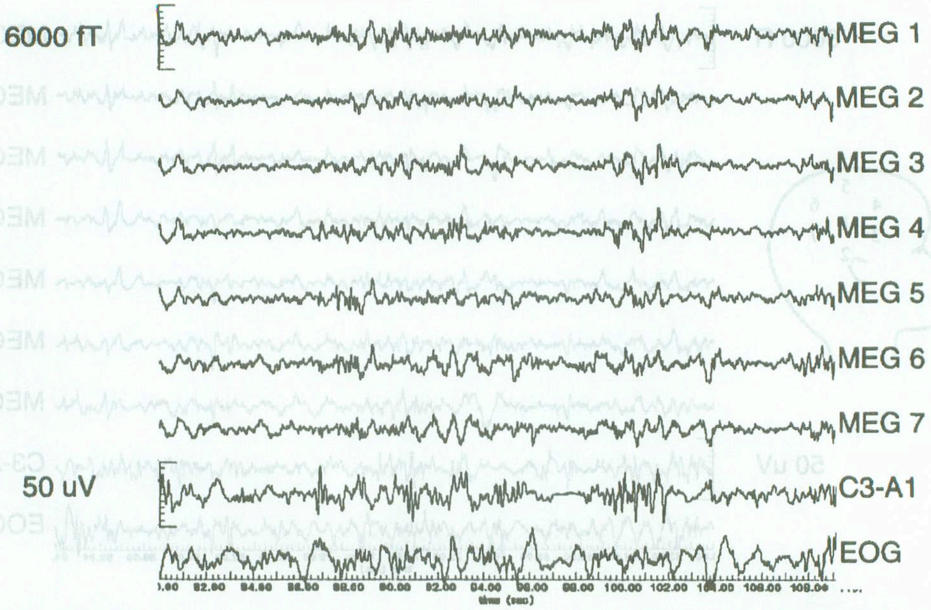

Fig. 3. Neonatal MEG/EEG recording showing *trace' alternant* (alternating trace). Notice how beautifully the pattern is expressed in the MEG, particularly in channels 2, 3, and 4.

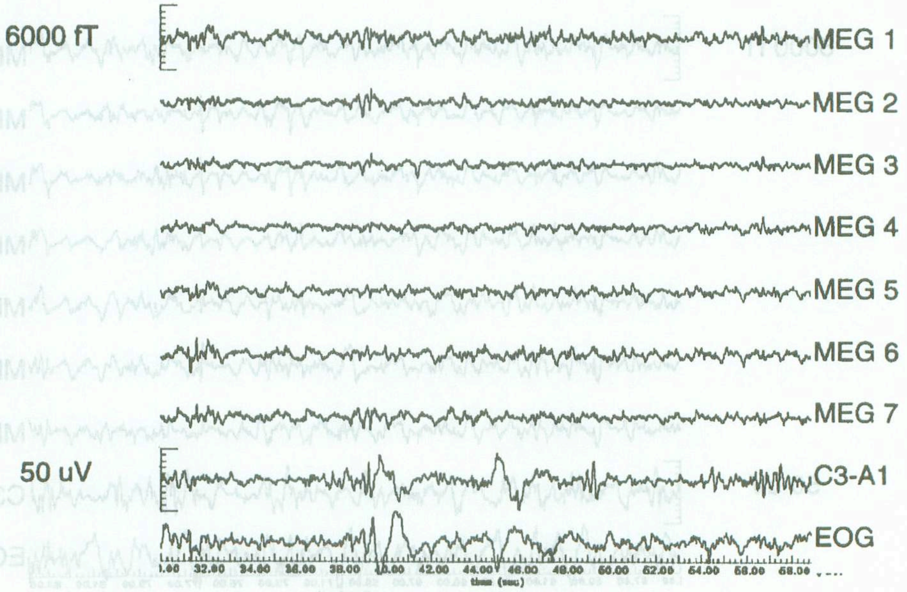

Fig. 4. Neonatal MEG/EEG during active (REM-like) sleep. Notice that eye movement artifact is strong in the EEG channel, but is absent from the MEG channels.

Discussion

Head movement was a significant problem, and may limit the practical utility of the neonatal MEG. Still, it was possible in this limited study to obtain some excellent recordings, and the amplitude of the MEG in some of our neonatal subjects was significantly larger than in most adults. This may result from the closer proximity of the detector to the generators in the neonatal brain.

In addition to large signal amplitude, the data indicate several advantages of the neonatal MEG. Some patterns, such as *trace' alternant*, were more prominent in the MEG than in the EEG, while eye movement artifact was greatly reduced.

In general, our initial observations in the neonate are consistent with those reported in adults during sleep [4-6]: that while the dominant frequencies of the MEG and EEG often diverge during sleep, similar progressive changes in frequency occur over time and sleep specific transient events are frequently represented in both signals. Thus, we anticipate that conventional neonatal sleep stages are identifiable on the basis of relative changes in MEG frequency and amplitude, when evaluated in combination with the traditional ancillary indices of behavioral activity and respiratory variability.

Acknowledgements

The study was supported in part by PHS grant R-01 NS37740.

References

[1] Chuang, S.H., Otsubo, H., Hwang, P., Orrison,, W.W., and Lewine, J.D. (1995) Pediatric magnetic source imaging, Neuroimaging Clinics of North America 5(2):289-303.

[2] Blum, T., Saling, E. and Bauer, R. (1985) First magnetoencephalographic recordings of the brain activity of a human fetus. Br J Obstet Gynaecol. 92, 1224-1229.

[3] Wakai, R.T., Leuthold, A.C., and Martin, C.B. (1996) Fetal auditory evoked responses detected by magnetoencephalography, Am. J. Obstet. Gynecol. 174:1484-1486.

[4] Hughes, J.R., Hendrix, D.E., Cohen, J., Duffy, F.H., Mayman, C.I., Schol, M.L., and Cuffin, B.N. (1976) Relationship of the magnetoencephalogram to the electroencephalogram. Normal wake and sleep activity, Electroenceph. Clin. Neurophysiol. 40:261-278.

[5] Lu, S.T., Kajola, M., Joutsiniemi, S.L., Knuutila, J., and Hari, R. (1992) Generator sites of spontaneous MEG activity during sleep, Electroenceph. Clin. Neurophysiol. 82:182-196.

[6] Nakasato, N., Kado, H., Nakanishi, M., Koyanagi, M., Kasai, N., Niizuma, H., and Yoshimoto, T. M (1990) Magnetic detection of sleep spindles in normal subjects, Electroenceph. Clin. Neurophysiol. 76:123-130.

New Developments in Magnetocardiology

Stroink G

Physics Department; Department of Physiology & Biophysics, Dalhousie University, Halifax, N.S., Canada B3H 3J5

Introduction

During the last few years, significant developments in magnetocardiology have taken place in instrumentation, in methods to calculate from heart models magnetic field maps (MFMs), in methods to use MFMs to image cardiac sources, and in clinical applications. In this short review we will describe some of the highlights in each of these areas.

Instrumentation

Sixty-seven channel MCG systems have been installed in Helsinki, and in Bochum (Germany). A third one (55 channels) is soon available in Ulm (Germany). This latest generation of low-Tc SQUID multichannel systems is capable of obtaining MFMs every millisecond over the whole chest area. They are easy to use and provide non-invasively a wealth of high-resolution temporal and spatial information on cardiac function for further analysis. They are ideal for clinical studies. However, such systems are expensive and relatively costly in their operation. Several groups have expressed the need for a low cost system with one or a few channels that can be used near the bedside (with no shielding). Although a bedside low-Tc SQUID system was described several years ago [1], recent dramatic improvements in the noise performance of high-Tc SQUIDs now make MCG studies with these SQUIDs in an unshielded environment possible (see Fig.1).

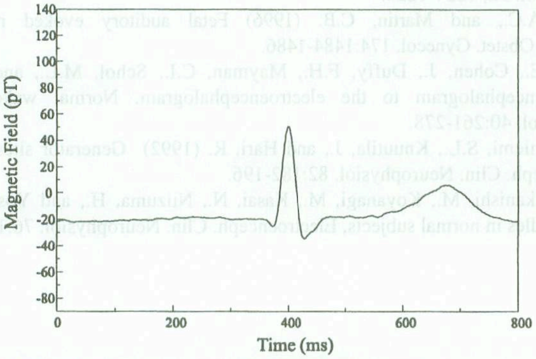

Fig.1: Averaged MCG obtained with high-Tc rf SQUIDs arranged as a second order gradiometer in a harsh laboratory environment [2]. Thirty complexes were averaged. The bandwidth is between 0.1 and 47 Hz. (Courtesy of J. Borgmann, University of Twente, The Netherlands).

Several clinical studies with high-Tc SQUID systems in a shielded environment were reported at this conference; one such study involves a 16-channel system [3]. The MCG community now has a range of MCG instruments available: single channel systems to study temporal MCG features or maps of patients in sinus rhythm, and multichannel systems with any number of channels arranged in the desired geometry. Such systems can measure any type of magnetic field component. It is up to the researchers to specify their needs, given their research goals and financial resources available.

Forward Solutions

Over the last few years we have seen important developments in physiologically and anatomically accurate models of cardiac activation. For example, the ventricular model described by Hren et al. [4] uses information about the fiber direction, anisotropic conduction, and action potential at about two million cellular units (mm scale resolution) within the myocardium to calculate the activation sequence. The activation propagation is ruled by cellular automata and is initiated when the transmembrane potential of the cellular unit exceeds a threshold value. The magnetic fields and potentials at the body surface are calculated using the oblique dipole model of cardiac sources [5] in combination with the Boundary Element Method [6]. Such models can be used to calculate the time series of magnetic field and potential body surface maps following epicardial or endocardial pacing. Fig. 2 shows the calculated MFMs resulting from initiating an activation sequence at an anterior endocardial site. Comparing the topography of such theoretical maps or their summation in time (QRS integral maps) with that observed during the onset of life-threatening Ventricular

©1999, Tohoku University Press
Recent Advances in Biomagnetism
T. Yoshimoto et al. (Eds)

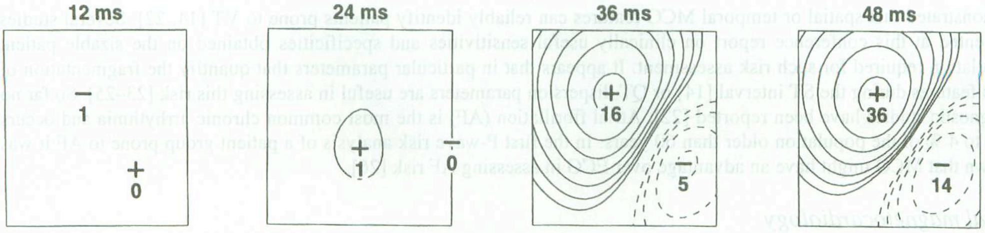

Fig. 2: Calculated MFMs after onset (in milli-seconds) of the activation sequence at an endocardial anterior pacing site midway between the apex and basal level [7]. The magnetic field component normal to the chest was simulated at 64 points on a 8 x 8 grid with 4 cm spacing, situated 2 cm in front of the anterior chest. Extrema are in pT. (Courtesy of R. Hren).

Tachycardia (VT) can assist the physicians in locating non-invasively the site of origin of VT, and in planning for possible ablation of that site [7].

Inverse Solutions and Electrophysiological Imaging

Over the last few years we have seen substantial progress in inverse solutions that go beyond those with a single dipole as the source model. Nevertheless, questions related to the accuracy of the single dipole inverse solution remain; some are addressed in these proceedings. The single dipole equivalent generator is an adequate generator when the bioelectric activity of the heart is confined to a small volume near the onset (the first tens of milliseconds) of activation. The accuracy of the single dipole inverse solution has been studied using the detailed heart model, described above, to generate magnetic field and body surface potential maps (BSPM). Noise is added to simulate realistic data. These studies indicate that similar accuracy can be obtained for both types of maps [4, 8]. However, a more direct method to assess the localization accuracy is through the use of tank models of realistic torsos. Recently, such studies [9] suggest that MFM might have some advantages over potential measurements, and that the overall accuracy increases when both electric and magnetic data are used for the inverse solution, confirming earlier theoretical results [10].

The most direct method of validating the single dipole inverse solution is with the use of a non-magnetic catheter configured as a current dipole. Results obtained by comparing the single dipole inverse solution with fluoroscopy localization of the current dipole tip of this catheter inserted in 10 patients show a location accuracy of about 5 mm [11]. The results also suggest that a more accurate localization can be obtained by using the MFM rather than the equivalent BSPM [12]. This catheter is designed to allow the physician to measure action potentials at the well-defined endocardial locations, determined with the inverse solution, without extensive use of fluoroscopy [13]. The accuracy achieved in locating a current dipole source supports the notion that MFMs are useful in locating non-invasively accessory pathways of WPW-patients, or the onset of ectopic beats. This knowledge is useful in planning an ablation procedure [8, 14].

Exciting is the development of computer programs that aim to calculate from the sequence of MFMs or BSPMs the activation sequence on the ventricular surface [15–19]. This noninvasive imaging of cardiac electric function on anatomical images of the endo- or epicardial surface (obtained from MR or CAT) promises to assist cardiologists in assessing cardiac damage. Several groups have validated such MFM-derived activation time maps by comparing them with those similarly calculated from BSPMs [16, 19], or by using epicardial surface recordings [18]. Others have used the location of wall abnormalities in patients with myocardial infarction to establish that the activation sequence obtained is as expected [20]. Validation of the reconstructed epi- or endocardial source distributions is a major issue which is not easily solved [21]. Although progress in deriving activation maps is substantial and their clinical value in assessing cardiac function clear, it will continue to require the combined efforts of mathematicians, experimentalists and clinicians to determine the reliability of the produced electrophysiological images before they will be acceptable as a clinical tool.

Clinical Applications

Risk analysis

About one-half of the cardiac deaths per year is of rhythmogenic origin. Ventricular fibrillation following ventricular tachycardia (VT) is the most common cause for sudden cardiac death. Consequently, there is a need for a relatively simple, non-invasive method of identifying patients at risk of VT. Over the years, both the MCG and ECG communities have proposed the use of particular temporal or spatial features as risk indicators. Studies establishing the validity of such indicators frequently focus on a group of patients suffering from a particular underlying cardiac dysfunction, such as myocardial infarction. Comparing such patient groups with and without VT, MCG studies have demonstrated that spatial or temporal MCG features can reliably identify patients prone to VT [14, 22]. Several studies presented at this conference report on clinically useful sensitivities and specificities obtained on the sizable patient population required for such risk assessment. It appears that in particular parameters that quantify the fragmentation of map features during the ST interval [14] or QT dispersion parameters are useful in assessing this risk [23–25]. So far no prognostic studies have been reported [22]. Atrial fibrillation (AF) is the most common chronic arrhythmia and occurs in 2 to 4 % of the population older than 60 years. In the first P-wave risk analysis of a patient group prone to AF it was shown that MCG might have an advantage over ECG in assessing AF risk [26].

Fetal magnetocardiology

The now well-documented advantages of fetal magnetocardiology over fetal electrocardiology have been exploited by several research groups in assessing non-invasively the fetal conduction system [27], fetal well being, as well as fetal growth and behavior [28]. In particular, the study and possible implications of fetal arrhythmias detected by fetal MCG have been documented by several authors. This field has emerged as a major MCG research area [14].

Ischemia

Several research groups have now recorded the changes in the repolarization maps of healthy subjects during exercise. Such changes were first recorded by Brockmeier et al. [29]. The origin of these signals is not clear although changes in heart position, blood volume, or cardiac mass as well as action potential changes and a more pronounced anisotropic conduction during exercise have been suggested. Although in the original experiments similar BSPM shift under the same experimental conditions were not observed [29], recent BSPM and MFM studies using a different method to induce stress show equivalent elevations in BSPMs and MFMs [30]. These BSPMs cover a larger area than in the original study. More research is required to understand these phenomena.

The report of ST shifts in exercise MCG has renewed interest in the analysis of MCG data of patients with coronary artery disease (CAD). Such studies were started by Cohen and his collaborators [31]. Several reports on the analysis of multichannel MCG of exercise induced myocardial ischemia are contained in these proceedings. The tentative conclusion that exercise MCG can be used to detect myocardial ischemia in CAD patients opens a promising new area of research with clearly defined clinical applications. Fig. 3 shows an example of exercise induced ST-shifts in a CAD patient.

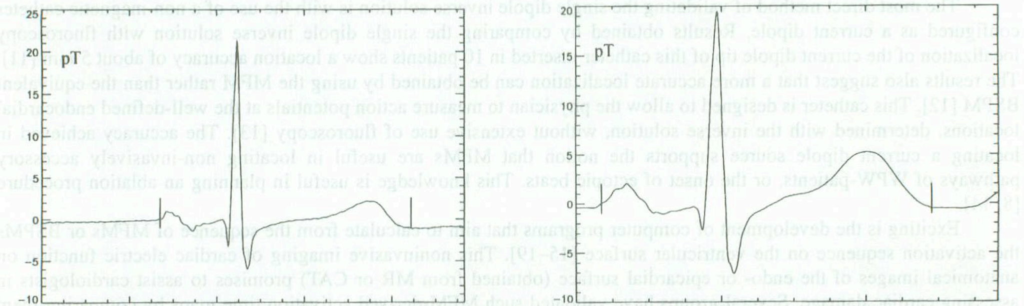

Fig. 3: MCG of a patient with CAD: at rest (left), and during pharmacologically induced stress (right). The MCGs are measured with the same channel (no. 30) of a 36-channel system in a shielded room. For details see [32].

References

[1] Matlashov A, Slobodchikov V, Bakharev A, et al: Miniature DC SQUID magnetometers for clinical use, Baumgartner C, Deecke L, Stroink G, et al (eds): Biomagnetism: Fundamental Research and Clinical Applications. Amsterdam: Elsevier/IOS-Press, 1995, pp 526–529

[2] Borgmann J, Rijpma AP, ter Brake HJM, et al: Highly balanced gradiometer system based on HTS-SQUIDs for the use in magnetically unshielded environment. Appl Supercond Conf, Palm Springs, California, 1998

[3] Sai KY, Uchikawa Y, Kotani M: MCG measurements using high-Tc SQUID. These proceedings.

[4] Hren R, Stroink G, Horacek BM: Spatial resolution of body surface potential maps and magnetic field maps: A simulation study applied to the identification of ventricular preexcitation sites. Med Biol Eng Comp 36: 145–157, 1998

[5] Leon LJ, Horacek BM: Computer model of excitation and recovery in the anisotropic myocardium. J Electrocardiol 24: 1–15, 1991

[6] Ferguson AS, Stroink G: Factors affecting the accuracy of the boundary element method in the forward problem—I: Calculating surface potentials. IEEE Trans Biomed Eng 44: 1139–1155, 1997

[7] Hren R, Stroink G: Value of magnetocardiographic QRS integral maps in locating ventricular tachycardia foci. These proceedings.

[8] Hren R, Stroink G, Horacek BM: Accuracy of single-dipole inverse solution when localising ventricular pre-excitation sites: Simulation study. Med Biol Eng Comp 36: 323–329, 1998

[9] Tenner U, Haueisen J, Nowak H, et al: A realistic torso phantom for calibration and testing of MCG and BSPM systems. These proceedings.

[10] Hren R, Zhang X, Stroink G: Comparison between electrocardiographic and magnetocardiographic inverse solutions using the boundary element method. Med Biol Eng Comp 34: 110-114, 1996

[11] Fenici R, Pesola K, Nenonen J: Clinical validation of three-dimensional cardiac magnetic source imaging accuracy with simultaneous magnetocardiographic mapping, monophasic action potential recordings and amagnetic pacing. These proceedings.

[12] Pesola K, Fenici R, Nenonen J, et al: Comparison of the localization accuracy of magnetocardiographic and body surface potential mapping using an amagnetic catheter. These proceedings.

[13] Fenici R, Giorgi A, Ruggieri MP, et al: Clinical validation of a multipurpose amagnetic catheter and the method for non-fluoroscopic, MCG guided, high resolution monophasic action potential recordings. These proceedings.

[14] Stroink G, Moshage W, and Achenbach S: Cardiomagnetism, Andrä W, Nowak H (eds.): Magnetism in Medicine: A Handbook. Berlin: Wiley-VCH, 1998, pp 136–189

[15] Wach P, Tilg B, Lafer G, et al: Magnetic source imaging in the human heart. Med Biol Eng Comp 45: 157–166, 1997

[16] Nenonen J: Multimodal cardiac source imaging in the BioMag Laboratory. NFSI 97 Symposium. Biomed Technik 42(1): 29–32, 1997

[17] Modre R, Tilg B, Nenonen J, et al: Reconstruction of cardiac propagation sequence from clinical magnetocardiographic data. These proceedings.

[18] Pesola K, Oosterdorp T, Nenonen J, et al: Uniform double layer solutions for magnetocardiographic and body surface potential mapping data. These proceedings.

[19] Tilg B, Wach P, Lesh MD, et al: Imaging surface activation time maps from magnetic field and body surface potential data. These proceedings.

[20] Nowak H, Leder U, Pohl P: Assessment of local electrical properties of the left atrial ventricle by inverse solution of MCG. These proceedings.

[21] MacLeod RS, Brooks DH: Recent progress in inverse problems in electrocardiology. IEEE Eng in Med and Biol 1: 73–82, 1998

[22] Mäkijärvi M: Magnetocardiography and cardiac risk. Herzschr Elektrophys 8: 178–183, 1997

[23] van Leeuwen P, Hailer B, Wehr M: Spatial distribution of QT intervals: Alternative approach to QT dispersion. PACE 19: 1894–1899, 1996

[24] Oikarinen L, Paavola M, Montonen J, et al.: Magnetocardiographic QT interval dispersion in post myocardial infarction patients with sustained ventricular tachycardia—validation of automated QT measurements. PACE 21:1998

[25] Yukinaka M, Nomura M., Nada T, et al: QTc dispersion using magnetocardiogram: Analysis in patients with myocardial infarction. These proceedings.

[26] Winklmaier M, Pohle C, Achenbach S, et al: P-wave analysis in MCG and ECG after conversion of atrial fibrillation. These proceedings.

[27] Huirne JAF, Krooshoop HJG, Quartero HCW, et al: The classification of fetal cardiac conduction disorders by means of magnetocardiography. These proceedings.

[28] van Leeuwen P, Lange S, Hailer B, et al: Assessment of fetal development on the basis of fetal magnetocardiography. These proceedings.

[29] Brockmeier K, Schmitz L, Chavez JJB, et al: Magnetocardiography and 32-lead potentials: repolarization in normal subjects during pharmacologically induced stress. J Cardiovasc Electrophys 8: 615–626, 1997

[30] Takala P, Hanninen H, Montonen J, et al: Comparison of magnetocardiographic and electrocardiographic exercise mapping in healthy volunteers. These proceedings.

[31] Cohen D, Savard P, Rifkin RD, et al: Magnetic measurement of S-T and T-Q segment shifts in humans. Part II: Exercise induced S-T segment depression. Circ Res 53: 274–279, 1983

[32] Adams A, Stroink G, Van Leeuwen P, et al: KLT-analysis of QRST integral magnetic field maps of patients with and without coronary artery disease at rest and during pharmacological stress. These proceedings.

Acknowledgment

This work has been supported in part by the National Sciences and Engineering Research Council (NSERC) of Canada.

Magnetocardiography - an Useful Tool for the Study of Electromotive Forces

Nakaya Y , Nomura M
The Second Department of Internal Medicine and Department of Nutrition,
University of Tokushima, School of Medicine
3-18 Kuramoto-cho, Tokushima 770-8503, Japan

Introduction

Studies by the magnetocardiography (MCG) on the origin of the electromotive forces of the heart are intriguing problem for electrocardiologists. It is still difficult to deduce correctly current source by the measurements of electrical potential from the body surface. The MCG can potentially provide new information, which is difficult to be detected by electrocardiogram (ECG). Especially, localization of electrical current source. Visualization with current density images also provides useful information in the clinical environment. Many research groups have studied on these topics, i.e. the localization of origin of ventricular arrhythmias or accessory pathway using MCG mapping. Other applications are diagnosis of various diseases, i.e., myocardial ischemia, fetal MCG and risk analysis for cardiac sudden death. We can use MCG to study theoretically the genesis of electrocardiographic waves as well.

Recent reviews of the MCG by Siltanien [1], Fenici [2], Nakaya [3] and Stroink [4] summarizes development of the MCG research. However, there are still less clinical application in the field of the MCG compared to those of the neuromagnetism. In this workshop, we discuss the usefulness and limitations of the MCG in clinical cardiology.

Source localization

In early MCG research, current source was deduced by isofield map using Biot Savart law by simple observation. This simple method provides useful information about the electric current source in clinical cardiology, such as T wave abnormality, injury current. Opposing dipole is one which the MCG can tell more easily than the ECG. Least square method was used to determine a single equivalent dipole. However, the electromotive force at most of the time during the excitation is not single dipole. Many activation fronts to various direction are reported in experimental models. For multiple-dipole estimation, detailed models (for instances more than 1000 dipoles) were used to calculate. Such model is extremely useful to study activation sequences of the heart in normal and abnormal conditions.

We also used the MCG to investigate the current source of initial QRS wave in normal, inferior wall infarction and left ventricular hypertrophy [5]. In textbooks of electrocardiology, initial QRS force is directed to the right and anteriorly and originated from the intraventricular conduction from the left- to the right-sided ventricles. Therefore, this force is called septal vector. This hypothesis is supported by the fact that in anteroseptal infarction (loss of electric current in the septum) the normal initial QRS force is absent. The absence of initial QRS force (absence of rightward or anterior force) in left ventricular hypertropy is considered to be due to the fibrosis of the intraventricular septum, in which conduction disturbance of the left bundle branch occurs and the initial QRS force is displaced to the left and posteriorly. However, the MCG shows that the absence of the initial QRS force is due to the increased posterior and leftward force of the hypertrophied left ventricle. Vector arrow map study (Fig. 1) shows that initial rightward force still exist on the right side of the heart but vector located on the left and directing posterior and to the left is increased. The summation of these vectors might direct to the left as indicated by the isofield map. These results indicated that initial QRS force is originated from septum alone but is a summation of electromotive forces of whole ventricles (Fig. 2). We can use the MCG to study electromotive force of ECG, especially location of current sources. As the ECG wave form is empirically determined, new findings will appear by the MCG.

Many researchers studied the localization of accessory pathway in WPW syndrome. With development of multi-channel recorder, ventricular arrhythmias were also studied in addition to WPW syndrome. Accuracy in determining the 3D location of preexcitation area has been reported by many investigators [6-8]. Most of the studies used the homogeneous semi-infinite models to deduce current source, but there was a significant error in detection of the current source in the left ventricle. Makijarvi et al [9], and Stroink et al [10] reported that realistic torso model improved accuracy in localization. Surgical treatment, and more recently catheter ablation of arrhthmogenic tissues became popular. Prior knowledge of the location of the arrhythmogenic sites would shorten the time of invasive mapping and diminish complication to the patients.

There might be small error even if we considered to be a single dipole in arrhythmogenic tissues. However, even in

©1999, Tohoku University Press
Recent Advances in Biomagnetism
T. Yoshimoto et al. (Eds)

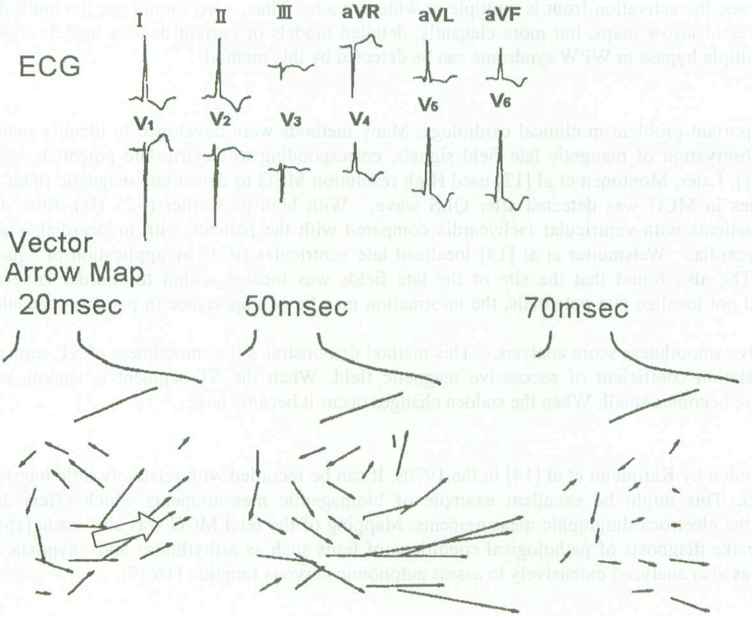

Fig. 1 Vector arrow map in a patient with left ventricular hypertrophy (27-year- old man, aortic valvular disease)
The initial rightward and anterior force is decreased in the ECG. The vector arrow map at 20 msec shows the initial QRS forces in the right portion directed to the right but those in the left directed to the left. The summation vector is directed to the left ⇨

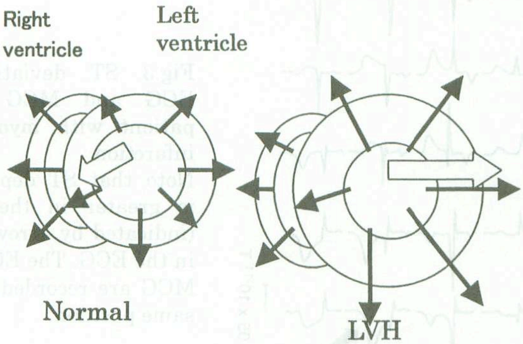

Fig.2 Mechanism of Displaced initial QRS force
The initial QRS force is derived many dipoles of the both ventricle. When left ventricle is hypertrophied (LVH), the electromotive force in the left ventricle is increased. Subsequently, initial QRS vector is displeced to the left.

the onset of the QRS waves, the activation front is multiple or wide spread. Thus, we should use the multi-diplole models. Easiest way is vector arrow maps, but more elegantly, detailed models or current density models should be used for this purpose. Multiple bypass in WPW syndrome can be detected by this method.

Risk analysis

Risk evaluation is an important problem in clinical cardiology. Many methods were developed to identify malignant cardiac arrhythmias. Observation of mangetic late field signals, corresponding to electric late potentials was first reported by Erne et al [11]. Later, Montonen et al [12] used High resolution MCG to detect late magnetic fields. They reported 0.4-3pT activities in MCG was detected after QRS wave. With high pass filter (>25 Hz), filtered QRS duration was longer in patients with ventricular tachycardia compared with the patients with myocardial infarction without ventricular tachycardia. Weismuller et al [13] localized late ventricular fields by application of equivalent current dipole model. The also found that the site of the late fields was located within the border zone of the infarction. As ECG could not localize late potentials, the information may be of importance in patients scheduled for catheter ablation.

Another methods is relative smoothness score analysis. This method demonstrates the smoothness of ST segment, by calculating sum of correlation coefficient of successive magnetic field. When the ST segment is smooth and no fluctuation occur, the score becomes small. When the sudden changes occur it became larger.

Fetal MCG

Fetal MCG was first recorded by Kariniemi et al [14] in the 1970s. It can be recorded with relatively little interference from the maternal MCG. This might be excellent example of biomagentic measurements which offers distinct advantages compared to the electrocardiographic measurements. Mapping of the fetal MCG was also made [15]. The fetal MCG is useful to make diagnosis of pathological conditions of fetus such as arrhythmias and hypoxia. Heart rate variability of fetus was also analyzed extensively to assess autonomic nervous function [16,17].

Myocardial ischemia

In clinical cardiology, diagnosis of myocardial ischemia is one of the most important problem. However, the ECG diagnosis of myocardial ischemia is not satisfactory, as it shows high false positive and false negative results. There have been few studies on myocardial ischemia by the MCG. The MCG can potentially detect the existence of myocardial ischemia. Repolarization current flows parallel to the ventricular surface, which is difficult to be detected by the ECG and easy by the MCG [18]. Thus, MCG can detect more easily than the ECG in some cases with myocardial ischemia (Fig. 3). Direct current recording can differentiate the normal variant from ischemic changes [19]. However, this is extremely difficult to record stable DC levels even in a magnetically-shielded room.

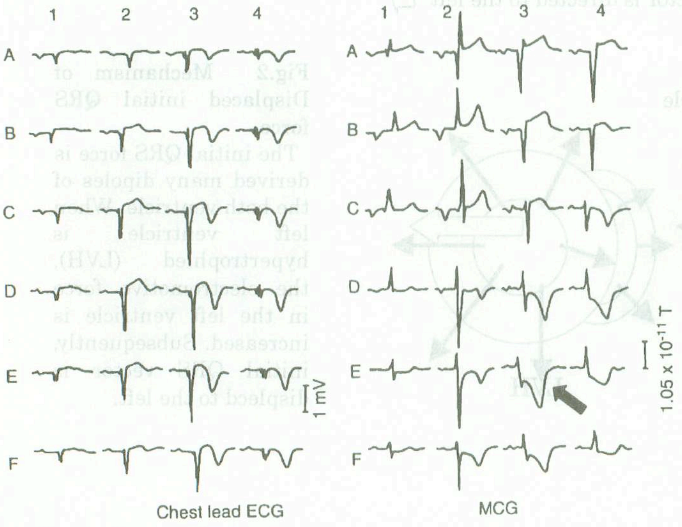

Fig.3 ST deviation in ECG and MCG in a patient with myocardial infarction

Note that ST depression is greater in the MCG (indicated by arrow) than in the ECG. The ECG and MCG are recorded at the same position.

The MCG has better spatial resolution and can detect local ischemic area. In this workshop Makijarvi et al. developed a new and accurate method for recognition of acute and chronic ischemia by calculating current density distribution. The necrotic area shows reduced current density and injury current can be recorded by this methods in acute ischemia. This method is one of the promising noninvasive method to detect myocardial ischemia.

Conclusion

The considerable amount of information has been accumulated about MCG. The next step for the MCG might be clinical application. To achieve this, cost of MCG recording should be reduced as the ECG is cheap although many important information. For easiness of recording, the MCG should be recorded in noisy hospital environment and ideally it should be handy or movable. Fenici's group extensively studied the MCG using an MCG system which can record in clinical electrophysiological laboratory (in this book). This might be the one way for the future MCG. Another way might be to study precisely small signals using a high resolution MCG system. The accumulation of information under these conditions will help development of the MCG research and clinical application.

References

[1] Siltanen P: Magnetocardiography. MacFarlene PW, Lawrie TDV (eds): Comprehensive Electrocardiography, Pergamon Press, New York, 1989 pp. 1405-1438

[2] Fenici RR, Mlillo G, Masselli M: Clinical magnetocardiogrrphy. 10 years experience at the catholic university. J Cardiac Imag 7: 151-167, 1991

[3] Nakaya Y, Mori H: Magnetocardiography. Clin Phys Physiol Meas 13: 191-229, 1992

[4] Stroink G, Lamothe MJR, Gardner MJ: Magnetocariographic and electrocardiographic mapping studies, Weinstock H, Kluwer (eds): SQUID Sensors. the Nederlands, 1996 pp. 413-444

[5] Nakaya Y, Nomura M, Saito K. Analysis of electoromotive force by magnetocariogram – Is the origin of initial QRS force (septal vector) intraventricular septum? Biomag 96 (in press).

[6] Moshage W, Abraham-Fuchs K, Weikl A, et al: Magnetocariography (MCG): Noninvasive localization of accessory conduction pathways in patients with the WPW syndrome. Electromedica 57: 233-128, 1989

[7] Fenici R, Melillo G, Cappelli A, et al: Magnetocariographic localization of Kent bundle. Williamson SJ, Hoke M, Stroink G, et al (eds): Advances in Biomagnetism, Plenum Press, New York and London, 1989 pp. 365-368

[8] Nomura M, Nakaya Y, Saito K, et al: Noninvasive localization of accessory pathways by magentocardiographic imaging. Clin Cardiol 17: 239-244, 1994

[9] Makijarvi M, Montonen,J, Toivonen L, et al: Localization of accessory pathways in the Wolff-Parkinson-White syndrome by high-resolution magnetocariographic mapping. J Electrocardiol 25: 143-155, 1992

[10] Stroink G, Greek LS, Elliott P, et al: Is there a need for individual torso models in magnetic inverse solution? Hoke M, Erne SN, Okada YC, et al (eds): Biomagnetism: Clinical Aspects, Excerpta Medica, Amsterdam, 1992, pp. 813-818

[11] Erne SN, Fenici RR, Hahbohm HD, et al: High-resolution magenetcardiographic recordings of the ST segment in patients with electrical late potentias. II Nuovo Cimento 2D: 340-345, 1983

[12] Montonen J, Katila T, Leinio M, et al: Analysis of high resoluton MCG recordings of patients with ventricular tachycardia. Williamson SJ, Hoke M, Stroink G and Kotani M ed. Advances in Biomagnetism Plenum Press, New York, 1989 pp 385-388.

[13] Weismuller P, Abraham-Fuchs K, Killmann R, et al: Localization of the site of origin of ventricular late fields in the signal averaged magnetocariogram in patients with ventricular late potentials. Baumgartner C, Deecke L, Stroink G, et al (eds) Biomagnetism: Fundamental Research and Clinical Applications. Amsterdam: Elsevier/IOS-Press, 1995, 566-570

[14] Kariniemi V, Ahopelto J, Karp PJ, et al: The fetal magnetocariogram. J Perinat Med 2: 214-216. 1974

[15] Wang M, Wakai RT, Henry J, et al: Mapping of the fetal magnetocariogram. Baumgartner C, Deecke L, Stroink G, et al (eds) Biomagnetism: Fundamental Research and Clinical Applications. Amsterdam: Elsevier/IOS-Press, 1995, pp 696-699

[16] Rassi D, Lewis MJ: Power spectral analysis of the foetal magnetocardiogram. Physiol Meas 16: 111-20, 1995

[17] Wakai RT, Wang M, Leuthold AC: Foetal magnetocardiogram amplitude oscillations associated with respiratory sinus arrhythmia. Physiol Meas 16: 49-54, 1995

[18] Trahms L, Burghoff M, Brockmeier K, et al: Vortex current detected by the magnetocaridogram. Abstracts of Biomag 96 p. 247 (in press).

[19] Cohen D, Savard P, Rifkin RD, et al Manetic measurement of S-T and T-Q segment shifts in humans. Part II: Exercise-induced S-T segment depression. Circ res 53: 274-279, 1983

Magnetocardiography - research tool or diagnostic modality with potential clinical value?

Stephan Achenbach, Werner Moshage

Department of Internal Medicine II
University of Erlangen-Nürnberg, Germany

Introduction

Magnetocardiography (MCG), the registration of the magnetic fields generated by the human heart's electrical activity, has advantages over the recordings of the electric potential at the body surface, the electrocardiogram. Theoretically, it provides higher spatial resolution and the magnetic fields are influenced by the electrical properties of the body tissues to a lesser extent than the electric potentials. Therefore, the magnetocardiogram can provide unique data for clinical and research applications. The first recording of the magnetocardiogram was published in 1963 [1]. Even though technology has progressed tremendously, the technical requirements to record the magnetocardiogram are still extremely high [2]. Superconducting, low-temperature equipment and magnetically shielded rooms are necessary to detect the weak signals and suppress background noise. Even though several interesting applications of magnetocardiography in cardiac diagnosis have been developed in the past several years, it is unclear whether their advantages over conventional diagnostic modalities outweigh the disadvantages caused by the extremely high efforts necessary to record the MCG.

1) Localization of cardiac arrhythmias

Magnetocardiography, in conjunction with magnetic resonance imaging, permits the localization of ventricular and supraventricular arrhythmias, including ventricular tachycardia and the accessory pathway in WPW-syndrome [3,´4, 5, 6, 7]. The localization accuracy depends on the equipment used and on the distance between the sensors and the sourse, but usually it is around 2 cm [3]. It has been demonstrated that non-invasive localization of the position of accessory pathways and the site of origin of ventricular arrhythmias can shorten the time necessary for interventional ablation procedures [8, 9]. However, electrophysiologic procedures have matured to a point where prior knowledge of the exact target site is hardly necessary. Additionally, body surface potential mapping can also provide information on the rough position e.g. of accessory pathways. It has turned out that only in rare circumstances the determination of the site of origin is helpful in the clinical management of patients with cardiac arrhythmias (see Fig. 1)

2) Risk stratification

Stratification of an individual's risk to experience malignant cardiac arrhythmias would be of utmost clinical importance. In clinical practice, the only reliable marker so far seems to be reduced left ventricular function, even though a number of parameters based on the surface ECG, such as "late potentials" and "QT

©1999, Tohoku University Press
Recent Advances in Biomagnetism
T. Yoshimoto et al. (Eds)

dispersion" have been proposed. A number of small studies could demonstrate potential advantages of MCG parameters to investigate depolarization (e.g. QRS fragmentation, late fields) or repolarization (e.g. RS-score, QT dispersion) over conventional ECG parameters (see table 1). However, to gain clinical acceptance, these parameters would have to be evaluated in very large clinical trials to prove MCG's superiority over current tools for risk stratification. Additionally, the technical requirements to record the magnetocardiogram would have to be greatly reduced before the method could be applied as a mass screening.

	MCG parameters
Depolarization	QRS Fragmentation [10] Late Fields [11, 12]
Repolarization	RS Score [13] QT Dispersion Field Extrema Trajectory Plots [14]

Table 1: Methods described for the investigation of depolarization and repolarization of ventricular excitation by magnetocardiography

3) Stress MCG and detection of ischemic and viable myocardium

Recent studies published by a number of groups demonstrated striking differences between stress ECG and MCG even in normal subjects. Also, tools have been developed which seem to allow the visualization and quantification of electrical activity within the myocardium and use this information to determine ischemic myocardium and viable myocardium after infarction. These applications would indeed consititute an important application of MCG, since currently only PET (positron emission tomography), an even more expensive method, seems to be able to provide similar information.

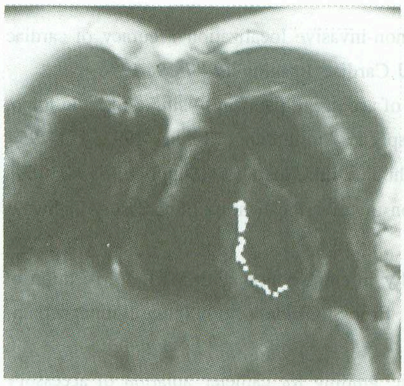

Fig 1: Localization of ectopic activity

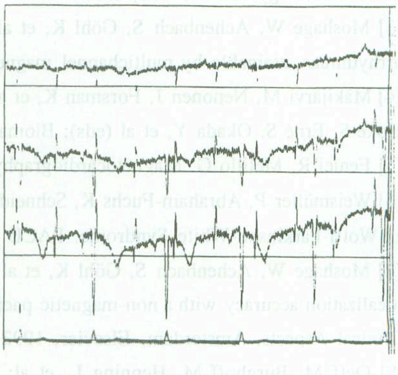

Fig 2: Recording of the fetal MCG (33rd gestational week)

4) Fetal magnetocardiography

The fetal magnetocardiogram has been shown to be an excellent tool to investigate fetal cardiac activity throughout pregnancy [15, 16, 17]. The earliest recordings have successfully been performed as early as the 13th week of pregnancy [18], and the fetal QRS complexes remain detectable throughout late pregnancy (see fig. 2). Fetal magnetocardiography (fMCG) therefore constitutes a virtually completely non-invasive tool for the detection, monitoring, and analysis of fetal cardiac activity. Several studies have demonstrated the development of the fetal magnetocardiogram during pregnancy and the possibility to analyze fetal arrhythmias using magnetocardiography [16, 17, 19).

The fetal MCG can therefore contribute to the management of pregnancies complicated by fetal brady- and tachycardia and provide information not attainable by any other method. It has been used in clinical decision-making. Currently, only the limited availability and enormous technical requirement of fetal magnetocardiography prohibit more extensive applications of the method. However, it seems to be possible to conduct such investigations with low-cost, high-temperature superconducting sensors, since the signals - in comparison to other applications of the MCG and MEG - are relatively large.

Summary

Magnetocardiography has demonstrated clinical utility in several fields. However, broad clinical application has so far not been achieved for three reasons: The clinical cases in which MCG can provide necessary information are rare (such as in MCG localization of arrhythmias), large studies to prove the clinical utility are missing (such as in MCG risk analysis), or the technical requirements prohibit clinical routine use even though the advantages have been clearly shown (such as in fetal magnetocardiography). It therefore seems well possible that MCG could establish a clinically relevant role, but further applications research and development of low-cost, user-friendly and robust systems are necessary if the method is to survive in clinical cardiology.

References

[1] Baule GM, McFee R: Detection of the magnetic field of the heart. Am Heart J 55:95-96, 1963.

[2] Schneider S, Hoenig E, Reichenberger H, et al: Multichannel biomagnetic system for the study of brain and heart. Radiology 176:825-831, 1999

[3] Moshage W, Achenbach S, Göhl K, et al: Evaluation of the non-invasive localization accuracy of cardiac arrhythmias attainable by multichannel magnetocardiography. Int J Cardiac Imaging 12:47-59, 1996

[4] Mäkijärvi M, Nenonen J, Forsman K, et al: MCG localization of accessory pathways using a realistic torso, Hoke S, Erné S, Okada Y, et al (eds): Biomagnetosm: Clinical Aspects. Amsterdam, Elsevier 1992, 491-495

[5] Fenici R, Melillo G. Magnetocardiography; Ventricular arrhythmias. Eur Heart J 14(Suppl. E):53-60, 1996

[6] Weismüller P, Abraham-Fuchs K, Schneider S. Biomagnetic non-invasive localization of accessory pathways in Wolff-Parkinson-White Syndrome. PACE 14:1961-1965, 1991

[7] Moshage W, Achenbach S, Göhl K, et al: Magnetocardiography in combination with MRI: Verification of localization accuracy with a non-magnetic pacing catheter, Hoke M, Erné S, Okada Y, et al (eds): Biomagnetism: Clinical Aspects, Amsterdam, Elsevier, 1992, 447-451

[8] Oeff M, Burghoff M, Henning L, et al: Magnetocardiographic guiding for catheter ablation of accessory pathways, Deecke L, Baumgartner C, Stroink G (eds): Recent Advances in Biomagnetism, Vienna, 1993, 318

[9] Moshage W, Göhl K, Achenbach S, et al: Ablation of idiopathic ventricular tachycardias and accessory conduction pathways guided by multichannel MCG, Baumgartner C, Deecke L, Stroink G, et al (eds): Biomagnetism: Fundamental Research and Clinical Applications, Amsterdam, IOS Press, 1995, 599-601

[10] Endt P, Hahlbohm H, Kreiseler D, et al: Ein Algorithmus zur Quantifizierung der Fragmentation des MKGs im QRS-Komplex. Biomed Tech 40(Suppl. 1):279-280, 1995[

11] Mäkijärvi M, Montonen J, Toivonen L, et al: Identification of patients with ventricular tachycardia after myocardial infarction by high-resolution magnetocardiography and electrocardiography. J Electrocardiol 26:117-124, 1993

[12] Weismüller P, Richter P, Abraham-Fuchs K. et al: Spatial differences of the duration of ventricular late fields in the signal-averaged magnetocardiogram in patients with ventricular late potentials. PACE 16:70-79, 1993

[13] Schmitz L, Brockmeier K, Trahms L, Erné SN: Magnetocardiography in patients with cardiomyopathy and operated congenital heart disease, Hoke M, Erné SN, Okada Y, Romani G (eds): Advances in Biomagnetism, New York, Plenum Press, 1989, 453-456

[14] Stroink G, Vardy D, Lamothe R, Gardner M: Magnetocardiography and electrocardiographic recordings of patients with ventricular tachycardia, Williamson SJ, Hoke M, Stroink G, Kotani M (eds): Advances in Biomagnetism, New York, Plenum Press, 1989, 437-440

[15] Kariniemi V, Ahopelto J, Karp PJ, Katila TE: The fetal magnetocardiogram. J Perinat Med 2:214-216, 1974

[16] Van Leeuwen P, Schussler M, Bettermann H, Lange S, Hatzmann W: Magnetocardiography for the assessment of fetal heart actions. Gepurtshilfe Frauenheilk 55:642-646, 1995

[17] Menéndez T, Achenbach S, Moshage W, Flüg M, Beinder E, Kollert A, Bittel A, Bachmann K: Prenatal recording of fetal heart actions by magnetocardiography. Z Kardiol 87:111-118, 1998

[18] Dunajski Z, Peters M: Development of the fetal magnetocardiogram from the 13th week of gestation onward, Baumgartner C, Deecke L, Stroink G, Williamson SJ (eds): Biomagnetosm: Fundamental Research and Clinical Applications, Amsterdam, IOS Press, 1995, 704-708

[19] Achenbach S, Moshage W, Menendéz T, Beinder E, Hofbeck M, Buheitel G, Bachmann K, Lang N, Singer H: Clinical results of fetal magnetocardiography. PACE 18:837, 1995

Non-Invasive Determination of the Accessory Pathway Localization by Magnetocardiography

HIRAOKA,M.[1], HIYOSHI,Y.[3], SAKURADA,H.[3], IZUMIDA,N.[2], KAWANO,S.[1], SAWANOBORI,T[1].

Department of Cardiovascular Diseases, Medical Research Institute[1] and Department of Pediatrics, School of Medicine[2], Tokyo Medical and Dental University, Tokyo; Department of Cardiology, Metropolitan Hiroo Hospital[3], Tokyo, Japan.

Introduction

Catheter ablation technique has become a feasible and safe method to cure symptomatic patients of WPW syndrome (1). The method requires a skillful technique of catheter mapping under fluoroscopy with time-consuming process for determination of the accessory pathway localization. It is, therefore, desirable to obtain a non-invasive method for diagnosis of accurate localization of the accessory pathway.

Magnetocardiography (MCG) is applied to detect a weak magnetic field caused by a current flow from the electrical source or generator in the heart (2,3). It has an advantage to detect three-dimensional localization of the current source in the human body with less influenced by different body build and air contained in the lung surrounding the heart as compared to electrical measurements. Therefore, we studied diagnostic accuracy of the accessory pathway localization determined by MCG with comparison to that determined by catheter mapping during electrophysiological study (EPS).

Methods

Seven cases of manifest WPW syndrome and 15 healthy individuals as the control group were studied by MCG. Patients with manifest WPW syndrome had typical ECG findings and frequent episodes of palpitation attacks due to paroxysmal supraventricular tachycardias. Because of these symptoms, they were referred to our hospital for arrhythmia evaluation and possible catheter ablation for the accessory pathway. All seven cases underwent EPS and subsequent ablation procedure. Informed consent of these procedures was obtained from all the patients. Six of 7 patients were also examined chest X-

©1999, Tohoku University Press
Recent Advances in Biomagnetism
T. Yoshimoto et al. (Eds)

ray, CT and MRI as well as MCG before EPS. Information obtained from these images as to the shape and location of the heart relative to other body structures were incorporated into estimation of the location on three-dimensional planes and display of the the current source in MCG data. One case was recorded MCG twice before and after catheter ablation of the accessory pathway.

MCG was recorded using a biomagnetometer with 37 channels (SMI-1004; Sumitomo Metal Inc., Tokyo and Biomagnetic Technology Inc.) placed in a magnetically shielded room (type Ak 3b; Vacuumschmelze GmbH, Germany). Recorded MCG wave data of each channel were clustered by their wave morphologies and averaged for the following analysis. For the dipole estimation, the thorax was imaged as a sphere with a homogeneous conductivity (4). A radius of the thoracic plane was estimated in each subjects and recorded by the digitizer. The estimated sphere was positioned and adjusted for a best-fit to the semi-circular region of the thorax under the biomagnetometer probe during data acquisition according to the digitizer recorded data. The information of the heart silhouette and other body structures from the images of X-ray, CT and MRI was also incorporated into data acquisition and display of MCG data. Then, the source localization of a single equivalent current dipole (single dipole) at each instance of the excitation was estimated in three dimensional planes of the thorax using the Sarvas' formula for the sphere model (4).

Results

1.A single dipole and its movement during ventricular excitation detected by MCG

In the control group, a single dipole first appeared in the middle anterior chest along left sternum edge, with the source current directed toward right and right-inferior. Then, the dipole moved to the right and right anterior-inferior direction with inferior-oriented current. Subsequently, the dipole movement shifted to the left and left posterior direction. The movement of the dipole was smooth and continuous up to 20-30 msec of QRS in 11 of 15 cases. Four cases showed a sudden jump of a dipole movement to the right upper anterior portion at 10-20 msec of QRS. In patients with WPW syndrome, initial appearance of the dipole, their locations and subsequent movements, and current directions were quite different from those of the control and were variable among individual cases depending on types of ECG findings, possibly reflecting the location of accessory pathway and fusion of ventricular excitation. The movement of the dipole was little and stayed around the same area up to 20-30 msec of QRS. After the accessory pathway was successfully ablated, the movement of the dipole and current direction became similar to those of the control.

2. Accessory pathway localization detected by MCG: Comparison with the location determined by catheter mapping during EPS.

We estimated the accessory pathway location by MCG with incorporation of the body information obtained by chest-Xray, CT and MRI examinations in 6 patients of WPW syndrome. The findings of MCG were compared to the accessory pathway location determined by catheter mapping during EPS under fluoroscopy. Four of 6 cases showed a fairly good agreement of the estimated location of the accessory pathway by MCG to that determined by catheter mapping at or less than 2 cm difference. One case had an estimated location by MCG at about 3 cm anterior to that determined by catheter mapping: Catheter mapping disclosed the accessory pathway at the right posterior septum, while MCG estimated the location at 3 cm anterior to this location. Another case of the left posterior accessory pathway showed the MCG determination at the right ventricular outflow tract.

Discussion

MCG measurements could determine the dipole location at each instance, their movements, and dipole current directions for the initial 30 msec of ventricular excitation in the normal subjects. In WPW syndrome, the dipole locations, their movements and dipole current directions were quite abnormal compared to those of the normal individuals, suggesting abnormal ventricular excitation through the accessory pathway. This was confirmed by normalization of these dipole movements and locations after a successful catheter ablation of the accessory pathway. MCG measurements were applied to diagnose the accessory pathway localization (5,6), but their measurements were not compared to other diagnostic methods to confirm their accuracy. As to diagnostic accuracy for non-invasive determination of the accessory pathway localization, we employed MCG measurements using the sphere model of Sarvas' formula and the results were compared to those determined by catheter mapping during EPS. MCG measurements gave a fairly good agreement with those of catheter mapping within 2 cm difference in 4 of 6 cases. MCG determination, however, had a tendency to estimate the accessory pathway slightly anterior direction than the site determined by catheter mapping. This may be caused by differences in timing of the two recordings and probably due to the sphere model employed for the MCG measurements. We may need further refinement for the theoretical calculation of the sphere model more closely to the human thorax. The reason for inaccurate determination by MCG in one case was not known.

Summary

MCG could determine the location and movements of a single dipole within the heart at each instance of ventricular excitation. We estimated the accessory pathway localization by MCG measurements and the results were compared to the sites determined by catheter mapping during EPS in 6 cases of WPW syndrome. In 4 of 6 cases, the accessory pathway localization was in a fairly good agreement between the two measurements. Therefore, MCG can be applied to non-invasive estimation of the accessory pathway localization, which may help to shorten fluoroscopic time for catheter ablation procedure.

References

1) Jackman WM, Wang X, Friday KJ, et al. Catheter ablation of accessory atrioventricular pathways (Wolf-Parkinson-White syndrome) by radiofrequency current. N Eng J Med.324:1605-1611,1991.

2) Baule GM, McFee R. Detection of the magnetic field of the heart. Am Heart J.66:95-96,1960.

3) Hart G. Biomagnetometry: Imaging the heart's magnetic field. Br Heart J.65:61-62,1990.

4) Sarvas J. Basic mathematical and electromagnetic concepts of the biomagnetic inverse problem. Phys Med Biol.32:11-22,1987.

5) Makijarvi M, Nenonen J, Toivonen L, et al. Magnetocardiography: Supraventricular arrhythmias and preexcitation syndromes. Eur Heart J.14:46-52,1993.

6) Nomura M, Nakaya Y, Saito K, et al. Noninvasive localization of accessory pathways by magnetocardiographic imaging. Clin Cardiol.17:239-244,1994.

Detection and Localization of Myocardial Ischemia and Viability by Magnetocardiography

Mäkijärvi M[1,2], Hänninen H[2], Takala P[4], Pesola K[4], Nenonen J[4], Lauerma K[3], Montonen J[4], Korhonen P[1,2], Oikarinen L[1,2], Toivonen L[1,2], Katila T[4]
Division of Cardiology[1], BioMag Laboratory[2] and Department of Radiology[3], Helsinki University Central Hospital, Helsinki, Finland;
Laboratory of Biomedical Engineering[4], Helsinki University of Technology, Espoo, Finland

Introduction

Detection, quantification and localization of ischemia is clinically important. New therapeutic interventions for revascularization enable treatment of new and larger patient groups. These techniques include coronary angioplasty and stenting, debulking methods like rotablation, mini-invasive surgery as well as surgical or percutaneous transmyocardial laser revascularization. Several noninvasive technologies for ischemia detection already exist: radionuclide methods, magnetic resonance imaging, stress echocardiography and positron emission tomography. However, many of these methods are either expensive or not available for most clinical centers. Therefore, new techniques for detection of myocardial ischemia are still warranted.

Electromagnetic changes caused by ischemia

Myocardial ischemia and necrosis cause clearcut changes in the electrophysiological properties of the myocardium. The resting transmembrane potential decreases and the upstroke amplitude of the action potential and its velocity is lowered [1]. The conduction velocity decreases markedly and unhomogenously in the ischemic areas resulting in the dispersion of the activation front. Ischemic and infarcted regions should therefore have different electromagnetic properties reflecting e.g. changes in the amplitudes and current densities of the recorded signals. The ST-segment changes have been experimentally shown to be a secondary result of a primary injury current that is interrupted during the ST interval [2].

The magnetic field generated by the heart is produced by the same ionic currents in the volume conductor, which produce the ECG [3]. Since the MCG and ECG are produced by the same class of currents, the MCG has the same morphological features as the ECG, such as QRS complex and T, P and U waves. However, there are some fundamental differences: the MCG is sensitive to closed loop currents (so called vortex currents) and the magnetic signals do not depend on the skin resistivity and other troublesome fields unlike the ECG [4]. Observed differences in the patterns of repolarization in the epicardium and endocardium could also be caused by ischemia and thus support a current distribution with possible loop (vortex) character [5,6].

These experimental findings are supported by the study of Brockmeier et al. producing stress by pharmacological agents in normal subjects and recording multichannel magnetocardiography and electrocardiography simultaneously [7]. During peak stress and maximum heart rates, comparison of the repolarization showed substantial changes in the MCG up to T-wave inversions. In the ECG only junctional ST-segment shifts were present. In detailed analysis of the electromagnetic fields, it was found that when the current dipole moment change at the onset of the T wave were marginal, the magnetic dipole moment changed drastically. The authors hypothesized the changes in the intensity and the orientation of the magnetic dipole to reflect the so called vortex currents as the biophysical basis of these differences of nonpathological origin between MCG and ECG.

Ischemia in magnetocardiogram

Basicly, detection of all different types of ischemia by MCG has been reported in the literature. MCG has been shown to be able to detect and localize acute ischemia caused by acute myocardial infarction [8] or induced by exercise [8,9]. Changes on magnetocardiograms in chronic ischemic heart disease have also been reported [10,11,12]. In these studies, acute and chronic ischemia have caused both morhological and spatio-temporal changes in MCG map patterns. QRS changes, ST-segment shifts and T-wave inversions have been seen resembling the alterations in the ECG recordings. In addition, the orientation of the magnetic field maps seems to change drastically during acute or silent ischemia [13,9].

On the contrary, chronic ischemia is typically characterized by reduced amplitude and decreased current densities reconstructed by the minimum norm estimation [10,8,11,14]. Qualitative identification of ischemia by MCG can be easily done by comparing normals and ischemic patients during resting state and exercise, but reliable quantification and localization of ischemic myocardial areas requires still high-quality 3-D imaging (i.e.

©1999, Tohoku University Press
Recent Advances in Biomagnetism
T. Yoshimoto et al. (Eds)

magnetic resonance imaging) and preferably sophisticated individualized torso models [14].

Exercise induced ischemia in MCG

Already in the 1970's ischemic ST-segment depressions similar to ECG has been reported after an exercise test of coronary heart disease patients [15,16]. Saarinen et al. showed that the ratio of ST-segment depression to R-wave amplitude after exercise is even greater in the MCG than in the ECG [15]. Cohen et al. reported ST depression visible in the MCG but not in the standard exercise ECG [16]. In the beginning of 1980's Cohen et al. demonstrated exercise induced ischemic ST-segment shifts in the direct current MCG in a patient with coronary artery disease after a step stress test [17].

Many years later Seese et al. investigated 11 patients with coronary heart disease and positive exercise ECG [8]. They were studied using an amagnetic bicycle ergometer in the magnetically shielded room. MCG was recorded before and immediately after exercise when signs of ischemia were still present in ECG. The minimum norm estimation was used to reconstruct the current density distribution during the ST-segment and the data were combined with X-ray and MRI images. The results were compared with coronary angiography and myocardial scintigraphy. During ischemia there was a significant elevation or depression of the ST segment both in MCG and ECG in all patients. The injury currents were in most cases directed from the ischemic area to the non-ischemic area. For example, anterior ischemia caused an injury current directed from the apex to the base of the heart. The anatomical location of the injury currents was in topographical agreement with the results of the reference methods.

Very recently Hänninen et al. have shown further evidence of the diagnostic power of MCG to detect ischemia and viability [9]. In this study they investigated 18 patients with single vessel coronary artery disease compared with 18 normals. The subjects performed a symptom limited exercise test pedalling a nonmagnetic ergometer in supine position. The rotation of the magnetic field vector was found to be a good parameter for identification of coronary artery disease. Patients with a stenosis of the left anterior descending artery showed a mean rotation of 94 degrees of the field vector during the ST segment compared to 49 degrees in patients with right coronary stenosis and 33 degrees in normals. On the other hand, patients with right coronary stenosis had their T-wave field rotated up to 44 degrees 4 minutes post exercise compared to 29 degrees of the left anterior descending stenosis and 8 degrees of the normals. The clinical reference methods were coronary angiography and thallium stress test. This preliminary study shows that exercise MCG can detect and localize ischemia at least in patients with single vessel coronary artery disease.

Acute myocardial infarction and MCG

So far there are very few clinical MCG observations from the acute phase of myocardial infarction in man. Seese et al. have reported 5 patients studied during the very first days of acute myocardial infarction [8]. Patients were examined in the acute phase of myocardial infarction. The minimum norm estimation was used to reconstruct the current density distribution during the ST-segment and the data were combined with X-ray and MRI images. The results were compared with coronary angiography and myocardial scintigraphy. Acute myocardial infarction (ischemia and necrosis) caused a significant elevation or depression of the ST segment both in MCG and ECG in all patients. The injury currents induced by transient ischemia and infarction of the same anatomical region were found to flow in opposite direction. This change of direction was reflected to either ST-depression or ST-elevation in morphological signals.

MCG changes owing to previous myocardial infarction have earlier been reported by several authors. However, the total number of reported cases is small and does not allow much detailed analysis of the MCG patterns in various infarct locations. Lant et al. have demonstrated the complementary nature of electrocardiographic and magnetocardiographic data also in patients with ischemic heart disease [18]. In post infarction patients they have shown that the differences between MI patients and normals were greater in ECG mapping especially during Q wave and in MCG mapping, on the contrary, during the repolarisation. In particular, MCG mapping showed complex, nondipolar structure in patients with non Q wave infarction. According to these investigators this could have been caused by prolonged ischemic injury increasing tangential current flow through the spared subendocardial tissue.

Lately, Van Leeuwen and collegues have developed an index for the varibility of the QT interval dispersion called Smoothness Index. With this index they could reliably separate myocardial infarction patients from normals [13].

Chronic ischemia and myocardial viability

There are still very few clinical studies on chronic myocardial ischemia and viability by MCG. Leder et al. investigated 40 subjects half of them patients with a history of myocardial infarction [11]. All patients underwent 12-lead-electrocardiogram, stress-test, echocardiography, coronary angiography, and most of them T1-SPECT. Individual volume conductor properties and physiologically meaningful constraints for current generator reconstructions were extracted from T1-weighted 3D-MR-images. Current density was calculated for myocardial support points using depth normalized minimum norm least square estimates and overlayed with 3D-MR-images. Results show that the current density is increasing from QRS onset to QRS maximum. The majority of healthy myocardial regions has high current densities. Corresponding to the absence of electrical active myocardial tissue, MCI shows reduced current density for regions of infarcted myocardium. Infarcted areas have current densities < 1 $\mu A/mm^2$. The current density distribution correlates with other cardiological investigations (eg. left heart catheterization, scintigraphy, echocardiography). These are promising results for further application of current density reconstruction algorithms. In 55% of 40 patients/normals investigated, MCI had complete correspondence with the other cardiological findings, in 27% they found partly correspondence and 18% MCI failed to provide correct diagnosis.

Recently same authors published a very detailed analysis of two infarction patients (one anterior and one inferior) and two healthy controls using the same methods and confirming the results of the initial series [14]. The main finding of these studies was the markedly decreased regional current densities in the areas corresponding to the infarcted segments of the heart defined by the clinical reference methods. The authors conclude that the proposed multiple dipole model may in the best case be able to distinguish viable from scarred myocardium. However, further studies are needed in order to define the spatial resolution and the diagnostic performance of this method. In addition, the ability of this method to identify and localize chronic ischemia or hibernation (not scar) remains unknown.

Specific changes during the repolarization phase of the cardiac electric cycle have recently been proposed to be related to coronary heart disease and possible silent chronic ischemia [12,13]. In the study by Van Leeuwen et al. patients with significant coronary stenosis but without myocardial infarction were found to have alterations of the magnetic field map orientation resembling the changes detected in infarction patients although there were no changes in the standard 12-lead ECG [13]. Moreover, the QT interval of the coronary patients was found to be more dispersed, more variable between neighboring channels and map pattern globally altered [12].

We have recently started a study, which is designed to test the diagnostic performance of MCG mapping to detect and localize areas of hibernating myocardium. The viability of the myocardium is confirmed by a full set of other diagnostic tests: exercise ECG, thallium stress test, dobutamine MRI and positron emission tomography (PET). The preliminary results of the first three patients look promising but there is a clear need for better software and modelling concerning chronic ischemia.

Advantages and disadvantages of MCG

Magnetocardiography has many advantages for a clinical method. First of all, it is fully noninvasive. There is no real need to attach anything extra to the patient. Current operating multi-channel systems are also very fast. A full measurement is carried out in just a couple of minutes. Both of these features mean highest patient comfort. Magnetocardiography can offer multiple electromagnetic parameters at one shot for complete electromagnetic characterization of the patient's heart. In addition, the spatio-temporal resolution is much higher than in conventional electric methods. Moreover, this novel technology always carries a substantial potential for extracting new physiological and pathophysiological information of the heart's electric acitivity.

There are ofcourse some disadvantages. The equipment is still expensive. The need of a shielded room excludes the wide applicability of the method as a quick bed-side test. The system is sensitive to any metal objects, which is an exclusion criteria for some patients.

Conclusions

Untill now the information content of the electromagnetic signals of the heart is used clinically only in the form of very limited standard 12-lead electrocardiogram. The more extensive electric mapping methods are time consuming to apply clinically and complicated to analyze. The fast technical development during the last years resulting in increased computer performance together with new algorithms and advanced source modelling, magnetocardiography (MCG) is offering now new independent information from normal and pathological cardiac function. Detection and localization of ischemia and viability would concern a large number of cardiac patients, if MCG method proves to be useful. Studies on the prognostic value of MCG after myocardial infarction are currently under way.

In the present state, we can conclude that detection of acute ischemia by MCG is definitely possible and the MCG method might even be more sensitive than the ECG in this task. This is probably related to the special properties of the MCG such as the ability to detect so called tangential injury currents (loop currents, vortex currents). Also the localization of ischemic areas should be possible accurately enough for clinical purposes. This application still needs more development and validation work. For the moment, the identification of chronically ischemic or hibernating myocardium by MCG has to be proven although the initial experience seems to be promising. There is still a clear need for better mathematical models for ischemia and large enough clinically appropriate patient studies. The increasing availability of high performance multichannel MCG systems in clinical environment will strongly contribute to these efforts.

References

[1] Janse MJ, Kleber AG. Electrophysiological changes and ventricular arrhythmias in the early phase of regional myocardial ischemia. Circ Res 1981;49:1069-1081.

[2] Cohen D, Kaufman LA. Magnetic determination of the relationship between the S-T segment shift and the injury current produced by coronary artery occlusion. Circ Res 1975;36:414-424.

[3 Cohen D, McCaughan D. Measurements and a simplified interpretation of magnetocardiograms from humans. Circulation 1969;39:395-402.

[4] Plonsey R. Comparative capabilities of electrocardiography and magnetocardiography. Am J Cardiol 1972;29:735-736.

[5] Antzelevitch C, Litowsky SH, Lukas A. Epicardium versus endocardium: Electrophysiology and pharmacology. In Zipes DP, Jalife J, eds.:cardiac Electrophysiology: From Cell to Bedside. WB Saunders, Philadelphia, 1990, pp. 386-395.

[6 Wikswo JP Jr, Barach JP. Possible sources of new information in the magnetocardiogram. J Theoret Biol 1982;95:721-729.

[7] Brockmeier K, Schmitz L, Bobadilla Chavez J, Burghoff M, Koch H, Zimmermann R, Trahms L. Magnetocardiography and 32-lead potential mapping: Repolarization in normal subjects during pharmacologically induced stress. J Cardiovasc Electrophysiol 1997;8:615-626.

[8] Seese B, Moshage W, Achenbach S, Killmann R, Bachmann K. Magnetocardiographic (MCG) analysis of myocardial injury currents. In: Biomagnetism: Fundamental Research and Clinical Applications. Baumgartner C, Deecke L, Stroink G, Williamson SJ (eds). Elsevier Science, IOS Press, Amsterdam, 1995, pp 628-632.

[9] Hänninen H, Takala P, Mäkijärvi M, Montonen J, Nenonen J, Katila T, Toivonen L. Dtection of exercise induced myocardial ischemia by multichannel magnetocardiography in patients with single vessel coronary artery disease. 8th International Congress of Holter and Noninvasive Electrocardiology, Annals of Noninvasive Electrocardiology 1998.

[10] Saarinen M. Magnetocardiogram in coronary artery disease. Ann Clin Res 1989.

[11] Leder U, Hemmann A, Eichorn J, Pohl HP, Hoffmann M, Huck MP, Nowak H, Haueisen J, Michaelsen S, Kuhnert H, Muller S. Segmentation of realistically shaped surfaces from 3D MRI for biomagnetic myocardial

[12] Hailer B, Van Leeuwen P, Pilath M, Lange S, Grönemeyer D, Wehr M. Changes in the spatial dispersion of QT interval in patients with coronary artery disease. PACE 1998;21(4 Part II):908.

[13] Van Leeuwen P, Hailer B, Wehr M. Spatial distribution of QT intervals: an alternative approach to QT-dispersion. PACE 1996;19:1894-1899.

[14] Leder U, Pohl H-P, Michaelsen S, Fritschi T, Huck M, Eicchorn J, Muller S, Nowak H. Noninvasive biomagnetic imaging in coronary artery disease based on individual current density maps of the heart. Int J Card 1998;64:83-92.

[15] Saarinen M, Karp PJ, Katila TE, Siltanen P. The magnetocardiogram in cardiac disorders. Cardiovasc Res 1974;8:820-834.

[16] Cohen D, Lepeschkin E, Hosaka H, Massell BF, Myers G. Abnormal patterns and physiological variations in magnetocardiograms. J Electrocardiol 1976;9:398-409.

[17] Cohen D. Steady fields of the heart. In: Williamson SJ, Romani G-L, Kaufman L, Modena I, eds. Biomagnetism. An Interdisciplinary Approach. New York, Plenum Press, 1983, pp. 265-274.

[18] Lant J, Stroink G, ten Voorde B, Horacek BM, Montague TJ. Complementary nature of electrocardiographic and magnetocardiographic data in patients with ischemic heart disease. J Electrocardiol 1990;23:315-322.
current imaging. Proceedings of the 10th International Conference on Biomagnetism, Sante Fe, 1996.

[19] Van Leeuwen P, Hailer B, Donker D, Lange S, Wehr M. Noninvasive diagnosis of coronary artery disease at rest on the basis of multichannel magnetocardiography. PACE 1998;21(4 Part II):908.

Diagnosis of Complex Arrhythmias: Advanced Technology Utilizing Magnetic Fields and the Limitations of Magnetocardiography

Shoda M, Fuda Y, Kasanuki H

Department of Cardiology, The Heart Institute of Japan, Tokyo Women's Medical College, Tokyo, Japan

Introduction

Radiofrequency catheter ablation has been widely used for treatment of tachyarrhythmias. It has become the first-line therapy especially for Wolff-Parkinson-White syndrome and atrioventricular reentrant tachycardia. Therefore, at present the main aim of electrophysiological testing is the diagnosis of tachyarrhythmias for ablation procedures. Magnetocardiography (MCG) has become available as a noninvasive diagnostic tool for arrhythmias and can identify the rough location of accessory pathways and the focus of arrhythmias. However its diagnostic accuracy may not be sufficient to navigate the electrophysiologist to the site to be ablated, especially in the case of the more complicated arrhythmias.

Recently, a novel mapping system utilizing magnetic fields has been developed and used to analyze the mechanism of arrhythmias, and to locate the appropriate site of ablation. This system is a non-fluoroscopic, computer-based, three-dimensional and electro-anatomical mapping instrument. We investigated complex atrial tachycardias in patients following open heart surgery and performed radiofrequency ablation procedures.

Methods

1) Patients

A 22-year-old female with tricuspid atresia following Fontan operation and a 50-year-old male with tetralogy of Fallot after surgical repair were referred for electrophysiologic study and radiofrequency catheter ablation of symptomatic supraventricular tachycardias.

2) Electrophysiologic Study

A routine electrophysiologic study was performed in the fasting, non-sedated state, after written informed consent was obtained. Duodecapolar Crista, decapolar and octapolar deflectable catheters (Cordis-Webster) were introduced via sheaths inserted in the bilateral femoral and left subclavian veins and positioned in the right atrium, coronary sinus and His-bundle region, respectively. Simultaneous recording of the intracardiac electrograms in the right atrium and coronary sinus was performed to observe the atrial activation sequence during the tachycardia.

3) Electroanatomical Mapping

System components: The mapping system (Fig. 1) consisted of an external ultra low magnetic field emitter, the CARTO processor (Biosense), monitor, workstation (Silicon Graphics Inc.) and set of two catheters with miniature magnetic field sensors (Cordis-Webster). The details of the system have been described in previous reports (1-5).

Mapping procedure: Electroanatomical mapping was performed during stable tachycardia. The reference catheter was placed in a stationary position within the coronary sinus. The mapping catheter was introduced to the upper part of the right atrium and dragged down over the endocardium. The system was used in conjunction with conventional fluoroscopic catheter orientation and navigation methods at the beginning of the procedure until an understanding of the

©1999, Tohoku University Press
Recent Advances in Biomagnetism
T. Yoshimoto et al. (Eds)

obvious configuration of the right atrium was obtained. Thereafter, the mapping catheter was navigated mainly with the electroanatomical mapping system and without the use of fluoroscopy. The data collection in the right atrium and the construction of a three-dimensional electroanatomical map were performed as described previously (4, 5). The distance between each data point was less than 3 cm in order to delineate important anatomical structures such as the superior vena cava, inferior vena cava, tricuspid annulus, surgical scars and surgical patches. A plurality of points was acquired within the zone of slow conduction and other areas of interest. Intracardiac electrograms were recorded with a 30-400 Hz band-pass filter.

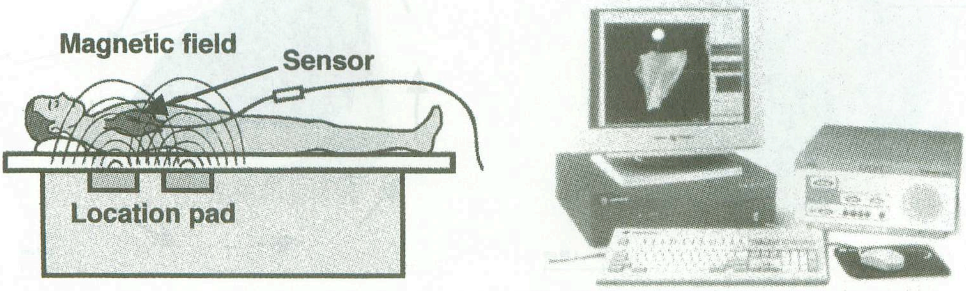

Fig. 1: Components of the electro-anatomical mapping system. Three independent magnetic fields are created by a location pad which is set under the examination bed. The magnetic sensor in the tip of catheter can recognize the strength and direction of each magnetic field. The CARTO processor and computer workstation analyze the location of the catheter and intracardiac electrograms simultaneously.

4) Radiofrequency Catheter Ablation

The patients subsequently underwent radiofrequency catheter ablation for their tachycardia. A RF Marinr (7F deflectable quadrapolar 4 mm-tipped electrode ablation catheter with a thermocouple; Medtronic) was used in conjunction with an Atakr (500kHz radiofrequency generator; Medtronic). Using conventional fluoroscopy, an ablation catheter was inserted into the right atrium and navigated to the site of ablation determined by the electroanatomical mapping.

Results

1) Electroanatomical Mapping

Three-dimensional electroanatomical mapping precisely revealed the morphology of the right atrium and activation pattern during the tachycardia (Fig. 2). Furthermore, it delineated the arrhythmogenic substrates created by previous surgeries such as atriotomies and baffles, and other scar tissue, by measuring the low-voltage areas in the right atrium. The mechanism of tachycardia was revealed to be macro-reentry (anterior to posterior in the right atrial free wall and posterior to anterior in the intraatrial septum) in both patients.

2) Radiofrequency Ablation

Radiofrequency pulses were applied to the site which fulfilled concealed entrainment and a post-pacing interval equal to the tachycardia cycle length at every site in which intracardiac electrograms were recorded in the zone of slow conduction detected by the three-dimensional electroanatomical mapping. Radiofrequency ablation was performed by the temperature-controlled technique at 60 degrees centigrade for 60 seconds. The location of the ablation catheter was fixed during the radiofrequency application. The tachycardia was terminated by single-site radiofrequency applications (Fig. 3, right panel) and was no longer inducible after the ablation procedure.

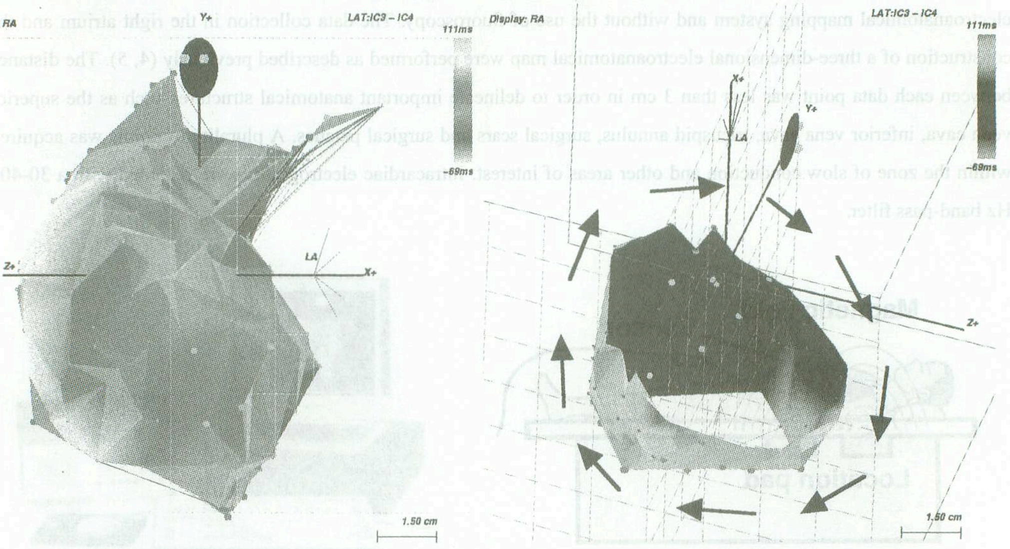

Fig. 2: Three-dimensional electro-anatomical map of the right atrium in a patient with tricuspid atresia after a Fontan operation (left panel: left anterior oblique view, right panel: clipped right posterior oblique cranial view). The three-dimensional morphology of the right atrium was reconstructed by the workstation demonstrating the activation pattern during the tachycardia. The mechanism of tachycardia was revealed to be macro-reentry (anterior to posterior in the right atrial free wall and posterior to anterior in the intraatrial septum).

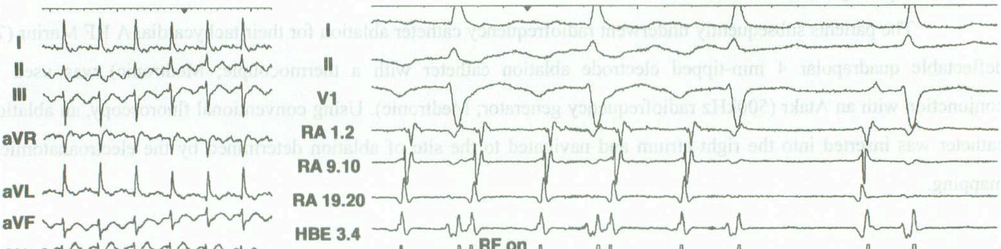

Fig.3: 12-lead ECG during the tachycardia (left panel) and termination of the tachycardia during the radiofrequency application (right panel) in the same patient. The tachycardia was terminated shortly after the onset of the radiofrequency application which was delivered at the site where fragmented activity was recorded. This site was close to the scar area due to the previous open heart surgery. (RA: right atrium, HBE: His bundle electrogram, ABL: ablation, CS: coronary sinus)

Conclusions

1) The new three-dimensional electroanatomical mapping could define in detail the anatomical relationships and electrophysiologic properties that defined the true substrate of the arrhythmia.

2) The three-dimensional electroanatomical map played an important role in understanding where to successfully deliver the radiofrequency energy.

References

(1) Ben-Haim SA, Osadchy D. Schuster I, et al. Nonfluoroscopic, in vivo navigation and mapping technology. Nature Medicine 1996: 2: 1393-5.

(2) Gepstein L, Hayam G, Ben-Haim SA. A novel method for nonfluoroscopic catheter-based electroanatomical mapping of the heart. In vitro and in vivo accuracy results. Circulation 1997; 95: 1611-22.

(3) Shpun S, Gepstein L, Hayam G, et al. Guidance of radiofrequency endocardial ablation with real-time three-dimensional magnetic navigation system. Circulation 1997; 96:2016-21.

(4) Shah DC, Jais P, Haissaguerre M, et al. Three-dimentional mapping of the common atrial flutter circuit in the right atrium. Circulation 1997; 96: 3904-12.

(5) Kottkamp H, Hindricks G, Breithardt G, et al. Three-dimentional electromagnetic catheter technology: electroanatomical mapping of the right atrium and ablation of ectopic atrial tachycardia. J Cardiovasc Electrophysiol 1997; 8: 1332-7.

Clinical Validation of a Multipurpose Amagnetic Catheter and of the Method for Non Fluoroscopic, MCG guided, High Resolution Monophasic Action Potential Recordings

Fenici R, Giorgi A, Ruggieri MP, Brisinda D, Fenici P.

Clinical Physiology - Biomagnetism Research Center, Catholic University, Rome, Italy,

Introduction

Monophasic action potential (MAP) recording is a method for clinical investigation of cardiac arrhythmias, which bridges the gap between experimental and clinical electrophysiology [1-3]. The safest method for MAP recording is the contact electrode technique [4-6] Since the early seventies multiple MAP recordings, either sequential or simultaneous with more than one catheter, were used to quantify, in patients, the dispersion of repolarization and refractoriness [7-10] local conduction disturbances [11] and afterdepolarizations [12-15], on a beat-to beat basis. However major limitations for multiple recordings were: 1) the need of multiple catheters, 2) the spatial resolution of local recordings, which cannot be precisely defined and maintained stable during long-term studies, 3) the lack of electro-anatomical integration of the EP information obtained and 4) the lack of preoperative knowledge of the three-dimensional coordinates of the arrhythmogenic substrate, where the MAP catheter would more easily detect electrophysiological abnormalities. In this paper a new method is described for multiple simultaneous MAP recording based on a single amagnetic catheter (AC) [16,17] which can be localized with magnetocardiographic mapping (MCG) [18-20] and imaged into a 3D model or MRI slices of the patient's heart, to integrate spatially the EP information obtained with MAP recording.

Methods

The multipurpose amagnetic catheter for MCG-guided multiple simultaneous MAP recording is a patent of the Italian National Research Council [21]. The catheter, 6F or 7F size, in the simplified configuration, shown in Fig.1a features four non-polarizable amagnetic electrodes at the tip, arranged in such a way that four monophasic action potentials can be simultaneously recorded, with a spatial resolution of 4 mm^2. Alternatively current dipoles of different geometry and strength, can be generated in the patient's heart, without artifacts induced by ferromagnetic materials. In other versions the AC features also additional lumens for fluid infusion and to insert a steerable wire and an optic fiber, suitable for laser ablation [21]. The pacing thresholds obtained with this catheter are ranging between 0.1 and 0.5 mA. For analog recording all tip electrodes are connected to the positive input of high impedance DC-coupled optically isolated differential preamplifiers. The reference electrode to the negative input of the amplifier. With this recording setup MAP signals are oriented upward. For digital processing, although MAP of apparently comparable morphology can be recorded with the new standard digital recorders for electrophysiology, which generally provide a band-pass filtering of 0.05-500 Hz and digitization at 1 kHz (Fig. 1c), a proper bandwidth for MAP recording is DC - 1kHz, with a sampling frequency of 4 kHz (at 12 bit resolution).

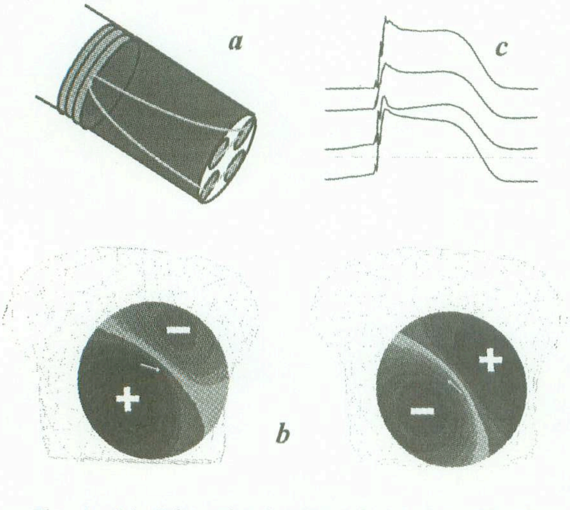

Fig. 1. **(a)** Schematic drawing of the AC. **(b)** The configuration of the fields generated by the AC changes according to the polarity of the current impressed and to the geometry of the dipoles **(c)** Single catheter multiple MAP recording.

For automatic analysis of MAP signals a custom software was developed, which provides automatic calculation of MAP duration at 50% (d50%) and 90% (d90%) of repolarization and local activation time (AT) for each MAP. As indexes of local dispersion of conduction and repolarization, the coefficient of variation (CV) of local AT and of d50% and d90% can be also automatically calculated and displayed.

The 3D position of the catheter's tip can be automatically calculated using the MCG method and displayed into the realistic torso

©1999, Tohoku University Press
Recent Advances in Biomagnetism
T. Yoshimoto et al. (Eds)

model, constructed with the boundary element method (BEM), or on MRI slices of the patient's heart (Fig. 2).

First magnetocardiographic (MCG) localization of the AC was done first in the unshielded catheterization room of the Biomagnetism Center at the Catholic University of Rome [22,23]. More recently the method has been validated also in the BioMag shielded room at the Helsinki University Central Hospital (HUCH) [24,25].

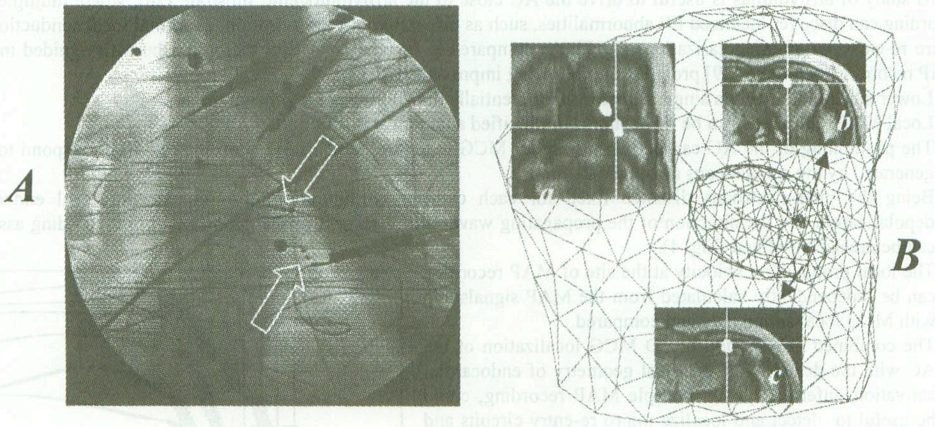

Fig. 2. (A) Frontal fluoroscopy of two amagnetic catheters, placed in the right ventricle, at the mid-anterior wall (upper arrow) and at the apex of the right ventricle (lower arrow). (B) MCG localization of the AC in the BEM torso model and in frontal (a), and axial MRI slices [(b) mid-anterior and (c) apex].

Results

The amagnetic catheter is very reliable for multiple simultaneous MAP recording with a well defined and high spatial resolution [16]. In patients without arrhythmias the average amplitude of the right ventricular (RV) MAP was 23 ± 9 mV. The average amplitude of right atrial MAP was 5.9 ± 2 mV. Local CV of RV MAP duration at 50% and 90% level of repolarization were 7.4% and 3.1%, respectively. The CV of local AT was 1.1%.

Once the catheter is properly placed in contact with the endocardial surface, the MAP signals remain stable for more than two hours, although the recording electrodes are alternatively used to induce different pacing dipoles for MCG localization of the catheter. In two hours the amplitude of the MAP signal decreases of about 50%.

The orthogonal position of the catheter against the endocardium can be easily monitored. In fact, if all the tip electrodes are equally in contact with the endocardium, the quality of all the four MAP recordings is comparable. If one electrode is not touching properly the endocardium the corresponding MAP is distorted or even reversed in polarity (Fig. 3).

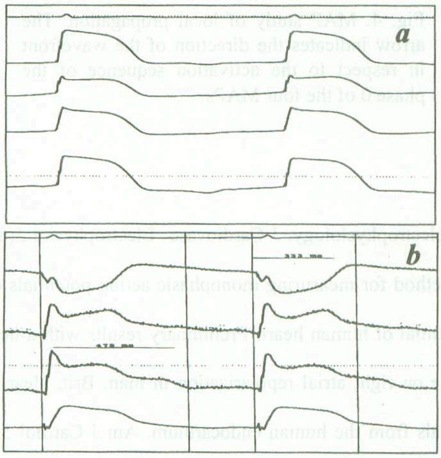

Fig. 3. MAP monitoring of (a) good, or (b) bad endocardial contact of the AC .

Being the inter-electrodes distance fixed for each catheter configuration, the sequence of local endocardial depolarization, the direction of the propagating wavefront and the propagation velocity in respect of the geometry of the recording assembly can be precisely defined (Fig. 4). In patients with arrhythmias, local abnormalities of repolarization and of conduction can be evidenced with single catheter multiple MAP recording.

With a single channel MCG instrumentation the average 3D localization error was 11.2 ± 5.6 mm [17,22,23]. Multichannel MCG recording in high performance shielded rooms provides much better accuracy, and allows quasi real-time localization and imaging of the tip of the AC on a beat-to-beat basis, using a moving equivalent current dipole in a realistic homogeneous torso model. The heart model, placed inside the torso after the calculations, is necessary for the anatomical imaging of the localization figures. Moreover a real-time dynamic interpolation of subsequent localizations of the AC during the EPS, can be used to draw more realistic endocardial boundaries of the patient's BEM model. This might improve electroanatomical integration of the EP information gained with MAP recording.

Discussion

New catheter-based technologies have been recently developed, for accurate single catheter endocardial activation mapping and for non-fluoroscopic three-dimensional (3D) navigation of EP catheters [26,27]. None of them can be used for preoperative non-invasive localization of the arrhythmogenic target and to combine such “a priori” knowledge with the navigation of MAP catheters. On the contrary preliminary observations suggest that preoperative MCG study of arrhythmias is useful to drive the AC close to the arrhythmogenic substrate [28], where multiple MAP recording can discover localized EP abnormalities, such as dispersion of repolarization, abnormal local conduction with micro re-entry, or afterdepolarizations [7,17]. As compared to conventional EPS therefore, the MCG-guided multiple MAP recording technique [29] provides the following improvements:

1. Lower invasivity, being a single catheter and potentially non-fluoroscopic procedure.
2. Local MAP recordings can be associated to a specified anatomical position.
3. The positioning of the AC can be refined under MCG mapping, until its 3D coordinates will correspond to those generated by the spontaneous arrhythmia.
4. Being the inter-electrodes distance fixed for each catheter configuration, the sequence of local endocardial depolarization and the direction of the propagating wavefront in respect of the geometry of the recording assembly can be precisely defined (Fig. 4).
5. The local propagation velocity at the site of MAP recording can be independently calculated from the MAP signals and with MCG localization data and compared.
6. The combined information of 3D MCG localization of the AC with the detection of the local geometry of endocardial activation, inferred by the multiple MAP recording, could be useful to detect and localize micro re-entry circuits and multiple simultaneous activation wavefront in patients with atrial fibrillation [30].

In conclusion, MCG-guided multiple MAP recording is a new low-invasivity method for high resolution detection of local electrophysiological abnormalities, from (or very close to) arrhythmogenic areas. The major limitation of the method, at the moment, is the lack of commercially available multichannel MCG mapping systems, working in the EP laboratory with the same sensitivity achievable in high performance shielded rooms. Moreover additional effort in mathematical modeling and software development are needed, to integrate the electro-anatomical information provided by MCG localization of arrhythmias, with that inferred by multiple local MAP recording and to improve the 3D anatomical imaging of the AC. Also body surface potential mapping can localize of the AC and arrhythmias [31], however at the moment its accuracy is lower as compared to MCG [32].

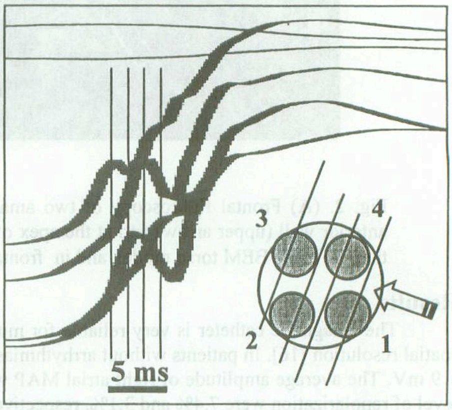

Fig. 4. MAP study of local propagation. The arrow indicates the direction of the wavefront in respect to the activation sequence of the phase 0 of the four MAPs.

References

[1] Franz MR: Bringing the gap between the basic and clinical electrophysiology. J Cardiovasc Electrophysiol 5(8): 699-710, 1994

[2] Olsson SB, Varnauskas E, Korsgren M: Further improved method for measuring monophasic action potentials of the intact human heart. J Electrocardiol 4: 19-23, 1971

[3] Fenici R, Bellocci F, Zecchi P, et al: Monophasic action potential of human heart. Preliminary results with a new technique. Acta Med Rom 11: 300-312, 1973

[4] Fenici R, Marchei M, Bellocci F, et al: Effect of Bunaphtine on right atrial repolarization in man. Brit. Heart J XXXIX: 787-794, 1977

[5] Franz M: Long-term recording of monophasic action potentials from the human endocardium. Am J Cardiol 51: 1629-1634, 1983

[6] Franz MR: Method and theory of measuring monophasic action potential recording. Prog Cardiovasc Vol XXXIII, No 6: 33:347-368, Dis 1991

[7] Morgan JM, Cunningham D, Rowland E: Dispersion of monophasic action potential duration: demonstrable in humans after premature ventricular extrastimulation but not in steady state. J Am Coll Cardiol 19:1244-1253, 1992

[8] Yuan S: Dispersion of ventricular repolarisation. A study in patients with ventricular arrhythmias using monophasic action potential recording technique. (Ph. D. dissertation) University of Lund, Grahns Boktrykeri AB, 1995.

[9] Yuan S, Wohlfart B, Olsson SB, et al: The dispersion of repolarization in patients with ventricular tachycardia. Eur Heart J 16: 68-76, 1995

[10] Levine JH, Spear JF, Guarnieri T et al: Cesium-chloride-induced long QT syndrome: Demonstration of

afterdepolarizations and triggered activity *in vivo*. Circulation 72: 1092-1103, 1985

[11] Fenici R, Masselli M, Zeppilli P, et al: Clinical recordings of monophasic action potentials: demonstration of intra-atrial conduction block in Sinus Node region and possible role in reentrant supraventricular tachycardia. Am Heart J Vol. 102, N. 1:124-128, 1981

[12] Fenici R, Marchei M, Colonna P, et al: Right Ventricular Monophasic Action Potential recording in man after suicidal Digoxin ingestion. VIII World Congress of Cardiology, abstr.n.1480, Tokyo 1978.

[13] Fenici R: Right Ventricular Monophasic Action Potentials in Patients with Long Q-T Syndrome. Br. Heart J 42: 615-616, 1981

[14] Gough WB, Raphael H: The early afterdepolarization as recorded by monophasic action potential technique: Fact or artifact?. Circulation (suppl II) 80:II-130, 1989

[15] El-Sherif N, Bekheit SS, Henkin R: Quinidine-induced long QT interval and torsade de pointes: Role of bradycardia-dependent early after depolarizations. J Am Coll Cardiol 14:252-257, 1989

[16] Fenici P, Ruggieri MP, Fenici R: Multiple simultaneous Monophasic Action Potential recordings with a single biomagnetically localizable amagnetic catheter. Eur. Heart J Vol 17, ISSN 0195 668X, P1560:282A, 1996

[17] Fenici R, Melillo G: Biomagnetically localizable multipurpose catheter and method for MCG guided intracardiac electrophysiology, biopsy and ablation of cardiac arrhythmias. Int J Card Imaging 7: 207-215, 1991

[18] Fenici RR, Melillo G, Masselli M: Clinical Magnetocardiography: ten years experience at the Catholic University of Rome. Int J Card Imaging 7: 3-4: 151-167, 1991

[19] Nakaya Y: Magnetocardiography. Clin Phys Physiol Meas 13: 191-229, 1992

[20] Moshage W, Achenbach S, Göhl K, Bachmann K: Evaluation of the non-invasive localization accuracy of cardiac arrhythmias attainable by multichannel magnetocardiography (MCG). Int J Card Imaging 12: 47-59, 1996

[21] Fenici R, Consiglio Nazionale delle Ricerche: Biomagnetically localizable multipurpose catheter and method for MCG guided intracardiac electrophysiology, biopsy and ablation of cardiac arrhythmias. United States Patent Documents, Patent N.5 056 517, Oct.15, 1991

[22] Fenici R, Melillo G, Cappelli A, et al: Magnetocardiographic localization of a pacing catheter. In: Williamson SJ, Hoke M, Stroink G, et al (eds): Advances in Biomagnetism. New York: Plenum Press, 1989, pp 361-364

[23] Fenici R, Melillo G: Magnetocardiography: ventricular arrhythmias. Eur Heart J 14(suppl.E): 53-60, 1993

[24] Fenici R, Nenonen J, Pesola K, et al: Non-fluoroscopic localization of an amagnetic catheter by multichannel magnetocardiography *(PACE 1997, - under revision)*

[25] Fenici RR, Pesola K, Korhonen P, et al: Magnetocardiographic Pacemapping For Non-Fluoroscopic Localization Of Intracardiac Electrophysiology Catheters . Arch Coeur Vais 91 (III): Abs 193-PW16, 345, 1998

[26] Peters SN, Jackman WN, Schilling RJ, et al: Human left ventricular Endocardial Activation mapping using a novel Noncontact Catheter. Circulation 95: 1658-1660, 1997

[27] Gepstein L, Hayam G, Ben-Haim S: A novel method for nonfluoroscopic catheter-based electroanatomical mapping of the heart. Circulation 95: 1611-1622, 1997

[28] Fenici R, Covino M, Cellerino C, et al: Magnetocardio-graphically guided catheter ablation. J Interv Cardiol 8(Suppl): 825-836, 1995

[29] Fenici R, Fenici P, van Bosheide J: Amagnetic catheter for biomagnetically guided endocardial mapping and ablation of cardiac arrhythmias. In: Reichl H, Heuberger A, eds. Micro System Technologies. Berlin: VDE-Verlag GmbH, 1996, pp 711-716.

[30] Holm M, Johansson, Brandt J, et al: Epicardial right free wall mapping in chronic atrial fibrillation. Eur Heart J 18: 290-310, 1997

[31] Stroink G, Lamothe R, Gardner MJ: Magnetocardiographic and electrocardiographic mapping studies. In: Weinstock H (ed): SQUID Sensors: Fundamentals, Fabrication and Applications. NATO ASI Series, Kluwer, the Netherlands, 1996, pp 413-444

[32] Pesola K, Fenici R, Mäkijärvi M, et al: Comparison of localisation accuracy of magnetocardiographic and body surface potential mapping using an amagnetic stimulation catheter *(this Conference)*

Acknowledgments

This work was supported by the Italian National Research Council (CNR), owner of patents: Ital. Patent N. 1219855, May 24,1990; US Patent N. 5 056 517, Oct.15, 1991; Eur. Patent N. 0428812, March. 08, 1995 and by the MURST (cofinanziamento 97) project N. 9706577608. We are grateful to Professor Luigi Donato for providing the financial support, and to Mr. Luigi Venturelli for developing the prototypes of the amagnetic catheters. We are also indebted to Dr. Jukka Nenonen, Dr. Markku Makijarvi, Dr. Katja Pesola, Dr. Lauri Toivonen, Dr. Petri Korhonen and Prof. Toivo Katila, for invaluable contribution in re-testing the catheter and method also in the BioMag Laboratory of the Helsinki University Central Hospital, within the EU HCM BIRCH Programme. The Neuromag Ltd. (Helsinki) is acknowledged for supporting this research with their advanced software for MSI.

Comparison of the Localization Accuracy of Magnetocardiographic and Body Surface Potential Mapping using an Amagnetic Stimulation Catheter

Pesola, K.[1,2], Fenici, R.[3], Nenonen, J.[1,2], Mäkijärvi, M.[4], Fenici, P.[3], Jokiniemi, T.[1,2], Korhonen, P.[4], Lauerma, K.[5], Lötjönen, J.[1], Valkonen, M.[1,2], Toivonen, L.[4], and Katila, T.[1,2]

Laboratory of Biomedical Engineering[1], Helsinki University of Technology, Espoo, Finland; BioMag Laboratory[2] Medical Engineering Centre, Helsinki University Central Hospital, Helsinki, Finland; Clinical Physiology - Biomagnetism Research Center[3], Catholic University of Rome, Rome, Italy; Department of Internal Medicine, Division of Cardiology[4], Department of Radiology[5], Helsinki University Central Hospital, Helsinki, Finland

Introduction

Magnetocardiographic (MCG) mapping has provided promising results in locating various intracardiac sources, e.g., the origin sites of life-threatening arrhythmias [1]. Reported clinical MCG localisation accuracies, obtained using an equivalent current dipole (ECD) as the source model, range from about 5 mm to 30 mm [2, 3, 4, 5, 6, 7]. In these studies, the ECD has been applied in locating ventricular pre-excitation sites associated with the Wolff-Parkinson-White syndrome, ventricular extrasystolic beats, and the origin of ventricular tachycardia, thus providing valuable information for pre-ablative evaluation of the patients. The ECD is an idealized, focal source model but, as shown above, has been proven to be useful in locating sources which are confined in a small volume of tissue.

The body surface potential mapping (BSPM) can also be used in the localization of sources within the heart. It has been used successfully in arrhythmia localization and in pacemapping studies, as well [8, 9, 10].

The accuracy of the non-invasive MCG and BSPM localisation is mainly influenced by the source and by the volume conductor models, and by the calculation method used in solving the inverse problem. In this study, the obtainable accuracy of MCG and BSPM localizations was investigated in 10 patients using an amagnetic stimulation catheter (AC). The tip of the catheter provides an exactly defined current-dipole source. Thus, it provides an excellent validation for the ECD localizations, calculated from simultaneously recorded MCG and BSPM data. The accuracy of the MCG localizations was investigated in more detail in a separate study [11].

Methods

Ten patients underwent standard electrophysiological studies (EPS) at the Cardiovascular Laboratory of Helsinki University Central Hospital (HUCH). Before the procedure, an informed consent to participate the MCG and BSPM recordings was asked. After the standard EPS, a catheter specially designed to produce no magnetic disturbances was applied [12]. In all ten cases, the AC was placed in the right ventricle. The position of the tip of the AC was recorded in X-ray fluoroscopy, which also showed a set of lead markers serving as reference points. Before moving the patient from the catheterization bed, 123 BSPM signals were recorded for 30 s during cardiac pacing with the BSPM device of the Laboratory of Biomedical Engineering [10]. The layout of the 123 BSPM electrodes is shown in Fig. 1a.

The patient was next transferred to the BioMag Laboratory at HUCH [13]. The locations of the frontal BSPM electrodes as well as the lead markers and the positions of the markers later used in magnetic resonance imaging were recorded with a 3D digitization system (3SPACE, Polhemus Inc., Colchester, VT, USA). In the magnetically shielded room of the BioMag Laboratory (Euroshield Ltd., Eura, Finland), current stimuli of 10 mA in amplitude and of 2 ms in duration were fed into the 5 mm long dipolar sources in the tip of the AC, while simultaneously recording 54 MCG and 51 BSPM channels. Five of the MCG channels were coaxial gradiometers while the rest were ordered in planar gradiometer pairs. The number of the MCG and BSPM channels was limited due to the properties of the data acquisition system. The signals were band-pass filtered to 0.03-500 Hz and digitized with the sampling rate of 2000 Hz. The locations of the 51 BSPM electrodes used in the recordings at the BioMag Laboratory are shown in Fig. 1b.

After the recordings in BioMag, the patient was transported back to the Cardiovascular Laboratory where biplane fluoroscopy imaging with the reference markers and the registration of the 123 BSPM signals were again performed in order to validate the position of the tip of the AC.

In order to perform the calculations from the BSPM data, the locations of the BSPM electrodes in the

©1999, Tohoku University Press
Recent Advances in Biomagnetism
T. Yoshimoto et al. (Eds)

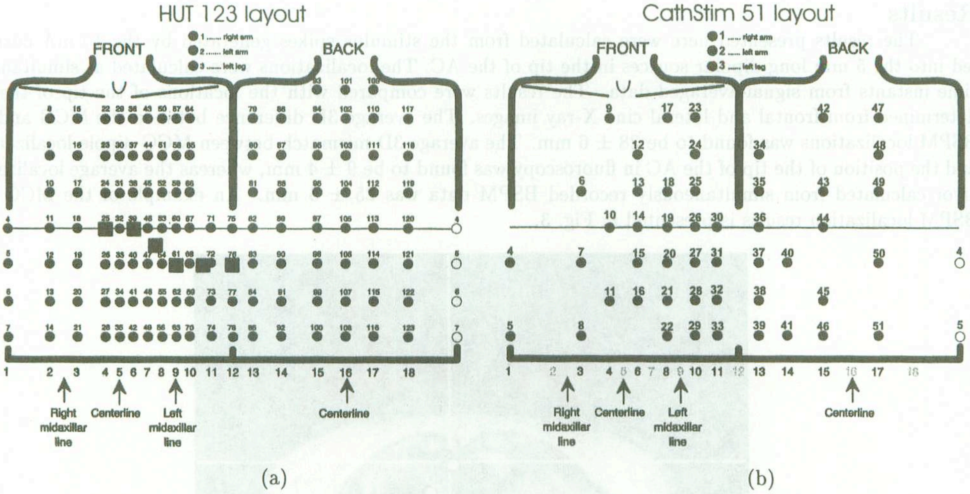

Fig. 1: *The layout of the BSPM electrodes used (a) in the Cardiovascular Laboratory and (b) in the BioMag Laboratory.*

back were generated by taking a set of standard locations and by projecting these locations onto the surfaces of the individual torso models. Typical contour patterns of the MCG and BSPM data at the peak of a stimulus are shown in Fig. 2. In Fig. 2a, the locations of the MCG sensors are also visible. The circles show the positions of the axial gradiometers while the squares denote to the planar gradiometer pairs.

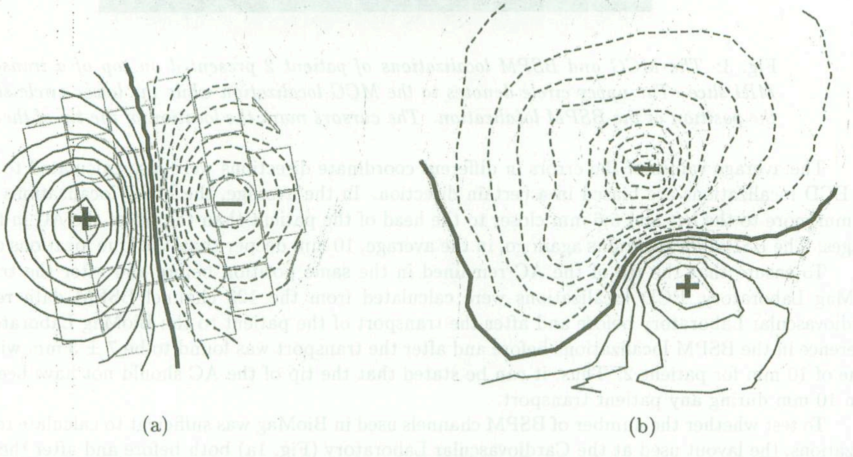

Fig. 2: *The isocontour lines at the spike of a stimulus of (a) the magnetic field perpendicular to the dewar bottom and (b) the electric potential on the surface of the torso. The step between the magnetic isocontour lines is 5 pT, and the electric isocontours are drawn at 200 μV intervals.*

Non-invasive localizations of the tip of the AC were computed from the stimulus spikes in the MCG and BSPM data using the ECD as the source model. The current dipole parameters were estimated with the Levenberg-Marquardt non-linear least squares fitting. The calculations were performed with individual, homogeneous boundary element (BE) torso models.

Results

The results presented here were calculated from the stimulus spikes generated by the 10 mA current, fed into the 5 mm long dipolar sources in the tip of the AC. The localizations were calculated at simultaneous time instants from signal-averaged data. The results were compared with the locations of the tip of the AC determined from frontal and lateral cine X-ray images. The average 3D difference between the MCG and the BSPM localizations was found to be 28 ± 6 mm. The average 3D mismatch between MCG dipole localizations and the position of the tip of the AC in fluoroscopy was found to be 9 ± 4 mm, whereas the average localization error calculated from simultaneously recorded BSPM data was 25 ± 6 mm. An example of the MCG and BSPM localization results is presented in Fig. 3.

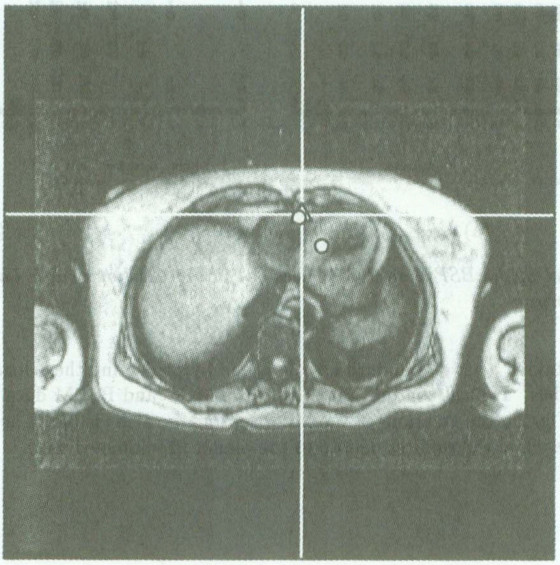

Fig. 3: *The MCG and BSPM localizations of patient 2 presented on top of a transaxial MRI slice. The upper circle denotes to the MCG localization while the lower circle shows the position of the BSPM localization. The cursors mark the location of the tip of the AC.*

The average values of the errors in different coordinate directions were also calculated to check whether the ECD localizations are biased in a certain direction. In the average, the MCG localizations are positioned 5.4 mm more to the left and 6.6 mm closer to the head of the patient than the tip of the AC in the fluoroscopy images. The BSPM localizations again go, in the average, 10 mm deeper than the true locations of the catheter.

To ensure that the tip of the AC remained in the same position before and after the transport to the BioMag Laboratory, ECD localizations were calculated from the 123 channel BSPM data recorded at the Cardiovascular Laboratory before and after the transport of the patient to the BioMag Laboratory. The mean difference in the BSPM localizations before and after the transport was found to be 7 ± 3 mm with a maximum value of 10 mm for patient 2. Thus, it can be stated that the tip of the AC should not have been moved more than 10 mm during any patient transport.

To test whether the number of BSPM channels used in BioMag was sufficient to calculate reliable ECD localizations, the layout used at the Cardiovascular Laboratory (Fig. 1a) both before and after the patient transport was reduced to the layout used at the BioMag Laboratory (Fig. 1b). The first five patients were included in the test. ECD localizations were then calculated at the same time instants from the 123 channel and from the 51 channel BSPM data to see whether the reduced number of electrodes would affect the quality of the BSPM localizations. The average 3D change in the localizations was found to be 6 ± 2 mm while the maximum difference was 8 mm. Thus, it can be stated that the BSPM localization results would not have significantly improved by using the 123 channel electrode set.

Discussion

In this study, the 3D localizations calculated from MCG recordings were found to be more accurate than the corresponding BSPM localizations. The BSPM localization accuracy is inherently affected, e.g., by the inaccuracies in the electrode positions. Even if the locations of the frontal electrodes were digitized in this study, errors up to 3 cm can be estimated to relate to the electrode locations in the back.

The ECD localizations in this study were calculated with homogeneous BE torso models. In the near future, the effect of certain inhomogeneities, e.g., the lungs and the cavities, will be investigated. It can be expected that more accurate BSPM localizations will be obtained by improving the volume conductor models.

References

[1] Nenonen J: Solving the inverse problem in magnetocardiography. IEEE Eng Med Biol Magazine 13: 87-96, 1994

[2] Fenici R, Melillo G. Magnetocardiography: ventricular arrhythmias. Eur Heart J 14 (suppl.E): 53-60, 1993

[3] Moshage W, Achenbach S, Göhl K, et al: Evaluation of the non-invasive localization accuracy of cardiac arrhythmias attainable by multichannel magnetocardiography (MCG). Internat J Cardiac Imaging 12: 47-59, 1996

[4] Mäkijärvi M, Nenonen J, Toivonen L, et al: Magnetocardiography: supraventricular arrhythmias and pre-excitation syndromes. Eur Heart J 14 (suppl.E): 46-52, 1993

[5] Nenonen J, Mäkijärvi M, Toivonen L, et al: Non-invasive magnetocardiographic localization of ventricular pre-excitation in the Wolff-Parkinson-White syndrome using a realistic torso model. Eur Heart J 14: 168-174, 1993

[6] Oeff M, Burghoff M: Magnetocardiographic localization of the origin of ventricular ectopic beats. PACE 17: 517-522, 1994

[7] Stroink G, Lamothe R, Gardner MJ: Magnetocardiographic and electrocardiographic mapping studies, Weinstock H (ed): SQUID Sensors: Fundamentals, Fabrication and Applications. The Netherlands: NATO ASI Series, Kluwer, 1996, pp 413-444

[8] Dubuc M, Nadeau R, Tremblay G, et al: Pace mapping using body surface potential maps to guide catheter ablation of accessory pathways in patients with Wolff-Parkinson-White Syndrome. Circulation 87: 135-143, 1993

[9] SippensGroenewegen A, Spekhorst H, van Hemel H, et al: Localization of the site of origin of postinfarction ventricular tachycardia by endocardial pace mapping. Circulation 88: 2290-2306, 1993

[10] Simelius K, Tierala I, Jokiniemi T, et al: A body surface potential mapping system in clinical use. Med Biol Eng Comput 34 (Suppl. 1, Part 2): 107-108, 1996

[11] Fenici R, Pesola K, Nenonen J, et al: Clinical validation of three-dimensional cardiac magnetic source imaging accuracy with simultaneous magnetocardiographic mapping, monophasic action potential recordings and amagnetic catheter pacing, In these proceedings

[12] Fenici R, Fenici P, van Bosheide J: Amagnetic catheter for biomagnetically guided endocardial mapping and ablation of cardiac arrhythmias, Reichl H, Heuberger A (eds): Micro System Technologies. Berlin: VDE-Verlag GmbH, 1996, pp 711-716

[13] Montonen J, Ahonen A, Hämäläinen M, Ilmoniemi R, Laine P, Nenonen J, Paavola M, Simelius K, Simola J, Katila T: Magnetocardiographic functional imaging studies in BioMag Laboratory, Aine C, Okada Y, Stroink G, Swithenby S, Wood C (eds): Advances in Biomagnetism Research: Biomag96. New York: Springer Verlag, 1998, in press

Acknowledgments

This work was supported by the EU HCM Large Scale Installation in Biomagnetic Research (BIRCH) at Helsinki University of Technology, by the Italian National Research Council (CNR), owner of patents: Ital. Patent N. 1219855, May 24,1990; US Patent N. 5 056 517, Oct.15, 1991; Eur. Patent N. 0428812, March. 08, 1995 and by the MURST (cofinanziamento 97) project N. 9706577608. The authors wish to thank Dr. Helena Hänninen, Dr. Terhi Husa, Dr. Lasse Oikarinen, and nurse Leila Sikanen for assistance in the measurements.

KLT-analysis of QRST integral magnetic field maps of patients with and without coronary artery disease at rest and during pharmacological stress

Adams A[1], Stroink G [1,2], Van Leeuwen P [3], and Hailer B [4]

Department of Physics, Dalhousie University [1], Halifax, Canada B3H 3J5
Department of Physiology & Biophysics, Dalhousie University [2], Halifax, Canada B3H 4H7;
Research & Development Center for Microtherapy (EFMT) [3], Bochum, Germany
Augusta Kranken Anstalt [4], Bochum, Germany

Introduction

Distinguishing patients with coronary artery disease (CAD) from those without CAD is presently performed by a number of techniques including electrocardiogram, echocardiogram and angiography. These techniques are either invasive or not particularly reliable in detecting CAD.

The method explored here uses magnetic field maps (MFM) derived from multiple magnetocardiograms (MCG) obtained with a multichannel system. We used QRST integral maps of patients with and without CAD to determine the non-dipolar content of patient MFMs at rest and under pharmaceutically induced stress. The aim of this study is to determine if the non-dipolar content of these QRST integral maps varies between rest and stressed conditions, and whether such variations can be used to determine the presence of CAD.

Methods

This study involved the analysis of 15 cardiac patients (age 54 ± 7 yrs, 9 male) using a 37-multichannel magnetocardiographic acquisition system (Siemens) while simultaneously recording the 3-limb lead ECG. The procedures used to obtain the data of these 15 patients in both rest and stressed conditions have been presented elsewhere [1]. Briefly summarized, all patients originally reported chest pain, but had no recorded history of coronary artery disease. Electrocardiograms (ECGs) and echocardiograms were performed on all 15 patients at rest, with all patients falling within normal ECG cardiac function and displaying no evidence of wall motion abnormality on the echocardiogram. A pharmacological stress (using arbutamine) echocardiogram with simultaneous 12 lead ECG was subsequently performed followed by rest and stress (again using arbutamine) magnetocardiograms (MCGs). The selected heart rate target for the stress measurements was 120 bpm in order to avoid fusion of the T-wave and the subsequent P-wave. Finally, left heart catheterization and coronary angiography were performed. As a result 7 of the 15 were diagnosed with stenosis ≥ 75 % of at least one coronary artery; in 8 patients relevant CAD could be excluded.

The 37-channel MCG recordings and 3-limb lead ECG recordings for each patient under rest and stressed conditions were averaged using DALECG software [2]. The averaged traces were marked for established cardiac intervals, and QRST integral maps were calculated by summing the MCG values over the QRST interval at each lead. This allowed for 15 rest and 15 stress integral maps to be compared.

The Karhunen-Loève Transformation (KLT) of the 15 rest and 15 stress maps was performed separately. The KLT has also been described elsewhere [3,4,5]. From previous work [5], it was established that the first three eigenvectors represent the dipolar nature of the cardiac signal. Thus, these three eigenvector/eigenvalue combinations were summed together and subtracted from the remaining signal to produce the non-dipolar content of the QRST integral map.

A statistical analysis (Mann-Whitney U test - two sided) was then performed on the resulting non-dipolar content to determine if there were any significant differences in the rest and stress data that may suggest whether the non-CAD and CAD patient maps could be statistically separated. We used the Wilcoxon test for paired variables to compare the differences between rest and stress data.

Results

The maxima, minima and root-mean-squared values (RMS) of the QRST integral maps were determined for both the rest and stress data. Tables 1 and 2 summarize the results for the rest and stress data sets, respectively. We observe significant increases in the QRST map values when stress is induced. Comparing Table 1 and 2 we find, for example, that the average RMS of the QRST integral value increases from (49 ± 21) x 10 pT · ms to (85 ± 35) x 10 pT · ms for

©1999, Tohoku University Press
Recent Advances in Biomagnetism
T. Yoshimoto et al. (Eds)

the non-CAD patient group ($p < 0.023$) and from (45 ± 16) x 10 pT · ms to (95 ± 27) x 10 pT · ms for the CAD group ($p < 0.031$).

Table 1: Average QRST integral map values in multiples of 10 pT · ms during rest (± S.D.).

REST patients	QRST integral maximum	QRST integral minimum	RMS QRST integral
Non-CAD	75±36	-89±43	49±21
CAD	85±36	-70±22	45±16
p-value	0.60	0.60	0.96

Table 2: Average QRST integral map values in multiples of 10 pT · ms during stress (± S.D.).

STRESS patients	QRST integral maximum	QRST integral minimum	RMS QRST integral
Non-CAD	140±62	-133±79	85±35
CAD	160±53	-115±81	95±27
p-value	0.69	0.69	0.54

As part of the KLT analysis we calculated the first 12 eigenvectors for both the rest data and stress data of all subjects. Figure 1 shows the 12 rest eigenvectors, while Figure 2 shows the 12 stress eigenvectors. As can be observed, the first three eigenvectors of the patients at rest and stress are dipolar in nature, while the remaining eigenvectors of each set are multipolar. The addition of each of these eigenvectors with their corresponding, subject specific eigenvalues, form the reconstructed integral map of that subject. The subtraction of the first 3 eigenvector reconstructed map from the 12 eigenvector reconstructed map, averaged over all subjects, leads to the non-dipolar percentages shown in Tables 3 and 4. Table 3 shows the results for the patients at rest. Table 4 shows the results for the patients with induced stress. The p-values express the significance of the difference in the calculated value for the CAD and non-CAD patient groups.

Table 3: Signal content (in %) in the first 3 and first 12 KL-eigenvectors.

REST patients	Percent signal in first 3	Percent signal in first 12	Percent non-dipolar
non-CAD	81±17	98±1	18±17
CAD	83±20	98±3	15±16
p-value	0.93	0.87	1

Table 4: Signal content (in %) in the first 3 and first 12 KL-eigenvectors.

STRESS patients	Percent signal in first 3	Percent signal in first 12	Percent non-dipolar
non-CAD	91±5	99±1	8.4±4.6
CAD	95±2	99±1	4.0±1.5
p-value	0.094	0.56	0.043

Discussion

Recently, several authors [e.g., 6] have observed increases in MCG signal strength of normal subjects during and immediately following exercise. Such increases are also observed here as is evident from the differences in the average map values given in Table 1 and 2. In fact, for all subjects the RMS QRST increases on average by a factor of 2.5. Increases due to exercise of normal subjects do not occur in BSPM data [6] or BSPM QRST integral maps [7]. From Table 1 and 2 we also observe that there are no significant differences between the QRST integral map values of the non-CAD and CAD subject group under either the rest or stress condition.

We have used KLT expansions to calculate the non-dipolar content in QRST integral maps to differentiate between patients with and without coronary artery disease under resting and stressed conditions. Our findings indicate that the statistical differences between the two patient groups, when measured at rest, are minimal. When measured during cardiac stress, however, the differences in the non-dipolar content between the CAD and non-CAD patient groups become significant ($p < 0.05$) (Table 4). The results support the findings of Hailer et al. [1] that MCG results can be used to differentiate between these patient groups. They found, for the same patient group as studied here, that spatial variations in the QT dispersion differences between the resting and stress states could also separate the CAD from the non-CAD group ($p < 0.005$). The difference between the two methods is that the method described here does not rely on

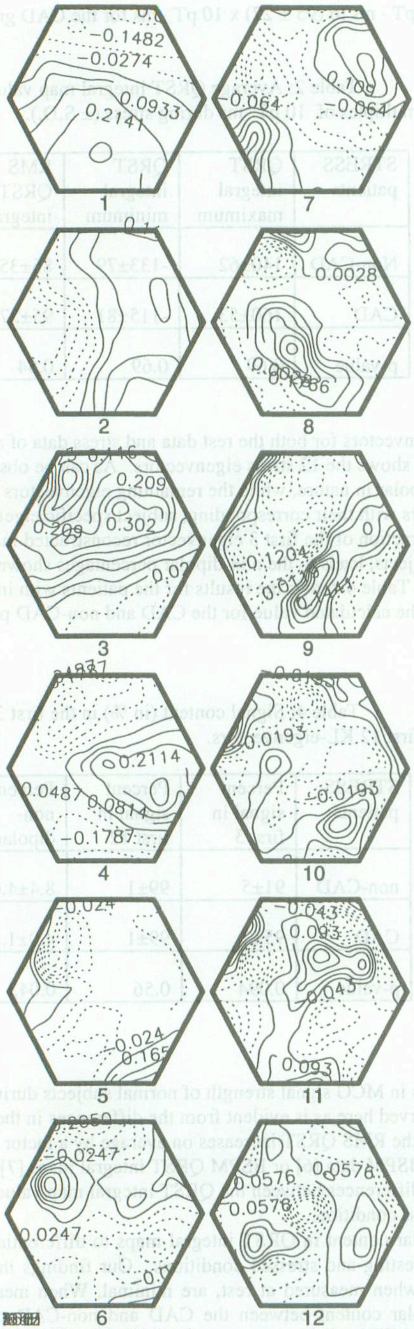

Figure 1: The 12 KLT eigenvectors of the MFM QRST integral maps of all subjects at rest.

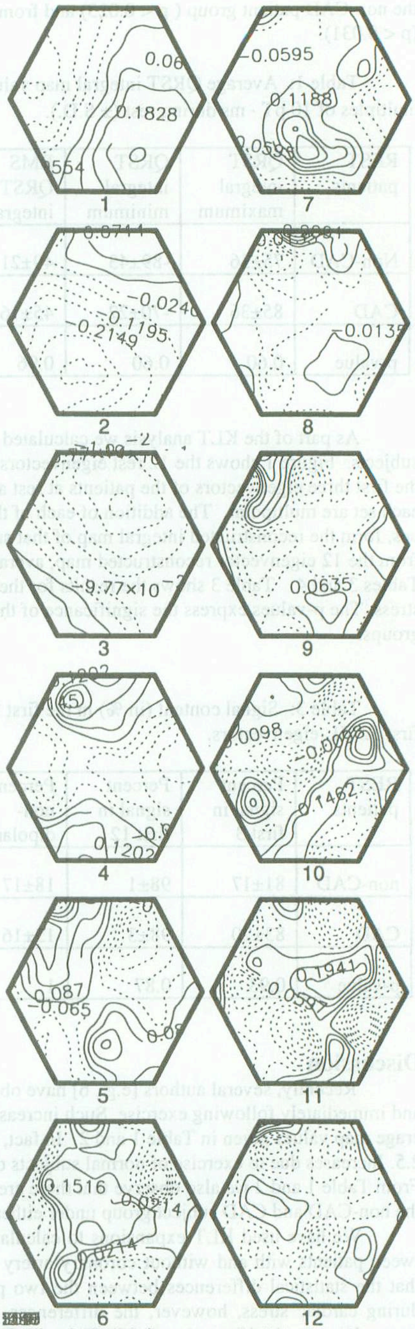

Figure 2: The 12 KLT eigenvectors of the MFM QRST integral maps of all subjects during stress.

distribution patterns of the de- and re-polarization times, but deals more directly with differences in the spatial features of the QRST integral maps between the two groups.

It should be noted, however, that further investigation in this area is necessary since our data were acquired from relatively few patients. Furthermore, the influence of stress inducing drugs on map features is not known.

References

[1] Hailer B, Van Leeuwen P, Lange S, et al: The influence of stress on the spatial distribution of QT dispersion in patients with coronary artery disease (To be published).

[2] Wolf HK, MacInnes PJ, Stock S, et al: Computer analysis of rest and exercise electrocardiograms. Comp Biomed Res 5: pp 329-346, 1972

[3] Gerbrands JJ, On the relationship between SVD, KLT and PCA. Pattern Recognition 14: pp 375-381, 1981

[4] MacAulay C, Stroink G, and Horacek BM: Signal analysis of MCGs and ECGs to test their independence, H. Weinberg H, Stroink G, and Katila T, (eds): Biomagnetism: Application and Theory. New York: Pergamon Press, 1984, pp 115-120

[5] Hubley-Kozey CL, Mitchell LB, Gardner MJ, et al: Spatial features in body-surface potential maps can identify patients with a history of sustained ventricular tachycardia. Circulation 92: pp 1825-1838, 1995

[6] Brockmeier K, Schmitz L, Chavez JJB, et al: Magnetocardiography and 32-lead potentials: repolarization in normal subjects during pharmacologically induced stress. J Cardiovasc Electrophysiol 8: pp 615-626, 1997

[7] McPherson D, Horacek BM, Sutherland DJ, et al: Exercise electrocardiographic mapping in normal subjects. *J Electrocardiol* 18(4): pp 351-360, 1985

Acknowledgement

This work has been supported in part by the National Sciences and Engineering Research Council (NSERC) of Canada. We thank S. Lange (EFMT) for the statistical analysis.

Magnetic localization of reentrant activation in isolated rabbit atrium

Costa Monteiro E[1], Andrade Lima E[1], Hall Barbosa C[1], Ornelas P H[1], Cavalcante E G[1], Santos S F[1], Marchesin D[2], Plohr B[3], Gundelach B[2], Marchesin A[2], Brio M[4], Costa Ribeiro P[1]

Pontifícia Universidade Católica[1], Rio de Janeiro, Brazil;
Instituto de Matemática Pura e Aplicada[2], Rio de Janeiro, Brazil;
State University of New York at Stony Brook[3], Stony Brook, USA;
University of Arizona[4], Tucson, USA

Introduction

The arrhythmia known as atrial flutter is usually associated with a reentrant excitation of atrium cells. In such situation, instead of the normal linear activation originating at the right atrium sinus node and propagating toward the ventricles, the electrical activity begins to continuously rotate within the atrium. The detection of the anatomical path of such reentrant excitation is of special interest for its therapy through catheter ablation [1], which is the treatment of choice for drug resistant or drug intolerant atrial flutter. This technique consists of application of radiofrequency energy in specific areas, in order to interrupt the reentry path. The curative success of the selective catheter ablation technique is presently fully acknowledged, but one of the main concerns is the optimal method for localization of the reentry path, which vary from patient to patient. The localization is traditionally performed by intracardiac electrophysiology techniques, requiring a long exposition to X-rays by both the patient and the procedure team. Thus, the possibility of non-invasive localization of the reentrant electrical path in the tissue during atrial flutter in humans is of great clinical interest.

In order to locate the reentry path, an inverse problem has to be solved, that is, given the magnetic field generated by the heart tissue, determine the associated configuration of currents. Inverse problem methods specially tailored to take into account the rotating pattern characteristics of the flutter arrhythmia will make optimal usage of the available experimental data.

In the present work, a SQUID system was used to detect the magnetic field associated with atrial flutter, which has been experimentally induced in isolated rabbit hearts. Through the analysis of the magnetic field spatial behavior, the propagation pattern of activation is identified, and the location of the center of the reentrant circuit can be assessed.

Materials and Methods

Rabbits of either sex, weighing between 3.0 kg and 4.5 kg, were submitted to a midsternal thoracotomy, after being decerebrated. The hearts were rapidly removed and connected to a Langendorff perfusion system with a Tyrode solution (NaCl, glucose, $NaHCO_3$, KCl, NaH_2PO_4, $MgCl_2$ and $CaCl_2$), bubbled with carbogen (95% O_2 and 5% CO_2). After separating the atria from the ventricles, the former were arranged in a planar configuration between two netlike supports on the surface of a Tyrode solution bath continuously gassed with carbogen. The isolated atrial tissues had 3 cm × 2 cm and about 1.5 mm thick. The tissue bath was continuously superfused with Tyrode solution with controlled input and output flow, therefore keeping the solution at a constant level. A temperature control system maintained the bath temperature at 37° C.

Tachycardias were induced by adding acetylcholine, which is known to increase the tissue vulnerability to reentry [2], to the nutrient solution bath (26.4×10^{-7} mM) and by pacing (16 V, 100 Hz, 1 ms).

Electrical measurements were performed to provide time and amplitude references to the propagation patterns, by means of silver wire extracellular glass electrodes immersed in the solution. One of the electrodes was positioned close to the tissue surface, thus generating a signal very similar to an electrogram record.

Magnetic field measurements were carried out inside a shielded chamber consisting of two concentric cylindrical μ-metal layers with 1 m diameter and 2 m height. The MCG system used consists of a single channel rf-SQUID coupled to a symmetric second order gradiometer, with 1.5 cm diameter and 4 cm baseline. The pick-up coil was positioned between 1.5 and 2 cm above tissue samples. A non-magnetic sample positioner controlled by an acquisition software was used to perform successive magnetic recordings at 21 different locations of two horizontal straight lines with an angle of 83° between them, as shown in Fig. 1. During each recording, the carbogen injection and the temperature control system pump were turned off in order to reduce magnetic noise. The shape and surface area (254 cm^2) of the sample holder were designed to reduce the magnetic contribution of the volume conductor surrounding the tissue sample to a negligible value [3], leading to a more accurate solution of the inverse problem.

©1999, Tohoku University Press
Recent Advances in Biomagnetism
T. Yoshimoto et al. (Eds)

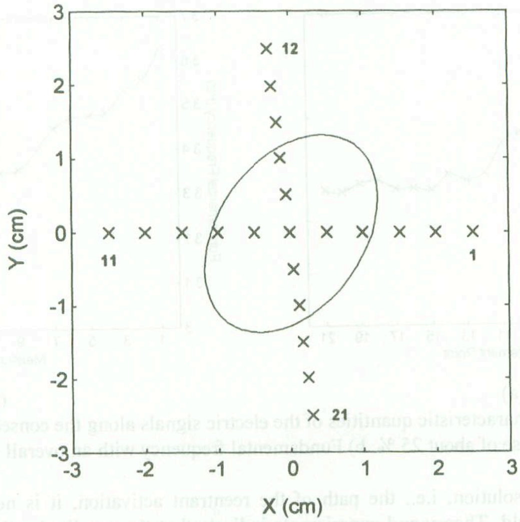

Fig. 1: Measurement positions located in a plane parallel to the sample, with a distance of 2 cm. The gray ellipse represents the atrial tissue, and the numbers show the order in which the magnetic signals were acquired by the SQUID system. The angle between the two lines is 83°

Results

The magnetic signal output from the SQUID was recorded in each measurement position during 3 seconds, corresponding to about 12 periods of reentrant excitations. Fig. 2 shows the magnetic signal recorded at position 3, and the electrical signal simultaneously recorded.

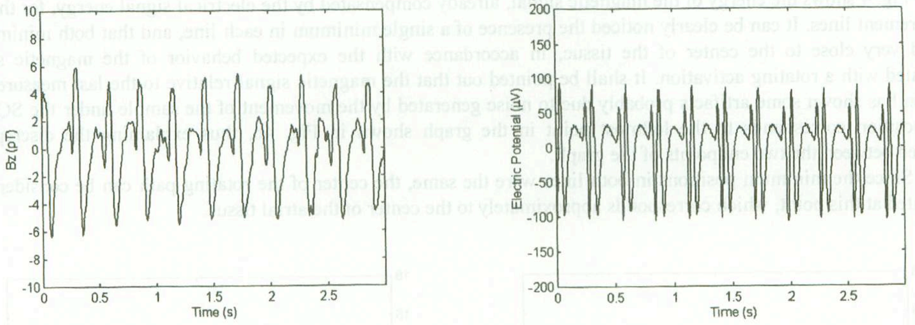

(a) (b)

Fig. 2: Example of acquired waveforms obtained inside a shielded chamber during an episode of experimentally induced flutter arrhythmia in isolated rabbit atrium. a) Magnetic signal measured over position 3 by a SQUID system, at a distance of about 2 cm. b) Electric signal simultaneously recorded by extracellular silver electrodes located inside the volume conductor.

During the experiment, it was observed that the amplitude of the electrical signal has varied with time, with a clear decrescent trend, as shown in Fig. 3a. The amplitude of the electrical signal for the last measured position was about 25 % smaller. Also, the fundamental frequency of the periodic signal has presented a similar decreasing with time, as can be seen in Fig. 3b, that represents an overall decrease of about 12 %.

Since the measurement electrodes were located in a constant position throughout the whole experiment, such changes in amplitude and frequency indicate an actual variation of the flutter arrhythmia. Thus, this behavior must be taken into account when analyzing the amplitude of the magnetic signal.

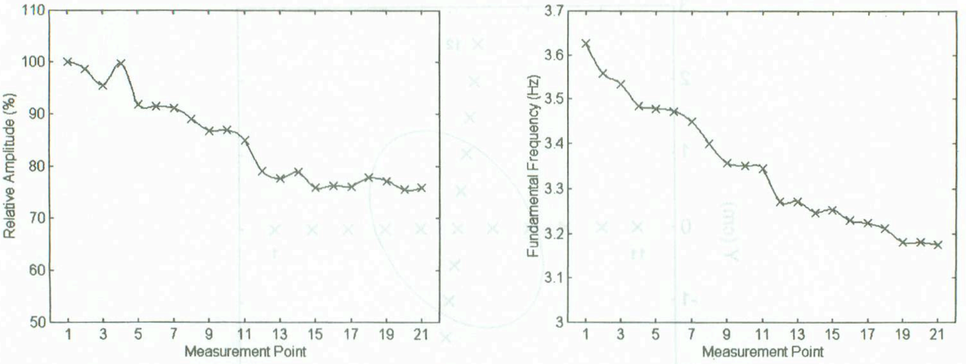

(a) (b)

Fig. 3: Variation of characteristic quantities of the electric signals along the consecutive positions. a) Relative amplitude, showing a decrease of about 25 %. b) Fundamental frequency with an overall variation of about 12 %.

To find the inverse solution, i.e., the path of the reentrant activation, it is necessary to assess the spatial behavior of the magnetic field. Theory and experiments indicate that the amplitude of the associated magnetic field should present a circularly symmetric surface, with a single point of minimum located over the center of the reentry path [4][5][6][7][8].

In order to analyze the magnetic field behavior over the two measurement lines, the average energy of the magnetic signal has been computed at each position. To do so, a Welch's periodogram algorithm [9] has been applied and the first ten harmonics obtained, considering also the frequency variation observed. After that, the energy can be obtained by means of Parseval's relation [10]. This procedure reduces significantly the noise influence on the magnetic distribution.

The same algorithm has been applied to the electric signal, then obtaining the variation of the electric signal energy along the measurement positions. Such values can be used to compensate for the alterations in the flutter arrhythmia shown in Fig. 3.

Fig. 4 shows the energy of the magnetic signal, already compensated by the electrical signal energy, for the two measurement lines. It can be clearly noticed the presence of a single minimum in each line, and that both minima are located very close to the center of the tissue, in accordance with the expected behavior of the magnetic signal associated with a rotating activation. It shall be pointed out that the magnetic signal relative to the last measurement position has shown some artifacts probably due to noise generated by the movement of the sample under the SQUID. This position corresponds to the leftmost point in the graph shown in Fig. 4b, thus explaining the discrepancy observed between the two endpoints of the graph.

Since the minimum positions in both lines were the same, the center of the rotating path can be considered to be located at this point, which corresponds approximately to the center of the atrial tissue.

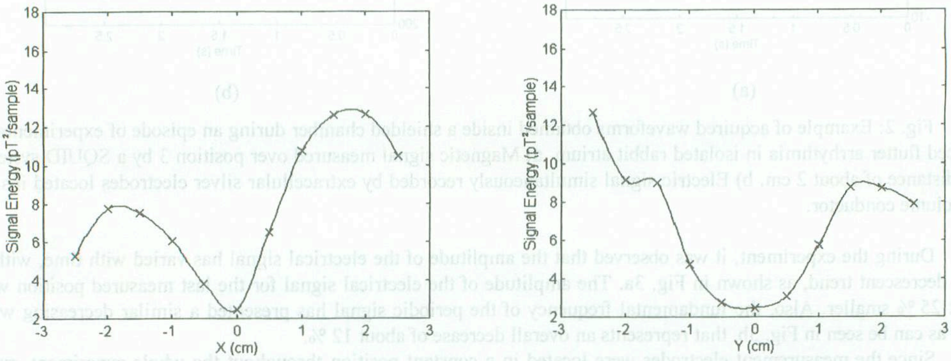

(a) (b)

Fig. 4: Variation of the energy of the magnetic signal between positions for the two lines of measurement shown in Fig. 1. The single minima characteristic of a rotating pattern can be clearly observed in both lines.

Discussion

In this work, it was studied the magnetic field produced by reentrant excitation observed during atrial flutter arrhythmia experimentally induced in rabbit heart tissues. The experimental protocol for isolation of the atrium was developed in order to control the position of the plane containing the rotating wave [5]. During the flutter episodes, systematic variability of the electrical signal amplitude and frequency has been observed. Nevertheless, such quantities should be invariable over time, as the electrodes were located in a fixed position throughout the whole measurement. These changes could be due to variations over time of eletrophysiologic characteristics of the tissue, such as activation recovery time.

The frequency variations have already been taken into account inherently during the calculation of the energy graphs, as the energy is determined over a single period. The other variability present, that is, the electrical signal amplitude, has been considered by compensating the magnetic field energy in accordance to the variations of the electric signal energy along the successive measurement points. After this procedure, the asymmetry has been reduced, but can still be observed (Fig. 4a). This effect could be due to other factors such as uneven thickness of the tissue and tilting in the sample holder.

An inverse solution method has been previously developed to recover the reentry path parameters such as center of rotation, radius and distance between the source and the detecting coil [5][11]. This method was applied to the data shown in this paper, but the obtained results appeared not to be completely reliable, probably due to the observed asymmetry. The recovery method is presently being modified to take into account possible sources of asymmetry, so as to better evaluate the parameters that describe the circulating wave. Although the present work has used a single channel equipment, the method could be extended to multichannel systems, leading to an improved recovery of cardiac phenomena.

References

[1] Poty H, Saoudi N, Haïssaguerre M, Daou A, Clémenty J and Letac B: Radiofrequency catheter ablation of atrial tachycardias. Am Heart J 131: 481-489, 1986

[2] Allessie M A, Lammers W J E P, Bonke I M and Jan Hollen E E: Intra-atrial reentry as a mechanism for atrial flutter induced by acetylcholine and rapid pacing in the dog. Circulation 70-1: 123-135, 1984

[3] Eghrari I R, Costa Monteiro E, Costa Ribeiro P, von der Weid J P, Oliveira P M and Paes de Carvalho A: On the influence of the volume conductor in magnetocardiography, Il Nuovo Cimento, 1983, 2: 346-356.

[4] Costa Ribeiro P, Bruno A C, Saboia e Silva P L, Hall Barbosa C R, Parente Ribeiro E, Costa Monteiro E and Fonseca Costa A: Detection of reentry currents in atrial flutter by magnetocardiography. IEEE Trans Biomed Eng 39-8: 818-824, 1992

[5] Costa Monteiro E, Andrade Lima E, Ornelas P H, Cruz R S, Picon A P, Kühner G S, Kelber C, Parente Ribeiro E, Bruno A C, Costa Ribeiro P, Marchesin D, Brio M, Leite T T: Induced Atrial Flutter in Rabbit Hearts Tissue and Inverse Magnetocardiography. Aine C J, Okada Y, Stroink G, Swithenby S J, Wood C C (eds): Advances in Biomagnetism Research, Volume I: Instrumentation; Forward and Inverse Problems; Magnetocardiography, 1997

[6] Costa Ribeiro P, Bruno A C, do Carmo J S, Parente Ribeiro E, Costa Monteiro E and Fonseca Costa A: Detection of magnetic atrial flutter waves in isolated rabbits hearts. Willianson S J, Hoke M, Stroink G, Kotani M (eds): Advances on Biomagnetism. New York: Pergamon Press, 1989, pp 389-393

[7] Costa Monteiro E, Correia M P, Hall Barbosa C, and Costa Ribeiro P: Cellular automata simulation in the magnetic study of rotating propagation models associated to cardiac arrhythmias, Cheryl J. Aine, Yoshio Okada, Gerhard Stroink, Stephen J. Swithenby, Charles C. Wood, (Eds.): Advances in Biomagnetism Research, Volume I: Instrumentation; Forward and Inverse Problems; Magnetocardiography. Pergamon Press, in press.

[8] Costa Monteiro E, Miranda LC, Bruno AC, Costa Ribeiro P: A cellular automaton computer model for the study of magnetic detection of cardiac tissue activation during atrial flutter. IEEE Transactions on Magnetics, in press.

[9] Marple Jr S L: Digital spectral analysis with applications. New Jersey: Prentice-Hall, 1987, pp.152-158

[10] Oppenheim A V and Willsky A S: Signals and Systems. New Jersey: Prentice-Hall, 1983, pp. 321-327

[11] Brio M, Marchesin D, Costa Monteiro E, Bruno A C and Costa Ribeiro P: Inverse magnetocardiography for reentry currents, Cheryl J. Aine, Yoshio Okada, Gerhard Stroink, Stephen J. Swithenby, Charles C. Wood. Advances in Biomagnetism Research, Volume I: Instrumentation; Forward and Inverse Problems; Magnetocardiography, 1997

Acknowledgements

We thank Kühner G S for building sample positioning system and Bruno A C for valuable discussions and help with the SQUID system. This work was partially supported by CNPq, FAPERJ and FINEP.

On the Spatial Distribution of Intra-QRS Fragmentation in MCG mapping of Post-Infarction Patients

Endt P[1,4], Montonen J[1,3], Korhonen P[2,3], Mäkijärvi M[2,3], Nenonen J[1,3], Trahms L[4], Katila T[1,3]

[1]Helsinki University of Technology, Helsinki, Finland; [2]Department of Internal Medicine, Division of Cardiology, Helsinki Central Hospital, Helsinki, Finland; [3]BioMag Laboratory, Helsinki Central Hospital, Helsinki, Finland; [4]Physikalisch-Technische Bundesanstalt, Berlin, Germany

Introduction

Different means for the assessment of the risk for malignant arrhythmias of post-myocardial infarction patients have been suggested. One way to evaluate this risk is the evaluation of the electromagnetic activity of the heart. The recording of the magnetocardiogram (MCG) is a non-contact fully noninvasive method to measure the cardiac electric activity. Risk-assessment has been carried out by the application of algorithms to the signal-averaged and filtered QRS complex in MCG in different domains, e.g. time-domain [1, 2, 3], or spatio-temporal domain [4, 5]. We have suggested the application of binomial filters allowing the study of intra-QRS fragmentation in the entire QRS-complex [6]. In former studies, parameters of a single channel or based on the mean of several channels have been used for risk-evaluation [7]. Here we present the spatial distribution of intra-QRS-fragmentation and its performance.

Methods

Patients

A total of 31 patients with old myocardial infarction and without bundle branch block was studied, 20 of whom had suffered from a documented paroxysmal sustained ventricular tachycardia (VT).

Measurements

High-resolution MCG measurements were rercorded in the Otaniemi magnetically shielded room, using a first order axial gradiometer and a dc -SQUID with field noise spectral density of about $4\ fT/Hz^{1/2}$ [7]. Single MCG-recordings were taken from positions C3, C4, C5, D3, D4, D5, E3, E4 and E5 of the standard grid [8] (see figure 1). This setup is also known as the minigrid.

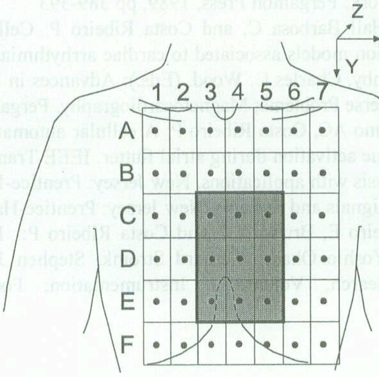

Figure 1: The minigrid (depicted in grey) within the standard Saarinen grid was used in this study (corner locations C3, C5, E3, E5).

High-resolution electrocardiogram (ECG) acquisition was performed using orthogonal bipolar x-, y- and z-leads. Each recording for every location of the MCG and the ECG was of 120 s duration.

©1999, Tohoku University Press
Recent Advances in Biomagnetism
T. Yoshimoto et al. (Eds)

Signal-processing

The signals were automatically averaged with a selective algorithm yielding SAECG (signal-averaged ECG) and SAMCG (signal-averaged MCG), respectively [9] Afterwards, they were filtered using a digital binomial highpass-filter (fc = 37Hz) and a lowpass filter (fc = 90 Hz). QRS onset and offset were automatically determined using a Simson-like method for the single MCG-channels [10]. The formerly introduced parameters M, describing the number of extrema, and S, describing the number of extrema and their heights, were calculated for each channel [11].

Results

For post-infarction patients, only few curvature-changes of the QRS-morphpology are visible (figure 2a), whereas the postinfarction-patient with a documented sustained ventricular tachycardia (VT) show more such changes (figure 2b). However, changes that can be hardly seen in the unfiltered signals, are evident in the filtered signals (2c-d).

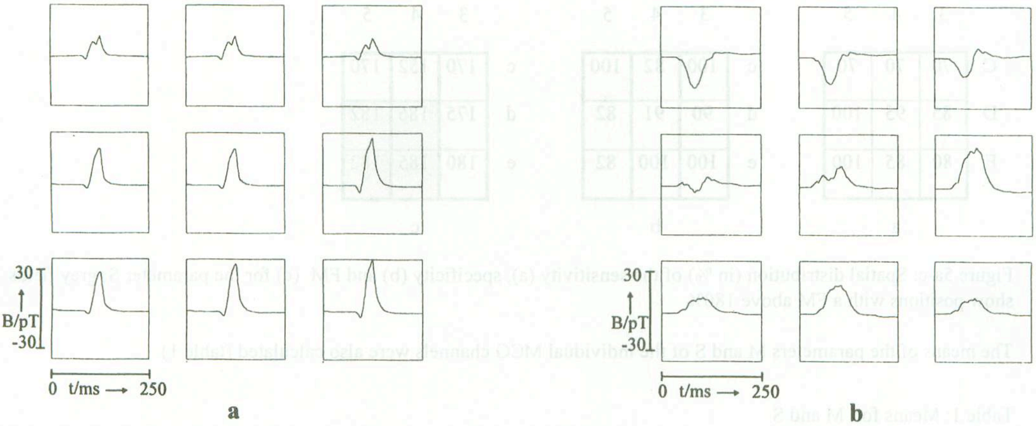

Figure 2 a-b: Unfiltered signals for a MI-patient without ventricular arrhythmia (figure 2a) and a MI-patient with documented sustained ventricular tachycardia (figure 2b) are shown corresponding to the locations in the minigrid.

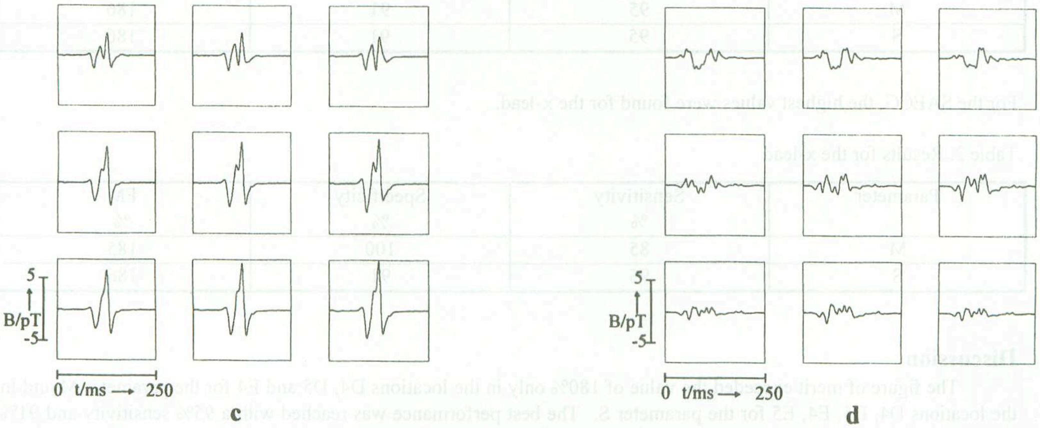

Figure 2 c-d: Filtered signals for the same MI-patient without ventricular arrhythmia (figure 2c) and the same MI-patient with documented sustained ventricular tachycardia (2d) are shown corresponding to the locations in the minigrid.

Thresholds for both parameters M and S were obtained for each MCG-location and each ECG-lead by maximizing the sum of sensitivity and specificity. This sum was also used as a figure of merit (FM). The spatial distribution of the sensitivity, specificity and FM for the M and S are shown in following figures.

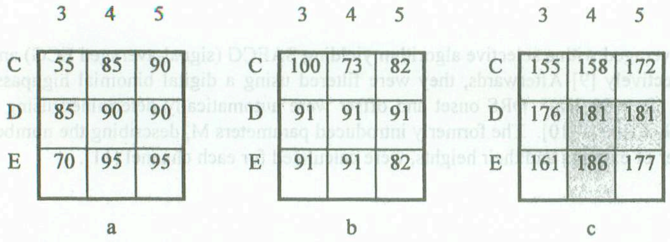

	3	4	5
C	55	85	90
D	85	90	90
E	70	95	95

a

	3	4	5
C	100	73	82
D	91	91	91
E	91	91	82

b

	3	4	5
C	155	158	172
D	176	181	181
E	161	186	177

c

Figure 4a-c: Spatial distribution (in %) of the sensitivity (a), specificity (b) and FM (c) for the parameter M; grey fields show positions with a FM above 180%

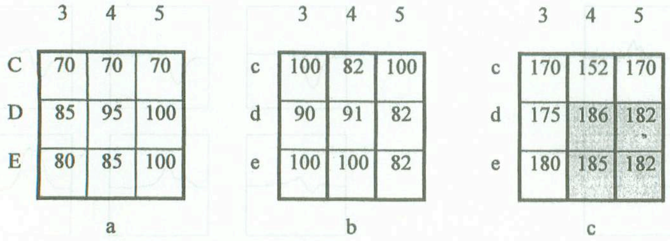

	3	4	5
C	70	70	70
D	85	95	100
E	80	85	100

a

	3	4	5
c	100	82	100
d	90	91	82
e	100	100	82

b

	3	4	5
c	170	152	170
d	175	186	182
e	180	185	182

c

Figure 5a-c: Spatial distribution (in %) of the sensitivity (a), specificity (b) and FM (c) for the parameter S; grey fields show positions with a FM above 180%

The means of the parameters M and S of the individual MCG channels were also calculated (table 1).

Table 1: Means for M and S

Parameter	Sensitivity %	Specificity %	FM %
M	95	91	186
S	95	91	186

For the SAECG, the highest values were found for the x-lead.

Table 2: Results for the x-lead

Parameter	Sensitivity %	Specificity %	FM %
M	85	100	185
S	95	91	186

Discussion

The figure of merit exceeded the value of 180% only in the locations D4, D5 and E4 for the parameter M and in the locations D4, D5, E4, E5 for the parameter S. The best performance was reached with a 95% sensitivity and 91% specificity in location E4 for parameter M and in location D4 for parameter S. For the SAECG a similar performance was found only for the x-lead. These figures are clinically very satisfactory, especially taking into account, that they refer to the identification of VT-patients within an MI patient population. Intra-QRS fragmentation of the MCG seems to be a sensitive and specific method for identification of patients with prosperity to VT after MI.

References

[1] Weissmüller P, Richter P, Abraham-Fuchs K, et al: Spatial-differences of the duration if ventricular late fields in the signal-averaged magnetocardiogram in patients with ventricular late potentials, PACE, 1993, 16(19), pp. 70-79

[2] Leder U, Huck M, Pohl H, et al: Detection of ventricular late fields by multichannel magnetocardiography. In: Biomagnetism: Santa Fe, 1996, p. 222

[3] Montonen J, Korhonen P, Paavola M, et al: Spatial aspects in magnetocardiographic time domain and spectrotemporal post-infarction arrhythmia risk assessment. In: Biomagnetism: Santa Fe, 1996,

[4] Stroink G., Lant J, Elliot P, et al: Disrimination between myocardial infarct and ventricular tachycardia patients using magnetocardiographic trajectory plots and iso-integralmaps. J. Electrocardiol. 25: pp 129-142, 1992

[5] Czerski, K, Gödde P, Müller, H-P, Agrawal, R, Oeff, M, Schultheiss, H-P: Magnetoccardiographic QT-dispersion in patients with coronary heart disease, A.N.E., July 1998, Vol 3, No.3, Part 2, S. 61

[6] Endt P, Hahlbohm H-D, Kreiseler D, et al: Fragmentation of the bandpass filtered QRS-complex of patients prone to malignant arrhythmia, accepted for publication by Medical & Biological Engineering & Computing

[7] Endt P, Montonen J, Mäkijärvi M, et al: Time domain analysis of the main QRS complex can identify myocardial infarction patients with ventricular Tachycardia, World Congress on Medical Physics and Biomedical Engineering, Nice 14-19. Sep 1997, p. 438

[8] Kelhä, V, Pukki, J, Peltonen, R, et al: Design, construction and performance of a large-volume magnetic shield, IEEE Trans. Magn. MAG-18,pp.260-270, 1982

[9] Saarinen M, Siltanen P , Karp P, et al: The normal magnetocardiogram: I morphology. Ann. Clin. Res. , 10 (S21), pp. 1- 43

[10] Paavola M: Feature analysis of magnetocardiographic mappings, Master's thesis, Helsinki University of Technology, 1995. In Finnish.

[11] Montonen J, Mäkijärvi M, Paavola M, et al: Comparison of time domain and spectrotemporal domain analysis of high resolution magneto- and electrocardiographic recordings of myocardial infarction patients with and without ventricular tachycardia, in Biomagnetism: Fundamental Research and Clinical Applications, eds: C. Baumgartner, L. Deecke, G. Stroink, S.J. Williamson, Elsevier Science/IOS Press, pp. 624-627, 1995.

Acknowledgements

This work has been supported by the Bundesministerium für Bildung, Wissenschaft und Forschung (BMBF) under grant number 13N6930, the EU large scale research facility BIRCH, the German Academic Exchange Service (DAAD) and the Finnish Academy of Science (SA).

Clinical Validation of Three-Dimensional Cardiac Magnetic Source Imaging Accuracy with Simultaneous Magnetocardiographic Mapping, Monophasic Action Potential Recordings and Amagnetic Cardiac Pacing

Fenici R[1], Pesola K[2,3], Nenonen J[2,3], Mäkijärvi M[4], Fenici P[1], Giorgi A[1], Jokiniemi T[2,3], Korhonen P[4], Lauerma K[5], Lötjönen J[2], Ruggieri MP[1], Brisinda D[1], Valkonen M[2,3], Toivonen L[4], and Katila T[2,3]

Clinical Physiology - Biomagnetism Research Center, Catholic University, Rome, Italy[1]; Laboratory of Biomedical Engineering, Helsinki University of Technology, Espoo, Finland[2]; BioMag Laboratory, Medical Engineering Center[3], Department of Internal Medicine -Division of Cardiology[4], Department of Radiology[5], Helsinki University Central Hospital, Helsinki, Finland

Introduction

Magnetocardiographic mapping (MCG) is the most promising non-invasive method for quantitative three-dimensional (3D) localization and imaging of cardiac arrhythmias [1-8]. However its spatial accuracy is still debated [9-11]. An MCG based pacemapping protocol was developed at the Catholic University of Rome [12], to quantify the accuracy of the MCG method for localization of intracardiac sources, using an amagnetic catheter (AC). The localization error was estimated by comparison between fluoroscopic position and 3D MCG coordinates of the AC. The reported localization accuracy, with single channel MCG, ranged between 5 and 25 mm [12-14].

The present study was carried out, with a state-of-art multichannel system, in order to: 1) quantify the 3D accuracy of MCG to localize an intracardiac source; 2) evaluate the accuracy of MCG to image the 3D position of the tip of the amagnetic catheter, without the use of fluoroscopy; 3) validate the reliability of the new multipurpose AC for high resolution (HR) multiple Monophasic Action Potential (MAP) recording; 4) evaluate the possible use of the MCG method for multimodal 3D electroanatomical integration of electrophysiological recordings carried out as close as possible to the arrhythmogenic substrate.

Methods

The multipurpose amagnetic catheter used in our study is patented by the Italian National Research Council [15]. The catheter, 5F to 7F size, has different configurations. The one used in this study features four non-polarizable amagnetic electrodes at the tip, arranged in such a way that current dipoles of different geometry and strength can be generated in the patient's heart, without artifacts induced by ferromagnetic materials. The same electrodes can record four monophasic action potentials (MAP) simultaneously, with a spatial resolution of $4\ mm^2$.

After standard electrophysiological study (EPS) was completed, the multipolar AC was placed in the right ventricle (RV) of 10 patients, who had volunteered with written informed consent to the MCG additional procedure. In 3 patients a second (5F) bipolar AC was also inserted in the RV. The research project was approved by the Ethical Committee of the Helsinki University Central Hospital (HUCH).

Four right ventricular MAPs were simultaneously recorded with the AC, to monitor the stability of its endocardial contact before, during and after the MCG procedure. The position of the tip of the AC was also imaged by biplane fluoroscopy (XR), together with lead markers, which were used as reference points to integrated XR, MCG and MRI images.

MCG studies were performed in the BioMag magnetically shielded room at HUCH, with a 67-channel instrumentation featuring 7 co-axial (baseline 80 mm) and 60 planar (baseline 16.2 mm) dc-SQUID gradiometers, covering a surface with a diameter of 30 cm [16]. Before MCG recordings, thorax co-ordinate were defined by digitizing a set of reference points, which were used to transfer MCG localization in MR images and for comparison with fluoroscopic images (XR) with the same coordinate system. For the MCG localization, current dipoles (5 mm; 10 mA) were impressed at the tip of the AC. 3D MCG localization of the tip of the catheter were calculated from signal peaks induced by the artificial dipoles. The polarity of the magnetic field varied in the individual patients, depending on the direction of the artificial current dipoles.

The position of the tip of the AC was calculated using a moving equivalent current dipole (ECD) in a realistic, homogeneous boundary element (BEM) torso model, which surface is tessellated with plane triangles (Fig. 1a and 1b). The BEM model of the torso was constructed from individual patients MRI, using a specific triangle mesh generation technique [17]. The electric potential is assumed to be linear in each triangle, and the discretized integral equations for the electric potential and the magnetic field can be manipulated into matrix equations which are fast to solve [18]. The six parameters (position and moment) of a current dipole were estimated with non-linear least squares fitting [19]. All inverse computations were performed from raw MCG data, neither signal-averaging nor digital filtering were applied. The accuracy of the MCG localization was evaluated by: 1) mismatch with XR and 2) anatomical location of the ECD

©1999, Tohoku University Press
Recent Advances in Biomagnetism
T. Yoshimoto et al. (Eds)

in MRI slices. The reproducibility of the measure was tested by repeating the same measurement 5 times and computing the coefficient of variation and the coefficient of reproducibility [20].

Magnetic resonance imaging (MRI) was performed in a separate session. MRI data were collected using a functional 1.5 tesla superconducting magnet device (Magnetom Vision, Siemens AG, Erlangen, Germany) at the Department of Radiology of HUCH. A set of 10-mm thick transaxial slices were acquired from the waist to the neck during early systole. In addition, 8-mm or 10-mm slices were collected transaxially or in the direction of the short axis of the heart to extract the endo- and epicardial surfaces more accurately. Cross-shaped markers filled with MgCl-solution were applied in the marker positions defined during the MCG recordings in order to match the MRI and MCG coordinate frames [16]. In this study, the MRI data were used for accurate representation of the individual geometry of the thorax and the heart for boundary element computations. They also allow accurate registration of MCG localization results with respect to the anatomy of the patient's heart [21] (Fig. 1c).

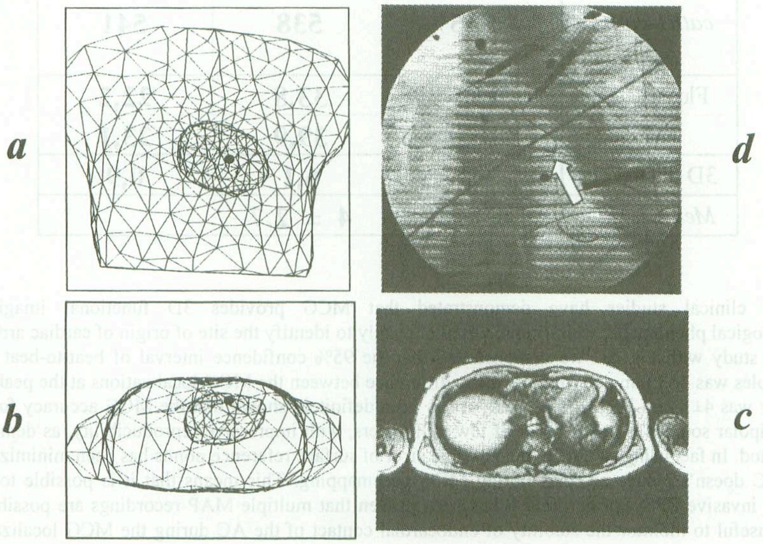

Fig. 1. Frontal and axial views of the BEM torso model (*a* and *b*) and of axial MRI (*c*), which show proper localization of the catheter placed at the mid anterior wall of the right ventricle *(white and black dots)*. (*d*) Frontal fluoroscopic image is shown for comparison *(the AC is marked by the white arrow)*.

Results

MAP recording demonstrated that the AC was in stable endocardial contact during the procedures in all patients. Indeed the MAP signal remained of good quality for even two hours (Fig. 2), in spite of patient transfer from the catheterization bed, where the AC was inserted, to the BioMag laboratory and back.

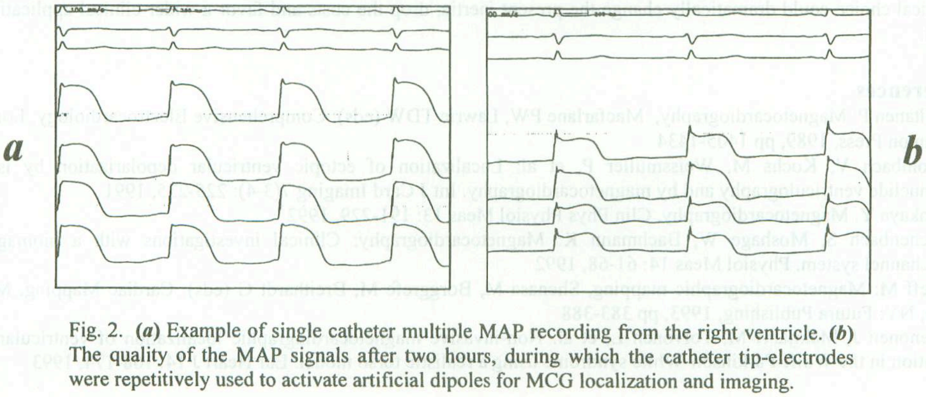

Fig. 2. (*a*) Example of single catheter multiple MAP recording from the right ventricle. (*b*) The quality of the MAP signals after two hours, during which the catheter tip-electrodes were repetitively used to activate artificial dipoles for MCG localization and imaging.

As inferred by MRI, the ACs were correctly localized in the right ventricle of all patients (Fig. 1). All localizations were reproducible, although computed from raw data. The mean 3D mismatch between XR and MCG localizations was 9 ± 4 mm (beat-to-beat analysis) (Table I). The coefficient of variation of 3D localization was 1.37% and the coefficient of reproducibility was 2.6 mm. As compared to fluoroscopy, the MCG estimation error of the 3D distance between the tips of two amagnetic catheters, simultaneously inserted in the RV, was 4 ± 2.7 mm.

Table 1: MCG and fluoroscopic estimate of the 3D distance between two amagnetic catheters inserted in the right ventricle of three patients.

	Patient identification		
3D distance cath1-cath2 (mm)	**535**	**538**	**541**
Fluoroscopy	**13,9**	**33,8**	**22,2**
MCG	**18,9**	**39,9**	**23,1**
3D difference	**5**	**6,1**	**0,9**
Mean ± SD	**4 ± 2.7**		

Discussion

Recent clinical studies have demonstrated that MCG provides 3D functional imaging of cardiac electrophysiological phenomena, which can be used clinically to identify the site of origin of cardiac arrhythmias [1-14]. In a previous study with the AC we demonstrated that the 95% confidence interval of beat-to-beat localizations of catheter's dipoles was 4±3 mm and that the mean difference between the MCG localizations at the peak of the stimulus and 3 ms later was 4±1 mm [22]. In this study it has been definitely shown that the MCG accuracy for localization of intracardiac dipolar sources is in the order of few millimeters, with impressive reproducibility, as demonstrated by the two ACs method. In fact using two ACs the possible error of surface reference points has been minimized.

The AC doesn't induce artifacts during MCG pacemapping. This means that it is possible to combine MCG mapping with invasive EPS. Furthermore it has been proven that multiple MAP recordings are possible with a single AC. This is useful to monitor the stability of endocardial contact of the AC during the MCG localization procedure, without the need of fluoroscopy and, at the same time, might be a new high resolution method to discover localized electrophysiological abnormalities close to the site of origin of focal arrhythmias [23-25]. Indeed MCG is adequate not only for preoperative non-invasive localization of arrhythmogenic targets but also for intraoperative three-dimensional imaging of multiple ACs into the 3D BEM model of the heart. Such images can be rotated by the operator in real time during the EPS and represent a new user-friendly interface for electro-anatomical integration of the electrophysiological information, competitive with standard endocardial mapping and with other novel catheter-based method [26-28].

In conclusion, it seems to us that the combination of MCG mapping with the AC technique has the potential to open a new age in clinical electrophysiology [29]. The interest for such new method is obvious because it might simplify interventional EP procedures, with lower invasivity and exposure to radiation for patients and operators. Nevertheless further development is needed to optimize the integration of preoperative information with interventional procedures, to construct more compact multichannel MCG systems, reliable in unshielded EP laboratories and to develop new software tools to make them really manageable by clinicians. Technological progress is very fast and such a tactical choice could dramatically change the present inertia, drop the costs and favor a wider clinical application of MCG.

References

[1] Siltanen P: Magnetocardiography, Macfarlane PW, Lawrie TDW (eds): Comprehensive Electrocardiology. London: Pergamon Press, 1989, pp 1405-1434

[2] Hombach V, Kochs M, Weissmuller P, et al: Localization of ectopic ventricular depolarization by ispect-radionuclide ventriculography and by magnetocardiography. Int J Card Imaging 7(3-4): 225-235, 1991

[3] Nakaya Y. Magnetocardiography. Clin Phys Physiol Meas 13: 191-229, 1992

[4] Achenbach S, Moshage W, Bachmann K: Magnetocardiography: Clinical investigations with a biomagnetic multichannel system. Physiol Meas 14: 61-68, 1992

[5] Oeff M: Magnetocardiographic mapping, Shenasa M, Borggrefe M, Breithardt G (eds): Cardiac Mapping. Mount Kisco, NY: Futura Publishing, 1993, pp 383-388

[6] Nenonen J, Mäkijärvi M, Toivonen L, et al: Non-invasive magnetocardiographic localization of ventricular pre-excitation in the Wolff-Parkinson-White syndrome using a realistic torso model. Eur Heart J 14: 168-174, 1993

[7] Mäkijärvi M, Nenonen J, Toivonen L, et al: Magnetocardiography: Supraventricular arrhythmias and pre-excitation syndromes. Eur Heart J 14(suppl.E): 46-52, 1993

[8] Oeff M, Burghoff M: Magnetocardiographic localization of the origin of ventricular ectopic beats. PACE 17: 517-522, 1994

[9] Fenici R, Covino M, Cellerino C, et al: Magnetocardio-graphically guided catheter ablation. J Interv Cardiol 8(Suppl): 825-836, 1995

[10]Stroink G, Lamothe R, Gardner MJ: Magnetocardiographic and electrocardiographic mapping studies. In: Weinstock H (ed): SQUID Sensors: Fundamentals, Fabrication and Applications. NATO ASI Series, Kluwer, the Netherlands, 1996, pp 413-444

[11]Moshage W, Achenbach S, Göhl K, et al: Evaluation of the non-invasive localization accuracy of cardiac arrhythmias attainable by multichannel magnetocardiography (MCG). Int J Card Imaging 12: 47-59, 1996

[12]Fenici R, Melillo G, Cappelli A, et al: Magnetocardiographic localization of a pacing catheter. In: Williamson SJ, Hoke M, Stroink G, Kotani M (eds): Advances in Biomagnetism. New York: Plenum Press, 1989: 361-364

[13]Fenici R, Melillo G: Biomagnetically localizable multipurpose catheter and method for MCG guided intracardiac electrophysiology, biopsy and ablation of cardiac arrhythmias. Int J Card Imaging 7: 207-215, 1991

[14]Fenici R, Melillo G: Magnetocardiography: ventricular arrhythmias. Eur Heart J 14(suppl.E): 53-60, 1993

[15]Fenici R., Consiglio Nazionale delle Richerche: Biomagnetically localizable multipurpose catheter and method for MCG guided intracardiac electrophysiology, biopsy and ablation of cardiac arrhythmias. United States Patent Documents, Patent N.5 056 517, Oct.15, 1991

[16]Montonen J, Ahonen A, Hämäläinen M, et al: Magnetocardiographic functional imaging studies in BioMag Laboratory. In: Aine C, Okada Y, Stroink G, et al. (eds): Advances in Biomagnetism research: Biomag96. New York, Springer Verlag, in press.

[17]Lötjönen J, Reissman PJ, Magnin I, et al: A triangulation method of an arbitrary point set selected from medical volume data. IEEE Trans Magn, in press.

[18]Nenonen J: Solving the inverse problem in magnetocardiography. IEEE Eng Med Biol Magazine 13: 87-96, 1994

[19]Marquardt DW:. An algorithm for least-squares estimation of nonlinear parameters. J SIAM 11: 431-441, 1963

[20]Altman DG, Bland JM: Measurements in Medicine: The analysis of method comparison studies. Statisticians 32:307-317, 1983

[21]Lötjönen J, Sipilä O, Nenonen J, et al: Individual boundary element models for magnetocardigraphic applications. Proc 18th Annu Int Conf of IEEE Eng Med Biol Soc, 1996: CD-rom

[22]Fenici R, Nenonen J, Pesola K, et al: Non-fluoroscopic localization of an amagnetic catheter by multichannel magnetocardiography (*PACE 1997, - under revision)*

[23]Fenici R, Masselli M, Zeppilli P, et al: Clinical recordings of monophasic action potentials: demonstration of intra-atrial conduction block in Sinus Node region and possible role in reentrant supraventricular tachycardia. Am Heart J Vol. 102, N. 1:124-128, 1981

[24]Yuan S, Wohlfart B, Olsson SB, et al: The dispersion of repolarization in patients with ventricular tachycardia. Eur Heart J 16:68-76, 1995

[25]El-Sherif N, Bekheit SS, Henkin R: Quinidine-induced long QT interval and torsade de pointes: Role of bradycardia-dependent early after depolarizations. J Am Coll Cardiol 14:252-257, 1989

[26]Peters SN, Jackman WN, Schilling RJ, et al: Human left ventricular Endocardial Activation mapping using a novel Noncontact Catheter. Circulation 95:1658-1660, 1997

[27]Johnson SB, Packer DL: Intracardiac ultrasound guidance of multipolar atrial and ventricular mapping basket applications (abstract), JACC 29: 202A, 1997

[28]Gepstein L, Hayam G, Ben-Haim S: A novel method for nonfluoroscopic catheter-based electroanatomical mapping of the heart. Circulation 95: 1611-1622, 1997

[29]Fenici R, Fenici P, van Bosheide J: Amagnetic catheter for biomagnetically guided endocardial mapping and ablation of cardiac arrhythmias. In: Reichl H, Heuberger A (eds): Micro System Technologies. Berlin: VDE-Verlag GmbH, 1996, pp 711-716

Acknowledgments

This work was supported by the EU HCM Large Scale Installation in Biomagnetic Research (BIRCH) at Helsinki University of Technology, by the Italian National Research Council (CNR), owner of patents: Ital. Patent N. 1219855, May 24,1990; US Patent N. 5 056 517, Oct.15, 1991; Eur. Patent N. 0428812, March. 08, 1995 and by the MURST (cofinanziamento 97) project N. 9706577608. We are grateful to Professor Luigi Donato for providing the financial support, and to Mr. Luigi Venturelli for developing the prototypes of the amagnetic catheters. We are also indebted to Dr. Lutz Reinhardt for creative discussion and suggestions. The Neuromag Ltd. (Helsinki) is acknowledged for supporting this research in Rome, with their advanced software for MCG.

Analysis of magnetocardiographic QRST integral maps for the prediction of vulnerability to ventricular arrhythmias

Hren R[1], Steinhoff U[2], Gessner C[2], Endt P[2], Goedde P[3], Agrawal R[3], Oeff M[3], Lux RL[4], Trahms L[2]

Institute of Mathematics, Physics, and Mechanics, University of Ljubljana, 1000 Ljubljana, Slovenia[1]
Physikalisch-Technische Bundesanstalt, D-10587, Berlin, Germany[2]
Universitätsklinikum Benjamin Franklin, Freie Universität, D-12200, Berlin, Germany[3]
Nora Eccles Harrison CVRTI, University of Utah, Salt Lake City, UT 84112[4]

Introduction

Sudden cardiac death is one of the challenging clinical problems in cardiology due to its significant incidence among the population of the Western world. It is thus of great diagnostic interest to identify subjects who are at risk of lethal ventricular arrhythmias that immediately precede sudden death. It has been shown that regional ventricular repolarization properties can be reflected in body surface distributions of electrocardiographic QRST deflection areas (integrals) [1]. To quantitatively assess spatial features of QRST integral maps, an index of nondipolar content [1,2] was introduced demonstrating that patients who are at risk of lethal arrhythmias have a markedly higher nondipolar index than do healthy subjects [1,3].

Magnetic field maps (MFMs), constructed from multiple recordings of the magnetic field above the anterior chest, also offer information about the regional cardiac events and complement that of electrocardiographic surface distributions [4,9]. The purpose of this study was to test the hypothesis that it is possible to identify distinct morphological features of MFMs recorded during sinus rhythm in patients at risk of ventricular arrhythmias. There is a sound biophysical basis and promising preliminary evidence [4,5] that magnetocardiographic QRST integral maps may supplement electrocardiographic QRST integral maps and thus provide additional information about nonuniform repolarization properties of the ventricles.

Methods

MFMs were obtained during sinus rhythm from 49 leads above the anterior chest in 22 healthy control subjects and in 29 patients with spontaneous episodes of ventricular arrhythmias (ventricular tachycardia or ventricular tachycardia/ventricular fibrillation). Magnetocardiographic recordings were performed in the magnetically shielded room located in Universitätsklinikum Benjamin Franklin, Berlin using the multichannel system developed at the Physikalisch-Technische Bundesanstalt, Berlin [6]. The sensors were arranged in a planar array which was parallel to the tangential plane of the subjects' torso and situated approximately 4 cm above the anterior chest surface.

All 49 leads were simultaneously recorded at a sampling rate of 1000 Hz (with a 15-bit amplitude resolution) using a set of dcSQUID (superconducting quantum interference device) first-order gradiometers (baseline 7 cm). Analog high-pass (RC type) and low-pass (Bessel type) filtering was applied to magnetocardiograms from 0.16 to 250 Hz. The mean value (± SD) of the measured noise level was (260 ± 100) fT, peak to peak over all recordings. The UP segment was taken as the zero reference line for all measurements. Magnetocardiographic signals were processed off-line and averaged over about 80 cardiac cycles.

In each subject, the QRST time integral was calculated for each lead as algebraic sum of all magnetic field values from the onset of the QRS complex to the offset of the T wave, multiplied by the sampling interval. Such an integral (with values expressed in pTms) represented the net area of the ventricular deflection of the magnetocardiogram. For visualization, the QRST integral maps were displayed using contour lines that connect points of equal integral value; a cubic spline function was used to interpolate integral values between the sensor positions.

Magnetocardiographic QRST integral maps were examined using spatial Karhunen-Loeve (KL) transformation as has been described in detail elsewhere [7,8]. Briefly, from the entire set of 51 QRST integral maps (each

©1999, Tohoku University Press
Recent Advances in Biomagnetism
T. Yoshimoto et al. (Eds)

comprising 49 values), we first calculated the covariance matrix Σ (49×49). Next, we calculated the eigenvalues and eigenvectors (basis functions) of this covariance matrix using the following decomposition (IMSL library),

$$\Sigma = \Gamma \Lambda \Gamma^{\mathrm{T}} , \tag{1}$$

where Γ is a square matrix of eigenvectors (49×49), Γ^{T} is its transpose, and Λ is a diagonal matrix of 49 eigenvalues ordered by magnitude. Then, we applied the KL transform to each vector of integral values x_j (49×1) recorded from the jth subject to obtain the vector of weighting coefficients γ_j (49×1),

$$\gamma_j = \Gamma^{\mathrm{T}} x_j , \tag{2}$$

Finally, we represented each individual integral map as a truncated linear combination of the first 24 eigenvectors and corresponding 24 weighting coefficients of γ_j. We calculated the percentage nondipolar content defined as the information (i.e., variation) content of the eigenvectors 4 through 24 relative to the total signal energy of a given reconstructed map (eigenvectors 1 through 24) [1,2]. Eigenvectors for the entire study group were displayed in the same format as QRST integral maps.

Statistical analysis was performed using the Wilcoxon rank sum test since a normal distribution of the values could not be assumed. A probability value of less than 0.05 was considered significant. Values were expressed as mean ± SD separately for the two group sets.

Results

In general, the QRST integral maps of patients with ventricular arrhythmias exhibited marked differences in the distribution patterns and in comparison to those of control subjects often had much smaller magnitudes of the extrema ((-560 ± 480) and (582 ± 547) pTms for the patient group versus (-915 ± 450) and (1626 ± 694) pTms for the control group); both differences were statistically significant). We represented the entire pattern space of 49 integral values in 51 subjects (22 controls and 29 patients) with 24 eigenvectors. The first three eigenvectors had a relatively smooth bipolar distribution, while the higher-order (> 3) eigenvectors were multipolar with an increasing number of extrema.

The contribution of eigenvectors beyond the third to the total signal energy (index of nondipolar content) was significantly higher in the group of patients with ventricular arrhythmia than in the control subject group ((13.01 ± 9.13) per cent versus (2.62 ± 2.02) per cent, $p < 0.0001$). To determine the decision threshold of nondipolar content index for the best accuracy in distinguishing between the two group sets, we calculated a receiver operating characteristic curve. A threshold of 6.7 per cent yielded an optimal accuracy with a sensitivity of 75.9 per cent and a specificity of 100 per cent. Nondipolarity index values higher than the decision threshold of 6.7 per cent were exclusively present in the group of patients with ventricular arrhythmia, while seven patients had a nondipolar content lower than this threshold.

Discussion

Our study represents an attempt to investigate the utility of spatial features derived from the magnetocardiographic QRST integral maps for predicting ventricular arrhythmia vulnerability. Our results suggest that differences in index of nondipolarity can quantitatively distinguish between the control subjects and patients with ventricular arrhythmia.

In this study, we applied the K-L transform, which has been successfully used in the previous electrocardiographic and magnetocardiographic studies [1,2,3,9]. Mean values for the nondipolar content of the two group sets ((13.01 ± 9.13) per cent in the VT group and (2.62 ± 2.02) per cent in the control group) were similar to those obtained by Abildskov et al. [1] ((33.6 ± 22.6) per cent in the VT group and (11.4 ± 7.6) per cent in the control group). However, both sensitivity and specificity found in the study of Abildskov et al. [1] (72 per cent and 84 per cent, respectively) were lower than in our study, suggesting that nondipolarity content of the magnetocardiographic QRST integral maps may be a more potent diagnostic marker than nondipolarity content of the electrocardiographic QRST integral maps. Further measurements using both modalities on the same patient group and applying the same protocol may help to understand the differences between the content of magnetocardiographic and electrocardiographic signals.

Here, we have supplied empirical and statistical evidence that magnetic field mapping (similarly as body surface potential mapping [1,3]) of the QRST integrals may provide noninvasive means in assessing alterations in the primary repolarization properties of the ventricles. Although the efficacy of magnetic field mapping has been demonstrated in the neurological clinical applications, cardiological clinical applications of this modality are still relatively scanty. The findings of our study indicate that magnetic field mapping in combination with quantitative assessment of ventricular repolarization properties may be a potentially useful screening tool for ventricular arrhythmia vulnerability.

References

[1] Abildskov JA, Green LS, and Lux RL: Detection of disparate ventricular repolarization by means of the body surface electrocardiogram, Zipes DP and Jalife J (eds): Cardiac electrophysiology and arrhythmias. New York: Grune & Stratton, 1985, pp 495–499

[2] De Ambroggi L, Bertoni T, Locati E, et al: Mapping of body surface potentials in patients with the idiopathic long QT syndrome. Circulation 74: 1334–1345, 1986

[3] Hubley-Kozey CL, Mitchell LB, Gardner MJ, et al: Spatial features in body-surface potential maps can identify patients with a history of sustained ventricular tachycardia. Circulation 92: 1825–1838, 1995

[4] Brockmeier K, Schmitz L, Chavez JJB, et al: Magnetocardiography and 32-lead potentials: Repolarization in normal subjects during pharmacologically induced stress. J Cardiovasc Electrophysiol 8: 615–626, 1997

[5] Stroink G, Lant J, Elliott P, et al: Discrimination between myocardial infarct and ventricular tachycardia patients using magnetocardiographic trajectory plots and iso-integral maps. J Electrocardiol 25: 129–142, 1992

[6] Drung D: The PTB 83-SQUID system for biomagnetic applications in a clinic. IEEE Trans Appl Supercond 5: 2112–2117, 1995

[7] Lux RL, Smith CR, Wyatt RF, and Abildskov JA: Limited lead selection for estimation of body surface potential maps in electrocardiography. IEEE Trans Biomed Eng 25: 270–276, 1978

[8] Lux RL, Evans AK, Burgess MJ, et al: Redundancy reduction for improved display and analysis of body surface potential maps. I. Spatial compression. Circ Res 49: 186–196, 1981

[9] Rovamo L, Paavola M, Montonen J, et al: Magnetocardiographic repolarization maps in children with long QT syndrome, Baumgartner C, Deecke L, Stroink G, et al (eds): Biomagnetism: Fundamental Research and Clinical Applications. Amsterdam: Elsevier/IOS-Press, 1995, pp 615–618

Acknowledgments

This work was supported in part by the German Federal Ministry of Education, Science, Research and Technology under grant number 13N6930 and in part by the Ministry of Science and Technology of Republic of Slovenia under grant number 3411-98-22 0558.

Value of magnetocardiographic QRS integral maps in localizing ventricular tachycardia foci

Hren R[1], Stroink G[2]

Institute of Mathematics, Physics, and Mechanics, University of Ljubljana[1], 1000 Ljubljana, Slovenia; Department of Physics, Dalhousie University[2], Halifax, Canada B3H 3J5

Introduction

Radiofrequency (RF) catheter ablation has recently become a method of choice in treating patients suffering from ventricular tachycardia (VT). The precise localization of ventricular tachycardia foci arising from triggered activity or micro-reentry is a prerequisite for the successful RF catheter ablation in patients. Magnetic field maps (MFMs), which are constructed from multiple magnetocardiograms recorded simultaneously above the anterior chest, has shown promise in facilitating such a localization.

Recently, Green et al. [1] performed an animal pace mapping study in combination with statistical analysis and concluded that pacing at sites separated by only 4 mm gives rise to electrocardiographic QRS integral maps that significantly differ in quantitative features. No attempt has yet been made to determine how precisely it is possible to discriminate between patterns of magnetocardiographic QRS integral maps.

Here, we used an anatomical computer model of the human ventricular myocardium to systematically pace the left ventricular (LV) and right ventricular (RV) epicardial surfaces. The overall objective of this simulation study was to determine the spatial resolution with which epicardial breakthrough sites near the origin of VT could be distinguished by magnetocardiographic QRS integral maps. Specific purpose of the study was to quantitatively assess how the spatial resolution of integral maps may depend on the location of a given activation site over the epicardial surface.

Methods

Our computer model of the human ventricular myocardium has been presented in detail elsewhere [2, 3]. It features anatomically accurate geometry, intramural anisotropic structure, and a computational implementation of propagation based on excitatory current flow [2, 3]. Extracardiac potentials and magnetic field are calculated using the oblique dipole model [2, 3] in combination with the boundary element method [4].

We simulated sets of MFMs (based on 64 lead sites near the anterior torso) for a total of 183 pacing sites: 72 pacing sites were positioned in the basal level (70 mm above the epicardial apex), 64 pacing sites were positioned in the middle level (45 mm above the epicardial apex), and 47 pacing sites were positioned in the apical level (20 mm above the epicardial apex). The distance between the neighboring sites on the same epicardial level was approximately 4 mm. For each pacing sequence, we calculated MFMs every 4 ms within the first 120 ms after the onset of activation. We also calculated magnetocardiographic QRS integral maps extending from the onset of activation to the time when activation of the ventricles was completed.

To mimic measuring conditions, we calculated for each of 183 pacing sites 10 magnetocardiographic QRS integral maps with added Gaussian noise; noise level was kept constant for all pacing sites and corresponded to 4 per cent of the mean range of magnetocardiographic QRS integral values. Next, we cross-correlated sets of maps for all possible pairs of pacings sites on the same epicardial level. Beat-to-beat variability of QRS maps was assessed for each pacing site by correlating two sets of maps resulting from identical pacing site. Finally, we applied the nonparametric unpaired Kolmogorov-Smirnov test and defined the spatial resolution as the pacing sites separation at which the differences in correlation coefficients were significant (level $p < 0.05$).

Results

Fig. 1 shows magnetocardiographic QRS integral maps for 36 (of 72) pacing sites located in the basal level. QRS integral maps feature a counterclockwise rotation of the axis joining the extrema as the pacing site is shifted from the left lateral, to the left anterior, right anterior, right lateral, right posterior, and left posterior aspects of the epicardium. The rotation of the axis (extrema) is accompanied by progressive changes of the amplitudes of the QRS integral values. QRS integral maps corresponding to the left lateral sites (sites 69 through 3) are

©1999, Tohoku University Press

Recent Advances in Biomagnetism
T. Yoshimoto et al. (Eds)

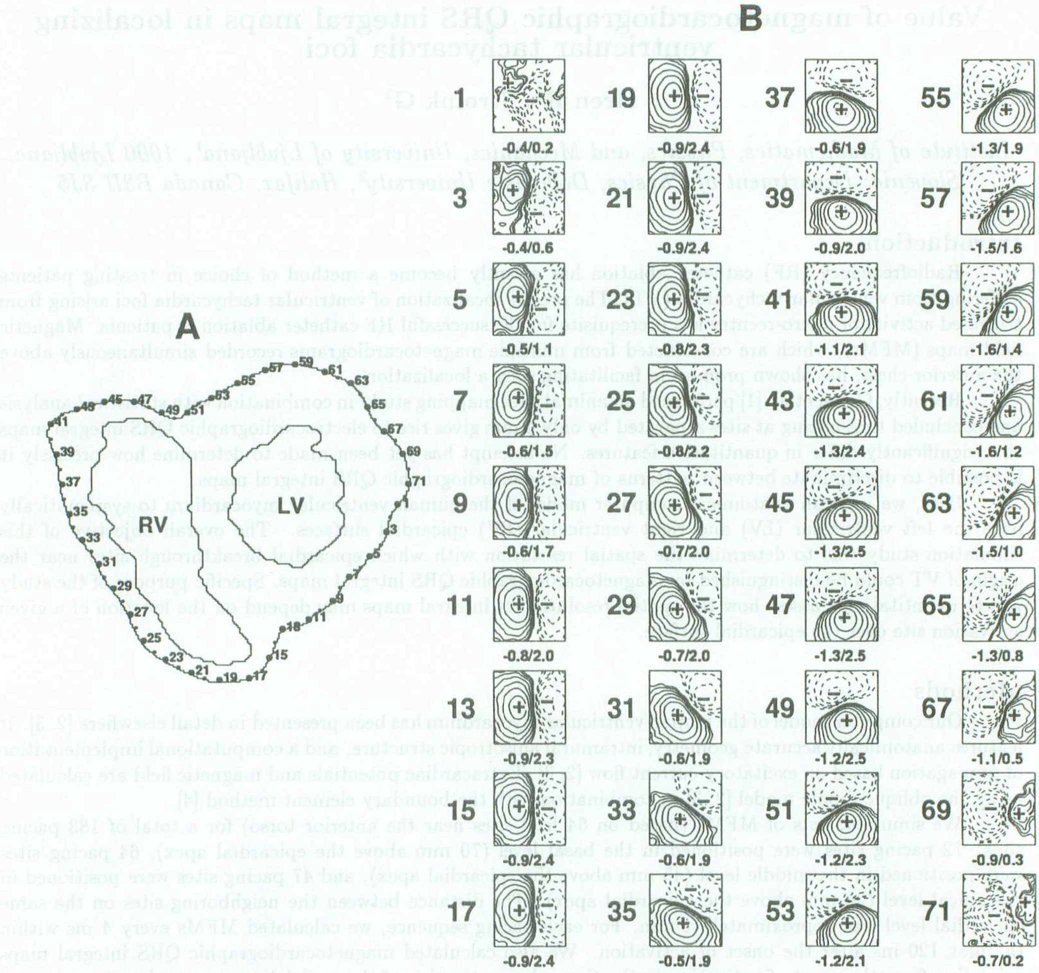

Figure 1: (A) Axial cross-section taken through the model at 70 mm (basal level) above the epicardial apex shown with 72 epicardial pacing sites. RV, right ventricle; LV, left ventricle; posterior aspect of the ventricles is to the top. (B) Magnetocardiographic QRS integral maps calculated (in the presence of Gaussian noise) for activation sequences initiated at 36 (of 72) pacing sites in the basal level of the LV (70 mm above the epicardial apex). The number of a given pacing site is shown at each map and corresponds with the site numbering of panel A. The extrema are denoted in pT·s below the map and isointegral lines are plotted for equal intervals.

characterized by low-amplitude values of the extrema since, as shown in our recent BSPM study [5], for these sites the primary sources point predominantly from the posterior to the anterior torso, that is, perpendicularly to the MFM measuring plane. Similar features as described above were found in magnetocardiographic QRS integral maps corresponding to the pacing sites in the middle and apical levels.

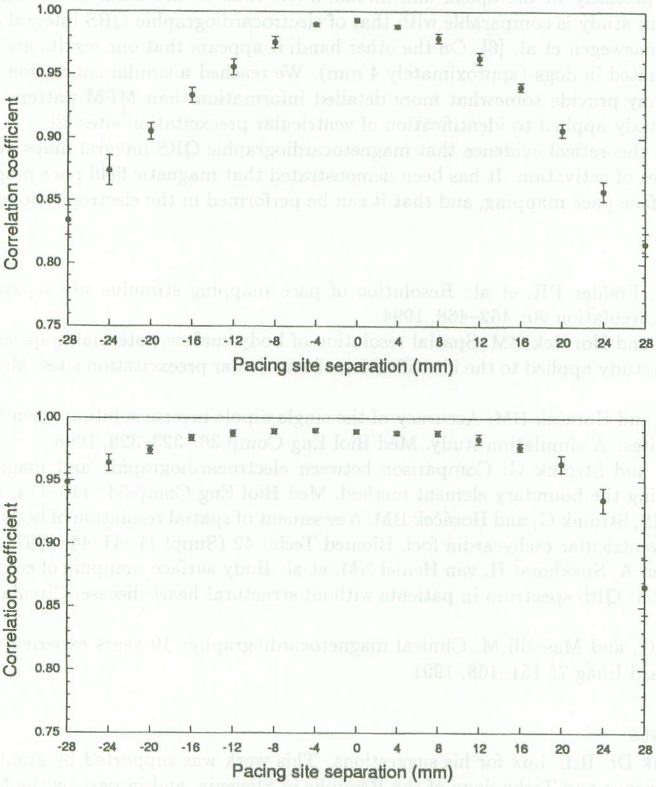

Figure 2: Correlation coefficients of QRS integral maps as a function of pacing site separation for (upper panel) the lateral pacing site in the basal level of the RV and for (lower panel) the anterior pacing site in the middle level of the RV. Abscissa: distance from the reference pacing site (0 mm); ordinate: mean correlation coefficients with SD indicated by error bars.

Fig. 2 shows the correlation coefficients as a function of the pacing site separation for the lateral pacing site in the basal level of the RV and for the anterior pacing site in the middle level of the RV. These plots reveal that correlation coefficients decrease with the increasing pacing site separation. Nonparametric statistical comparison showed for these particular examples that pacing sites can be separated within 4 mm (at the level of $p < 0.015$) and 16 mm (at the level of $p < 0.0001$), respectively.

The average spatial resolution (±SD) for magnetocardiographic QRS integral maps was 9.7 ± 5.4 mm in the basal level, 7.6 ± 4.1 mm in the middle level, and 7.9 ± 3.4 mm in the apical level (8.4 ± 4.6 mm for all levels combined). In 36 per cent of pacing sites (66/183), the significant differences in maps were observed within 4 mm, while 26 per cent of pacing sites (48/183) could not be separated within 12 mm or more. We were better able to distinguish LV than RV pacing sites (6.8 ± 3.9 mm versus 10.3 ± 4.7 mm).

Discussion

Our study represents the first attempt in systematically assessing the spatial resolution of magnetocardiographic QRS integral maps for localization of ectopic pacing sites. The findings of our study indicate that the localization of epicardial pacing sites can be on average (± SD) within 8.4 ± 4.6 mm. Pacing sites can be distinguished more precisely in the apical and middle levels than in the basal level. The average spatial resolution assessed in our study is comparable with that of electrocardiographic QRS integral maps obtained in humans by SippensGroenewegen et al. [6]. On the other hand, it appears that our results are worse than those of Green et al. [1] estimated in dogs (approximately 4 mm). We reached a similar conclusion—that the BSPM pattern classification may provide somewhat more detailed information than MFM pattern classification—in our recent simulation study applied to identification of ventricular preexcitation sites [2].

Here, we provide theoretical evidence that magnetocardiographic QRS integral maps may offer guidance to localizing ectopic sites of activation. It has been demonstrated that magnetic field pace mapping is a feasible alternative to body surface pace mapping, and that it can be performed in the electrophysiology laboratory [7].

References

[1] Green LS, Lux RL, Ershler PR, et al: Resolution of pace mapping stimulus site separation using body surface potentials. Circulation 90: 462–468, 1994

[2] Hren R, Stroink G, and Horáček BM: Spatial resolution of body surface potential maps and magnetic field maps: A simulation study applied to the identification of ventricular preexcitation sites. Med Biol Eng Comp 36: 145–157, 1998

[3] Hren R, Stroink G, and Horáček BM: Accuracy of the single dipole inverse solution when localising ventricular preexcitation sites: A simulation study. Med Biol Eng Comp 36: 323–329, 1998

[4] Hren R, Zhang X, and Stroink G: Comparison between electrocardiographic and magnetocardiographic inverse solutions using the boundary element method. Med Biol Eng Comp 34: 110–114, 1996

[5] Hren R, MacLeod RS, Stroink G, and Horáček BM: Assessment of spatial resolution of body surface potential maps in localizing ventricular tachycardia foci. Biomed Techn 42 (Suppl 1): 41–44, 1997

[6] SippensGroenewegen A, Spekhorst H, van Hemel NM, et al: Body surface mapping of ectopic left and right ventricular activation: QRS spectrum in patients without structural heart disease. Circulation 82: 879–896, 1990

[7] Fenici RR, Melillo G, and Masselli M: Clinical magnetocardiography: 10 years experience at the Catholic University. Int J Card Imag 7: 151–168, 1991

Acknowledgements

We wish to thank Dr. R.L. Lux for his suggestions. This work was supported by grant 3411-98-22 0558 from the Ministry of Science and Technology of the Republic of Slovenia, and in part by the Nova Scotia Heart and Stroke Foundation.

Detection of Exercise Induced Myocardial Ischemia by Multichannel Magnetocardiography in Patients with Single Vessel Coronary Artery Disease

Hänninen H, MD[1,2], Takala P, MSc[2,3], Mäkijärvi M, MD[1,2], Montonen J, PhD[2,3], Korhonen P, MD[1,2], Oikarinen L, MD[1,2], Nenonen J, PhD[2,3], Katila T, PhD[2,3], Toivonen L, MD[1,2]

[1]Division of Cardiology and [2]BioMag Laboratory, Helsinki University Central Hospital;
[3]Laboratory of Biomedical Engineering, Helsinki University of Technology; Helsinki, Finland

Introduction

New therapeutic interventions for coronary revascularization enable treatment of new patient groups. This makes the detection, quantification and localisation of ischemia clinically even more important.

Magnetocardiography (MCG) is a noncontact multichannel mapping technique. The magnetic field generated by the heart is produced by the same ionic currents which produce the ECG. However, there are some fundamental differences: the MCG is sensitive to closed loop currents, and the magnetic signal does not depend on the skin resistivity or intervening tissue distortion unlike the ECG [1,2]. The mathematical modelling of magnetic fields is easier than that of electrical fields [3]. One of the first clinical studies was reported by Saarinen et al. [4] in 1974, where ischemic ST-segment depressions were found both in the ECG and the MCG of coronary artery disease patient after stress. Cohen et al. [5] created an experimental occlusion of a coronary artery in a dog, and found within 20 seconds after occlusion equal and opposite ST-segment and baseline shifts on direct current MCG. Lant et al. [6] found MCG to carry complimentary information compared with body surface potential mapping in patients with ischemic heart disease especially during the terminal phase of ventricular depolarization and during the whole repolarization phase.

This study assessed the ability of multichannel MCG to detect myocardial ischemia in patients with well defined coronary artery disease (CAD) during supine bicycle ergometry.

Methods

Patients and controls

The study population consisted of 18 patients (10 male and 8 female; mean age 56 years; range 37-75 years) with single vessel coronary artery disease, and 17 healthy middle-aged volunteers (12 men and 5 female; mean age 55; range 45-67 years) (Table 1). Ten patients showed significant (>50% luminal diameter) stenosis of the proximal left anterior descending coronary artery (LAD) (mean±SD, 81±13%), and 8 patients significant stenosis of the right proximal coronary artery (RCA) (mean±SD 92±5%) in coronary angiograms. All patients had documented exercise induced ischemia in standard bicycle ergometry (3 minute and 50W or 25W steps). Importantly, none of the patients had suffered from a previous transmural myocardial infarction and 12-lead ECG showed no abnormal Q-waves or bundle branch block. Both left ventricular cine-angiography and transthoracic echocardiography were considered normal. All the patients were under appropriate CAD medication during the study (Table 2). The healthy controls had no history of heart disease, and had normal findings in transthoracic echocardiography and bicycle ergometry stress test.

Table 1. Clinical characteristics of the study groups.

GROUP	LAD	RCA	CONTROLS
N	10	8	17
AGE (years)	55±9	58± 12	55±7
MALE / FEMALE	5/5	5/3	12/5
EF (%)	64±6	62±8	66±7
STENOSIS (%)	81±13	92±5	-

Number of patients or mean±SD

Table 2. Coronary artery disease medication.

GROUP	N	β-blockers	Ca-antag	nitrates	aspirin
LAD	10	100 %	10 %	80 %	100 %
RCA	8	100 %	25 %	75 %	100 %

©1999, Tohoku University Press
Recent Advances in Biomagnetism
T. Yoshimoto et al. (Eds)

Magnetocardiography

MCG recordings were performed in Helsinki University Central Hospital at the high performance magnetically shielded room of the BioMag Laboratory with 67 channel magnetometer.

A rest measurement was recorded for five minutes and after that supine bicycle exercise test was performed using a nonmagnetic stress ergometer, which was designed in the Laboratory of Biomedical Engineering of Helsinki University of Technology. The amagnetic ergometer was calibrated against commercially available Siemens bicycle stress ergometer used in cardiac catheterization laboratory for supine exercise testing. During exercise test the stress level was increased and blood pressure monitored every two minutes. The cessation criteria were severe fatique or dyspnea, severe chest pain, ischemic ST-depression ≥ 1.0 mm in ECG, progressive decrease or abnormal elevation of systolic blood pressure. Both MCG and 12-lead ECG were continuously recorded during the exercise and up to ten minutes postexercise.

MCG analysis

MCG recordings were base-line corrected and signal averaged to increase the signal-to-noise ratio. Four different test phases were taken into analysis: 1) rest, 2) cessation of exercise 3) two and 4) four minutes postexercise. The following two time intervals chosen for the analysis were determined using the signals from seven central gradiometers (Fig. 1):

1) An integral of the ST-segment (the second quarter from the J-point to the T wave maximum)

2) The T-wave maximum.

Signal averaged MCG at these test phases were used to create isofield maps. A change in the isofield map was determined as a turn of the magnetic field vector between the minimum and maximum compared to the field orientation of the baseline measurements. This change was quantified as a rotation of an imaginary line connecting the magnetic field minimum and the maximum in the isofield maps.

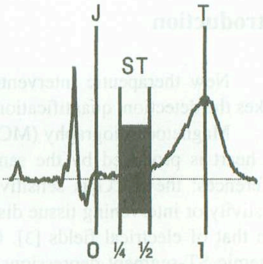

Fig. 1. The time instants analysed. An integral of the ST-segment and T-wave maximum.

Statistical Analysis

The statistical analysis was performed with SPSS statistical software for Windows (Version 7.5) using Mann-Whitney U test. Two-tailed p-value < 0.05 was considered statistically significant.

Results

ST-segment maps

The average changes of the magnetic field orientation during the ST-segment are summarized in Table 3.

The rotation of the ST-segment isofield maps (Fig. 2) at cessation of exercise was significantly larger in coronary artery disease (CAD) patients than in controls (74° vs 33°, $p < 0.01$). The ST-segment maps at cessation of exercise also separated LAD patients from controls (94° vs 33°, $p < 0.01$), whereas RCA patients could not be separated from controls (49° vs 33°, p = ns). The rotation of the ST-segment maps at cessation of exercise was statistically significantly larger in LAD than in RCA patients ($p < 0.05$). The ST-segment maps 2 minutes postexercise separated LAD patients from controls (94° vs 37°, $p < 0.05$), but did not separate the combined CAD patient group or RCA patients from controls (p = ns). The ST-segment maps 4 minutes postexercise did not separate CAD patients from controls (Table 3).

Table 3. Rotations in the ST-segment isofield maps. Mean / range (in degrees).

GROUP	cessation of exercise	2 min postexercise	4 min postexercise
LAD	94 / 25-163	94 / 20-180	71 / 10-165
RCA	49 / 15-145	44 / 5-165	32 / 0-145
CAD	74 / 15-163	72 / 5-180	54 / 0-165
CONTROLS	33 / 0-107	47 / 0-117	36 / 0-115

T-wave maps

The average changes of the magnetic field orientation at the T-wave apex are summarized in Table 4.

The rotation of T-wave maps (Fig. 3) at cessation of exercise separated RCA patients from controls (32° vs 8°, $p < 0.01$), whereas they were not able to separate

Table 4. Rotations in the T-wave isofield maps. Mean / range (in degrees).

GROUP	cessation of exercise	2 min postexcercise	4 min postexcercise
LAD	13 / 0-40	40 / 0-170	29 / 5-177
RCA	32 / 0-120	46 / 15-85	44 / 10-95
CAD	21 / 0-120	43 / 0-170	36 / 5-177
CONTROLS	10 / 0-25	7 / 0-30	8 / 0-60

the LAD patients or the combined CAD patient group from controls (13° vs 8°, 21° vs 8°, $p = ns$, both). The rotation of the isofield maps of T-wave 2 and 4 minutes postexercise was significantly larger in CAD patients than in controls (43° vs 7°, 36° vs 14°, $p < 0.01$), and also separated both LAD and RCA patients from controls ($p < 0.05$, all). The rotation of the T-wave isofield maps 4 minutes postexercise was significantly larger in RCA than in LAD patients (44° vs 29°, $p < 0.01$).

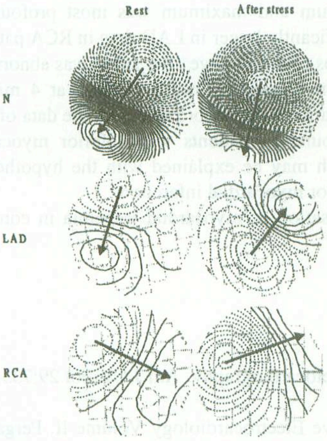

Fig. 2. An example of rotation of the ST-segment maps at cessation of exercise in a control, LAD and RCA patient. Step 0.2pT.

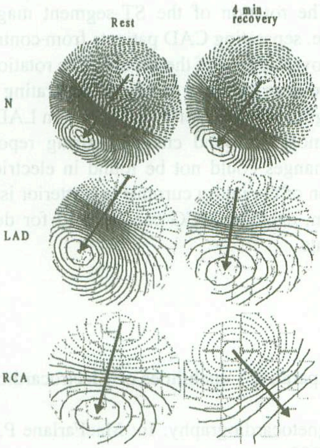

Fig. 3. An example of rotation of the T-wave maps 4 minutes postexercise in a control, LAD and RCA patient. Step 0.5pT.

Table 5. Rotation of maps when compared to rest measurements.

GROUPS	ST-maps after Stress	T-wave maps 2 min postexercise	T-wave maps 4 min postexercise
CAD vs CONTROLS	$p < 0.01$	$p < 0.01$	$p < 0.01$
LAD vs CONTROLS	$p < 0.01$	$p < 0.05$	$p < 0.05$
RCA vs CONTROLS	ns	$p < 0.01$	$p < 0.01$
LAD vs RCA	$p < 0.05$	ns	$p < 0.05$

The statistical significance of the magnetic field map rotations between different exercise test phases and patient groups is shown in Table 5. The measured differences of MCG maps could always separate study groups except ST-maps for RCA and controls and for T-wave maps for LAD and RCA patients (Table 5).

Discussion

The present study demonstrated that exercise induced myocardial ischemia causes recognisable and significant repolarization changes in MCG maps of coronary artery disease patients. The first study of MCG in acute myocardial ischemia was reported by Cohen et. al. [8] in 1971, where an occlusion of dog´s coronary artery was created. Opposite baseline and ST-segment shifts were recorded in direct current MCG indicating that ST-segment elevation during acute myocardial infarction might be secondary to injury current causing baseline depression. This primary injury current discontinues during the ST-segment. Saarinen et al. [4] reported the first MCG recording on CAD patient in 1974, where both 12-lead ECG and single channel MCG from 3 different locations were recorded after physical stress. The ischemic postexercise ST segment depressions were seen in MCG, in which the ST shift amplitude / R ratio was even greater than in ECG.

Lant et al. [6] reported in 1990 the complementary nature of the magnetic and electric mapping. The most profound changes of MCG for anterior myocardial infarction (MI) patients were found during depolarization and for the inferior MI patients during repolarization. The authors concluded that the repolarization changes in MCG could have been caused by prolonged ischemic injury increasing tangential current flow through the spared subendocardial tissue.

In the present study the change of the magnetic field orientation after exercise was quantified as a rotation of the imaginary line connecting the magnetic field minimum and maximum compared to the rest measurements. Two different time intervals were used for the analysis: An integral of the ST-segment and a single time instant on the T-wave maximum. The rotation of the ST-segment magnetic field minimum and maximum was most profound at cessation of exercise, separating CAD patients from controls, and was significantly larger in LAD than in RCA patients, although there was overlapping of the groups. The rotation of the MCG maps of the T-wave after stress was abnormally increased during exercise induced ischemia separating CAD patients from controls. T-wave rotation at 4 minutes postexercise was significantly larger in RCA than in LAD patients. This finding is in concordance with the data of Lant et al., where the most profound changes during repolarization were found in patients with inferior myocardial infarction. These changes could not be found in electrical mapping, which may be explained with the hypothetized tangential orientation of the injury currents in posterior ischemia and posterior myocardial infarction.

In conclusion, exercise MCG can be used for detection and localisation of myocardial ischemia in coronary artery disease patients.

References:

[1] Plonsey R. Comparative Capabilities of Electrocardiography and Magnetocardiography. Am J Cardiol 29:735-736, 1972.

[2] Siltanen P. Magnetocardiography. In: MacFarlane P, ed. Comprehensive Electrocardiology Volume II. Pergamon Press, 1405-1438, 1989.

[3] Nenonen J: Solving the Inverse Problem in Magnetocardiography. IEEE Engineering in Medicine and Biology 13:487-496, 1994.

[4] Saarinen M, Karp PJ, Katila TE, Siltanen P. The Magnetocardiogram in Cardiac Disorders. Cardiovasc Res 8:820-834, 1974.

[5] Cohen D, Kaufman LA. Magnetic Determination of the Relationship between the S-T-segment Shift and the Injury Current Produced by Coronary Artery Occlusion. Circ Res 36:414-424, 1975.

[6] Lant J, Stroink G, ten Voorde B, Horacek BM, Montague TJ. Complementary Nature of Electrocardiographic and Magnetocardiographic Data in Patients with Ischemic Heart Disease. J Electrocardiol 23:315-322, 1990.

[7] Cohen D, Norman JC, Molokhia F, Hood W. Magnetocardiography of Direct Currents: S-T Segment and Baseline Shifts during Experimental Myocardial Infarction. Science 172:1329-1333, 1971.

Classification of WPW Cases with Cluster Analysis of Accessory Conduction Pathway Direction of Propagation

Jazbinšek V[1], **Trontelj Z**[1], **Oeff M**[2], **Burghoff M**[3]

[1]*Institute of Mathematics, Physics and Mechanics, University of Ljubljana, Slovenia;*
[2]*Klinikum Benjamin Franklin, Freie Universitaet Berlin, Berlin, Germany;*
[3]*Physikalisch-Technische Bundesanstalt, Institut Berlin, Berlin, Germany*

Introduction

Recently, several studies have been performed [1, 2, 3, 4, 5] where the functional localization of accessory pathway (AP) in Wolff–Parkinson–White (WPW) syndrome patients, obtained by non-invasive magnetocardiographic (MCG) mapping, were compared with results of invasive electrophysiological study (EPS). Main restrictions of comparing spatial differences in these studies are some methodological incompatibilities between MCG and EPS. Some papers report alternative approach where the MCG mapping data is used to classify different types of WPW cases either from magnetic field distribution [6] or from propagation of the calculated equivalent current source, superimposed on the magnetic resonance image (MRI) [7].

In this study we have introduced cluster analysis of AP direction of propagation to classify different types of WPW patients. We have studied 22 WPW syndrome patients. All patients underwent non-invasive MCG mapping and the invasive EPS before catheter ablation of AP was performed. Spatial coordinates of a moving equivalent current dipole source within different volume conductor models (a half space and a realistic torso model) were calculated from the MCG data in the localization procedure. The current dipole direction of propagation within the AP has been used in clustering procedure.

Methods

All MCG measurements were recorded in the Berlin Magnetically Shielded Room [8] by means of 37-SQUID multichannel magnetometer system [9]. The measured plane was tangential to the patient's chest (frontal plane). The magnetic field component perpendicular to the frontal plane was measured (see Fig. 1). Recording time was 100 seconds, sampling rate 1000 Hz, and frequency band $0.016 - 250\,Hz$. Preprocessing of recorded data included averaging and automatic rejection of artifacts. The patient positioning during all MCG measurements was done manually. The estimated error of this procedure was around 0.5 cm for the frontal (xy) plane and about 1 cm for the z coordinate (depth).

All EPS were performed at the University Hospital Benjamin Franklin in Berlin–Steglitz. Positioning of patient during EPS was done with markers on the skin. The ablation catheter was recorded by X-rays in frontal and sagittal planes. For each projection the 1 cm grid was put perpendicular to X-rays to reconstruct the catheter position. The X-ray film was afterwards projected on the screen and the position of catheter ablation tip was determined manually by using the above mentioned grids. The estimated error of this procedure was up to 1.5 cm for each coordinate.

The AP is usually clearly manifested by a small deflection called Δ–wave in a time evolution of the ECG and the MCG signal. For each of 37 channel MCG signals a baseline is determined by selecting a 10 ms reference interval before Δ–wave. The reference signal, determined by the mean value of the MCG signal on the reference interval, was then subtracted from the data on the whole heart cycle. Besides baseline correction, the subtraction of the reference signal reduces the influence of the P–wave repolarization [1]. For all studied cases the very beginning of the AP was automatically determined as well as selection of the best reference interval for baseline correction [10].

We have used a moving current dipole model within different volume conductors to find location of the AP from the measured data. We have applied two types of volume conductor models – the simplified half-space model and realistically shaped human torso using boundary element method (BEM). We have constructed such torso model from MRI (see Fig. 2). We have applied the same torso for all studied cases. We have calculated spatial coordinates of equivalent current dipole for each ms on 30 ms time interval after the AP onset. For each

©1999, Tohoku University Press
Recent Advances in Biomagnetism
T. Yoshimoto et al. (Eds)

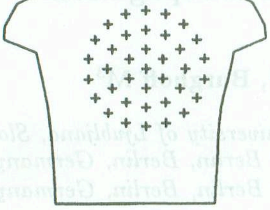

Fig. 1: The 37-channel MCG measurement grid.

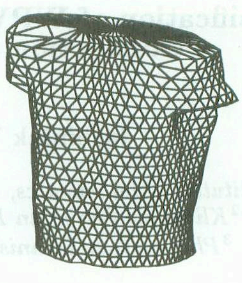

Fig. 2: The triangulated BEM torso model.

volume conductor model and time point the tolerance of calculated localization site was estimated by averaging results of five neighboring time points, two before and two after the current time point. Additionally a velocity of the moving equivalent current dipole between two neighboring averaged localizations and mean goodness of fit were calculated. Results published elsewhere in more details [5] showed that for almost all cases the MCG solutions become more stable 10 to 20 *ms* after the AP onset. This is due to very low magnetic signals in the very beginning of AP that are slightly above the noise level. This was even more evident if the MCG inverse solutions with reference intervals before the P wave were also examined [10]. In further analysis we considered only 16 patients (other were omitted due to the poor goodness of fit or large fluctuations of localization results).

To compare invasive EPS with noninvasive MCG localization results one has to match coordinate systems used in both modalities. Direct comparison of coordinates obtained by EPS and MCG does not give a clear evaluation in our case due to the positioning methods. However, these errors are mainly translational. So we have also studied direction of AP propagation that is invariant to translational changes of coordinate system. We divide the AP into segments that connect two successive points obtained by MCG localization procedure, see Fig. 3. $\Delta\vec{R}_{i,j}$ and $\Delta\vec{R}_{i,k}$ represent the i–the segment direction of propagation for the j–th and k-th case,

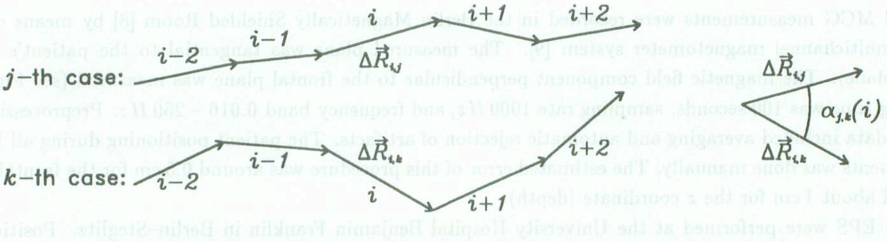

Fig. 3: Schematic presentation of two AP for the two cases (j) and (k).

respectively. A cosine of an angle $\alpha_{j,k}(i)$ between two directions is determined by

$$\cos\alpha_{j,k}(i) = \frac{\Delta\vec{R}_{i,j}\cdot\Delta\vec{R}_{i,k}}{|\Delta\vec{R}_{i,j}||\Delta\vec{R}_{i,k}|}\ . \tag{1}$$

We introduce the quantity

$$S_{j,k} = 1 - \frac{1}{N}\sum_{i=1}^{N}\cos_{j,k}(i) \tag{2}$$

as a measure of similarity between two different AP which belong to the j-th and the k-th patient, respectively. N is a number of segments in AP which is equal to a number of time points in AP minus one. $S_{j,k}$ is equal zero if two AP are parallel and equal two if they are antiparallel. Otherwise the $S_{j,k}$ is between both limit values. Similarities in Eq. (2) calculated for M patients ($j,k = 1,2,\ldots,M$) form a symmetric similarity matrix S. The agglomerative hierarchical clustering method has been applied subsequently. At any particular stage the method fuses individuals or group of individuals that are more similar (has the lowest $S_{j,k}$) into a new group or cluster. A group average method was used to update the S at each step. This approach defines similarity between two groups as the average of similarity between all pairs of individuals in the two groups [11]. The end-product of the method is a dendogram showing the successive fusions of individuals (Fig.4). The dimension of S reduces by one at each stage until all individuals are in one group.

Results

According to the EPS classification the initial group of 22 patients has been divided into two subgroups: left postero-lateral (LPL) and postero-septal (PS) with 12 and 9 members, respectively. Only 16 patients with more stable MCG inverse problem solutions were considered. Several different time intervals of calculated AP were tested during the cluster analysis. The best match between the EPS and the cluster classification was found for the AP time sequence 10-30 *ms* after the AP onset calculated with the current dipole in the torso model. The clustering classification has formed two main clusters in this case. There were (7 PS + 2 LPL) and (6 LPL + 1 PS) patients in the first and in the second cluster, respectively (see Table 1 and Fig. 4). AP time sequences calculated with the half space model failed to match the EPS classification. Fig. 5 shows the average AP for the two groups of patients.

We have also calculated spatial differences between MCG and EPS localization results. Average differences became smaller in the sequence 10–20 *ms* after the AP onset when also the MCG inverse solutions were more stable. The average differences for the time AP onset + 20 *ms* obtained by realistically shaped torso model and half space model were (3.6±2.3) *cm* and (6.2±2.5) *cm*, respectively. These results agreed with similar studies on a group of 12 patients [1, 2] where errors (2.8 ± 1.4) *cm* and (8.5 ± 3.2) *cm* were reported, respectively.

Table 1: Comparison between EPS and cluster classification.

Group	EPS classification types	EPS Codes	Initial Cases	Considered Cases	Matched Cases
LPL(o)	Left Lateral	K	2	1	0
	Left Postero-Lateral	L	5	4	3
	Left Posteral / Postero-Lateral	M	1	0	0
	Left Posteral	N	4	3	3
PS(x)	Left Postero-Septal	O	3	3	2
	Postero-Septal	P	4	4	4
	Posterial / Postero-Septal	Q	1	1	1
	Right Postero-Septal	R	0	0	0
–	Right Antero-Septal	S	1	0	0

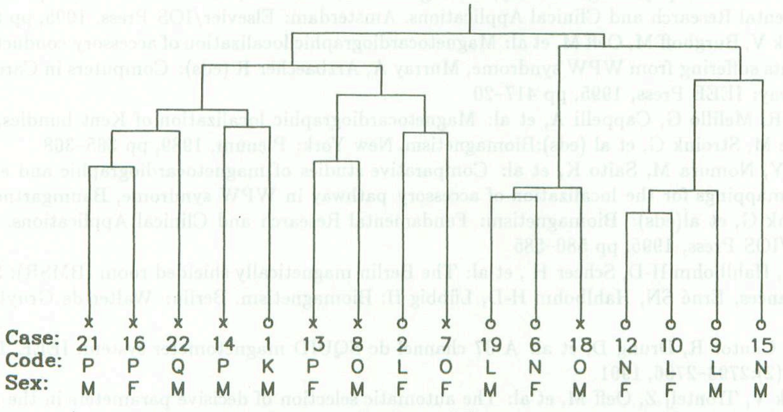
x x x x o x x o x o o x o o o o
Case: 21 16 22 14 1 13 8 2 7 19 6 18 12 10 9 15
Code: P P Q P K P O L O L N O N L L N
Sex: M F M M M F M F F M F M F F M M
PS(x)
LPL(o)

Fig. 4: The result of cluster analysis in the interval 10–30 *ms* after the AP onset. Types of patients (PS and LPL) are denoted by (x) and (o), respectively.

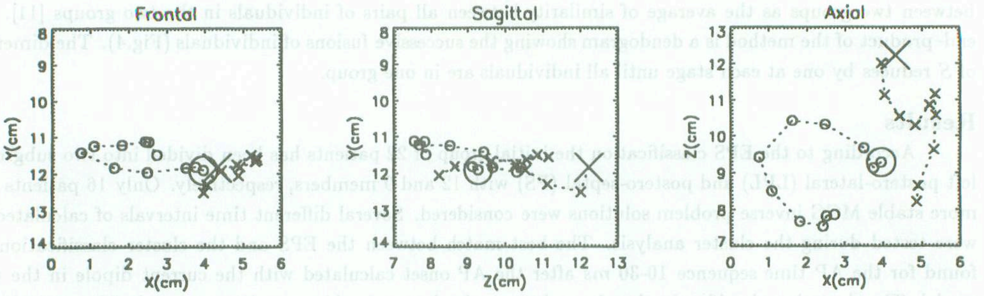

Fig. 5: Average AP for the two groups of patients: LPL(o) and PS(x) from the Fig. 4. The starting point (AP onset + 10 *ms*) is denoted by three times larger label. The step between two successive points is 2 *ms*. Coordinate system origin is in manubrium with axes pointing to: $x \rightarrow$ left, $y \rightarrow$ feet, and $z \rightarrow$ posterior direction.

Discussion

One has to keep in mind some methodological errors when comparing localization results from both modalities. The EPS localization, which is the golden standard in all cases, detects the atrial end of the AP, while the MCG signals reflect the ventricular end. Both ends are expected to be 1–2 *cm* apart [2]. Another major contribution to the uncertainty of results is patient's positioning during both EPS and MCG measurements.

Pathways obtained in WPW-patients (LPL and PS) show significant differences allowing to distinguish these groups by using a clustering procedure. However, further studies on larger groups with different WPW-patients should be performed to prove that the cluster analysis of AP direction of propagation, obtained by the non–invasive MCG localization procedure, can be used for classification of WPW cases.

References

[1] Nenonen J, Katila T, Leiniö M, et al: Magnetocardiographic functional localization using current multipole models. Trans. Biomed. Eng. BME-38(7):648–657, 1991

[2] Nenonen J, Purcell CJ, Horacek BM, et al: Magnetocardiographic functional localization using a current dipole in a realistic torso. IEEE Trans. Biomed. Eng. BME-38(7):658–664, 1991

[3] Moshage W, Achenbach S, Schneider S, et al: Application of multichannel systems in magnetocardiography, Hoke M, Erné SN, Okada YC, et al(eds): Biomagnetism: Clinical Aspects. Amsterdam: Elsevier, 1992, pp 439–446

[4] Kokubun T, Awano N, Kido K, et al: Magnetocardiographic source localization of accessory pathway: Comparison with electrophysiological study, Baumgartner C, Deecke L, Stroink G, et al(eds): Biomagnetism: Fundamental Research and Clinical Applications. Amsterdam: Elsevier/IOS Press, 1995, pp 586–590

[5] Jazbinšek V, Burghoff M, Oeff M, et al: Magnetocardiographic localization of accessory conduction pathway in patients suffering from WPW syndrome, Murray A, Arzbaecher R (eds): Computers in Cardiology 1995. Piscataway: IEEE Press, 1995, pp 417–20

[6] Fenici RR, Melillo G, Cappelli A, et al: Magnetocardiographic localization of Kent bundles, Williamson SJ, Hoke M, Stroink G, et al (eds):Biomagnetism. New York: Plenum, 1989, pp 365–368

[7] Nakaya Y, Nomura M, Saito K, et al: Comparative studies of magnetocardiographic and electrocardiographic mappings for the localization of accessory pathway in WPW syndrome, Baumgartner C, Deecke L, Stroink G, et al(eds): Biomagnetism: Fundamental Research and Clinical Applications. Amsterdam: Elsevier/IOS Press, 1995, pp 580–585

[8] Erné SN, Hahlbohm H-D, Scheer H , et al: The Berlin magnetically shielded room (BMSR): Section B — performances, Erné SN, Hahlbohm H-D, Lübbig H: Biomagnetism. Berlin: Walter de Gruyter, 1981, pp 79–87

[9] Koch H, Cantor R, Drung D, et al: A 37 channel dc SQUID magnetometer system. IEEE Trans. Magn. MAG-27(2):2793–2796, 1991

[10] Jazbinšek V, Trontelj Z, Oeff M, et al: The automatic selection of decisive parameters in the magnetocardiographic localization of the accessory pathway in patients suffering from the WPW syndrome, Wood C, et al: Advances in Biomagnetism. Elsevier, 1998 (In press)

[11] Everitt B: Cluster Analysis. London: Heinmann Educational Book Ltd, 1974

Time Domain Late Field Analysis of Multichannel MCG in Post-Infarction Ventricular Arrhythmia Risk Assessment

Korhonen P [1,2], Montonen J [2,3], Mäkijärvi M [1,2], Toivonen L [1,2], Katila T [2,3]
Division of Cardiology[1] and BioMag Laboratory[2], Helsinki University Central Hospital, Finland;
Laboratoty of Biomedical Engineering[3], Helsinki University of Technology, Espoo, Finland

Introduction

The assessment of the risk for ventricular arrhythmias and sudden cardiac death after myocardial infarction (MI) remains a clinical challenge although in the thrombolysis era the incidence of these serious events has decreased [1]. Several nonivasive methods have been used for this purpose. Clinical variables and the extent of myocardial dysfunction estimated as left ventricular ejection fraction (LVEF) [2], reduced heart rate variability [3] as an index of autonomic imbalance, as well as inhomogeneities of repolarization measured as increased QT dispersion [4] all indicate increased risk after myocardial infarction.

Low amplitude deflections at the end of the magnetic QRS complexes in patients prone to ventricular arrhythmias were first reported by Erne et al in 1983 [5]. These so called **late fields** (LF) have later been suggested in other studies to be associated with a history of ventricular arrhythmias after MI in a manner analogous to electrical late potentials [6]. This late activity is presumed to indicate abnormal, delayed conduction in the border zone of myocardial necrosis which serves as a substrate for re-entrant ventricular tachycardias (VT) which in turn may degenerate into ventricular fibrillation (VF). The ability of time domain indexes of LF to identify patients with ventricular arrhythmias after MI seems promising [7]. So far the materials studied have been relatively small due to the limited availability of the method in clinical use. In recent years it has become possible to perform MCG recordings in hospital environment [8] which has made it more convenient to study larger patient populations.

The aim of the present study was to assess the ability of time domain late fields to separate patients with documented sustained VT after MI from those without arrhythmias in a larger clinical patient material.

Patients

The study population consisted of 103 patients with old MI. 61 patients had not had any significant ventricular arrhythmias during a period of minimum 6 months after MI and these patients comprised the non-VT group. The VT group consisted of 42 patients with old MI who had had a sustained ventricular arrhythmia after MI without associated new infarction. Sustained monomorphic ventricular tachycardia (MVT) had been the clinical arrhythmia in 37 patients, with 4 of them having also ventricular fibrillation (VF). 5 patients had VF only, and were inducible to sustained MVT in electrophysiologic testing indicating chronic propensity to arrhythmias. LVEF was lower in the VT group whereas there were no significant differences in the ages and infarct locations between the groups (table 1). None of the patients had complete bundle branch block in 12-lead electrocardiogram. The patients did not have any anti-arrhythmic medication except beta-blockers during the measurement.

Table 1: Clinical characteristics of the study patients.

	non-VT patients	VT patients	p-value
N	61	42	
Age (yrs)	59 ± 9	62 ± 8	NS
EF (%)	43 ± 17	30 ± 8	< 0.001
Infarct location:			
anterior	30	21	
inferior	24	14	NS
multiple	7	7	

©1999, Tohoku University Press
Recent Advances in Biomagnetism
T. Yoshimoto et al. (Eds)

Methods

MCG recordings were performed in the magnetically shielded room (Euroshield Ltd., Eura, Finland) of the BioMag Laboratory at Helsinki University Central Hospital. High-resolution 67-channel MCG was recorded over the left anterior chest for 5 minutes. Six of the MCG channels were coaxial gradiometers and the remaining were ordered as planar gradiometer pairs. The signals were band-pass filtered 0.03-300 Hz and digitized with a sampling frequency of 1000Hz. After signal averaging, a transformation of the original signals registered with all 67 channels was performed to signals which would have been registerd if only axial gradiometers had been used in the same sensor locations. Minimum norm estimate for the current dipole generating the axially measured signals was utilized in this transformation [9] . After 40Hz high pass filtering the time domain parameters were calculated as mean values over the seven central channels closest to the chest. The time domain parameters calculated were: filtered QRS duration (QRSd), duration of low amplitude signal < 1pT (LAS) and root mean square amplitude of the last 50 ms of the QRS (RMS). Channels with a noise level > 35 fT, measured in a 40 ms interval in the ST segment, were discarded from the analysis.

Results

The time domain parameter values of late fields in both groups are shown in table 2. All parameters differed significantly between the groups. Using the cut point value of QRSd 120 ms yielded a sensitivity of 55% and a specificity of 90% for VT detection. Using the criteria of QRSd > 120ms or RMS < 600 fT yielded a sensitivity of 67% and a specificity of 74% for VT detection.

Table 2. The time domain parameter values (* fT= 10^{-15}Tesla).

	non-VT patients	VT patients	p-value
QRSd (ms)	103 ± 17	126 ± 27	< 0.0001
LAS (ms)	37 ± 13	52 ± 22	< 0.0001
RMS (fT*)	1170 ± 769	621 ± 403	< 0.0001

A sub-group analysis in patients with a moderate to severe left ventricular dysfunction (EF< 40%) was also performed to see if time domain parameters would also identify VT patients in this subgroup. This was performed because left ventricular dysfunction as such is associated with ventricular arrhythmias and sudden cardiac death [2]. Also in patients with a larger infarction the parameter values differed between VT patients and non-VT patients (table 3). Thus the late fields reflected not only the extent of myocardial infarction but most importantly also the abnormal delayed depolarization that is a typical marker of re-entrant ventricular arrhythmias after MI.

Table 3: The left ventricular function and time domain parameter values in patients with ejection fraction < 40% (* fT= 10^{-15}Tesla).

	non-VT patients	VT patients	p-value
N	28	39	
EF (%)	30 ± 9	29 ± 6	NS
QRSd (ms)	114 ± 16	127 ± 27	0.023
LAS (ms)	43 ± 14	53 ± 22	0.044
RMS (fT*)	850 ± 520	591 ± 389	0.023

Discussion

This study shows that magnetocardiographic time domain late field parameters can identify patients with a propensity to severe ventricular arrhythmias after MI. The specificity of the method is good and magnetocardiographic QRS duration <120 ms indicates a favourable prognosis concerning VT/VF. Combining QRSd and RMS yields clinically acceptable sensitivity and specificity. Late fields reflect the arrhythmogenic abnormal delayed conduction typical of patients with VT after MI and not only the extent of myocardial damage.

References

1. Touboul P, Andre-Fouet X, Leizorovicz A, et al. for the Groupe d'etude du pronostic de l'infarctus du myocarde (GREPI): Risk stratification after myocardial infarction. Eur Heart J **18**: 99-197, 1997
2. McClements B M, Adgey A A J: Value of signal-averaged electrocardiography, radionuclide ventriculography, Holter monitoring and clinical variables for prediction of arrhythmic events in survivors of acute myocardial infarction in the thrombolysis era. J Am Coll Cardiol **21** (6): 1419-27, 1993
3. Cripps T R, Malik M, Farrell T G, Camm A J: Prognostic value of reduced heart rate variability after myocardial infarction: clinical evaluation of a new analysis method. Br Heart J **65**: 14-19, 1991
4. Perkiömäki, J S, Koistinen J M, Yli-Mäyry S, Huikuri H: Dispersion of QT interval in patients with and without susceptibility to ventricular arrhythmias after previous myocardial infarction. J Am Coll Cardiol **26** (1): 174-179, 1995
5. Erne S N, Fenici R R, Hahlbom H-D, et al: High-resolution magnetocardiographic recordings of the ST segment in patients with electrical late potentials. Il Nuovo Cimento 2D N 2: 340, 1983
6. Simson MB: Use of signals in the terminal QRS complex to identify patients with ventricular tachycardia after myocardial infarction. Circulation; **64**: 235-242, 1981
7. Montonen J, Leiniö M, Mäkiniemi K, et al: Analysis of high resolution MCG recordings of patients with ventricular tachycardia. In: Williamson SJ, Hoke M, Stroink G, Kotani M, eds. Advances in Biomagnetism. New York: Plenum Press,: 385-8, 1989
8. Montonen J, Ahonen A, Hämäläinen M, et al: Magnetocardiographic functional imaging studies in BioMag laboratory. In: Aine C, Okada Y, Stroink G, Swithenby S, Wood C (eds). Advances in Biomagnetism Research: BioMag96. New York: Springer Verlag, 1988 (in press)
9. Numminen J, Ahlfors S, Ilmoniemi R, et al: Transformation of multichannel magnetocardiographic signals to standard grid form . IEEE Trans.Biomed. Eng. **42**:1:72-78, 1995

Reconstruction of Cardiac Propagation Sequence From Clinical Magnetocardiographic Data

Modre R[1], Tilg B[1], Nenonen J[2], Fischer G[1], Lafer G[1], Wach P[1], Katila T[2]

Department of Biophysics, Institute of Biomedical Engineering,
Technical University Graz, Graz, Austria[1]
Laboratory of Biomedical Engineering, Helsinki University of Technology,
and with the BioMag Laboratory, Helsinki University Central Hospital,
Helsinki, Finland[2]

Introduction

The noninvasive imaging of cardiac electrical function from magnetic field or body surface potential data has attained increasing interest in clinical and basic research [4, 6÷11]. In combination with imaging modalities like magnetic resonance imaging or computed tomography it has become possible to reconstruct the primary sources in the human heart fully noninvasive with a temporal resolution in the order of milliseconds and with a spatial resolution in the order of millimeters. Till now no other modality for functional imaging allow a temporal (and spatial) resolution of electrical function of comparable order [6]. This modality for noninvasive electrical source imaging should assist cardiologists performing functional electrical diagnostics locating arrhythmogenic substrates prior to invasive surgery treatment.

The objective of this study was the reconstruction of the cardiac propagation sequence on the surface of the heart (endocardium and epicardium) from clinical magnetocardiographic data in the case of a sinus rhythm, a ventricular extrasystolic beat and an old myocardial infarction.

Methods

Magnetocardiogram (MCG) recordings were performed at the BioMag Laboratory at Helsinki University Central Hospital (HUCH). The BioMag Laboratory was established recently to provide facilities both for basic research and clinical applications in neuro- and cardiomagnetic studies [6, 9]. A three-layer magnetically shielded room (MSR; Euroshield Ltd., Eura, Finland) provides excellent shielding against ambient urban magnetic noise. A 67-channel magnetometer (Neuromag Ltd., Helsinki, Finland) is employed in MCG recordings. The sensor array consists of seven axial and 60 planar dc SQUID gradiometers immersed in a large cryogenic dewar. The cryogenic dewar is a 0.130 m long cylinder with the outer diameter of 0.42 m. It has a curved bottom with a radius of curvature of 0.79 m, and the diameter of the inner bottom is 0.30 m. The dewar is held by an easily movable gantry system, which allows both vertical adjustment and tilting by 20 degrees around two axes perpendicular to the longitudinal axis of the cylinder [6].

Before the MCG measurement, electrocardiographic (ECG) recording electrodes and marker coils to determine the sensor array position are attached to the patient's chest. A digitizer pen is used to record the coordinates of reference points defining the MCG coordinate system, and the coordinates of marker points later used in X-ray or magnetic resonance imaging (MRI). The marker points are stamped with invisible ink, which can be made visible in ultraviolet light so that either lead (for X-ray) or MgCl-filled (MRI) crosses can be attached exactly to the digitized locations.

The data acquisition is performed with a sophisticated X-Windows based software allowing feasible detection, monitoring and averaging of all channels during the recording. Analog signals are band-pass filtered (Bessel-type filters, 0.05 to 300 Hz) and digitized with an adjustable sampling rate (typically 1000 Hz). The magnetocardiogram was measured on the anterior and posterior side of two patients. Torso geometries were imaged with a Siemens 1.5 Tesla magnetic resonance imaging machine.

The volume conductors of the patients were modeled applying an isotropic boundary element formulation including the blood masses, the lungs and the outer torso surfaces [1, 2, 11]. One of the patients (P1) was suffering from idiopathic ventricular tachycardia. A normal sinus beat was here followed by a ventricular extrasystole. The other one (P2) had an old myocardial infarction. Case P1 was treated with catheter ablation. In case P2, the infarction site was diagnosed from cine-angiographic X-ray images. P2 also underwent surgery to by-pass the left anterior descendent coronary artery.

The transfer matrices calculated by the boundary element method (BEM) described the relationship between the transmembrane potential on the surface of the heart and the MCG at the observation points [1, 2, 11÷13]. In the BEM approach applied we assumed electrical isotropy in the myocardium (uniform dipole layer theory) [14]. In the inverse formulation the transmembrane potential at each source point on the surface of the heart was described by an analytical formula with the parameters resting membrane potential, action potential amplitude, rise time and activation

©1999, Tohoku University Press
Recent Advances in Biomagnetism
T. Yoshimoto et al. (Eds)

time (onset of the transmembrane potential). All parameters except the activation time were assumed to be constant [11]. The activation time pattern was estimated applying the *critical point theorem* (for a proper determination of the starting vector) [3÷5] and a subsequent nonlinear optimization routine (E04UCF, NAG library) [11, 13].

Results

The MCG from patient P1 is depicted on the left side of Fig. 1 for the sinus rhythm (upper panel, anterior probe, channel No. 1) and for the extrasystolic beat (lower panel, anterior probe, channel no. 1). The MCG for the old myocardial infarction (patient P2) is shown on the right side of Fig. 1. The upper panel depicts the MCG at the anterior probe (channel no. 1), the lower panel at the posterior probe (channel no. 55 (no. 122 in the whole MCG data set)). Imaging of the propagation sequences was perfomed in all three cases only from the anterior MCGs.

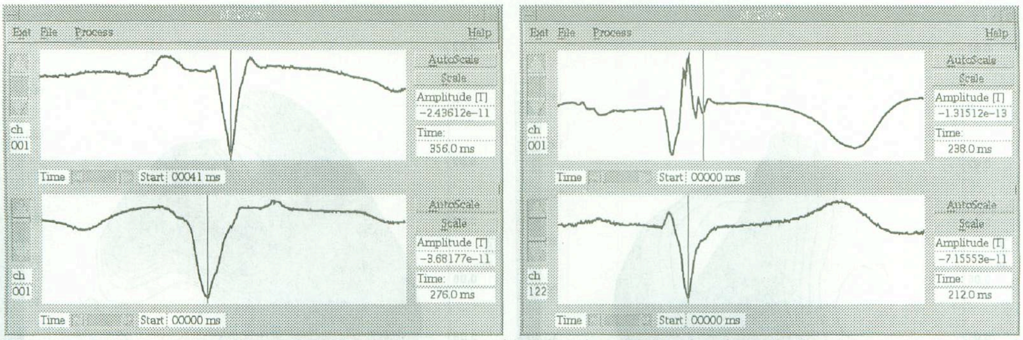

Left window, upper panel: ch 001; Amplitude [T] -2.43612e-11; Time: 356.0 ms; Time Start: 00041 ms

Left window, lower panel: ch 001; Amplitude [T] -3.68177e-11; Time: 276.0 ms; Time Start: 00000 ms

Right window, upper panel: ch 001; Amplitude [T] -1.31512e-13; Time: 238.0 ms; Time Start: 00000 ms

Right window, lower panel: ch 122; Amplitude [T] -7.15553e-11; Time: 212.0 ms; Time Start: 00000 ms

Fig. 1: Left: Magnetocardiogram (MCG) on the anterior side of patient P1 for the sinus rhythm (upper panel, channel no. 1) and for the ventricular extrasystolic beat (lower panel, channel no. 1). Right: MCG for patient P2 collected on the anterior (upper panel, channel no. 1) and posterior (lower panel, channel no. 55 (122)) side, respectively – source imaging was performed only from the anterior MCGs.

For the sinus rhythm the earliest activation was reconstructed on the septal side of the endocardial surface. After the first epicardial breakthrough the depolarization wave propagates towards the right and left heart base, as can be seen from Fig. 2. The estimated activation times were in between the interval 10 to $90 \cdot 10^{-3}$ s for the whole process of ventricular depolarization. These findings were in close qualitative agreement with the well-known normal cardiac propagation pattern.

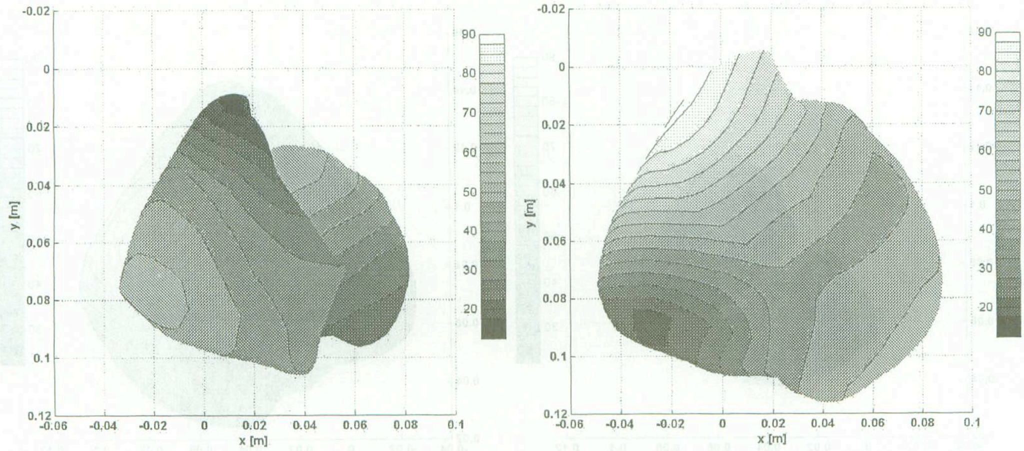

Fig. 2: Propagation sequence in 10^{-3} s estimated from 67-channel anterior MCGs for the sinus rhythm of patient P1 on the endocardium (left panel) and epicardium (right panel) from an anterior view. Isochrones are shown in steps of $5 \cdot 10^{-3}$ s. The activation times were estimated at 202 and 212 source points on the endocardium and epicardium, respectively.

For the sinus rhythm as well as for the extrasystolic beat the activation times were reconstructed at 414 source points on the surface of the heart (202, 212).

For the abnormal beat the origin of the extrasystole was determined in the anterior part of the ventricle, near the atrio-ventricular ring. The propagation sequence is depicted in Fig. 3. The isochrones are shown in steps of $10\cdot10^{-3}$ s. One can see from Fig. 3 that the propagation wave spreads from the origin of the extrasystolic beat down to the apex. The origin of the extrasystolic beat (i.e. of the arrhythmogenic substrate) was within about $10\cdot10^{-3}$ m from the result obtained by invasive catheterization during the ablation.

In case of the infarction we found that an area on the anterior left ventricle was activated later than for normal activity. Therefore, we concluded that the pathological substrate must be located in this area. Cine-angiograms revealed that this patient has an old and small infarction in an anteroseptal apical location. Fig. 4 depicts the propagation sequence from a cranial view on the endocardium (left panel) and epicardium (right panel). As shown, the anterior side of the left ventricle is depolarized much later than during normal activation (for a qualitative comparison with a sinus rhythm, see Fig. 2). Source imaging in case of P2 was performed at 372 source points (160, 212).

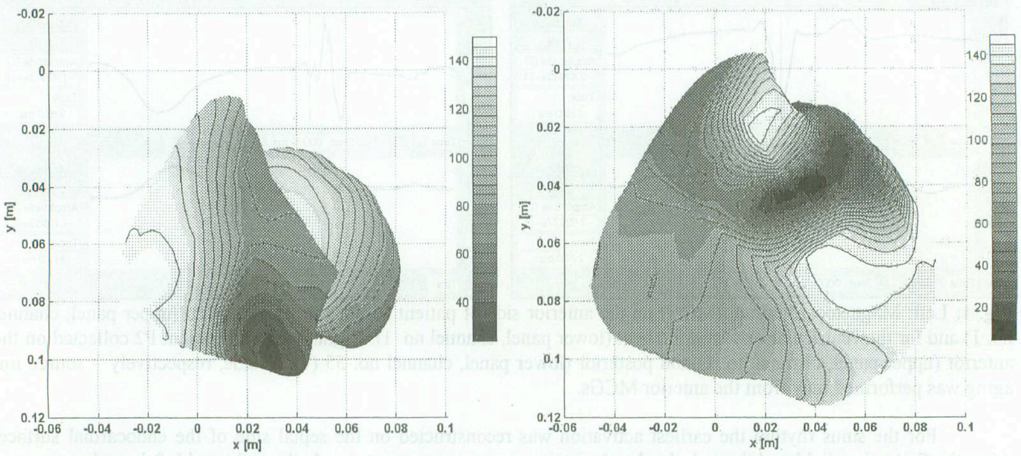

Fig. 3: Propagation sequence in 10^{-3} s estimated from 67-channel anterior MCGs for the ventricular extrasytolic beat of patient P1 on the endocardium (left panel) and epicardium (right panel) from an anterior view. Isochrones are shown in steps of $10\cdot10^{-3}$ s. The activation times were estimated at 202 and 212 source points on the endocardium and epicardium, respectively.

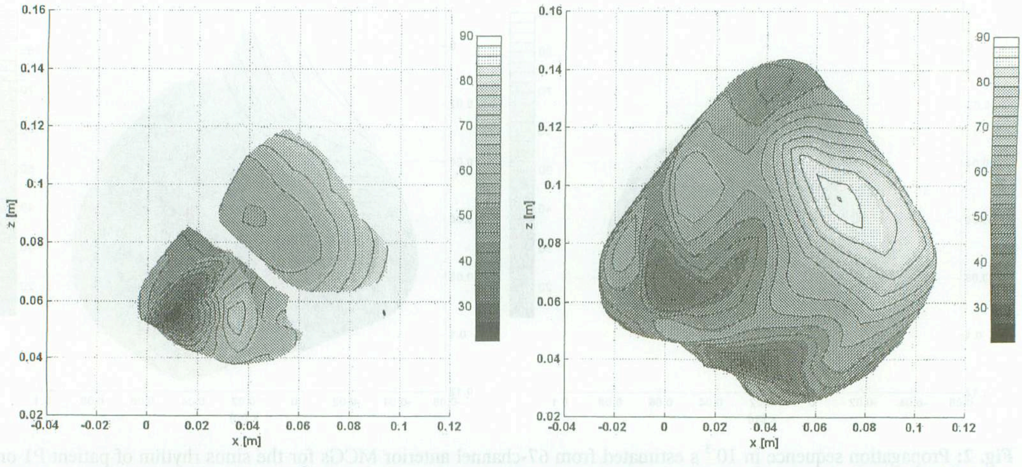

Fig. 4: Propagation sequence in 10^{-3} s on the endocardium (left panel) and epicardium (right panel) from a cranial view estimated from 67-channel anterior MCGs for patient P2 with the old myocardial infarction. Isochrones are shown in steps of $5\cdot10^{-3}$ s. The activation times were estimated at 160 and 212 source points on the endocardium and epicardium, respectively.

Conclusion

We demonstrated that the activation time inverse approach was able to describe normal and pathological cardiac propagation. The reconstructed propagation sequence for the sinus rhythm was in agreement with the well-known normal spread of excitation. The origin of the extrasystolic beat was found to be located on the epicardium. Therefore we concluded that the arrhythmogenic substrate was located in between the opposite endocardium and epicardium. Because invasive catheter measurements showed that the pre-excitation site was on the endocardial surface near the atria-ventricular ring, we concluded that the localization error was in the order of $10\cdot10^{-3}$ m. The remaining reconstructed pattern on the epicardium was in agreement with the physics of cardiac propagation. The pattern on the endocardium was found to be very stable by varying the regularization parameter in the nonlinear optimization procedure (and by varying the effective rank in the *critical point theorem*). In whole, the reconstructed activation time pattern was found to be very stable, and therefore assumed to be a proper estimate. The reconstructed late activation in the area of the infarcted substrate was stable in a mathematical sense; the activation time pattern at the remaining source points was more numerically instable than in the cases before. Although, the solution achieved from the *critical point theorem* was stable regarding the choice of the effective rank, the optimized inverse solution showed less continuity by varying the regularization parameter. This was caused maybe by several aspects. One reason could be that some of the MCG channels had a significant high noise-level, the second one that the surface of the heart was modeled to less realistic.

The performance of the inverse method was analyzed using the estimated MCG inverse solution for the sinus rhythm as a synthetic forward solution. The relative residual difference of the activation time pattern than calculated from the synthetic MCG adding Gaussian noise (35dB) was found to be less than 0.01.

Although no invasive activation time mapping data were available the results achieved were found to be of high clinical relevance, because they were in agreement with routine clinical diagnosis. Also, because all the characteristally events like breakthroughs were found to be properly located.

References

[1] Fischer G, Tilg B, Wach P, et al: Application of high-order boundary elements to the electrocardiographic inverse problem. Comput Meth Prog Bio, 1998 (in press)

[2] Fischer G, Wach P, Tilg B, et al: Application of second-order boundary elements to inverse magnetocardiography. (in these proceedings)

[3] Greensite F: Remote reconstruction of confined wavefront propagation, Inverse Problems 11: 361-370, 1995

[4] Huiskamp GJM, van Oosterom A: The depolarization sequence of the human heart surface computed from measured body surface potential. IEEE Trans Biomed Eng 35: 1047-1058, 1988

[5] Huiskamp GJM, Greensite F: A new method for myocardial activation imaging. IEEE Trans Biomed Eng 44: 433-446, 1997

[6] Nenonen J: Multimodal cardiac source imaging in the BioMag Laboratory. NFSI 97 Symposium, Noninvasive Functional Source Imaging, Graz, Austria, Biomed Technik 42(1): 29-32, 1997

[7] Oster HS, Taccardi B, Lux RL, et al: Noninvasive electrocardiographic imaging – reconstruction of epicardial potential, electrograms, and isochrones and localization of single and multiple electrocardiac events. Circulation 96: 1012-1024, 1997

[8] Pesola K, Nenonen J, Fenici R, et al: Comparison of regularization methods when applied to epicardial minimum norm estimates. NFSI 97 Symposium, Noninvasive Functional Source Imaging, Graz, Austria, Biomed Technik 42 (1): 273-276, 1997

[9] Simelius K, Katila T, Montonen L, et al: Biomag: Functional brain and heart research in clinical environment, IEEE Engineering in Medicine and Biology 17th Annual Conference & 21st Canadian Medical and Biological Engineering Conference, IEEE Engineering in Medicine and Biology Society (CD-ROM), 1995

[10] Taccardi B, Punkse BB, Lux RL, et al: Useful lessons from body surface mapping. J Cardiovasc Electrophysiol 9: 773-786, 1998

[11] Tilg B: Noninvasive functional cardiac electrical source imaging. Shaker Verlag, Aachen, Germany, 1998.

[12] Tilg B, Nenonen J, Lafer G, et al: A comparison study on source imaging from BSP and MCG data. NFSI 97 Symposium, Noninvasive Functional Source Imaging, Graz, Austria, Biomed Technik 42(1): 151-154, 1997

[13] Tilg B, Wach P, Lesh MD, et al: Imaging surface activation time maps from magnetic field and body surface potential data. (in these proceedings)

[14] Yamashita Y, Geselowitz DB: Source-field relationships for cardiac generators on the heart surface based on their transfer coefficients. IEEE Trans Biomed Eng 32(11): 964-970, 1985

Acknowledgment

This work was supported by the Austrian Science Foundation, grants P12267-MED, P11448-MED and by the European Large Scale Facility in BIomagnetic Research at Center Helsinki University of Technology (BIRCH).

Magnetocardiographic Measurement from the Left Side of the Patient Improves Detection of Prolonged Ventricular Depolarization in Post-Infarction Patients with Malignant Arrhythmias

Montonen J[1,2], Korhonen P[2,3], Mäkijärvi M[2,3], Toivonen L[2,3], Katila T[1,2]

Laboratory of Biomedical Engineering[1], Helsinki University of Technology, Helsinki, Finland; BioMag Laboratory[2], and Division of Cardiology[3], Helsinki University Central Hospital, Finland

Introduction

Means for post-infarction arrhythmia risk stratification are of considerable clinical interest, even though the thrombolytic therapy has significantly reduced the number of malignant arrhythmias . For this purpose, signal averaged magnetocardiography (MCG) has been suggested [1,2,3]. In earlier studies, a very significant difference in QRS duration determined by time domain analysis (TDA) of MCG signals measured frontally right above the heart was found between infarction patients with and without malignant arrhythmias [4].

In a more recent single channel MCG mapping study the longest QRS durations were frequently found on the lower left part of the frontal plane covered in the measurement [5]. The aim of the present study was to find if it were advantageous for arrhythmia risk evaluation to measure multichannel MCG from the left side of a supine patient rather than in the frontal plane.

Methods

Altogether 84 post-infarction patients were studied, including 32 with history of ventricular tachycardia or fibrillation (VT/VF). The patient material is described in Table 1.

For each patient, high-resolution 67-channel MCG at rest was recorded for 5 minutes in the BioMag Laboratory (see Fig. 1) with the center of the dewar in two locations: 1) 15 cm below the jugulum and 5 cm to the left (see Fig. 2), and 2) 15 cm below the jugulum and with, at maximum, 20 degree tilt to the left side of the thorax. The MCG device was equipped with 7 gradiometers of axial type and with 30 units including two orthogonal planar gradiometers [6]. The sensitivity of the sensors is about 3 fT/sqrt(Hz) and 5 fT/cm·sqrt(Hz), respectively, in the frequency range of 5 to 100 Hz.

The MCG signals were digitized with 1 kHz sampling rate. After selective signal averaging, a transform from the original signals, measured with the planar and axial gradiometers, to signals which would have been measured if only axial gradiometers were used in the same sensor locations, was performed utilizing a minimum norm estimate for the current distribution generating the actually measured signals [7]. Next, conventional TDA with 40 Hz high-pass filtering was performed for the transformed signals in the seven central grid locations (see Fig. 3).

Table 1: The patient material. Values are given as mean ± standard deviation. VT/VF = ventricular tachycardia / fibrillation, LVEF = left ventricular ejection fraction.

	VT/VF	non-VT/VF	p-value
N	32	52	
Age (yrs)	60 ± 8	59 ± 9	NS
LVEF (%)	30 ± 8	44 ± 16	< 0.0005
Infarct location:			
anterior	18	26	
inferior	9	20	NS
multiple	5	6	

©1999, Tohoku University Press
Recent Advances in Biomagnetism
T. Yoshimoto et al. (Eds)

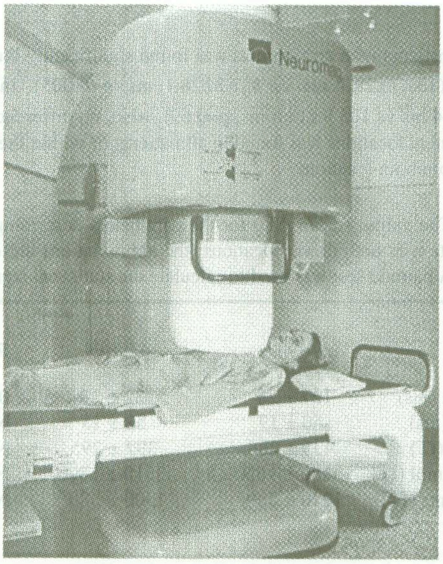

Fig. 1: The Magnetocardiographic (MCG) measurement setup used in the BioMag Laboratory.

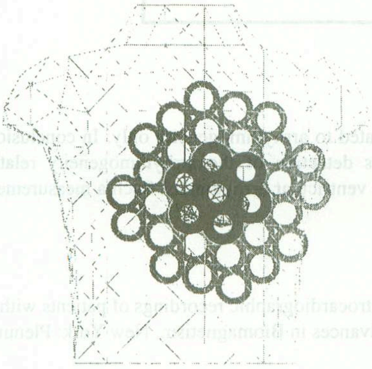

Fig. 2: The frontal MCG measurement grid. Mean value of each parameter in the seven central locations (black circles) was used.

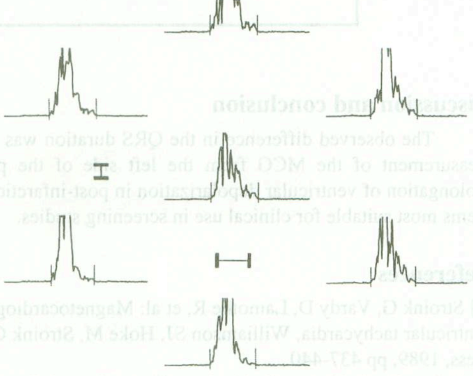

Fig. 3: Filtered magnetic QRS complexes in the central locations with a low amplitude tail (late filed) in a patient with ventricular tachycardia. The horizontal scale tick corresponds to 100 ms and the vertical one to 0.5 pT.

The following five parameters were calculated to describe the filtered QRS complexes (the abbreviations refer to Table 2): 1) Duration of the filtered QRS (QRSd), 2) duration of the low amplitude signal below 1 pT at the end of the filtered QRS (LAS), 3) root mean square magnitude of the last 40 ms of the filtered QRS (RMS), 4) the maximum amplitude of the filtered QRS (QRSampl), and 5) the root mean square magnitude of the whole filtered QRS complex (QRSrms). A mean value over these seven locations was used to calculate the final TDA parameters (see Table 2). Statistical paired samples t-test was used to compare data from the two measurement locations.

Results

The QRS duration in the patients with arrhythmias was found significantly longer in measurements from the left side than in the frontal plane (131.7±28.1 ms vs 127.2±28.1 ms, $p<0.005$). In patients without arrhythmias no difference was found (104.4±18.4 ms vs 103.9±18.5 ms, $p=0.69$). Also, no difference in the filtered QRS amplitude or power between the two measurement locations was found in all patients or within the two subgroups. The level of noise was the same in all recordings from both locations.

Table 2: The values (mean±SD) for the parameters describing ventricular depolarization in both dewar locations (the abbreviations are explained in the text). A paired t-test was used to calculate the statistical significance.

	Center	Left side	p-value
VT/VF			
QRSd (ms)	127 ± 28	132 ± 28	0.004
LAS (ms)	50 ± 19	52 ± 15	NS (0.15)
RMS (fT)	435 ± 286	397 ± 295	NS (0.40)
QRSampl (fT)	3180 ± 1620	3510 ± 1790	NS (0.11)
QRSrms (fT)	1210 ± 580	1300 ± 580	NS (0.17)
non-VT/VF			
QRSd (ms)	104 ± 19	104 ± 18	NS (0.69)
LAS (ms)	38 ± 13	39 ± 13	NS (0.57)
RMS (fT)	826 ± 604	762 ± 579	NS (0.09)
QRSampl (fT)	3700 ± 1700	3880 ± 2100	NS (0.30)
QRSrms (fT)	1390 ± 570	1460 ± 710	NS (0.27)

Discussion and conclusion

The observed difference in the QRS duration was found to be related to arrhythmogeneity only. In conclusion, measurement of the MCG from the left side of the patient improves detection of the arrhythmogeneity related prolongation of ventricular depolarization in post-infarction patients with ventricular arrhythmias. Such a measurement seems most suitable for clinical use in screening studies.

References

[1] Stroink G, Vardy D, Lamothe R, et al: Magnetocardiographic and electrocardiographic recordings of patients with ventricular tachycardia, Williamson SJ, Hoke M, Stroink G, et al (eds) Advances in Biomagnetism, New York: Plenum Press, 1989, pp 437-440.

[2]Weismuller P, Richter P, Abraham-Fuchs K, et al: Spatial differences of the duration of ventricular late fields in the signal-averaged magnetocardiogram in patients with ventricular late potentials. PACE 16(1(I)):70-79, 1993.

[3] Mäkijärvi M, Montonen J, Toivonen L, et al: Identification of patients with ventricular tachycardia after myocardial infarction by high-resolution magnetocardiography and electrocardiography. J. of Electrocardiol. 26(2):117-124, 1993

[4] Montonen J, Mäkijärvi M, Paavola M, et al: Comparison of time domain and spectrotemporal domain analysis of high resolution magneto- and electrocardiographic recordings of myocardial infarction patients with and without ventricular tachycardia, Baumgartner C, Deecke L, Stroink G, et al. (eds) Biomagnetism: Fundamental Research and Clinical Applications. Elsevier Science/IOS Press, 1995, pp 624-627

[5] Montonen J, Korhonen P, Paavola M, et al: Spatial aspects in magnetocardiographic time domain and spectrotemporal post-infarction arrhythmia risk assessment, Advances in Biomagnetism Research: Biomag96, Springer Verlag, in press.

[6] Montonen J, Ahonen A, Hämäläinen M, et al: Magnetocardiographic Functional imaging studies in BioMag Laboratory, Advances in Biomagnetism Research: Biomag96, Springer Verlag, in press.

[7] Numminen J, Ahlfors S, Ilmoniemi R, et al: Transformation of multichannel magnetocardiographic signals to standard grid form. IEEE Trans. Biomed. Eng. 42(1):72-78, 1995.

Assessment of Local Electric Properties of the Left Ventricle by Inverse Solutions Based on MCG

Nowak H[1], Leder U[2], Pohl P[2], Haueisen J[1]

Biomagnetic Centre[1]; Clinic of Internal Medicine[2], University of Jena,
Philosophenweg 3, 07743 Jena, Germany

Introduction

From 1960´s through the 1970´s and the 1980´s magnetocardiography data were used predominantly for time domain and signal shape analysis of single leads or non-simultaneously obtained mapping data respectively [1]. This has provided insights into patient risk stratification and prognosis. In the 1990´s, however, magnetocardiography began to play an increasingly important role in diagnosing and localizing the sources of cardiac magnetic fields [2]. This new application of inverse-solution-based analysis of magnetic fields has become known as Magnetic Source Imaging (MSI). In this respect, the developement of source imaging techniques and multisensor devices had advantageous interdependence [3].

Therefore, magnetocardiography developed as a new experimental discipline of functional imaging. The discipline has moved from the no-model signal analysis to a broad emphasis on the functional localization of cardiac electrical activity and characterization of patients with known disease. Since that time, application of new techniques of data analysis has evolved progressively, while the clinical relevance of currently available procedures is being assessed on an ongoing basis.

Coronary Artery Disease

Ischemic heart disease is usually due to obstruction of the coronary arteries, which in turn most commonly results from artherosclerosis. The importance of coronary artery disease in contemporary society is attested by the almost epidemic number of persons afflicted. It causes more deaths, disability, and economic loss in industrialised nations than any other group of diseases.

Myocardial infarctions may be divided into two major types: transmural infarcts, in which myocardial necrosis involves the full thickness of the ventricular wall, and subendocardial (nontransmural) infarcts, in which the necrosis involves the subendocardium, the intramural myocardium, or both without extending all the way through the ventricular wall. Eight to 10 days following infarction, the thickness of the cardiac wall in the area of the infarct is reduced as necrotic muscle is removed by mononuclear cells. A loss of functioning myocardium results. As a consequence of infarction, changes in left ventricular size, shape, and thickness involving both the infarcted and the noninfarcted segments of the ventricle often occur. These changes are referred to as „ventricular remodeling„, a process that in turn can influence function and prognosis.

One of the most important developments in the treatment of patients with infarction consists of establishing reperfusion of ischemic heart muscle. It improves hemodynamics and decreases infarction size (the latter in early reperfusion).

Significant stenosis of one or more major epicardial arteries, which supply at least a moderate-sized area of viable myocardium, in a patient who has ischemia episodes, angina or major ventricular arrhythmia has to be treated by coronary revascularisation. Efforts to prevent and/or treat the disease have the potential for success. Diagnostic procedures are essential for the correct selection of patients and coronary vessels prior to revascularisation. In this respect it would be of great importance for the future of magnetocardiography to enter the field of assessment of myocardial viability.

Diagnostic Procedures

The crucial problem in coronary artery disease refers to the identification of viable myocardium. Stunning and hibernation of myocardial segments may lead to reduced kinesis of viable tissue. Therefore, wall motion analysis fails to correctly diagnose vibility. Additional procedures are required.

Myocardial infarction can become visualised by nuclear cardiology either as a „cold spot„ or as a „hot spot„. Cold spot imaging is based on perfusion defects, the infarct can become visualised as a „hot spot„ using monoclonal antibody specific for intracellular myosin.

©1999, Tohoku University Press
Recent Advances in Biomagnetism
T. Yoshimoto et al. (Eds)

Since the gold standard in the diagnosis of myocardial viability (PET: combined perfusional/metabolic imaging) is available not everywere, stress-echocardiography or ^{201}Tl- or ^{99m}Tc-SestaMIBI stress imaging respectively are the widely used standard procedures.

A precise localisation of myocardial infarction based on the standard ECG is not always possible. Accuracy of such a localisation is influenced, for example, by distance of the electrode from the heart, which varies considerably amoung individuals. Therefore, additional anatomical constraints and the application of algorithms which solve the inverse problem of electrocardiography or magnetocardiography respectivlely are desirable.

Method

23 patients with prior myocardial infarction and 25 healthy subjects/patients without infarction were investigated. The presence of infarction (ECG, history, elevated blood level of cardiac enzymes) was proven by angiography. Fig. 1 displays an example of ECG (Einthoven leads) and angiography of a patient suffering from an inferobasal-inferomedial aneurysm of the left ventricle.

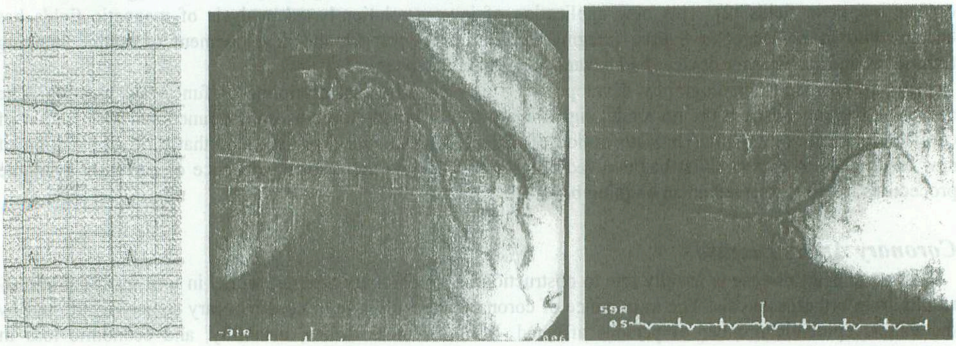

FIG. 1: left: ECG (EINTHOVEN LEADS); right: ANGIOGRAM (30° RAO, 60° LAO)
of a patient with an INFEROBASAL-INFEROMEDIAL MYOCARDIAL iNFARCTION

Magnetocardiograms were taken using a multisensor device (Philips). The device consists of two sensor heads, each of them holding 31 sensors [4]. The recording time was set to 100 to 600 s (1000 Hz sampling rate). The sensor heads were tilted by about 30°. The coordinates of the torso relative to the multichannel system were determined by localizing the center coordinates of 10 coilsets.

MRIs were taken with a 1.5 T machine (Philips Gyroscan® ACS II. Prior to the investigation, coilsets were replaced by oil pills. A series of 40 to 60 transverse slices (5 mm thick, T1 weighted turbo field echo scan) were taken. The scan time window was placed in the late enddiastolic heart phase at R upstroke.

The data processing, i.e. segmentation of three-dimensional surfaces, calculation of current densities, and presentation of results was done with the software package Curry® made by Philips. The resulting stack of MRI slices was transformed into an three-dimensional dataset.

The surfaces required for the volume conductor modeling were segmented by a threshold steered region growing algorithm.The following thinning procedure resulted in a reduced list of surface points. This list was used for the computation of a boundary element volume conductor model. The segmentation of the source structure (left ventricle) was done by hand using a freehand cursor brush in three zoomed orthogonal image planes. The left ventricular endocardial surface was divided into a grid of several hundred points of equal distance using a thinning algorithm. The list of myocardial point coordinates served as dipole positions for reconstruction. The overall time for MRI preparation took about one hour (30 minutes scan preparation and scan time, 30 minutes for 3D surface processing).

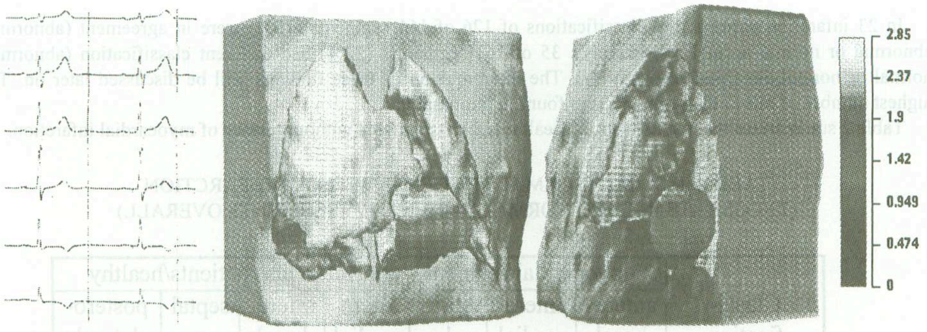

FIG. 2: left: ECG (WILSON leads); right: MSI (30° RAO, 60° LAO) of the same patient as in Fig. 1, a patient suffering from an INFEROBASAL-INFEROMEDIAL MYOCARDIAL infarction

Current density was calculated for a few hundred support points at the peak of the QRS complex. The reconstruction points were regularly spaced on the left ventricular endocardial surface with a mean distance of 5 mm. The current density had to satisfy the constraints of minimum norm least sqares, lead field regularization, and noise regularization. Noise regularization was performed using the bend values of a L-curve. The resultant current density distribution was presented as a colour coded surface plot of the left ventricle for the assessment of regional electrical activity. Figure 2 shows an MSI example of a patient with an INFEROBASAL-INFEROMEDIAL MYOCARDIAL infarction.

The localization and the extent of the area of low current density in the infarction patients was determined for seven segments of the left ventricle. Low current density was assumed for the currents below an arbitrarily defined value (1 µA/mm²). Localization results were compared to ECG, echocardiography, scintigraphy, and left heart angiography.

Results

There were marked differences in mean current strength, localization, and extent of areas of low current density between the infarction patients and the healthy subjects. Mean current densities of the patients turned out to be lower compared to the current densities of the healthy. A mean point distance of 5 mm for the generation of support point lists resulted in a standardised patch area of about 30 mm². According to the ventricular remodeling and enlargement after myocardial infarction, the number of points or currents respectively was considerably higher in patients. Nevertheless, the sum of all currents was lower in the patients compared to the healthy subjects.

The following Table 1 compares MSI to contrast angiography in the infarction group.

TABle.1: COMPARISON OF aNGIOGRAPHY AND MSI IN 23 iNFARCTION pATIENTS
(I.E. 7 segments in each patient, 161 sEGMENTS OVERALL)

	Myocardial segment – infarction patients						
classi-fication	antero-basal	antero-medial	Apical	Infero-medial	infero-basal	septal	postero-lateral
pp	3	13	13	9	1	11	7
nn	15	5	7	9	14	7	12
pn	2	2	2	5	8	0	1
np	3	3	1	0	0	5	3
Σpp+nn	18	18	20	18	15	18	19
Σpn+np	5	5	3	5	8	5	4
pp	abnormal laevocardiography and abnormal MSI						
nn	normal findings for both procedures						
pn	abnormal angiography and normal MSI						
np	Normal angiography and abnormal MSI						

In 23 infarction patients, the classifications of 126 of 161 segments (78%) were in agreement (abnormal-abnormal or normal-normal respectively). 35 of 161 segments (22%) had different classification (abnormal-normal or normal-abnormal respectively). The interpretation of these findings will be discussed later on. The highest number of mismatch segments was found inferobasally.

Table 2 summarizes the results from 25 healthy subjects/patients without history of myocardial infarction.

TABle.2: MSI IN 25 NORMALS/PATIENTS WITHOUT INFARCTION
(7 SEGMEnTS IN EACH NORMAL/PATIENT, 175 SEGMENTS OVERALL)

Classi-fication	myocardial segment – non-infarction patients/healthy						
	antero-basal	antero-medial	Apical	Infero-medial	infero-basal	septal	postero-lateral
P N	2 23	2 23	0 25	4 21	5 20	6 19	6 19
N P	normal MSI abnormal MSI						

25 of 175 Segments (14%) turned out to have an abnormal low current density. Notice that inferiorly and nearby located segments again had the highest rate of abnormal MSI results.

Discussion

Despite the obstacle posed by the non-uniqueness of inverse solutions, we have shown that an estimation of the myocardial source activity in coronary artery disease can be achieved by a solution which minimizes the square of power integrated over a left ventricular surface.

Low regional current density turned out to be the hallmark of infarcted myocardial tissue in coronary artery disease. In this study there are several reasons for the mismatch of angiography-MSI. The interpretation of the coherence between regional wall motion and regional current density is limited by a lack of knowledge about the regional amount of viable myocardium. Because hypokinesis may occur in stunning and hibernating myocardium, as well as in myocardial infarction with varying degrees of myocardial fibrosis, reference procedures (PET, scintigraphy, endocardial catheter mapping) are required in future studies. Reversibility of wall motion abnormalities should be the way of differentiating underperfused but viable myocardium from myocardial scar in a prospective study.

Assuming that MSI gives a true copy of regional electrical activity, the identification of hypokinetic but viable myocardium (pn-segments, Table 1) would become possible. Nevertheless, the results of this preparatory study should considered to be preliminary. Much work is to do in this field.

References

[1] Siltanen P: Magnetocardiography, MacFarlane PW, Lawrie TDV (eds): Comprehensive Electrocardiology. New York, Pergamon Press, 1989, pp 1405-1438

[2] Stroink G, Moshage W, Achenbach S: Cardiomagnetism, Andrä W, Nowak H (eds): Magnetism in Medicine. Berlin, WILEY-VCH, 1998, pp136-189

[3] Leder U, Pohl HP, Michaelsen S, et al: Noninvasive biomagnetic imaging in coronary artery disease based on individual current density maps of the heart. Int J Cardiol 64: 83-92, 1998

[4] Dössel O, David B, Fuchs M, et al: A 31-channel SQUID system for biomagnetic imaging. Appl Supercond 1 (10-12), 1813-1825, 1993

Acknowledgements

The authors would like to thank Ines Krummbein for providing MRI images, and Uwe Schulze for assistance during magnetocardiographic measurements. Special thanks go to the team of the Philips Research Laboratory (Hamburg, Germany) for the excellent data analysis software CURRY®.

This work was supported by the German BMBF grant 13N664 and the Thuringian research grant B 301-96082.

Three-Dimensional Distribution of Ventricular Action Potential Amplitude Estimated from Magnetocardiogram

S Ohyu[1], S Aida[1], K Komatsu[1], Y Okamoto[2], S Kuriki[3]
Medical Engineering Laboratory, TOSHIBA corporation[1], Tochigi, Japan;
Department of Electrical Engineering, Chiba Institute of Technology[2], Chiba, Japan;
Research Institute for Electronic Science, Hokkaido University[3], Sapporo, Japan

Introduction

Investigating the location and severity of ischemia is clinically important for making decisions on treating ischemic heart disease. There have been several studies to detect ischemia by using wave forms or spatial distributions of magnetocardiograms(MCG)[1–3]. However, they are not able to determine the exact location of the ischemia. It is well known that ischemic myocardium decreases the amplitude of the action potential. We have developed a new method in which the three-dimensional distribution of the action potential amplitudes and the ventricular excitation sequence are estimated from a measured QRS complex of the MCG, in order to detect and locate ischemic regions.

This method was tested using computer simulations. An artificial MCG was calculated based on a ventricular model with an ischemic region. Pseudo-gaussian noises were added to simulate measurement noise. Then, we applied our estimation method, and the action potential amplitude distributions(APAD) and the excitation onset time distributions(EOTD) were obtained. Typical results are shown in this report.

Electrophysiological Model

The excitation front with the steep change in a transmembrane potential is propagated through the ventricle(Fig.1). Current source which induces the QRS complex in the MCG is proportional to the spatial gradient of the transmembrane potential(Fig.2). The spatio-temporal distribution of the transmembrane potential is uniquely determined by the APAD and the EOTD. Therefore, MCGs during QRS period are also determined by APAD and EOTD. Conversely speaking, APAD and EOTD can be estimated from MCGs measured during QRS complex by means of the least-square-error method.

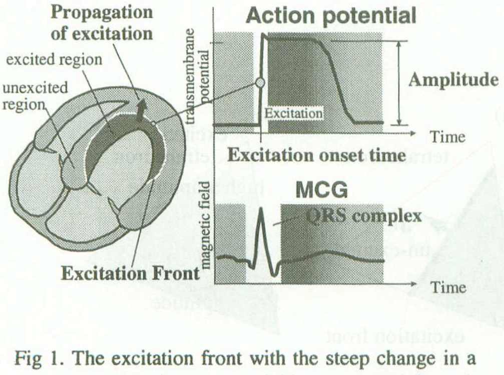

Fig 1. The excitation front with the steep change in a transmembrane potential is propagated through the ventricle. The QRS complex appears in the MCG during the ventricular excitation process.

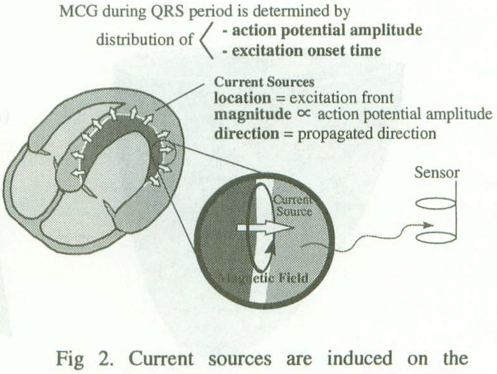
MCG during QRS period is determined by
distribution of
- action potential amplitude
- excitation onset time
Current Sources
location = excitation front
magnitude ∝ action potential amplitude
direction = propagated direction
Sensor
Current Source
Magnetic Field

Fig 2. Current sources are induced on the excitation front, generates the magnetic field.

©1999, Tohoku University Press
Recent Advances in Biomagnetism
T. Yoshimoto et al. (Eds)

Estimation Method

Our estimation algorithm, indicated as "inverse process" in Fig. 3, calculates the APAD and the EOTD from the measured MCG during the QRS complex by an iterative process. The estimation algorithm starts with the pair of initial distribution (1), and performs the "forward process" to calculate the MCG (2). Then, the calculated MCG is compared with the measured MCG (3). If these two MCGs do not agree with each other, the pair of distributions are modified (4). The two distributions are iterated over to minimize the square deviation between the MCGs.

Based on the electrophysiological model, the forward process calculates the QRS complex of the MCG using two serial processes: the "source calculation process" which calculates the current sources, and the "field calculation process" which calculates the magnetic field caused by the current sources. In the source calculation process, the excitation fronts in each tetrahedron are determined from the EOTD. The values of the action potential amplitudes and the excitation onset times are given at each node of the ventricular shape model shown in Fig. 4. Then, the current source on the each tetrahedron is calculated as $\mathbf{J}_f = \sigma_i A \Phi \mathbf{n}$ shown in Fig. 5(a), where σ_i is the effective conductivity of the intracellular network, A is area of the segmented excitation front in a tetrahedron, Φ is action potential amplitude on the tetrahedron, and $\mathbf{n}$ is the normal vector of the excitation front. In addition, another current source, "injury current", on the each excited tetrahedron is calculated as $\mathbf{J}_e = -V\sigma_i \nabla\Phi$ shown in Fig 5(b), where V is the volume of each tetrahedron. In the normal myocardium, $\mathbf{J}_e$ is almost zero because of uniformity of the action potential

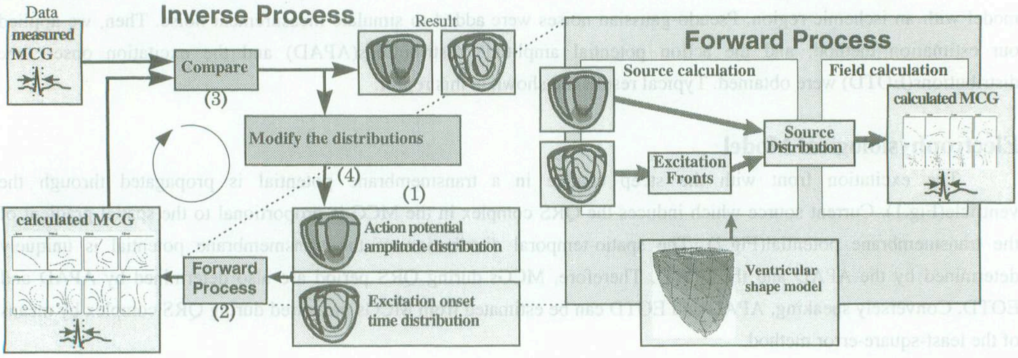

Fig. 3. Estimation Algorithm

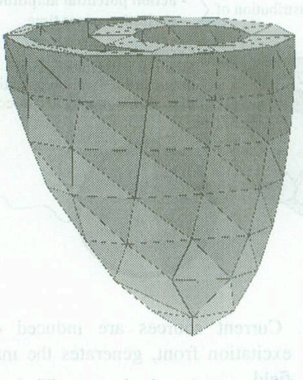

Fig. 4. The ventricular shape model consists of 162 nodes and 460 tetrahedrons.

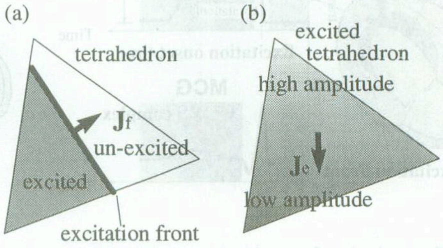

Fig. 5. Current sources in each tetrahedron. The current source $\mathbf{J}_f$ is induced on the excitation front. The injury current source $\mathbf{J}_e$ is induced in the excited tetrahedron.

amplitude, but a myocardial injury causes a low amplitude region, and it induces $\mathbf{J}_e$ which causes an ST displacement in the MCG. Then, the field calculation process produces the magnetic field outside the chest from the current sources using spherical volume conductor model [4].

Numerical Experiments

We tested the estimation method using numerical experiments. We assumed that the sensors and the ventricle were arranged as shown in Fig. 6 and Fig. 7. First, we prepared a APAD which include a low amplitude "ischemic" region (Fig.8). The action potential amplitude in a normal region was 100 mV. The low amplitude region was located on the septal wall with a 50 mV decrease in the center, and it has a 3-cm diameter. Next, we simulated the MCG as a measured data by using the "forward process". The "measured" MCG consists of the 17 samples with 5 ms interval during the QRS period. The gaussian noise was added to the MCG to simulate the measurement noise, and the resultant signal-to-noise-ratio was 30 dB which is about 5 times as large as the noise level of typical SQUID system. Finally, we applied our estimation algorithm to obtain the APAD and the EOTD.

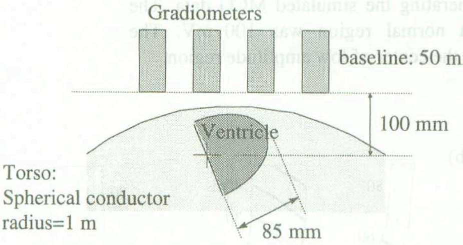

Fig. 6. The ventricle is in a spherical conductor torso.

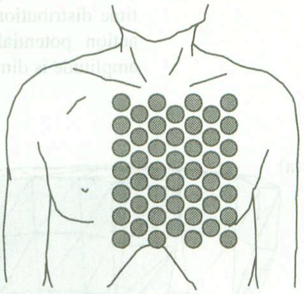

Fig. 7. Arrangement of 46 magnetic sensors.

Results

Fig. 9(a) and Fig. 9(b) show the estimated APAD and EOTD. They agreed well with the given APAD and EOTD in Fig. 8(a) and Fig. 8(b). Especially, the low amplitude region was reproduced close to the location in Fig. 8(a).

Conclusion

The action potential amplitude distribution and the excitation onset time distribution were estimated from the simulated MCG with gaussian noise. However, further study is necessary on the accuracy and stability of the method, and on the clinical validity of detecting ischemia through a decrease in the action potential amplitude.

References

[1] M. Saarinen, T. Katila, J. Nenonen, M. Seppänen, and P. Siltanen, Simulated and measured mangetocardiograms in localized myocardial abnormalities, Biomagnetism: Applications and Theory, Pergamon Press, 159-163 (1984)

[2] H. Mori, Y. Nakaya: Clinical value of the magnetocardiography, Biomagnetis '87, Tokyo Denki University Press, 82-89 (1989)

[3] J. ten Voorde, G. Stroink, T.J. Montague, Magnetocardiographic maps of subjects with old non-Q myocardial infarction, Biomagnetism'87, Tokyo Denki University Press, 326-329 (1987)

[4] J. Sarvas, Basic mathematical and electromagnetic concepts of the biomagnetic inverse problem, Phys. Med. Biol., Vol. 32, No. 1, 11-22(1987)

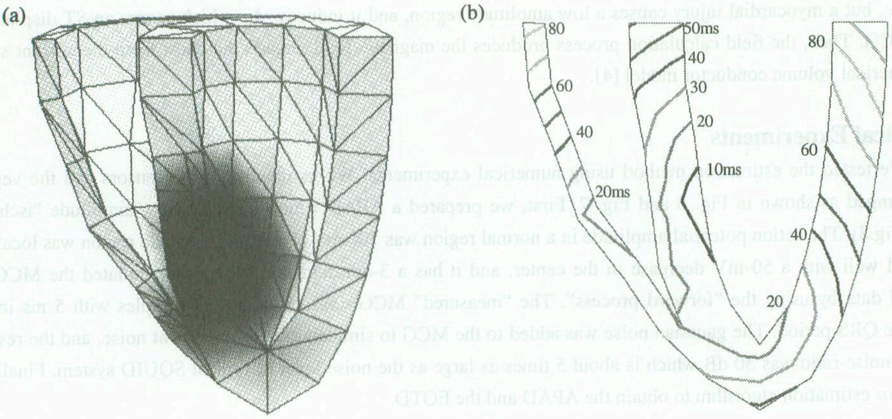

Fig. 8. Given action potential amplitude distribution (a), and excitation onset time distribution (b) used for generating the simulated MCG data. The action potential amplitude in a normal region was 100 mV. The amplitude is diminished to half on the center of low amplitude region.

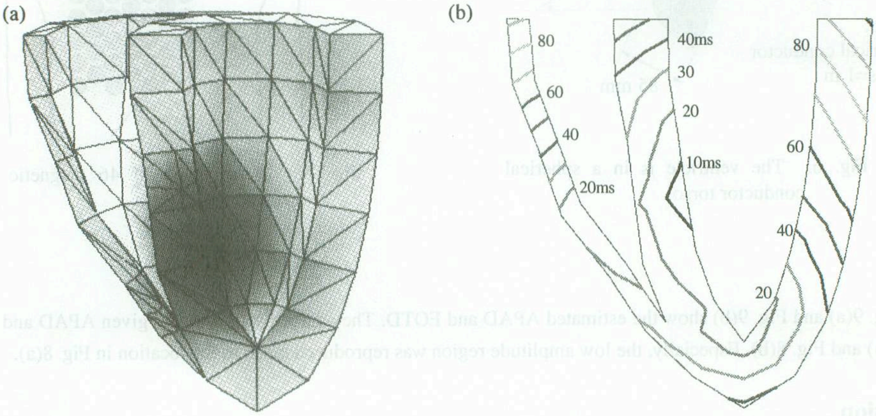

Fig. 9. Result of Estimation from the simulated MCG data: action potential amplitude distribution (a), and excitation onset time distribution (b). The low amplitude region was represented.

Magnetocardiographic Evaluation of a Genetically Characterized Family with Hypertrophic Cardiomyopathy

**Selbig D., Bode M., Soltner H., Ziegert K.[1], Halling H.,
Bousack H., Trahms L.[2], Stellbrink C.[1]**

Forschungszentrum Jülich, Jülich, Germany; Department of Cardiology RWTH Aachen, Aachen, Germany[1]; Physikalisch-Technische Bundesanstalt, Berlin, Germany[2]

Introduction

Hypertrophic cardiomyopathy (HCM) is a primary heart muscle disease characterized by left ventricular hypertrophy and myofibrillar disarray. Sudden cardiac death is frequently the first manifestation of the disease in apparently healthy young individuals. The majority of these individuals who survive an episode of SCD due to ventricular tachycardia or fibrillation will fulfill the conventional diagnostic criteria. Occasionally the echocardiographic features can not exactly identify the current diagnostic criteria or it existing only minor ECG abnormalities [1]. In the recent years a range of main mutations in four different contractile protein genes - ß-myosin heavy chain, cardiac troponin T, cardiac α-tropomyosin and myosin-binding protein C - have been shown to cause HCM as a hereditary disorder [2]. However, the identification of the mutation is at present a research procedure and not available as a routine clinical service.

Therefore an identification of SCD survivors with borderline clinical criterias and of apparently healthy gene carriers in HCM families is a substantial task. The aim of our study was to estimate the diagnostic value of the HTc-MCG in identifying patients and gene carriers in a genetically characterized HCM family.

Methods

We examined 27 phenotypically and genotypically characterized members of a HCM family (table 1).

The phenotype was identified using medical history, physical examination, electrocardiogram and echocardiography.

A previous study had discover the gene mutation: a frameshift mutation of the myosin binding protein C (MYBP-C) with a consecutive shortening of these protein.

Table 1

group	G+/P+	G+/P-	G-/P-
number	n=9	n=8	n=10
age±SD	48±12,6	35,25±12,25	39,7±10,27
sex	m=4/f=5	m=1/f=7	m=6/f=4

G+/P+= positive geno- and phenotype, G+/P-= positive genotype and negative phenotype, G-/P-= negative geno- and phenotype

MCG mapping was recorded from 36 precordial points using a first-order gradiometer with sensors from high-temperature superconductors (HTc-SQUID) in a magnetically shielded room.

A residual map score (RMS) of the QRST-integral was calculated by subtracting a mean normalized QRST-integral of a healthy, family independent group from the individual normalized QRST-integral of the examined family members. Furthermore a fragmentation index (FI) of the QRS complex indicating depolarization disturbances were analyzed [3].

Results

In result a significant separation between G+/P+ versus G+/P- and G-/P- was possible by RMS analysis (ANOVA p=0,0015; Tukey-Kramer-test p<0,001). There was no significant difference between G+/P- and G-/P-.

Figure 1 shows a typical residualmap of a HCM patient (G+/P+) and of a healthy family member (G-/P-).

©1999, Tohoku University Press
Recent Advances in Biomagnetism
T. Yoshimoto et al. (Eds)

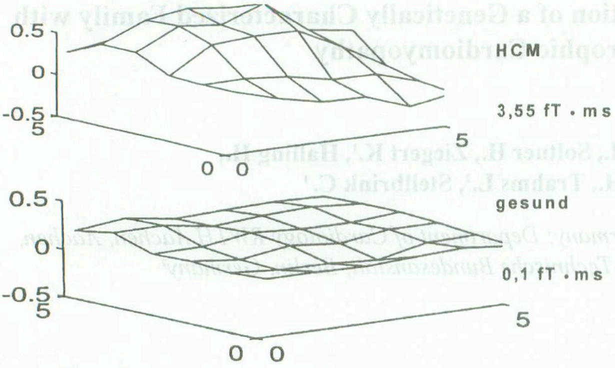

Figure 1

The FI was only significant between G+/P+ and G-/P-(ANOVA p=0,021; Tukey-Kramer-test p<0,05).
The mean MS and FI of the 3 patients groups are presented in table 2.

Table 2

group	G+/P+	G+/P-	G-/P-
FI	52,6±22,3	37,8±16,6	29,9±8,5
RMS	1,49±1,3	0,158±0,1	0,16±0,1

Discussion and conclusion

In our study HTc-MCG analysis detects de- and repolarization abnormalities in HCM patients. But it was not possible to identify asymptomatic gene carriers with the used analysis methods- the FI of the QRS complex and the RMS of the QRST-integral.

The theoretical background was the consideration that in such gene carriers exist a functional disorder due to a beginning or minor expressed myofibrillar disarray without visible hypertrophy in conventional diagnostic. We tried to discover these functional disorder in re- and depolarization period of the heart cycle. A subdividing of the QRST-integral in the first 40ms of the QRS-complex indicating the excitation of the ventricular septum, the QRS complex for the depolarization alone and the ST-Segment for the repolarization alone showed no significant results, too.

A possible explanation for failing of detecting of gene carriers without clinical symptoms until the evaluation would be a non existing of such myofibrillar disarray for instance due to a low penetrance of the discovered mutation. It is a known fact that mutations in the MYBP-C are associated with a low penetrance and mild form of the disease [2].

Another explanation could be the used analysis methods. Czerski et al reported about turbulence analysis in the first 20ms of the QRS complex with good results in all HCM patients. These method could be a potential alternative to identify borderline phenotypes [4].

We conclude that HTc-MCG detects de-and repolarization abnormalities in HCM patients but can not by itself identify gene carriers in the examined family with the used methods.

References

[1] Consensus Statement of the Joint Steering Committees of the Unexplained Cardiac Arrest Registry of Europe and of the Idiopathic Ventricular Fibrillation Registry o the United States: Survivors of Out-of-Hospital Cardiac Arrest with Apparently Normal Heart
Circulation 95: 265-272, 1997

[2] Marian AJ, Roberts R: Molecular Genetic Basis of Hypertrophic Cardiomyopathy: Genetic Markers of Sudden Cardiac Death
J Cardiovasc Electrophysiol 9: 88-99, 1998

[3] Brockmeier K, Schmidt S, Kreiseler D, Trahms L, Schmitz L, Oeff M, Hahlbohm HD: Fragmented Ventricular Depolarization Detectable in the QRS Complex of the Magnetocardiogram after Filtering with Binomial Non-recursive Filters
Proc. Computer in Cardiology, IEEE Computer Society Press: 685-687, 1994

[4] Czerski K, Gödde P, Agrawal R, Müller HP, Trahms L, Oeff M: Magnetokardiographische rämlich-zeitliche Turbulenzanalyse bei Patienten mit Hypertropher Kardiomyopathie
64. Jahrestagung der Deutschen Gesellschaft für Kardiologie: 157, 1998 (abstr.)

Risk Assessment after Myocardial Infarction with HTc-magnetocardiography by QRS Complex Analysis

**Selbig D., Soltner H., Bode M., Ziegert K.[1], Halling H.,
Bousack H., Trahms L.[2], Stellbrink C.[1]**

Forschungszentrum Jülich, Jülich, Germany; Department of Cardiology RWTH Aachen, Aachen, Germany[1]; Physikalisch-Technische Bundesanstalt, Berlin, Germany[2]

Introduction

Risk stratification for sudden cardiac death (SCD) of patients after myocardial infarction (MI) using electrical signals (e.g. signal averaged ECG, SAECG) has shown only modest prediction of SCD. Different study groups demonstrated a sensitivity of 63-93%, a specifity of 55-76%, a high negative predictive value with 95-99% but a low positive predictive value of 12-27% [1, 2, 3, 4, 5, 6], i.e. only 1 from 4 -7 patients (pts) with positive late potentials are at risk for SCD due to sustained ventricular tachyarrhythmia (sVT).

Magnetocardiography (MCG) is a technique that may have a higher sensitivity for the detection of minor depolarization abnormalities. First late field analysis were not superior to late potentials [7].

Late potentials and late fields detecting only strong delayed depolarization but not slow conduction areas in the entire QRS complex. The aim of our study was to examine if a HTc-magnetocardiographic analysis of the whole depolarization period will have a higher sensitivity and specifity in pts after transmural MI.

Methods

We examined 29 pts (m=23, f=6) after transmural MI with sVT (n=9; age 60,6±7,5 years), without sVT until the evaluation (n=20; age 57,9±14,1 years) and 19 controls without underlying heart disease (m=14, f=5; age 47,7±13,3 years). All pts and controls were clinical characterized by medical history, physical examination, ECG, long time ECG, SAECG, exercise ECG and echocardiography. All pts with sVT (CAD/VT+) and without sVT (CAD/ VT-) underwent coronarography/laevography. Exclusion criteria's were complete bundle branch block, atrial fibrillation non transmural MI and signal to noise ratio of the MCG-measurement <40.

A MCG (sensorpostion: 12.5cm below the manubrium sterni) was recorded in a magnetically shielded room with a single channel measurement system (first-order gradiometer, sensors from high-temperature superconductors). ECG (bipolar) was carried out at the same position like MCG recording. After averaging and bandpass filtering of the MCG and ECG signals an index characterizing the fragmentation of the QRS complex (Fragmentationscore, FS) was determined [8].

Results

In result there was a significant difference between the three groups in the fragmentation score using HTc-magnetocardiography (ANOVA; p<0,001) but not in the ECG analysis (ANOVA; p=0,059). In table 1 are presented the results of the mean FS in MCG and ECG, results of SAECG and long time ECG.

Table 1

		CAD/VT+	CAD/VT-	control
Number		9	20	19
	> 10 VES/h	6/9	7/18	2/11
Holter	Couplet	3/9	4/18	2/11
	Salvos	1/9	0/18	0/11
SAECG +		5/8	2/18	0/19
FS (MCG)		79,4 ± 23,5	41,6 ±19,6	32,2 ± 8,9
FS (ECG)		46,1 ± 19,6	35,4 ± 14,4	31,2 ±16,3

©1999, Tohoku University Press
Recent Advances in Biomagnetism
T. Yoshimoto et al. (Eds)

Statistical analysis (Tukey-Kramer-test) between the subgroups shows a significant discrimination between CAD/VT+ versus CAD/VT- and controls but was not significant CAD/VT- versus controls in HTc-MCG (table 2).

Table 2

	MCG	ECG
CAD/VT+ vs CAD/VT-	p<0,001	p<0,05
CAD/VT+ vs control	p<0,001	p<0,05
CAD/VT- vs control	p<0,05	p<0,05

Under the assumption of Gauss distribution a sensitivity of 95% resulting in a threshold of 46 and a specifity of 59% in CAD/VT+ versus CAD/VT- and a specifity of 94% in CAD/VT+ versus controls (Figure 1).

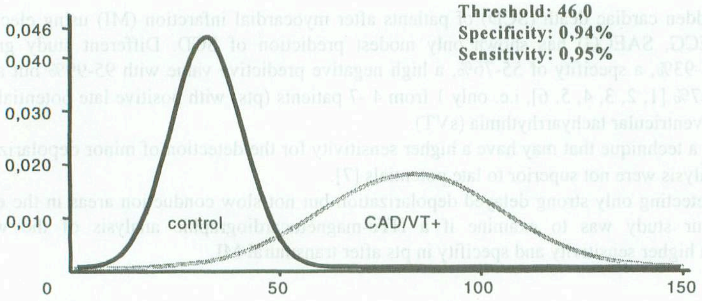

Figure 1

The SAECG shows high specifity (94%) too but only 63% sensitivity for differentiation of VT+ versus controls and VT-.

Discussion and Conclusion

In our study HTc-MCG analysis of the QRS- fragmentation is a more sensitive method than ECG or SAECG for the evaluation of the depolarization in pts with coronary artery disease at risk for SCD.

The FS reflects not only high frequent signals with low amplitude in the end of the QRS complex like the SAECG or late fields, it allows an examination of the whole depolarization period. This should be the explanation for the more sensitive detection of the pathophysiological substrate of VT´s (reentrytachycardia) after myocardial infarction -the slow conduction area.

The low specifity in the comparison of CAD/VT+ versus CAD/VT- pts may be caused by inclusion of pts with high risk for VT. Most of the VT- pts were measured in the first quarter of the year after the MI. It is a limiting factor that a retrospective study design with only a small pt number was used. Prospective analysis has to clarify the real specifity value.

Our first results demonstrating a good possibility of risk assessment after transmural MI by QRS complex analysis with a HTc-MCG-measurement system and according to the results with Fragmentation Index using LTS-MCG-System from Oeff et al [9].

References

[1] Breithardt G, Borggrefe M, Karbenn U,: Prevalence of late potentials in patients with and without ventricular tachycardia: correlation to angiographic findings.
Am J Cardiol 49: 1932-1937, 1982

[2] Kuchar DL, Thorburn CW, Samuel NL: Late potentials detected after myocardial infarction: natural history and prognostic significance
Circulation 74: 1280-1289, 1986

[3] Denniss AR, Richard DA, Cody DV, Russell PA, Young AA, Cooper MJ, Ross DL, Uther JB: Prognostic significance of ventricular tachycardia induced at programmed stimulation and delayed potentials detected on the signal-averaged electrocardiograms of survivors of acute myocardial infarction
Circulation 74: 31-754, 1986

[4] Gomes JA, Winters L: The prognostic significance of the signal-averaged electrocardiogram in the infarct

survivors
In: Gersh BJ, Rahimtoola SA; Acute myocardial infarction, Circulation 40: 19 (Abstract), 1984

[5] Cripps T, Bennett ED, Camm AJ, Ward DE: High gain signal-averaged electrocardiogram combined with 24-hour monitoring in patients early after myocardial infarction for bedside prediction of arrhythmic events
Br Heart J 60: 181-187, 1987

[6] El-Sherif N, Ursell SN, Bekheit S: Prognostic significance of the signal-averaged electrocardiogram depends on the time of recording in the postinfarction period
Am Heart J 118: 256-264, 1989

[7] Weismüller P: Magnetocardiographic diagnostic of late fields. Current state and future perspectives
Herzschr Elektrophys 8: 159-166, 1997

[8] Brockmeier K, Schmidt S, Kreiseler D, Trahms L, Schmitz L, Oeff M, Hahlbohm H.D.
Fragmented Ventricular Depolarization Detectable in the QRS Complex of the Magnetocardiogram after Filtering with Binomial non-recursive Filters
Proc. Computer in Cardiology, IEEE Computer Society Press: 685 – 687, 1994

[9] Magnetocardiographic Detection of Abnormal Intraventricular Activation in Patients with Ischemic Heart Disease with and without Tachycardia
Herzschr Elektrophy 8: 195-204, 1997

Risk Stratification in Patients with Coronary Artery Disease by Mapping of the Cardiac Magnetic Field Distribution

Selbig D., Gapelyuk A. Schuett H., Zimmermann R., Polak S., Sawitzki B., Schirdewan A.

Franz-Volhard-Hospital, Humboldt-University, Berlin, Germany

Introduction

Sudden cardiac death (SCD) in patients with coronary artery disease (CAD) is mainly caused by ventricular tachyarrhythmia. Every year 200.000 persons dying in the United States due to SCD [1]. These fact and the development of new therapeutic strategies (i.e. the implantable cardioverter defibrillator) in the recent years makes more accurate screening methods necessary. To identify such patient at high risk with a noninvasive screening method is an important clinical task. QT dispersion (QT interval maximum minus minimum) has been shown to reflect regional variations in ventricular repolarization and is increased in patients with life-threatening ventricular arrhythmias [2]. Reproducibility of this parameter vary significantly between studies and there existing controversy remains regarding the prognostic value of ventricular repolarization abnormalities in the risk stratification of patients surviving acute myocardial infarction [3].

The aim of our study was to estimate a noninvasive risk stratification method based on evaluation of the magnetic field distribution inhomogeneity in the ventricular repolarization period.

Methods

The study population consisted of three groups: 33 patients (pts) with angiographically proved CAD with events of ventricular tachyarrhythmia (VT) and mainly inducible ventricular tachycardia or fibrillation in the electrophysiological study (CAD/VT+), 42 coronary artery diseased pts without VT until the evaluation (CAD/VT-) and 28 controls without underlying heart disease (table 1).

Table 1

group	**CAD/VT+**	**CAD/VT-**	**controls**
number	n=33	n=42	n=28
age±SD	60,87±8,7	60,47±11,05	41,86±10,77
sex (m/f)	31/2	39/3	25/3

The pts and controls were characterized by medical history, physical examination, ECG, longtime ECG, echocardiography and exercise ECG. The clinical patient characteristics are figured in table 2.

Table 2

group	**CAD/VT+**	**CAD/VT-**
CAD: 1vessel	10 (30,3%)	18 (43,9%)
2vessel	7 (21,21%)	16 (39,02%)
3vessel	16 (48,48%)	7 (17,07%)
MI: no MI	10 (30,3%)	19 (46,34%)
anterior MI	10 (30,3%)	13 (31,7%)
inferior MI	14 (42,42%)	8 (19,51%)
EF±SD	42,79±16,44	61,2±13,74
EPU (inducible)	25 (75,75%)	no

In all pts and controls a MCG-map was recorded from 36 points on the anterior thorax using a single channel magnetic measurement system (Cryoton, Cryonit, Moscow). Isomagnetic field maps were constructed for 32 time steps of the repolarization period. after normalizing a parameter describing the inhomogeneity (IHc) of the repolarization was calculated by using the sum of magnetic field strength differences between local extrema and corresponding points [4].

©1999, Tohoku University Press
Recent Advances in Biomagnetism
T. Yoshimoto et al. (Eds)

Results

In result there was a mean IHc of 369,51±170,32 in CAD/VT+ pts, 184,35±87,28 in CAD/VT- pts and 112,32±41,89 in the control group. The discrimination was highly significant between all 3 groups (t-test: $p<0{,}0001$ CAD/VT+ versus CAD/VT- and controls, $p=0{,}00013$ CAD/VT versus controls). Under the assumption of IHc threshold of 250 a separation of CAD/VT+ versus CAD/VT- was possible with a specifity of 91,42% and a sensitivity of 87,78% (figure 1). These first analysis are independently from left ventricular ejection fraction (EF), coronary vessel status and the medical history of an acute myocardial infarction. Because the 3 groups were not exactly matched in these parameters (table 2) the data's were analyzed in subgroups.

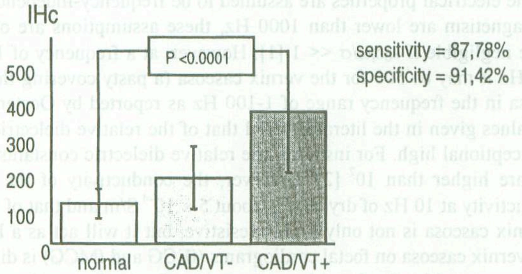

Figure 1

CAD/VT+ pts with a strong (<30%) and middle reduced EF (30-45%) presented no significant IHc difference, but the IHc was significant lower in pts with an EF >45% (t-test: $p=0{,}024$). The IHc is consequently depending from the EF. That's why we compared CAD/VT+ and CAD/VT- with an EF only greater 45%. In result a significant separation (t-test: $p= 0{,}00294$) between these two groups with a sensitivity of 90,9% and specifity of 91,42% was possible, too.

The analysis of the relationship between the number of diseased coronary vessels respectively the existing of a myocardial infarction and IHc showed no significance (t-test: $p>0{,}05$).

Discussion and Conclusion

Our MCG approach - the IHc- allows to identify CAD pts at risk for ventricular tachyarrhythmia with high sensitivity and specifity. The IHc is not depending from the coronary vessel status and the presence of a myocardial infarction but it exist a significant relationship between EF and IHc.

These first results are limited through a small pts number and the retrospective study design. On this way it is not possible to evaluate the important negative and positive predictive value. Only a following prospective study will clarify if the IHc shows a high predictive value in addition and will be consequently a powerfull noninvasive screening method to identify pts with CAD at risk for SCD.

References

[1] Gordon T, Kann WB: Premature Mortality from Coronary Heart Disease: the Framingham Study. J.Amer.med.Ass. 215: 1617-1625, 1971

[2] Glancy JM, Garratt CJ, Woods KL, de Bono DP: QT Dispersion after Myocardial Infarction. Lancet 345: 945-948, 1995

[3].Kautzner J, Malik M: QT Intervall Dispersion and its Clinical Utility Pace 20(Pt II): 2625-2640; 1997

[4] Gapelyuk A, Schütt H., Reinsperger F, Primin M, Meyerfeldt U, Wiedemann M, Schirdewan A: Magnetocardiographic Evaluation of Repolarization Process in Coronary Artery Disease Patients Prone to Malignant Ventricular Tachycardia
Proc. of World Congress on Medical Physics and Biomed. Ing. (Nice, France), Sept.14-19: p. 16, 1997

The Influence of the Vernix Caseosa on foetal Cardiograms

Stinstra JG [1], Krooshoop HJG [1], Muis B[1], Huirne JAF [2], Quartero HWP [2], Peters MJ [1]

University of Twente[1], Low Temperature Division, Graduate School iBME, Enschede, The Netherlands; Hospital Medisch Spectrum Twente[2], Enschede, The Netherlands

Introduction

The volume conductor is usually described by homogeneous, isotropic and ohmic compartments. Capacitive effects are not taken into account and the electrical properties are assumed to be frequency-independent. Although the frequencies that are important in biomagnetism are lower than 1000 Hz, these assumptions are only approximately true. For instance, capacitive effects are negligible if $\varepsilon_0\varepsilon_r\omega/\sigma \ll 1$ [1]. However, at a frequency of 10 Hz this value is about 0.6 for adipose tissue and at 100 Hz it may be 500 for the vernix caseosa (a pasty covering the skin of a foetus) [2,3]. The conductivity of vernix caseosa in the frequency range of 1-100 Hz as reported by Oostendorp *et al.* is 10^{-6} S/m (this value is in accordance with values given in the literature) and that of the relative dielectric constant 5×10^5 [3]. The latter has a value that is not exceptional high. For instance, the relative dielectric constants at 10 Hz of brain tissue, heart muscle, kidney, or liver are higher than 10^7 [2]. However, the conductivity of the vernix caseosa is exceptional low. For example, the conductivity at 10 Hz of dry skin is about 5×10^{-4} S/m and that of adipose tissue 10^{-2} S/m [2]. Consequently, the layer of vernix caseosa is not only highly resistive, but it will act as a leaky capacitor. In this paper, the influence of the layer of vernix caseosa on foetal cardiograms (fECG and fMCG) is discussed.

In early pregnancy, the currents generated by the foetal heart spread out in the foetus, the amniotic fluid, and the maternal abdomen. After about 30 weeks of gestation the fECG signal usually decreases, and around 32 weeks it is often immeasurable. This drop in signal strength is ascribed to the insulating effect of the vernix caseosa. Generally, the vernix caseosa cells are described as closely spaced squames. Due to the insulating effect of the vernix caseosa, the currents are presumably constrained within the foetus and only a small part of the current flows to the surface of the maternal abdomen. Consequently, practically no potential differences can be measured at the abdomen. In pregnancies of more than 34 weeks of gestation, the transfer of the current towards the maternal abdomen occurs probably through preferred pathways, possibly holes in the layer of vernix caseosa. Near term, at approximately the 37th to 38th week of pregnancy, this layer is sloughed from the surface of the foetal skin into the amniotic fluid and an fECG is easier to measure again. Presumably, the electrical properties of the layer of vernix caseosa play a dominant role in the transfer of currents from the foetal heart to the maternal abdomen, although other tissues may also have a considerable effect [4]. However, data on the electrical properties of tissues involved in the conduction of currents throughout the maternal abdomen are scarce in the literature. In this paper, an overview of the conductivity of the various tissues is given. Some conductivity measurements are repeated. Subsequently, some simulations are carried out to estimate the influence of the layer of vernix caseosa on foetal cardiograms.

Electrical properties of tissues involved in the volume conduction

Typical orders of magnitude of the conductivity of tissues involved in the ohmic (*i.e.* for small current density) conduction of currents generated by the foetal heart are given in table 1. Note that values given in the literature may vary a factor of ten. Moreover, the conductivity is a function of the frequency, the temperature, the individual, the direction, the position, and often it is not known for human tissues but for tissues of another mammal. Three values for the conductivity of the vernix caseosa were found in the literature [3,7,8]. All three of them found values of the order 10^{-6} S/m. A description of the measurement technique is only given by Oostendorp *et al.* In the complete frequency trajectory from 1-10^5 Hz they found a phase shift of $\frac{1}{2}\pi$ in two fresh samples with a thickness of 1.25 mm that were obtained from two different infants. In one of these samples, the phase shift after 24 hours was 0.4π at 1 Hz. The other authors did not mention any phase shift.

To get a confirmation of the fact that only for vernix caseosa $\varepsilon_0\varepsilon_r\omega/\sigma > 1$, measurements of the conductivity of vernix caseosa and of some other tissues are repeated, using an HP 4194A impedance analyser for the frequency range 100 Hz to 10 MHz. To cover the frequencies from 1 - 1000 Hz, a lock-in amplifier was used. The values obtained are indicated in table 1 with an asterisk. As the frequencies playing a role in fECG and fMCG signals are lower than 100 Hz, the currents flow through the extracellular fluid only. Consequently, care is taken that excised tissues are investigated promptly, because immediately after excision the cell membranes will break down, resulting in an increasing conductivity and a decreasing dielectric constant. Moreover, the frequency dependence at these low frequencies (*i.e.* the α-dispersion) may disappear in a few hours. For example, for muscles, at three days after excision, the dielectric constant at 0.1 Hz was decreased by a factor 20 and at 10 Hz by a factor 2. The conductivity at 0.1 Hz increased with a factor 2 and at 10 Hz with 40% [9].

©1999, Tohoku University Press
Recent Advances in Biomagnetism
T. Yoshimoto et al. (Eds)

Tissue	Conductivity (S/m)	Tissue	Conductivity (S/m)	Tissue	Conductivity (S/m)
Vernix caseosa	1.80×10^{-6} [3]	Placenta	0.6*	Bladder	1×10^{-1} [2]
	1.4×10^{-6} [7]	Uterus	5×10^{-1} [2]	Liver	2×10^{-2} [2]
	1.1×10^{-6} [8] $10^{-4} - 10^{-7}$*	Brain white matter	1×10^{-1} [6]	Spleen	10^{-1}[2]
		Brain grey matter	8×10^{-2} [2]	Kidney	1×10^{-1} [5]
Wharton's jelly	1.4 [3]	Muscle	2×10^{-1} [2]	Lung (inflated)	5×10^{-2} [2]
Blood	5×10^{-1} [6]	Cartilage	2×10^{-1} [5]	Ovary	3×10^{-2} [2]
Foetal membranes	0. 40 [3]	Bone (cortical)	2×10^{-2} [2]	Skin (dry)	2×10^{-5} [2]
Amniotic fluid	1.20 – 1.30 [5] 1.66 [7] 1.2 – 1.6*	Adipose tissue	1.2×10^{-2} [2] 1×10^{-1}*	Skin (wet)	2×10^{-1} [2]

Table 1- Conductivity of tissues surrounding the foetal heart (* indicates are own measurements)

Firstly, the measurement procedure was tested for a series of standard salt solutions (NaCl and KCl) at various temperatures and frequencies for samples with different lengths. The results were according to expectancy and the errors found were within a few percent. Secondly, the conductivity of amniotic fluid was determined. Seven samples of 10 ml of *in vitro* amniotic fluid were used. These samples came from women at different stages of gestation. The measurements were performed at 20°C and 37°C at various frequencies within the range 10 - 2000 Hz. No frequency dependence was found. The conductivities were higher at 37°C than at 20°C, which is according to expectancy, because the mobility of the ions will be higher at higher temperatures. Apart from one sample, which was contaminated with blood and meconium, it was found that the conductivity decreases with the duration of pregnancy. This can be explained by the fact that the phospholipid components and their concentrations change during pregnancy. The findings were in good accordance with those of De Luca *et al* [5]. Repeating the measurements after some days showed that the conductivity increased in time due to the break down of cells. Next, a freshly excised placenta, soaked in a physiological salt solution, was used to determine an average conductivity. The substance was fitted between two cylindrical tubes filled with a salt solution (NaCl 9 gram/litre). The diameter of the tubes was 1 cm and their length was 70 mm. The thickness of the sample of placenta was 10 mm. At 10 Hz at a temperature of 20°C, the average conductivity turned out to be about 0.6 S/m. This value is of the same order as the conductivity of human blood. The impedance of the foetal membranes (chorion and amnion) was too small to measure accurately, although 5 membranes were fitted between the tubes filled with the salt solution. Next, the in-phase and out-phase components of the (complex) impedance were measured of a sample of freshly excised abdominal adipose tissue attached to the skin (removed during a caesarean section). The length of the sample was about 14 mm, of which was 10 mm adipose tissue, and the diameter was 10 mm. The conductivity at 20°C in the frequency range of 10 to 1000 Hz was measured and was 1×10^{-1} S/m. We measured only a small phase shift (less than 8 degrees). Our conductivity was a factor ten higher than the conductivity reported for adipose tissue by Gabriel *et al.*[5]. They reported a conductivity for adipose tissue at 37°C of 1.1×10^{-2} S/m, that was independent of the frequency up to a frequency of 10^6 Hz. The difference can be explained by the presence of skin that has a higher conductivity.

Subsequently, the electrical properties of vernix caseosa were measured. Samples were scraped from the skin of normal newborn infants immediately after birth. Their gestational age varied between 36 and 41 weeks. (At 41 weeks the amniotic fluid that surrounded our sample was contaminated with meconium.) Some samples showed small traces of blood. The consistency of the various samples seemed to vary. The vernix caseosa was put in a small cylinder of perspex. The samples were fitted between tubes filled with a saline solution (NaCl 9gram/litre). Care was taken to ensure that no minute openings were present in the layer of vernix caseosa that could form salt-water junctions between the tubes filled with the saline solution. Samples obtained from different children were used to measure the electrical properties. The time interval between the measurement and the instant of birth varied between four and seven days. The thickness of the samples was 10 ± 1 mm or 5 ± 1 mm. The temperature was 25°C. To ensure a linear relationship between the conductivity and the potential gradient over the sample, the latter was kept as small as possible. The measured conductivities and relative dielectric constants are shown as a function of frequency in Fig. 1. It can be noticed that the electrical properties of the various samples differ a lot. Probably, these properties vary between individuals, they depend on the gestational age, on the contamination with blood or other fluids, and on the number of days after birth the sample was measured. Measurements were also carried out for a sample of 1 cm^3 of vernix caseosa, the specimen was kept in a freezer at minus 18°C for some months. Presumably, due the breaking-up of the cell membranes and loss of fluid, no phase shift was found. At 10 Hz the value of the conductivity was 9×10^{-4} S/m.

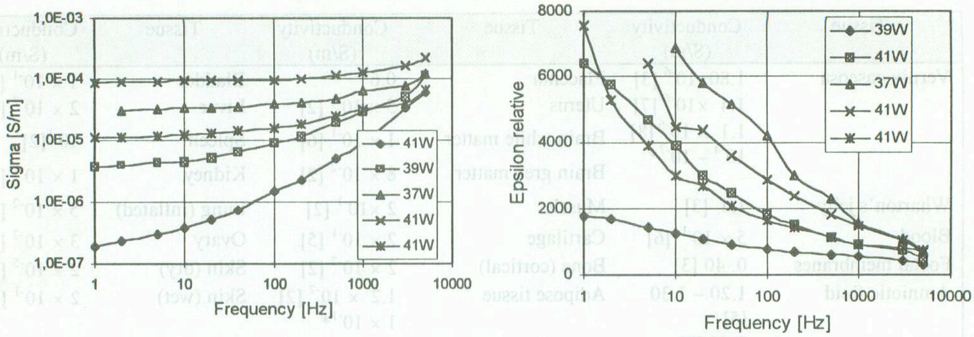

Fig. 1 – The conductivity and relative dielectric constant of the vernix caseosa against the frequency for different subjects and for different time intervals after birth, measured at 25°C.

Simulations

To estimate the effects of the layer of vernix caseosa on the foetal ECG, a model was used consisting of three concentric spheres representing the abdomen of the mother, the vernix caseosa, and the foetus. The compartments describing the foetus and maternal abdomen had a conductivity of 0.22 S/m. The sphere representing the foetus had a radius of 148 mm and the shell representing the maternal abdomen had a radius of 250 mm. The shell describing the vernix caseosa had a thickness of 0.2, 2, or 20 mm, a conductivity of 1×10^{-6} S/m, and a relative dielectric constant that varied (*i.e.* $\varepsilon_r = 5 \times 10^4, 5 \times 10^5$, or 5×10^6). The source was modelled by a current dipole $p = p_0 \cos \omega t$ in the centre of the spheres. (If the time varying fields are written in phasor form and the complex conductivity is used, the Poisson equations for the electrical potential and the appropriate boundary conditions are similar to the ones used when capacitive effects are not taken into account). When the dipole source is located in the centres of the spheres, the potential distribution at the interfaces can be described by one Legendre polynomial. The potential distribution at the surface of the outer sphere was calculated. Due to the spherical symmetry of the model used, only the amplitude of this potential distribution differs for each frequency. The transfer function, describing the relationship between the strength of the source and the potential in a point at the outer surface, was calculated. For the case that the layer of vernix caseosa had a thickness of 2mm it is given in Fig. 2 for three values of the dielectric constant. As can be seen, the high-frequency components are amplified in comparison to the low-frequency ones. The volume conductor acts as a first-order highpass filter for fECG. There is a phase shift between source and measured potential. For frequencies

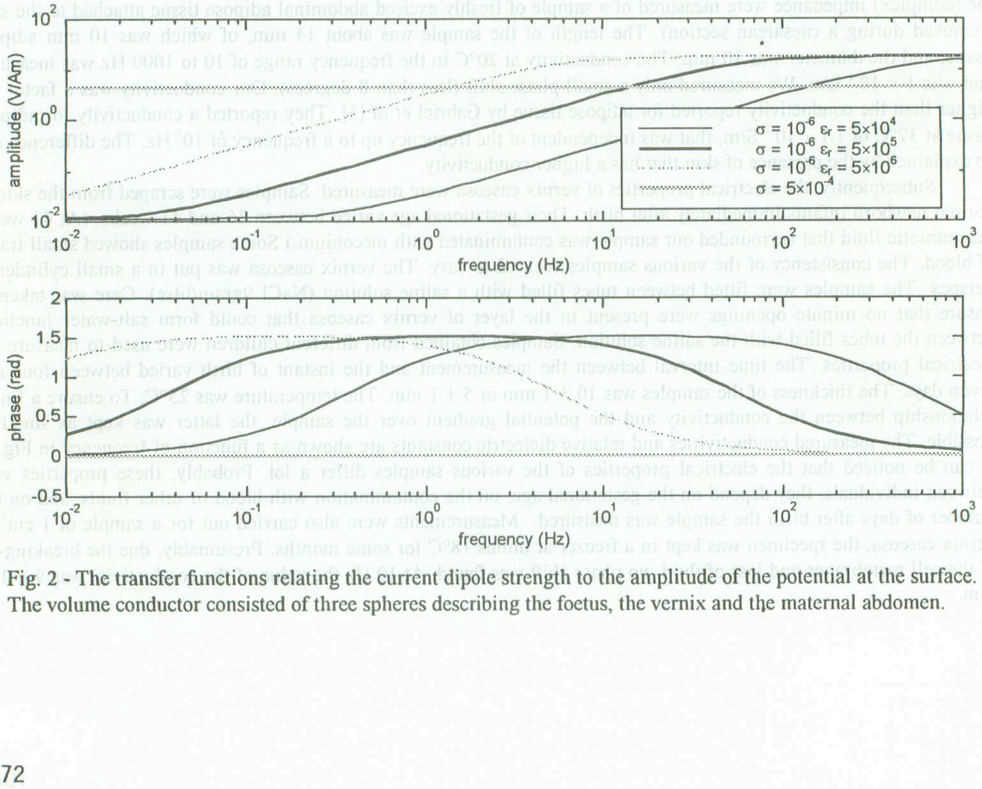

Fig. 2 - The transfer functions relating the current dipole strength to the amplitude of the potential at the surface. The volume conductor consisted of three spheres describing the foetus, the vernix and the maternal abdomen.

around 1 Hz this phase shift is about 90 degrees. For frequencies around 100 Hz the phase shift approaches 0 degrees. When the value of the dielectric constant is higher, the cut-off frequency of the high-pass filter is shifted to a lower frequency. When the value of the dielectric constant is lower, the opposite effect is found and the cut-off frequency is shifted to a higher frequency. A thicker layer of vernix caseosa results in a higher cut-off frequency and a thinner layer in a lower cut-off frequency. The effect of a 20 mm thick layer of adipose tissue under the skin was simulated in a similar way. The transfer function turned out to be frequency independent in this case. The simulations were repeated for the case that the layer of vernix caseosa had a conductivity of 5×10^{-4} S/m and the results are shown in Fig. 2.

In simulations of the fMCG, the volume conductor consisted of confocal spheroids describing the foetus and the layer of vernix caseosa surrounded by a sphere representing the maternal abdomen. The source was an oscillating current dipole along the z-axis. The amplitude of the current dipole was 0.5 μAm. The forward problem was solved by means of the boundary element method. The influence of the frequency of the source on the magnetic field was small [10].

Discussion

To confirm the dominant role of the vernix caseosa in the volume conduction, measurements of its electrical properties were performed and compared with those found in the literature. Our findings show that the conductivity and dielectric constants differ between individuals. Our samples were measured within a week after birth. For fresh samples, it is to be expected that the values for the conductivity are somewhat higher and those for the dielectric constant somewhat lower [9]. We did not measure at body temperature. The dependence on the temperature for both the dielectric constant and conductivity are tissue-type and frequency dependent [2]. Hence, our values cannot be translated to body temperature. Capacitive effects are expected when the ratio of $\varepsilon_0\varepsilon_r\omega$ and σ is larger than one. Consequently, the layer may act as a leaky capacitor (it depends on the patient and the frequency).

Two three-compartment models consisting of spheres or spheroids were used to estimate the capacitive effect of the layer of vernix caseosa on fECG and fMCG, when the layer acts as a leaky capacitor. From these model studies, one may conclude that the layer may act as a first-order highpass filter for fECG. When the thickness of the vernix in our model was 2 mm, the conductivity 1×10^{-6} S/m, and the relative dielectric constant 5×10^{5}, the ratio between the 1 Hz and 50 Hz component of the fECG was about 35. In this case, the P-and T-waves would hardly be measurable and even the QRS-complex would be diminished in amplitude. However, our measurements show that the layer will not always work as a leaky capacitor, although it always is a highly resistive layer. The thickness of the layer of vernix caseosa is unknown, it grows and shrinks during the last trimester of pregnancy and holes may appear in the layer. Moreover, the conductivity may vary from subject to subject. Thus, the influence of the volume conductor on the fECG in the last trimester of the pregnancy is of paramount importance, but cannot be predicted. In case of the fMCG, the influence of the presence of vernix caseosa on the waveform is smaller.

References

[1] Plonsey R, Heppner DB: Considerations of quasi-stationarity in electrophysiological systems, Bul Math Biophysics, 29: 657-664, 1967

[2] Gabriel S, Lau RW, Gabriel C: The dielectric properties of biological tissue: I Literature survey, II Measurements in the frequency range 10Hz to 20GHz, III Parametric models for the dielectric spectrum of tissues, Phys Med Biol, 41: 2231-2293, 1996

[3] Oostendorp TF, Oosterom A van, Jongsma HW: Electrical properties of tissues involved in the conduction of foetal ECG, Med & Biol Eng & Comp: 322-324, 1989

[4] Oostendorp TF, Oosterom A van, Jongsma HW: The effect of changes in the conductive medium on the foetal ECG throughout gestation, Clin Phys Physiol Meas 10: 11-20, 1989

[5] De Luca F, Cametti C, Zimatore G, *et al*: Use of low-frequency electrical impedance measurements to determine phospholopid content in amniotic fluid, Phys Med Biol, 41: 1863-1869, 1996

[6] Geddes LA and Baker LE: The specific resistance of biological material- A compendium of data for the biomedical engineer and physiologist, Med & biol Engng, 5: 271-293, 1967

[7] Bolte A: Zur Ableitung und Bewertung foetaler Herzaktionspotentiale bei schwangeren Frauen, Archiv für Gynäkologie, 194: 594-610, 1961

[8] Wimmer P: Ergebnisse der Abdominal-Elektrokardiography, Geburtsh. u. Frauenheilk., 14: 115, 1954

[9] Schwan HP: Dielectric properties of cells and tissues, Chiabrera A, Nicolini C, Schwan HP (eds): Interactions between electromagnetic fields and cells, NATO ASI series, 97, Plenum Press, 1985, pp 75-99

[10] Stinstra JG, Peters MJ: The volume conductor may act as a temporal filter on ECG and EEG, Med & Biol Eng & Comput, 36: 1-6, 1998

Estimation of Ventricular Excitation by MCG with Restrictions of Solution Area

Uesugi N[1], Sugaya H[1], Osozawa S[1], Ishiyama A[1] and Kasai N[2]

Dept. of Electrical, Electronics and Computer Engineering, Waseda University, Tokyo, Japan[1]
Electrotechnical Laboratory, Tsukuba, Japan[2]

Introduction

It is very important for the diagnosis of myocardia such as myocardial infarction to obtain the information regarding the viability of myocardial cells in the ventricle. A single-current dipole model is available for the source localization of small activated region in the heart; for example, localizing the ventricular pre-excitation site in Wolff-Parkinson-White (WPW) syndrome [1]. However, it is inadequate to use the single-current dipole model for the estimation of excited area in the ventricle, because the ventricular excitation begins from a localized place in the ventricular septum and a depolarization wavefront propagates spreading gradually over a wide area in the ventricle [2]. Several localization methods using a multi-current dipole model with anatomical restrictions and MRI information have been reported [3].

We developed a source localization method using a multi-current dipole model with restrictions of solution area in consideration of propagation of the depolarization wavefront [4].We applied this method to real MCG data of a normal subject. Only two-dimensional propagation of wavefront was obtained, though it is known that the wavefront propagates also to front and backside from electrophysiological study.

In this paper, we have improved this method about the restrictions. We have estimated the depolarization wavefront using this improved method. A solution area consists of three-dimensional grids and it is assumed that the dipoles are on the grids in this method. We have also investigated the effect of this assumption.

Localization methods

The localization method used in this work is based on the simulated annealing method (SA) with a multi-current dipole model. A solution area consists of three-dimensional grids and objective dipoles are assumed to be on the grids.

Since the wavefront proceeds smoothly in spatio-temporal space, dipoles at the time t_2 could be estimated using the conditions of the position and moment of the dipoles at the previous time t_1 ($t_2 = t_1 + \Delta t$). The solution area can be confined in the spherical cones shown in Fig. 1. The center of each spherical cone is on the position of a current dipole at t_1. The radius (r) and the angle (φ) of the spherical cone are determined with regard to the velocity and direction of wavefront propagation. The solution area at t_2 consists of the spherical cones selected by each dipole estimated at t_1.

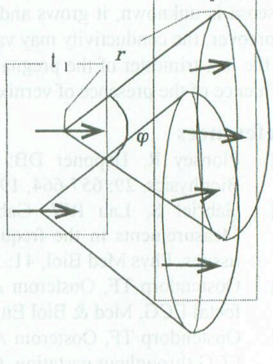

Fig. 1 Selected solution area

According to the physiological information, the excitation strength of cardiac muscle depends a little on the place in the heart. We assumed the dipole moment magnitude (m) is smaller than a certain magnitude.

The cost function E to be minimized is given by:

$$E = \frac{\sum_{i}^{coil} (B_i^m - B_i^c)^2}{\sum_{i}^{coil} {B_i^m}^2} + \alpha \sum_{j}^{dipole} F(m_j) + \beta \sum_{j}^{dipole} G(\theta_j^1, \theta_j^2) \qquad (1)$$

where B_i^m is the measured flux density and B_i^c is the flux density calculated from estimated current dipoles. $\alpha \Sigma F(m)$ is the penalty function concerned with the restriction for m. $\beta \Sigma G(\theta^1, \theta^2)$ is the penalty function concerned with the restriction for the dipole moment direction, where θ^1 is an angle between the moment vector of the dipole at t_2 and that at t_1 and θ^2 is an angle between the moment vector of neighboring estimated dipoles at t_2. The function G is given by (1-cosθ^1) and (1-cosθ^2). The α and β are the constant weight parameters. The most suitable values of these parameters were selected by changing the positions and number of dipoles randomly, so as to minimize the first term of Eq. 1.

©1999, Tohoku University Press
Recent Advances in Biomagnetism
T. Yoshimoto et al. (Eds)

Simulation

A computer simulation was carried out with two three-dimensional wavefront models. The schematic figure of the simulation model is shown in Fig. 2. The measuring plane was set at $z = 60$ mm and the area of the plane was 150 mm × 160 mm. Pick-up coils of 7ch SQUID system [4] were positioned on 18 points in the measurement plane. The axis of those coils were normal to the measuring plane. The dipoles constructed a simulated wavefront of cardiac excitation in the ventricle. These dipoles had the same moment magnitude and were directly parallel to the y-axis. The simulated wavefront was perpendicular to the measuring plane and proceeded in the positive y direction gradually, spreading the excited area.

In the case of one model, the dipoles were set on the grids. The estimated result agreed perfect with the source model. Even deep dipoles were estimated well.

In the case of the other model, the dipoles were not on the grids. Fig.3 shows the propagating wavefront plane. The proceeding speed of the wavefront plane were constant to be 2.5 mm/ τ . The single dipole at t_1 was set at the origin of the coordinate as an initial point in solving an inverse problem. By means of the proposed method, the position and moment of the current dipoles at t_2 were estimated. The following current dipoles at t_3, t_4, t_5 and t_6 were estimated sequentially. The values of parameters (r, φ) used in this simulation were first given as $\varphi = 120^\circ$ and $r = 6$ mm. The values of parameters were changed if a suitable solution was not obtained for the value of the parameter. The maximum values of parameters θ^1 and θ^2 are $\theta^1_{max} = 20^\circ$ and $\theta^2_{max} = 30^\circ$ .The estimated results agreed well with the distribution and direction of the source model. The results are shown in Fig. 4. Each dipole was not estimated precisely, but the wavefront propagation was estimated well. It seems that there is a possibility for the estimation of distributed current source such as cardiac excitation in the ventricle by means of this method.

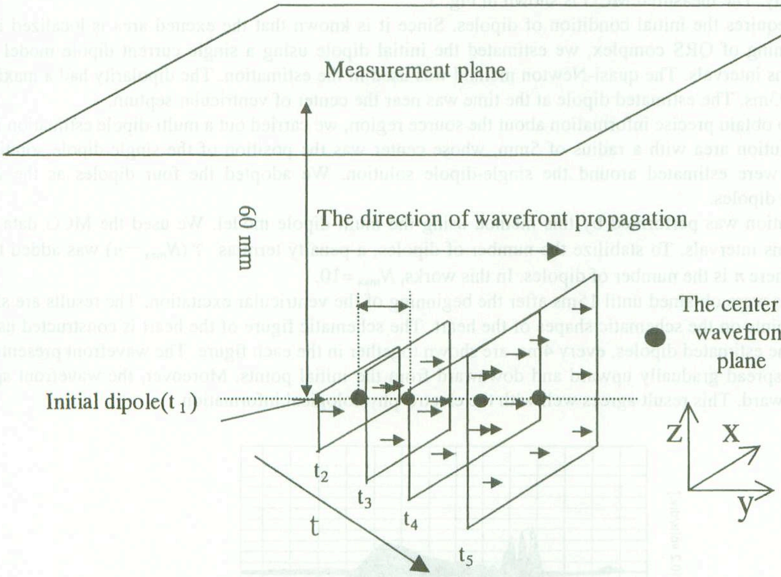
Measurement plane
60 mm
The direction of wavefront propagation
The center of wavefront plane
Initial dipole(t_1)
t_2
t_3
t_4
t_5
t
Z
X
y

Fig. 2 Simulation model

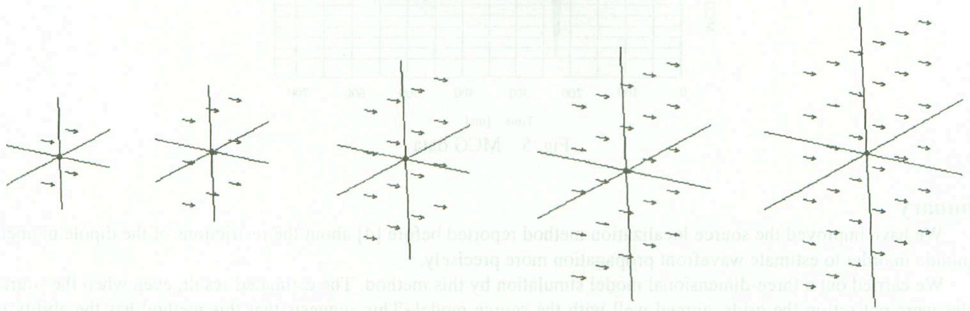

$t_2 = \tau$ $t_3 = 2\tau$ $t_4 = 3\tau$ $t_5 = 4\tau$ $t_6 = 5\tau$

Fig. 3 Source dipole model in the simulation

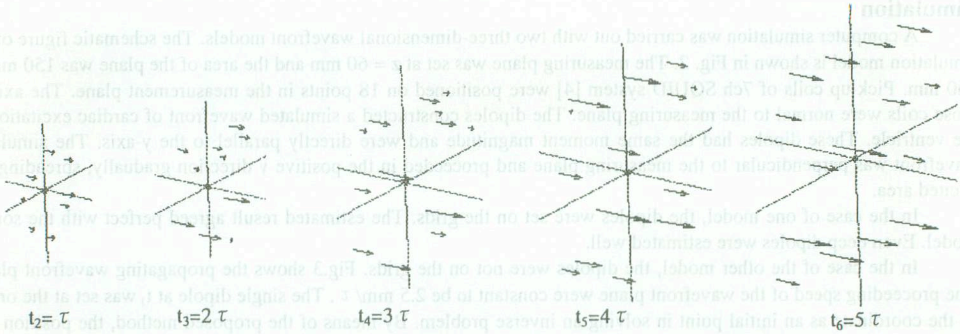

Fig. 4 Estimated results

Source localization of real MCG

We applied this method to a real MCG [4]. The details is reported in the reference [4]. We measured the normal component of the MCG of a normal male subject, 34 years old, using a 7-channel dc-SQUID system in a magnetically shielded room. The number of measurement points was 126 (7×18) in total. To fix the time, the electorocardiogram was gathered simultaneously. The measured MCG is shown in Fig. 5.

This method requires the initial condition of dipoles. Since it is known that the excited area is localized in the ventricle at the beginning of QRS complex, we estimated the initial dipole using a single current dipole model from 185ms to 215ms at 1ms intervals. The quasi-Newton method was used in the estimation. The dipolarity had a maximum value at 192ms and 193ms. The estimated dipole at the time was near the center of ventricular septum.

Furthermore, to obtain precise information about the source region, we carried out a multi-dipole estimation in the digitized spherical solution area with a radius of 5mm, whose center was the position of the single-dipole solution at 192ms. Four dipoles were estimated around the single-dipole solution. We adopted the four dipoles as the initial condition of following dipoles.

Source localization was performed by this method using the multi-dipole model. We used the MCG data from 192ms to 207ms at 1ms intervals. To stabilize the number of dipoles, a penalty term as $\gamma(N_{\max}-n)$ was added to the cost function Eq. 1, where n is the number of dipoles. In this works, $N_{\max}=10$.

Effective results were obtained until 15ms after the beginning of the ventricular excitation. The results are shown in Fig. 6 with black points on the schematic shapes of the heart. The schematic figure of the heart is constructed using a MRI of the subject. The estimated dipoles, every 4ms, are shown together in the each figure. The wavefront presented by the estimated dipoles spread gradually upward and downward from the initial points. Moreover, the wavefront spread also forward and backward. This result agrees well with the electro-physiological information.

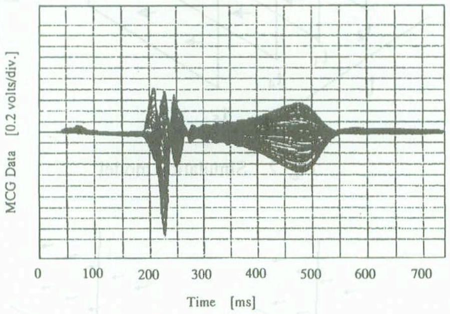

Fig. 5 MCG data

Summary

We have improved the source localization method reported before [4] about the restrictions of the dipole moment magnitude in order to estimate wavefront propagation more precisely.

We carried out a three-dimensional model simulation by this method. The estimated result, even when the source dipoles were not set on the grids, agreed well with the source model. This suggests that this method has the ability to visualize wavefront propagation.

We tried to apply this method to real MCG data of a normal subject. Effective results were obtained until 15ms after the beginning of the ventricular excitation. The estimated wavefront propagated not only upward and downward but also to posterior . This result agrees well with the physiological information.

This result seems the limit of using this method with the number of measurement points to estimate wavefront propagation. More investigations are required to estimation when the wavefront propagates more widely.

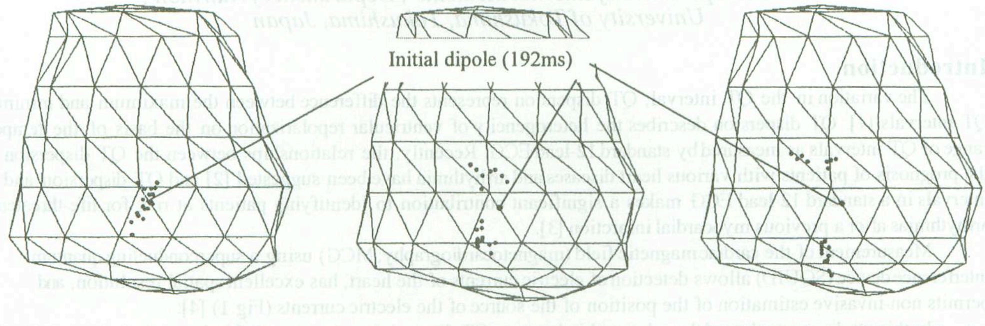

(1-a) Frontal view 192-195 [ms] (2-a) Frontal view 196-199 [ms] (3-a) Frontal view 200-203 [ms]

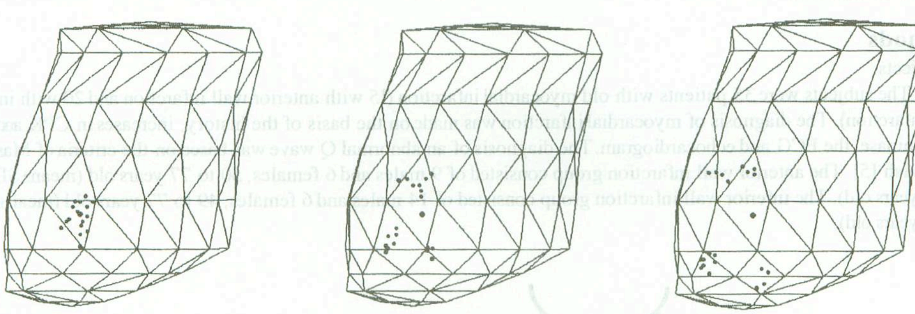

(1-b) Side view 192-195 [ms] (2-b) Side view 196-199 [ms] (3-a) Side view 200-203 [ms]

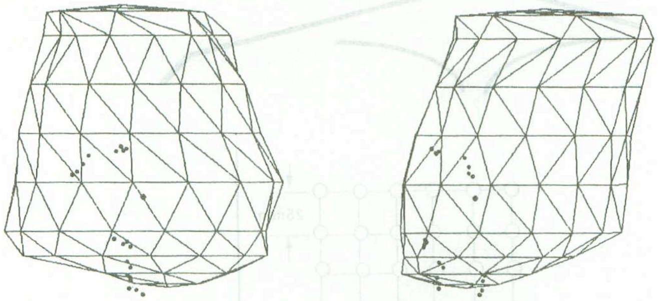

(4-a) Frontal view 204-207 [ms] (4-b) Side view 204-207 [ms]

Fig.6 Estimated results

References

[1] N. Kasai, T. Kokubun, K. Kido, N. Awano, K. Chinone: Source Localization of an Accessory Pathway by MCG - Comparison with Electrophysiological Study-. JJME 32: pp.231-237, 1994 (in Japanese)

[2] D. Durrer, R. Th. van Dam, G. E. Freud, M. J. Janse, F. L. Meijler, R. C. Arzbaecher: Total Excitation of Isolated Human Heart. Circulation 41: pp.899-912, 1970

[3] W. Moshage, B. Seese, S. Achenbach, R. Killmann, k. Bascmann: Abstracts of Biomag'93: pp.376-377, 1993,

[4] Sugaya H, Osozawa S, Ishiyama A, and Kasai N: Abstract of Biomag'96: pp.150, 1996

QTc Dispersion Using Magnetocardiogram: Analysis in Patients with Myocardial Infarction

Michiko Yukinaka[1], Masahiro Nomura[1], Tomomi Nada[1], Yuki Kondo[1], Ken Saito[1], Susumu Ito[1], Yutaka Nakaya[2]
Second Department of Internal Medicine[1]; Department of Nutrition[2],
University of Tokushima, Tokushima, Japan

Introduction

The variation in the QT interval, QT dispersion represents the difference between the maximum and minimum QT intervals [1]. QT dispersion describes the heterogeneity of ventricular repolarization on the basis of the temporal range of QT intervals as measured by standard 12-lead ECG. Recently, the relationships between the QT dispersion and the prognosis of patients with various heart diseases and arrhythmia have been suggested [2] and QT dispersion and QT intervals in a standard 12-lead ECG makes a significant contribution to identifying patients at risk for life-threatening arrhythmias after a previous myocardial infarction [3].

Measurement of the cardiac magnetic field (magnetocardiography; MCG) using a superconducting quantum interference device (SQUID) allows detection of electric currents of the heart, has excellent spatial resolution, and permits non-invasive estimation of the position of the source of the electric currents (Fig.1) [4].

In this study, we evaluated the relationship between QT dispersion and myocardial ischemia in patients with old myocardial infarction.

Methods

1) Subjects

The subjects were 35 patients with old myocardial infarction (15 with anterior wall infarction and 20 with inferior wall infarction). The diagnosis of myocardial infarction was made on the basis of the history, increases in CPK and transaminase, the ECG and echocardiogram. The diagnosis of an abnormal Q wave was based on the criteria of Massie and Walsh [5]. The anterior wall infarction group consisted of 9 males and 6 females, 50 to 77 years old (mean±SD; 58±4 years old). The inferior wall infarction group consisted of 14 males and 6 females, 49 to 77 years old (mean±SD; 59±5 years old).

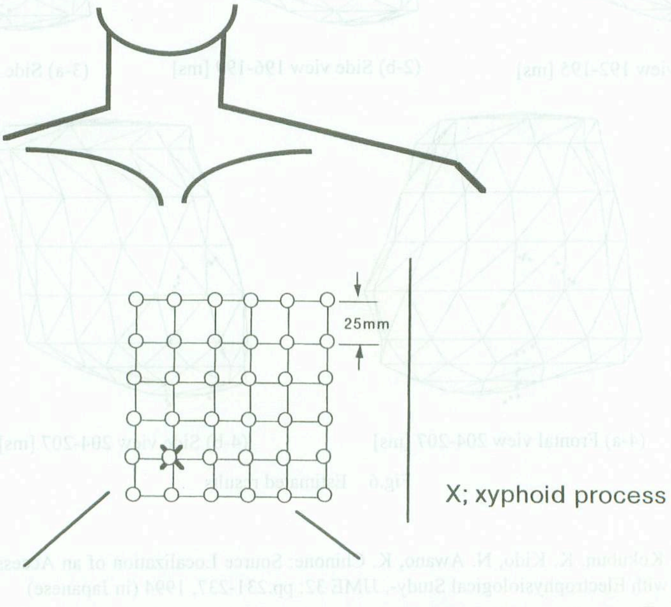

Fig. 1 Recording of the MCG

©1999, Tohoku University Press
Recent Advances in Biomagnetism
T. Yoshimoto et al. (Eds)

2) MCG recording

MCG was recordedusing a single-channel second-derivative type rf-SQUID (BTi Co). During measurement, the patients were kept in the supine position on a wooden bed; the dector almost touched the anterior chest wall and components perpendicular to the frontal plane of the magnetic field were recoded. The magnetic field parallel to the anterior chest wall was measured by 36 precordial leads using lead II ECG as a time reference (Fig 1) [4]. Standard 12-lead ECGs and magnetocardiograms were recordedat 25 mm/sec.

3) Analysis of the MCG

From the unipolar chest lead ECG and MCG of the 36 recording points (Fig 1), a body-surface isopotential map and isomagnetic map were constructed at the peak of the T wave of lead II of the standard 12-lead ECG. QT time and RR interval were determined from the MCG traces from all leads, and QTc was calculated by Bazett's equation. Also, to evaluate the space-time distribution in the anterior chest wall, isochronic contour lines of QTc time were constructed from the QTc data from each lead and compared with the position of the source of the electric current of myocardial ischemia estimated from the magnetic isofield map in the repolarization phase using a single - dipole model.

Results

1) QTc dispersion in standard 12-lead ECG and MCG

QTc dispersion was 86±25 msec by MCG and 66±23 msec by standard ECG, being significantly greater by MCG method ($p<0.05$) (Fig. 2). The values of minimum QTc determined by ECG and MCG were not significantly different.

2) Locational relationship between the isochronic contour lines of QTc in the magnetocardiogram and vector of myocardial ischemia

Fig. 3 shows examples of QTc isochronic contour lines (a) from MCG and a magnetic isofield map in the repolarization phase (b) of anterior myocardial infarction. In the QTc isochronic contour lines, QTc was prolonged in the left area of anterior chest wall. In the magnetic isofield map, a sink of magnetic field was observed in the upper middle area of the precordial region, and a source of magnetic field in the left lower area. From this distribution of the wave form of the T wave. A repolarization vector was deduced in the left area of the precordial region nearly corresponding to the site of prolonged QTc according to 'the corkscrew rule'.

Fig. 4 shows QTc isochronic contour maps (a) from MCG and a magnetic isofield map in the repolarization phase (b) of inferior wall infarction. In the QTc isochronic contour maps, QTc was prolonged in the lower part of the precordial region. In the magnetic isofield map, a sink of magnetic field was observed in the left lower part of the precordial region, and a source of magnetic field in the center of the precordial region. A repolarization vector was deduced in the lower part of the precordial region corresponding to the site of prolonged QTc.

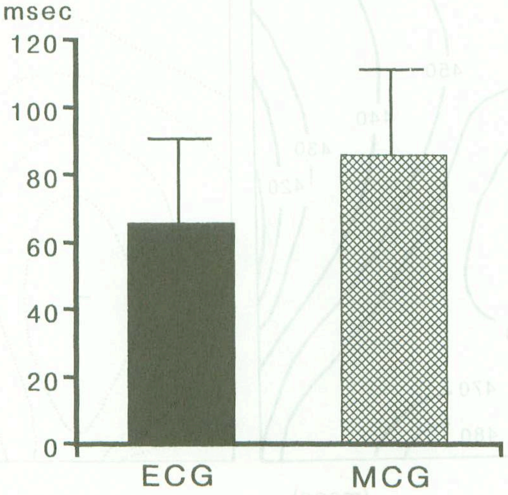

Fig. 2 QTc dispersion from ECG and MCG.

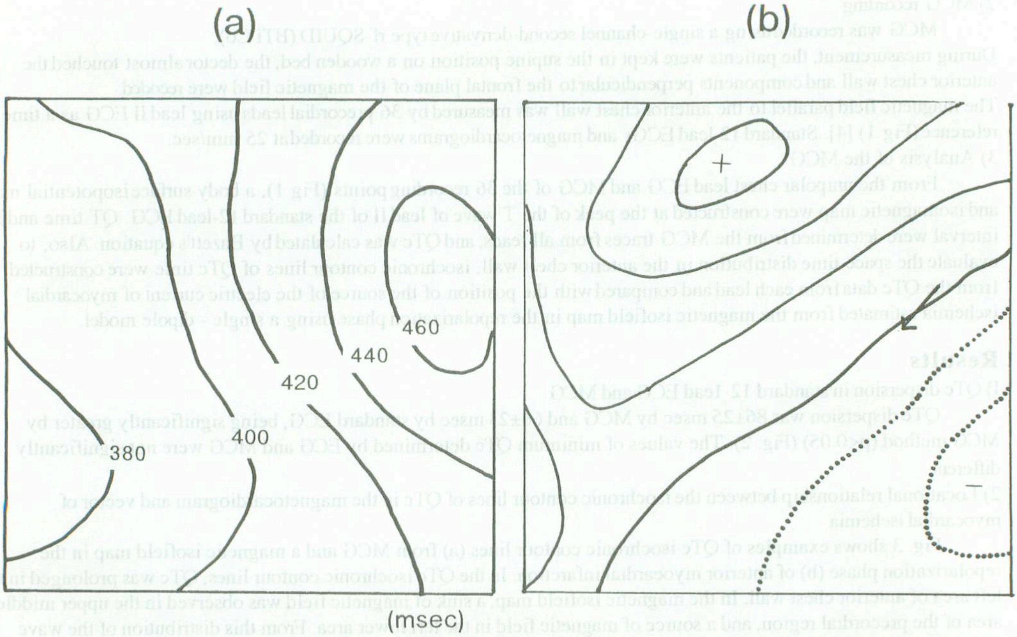

Fig. 3 Magnetocardiographic QTc isochronic contour lines in the anterior myocardial infarction. (a) Magnetic isofield map in the repolarization phase in the anterior myocardial infarction. (b)

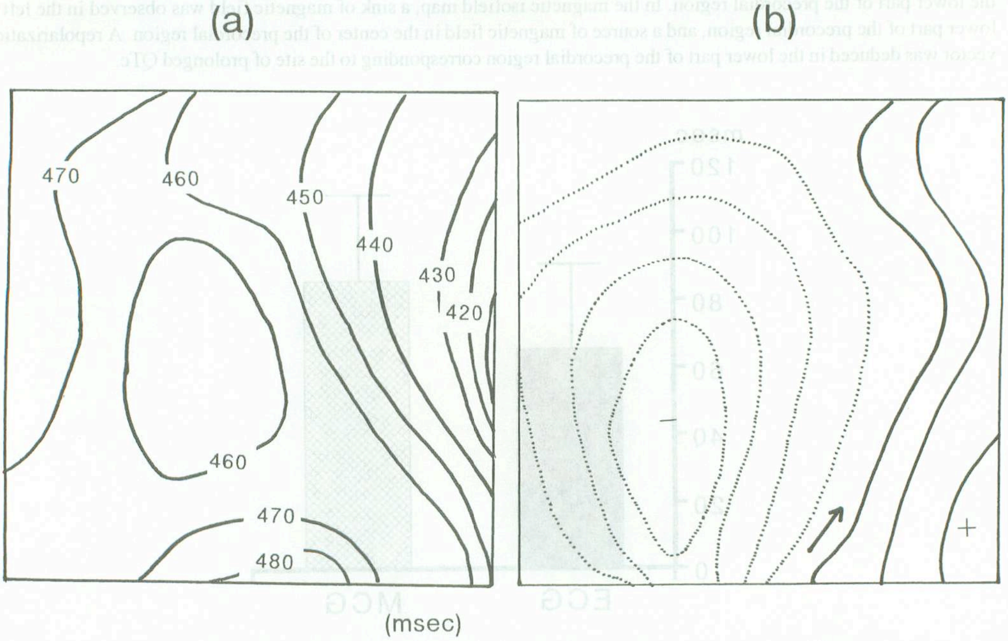

Fig. 4 Magnetocardiographic QTc isochronic contour lines in theinferior myocardial infarction. (a) Magnetic isofield map in the repolarization phase in theinferior myocardial infarction. (b)

Discussion

The concept of QT dispersion was introduced by Campbell et al [6]. Its relation with the prognosis of various heart diseases and arrhythmias have been reported [7]. Higham has reported QT dispersion is increased after myocardial infarction and degrees are greater in patients with ventricular fibrillation [8]. Glancy found QT dispersion serves variability in ventricular recovery time and may be a means of identifying patients at risk of arrtythmias and sudden death after acute myocardial infarction [9]. A few evaluations using MCG has been known. Leeuwen et al.have reported analysis of spatial QT dispersion in healthy subjects and patients after acute myocardial infarction showed clear differences in spatial distribution [10].

In this study, MCG, which detects the electric current immediately below the sensor [4], was significantly more sensitive to detect an increase in QT dispersion than by standard 12-lead ECG. Also, the dipole of myocardial ischemia in the repolarization phase was nearly in agreement with the site of the lead that showed QT prolongation, suggesting that myocardial ischemia is involved in the increase in QT dispersion.

The variation of QT interval among leads could be detectedaccurately by MCG, which has excellent spatial resolution, and prolongation of QTc was observed near the area of myocardial ischemia, suggesting a relationship between an increase in QTc dispersion and myocardial ischemia. Distribution patterns of QT dispersion which reflect localized repolarization abnormalities may thus represent a useful indicator for pathology and risk.

References

[1] Cowan JC, Yusoff K, Moore M, et al: Importance of lead selection in QT interval measurement. Am J Cardiol61: 83-87, 1988

[2] Higham PD, Campbell RW: QT dispersion. Br Heart J 71: 508-510, 1994

[3] Perkiomaki JS, Koistinen MJ, Yli Mayry S, et al: Dispersion of QT interval in patients with and without susceptibility to ventricular tachyarrhythmias after previous myocardial infarction. J Am Coll Cardiol 26: 174-179, 1995

[4] Mori H: Present status of clinical magnetocardiography. CV World Report 1: 78-86, 1988

[5] Massie E, Walsh TJ: Clinical vectorcardiography and electrocardiography. Year Book Medical Publishers, 1960

[6] Campbell RW, Gardiner P, Amos PA, et al: Measurement of the QT interval. Eur Heart J 6: Suppl D 81-83, 1985

[7] Barr CS, Naas A, Freeman M, et al: QT dispersion and sudden unexpected death in chronic heart failure. Lancet 343:327-329, 1994

[8] Higham PD, Furniss SS, Campbell RW: QT dispersion and components of the QT interval in ischemia and infarction. Br Heart J 73: 32-36, 1995

[9] Glancy JM, Garratt CJ, Woods KL, et al: QT dispersion and mortality after myocardial infarction. Lancet 345: 945-948, 1995

[10] Van Leeuwen P, Hailer B, Wehr M: Spatial distribution of QT intervals: an alternative approach to QT dispersion. Pacing Clin Electrophysiol 19: 1894-1899, 1996

Using Biosusceptometry AC to Study the Action of a Drug in Gastric Antral Contraction

Miranda JRA[1], Moraes R [2], Oliveira RB[3] and Baffa O[4]

Department of Physics and Biophysics, The Bio-sciences Institute, UNESP [1] ; The Botucatu Medical School, Botucatu – SP [2]; Department of Internal Medicine; The Medical School of Medicine USP Ribeirão Preto [3]; Department of Physics and Mathematics, FFCLRP-USP [4].
14.040-901 Ribeirão Preto – SP. Brazil.

Introduction

Gastrointestinal motor disorders play an important role in pathophysiology of several symptoms encountered in the clinical practice [1]. Several methods [2,3] have been used to study this condition and more recently biomagnetic techniques have been also successfully used [4-8]. Gastric antral contraction [9] was studied using susceptometric measurements of a magnetic test meal present in the stomach, showing a new application of biomagnetic measurements. Biomagnetic measurements are non invasive, harmless and radiation-free, making them ideal for repeated measurements. An interesting perspective for this novel technique is to study the efficiency of drugs that affect the gastrointestinal motility. Buscopan is known to reduce dramatically gastrointestinal motility and was used as a model drug in this study.

Materials and Methods

In vivo studies were initiated after approval of the experimental protocols by the ethics committee of the University Hospital (Medical School UNESP-Botucatu). The subjects ingested 100 ml of a chocolate yogurt (100 kcal) containing 4 g of manganese ferrite ($MnFe_2O_4$). The subjects stood in the upright position during the measurements, having the magnetic detector with a slight pressure against the abdominal wall over the epigastrium. Twenty one assymptomatic volunteers (15 men and 6 women, age ranging from 20 to 48 years) formed the study group. In these subjects the magnetic detection of GAC was repeated after intravenous hyoscine N-butyl bromide (Buscopan™- Boehringer/ Ingelheim 40 mg). The subjects had a saline infusion into a peripheral vein started before the experiments in order to facilitate drug injection during the biomagnetic measurements.

The magnetic detector employed in this study is an AC biosusceptometer (ACB), based on a differential (first order gradiometer) coil arrangement of two air core transformers, having one transformer for reference, and the other working as a measuring transformer on which the magnetic tracer having a high magnetic permeability acts like an external nucleus. The coils were mounted coaxially in a PVC tube and fixed with epoxy resin with a final diameter of 3.5 cm and 20 cm long. The primaries or excitation coils are fed by a power amplifier and the imbalance voltage produced by the test meal at the secondaries or detection coils, is detected by a lock-in amplifier (SR 570). A 8 pole low pass filter (HP 5489A) with a cutoff frequency set at 3 Hz was used. The signal was digitized at 10 Hz frequency yielding data files up to 6 Kb. Fig. 1 shows a general scheme of the apparatus and Fig. 2 a detail of the exciting and detection probe.

The measurements were performed within 1 hour after the ingestion of the magnetic test meal and each recording was 10 minutes long. Signals were digitized with sampling frequency of 10 Hz. Off line signal processing included filtering with a Butterworth filter (bi-directional, 2 poles, pass-band of 30 to 70 mHz), Fast Fourier Transformer (FFT) and Running Spectrum Analysis (RSA) of a 1 minute period, using the MatLab signal processing software. FFT and RSA were used to evaluate the amplitude of signal before and after the drug administration.

©1999, Tohoku University Press
Recent Advances in Biomagnetism
T. Yoshimoto et al. (Eds)

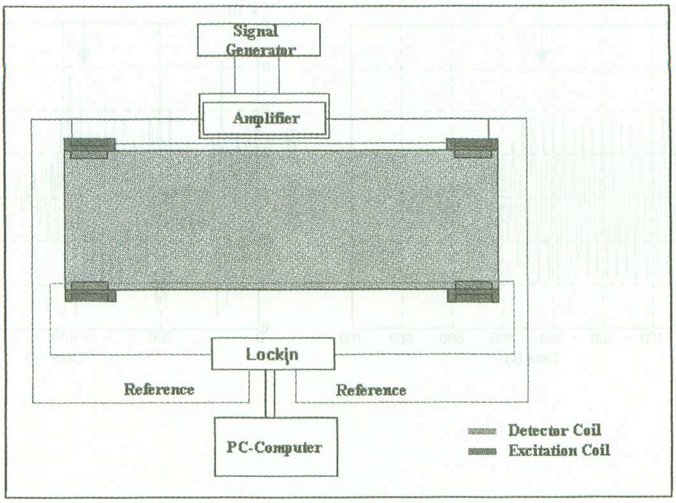

Fig. 1- General scheme of the AC Biosusceptometer. The excitation and detection coils are mounted coaxially, a block diagram of the electronics is also shown.

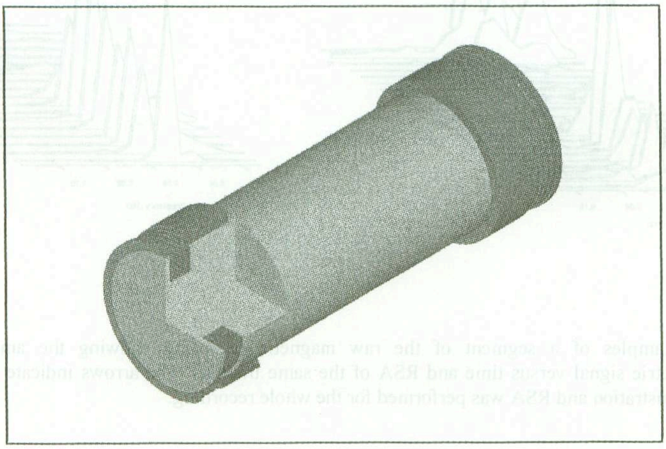

Fig. 2- Detail of the winding of the first order gradiometer employed for excitation and detection of magnetic flux variation due to the presence of magnetic tracers. The inner coil is used for signal detection and the outer for excitation of the sample.

Results

Examples of magnetic signal recording in different volunteers and the RSA are shown in Fig. 3. The tracing show only a portion of the whole data recorded and arrows indicate the instant of the drug administration. RSA was performed in the same signals for a longer period and it is possible to note the recovering of the mechanical activity after 70 and 40 minutes approximately. The mean value of the initial spectral intensity was considered 100% and the comparisons were made between the mean values of the ten minute periods before and after the intravenous infusion of Buscopan™. The amplitude in the ten minute period after the administration of the drug was a decreased to (12.11± 12.22) % (coefficient of variation of its initial value 101.4)

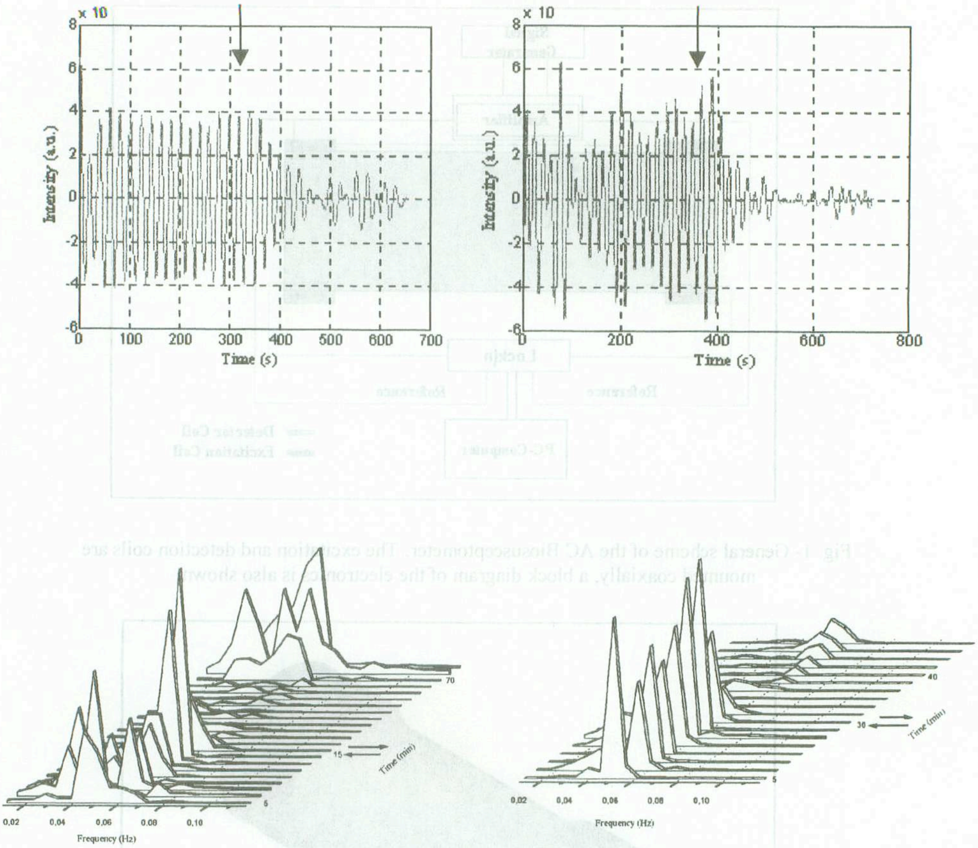

Fig 3- Examples of a segment of the raw magnetic recording showing the amplitude of the susceptometric signal versus time and RSA of the same tracings. The arrows indicate the moment of drug administration and RSA was performed for the whole recording.

Discussion

The main results of this study demonstrate that the biosusceptometric method herein employed is capable to detect the reduction of gastric antral contractions amplitude caused by Buscopan ™. The susceptometric signal has a high signal/noise ratio and was successful in detecting GAC in all measurements suggesting that this method could be more widely used as good tool to clinical evaluation of gastric motility. A possible and direct application of the technique could be the functional evaluation of gastroparesis, a secondary complication of diabetes mellitus. The effect of other drugs that affect the gastric motility can also be studied with this method.

Reference

[1] Drossaman D.A. Clinical research in the functional digestive disorders, Gastroenterology, 1987, 92:1267-1269.

[2] Brasseur JG and Dodds WJ Interpretation of intraluminal manometric measurements in terms of swallowing mechanics **Dysphagia 6**:100-9, 1991.

[3] Urbain JLC, Vekemans MC, Bouillon R, et al: Characterization of gastric antral motility disturbances in diabetes using a scintigraphic technique. **J. Nucl. Med.**, **34**:576-81, 1993.

[4] Miranda JR, Baffa O, Oliveira RB et al: An AC Biosusceptometer to Study Gastric Emptying. **Med. Phys.** 19(2):445-448, 1992.

[5] Baffa O, Oliveira RB, Arruda Miranda JR et al: Troncon Analysis and Development of a Simple AC Biosusceptometer for Orocaecal Transit Time Measurements.. **Med. & Biol. Eng. & Comput.** 33:353-357, 1995.

[6] Oliveira RB, Baffa O, Troncon LEA et al: Evaluation of a Biomagnetic Technique for Measurement of Orocaecal Transit Time. **Eur. J. Gastroent. & Hepatol.** 8:491-496 (1996).

[7] Daghastanli NA, Braga FJHN, Oliveira RB, et al: Oesophageal Transit Time Evaluated by a Biomagnetic Technique. e O. Baffa. **Physiol. Meas.**19(3): 413-420,1998.

[8] Baffa O, Wakai R, Leuthold A, et al: Studies in Magnetogastrography in the fasted and fed states. Med. & Biol. Eng. & Comput. 35(S-I):18, 1997.

[9] Miranda JRA, Oliveira RB, Sousa PL, et al: A novel biomagnetic method to study gastric antral contractions. **Phys. Med Biol.** 42(9):1791-1799, 1997.

Acknowledgements: We are grateful to E. Navas, M. Stelzer and L. Aziane for technical support. This work partially supported by: FAPESP, CNPq, FUNDUNESP, PRONEX and CAPES.

Biomagnetic Measurement of Small Intestinal Electrical Activity by 64-Channel Magnetographic Imaging

Nomura M[1], Kondo Y[1], Nada T[1], Yukinaka M[1], Saito K[1], Ito S[1], Nakaya Y[2]

Second Department of Internal Medicine[1], and Department of Nutrition[2],
University of Tokushima, Tokushima, Japan

Introduction

Non-ulcer dyspepsia (NUD) is a functional illness without any organic disease, and patients with this functional abnormality complain of various gastrointestinal symptoms (primarily symptoms of the upper digestive tract) [1]. Some cases of NUD are reported to involve functional abnormalities of the entire digestive tract, i.e., both the upper and lower digestive tracts. The diagnosis of NUD conventionally has relied on an exclusionary diagnosis, that is, ruling out all other possible conditions. However, if the coordination between upper and lower digestive tracts can be evaluated physiologically, the pathophysiology of NUD might be clarified. Recent advances in superconduction technology have made it possible to detect very weak magnetic fields produced by organisms. Several studies of gastric magnetic fields have been published [2-4], but there have been few studies of magnetic fields related specifically to the small intestine. The Superconducting Sensor Laboratory has manufactured a 64-channel superconducting quantum interference device (SQUID) [3]. The present study was undertaken to examine whether or not measurement of the small intestinal magnetic fields using this device would allow evaluation of small intestinal motility.

Subjects and Methods

The subjects were 2 healthy volunteers who had no history of gastrointestinal disease and without complaints concerning their gastrointestinal system. Magnetic fields produced by the digestive tract were measured using a 64-channel SQUID gradiometer in a magnetically shielded room. The SQUID gradiometer was composed of 64 magnetic coils, connected to Josephson elements and placed in liquid helium, to allow the detection of biomagnetic fields.

The subject, wearing no metal accessories or devices, lay on a bed made of non-magnetic materials. The magnetic sensors were placed immediately above the hypogastrium, as close as possible to the abdominal wall. Magnetic signals were collected for about 30 minutes, using a band pass filter (50 mHz - 30 Hz). The collected magnetic signals were Fourier analyzed, using a spectral analyzer (HP356A DYNAMIC SIGNAL ANALYZER). Moreover, the magnetic signals were filtered with a 500 mHz low-path filter.

Measurement of magnetic signals was performed on an empty stomach and after an intramuscular injection of a gastrointestinal anti-convulsant (scopolamine butylbromide, 20 mg).

Results

1. Magnetic signals of the 64 channels

Figs. 1 and 2 show the magnetic signals obtained with a 500 mHz low-path filter on an empty stomach and after an injection of scopolamine butylbromide, respectively. Ten to 15 cycles/min of magnetic signals were recorded under both conditions. The amplitude of the signals decreased after the injection.

2. Spectral analysis

Figs. 3 and 4 show the magnetic spectra on an empty stomach and after the injection, respectively. Two sharp peaks at 50 - 55 mHz and about 200 mHz, were observed under both conditions. The magnetic intensity decreased after injection of the anti-convulsant.

3. Magnetic isofield map

Fig. 5 is a magnetic isofield maps obtained from the 64-channel SQUID gradiometer. The location of the extrema varied at intervals of about 5 seconds, and the magnetic fields in the abdominal region oscillated at a rate of about 10 - 15 cycles/min.

©1999, Tohoku University Press
Recent Advances in Biomagnetism
T. Yoshimoto et al. (Eds)

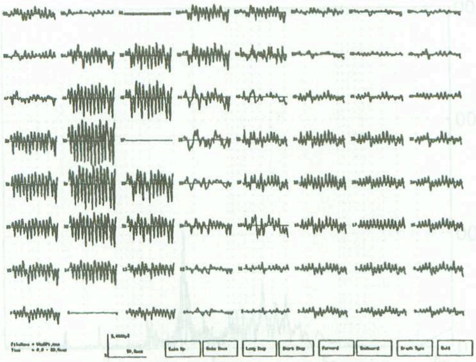

Fig. 1 Magnetic signals on an empty stomach

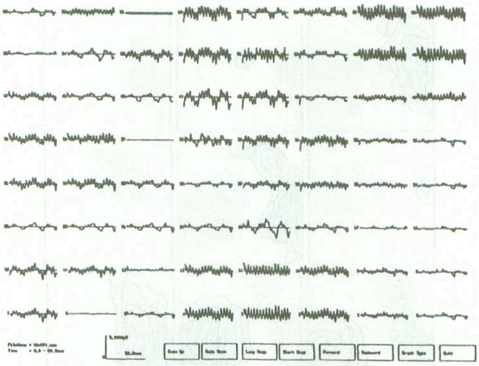

Fig. 2 Magnetic signals after the injection of scopolamine butylbromide

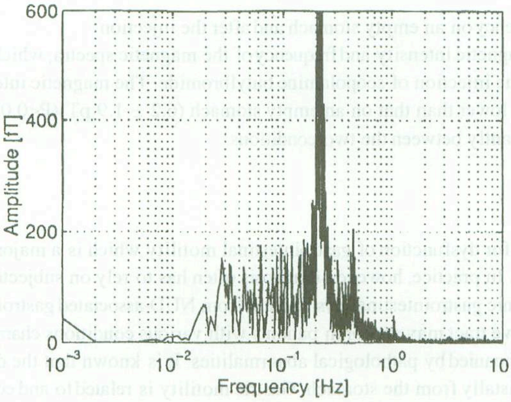

Fig. 3 Magnetic spectra on an empty stomach

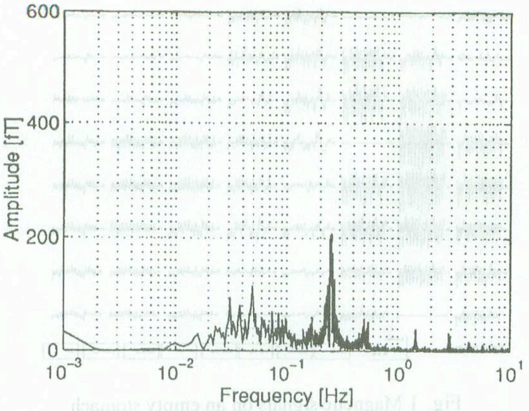

Fig. 4 Magnetic spectra after injection of scopolamine butylbromide

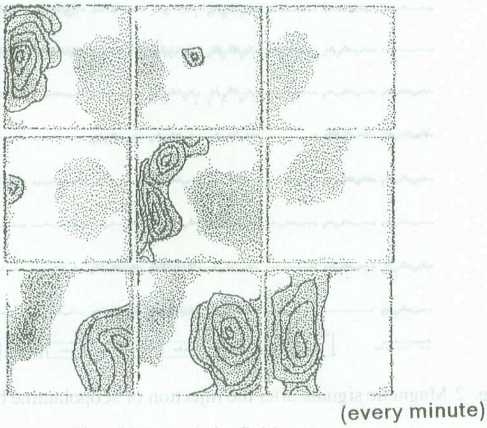

Fig. 5 Magnetic isofield maps

4. Magnetic intensity and frequency on an empty stomach and after the injection

Fig. 6 compares the magnetic intensity and frequency of the magnetic spectra, which had a peak at 200 mHz, on an empty stomach and after the injection of scopolamine butylbromide. The magnetic intensity after the injection (2.3 ± 1.6 pT) was significantly lower than that on an empty stomach (6.2 ± 1.9 pT)($P<0.05$). The frequency, on the other hand, did not differ significantly between the two conditions.

Discussion

It is essential to check for dysfunction of gastrointestinal motility which is a major feature of NUD, in order to make a diagnosis of NUD [1]. In practice, however, diagnosis often has to rely on subjective symptoms, making it difficult to distinguish psychogenic gastrointestinal dysfunction from NUD-associated gastrointestinal dysfunction. Diverse symptoms of the digestive tract may appear in patients with various conditions characterized by gastrointestinal dysfunction without being accompanied by pathological abnormalities. It is known that the digestive tract shows periodic motion which spreads distally from the stomach. Gastric motility is related to and coordinated with duodenal and gallbladder motility. However, the patterns of contraction vary from organ to organ. It is difficult to assess the motility of these organs separately by non-invasive measurement.

Electrogastrography is clinically available as an objective evaluation of gastric motility [2, 5]. However, only a few records of electric potentials of small intestines have been reported. It is difficult to isolate action potentials of the

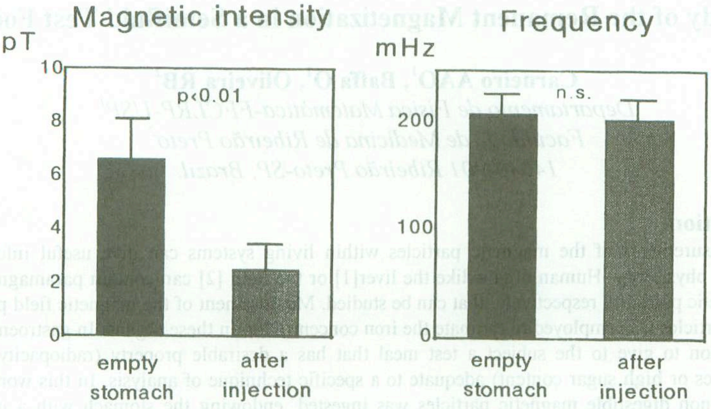

Fig. 6 Magnetic intensity and frequency of magnetic spectra on an empty stomach and after the injection of scopolamine butylbromide

digestive tract by measuring electric potentials. On the other hand, measurement of magnetic fields has a high spatial resolution, and it is possible to measure magnetic fields immediately below a magnetic sensor. Saijo *et al.* reported that gastric magnetic fields could be detected easily by the magnetic sensor placed in the epigastric area [3]. It seems therefore likely that if a magnetic sensor is placed in the hypogastrium, magnetic fields of the small intestine, produced by small intestinal action currents, can be detected.

In the present study, the magnetic spectral analysis revealed two sharp peaks at 50 - 55 mHz and 200 mHz. It has been reported that slow waves with a period of 3 cycles/min were recorded from the stomach and waves with a period of 11 - 12 cycles/min were recorded from the duodenum and ileum [2]. Of the magnetic signals collected in the present study, the signals with a peak at 50 - 55 mHz seem to represent gastric motility, and the signals with a peak a 200 mHz seem to represent duodenal and small intestinal motility. Thus, the magnetic sensor seems to allow separate detection of gastric magnetic fields and small intestinal magnetic fields.

This method of non-invasive measurement of gastrointestinal magnetic fields, which is capable of measuring magnetic fields from the stomach and small intestine (reflecting the motility of these digestive organs) separately in a physiological state, is clinically promising as a means of diagnosing regional disturbances of gastrointestinal motility.

References

[1] Colins-Jones DG: Management of dyspepsia: Report of a working party. Lancet 12:576-579, 1988

[2] Basile M: The biomagnetic approach to the study of gastrointestinal activity. Hoke M, Erne SN, Okada Y, et al (eds): Biomagnetism: Clinical Aspects. Amsterdam: Elsvier, 1992, pp613-619

[3] Saijyo T, Nomura M, Haruta Y, et al: Biomagnetic measurement of gastric electrical activity by 64-channel magnetogastrographic imaging. Gastroenterol 108:A681, 1995

[4] Staton D, Golzarian J, Wikswo JP, et al: Measurement of small bowel electrical activity in vivo using a high-resolution SQUID magnetometer. Baumgartner C, Deeke L, Stroink G, et al (eds): Biomagnetism: Fundamental Research and Clinical Applications. Amsterdam: Elsevier/IOS-Press, 1995, pp748-752

[5] Comani S, Basile M, Casciard S, et al: Extraporeal direct magnetic measurement of gastric activity. Hoke M, Erne SN, Okada Y, et al (eds): Biomagnetism: Clinical Aspects. Amsterdam: Elsvier, 1992, pp639-642

Study of the Remanent Magnetization in a Semifluid Test Food

Carneiro AAO[1], Baffa O[1], Oliveira RB[2]
Departamento de Física Matemática-FFCLRP-USP[1]
Faculdade de Medicina de Ribeirão Preto[2]
14040-901 Ribeirão Preto-SP, Brazil.

Introduction

Measurements of the magnetic particles within living systems can give useful information about their physiology. Human organs like the liver[1] or the lung [2] can contain paramagnetic and ferromagnetic particles, respectively, that can be studied. Measurement of the magnetic field produced by these particles was employed to estimate the iron concentration in these organs. In gastroenterology it is common to give to the subject a test meal that has a desirable property (radiopacity, shape, radioisotopes or high sugar content) adequate to a specific technique of analysis. In this work, a test meal with non digestible magnetic particles was ingested, endowing the stomach with a magnetic characteristic. Measuring the magnetic fields produced by these particles can give new information about gastrointestinal physiology [3-7]. The relaxation process can give information about the quantity of magnetic particles present but also about the internal dynamics of the stomach [7-8].

A system composed of magnetization coils and magnetic detectors was developed for measurements of remanent magnetization of magnetic tracers in the interior of the human stomach. The system of magnetization consists of two coils with 84 cm of diameter organized in a Helmholtz configuration. The magnetic detectors consist of two first order gradiometers made with fluxgate magnetometers.

Measurements of the time evolution of the Remanent Magnetization (RM) were performed *in vitro* and in a normal subject after the ingestion of a test meal labeled with magnetic particles. The time it takes for the RM to decay to half of its initial value ($T_{1/2}$) was measured.

Under normal circumstances the stomach has three major roles, i.e. providing a reservoir for the food, mixing and grinding the food with gastric secretion and controlling the emptying of the stomach contents into the duodenum. Contraction waves travelling along the stomach wall towards the antrum increase in intensity, pushing antral contents towards the pylorus and assisting in mixing and grinding gastric contents. The frequency of these mixing waves is 3 cycles/minute or 50mHz and its intensity varies with the prandial state. In this work a system developed to magnetize large samples and to measure the RM was to evaluated.

Materials and Methods

The magnetization of the particles was made with a magnetic pulse of 60 mT and 70 ms duration, generated by two coils in the Helmholtz configuration. These were energized with a capacitor group with 48 mF of capacitance and charged at 320 volts. The two coils were built with copper wire of 6 mm of diameter and each one possessing 48 loops, 84 cm of diameter, 40 mΩ of resistance and 1.25 mH of inductance. The magnetic sensor consists of two fluxgate magnetometers arranged in a first order electronically formed gradiometric configuration with base line of 15 cm. With this configuration, the environmental magnetic noise was minimized to a level of 10 nT. For a base line smaller than 10 cm the fluxgate magnetometers start to interfere wich each other. These sensors present a sensitivity of $0.5\,nT/\sqrt{Hz}$. Fig. 1 shows the general picture of the system. Non magnetic materials like wood and aluminum were employed in the construction and special care was taken to avoid coupling of vibrations from the coils, during the magnetic pulse, to the magnetometers. The signal detected by the fluxgates was digitized at 10 Hz and stored in a PC computer. The measurements were performed in an unshielded environment.

After fasting for at least two hours, the subject ingested a magnetic test meal consisted of yogurt (200 ml) and magnetite powder (Fe_2O_3, 1.5 grams) of diameter less than 27 μm. The subject laid down horizontally in a bed in a position of ventral decubitus leaving the stomach region centered between the two field coils . The RM was only measured with the inferior sensor positioned next to the stomach between the umbilical scar and the xiphoid. The distance between the sensor and the skin was 1cm. The study protocol was approved by the ethics committee of the University of São Paulo Hospital of Clinics.

©1999, Tohoku University Press
Recent Advances in Biomagnetism
T. Yoshimoto et al. (Eds)

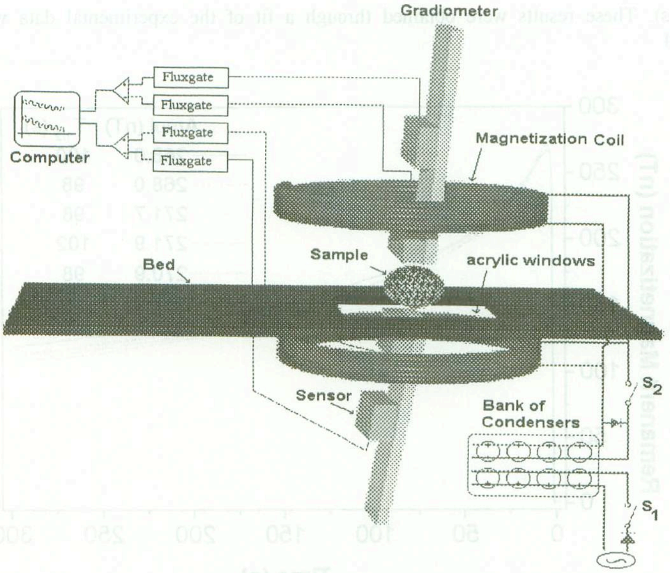

Fig.1: General picture of the gradiometric fluxgate system of measurement.

Simulation of the mixing process performed by the antrum was done with the device shown in the Fig. 2, that consists of a cylindrical reservoir with a volumetric capacity of 100 ml and a non magnetic blade in its interior. It moves the test food with controlled frequency, by means of a DC motor (12 volts and 3.6 W) linked to blade by a group of pulley and belts. The distance between the motor and the reservoir is 4 meters, to avoid interference from magnetic fields generated by the motor. This rotational movement applied in the particles is perpendicular to the magnetizing field on the measurement of RM

The sample, which was used in the simulation, had a magnetic concentration of magnetic tracers equal to the magnetic test meal ingested by voluntary. The rotation speed of the blade was adjusted to achieve a 3 cycles/minute frequency. Five measurements were made with the same sample at the same position.

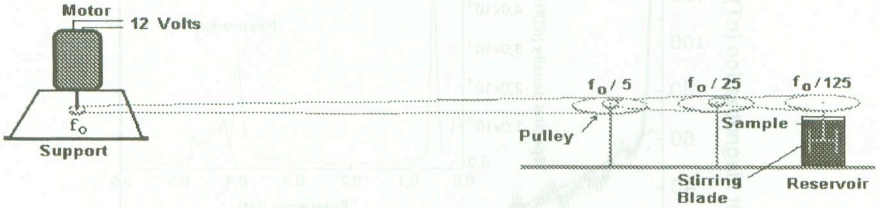

Fig. 2: System for simulation of the magnetic particle relaxation by an external mechanical force

Results

During the application of the magnetizing pulse the fluxgate detectors saturate. After the pulse the RM is detected and its initial value is very reproducible in a set of 5 magnetizations (B_o=270.1±1.9). The fact that there is no increase in the initial value of RM sugests that these particles are being aligned in the magnetizing field and there is no increase in domain size of the particles. After the pulse, the RM starts to decay due to the movement applied in the particles. This relaxation pattern was also reproduced in all measurements. The average decay time (*M_o/e*) was

(99.2±1.8 s). These results were obtained through a fit of the experimental data with a single exponential.

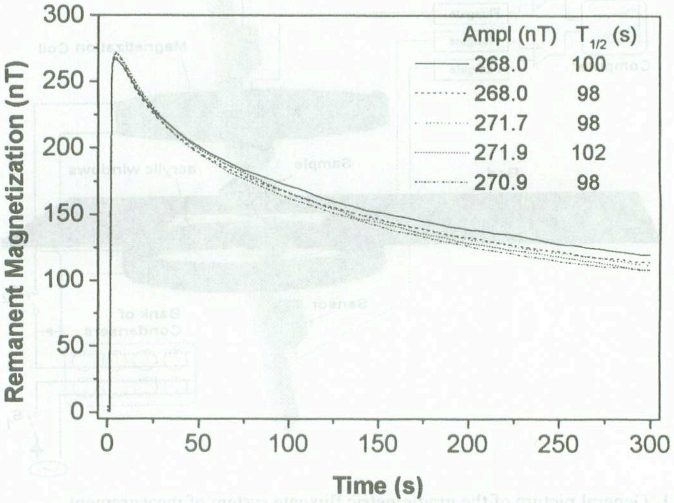

Fig. 3: Decay of the RM, experimentally simulated with device of the Fig. 2, showing the reproducibility in the measurements.

A typical decay plot of the RM measured in a normal subject is shown in the Fig. 4. The 3 cycles/minute and 12 cycles/minute undulation, due to contraction of the stomach and to respiration, is clearly seen. Fourier transform of this signal in the inset of Fig. 4, shows power density at the respiration and stomach contraction frequencies. The decay of the RM in this measurement ($T_{1/2}$=108 s) has the same characteristics of the measurements simulated *in vitro*.

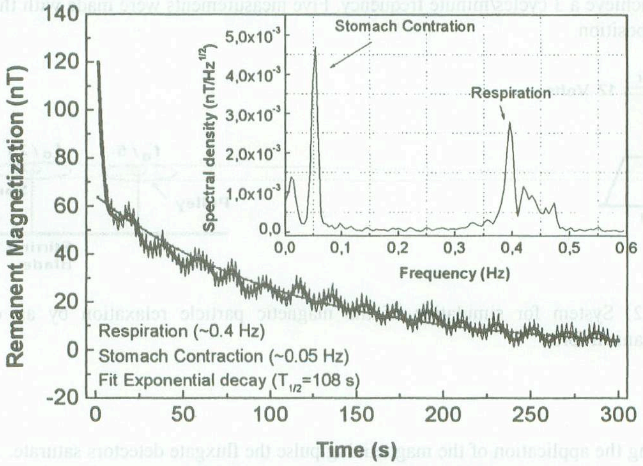

Fig. 4: Typical plot of the RM as a function of time showing the effect of the stomach's motility and its power spectrum plotted in the right superior corner.

Discussion

The system developed allows reliable measurements of the relaxation of the remanent magnetization of a magnetic test meal ingested by volunteers. These measurements show clearly the stomach contractions. A decay time associated with the mixing of the food can be determined. This new parameter needs to be further investigated to assess its importance in the gastric physiology. The system can also be employed to study RM produced in other organs.

Acknowledgments

We are grateful to the Brazilian Agencies FAPESP, PRONEX, CNPq and CAPES for partial financial support and to E. Navas, E. de Paula, L Aziani and M. Oliva for technical support.

References

[1] Engelhardt R, Tiemann C, Janka GE, et al: Biomagnetic Susceptibility Measurements of Liver and Spleen in Thalassemic Children. In **Biomagnetism: Fundamental Research and Clinical Applications.** Studies in Applied Electromagnetics and Mechanics, Elsevier Sci. Publ, pp 789-756, 1995.

[2] Forsman M and Högstedt P: Total Lung Dust Inverse Solutions in Single Plane SQUID Magnetopneumography. In **Biomagnetism: Fundamental Research and Clinical Applications.** Studies in Applied Electromagnetics and Mechanics, Elsevier Sci. Publ, pp 793-797, 1995.

[3] Miranda JR, Baffa O, Oliveira RB, et al: An AC Biosusceptometer to Study Gastric Emptying. **Med. Phys.** 19(2):445-448, 1992.

[4] Oliveira RB, Baffa O, Troncon LEA, et al: Evaluation of a Biomagnetic Technique for Measurement of Orocaecal Transit Time.. **Eur. J. Gastroent. & Hepatol.** 8:491-496, 1996.

[5] Baffa O, Basile M, Bradshaw A, et al: Biomagnetic Research in Gastroenterology. *in* **Biomag'96** (Proceedings da 10th International Conference on Biomagnetism), 1997.

[6] Daghastanli NA, Braga FJHN, Oliveira R B, et al: Esophageal Transit Time Evaluated by a Biomagnetic Methods. **Physiological Measurement**, august 1998.

[7] Baffa O, Oliveira RB, Miranda JRA, et al: Mixing Power of Food in the Stomach Evaluated by a Biomagnetic Technique, *in* **Biomagnetism: Fundamental Research and Clinical Applications.** Studies in Applied Electromagnetics and Mechanics, Elsevier Sci. Publ pp 753-756, 1995.

[8] Forsman M, Hultin L and Abrahamsson H: Messuraments of Gastrointestinal Transit using Fluxgate Magnetometers. *in* **Biomagnetism: Fundamental Research and Clinical Applications.** Studies in Applied Electromagnetics and Mechanics, Elsevier Sci. Publ pp 739-742.

AC susceptometer with a non homogeneous magnetising field

Della Penna S[1], Del Gratta C[1,2], Di Luzio S[1,2], Pasquarelli A[3], Pizzella V[4], Pulvirenti L[1],

Torquati K[1] and Romani G L[1,2]

Istituto di Tecnologie Avanzate Biomediche - Università Gabriele D'Annunzio[1], Chieti, Italy; Dipartimento di Scienze Cliniche e delle Bioimmagini - Università Gabriele D'Annunzio[2], Chieti, Italy; Zentralinstitut fuer Biomedizinische Technik - University Ulm[3], Ulm, Germany; Istituto di Elettronica dello Stato Solido – CNR[3], Roma, Italy

Introduction

SQUID based susceptometers have been used to measure the magnetic susceptibility of magnetised human tissue. The aim is the quantification of iron content in liver, spleen and other organs. An excess of iron-ferritine in such organs is the consequence of diseases such as thalassemia or hemocromatosis. The determination of the excretion rate of iron-ferritine in time is an important parameter for the follow-up of the patients undergoing chelation therapy [1].

In the operating SQUID based susceptometers, the tissue under investigation is magnetised by the magnetic field generated by an array of coils, while the magnetisation field is sensed by a SQUID inductively coupled to a gradiometer coil. The SQUID features the sensitivity and bandwidth, extending to dc, for the detection of quasi-static field variations when the distance between patient and sensor is slowly increased or reduced. The use of the susceptometer for *in vivo* studies requires a relatively large magnetised volume and an easy access for the patient.

The shapes of the magnetising and of the sensing coils are basic features, since they determine the quality of the spatial response. The operating instruments can be classified in two groups on the basis of the adopted geometry. The first [2] makes use of a superconducting magnetising coil array placed inside the cryostat containing the sensor. This configuration has the advantage of generating high fields whilst virtually avoiding any relative displacement between magnetising and sensing coils; on the other side, the field intensity decreases from the sensor to the magnetised body, thus increasing the importance of superficial tissues with respect to the deep ones. The second [3] uses a homogeneous field generated by large Helmoltz coils external to and mechanically decoupled from the SQUID cryostat. This instrument has the advantage that all tissues senses the same field, but still no enhancement of the signal coming from internal organs is present.

We present here an instrument that makes use of a non homogeneous magnetising field increasing from the sensor to the magnetised body with a constant gradient plus a cubic term at large distances. This configuration reduces the contribution of superficial tissues to the total signal, increasing that of internal organs. As a consequence, the dependence of the estimated concentrations of paramagnetic substances on modelling errors is decreased. Preliminary measurements have been carried out on samples of known magnetic susceptibility. A double layer phantom has been investigated in order to study the advantage of using a gradient field compared to a uniform field.. In comparing the estimated susceptibility values obtained using a homogeneous model, the relative error in susceptibility, when applying the non homogeneous field, results 2.5 times smaller than with the homogeneous field.

Methods

The magnetometer consists of a dcSQUID coupled to a superconducting first-order planar gradiometer (0.01 m diameter and 0.015 m baseline). This instrument has been used for the measurement of the magnetic susceptibility of large samples by using a low frequency AC homogeneous field [4]. Since the sensor is operated in a inhomogeneous applied field, the net signal in the SQUID would exceed its dynamic range without an additional active compensation. We thus inject a signal in the feedback loop in order to null the SQUID output: this signal is generated by sensing the current driving the field coils and by amplifying and shifting it. With the active compensation, the applied magnetic field is rejected with a relative residual smaller than 1×10^{-7}. A high signal to noise ratio is achieved by selecting the frequency of the AC magnetising field above the 1/f corner of the SQUID noise and using a digital lock-in detection, with the signal driving the magnetising coils as a reference. The overall system noise is reduced to less than 70 fT rms thanks to the filtering effect introduced by the lock-in detection.

©1999, Tohoku University Press
Recent Advances in Biomagnetism
T. Yoshimoto et al. (Eds)

The magnetising field increasing towards the patient is generated by using a Helmoltz pair oppositely wound. The coils are 1.35 m in diameter, separated by a 0.69 m distance, with 60 turns of wire. The coils are connected in series and driven by opposite currents generated by a power amplifier; the amplifier supplies the coils with a maximum rms current of 5.1 A at the frequency of operation, selected at 11 Hz, since higher current values cause a residual noise larger than 70 fT rms value.

Due to the field shape, the position of the gradiometer in the field coils determines the amplitude of the residual signal to be compensated. Any small displacement of the coils with respect to the sensor causes a spurious signal in the detection coils, that is not attenuated by the active compensation. Thus, in order to avoid vibrations, the object to be measured is placed under the detection coils, while the field coils are kept fixed with respect to the sensor. The detector response is nulled before the measurement, and the signal before and after positioning the object under the sensor is recorded as the baseline; a displacement of the sensor with respect to the coils results in a baseline shift. The net magnetisation signal is obtained as the difference between the measurement with the sample and the baseline.

The magnetic susceptibility is estimated from the comparison between the experimental field and the theoretical field of the model of the magnetised body. In the computation of the theoretical field, the vertical and radial components of the non homogeneous applied field are expressed with polynomial expansions; the polynomial coefficients are optimised to describe the field in the magnetised body within an error of 1%. The model consists of a group of stripes of magnetic dipoles uniformly distributed over the section orthogonal to the stripes; all dipoles are directed along the local magnetising field. The theoretical field is obtained by integrating the field of the stripes over the orthogonal section. Both the total field and the magnetic flux threading the gradiometer are obtained by discrete integration: with this technique we lower the computation errors introduced by other integration techniques and due to the averaging of the spatial fluctuation of the magnetising field in the magnetised object. For each geometry of the object under study, the number of integration points has been selected by increasing it until the relative variation of the theoretical field was less than 0.2%.

Results

We tested the apparatus with samples of known magnetic susceptibility. First a small sample, yielding a strong signal and high signal to noise ratio, was used to perform an overall test of the instrument. We then investigated the effect of the gradient field on a large sample consisting of two layers of different magnetic susceptibility.

In the small sample test, we compared the actual susceptibility of the sample with the value inferred from measurements of the magnetic field. The sample was chosen small enough to model the applied field as a constant gradient field. The small sample consisted of a glass cylinder ((9.50 ± 0.05) mm in internal diameter and (34.10 ± 0.05) mm in length) filled with hexaydrated iron sulfate powder, the volume magnetic susceptibility of which is 6.60×10^{-4} SI units. If we consider the powder uniformly distributed in the inner volume of the cylinder, the mean volume magnetic susceptibility of the sample is determined by the packing factor, which is the ratio between the effective volume occupied by the substance and the inner volume of the cylinder. In our case, the volume magnetic susceptibility of the sample was calculated to be $(3.995 \pm 0.091) \times 10^{-4}$ SI units.

We first measured the sample magnetisation field by applying a homogeneous field, obtaining a magnetic susceptibility of $(4.00 \pm 0.12) \times 10^{-4}$ SI units. A model consisting of two coaxial cylinders was used for the estimation of the magnetic susceptibility, in order to take into account the contribution of the glass container; the magnetic susceptibility of the glass was estimated from measurement of the field of the empty cylinder.

The sample was then investigated with the gradient field and the set of three measurements (background, sample, background) was repeated in order to check their reproducibility. In the susceptibility estimation the two cylinder model above described was used, whereas the applied field was expressed with a constant gradient field, describing the field within 1% in the sample volume:

$B_z = G\,z$

$B_\rho = 0.5\,G\,\rho$

with G = (0.85 ± 0.05) mT/m.. The magnetic susceptibility values obtained during six measurement sessions are displayed in Table 1, together with the estimate obtained from the homogeneous field measurement. The average value of the magnetic susceptibility was $(4.00 \pm 0.20) \times 10^{-4}$ SI.

In the measurement on the two layer sample, we used a plastic cylinder filled with pure water. The cylinder was (200.00 ± 0.1) mm long, with an internal radius of (40.70 ± 0.05) mm. The plastic thickness was (0.80 ± 0.05) mm. We studied the sample both in the gradient field and in a homogeneous field. Our aim was the evaluation of the effect of a superficial layer with different susceptibility on the estimated inner magnetic susceptibility, in the two magnetising field shapes. We thus compared the susceptibility values estimated using two models: a homogeneous cylinder, which did not take into account the plastic contribution, and two concentric cylinders with different magnetic susceptibilities. As in the case of the small sample, we first estimated independently the plastic magnetic susceptibility from field measurements of the empty container.

We studied the sample with a homogeneous ac magnetising field of (4.960 ± 0.005) Gauss. The estimated magnetic susceptibilities obtained by means of the two models were: $-(9.04 \pm 0.27) \times 10^{-6}$ SI for the two cylinders model and $-(9.20 \pm 0.27) \times 10^{-6}$ SI for the homogeneous cylinder model.

We then studied the sample with the gradient field. In the susceptibility estimation, we modelled the magnetising field components with the following polynomials of the third order, with a relative error of 1% in the object volume:

$B_z = G\,z\,(1 + 0.23\,z - 3.3\,z^2)$

$B_\rho = 0.5\,G\,\rho\,(1 + 0.3\,\rho - 7.7\,z^2)$

with G = (0.85 ± 0.05) mT/m. The data were analysed as described above for the homogeneous field. Table 2 reports the results obtained in four measurements, as well as the homogeneous field results. The magnetic susceptibilities estimated using two different models are displayed for each measurement.

Table 1. Magnetic susceptibility estimates for the small sample

Calculated	$(3.995 \pm 0.091) \times 10^{-4}$
Homogeneous field	$(4.00 \pm 0.12) \times 10^{-4}$
Gradient field	
1	$(4.03 \pm 0.12) \times 10^{-4}$
2	$(4.09 \pm 0.12) \times 10^{-4}$
3	$(3.98 \pm 0.12) \times 10^{-4}$
4	$(4.00 \pm 0.12) \times 10^{-4}$
5	$(3.86 \pm 0.12) \times 10^{-4}$
6	$(3.99 \pm 0.12) \times 10^{-4}$
Average	$(4.00 \pm 0.12) \times 10^{-4}$

Table 2. Magnetic susceptibility estimates for the large sample

	χ_{water} – two cylinders ($\times 10^{-6}$ SI)	χ_{water} – homogeneous cylinder ($\times 10^{-6}$ SI)	$\Delta\chi_{water}$ ($\times 10^{-6}$ SI)
Homogeneous field	-(9.04 ± 0.27)	-(9.20 ± 0.27)	0.16
Gradient field			
1	-(9.21 ± 0.28)	-(9.27 ± 0.28)	0.06
2	-(9.03 ± 0.27)	-(9.10 ± 0.27)	0.07
3	-(9.40 ± 0.28)	-(9.46 ± 0.28)	0.06
4	-(8.84 ± 0.26)	-(8.91 ± 0.27)	0.07
Average	-(9.12 ± 0.27)	-(9.185 ± 0.275)	0.065

Discussion

The feasibility of the measurement with the gradient field is assessed by the results shown in Table 1 and 2. First, the estimations of the magnetic susceptibility were reproducible with a maximum relative deviation of 3.5 % in the small sample case and 3.1% in the large sample case, pointing out the system is stable and the measurements are accurate . Moreover, all the values of the magnetic susceptibility, estimated by means of the two cylinders model, agree with the actual value within the experimental error. This indicates that the models and approximations used for the magnetising field and the forward model for the magnetisation field were consistent.

The other conclusion that can be drawn from Table 2 is that the importance of superficial layers is lowered when using the gradient field. In particular, the comparison between the magnetic susceptibilities, estimated by means of the homogeneous and the two cylinders models, gives information about the sensitivity of the gradient and the homogeneous field to a superficial layer surrounding the object of interest. The third column of Table 2 shows the relative error in the estimated magnetic susceptibility when considering the sample as homogeneous. From the values therein it can be seen that the relative error decreases from 1.8% to 0.7% when the gradient field is used, so that the sensitivity to superficial inhomogeneities in the susceptibility distribution is 2.5 times lower. The effect of the gradient field can also be evaluated by comparing the magnetic field values: the contribution of the plastic container in relation to the field of the water is 2% with the gradient field, while it rises to 5.6 % with the homogeneous field. This result shows how the gradient field reduces the contribution of superficial layers with respect to that of deeper layers, a feature useful for in vivo investigation of internal organs.

It is interesting to generalise the above results in the perspective of in vivo applications, by comparing the sensitivity profile of the gradient field with the homogeneous field. The sensitivity profile of the susceptometer depends on the geometry of both the detection coil and the magnetising coils and on their relative position. Indeed the reciprocity theorem asserts that:

$$\Phi = \mu_0^{-1} \int \chi(\mathbf{r}) \, \mathbf{B}_0(\mathbf{r}) \cdot \mathbf{B}_d(\mathbf{r}) \, dv$$

where $\mathbf{B}_0(\mathbf{r})$ is the applied external field and $\mathbf{B}_d(\mathbf{r})$ is the lead field of the detection coil, so that the function

$$s(\mathbf{r}) = \mathbf{B}_0(\mathbf{r}) \cdot \mathbf{B}_d(\mathbf{r})$$

actually represents the spatial sensitivity profile of the instrument. The normalised sensitivity profile isocontours are displayed in Fig. 1, in the plane y = 0 for the gradient (left) and the homogeneous (right) magnetising field configurations; here the baseline of the gradiometer is lying on the x axis. Again from this figure it is clear that the use of a inhomogeneous field increasing with the distance from the sensor improves the spatial sensitivity to deep sources. For example the 0.004 isocontour extends about 2.5 cm deeper in the case of the gradient field. This explains the results obtained in the study of the double layer sample. Indeed, the weight associated to internal volumes is higher than in the homogeneous field and we thus obtain a lower contribution of superficial layers to the total magnetisation; as a consequence, the sensitivity to modelling errors relative to layers near to the sensor is reduced.

In summary, our main target was to investigate how the use of a quasi-linear applied field lowers the sensitivity of an instrument for biosusceptometry to superficial layers with respect to inner layers. The successful investigation of samples of known magnetic susceptibility implies that the use of a quasi-linear field is possible. Moreover the comparison between the studies of a two layer sample in a gradient field and in a homogeneous field indicates that an inhomogeneous applied field is better suited for *in vivo* susceptometry. This suggest the study of a customized applied inhomogeneous field to be used in a clinical purpose instrument.

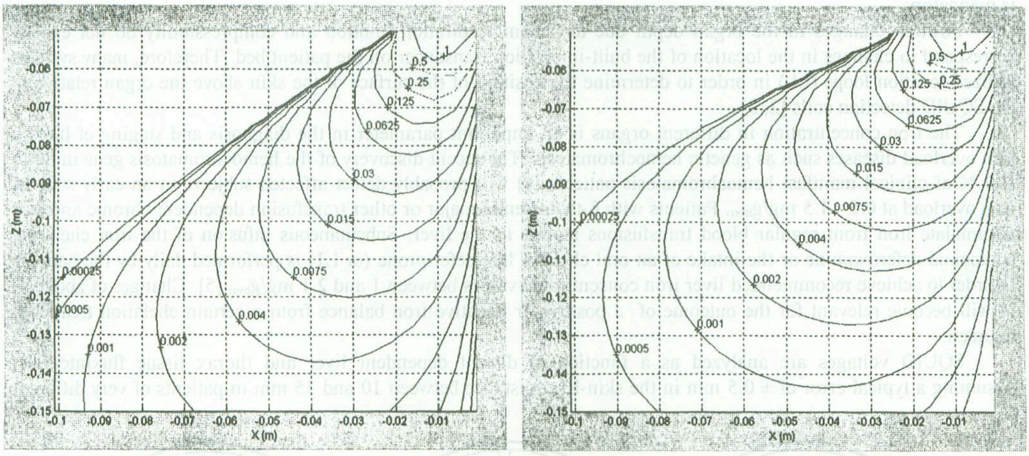

Fig. 1: Sensitivity profile isocontour lines of the gradient field (left) and the homogeneous field (right). The values at the isocontour lines are normalised to the value at the first isocontour line. The sensitivity profile function s(r) is displayed in the plane y=0, in the area occupied by the sample underneath one of the gradiometer coils; the center of the planar gradiometer is placed at z = -0.04 m, x= 0.0 m and the baseline lies on the x axis.

References

[1] Nielsen P, Fisher R, Engelhardt P, Tondüry P, Gabbe E E and Janka G E: Liver iron stores in patients with secondary haemosiderosis under iron chelation therapy with deferoxamine or deferiprone. British Journal of Haematology 91: 827-833, 1995

[2] Fisher R, Paulson D N, Fagaly R L and Toussaint R M: Biomagnetic Susceptometer with SQUID Instrumentation IEEE Trans. on Mag. 27: 3249-3252, 1991

[3] Bastuscheck C M and Williamson S J: Technique for measuring the ac susceptibility of portions of the human body or other large objects J.Appl.Phys. 58: 3896-3906, 1985

[4] Pasquarelli A, Del Gratta C, Della Penna S, Di Luzio S, Pizzella V and Romani G L: A SQUID based AC susceptometer for the investigation of large samples Phis. Med. Biol. 41: 2533-2539, 1996

Printed Circuit Locator Loop for X-Y-Positioning and Z-Distance Measurements

Engelhardt R[1], Valett K[2], Fischer R[1]

Abteilung Medizinische Biochemie, UKE, University Hamburg[1];
Positronic system technique, Ellerbek[2], Germany

Introduction

Magnetic flux in susceptometry changes rapidly with the distance of magnetized objects from the detection coils. For the quantification of liver iron in patients it is of crucial importance to measure the distance between the patient's skin and the gradiometer coil configuration, at the optimum measurement position above the liver, as precisely as possible, whereas the more distant skin-liver spacing is determined with sufficient precision by ultrasound imaging techniques. Moreover, as current biosusceptometer systems [1, 2] make use of a water coupling membrane as diamagnetic reference for biological tissues, the localization of the exact position below the water bag is mandatory.

Position changes in the organ depth due to patient respiration, motion and compressibility do not exactly correspond to changes in the location of the built-in position transducer on the patient bed. Therefore, many systems utilized location loops (LL) in order to determine the position of the surface of the skin above the organ relative to the SQUID detection coils [2, 3].

The iron concentration in different organs is an important parameter in the diagnosis and staging of human iron overload diseases such as genetic hemochromatosis. The recent discovery of the hemochromatosis gene in 80 to 100 % of clinical manifest hemochromatosis patients [4] will probably detect affected subjects in an early state of iron overload at 0.5 - 1.5 $\mathrm{mg/g_{liver}}$. Patients with ß-thalassemia major or other transfusion dependent chronic anemias accumulate iron from regular blood transfusions mainly in the liver. Subcutaneous infusion of the iron chelating compound deferoxamine or the intake of an oral chelator like deferiprone (or L1) is performed daily by the patients in order to achieve recommended liver iron concentration values between 1 and 2.1 $\mathrm{mg/g_{liver}}$ [5]. Changes of about 30 % will become relevant for the outcome of a positive or negative iron balance from a certain chelation treatment regimen.

SQUID voltages are analyzed as a function of distant dependent liver and thorax tissue fluxintegrals. Assuming a typical error of ± 0.5 mm in the skin-liver distance between 10 and 35 mm in patients of very different

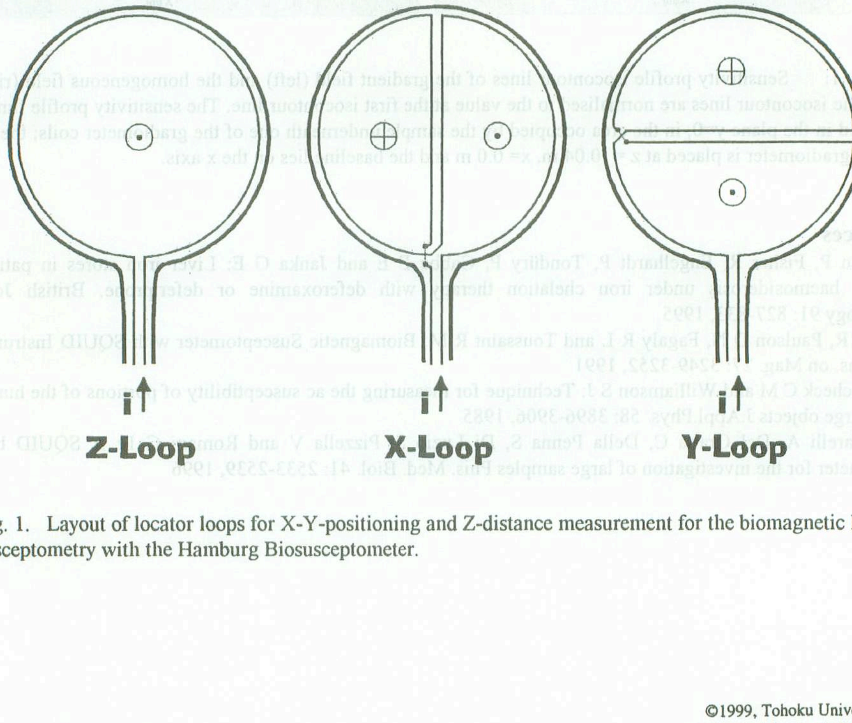

Fig. 1. Layout of locator loops for X-Y-positioning and Z-distance measurement for the biomagnetic liver susceptometry with the Hamburg Biosusceptometer.

©1999, Tohoku University Press
Recent Advances in Biomagnetism
T. Yoshimoto et al. (Eds)

stature results in an uncertainty in the liver iron concentration of 3.5 %. The location loops used so far [2] were hand crafted wire designs glued between thin quartz epoxy plates. Any replacement of these sensitive items at the end of their lifetime caused a recalibration with respect to distance and magnetic background. For routine patient measurements, we developed a new type of location loops for X-Y-positioning and Z-distance measurements under the latex membrane of a water bag (4 - 15 kg). Our aim was the development of a new locator loop design as a printed circuit with low background noise, reasonable mechanical stability and elasticity, with the advantage of high reproducibility.

Locator loop design

The LL-design for X-Y-positioning and Z-distance measurements (Fig. 1) is a combination of two double D-shaped coils (X- and Y-loops) and a single circular coil (Z-loop). The winding of belonging D-coils are opposite and X-, Y-loops are orthogonal to each other.

Both the singular circular Z-loop and the D-shapeded X-Y-loops have a diameter of 19 mm (Fig. 1). Due to the low background noise from prior magnetic measurements, a base material of 50 µm thick polyimid foils (capton) plated with 17 µm thin copper and 25 µm glue in-between was selected. The wire width of the printed circuit was chosen with 0.15 mm. Every loop (X, Y, Z) is located in one plane of a multilayer printed circuit. Wiring interconnection through the circuit planes have a diameter of 0.3 mm. Totally 4 polyimid foils with 3 layers of copper in-between were glued together (Fig. 2). The outer dimensions of the circular formed printed circuit (with a tail for electrical connections) are:

base material diameter = 20 mm, LL-thickness = 0.4mm, tail width = 4 mm, tail length = 300 mm.

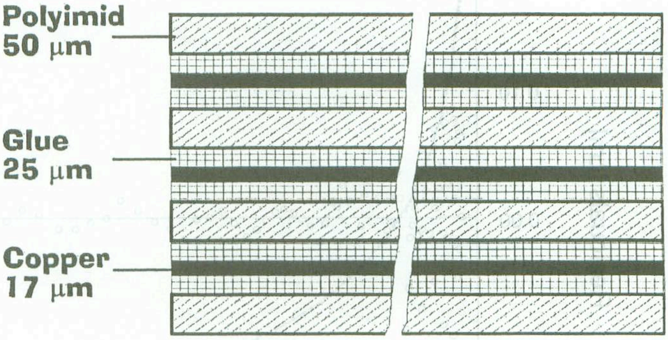

Fig. 2. Cut view through the locator loop printed circuit with a total thickness of 0.4 mm.

Principle of operation

X-Y-positioning of a patient is accomplished with the LL by an ac 2 mA$_{pp}$ sinusoidal current signal (206/286 Hz) of a pair of D-loops with opposite direction. Z-distance below the detection coils is determined in a similar way by an ac signal (2 mA$_{pp}$, 206 Hz) generated by the Z-loop positioned on the patient's skin above the liver.

The generated field of either the X-Y-loops or the Z-loop and the signals from biomagnetic organ susceptometry are detected simultaneously by the SQUID detection coils. Phase sensitive detection (by lock-in-amplifier) is used to extract the LL-signals and to reject noise. The locator loop signal (from unfiltered output of SQUID electronics) at 206 Hz or 286 Hz is far above frequencies of interest for organ susceptometry, with a bandwidth below 3 Hz.

If the LL is centred under the biomagnetometer detection coils, the magnetic field is cancelled out and the resulting signal is zero. Any deviation from the systems centre results in a positive or negative field. A real-time visualization of this deviation is made by a cross hair graphic on a monitor screen.

Calibration of the LL depth is done by lowering the LL below the biomagnetometer detection coil system and comparing the built-in bed position transducer against the LL-voltage (the LL has to be mounted rigidly on a holder). Measurement of background noise was done by registration of the magnetic background of the LL on a low susceptibility plastic phantom. This background contribution was fitted against the distance and stored in a data file for further subtraction from the raw SQUID-voltage in the data analysis procedure.

Results

The measurement for LL-calibration was performed by lowering the LL from 2.5 cm to 12 cm distance below the detector coil system. The measured voltage output of the lock in amplifiers from both SQUID channels (A and B) were fitted against the absolute Z-distance determined from the position transducer (Fig. 3). As a zero order fit, the formula for the magnetic flux Φ generated by a small coil (radius r, constant c) at far distance Z was used ($\Phi = c \cdot r^2/(Z^2 + r^2)^{3/2}$). For minimizing of deviations between measured LL-voltages and Z-distance, lower and higher order terms were used in Equ.1. Fit parameters of Equ. 1 for SQUID channel A and B are shown in Tab. 1. Finally, the parameters of Tab. 1 were stored in a parameter file and are available for online and final analysis of biomagnetic organ susceptometry. Z-distance determined from either SQUID-channel A or B has practically the same precision ($r^2_A = 0.99974$, $r^2_B = 0.99967$), but at far distances the residuals for the more sensitive SQUID-channel A are smaller. The reason is, because SQUID-channel A is more far distance sensitive.

Equu. 1 $$Z = a_0 + a_1 \times X + \frac{a_2}{X} + \frac{a_3}{\sqrt[2]{a_4 + X}} + \frac{a_5}{\sqrt[3]{X}}$$

Z = distance from LL to bottom of SQUID detector coils
X = LL-voltage
a_0, ...a_5 = fit parameters

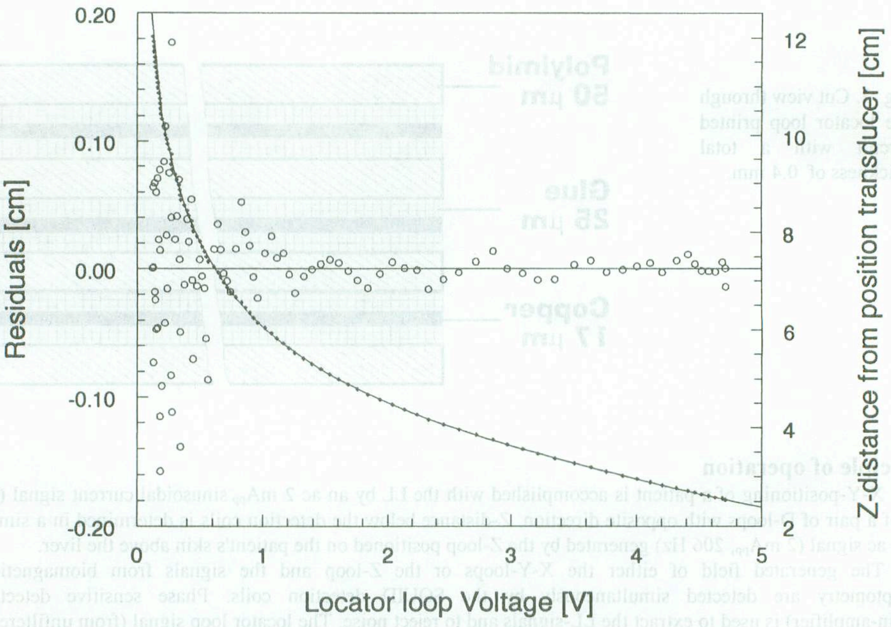

Fig. 3. Position transducer Z-distance as function of LL-voltage (right scale, black dots). The straight line is the fit of the measured LL-voltage according to Equ. 1. Open circles represent the residuals between measured data and the fit (left scale).

The present LL-design has only 40 % of the background noise compared to the former epoxy plate device [2]. In the data analysis of liver iron quantification, this background corresponds to a normal human liver iron concentration of 300 µg iron/g liver.

Discussion

As it is shown in Fig. 3, the described fit procedure converges at near (2.5 cm) and far distances (12 cm). In routine biomagnetic organ susceptometry only a span of 6 cm (from start to end of bed movement) will be used. From the residuals in Fig. 3 it is seen, that at distances below 6 cm the error in the Z-distance determination is smaller than 0.3 mm. Only at far distances above 8 cm the noise of the detected LL-signal is increasing the error of distance determination up to 1.5 mm, because the detectable signal for the lock in amplifier decreases below 15 mV. As shown in the layout of the LL (Fig. 1) the lead wires to the coils are parallel and in one horizontal plane and not twisted as in the system of Bastuscheck et al. [3]. Due to the small gap of 0.15 mm between the leads, the flux induced from the parallel wire components are not considered. However, any deviation from an ideal circular loop will be considered by the fit procedure. and is finally negligible.

Tab. 1. Fit parameters from the locator loop Z-distance calibration, according to Equ. 1 for SQUID channel A and B.

Locator loop A	Locator loop B
$r^2 =$ 0.99974	$r^2 =$ 0.99967
$a_0 =$ 5.4544	$a_0 =$ 0.6751
$a_1 =$ -0.4143	$a_1 =$ -0.1016
$a_2 =$ 0.9067	$a_2 =$ -0.1301
$a_3 =$ 13.0790	$a_3 =$ 0.9732
$a_4 =$ 0.1994	$a_4 =$ 0.0043
$a_5 =$ -11.8249	$a_5 =$ 3.3052

One main aspect in the development of a new LL was the reduction of background noise. The measured SQUID signal in human examination is a sum of background noise, e.g. liver and tissue signal. Before any iron analysis of SQUID measurements could be performed, the background from the locator loop must be known and subtracted. Especially in patients with low iron concentration, the signals from the liver are low. The achieved reduction of system background leads to more precise results.

Other important advantages of the new LL-construction are the high mechanical stability, the flexibility (it fits close to the body skin) and a very fast exchangeability. It's fast exchangeability without any new calibration is due to the high reproducibility of the fabrication process. Thus, this type of locator loop is well suited for the application in a clinical setting.

References

[1] Brittenham GM, Farrell DE, Harris JW et al: Magnetic susceptibility measurement of human iron stores. N Engl J Med 307: 1671-1675, 1982

[2] Paulsen DN, Fagaly RL, Toussaint RM, Fischer R: Biomagnetic susceptometer with SQUID instrumentation. IEEE Trans Magn 27: 3249-3252, 1991

[3] Bastuscheck CM, Williamson SJ: Technique for measuring the ac susceptibility of portions of the human body or other large objects. J Appl Phys 58 (10): 3896-3906, 1985

[4] Feder JN, Gnirke A, Thomas W et al: A novel MHC class I-like gene is mutated in patients with hereditary haemochromatosis. Nature Genetics 13; 399-408, 1996

[5] Olivieri N, Brittenham GM: Iron-chelating therapy and the treatment of thalassemia. Blood 89; 739-761,1997

Large-scale Study in Thalassemia Using Biomagnetic Liver Susceptometry

Fischer R[1], Piga A[2], De Sanctis V[3], Magnano C[4], Galanello R[5], Capra M[6], Di Gregorio F[7], Politis C[8], Brittenham GM[9], Töndury P[10], Engelhardt R[1], Longo F[2], Nielsen P[1], Dürken M[1], Gabbe EE[1]

Universität Hamburg[1], Germany; Università di Torino[2], Arcisp. S. Anna Ferrara[3], Osp. Garribaldi Catania[4], Università di Cagliari[5], Osp. Di Cristina Palermo[6], Università di Catania[7], Italy; University of Athens[8], Greece; Columbia University N. Y.[9], USA; Inselspital Bern[10], Switzerland.

Introduction

Iron overload from genetic disorders and/or regular blood transfusions is a serious health problem in many regions of the world. The precise quantitation and the continuous monitoring of liver iron stores is of particular importance in the treatment of these disorders. In order to improve the acceptance and to speed up the adoption of SQUID biomagnetic liver susceptometry (BLS) by clinical centers dealing with iron overload diseases, a total number of 700 patients with ß-thalassemia major and other hemoglobinopathies have been investigated between 1994 - 98. Most patients came from Italy or were of Italian origin. Others were of Greek, Turkish, or Near East origin. Preliminary results have been reported in recent years [1].

Methods and Patients

The Hamburg biosusceptometer facility (Ferritometer: BTi, USA) has been described in detail elsewhere [2]. Patients are lowered dynamically from the closest distance of 2.5 to 9.5 cm in a non-homogeneous magnetic field from 20 mT down to 1 mT. Data analysis is done by forward modeling of the magnetic flux change from ellipsoidal liver or spleen and spherical thorax geometries assessed by bed-side sonography (positioning, liver/spleen contour and volume determination). In this 2nd order approximation the SQUID voltages are fitted simultaneously to the precalculated flux integrals of liver and overlying thorax tissue scaled by their unknown magnetic volume susceptibilities [3]. In the routine application of the BLS method a rough estimation of the magnetic susceptibility of the thorax tissue from the body mass index is sufficient [1]. Beside inter-run statistics, total error estimation include systematic errors in the thorax tissue susceptibility of $\Delta\chi = 0.05 \cdot 10^{-6}$ SI units and in the skin-liver distance of $\Delta z = 0.5$ mm. The resulting total errors of liver iron concentration (LIC) range from 50 to 300 µg/g-liver in most patient measurements.

The clinical verification of the non-invasive BLS method was performed by comparing the in vivo results as µg/g-liver (µg/g-liv) with the physico-chemical determination of total, ferritin and hemosiderin iron as µg/g-wet weight (µg/g-ww) by atomic absorption spectroscopy (AAS) in liver biopsies [4]. The biopsy sample size is of crucial importance in the precise quantitation of LIC and a size of m > 3 - 5 mg-ww is recommended. Liver biopsies in most patients with ß-thalassemia major were performed as fine needle biopsies. The iron content was determined by AAS and calculated as µg/g-dry weight (µg/g-dw). From the water content of normal liver tissue of about 71% a drying factor of 3.46 is derived. Normal liver volumes were calculated from the body surface area. In thalassemic patients, livers were found to be enlarged relative to normal livers by a factor of about 1.5 (see Tab. 1). Thus, to compare the in vivo results from BLS on the same scale, a drying factor of 5 was assumed for "dry-weight" liver biopsies (n = 131). LIC determined from "wet-weight" biopsies (n=7) were not scaled.

Serum ferritin (SF) was performed by current methods in the different thalassemia centers. Additionally, ferritin was also determined at the time of the BLS measurement by a chemoluminescence assay (ACCESS® immunoassay: Sanofi Diagnostics Pasteur, Germany) calibrated by the international ferritin standard. No significant deviations could be attributed to the different ferritin assays used in the centers. Other clinical parameters such as serum levels of the liver enzyme alanine aminotransferase (ALT) and antibodies for a hepatitis C virus (HCV) infection were tested at the different centers.

Serum ferritin, liver iron concentration and ALT have skewed distributions in iron overload states. Therefore, median values, geometric means, and 2.5 or 97.5% percentiles were calculated instead of mean values and standard deviations (SD). Correlations between these parameters have been performed only after logarithmic transformation or equivalent power functions have been used.

Patients with ß-thalassemia major, intermedia and minor, ex-thalassemic patients after bone marrow transplantation (BMT), and patients with sickle cell disease and with a mixed gene mutation sickle cell / ß-thalassemia were investigated (see Tab. 1). The group of rare anemias included α-thalassemias, Lepore, dominant thalassemia, aplastic anemias, Blackfan Diamond, congenital dyserythropoetic anemia and hemolytic anemias. Patients between 5 and 63 y could be measured without any problems. In children younger than 5 y of age, a sedation had to be used in most cases. Nearly all patients were initially under the traditional subcutaneous chelation treatment with deferoxamine. For comparison, also data of patients with genetic hemochromatosis were used.

©1999, Tohoku University Press
Recent Advances in Biomagnetism
T. Yoshimoto et al. (Eds)

Results and Discussion

SQUID biosusceptometry results together with liver volumes are summarized in Tab. 1 for the different groups. For the iron concentration from BLS, median values are given together with 2.5% and 97.5% percentiles. Patients with ß-thalassemia major (n=596) were by far the largest group of patients with iron overload from regular blood transfusions. LIC values were found between 87 and 11470 µg/g-liv.

Tab. 1 Groups of different hemoglobinopathies and mean (median) values with range (percentiles) or standard deviation (SD) for age, liver iron concentration (LIC), liver volume, and liver volume enlargement ratio.

Diagnosis	**n**	**age [y]**			**LIC by BLS [µg/g-liv]**			**Liver Volume [ml]**		**Enlargement**	
		mean	min	max	median	2.5%	97.5%	mean	SD	mean	SD
normal					*300*	*100*	*400*	*1200*		*1.00*	
ß-thal. major	596	20.9	1.8	47.4	1586	287	7581	1610	588	1.35	0.37
ß-thal. intermedia	28	24.7	5.2	48.2	1517	327	4283	1886	660	1.46	0.30
ß-thal. minor	7	37.1	26.4	42.3	217	131	467	n.d.			
ex-ß-thal. a. BMT	26	17.1	4.9	25.0	1097	289	4806	1337	397	1.18	0.23
sickle c. / ß-thal.	17	22.0	10.5	35.6	1243	172	6395	1879	647	1.44	0.37
sickle cell disease	5	16.2	4.5	37.6	1188	225	3429	1954	1317	1.88	0.42
rare anemias	21	21.7	1.7	63.0	950	197	3995	1710	868	1.55	1.05

Liver biopsies were available in 138 patients with thalassemia. However, constraints in the biopsy weight (m-dw > 0.5 mg) and in the time between the biopsy and the last BLS measurement (< 12 months) reduced this number to 80. In Fig. 1 a linear functional relationship between the two methods of iron quantitation was performed for LIC < 5000 µg/g-ww in biopsies. For the more severely iron overloaded patients, liver cirrhosis is highly probable with resulting uneven iron distribution in the liver [5]. For comparison, iron quantitation in "wet-weight" biopsies from 40 patients with genetic hemochromatosis, performed for the verification of the BLS method [4] is superimposed in Fig. 1. LIC values with large error bars indicate patients where at least two biopsies were available from the same liver lobe. This obviously uneven iron distribution could also be interpreted as sign of cirrhotic liver tissue.

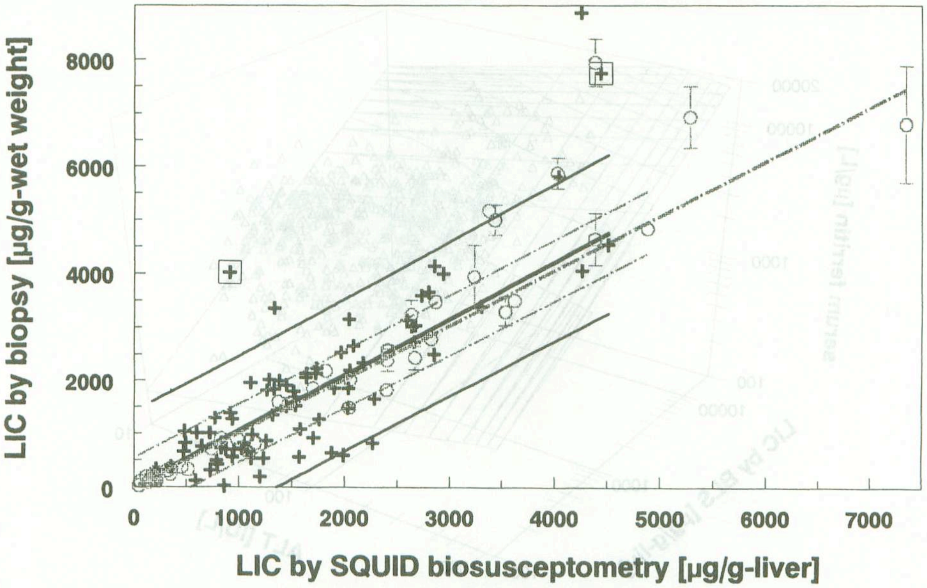

Fig. 1 Liver iron concentration (LIC) in patients with thalassemia major (crosses) and genetic hemochromatosis (circles) from chemical quantitation in biopsies and biomagnetic measurements. Linear functional relationship with 95% prediction range and coefficients of determination R²= 0.63 for thalassemia major (solid lines) and R² = 0.96 for hemochromatosis patients (dash-dot lines).

In principle, BLS should be superior to the physico-chemical quantitation of iron in liver biopsy samples due to the assessment of larger, more representative liver portions. Only a poor correlation could be achieved in the thalassemia patients ($R^2 = 0.63$) in contrast to patients with genetic hemochromatosis ($R^2 = 0.96$). The resulting 95% prediction range in Fig. 1 shows this difference even more clearly. Thus, liver biopsies allow a quantitation of iron only within a mean error range of 2800 µg/g-ww for thalassemic patients and within 1300 µg/g-ww for hemochromatotic patients, whereas the patient related error for BLS is between 50 and 300 µg/g-liv [3]. The higher degree of fibrosis due to frequent hepatitis C infection in patients with thalassemia may explain in part the uneven iron distribution. This may be especially true for elder patients. Typically, those patients with the largest deviations in Fig. 1 (squared crosses) were older than 20 y. Another explanation is an increase in the water content of the liver due to a significant liver enlargement as can be seen from Tab. 1. In hemochromatosis no significant liver enlargement could be observed in most patients. However, part of the deviations in thalassemia patients have also to be attributed to the smallness and imperfect determination of the weight of liver biopsies (50 % of biopsies < 3.7 mg-ww).

Serum ferritin is a standard laboratory parameter in the monitoring of iron overload at almost all thalassemia centers around the world. The rationale since decades is that this iron protein allows the estimation of the non-heme iron stores. There is no doubt about the benefit of this parameter in patients with subnormal or normal iron stores. In iron overload states the two iron pools (reticulo-endothelial system, hepatic iron stores) may influence the serum ferritin value in an individual manner. Moreover, acute or chronic inflammation processes indicated by the presence of hepatitis C virus infection (HCV) or by elevated serum levels of the liver enzyme ALT, usually increase the serum ferritin level.

Although, a highly significant correlation between LIC and SF was found by different authors and also in this work, only a poor prediction range for LIC estimation could be derived [6]. For the group of patients with ß-thalassemia major a correlation coefficient of $R=0.69$ ($p<10^{-3}$) was found for those patients positive for HCV and only a slightly better coefficient of $R=0.71$ for those patients tested negative for HCV infection. However, there was no significant difference in the logarithmic correlation between these two groups. Thus, a typical serum ferritin value at 1000 µg/L allows the prediction of LIC only within a 95% range from 150 to 3100 µg/g-liv.

Beside the standard correlation between serum ferritin and liver iron concentration, there is also a significant but weaker correlation of SF with serum levels of the liver enzyme ALT ($R=0.34$, $p < 10^{-3}$). A multiple logarithmic correlation of SF with BLS and ALT, improved the correlation (from $R = 0.69$ to $R = 0.77$) with significant contributions from BLS and ALT. In Fig. 2 the additional dependence of the SF - LIC correlation from the ALT values is demonstrated with a steeper slope at elevated ALT levels > 50 IU/L.

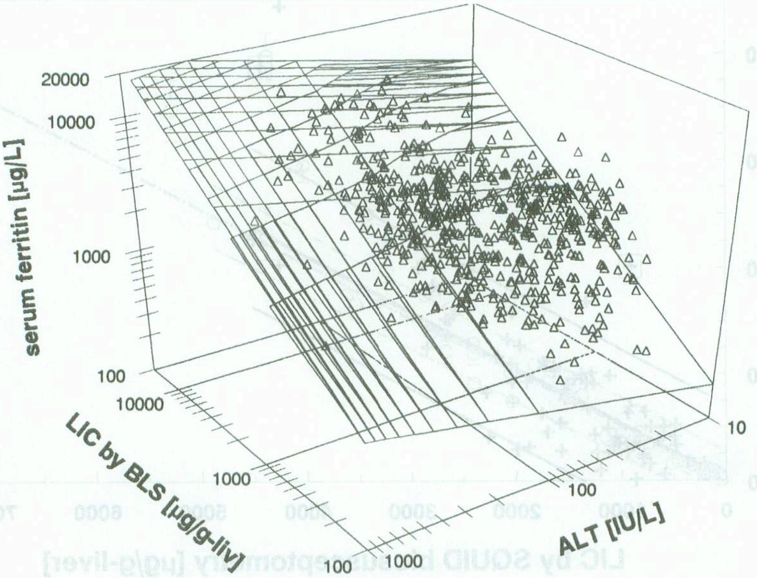

Fig. 2 Multiple linear correlation (after logarithmic transformation) between serum ferritin estimations and biomagnetic liver susceptometry results and serum values of the liver enzyme ALT ($R = 0.77$, $p < 10^{-4}$) in patients with ß-thalassemia major.

It is known that ex-thalassemic patients after bone marrow transplantation have relatively lower serum ferritin levels than patients with ß-thalassemia major at the same LIC value [7]. Patients of different thalassemic traits were investigated with respect to the logarithmic correlation between SF and LIC in Tab. 2. All correlations were highly significant at $p < 10^{-3}$. Significant differences could be observed between patients with ß-thalassemia major and patients of other thalassemic traits. Especially, the correlation of SF with BLS in patients with ß-thalassemia intermedia was steeper and similar to ex-thalassemics after BMT and to that of patients with genetic hemochromatosis for comparison [8]. Patients with the mixed gene mutation sickle cell disease / ß-thalassemia showed the best correlation with 82% of SF values within the range of ± 1 standard deviation.

Tab. 2 Statistical results in patients of different thalassemic traits and in patients with genetic hemochromatosis for comparison: antilogarithm means and correlation parameters between serum ferritin (SF) and liver iron concentration (LIC) from SQUID biosusceptometry $SF = a_0 \cdot LIC^{a_1}$.

patient group	**SF** [µg/L]	**LIC** [µg/g-liv]	**R²**	**$a_{0 \pm \Delta a0}$ [µg/L]**	**$a_{1 \pm \Delta a1}$**
ß-thalassemia major	1861	1644	0.48	11.6 ± 1.2	0.69 ± 0.03
ß-thalassemia intermedia	833	1267	0.65	0.3 ± 5.7	1.13 ± 0.24
ex-ß-thal. after BMT	383	711	0.55	0.2 ± 3.4	1.17 ± 0.19
sickle c. / ß-thalassemia	1984	1188	0.82	2.9 ± 2.4	0.92 ± 0.12
gen. hemochromatosis	746	1779	0.53	0.1 ± 2.3	1.16 ± 0.11

As many thalassemic patients are nowadays treated with the oral chelator deferiprone (DFP, former name L1) instead of the standard treatment by daily subcutaneous infusions of deferoxamine (DFO), the problem of differences in the serum ferritin response to the size of non-heme iron stores under different chelator treatment regimen may be raised. Comparing only thalassemic patients who were treated initially with DFO and thereafter with DFP, a clear difference was observed with relatively smaller serum ferritin values at liver iron concentrations below 2000 µg/g-liv. A larger regression coefficient was determined for the patients under DFP ($a_1 = 0.80 \pm 0.07$) than under DFO ($a_1 = 0.52 \pm 0.07$), whereas the scattering was the same under both therapies ($R^2 = 0.39$). Patients tested additionally negative for HCV, exhibited an even steeper response of serum ferritin ($a_1 = 0.94 \pm 0.13$).

SQUID biomagnetic liver susceptometry seems to be less affected by an uneven iron distribution than the iron quantitation in liver biopsies of patients with ß-thalassemia and may serve as the reference standard of primary choice. Monitoring iron overload by BLS is shown to be far superior to the standard laboratory parameter serum ferritin in nearly all thalassemic patients with mild or severe iron overload.

References

[1] Fischer R, Piga A, Tricta F, Nielsen P, Engelhardt R, Garofalo F, Di Palma A, Vullo C: The use of biomagnetic liver susceptometry in the Ferrara-Hamburg-Turin study on thalassemia. Aine C, Okada Y, Stroink G, Swithenby S, Wood C (eds): Biomag96: Advances in Biomagnetism Research. New York: Springer, in press, 1998

[2] Paulson DN, Fagaly RL, Toussaint RM, Fischer R: Biomagnetic susceptometer with SQUID instrumentation. IEEE Trans Magn 27: 3249-3252, 1991

[3] Fischer R: Liver iron susceptometry. Andrae W and Nowak H (eds): Magnetism in Medicine: A Handbook. Berlin: Wiley-VCH, 1998, pp 286-301

[4] Fischer R, Engelhardt R, Nielsen P, Gabbe EE, Heinrich HC, Schmiegel WH, and Wurbs D (1992): Liver iron quantification in the diagnosis and therapy control of iron overload patients. Hoke M, Erné SN, Okada YC, and Romani GL (eds): Advances in Biomagnetism '91. Amsterdam: Elsevier, 1992, pp 585-588

[5] Ambu R, Crisponi G, Sciot R, VanEyken P, Parodo G, Iannelli S, Marongiu F, Silvagni R, Nurchi V, Cost V, Faa G, and Desmet VJ: Uneven hepatic iron and phosphorous distribution in ß-thalassemia. J Hepatol 23: 544-549, 1995

[6] Brittenham GM, Cohen AR, McLaren CE, Martin MB, Griffith PM, Nienhuis AW, Young NS, Allen CJ, Farrell DE, and Harris JW: Hepatic iron stores and plasma ferritin concentration in patients with sickle cell anemia and thalassemia major. Am J Hematol 42: 81-85, 1993

[7] Fischer R, Nielsen P, Dürken M, Engelhardt R, Garofalo F, Gamberini MR, Zander A, Janka GE, Gabbe EE, and Piga A: The method of biomagnetic liver susceptometry in the follow-up of thalassemic patients after BMT. Bone Marrow Transpl 19 (suppl. 2): 136-138, 1997

[8] Nielsen P, Fischer R, Engelhardt R, Dresow B, and Gabbe EE: Neue Möglichkeiten in der Diagnose der hereditären Hämochromatose. Deut Ärztebl, in press, 1998

Possible Magnetic Detection of Injury Currents in Bean Plants

Jazbinšek V[1], Thiel G[2], Mueller W[3], Trontelj Z[1]

[1]*Institute of Mathematics, Physics and Mechanics, University of Ljubljana, Ljubljana, Slovenia;*
[2]*Pflanzenphysiologisches Institut, Universität Göttingen, Göttingen, Germany;*
[3]*Physikalisch-Technische Bundesanstalt, Institut Berlin, Berlin, Germany*

Introduction

Several animal [1, 2] and plant [3, 4] species respond to injury with electrical activity. In plants local burning injury on a leaf causes slow, often bi-phasic relaxation of the membrane potential (Vm) [5, 6]. These wound induced electrical events spread with a slow velocity (less than 1 *cm/s*) over the entire plant[3, 4]. There is now compelling evidence, that this systemic propagation of electrical signals is a mechanism by which local injury signals are transmitted over long distances [3, 6]. When reaching distant parts of the plant the electrical signal stimulates expression of wound induced genes as part of a defence reaction [3, 6].

The mechanism of electrical propagation is not yet fully understood. One possibility is that a travelling, but as yet unknown chemical substance causes depolarization of Vm [4]. Alternatively, it was proposed [3, 5, 6] that propagation is entirely electrical. In this context, a low resistance electrical continuum of the sieve-tube element/companion cell complex was envisaged as dominant electric conduction pathway [5]. Recent cell type specific recordings of injury evoked depolarization in tomato plants found that the entire vein contributes to electrical propagation. Due to poor electrical connections between these cells also a contribution of the apoplast was proposed in propagation [6].

In order to further elucidate the proposed current pathways and to better understand the global current distribution over the entire plant together with the nature of currents, biomagnetic measurements of electrical activity in bean plant tissue has been conducted. Before the analysis of measurements on all plants a very careful simulation study was accomplished.

Methods

Measurements were conduced on 21-23 day old Vicia faba (cv Hangdown) plants. Plants were grown in garden peat in the green house.

Electric measurements of the membrane potential of vascular leaf cells were conducted with conventional intracellular electrodes. The leaf of a bean plant was therefore fixed into a chamber and immersed in standard recording solution containing 1 mM KCl, 0.5 mM $CaCl_2$, 0.5 mM NaCl and 0.5 mM Mes/KOH pH 6.1 (see Fig. 1). The Vm recording electrode was impaled into cells of the vascular tissue on the lower surface of a leaf. A reference electrode was connected via an agar bridge (2% agar/ 200 mM KCl) with the bath solution. Ag/AgCl wires in both electrodes (filled with 200 mM KCl) were connected to a high impedance amplifier and Vm measured as voltage difference between the two electrodes. The injury was introduced by locally burning (approximately $2cm^2$) leafs downstream of the recording leaf.

Magnetic measurements were performed on 10 bean plants in the Berlin Magnetically Shielded Room [7] with 37-channel SQUID magnetometer system[8]. Since the expected injury currents are almost dc, measured signals were modulated (similarly as in [1]) by installing the plant on a moving table that was oscillating sinusoidally with frequency 0.5 Hz in vertical direction with peak-to-peak amplitude 3-5 cm. Duration of each measurement (T_{mes}) was 20-25 minutes. Sampling frequency was 250 Hz and the analog frequency band was 0.016 - 64 Hz. The measured data were compressed by applying low pass digital filter with cut-off frequency equal to 2 Hz and by re-sampling the filtered data with 5 Hz rate. Within the first 5 minutes the plant was injured by a burning candle placed for a few seconds under one of the leafs from the oldest leaf pair. Younger leafs were immersed in a chamber containing standard recording solution as it is shown in Fig. 5a.

Data analysis was performed in frequency domain by applying Fast Fourier Transform (FFT) to successive data intervals

$$D_i = [t_i - T/2, t_i + T/2], \quad t_i = T/2 + i \cdot \Delta_t, \quad i = 0, 1, \ldots N_t, \quad N_t = (T_{mes} - T)/\Delta_t, \qquad (1)$$

where T is length of data interval D_i around i-th time t_i. N_t and Δ_t denote number of time points and step between two successive points, respectively. For each step in the time signal reconstruction procedure – we called it STEP-FFT – we calculate:

$F_m^k(D_i)$ – FFT of magnetic k–th channel data on time interval D_i at modulation frequency f_m

©1999, Tohoku University Press
Recent Advances in Biomagnetism
T. Yoshimoto et al. (Eds)

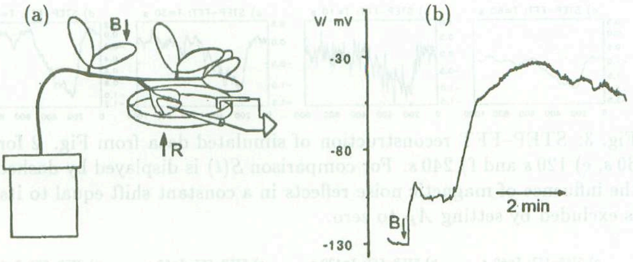

Fig. 1: Sketch of intracellular electrical membrane potential measuring set–up (a). The plant is burned on the leaf B downstream of the recording leaf R. In the typical example of an injury evoked membrane depolarization (b) the distance between B and R was 7 cm.

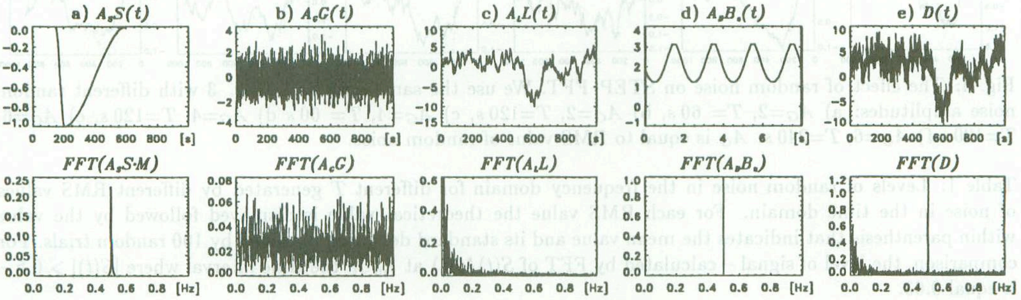

Fig. 2: Simulated data for $\vec{A} = [A_S, A_G, A_L, A_B]$= [-1,1,0.01,1] (displayed in the upper row) and their FFT amplitude low frequency spectra (displayed in the lower row): a) signal $A_S S(t)$, b) Gaussian noise $A_G G(t)$, c) low frequency noise $A_L L(t)$, d) magnetic dipole $A_B B_z(t)$ and e) whole simulated data $D(t)$. The FFT spectrum at a given frequency is equal to the amplitude of corresponding sine wave in the time domain.

$F^k_m(D_i)$ – FFT of magnetic k–th channel data on time interval D_i at modulation frequency f_m

$F^M_m(D_i)$ – FFT of moving table (modulation) data on time interval D_i at modulation frequency f_m

The signal amplitude at time t_i is determined by the absolute value of $F^k_m(D_i)$. The signal polarity is obtained by comparing angles between real and imaginary components of complex frequency domain data $F^k_m(D_i)$ and $F^M_m(D_i)$. A distance between discrete points in frequency domain Δ_f is equal to $1/T$, therefore one has to select in STEP-FFT such T that the modulation frequency f_m coincides with one of points in the frequency domain.

We have tested STEP-FFT procedure by the computer simulation. The biomagnetic signal is simulated with two cubic polynomials representing depolarization and repolarization response (see Fig.2a)

$$S(t) = \begin{cases} [1 - 3(\frac{t-t_s-t_r}{t_d})^2 - 2(\frac{t-t_s-t_r}{t_d})^3 & \text{if } t_s \geq t < t_s + t_r \\ [1 - 3(\frac{t-t_s-t_r}{t_r})^2 + 2(\frac{t-t_s-t_r}{t_r})^3 & \text{if } t_s + t_r \geq t < t_s + t_r + t_r \\ 0 & \text{otherwise} \end{cases} \tag{2}$$

where t_s denotes the signal beginning, t_d and t_r represent duration of depolarization and repolarization, respectively. Signal function $S(t)$ in Eq. (2) is then multiplied with modulation $M(t) = sin(2\pi f_m t + \phi)$ that simulates oscillating table with modulation frequency $f_m = 0.5\,Hz$ and phase shift ϕ. Measured noise is generated by composing three contributions. Random noise $G(t)$ (Fig. 2b) has Gaussian distribution with the root mean square value (RMS) equal 1. Low frequency (1/f) noise is generated by a sum of sine waves on frequency interval $[f_0, f_1] = [0.001, 1.0]\,Hz$ (Fig. 2c)

$$L(t) = \sum_{f=f_0}^{f_1} G(f)\frac{f_m}{f} sin(2\pi f t + \phi_u(f)) \tag{3}$$

where $\phi_u(f)$ denotes randomly distributed phase shifts on interval $[-\pi, \pi]$. Summation step is $0.001\,Hz$. Noise due to magnetic impurities on a moving sample is generated by magnetic dipole $\vec{Q}$ (Fig. 2d)

$$B_z(t) = \frac{\mu_0}{4\pi r^5(t)}[3z(\vec{Q}\cdot\vec{r}(t)) - r^2(t)Q_z] \tag{4}$$

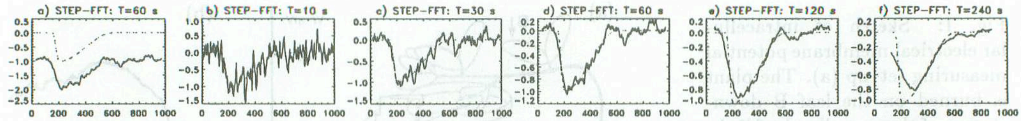

Fig. 3: STEP-FFT reconstruction of simulated data from Fig. 2 for different T : a) $60\,s$, b) $10\,s$, c) $30\,s$, d) $60\,s$, e) $120\,s$ and f) $240\,s$. For comparison $S(t)$ is displayed by dashed curve on each graph. Plot a) shows that the influence of magnetic noise reflects in a constant shift equal to its amplitude A_B. On other plots this noise is excluded by setting A_B to zero.

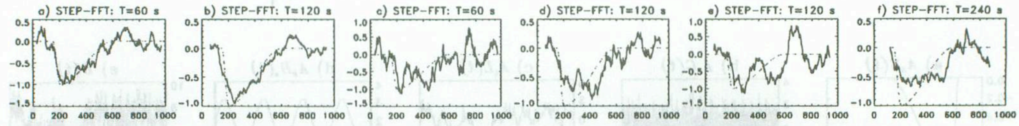

Fig. 4: The effect of random noise on STEP-FFT. We use the same data as in Fig. 3 with different random noise amplitudes: a) A_G=2, T= $60\,s$, b) A_G=2, T=$120\,s$, c) A_G=4, T= $60\,s$ d) A_G=4, T=$120\,s$, e) A_G=6, T=$120\,s$ f) A_G=6, T=$240\,s$. A_G is equal to RMS value of random noise.

Table 1: Levels of random noise in the frequency domain for different T generated by different RMS values of noise in the time domain. For each RMS value the theoretical value is displayed followed by the value within parenthesis that indicates the mean value and its standard deviation obtained by 100 random trials. For comparison, the level of signal – calculated by FFT of $S(t)M(t)$ at f_m in the time interval where $|S(t)| > 0.5$ – is equal 0.63.

$T[s]$	RMS=2.0	RMS=4.0	RMS=6.0	RMS=8.0	RMS=10.0
10	0.566(0.507±0.246)	1.131(1.020±0.517)	1.697(1.543±0.794)	2.263(2.060±1.061)	2.828(2.393±1.315)
30	0.327(0.309±0.144)	0.653(0.635±0.286)	0.980(0.813±0.424)	1.306(1.278±0.681)	1.633(1.491±0.795)
60	0.231(0.194±0.103)	0.462(0.397±0.203)	0.693(0.666±0.344)	0.924(0.800±0.416)	1.155(0.959±0.502)
120	0.163(0.132±0.070)	0.327(0.303±0.161)	0.490(0.412±0.225)	0.653(0.526±0.320)	0.816(0.743±0.361)
240	0.115(0.105±0.048)	0.231(0.211±0.110)	0.346(0.327±0.173)	0.462(0.401±0.211)	0.577(0.519±0.249)

where $\vec{r}(t) = [x, y, z(t)]$ – a vector pointing from the observer to the dipole position – is oscillating in vertical direction with amplitude z_m around z_0: $z(t) = z_0 + z_m \cdot M(t)$. The whole simulated data is (Fig. 2e)

$$D(t) = A_S S(t)M(t) + A_G G(t) + A_L L(t) + A_B B_z(t) = \vec{A} \cdot [S(t)M(t), G(t), L(t), B_z(t)] \tag{5}$$

where $\vec{A} = [A_S, A_G, A_L, A_B]$ denotes amplitude vector with components that represent amplitudes of signal, random noise, low frequency noise and magnetic impurities noise, respectively.

Results

In simulation calculations we have generated data in $1000\,s$ time sequence with the following parameters: $t_s = 150\,s$, $t_d = 50\,s$, t_r=$400\,s$. The magnetic dipole $\vec{Q}$ is normalized in such way that B_z in Eq. (4) generates the same peak-to-peak value as signal $S(t)\cdot M(t)$ defined in Eq. (2). Fig. 2 shows all contributions to simulated data and their amplitude frequency spectra for $\vec{A} = [A_S, A_G, A_L, A_B]$=[-1,1,0.01,1]. Fig. 3 shows STEP-FFT reconstruction of data from Fig. 2. The magnetic noise B_z produces a constant shift with amplitude A_B (Fig. 3a) that can be completely removed by subtracting it from the reconstructed data. Selection of longer T improves the signal to noise ratio (Figs. 3b,c,d), but it also distorts the signal if T is longer than signal rise time (Figs. 3e,f). Random noise $A_G G(t)$ and low frequency noise $A_L L(t)$ have similar influence on STEP-FFT. They both increase the value of FFT spectra at f_m and if their contribution become comparable to the signal FFT then STEP-FFT fails to reconstruct the signal. Fig. 4 shows the influence of $A_G G(t)$ on STEP-FFT and Table 1 displays levels of random noise in the frequency domain for different T.

Fig. 5 shows results of STEP-FFT analysis of magnetic measurements data for the two cases where we observed the response of a bean plant to the heat injury.

Discussion

The analysis of simulated signal together with the most important types of noise gives the limits beyond which the applied data analysis technique could not extract the signal. Inspecting all measurements we have seen that the instrumentation noise, the random environmental noise and the $1/f$ noise are within acceptable

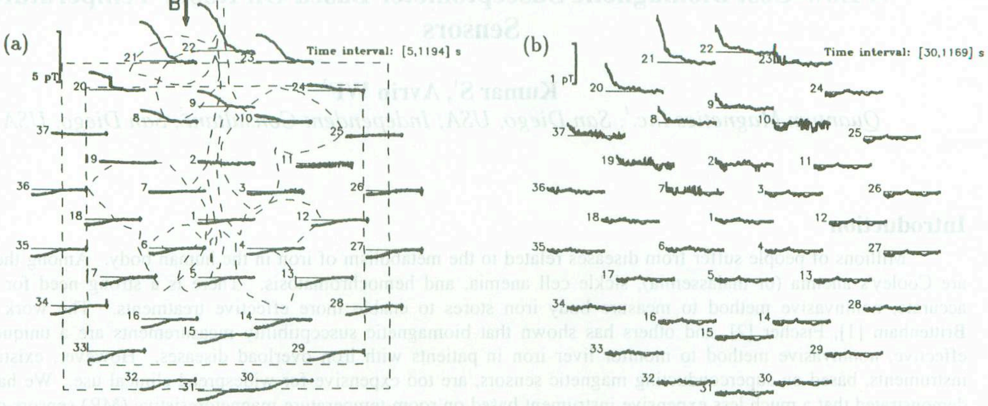

Fig. 5: Magnetic measurements reconstructed by STEP-FFT for two plants a) $T=10\,s$ and b) $T=60\,s$. Dashed lines in (a) show the plant position and a chamber into which we immersed plants during the measurement. The plant is burned on the leaf B. The measurement in case (a) was performed in total compensation mode – the mean signal over all channels was subtracted from the data in each acquisition point. The case (b) was measured with a normal mode and therefore a longer T was necessary.

limits in most of the measurements. The magnetic contamination could still remain after the usual inspection and preventive demagnetization and therefore some plants had to be excluded from further analysis. Fig. 5a,b demonstrates the two final cases where we believe that space and time evolution of biomagnetic signal reflects the propagating current from the place of heat injury along the plant. The signal time evolution, obtained after the STEP-FFT reconstruction, allows the estimation of signal spreading velocity. The approximate value is less than $1\,cm/s$ that is in agreement with the reported values [3, 4].

The possible dc part of measured magnetic field due to the part of injury currents driven by the trans-membrane resting potential gradient is difficult to determine. It could be easily masked by the contribution of magnetic impurities.

We conclude that our measurements and analysis demonstrate the possibility of biomagnetic detection of heat induced injury currents and their spreading velocity in bean plants.

References

[1] Curio G, Erné S N, Burghoff M, et al: Non-invasive neuromagnetic monitoring of nerve and muscle injury currents. Electroenceph Clin Neurophys 89:154–160, 1993

[2] Trontelj Z, Pirnat J, Lužnik J, et al: Measurement of magnetic field near an acute surgical injury on the rabbit's thigh, Williamson S J, Hoke M, Stroink G, et al (eds): Advances in Biomagnetism. New York: Plenum, 1989, pp 517–520

[3] Wildon D C, Thain J, Minshin P, et al: Electrical signalling and systemic proteinase inhibitor induction in wounded plant. Nature 360:62–65, 1992

[4] Roblin G, Bonnemain J-L: Propagation in Vicia faba stem of a potential variation induced by wounding. Plant Cell Physiol 26:1273-1283, 1985

[5] Rhodes J D, Thain J F, Wildon D C: The pathway for systemic electrical signal conduction in the wounded tomato plant. Planta 200:50-57, 1996

[6] Herde O, Pena-Cortes H, Willmitzer L: Remote stimulation by heat induces characteristic membrane-potential responses in veins of wild-type and abscisic acid-deficient tomato plants. Planta 206:146-153, 1998

[7] Erné S N, Hahlbohm H-D, Scheer H et al: The Berlin magnetically shielded room (BMSR): Section B – performances, Erné S N, Hahlbohm H-D and Lübbig H (eds): Biomagnetism. Berlin: Walter de Gruyter, 1981, pp 79–87

[8] Koch H, Cantor R, Drung D, et al: A 37 channel dc SQUID magnetometer system. IEEE Trans Magn MAG-27(2):2793–2796, 1991

A Low-Cost Biomagnetic Susceptometer Based On Room-Temperature Sensors

Kumar S[1], Avrin WF[2]

Quantum Magnetics Inc.[1], San Diego, USA; Independent Consultant[2], San Diego, USA

Introduction

Millions of people suffer from diseases related to the metabolism of iron in the human body. Among these are Cooley's anemia (or thalassemia), sickle cell anemia, and hemochromatosis. There is a strong need for an accurate, noninvasive method to measure body iron stores to enable more effective treatments. The work of Brittenham [1], Fischer [2], and others has shown that biomagnetic susceptibility measurements are a uniquely effective, noninvasive method to monitor liver iron in patients with iron overload diseases. However, existing instruments, based on superconducting magnetic sensors, are too expensive for widespread clinical use. We have demonstrated that a much less expensive instrument based on room-temperature magnetoresistive (MR) sensors can make magnetic susceptibility measurements with a precision more than adequate for monitoring liver iron. We have measured the magnetic susceptibility of a liver phantom, at a distance comparable to the depth of the liver below the abdominal surface, with a statistical uncertainty equivalent to an iron concentration of 30 μg/ml. This instrumental resolution is within 50% of that previously reported for SQUID-based instruments [3]. It is well below the normal range of liver iron (200 - 500 μg/ml), and 50 times lower than the level (1500 - 2000 μg/ml) that is typically maintained in patients undergoing iron chelation therapy [4].

Methods

The performance of the room-temperature instrument depends on two critical issues: (a) the instrument has to be sensitive enough to see the small magnetic signals produced by the magnetic susceptibility of the liver, and (b) the liver susceptibility has to be determined accurately in the presence of the interfering signal produced by the slight magnetic susceptibility of the abdominal wall and other surrounding tissues.

To measure a given magnetic susceptibility, we do not necessarily need the lowest possible noise in the magnetic sensors themselves. All we need to do is to ensure that the response of the sample is above the sensor noise. Since the magnetization of the sample is proportional to the applied field, we could in principle make the magnetic response as large as we want, by applying a large enough magnetic field. However, we have to be careful not to create excessive ohmic heating by applying too large a current in the coil used to provide the applied field. Excessive ohmic heating can cause thermal drifts and thereby reduce the system sensitivity.

We designed an applied field coil with which fields of sufficient strength could be applied without excessively heating the coil. With an applied field of 10^{-3} T a liver with a normal iron concentration will respond with a field about $3 \text{ X } 10^{-7}$ times, resulting in a response field of $3 \text{ X } 10^{-10}$ T. We can easily detect such fields by taking advantage of recent advances in the performance of room-temperature magnetic sensors. MR sensors with very low noise have been developed by Kodak [5], Honeywell, and other companies. With the Kodak sensors, we have observed noise spectral densities below 3×10^{-11} T/√Hz. With a measurement bandwidth of 0.1 Hz (three seconds of data averaging) these sensors would give us a rms sensor noise of 10^{-11} T. This noise level is thirty times below our estimated liver-iron signal of $3 \text{ X } 10^{-10}$ T.

Our requirements for noise-rejection are less stringent than those of the existing SQUID biosusceptometers. The SQUID systems use dc magnetic fields, since they are designed to exploit the extremely stable magnetic fields produced by persistent currents in a superconducting magnet. These systems produce a time-varying magnetic signal by moving the patient up and down at a frequency of 0.5 Hz. However, even with this modulation, the measurement takes place at a rather low frequency. At such frequencies, the background noise in many environments is quite large. Our room-temperature system applies an ac magnetic field at 270 Hz, and detects the magnetic response at the same frequency. At these frequencies, environmental background fluctuations are usually rather small, as long as we avoid the noise peaks at harmonics of the power-line frequency. We have experienced no major difficulty with background noise in our susceptibility measurements on the liver.

One key concern is the stability of the current in the coils that produce the applied field. Our instrument is designed so that fluctuations in the coil current have only a negligible effect on the magnetic measurements. Our technique is to configure the applied-field coil so that it produces almost no field at the location of the magnetic sensor. Were the magnetic sensor to see the full amplitude of the applied field, then the current in the field coils

©1999, Tohoku University Press

Recent Advances in Biomagnetism
T. Yoshimoto et al. (Eds)

would have to be stable to at least one part in 10^7 in order to resolve the weak magnetic signals we want to detect. However, if the sensor only sees 10^{-4} of the field applied to the sample, the coil current can vary by as much as one part in 10^4, and the variation in the magnetic measurement will then only be 10^{-8} of the field applied to the sample itself.

In addition to demonstrating the basic sensitivity necessary to see the weak magnetic response of the liver, our second main challenge was to distinguish the liver signal from the weak, but non-negligible response of the surrounding abdominal tissues. Most body tissues have weak diamagnetic susceptibility similar to that of water, roughly 9×10^{-6} in SI units. This diamagnetic response is actually 30 times greater than the 3×10^{-7} SI units that we estimate for liver iron at a concentration of 0.2 mg/ml.

The usual first step in eliminating the physiological background (abdominal) response is to use a water bag to fill the space between the instrument and the patient's body [1,6]. The existing SQUID instruments use this approach. The water bag approximately matches the susceptibility of the body tissues, and the effect is the same as if the entire magnetic measurement were being made in a medium with a uniform permeability. Within this uniform medium, the liver stands out as a paramagnetic anomaly. Unfortunately, the susceptibility of abdominal tissues is not exactly the same as that of water, and it is not exactly the same from one patient to another. In particular, since fat is slightly less diamagnetic than water, the abdominal wall of a fat patient tends to have a lower susceptibility than that of a thin patient. This varying tissue response is one of the main factors limiting the resolution of liver-iron measurements on real patients.

The work of Brittenham, et al., indicates that the basic water-bag technique is sufficient to monitor liver iron in patients with iron-overload diseases [1]. To measure very low iron concentrations associated with iron deficiency, Fischer and co-workers have developed a more elaborate method, which extracts the susceptibility of the abdominal tissue directly from the magnetic susceptibility measurements [2,6]. In this method, the liver is represented by a simple geometric shape, whose parameters are determined from ultrasound measurements. The outline of the body itself is determined from ultrasound, or estimated from magnetic measurements made in the absence of the water bag. It is assumed that the magnetic susceptibility has one value throughout the liver, and a second value throughout the rest of the body. Then, knowing the sample geometry, and knowing the geometry of the applied-field coils and magnetic sensors, it is possible to calculate how the response of both the liver and the surrounding tissue should vary as a function of the distance between the patient and the sensor system. One difficulty with this approach is that the contributions from the liver and the overlying tissues have rather similar dependences on the patient-sensor distance. As a result, the error in determining the contribution due to the liver iron is much greater than the error in measuring the overall magnetic signal.

We designed an applied field coil which would make the basic water-bag technique as effective as possible, and would also allow us the option of making a measurement similar to that of Fischer, et al. The coil design allows for the minimization of the abdominal response and that from the lung. The optimal coil design was obtained using an electromagnetic modeling program.

In order to eliminate the effects of slow drifts in the sensor output, likely to be caused by thermal effects, we modulated the distance between the sensor and the measurement sample. The signal appears at the modulation frequency, well above the characteristic time variation of the drift signal.

We did a systematic series of experiments. We first characterized the noise in the MR sensors. We then added the ac applied field, and refined our experimental technique until the applied field did not significantly increase the noise in the magnetic measurements. Next, we measured the magnetic response of a container of water. We performed repeated measurements of the water sample, and calculated the standard deviation, thus determining the noise-limited resolution of the magnetic susceptibility measurements. Finally, we performed a set of measurements using a phantom, in which a container of dilute manganese chloride solution, representing the liver, was enclosed within a larger container of water, representing the effect of surrounding body tissues. The results of these measurements are given below.

Results and Discussion

We first measured the magnetic susceptibility of water, and used this measurement to determine the noise-limited resolution of our measurement system. We characterized the noise in this magnetic susceptibility measurement by calculating the standard deviation of 16 successive measurements. With 32 seconds of data averaging for each measurement, the standard deviation of successive measurements was approximately 0.5% of the signal due to the water sample. This root-mean-square noise level corresponds to a liver iron concentration of approximately, 30 μg/ml. This noise level is within a factor of two of that obtained previously using SQUID instruments. Using our optimized ac field coil, we could achieve this resolution with the sensor unit separated from the water container by 2.6 cm at closest approach. This separation is comparable to the distance from the liver to the surface of the abdomen in a typical adult patient.

Subsequently we determined the ability of our measurement system to discriminate the liver from the abdomen in the phantom. To do this we introduced liquids of different magnetic susceptibility in the inner container of the phantom. With water in the outer container enclosing the inner container, the detection threshold of our system corresponds to the susceptibility of the liquid in the inner container being equal to about 1/3 the normal iron concentration in the liver. We feel that this threshold value can be further lowered by making improvements to our measuring system. This resolution is more than adequate to monitor iron concentrations in patients under treatment for a variety of disorders, including thalassemia, sickle cell anemia, and hemochromatosis. We have achieved this result using inexpensive, room-temperature magnetic sensors and applied field coils.

References

[1] Brittenham GM, et al: Hepatic iron stores and plasma ferritin concentration in patients with sickle cell anemia and thalassemia major. Amer J Hematology 42, 85, 1993; Brittenham GM et al: Magnetic susceptibility of human iron stores. New England J Med 307, 1671, 1982.

[2] Fischer R, et al: Liver iron quantification in the diagnosis and therapy control of iron overload patients. Hoke M. et al (eds): Biomagnetism: Clinical. Aspects. Amsterdam: Elsevier, Amsterdam, 1992, pp 585; Fischer R, et al: Williamson SJ, et al (eds): Advances In Biomagnetism, Plenum, New York, 1989, pp 501.

[3] Paulson DN, et al: Biomagnetic susceptometer with SQUID instrumentation. IEEE Trans Magnetics 27, 3249, 1991.

[4] Cohen A: Children's Hospital of Philadelphia, Philadelphia, Pa, private communication, 1998.

[5] Smith N, Jeffers F, and Freeman J: A high-sensitivity magnetoresistive magnetometer. J Appl Phys 69, 5082, 1991.

[6] Nielson, P, et al: Liver iron stores in patients with secondary haemisiderosis under iron chelation therapy with deferoxamine or deferiprone. Br J Hematol 91, 827, 1995.

Acknowledgements

This work was supported by a Small Business Innovation Research contract by the United States National Institutes of Health.

Magnetic and Electrical Measurements of Peripheral Nerves

Lang G[1], Shahani U[2], Weir AI[2], Maas P[2], Pegrum CM[1] and Donaldson GB[1]

University of Strathclyde[1], Glasgow, UK; Wellcome Biomagnetism Unit[2], Southern General Hospital, Glasgow, UK.

Introduction

Recently [1,2] neuromagnetic recordings have been extended to include human peripheral nerves. The evoked magnetic field from the peripheral nerve is one of the smallest fields in the body at less than 500fT. Peripheral nerves carry all somatosensory and motor information to and from the brain and as disease and damage in them can have serious consequences, a technique for non-invasive localisation and diagnosis is eagerly sought. Peripheral nerve conduction studies are routinely carried out using needle or surface electrodes, the former being a relatively invasive technique [3]. Particularly in the sensory system, deeply placed nerves are difficult to record from because of phase cancellation and the volume conductor characteristics leading to temporal dispersion and attenuation of responses [4]. Recording the magnetic field produced by a compound action potential (the magnetic compound action field, mCAF) using SQUIDs offers an alternative non-invasive technique. Unlike electric fields, dc and low frequency magnetic fields pass through human tissue unaltered.

To date neuromagnetic recordings of compound action potentials from the peripheral nerve have necessitated expensive magnetic shielding and substantial signal averaging. As many as 4000 averages with up to four repetitions are common using first-order axial gradiometers [5]. We have been able to measure mCAFs with a custom made planar gradiometers and a commercial BTi neuromagnetometer in an eddy-current shielded room with a small number of averages (256-2048). A low number of averages is desirable to reduce the measurement time and patient discomfort. The eddy-current shielded room is substantially less expensive than a magnetically shielded room but it offers little shielding from dc and low frequency magnetic fields. We compare the signal obtained from a travelling volley using both magnetic sensors with that obtained electrically. Electrically the signal attenuates and disperses as the nerve progresses further from the stimulus and deeper into the arm. We investigate if this also occurs in the magnetic measurement. As the magnetic measurement still requires up to 2048 averages, in order to reduce the measurement time, the effect of increasing the stimulus rate is investigated.

Methods

The recordings were made on eight normal healthy volunteers with ethical approval. The ulnar was stimulated at the wrist above threshold to evoke somatosensory evoked potentials (SEP) and fields (SEF). The stimulus was a constant current of ~12mA applied at 3pps with 10% randomness. At least two sequential recordings were taken per point. The recording sites were on the upper arm over the ulnar nerve at 4cm spacings.

The magnetic recordings were made in a simple eddy-current shielded room at the Wellcome Biomagnetism Unit (WBU) at the Southern General Hospital, Glasgow. The shield is fabricated from 25mm thick high-conductivity aluminium sheet, root-welded through its full thickness for electrical integrity and structural stability. The shield provides (increasing) attenuation of uniform magnetic fields of ~20dB per frequency decade above a corner frequency of 1.9Hz. The cost of the eddy-current shielded room was £23,000 when purchased in 1990. This is substantially cheaper than a magnetically shielded room.

Magnetic recordings were taken from peripheral nerve in the upper arm using a commercial BTi neuromagnetic SQUID magnetometer and a custom-built second-order planar gradiometer [6]. Patients lay supine with their arm abducted, and flexed over the head, as shown in Fig.1. The BTi sensor measures the second-order radial gradient of the radial component of the magnetic field. The SQUID of the BTi sensor is enclosed in a small niobium shield. The planar gradiometer measures the second-order radial gradient of the tangential component of the magnetic field. There is no extra shielding around the planar device. The plane of the planar gradiometer was oriented parallel to the nerve. The output from both devices was filtered between 1-300Hz. (Recordings were also made with a

©1999, Tohoku University Press
Recent Advances in Biomagnetism
T. Yoshimoto et al. (Eds)

wider bandwidth (1-1kHz), but no additional information was found). The signals were rms averaged by a Medelec Sapphire (2ME) data acquisition system. Both gradiometers were shielded in standard BTi BMD5x dewers. Cables carrying the output of the planar gradiometer were housed in a copper conduit for protection from rf interference. Standard flux-locked loop electronics (BTi's own electronics for the axial device and Quantum Design model 550 for the planar device) were used with no additional electronic cancelling or noise reduction techniques. Four runs of 256 (axial) or 512 averages (planar) each, were recorded at each point.

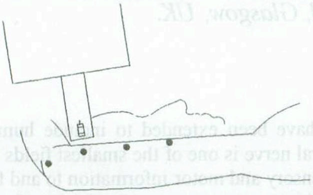

Fig. 1. Patient set up for magnetic measurements and orientation of planar gradiometer on the upper arm. Points were set 4cm apart on the ulnar nerve.

Electrical measurements were made with standard surface disk electrodes. The reference was kept at a point 4cm proximal to the recording electrode. The subject lay in a relaxed supine position. Bandpass settings for the electrical measurements were set between 1Hz and 1kHz. Two runs of 128 averages each were recorded at each point.

Results

Of the eight volunteers (5 male, 3 female) no signal was detected magnetically in four subjects. However in two of these subjects, the electrical signal was also unobtainable. The best results were recorded from those subjects where the nerve was fairly superficial. Data recorded from various points on the upper arm is shown in Fig. 2 for all three methods. The signal amplitude decreases as the nerve progresses further from the stimulus and deeper into the arm both electrically and magnetically. The electrical measurement shows a much clearer biphasic response compared with both magnetic measurements. The biphasic nature of the signal is only evident in some of the magnetic traces, due to the poorer signal to noise ratio. Both magnetic measurements are broader and occur slightly later than in the electrical measurements. This is probably an effect of using a narrower bandwidth. The signal amplitude is much larger in the BTi magnetic measurement than in the planar measurements. This is because the sensing area of the BTi device is ten times larger than that of the planar. The above findings are consistent in all patients. The slow sinusoidal waves in some of the traces of Fig. 2 are thought to be due to muscle activity.

Figure 3 shows how the signal latency varies with distance from the stimulus. (The data points are taken from the start of the signal). The conduction velocity for all three methods can be calculated from the gradient of these relationships and are given in Table 1.

TABLE 1
CONDUCTION VELOCITIES

Method	Conduction velocity (ms^{-1})
Electrical	84.5
Magnetic BTi	68.3
Magnetic Planar	68.6

It is known that an increase in the stimulus rate to the ulnar nerve causes a decrease in the amplitude of the measured electrical signal [7]. Fig. 4 show data measured magnetically with the BTi gradiometer with various stimulus rates. There is a small decrease in signal amplitude as the stimulus rate is increased and in a limited number of subjects there is also a slight shift in latency of ~0.5ms as the stimulus rate is increased from 3pps to 30pps.

Discussion

Conventional electrical measurements of ulnar nerve conduction velocity were compared with those obtained magnetically. The results indicate that presently available magnetic devices are sensitive enough to record travelling volleys from the peripheral nerve with only eddy-current shielding. The

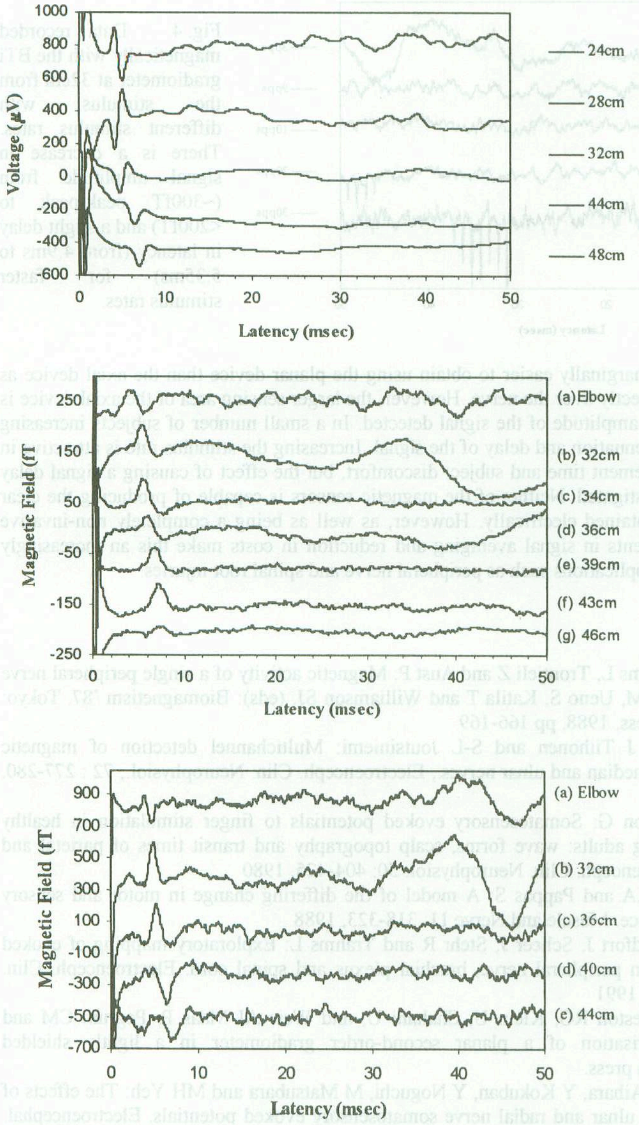

Fig. 2 Data recorded from the ulnar nerve at the elbow and in the upper arm following stimulation at the wrist, (a) electrically, traces are a grand average of two sequentially recorded runs of 128 averages each.
(b) magnetically with the BTi axial gradiometer. Traces are a grand average of four sequentially recorded runs of 256 averages each and
(c) magnetically with the planar gradiometer. Traces are a grand average of four sequentially recorded runs of 512 averages each. Traces are displaced vertically for clarity.

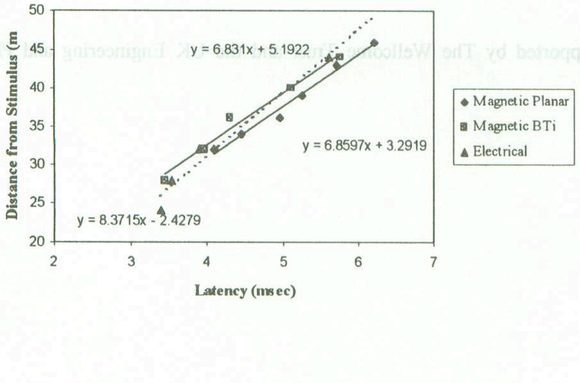

Fig. 3 Graph of dependence of latency on distance from stimulus for each of the three methods. The gradient of the graph is the conduction velocity; electrical 84[illegible].7ms^{-1}, Magnetic BTi 68.3ms^{-1} and magnetic planar 68.6ms^{-1}

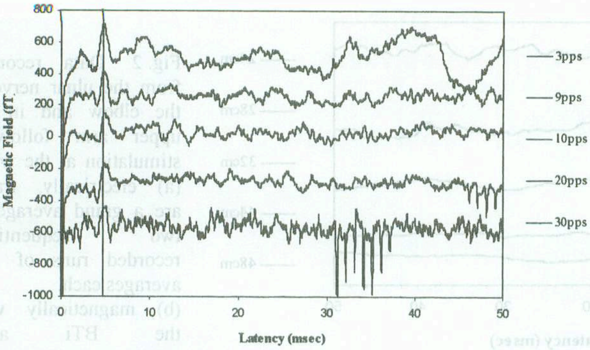

Fig. 4 Data recorded magnetically with the BTi gradiometer at 32cm from the stimulus, with different stimulus rates. There is a decrease in signal amplitude from (~300fT peak-peak to <200fT) and a slight delay in latency (from 4.9ms to 5.35ms) for faster stimulus rates.

magnetic measurement is marginally easier to obtain using the planar device than the axial device as the signal is a maximum directly over the nerve. However, the larger sensing area of the axial device is preferable to maximise the amplitude of the signal detected. In a small number of subjects increasing the stimulus rate caused attenuation and delay of the signal. Increasing the stimulus rate is attractive in order to reduce the measurement time and subject discomfort, but the effect of causing a signal delay must firstly be further investigated. Neither of the magnetic sensors is capable of producing the clear biphasic signals that are obtained electrically. However, as well as being a completely non-invasive technique, these improvements in signal averaging and reduction in costs make this an increasingly attractive tool for clinical applications such as peripheral nerve and spinal root injuries.

References

[1] Erne SN, Curio G, Trahms L, Trontjeli Z and Aust P: Magnetic activity of a single peripheral nerve in man. Atsumi K, Kotani M, Ueno S, Katila T and Williamson SJ, (eds): Biomagnetism '87. Tokyo: Tokyo Denki University Press, 1988, pp 166-169

[2] Hari R, J Hallstrom, J Tiihonen and S-L Joutsiniemi: Multichannel detection of magnetic compound action fields of median and ulnar nerves., Electroenceph. Clin. Neurophysiol., 72 : 277-280, 1989.

[3] Desmedt JE and Cheron G: Somatosensory evoked potentials to finger stimulation in healthy octogenarians and in young adults: wave forms, scalp topography and transit times of parietal and frontal components. Electroenceph. Clin. Neurophysiol. 50: 404-425, 1980

[4] Kincaid JC, Minnick KA and Pappas S: A model of the differing change in motor and sensory action potentials over distance. Muscle and Nerve 11: 318-323, 1988

[5] Curio G, Erne SN, Sandfort J, Scheer J, Stehr R and Trahms L: Exploratory mapping of evoked neuromagnetic activity from peripheral nerve, brachial plexus and spinal cord. Electroenceph. Clin. Neurophysiol. 81: 450-453, 1991

[6] Lang G, Hutson D, Weston RG, Klein U, Shahani U, and Weir AI Maas P, Pegrum CM and Donaldson GB: Characterisation of a planar second-order gradiometer in a lightly shielded environment. Biomag 96. In press.

[7] Fujii M, T Yamada, M Aihara, Y Kokuban, Y Noguchi, M Matsubara and MH Yeh: The effects of stimulus rate upon median, ulnar and radial nerve somatosensory evoked potentials. Electroencephal. Clin. Neurophysiol. 92: 518-526, 1994.

Acknowledgements

This work was supported by The Wellcome Trust and the UK Engineering and Physical Sciences Research Council.

Number of Active Muscle Fibers within a Single Motor Unit Estimated by Magnetomyography

Masuda T[1,2], **Endo H**[1,2], **Takeda T**[3,1,2]

National Institute of Bioscience and Human-Technology[1]*, Tsukuba, Japan; Core Research for Evolutional Science and Technology (CREST)*[2]*, Kawaguchi, Japan; Department of Mathematical Engineering and Information Physics*[3]*, University of Tokyo, Bunkyo, Japan*

Introduction

One of the advantages that magnetic measurement has over the conventional electrical potential measurement is the estimation of absolute intensity of an action current flowing inside the human body. By using this advantage we can estimate the total current flowing in a skeletal muscle from the distribution and amplitude of magnetomyographic (MMG) signals. If the current intensity of a single motor unit is estimated magnetically, we can calculate the number of active muscle fibers contained in the motor unit by dividing this current intensity with the average intensity of a single muscle fiber. This estimation should help clinically diagnose neuromuscular disorders, which may decrease the number or the thickness of muscle fibers. With the conventional electrical potential measurements, we cannot estimate action current intensity, unless the electrical conductivity and the shape of surrounding tissue are known.

Action currents in a muscle fiber is described as a current octupole [3]. For an octupole it is difficult to estimate the current intensity from the outside magnetic fields, because magnetic fields produced by currents in an octupole cancel each other out. We found that a magnetic field with a distinct dipolar pattern appears when the propagating action currents reach at the end of a muscle fiber [2]. At this moment only the repolarization current remains active. It then becomes possible to estimate the intensity of action currents from this dipolar magnetic fields.

In our previous paper [2] however we used only the intensity of the current dipole for calculating the number of muscle fibers. It should be necessary to take the duration of action currents into consideration for improving the accuracy of the estimation.

Methods

Subjects were three normal healthy adult males aged 22, 24, and 42 years. Muscles tested were the vastus medialis and vastus lateralis, which are extensors of the knee joint. We used a 64-channel SQUID system (Neuro SQUID Model-100, CTF Systems, Inc., Port Coquitlam, Canada) housed in a magnetically shielded room (AK3b, Vakuumschmelze, Hanau, Germany). The first-order gradiometer coils were uniformly distributed over a hemispherical surface (Figs. 1 and 2). The sampling frequency was 1.25 kHz. The frequency band ranged from 1 to 625 Hz.

The subjects lay on their backs and bent the knee joint to position the knee in the Dewar concavity (Fig. 2 a). During the recording, the subjects forced knee extension voluntarily without moving the body. Bipolar surface electrodes were placed on the innervation zones of the muscles to simultaneously record an electromyographic (EMG) signal with MMG. Innervation zones are the muscle areas where motor endplates are concentrated. EMG signals were recorded with a gain of 63 dB over a frequency range from 5 to 500 Hz.

For the detection of action potentials from a single motor unit, EMG signals were converted to sound and presented to the subjects. Using the EMG sound as feedback, the subjects adjusted contraction force to a minimum so that a spike train of single motor unit action potentials would appear at approximately regular intervals. We used zero-crossing timings in the EMG signal as triggers for averaging and extracting magnetic fields created by a single motor unit. We then estimated the location, orientation and moment of a current dipole from the averaged magnetic field. The dipole was estimated at the time point when MMG showed the maximal amplitude.

The currents in a single muscle fiber were approximated by an octupole model [3]. When the excitation region reaches the end of a muscle fiber (Fig. 2 c), the depolarization current disappears first, leaving only the repolarization

©1999, Tohoku University Press
Recent Advances in Biomagnetism
T. Yoshimoto et al. (Eds)

current. At this time point the cancellation of the magnetic fields disappears. The repolarization current then produces strong dipolar magnetic fields. This distinct dipolar pattern enables the current source to be estimated with a minimal error.

It is necessary to determine the geometrical configuration of muscle fibers to calculate the magnetic fields produced by action currents. We arranged a linear muscle fiber model whose distal end coincides with the estimated dipole (Fig. 2b). We used the parameters for action currents reported by Andreassen and Rosenfalck [1]. In their parameters, the sink of the membrane current was common to the depolarization and repolarization currents (Fig. 3a). We calculated the magnetic fields from these action currents based on the Biot-Savart formula.

To estimate the time shift between excitation on different muscle fibers we deconvolved the measured MMG signal with the calculated MMG of a modeled single muscle fiber. We deconvolved the MMG signal that had the largest amplitude among the 64 channels. The number of active muscle fibers was calculated from the deconvolved waveform. The ordinate of the deconvolved waveform indicates the number of active fibers per unit time 0.1 ms. For calculating the number of muscle fibers we chose the area of the deconvolved waveform where the time shift and the deflection are positive.

Results

Six motor units were detected from the three subjects. Similar waveform and distribution of MMG were observed in the vastus medialis and vastus lateralis of the three subjects. Fig. 1b shows the distribution of MMG at three typical time points. Fig. 1c shows the trigger-averaged MMG and EMG waveforms. In the upper trace 64 channels of MMG were superimposed. The initial deflection in the EMG indicated the start of muscle fiber excitation, because EMG electrodes were placed on the innervation zones, so this time was used as the reference or 0 ms.

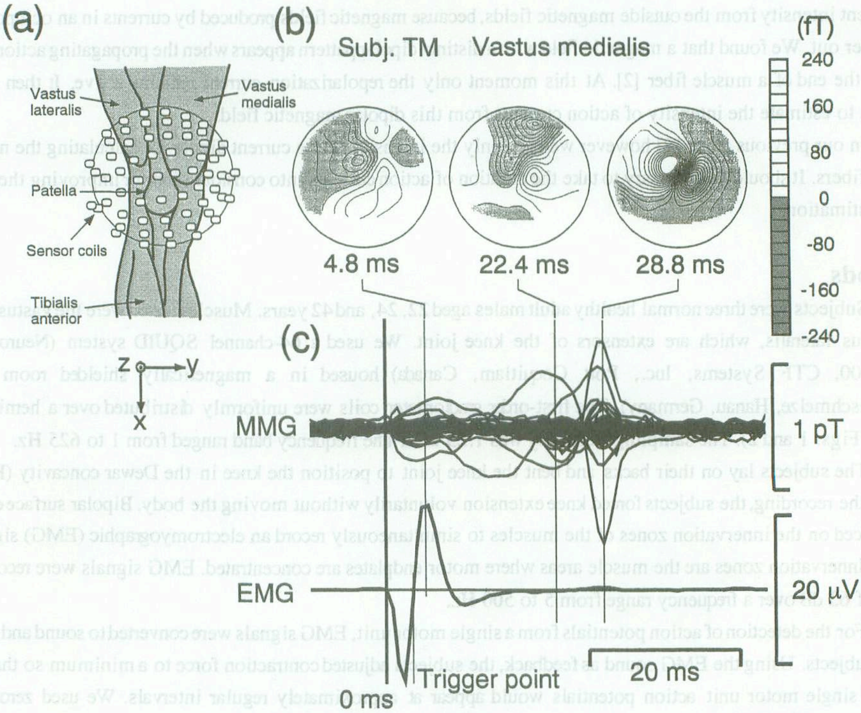

Fig. 1 (a) Configuration of sensor coils for magnetic recording with corresponding muscle regions. The actual coils were arranged on a hemispherical surface. (b) Distribution of magnetic fields at three typical time points. (c) Trigger-averaged waveforms of MMG and EMG. EMG was detected from the vastus medialis. MMG signals were trigger-averaged at the zero-crossing timings in EMG. The number of averaging was 84 for this record.

In Fig. 1 the distribution of MMG was complex during the initial 26.4 ms. Later at 28.8 ms, one entering and one exiting fluxes were arranged in a pattern of linear symmetry. This pattern indicates the magnetic field created by a current dipole at the center of symmetry. The position, orientation and moment of the current dipole were estimated at this time point when the magnetic field was strongest.

Fig. 3b shows the magnetic field calculated from a modeled muscle fiber (Fig. 2b). The calculated magnetic field differed from the measured one (Fig. 3c). Compared with the calculated signal, the measured MMG was longer in its duration and smaller in its ratio of entering and exiting fluxes. We considered that the measured MMG was a time-shifted superposition of single fiber MMGs. The measured MMG was therefore deconvolved with the calculated single fiber MMG (Fig. 3d). The deconvolved waveform became monophasic, whereas the measured MMG was biphasic.

The hatched region in Fig. 3d indicates an area whose time shift and deflection were positive. The number of muscle fibers was calculated from this area. The positive shift means the time after the depolarization reaches the fiber end. The number of muscle fibers thus estimated for the six motor units was 708 to 1,791 (average 1,088 ± 480). These figures were 6.5 times larger than the estimate of 84 to 400 (average 193 ± 120) that was obtained by simply dividing the dipole moment with that of a single muscle fiber [2].

Discussion

The monophasic waveform of the deconvolution results indicates that the measured MMG is a time-shifted superposition of the calculated single fiber MMG. If the deconvolved waveform shows a negative deflection, there must exist action currents with the reverse polarity. The deconvolved waveform was mostly positive as shown in Fig. 3d.

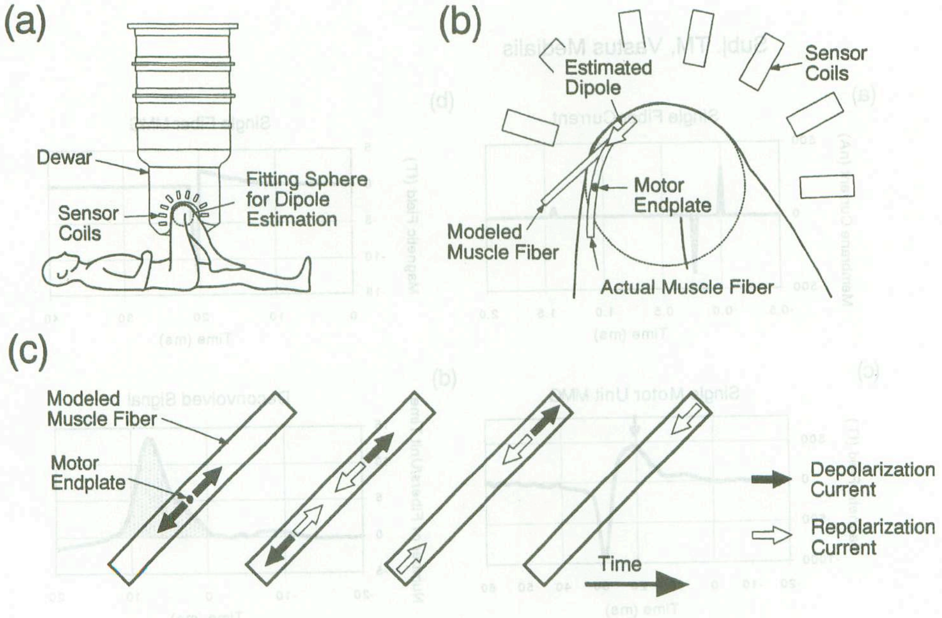

Fig. 2 (a) Subject posture during the measurement. The knee was flexed and put into the Dewar concavity. (b) A model of a muscle fiber. A linear fiber was arranged so that its distal end coincides with the position and orientation of the estimated current dipole. (c) Schematic diagram of action currents flowing in a muscle fiber. Depolarization and repolarization currents arise at the motor endplate and propagate to the fiber ends.

In large muscles including the vastus medialis and vastus lateralis, motor units contain several hundred or thousand fibers [4]. The number of fibers obtained in the present study was closer to these figures. The present estimation thus seems to show improvement. To prove the validation of the present results, we must conduct an animal experiment or a simulational study with a physical or numerical model.

There are four major reasons that cause the time shift between the excitation on different muscle fibers. They are the spatial distribution of motor endplates, the variation in timing of excitation in individual muscle fibers, the variation in muscle fiber conduction velocity, and the variation in muscle fiber length. The average time shift obtained from the deconvolution was 10.0 ms. If we assume that this time shift is solely caused by the spreading of motor endplates, the spreading becomes 40.0 mm, which was a multiple of the time shift 10.0 ms and the conduction velocity 4.0 m/s. This spreading seems to be too large for the motor endplate distribution. The other factors mentioned above should also contribute to the time shift. At the present stage it is impossible to isolate the contribution of the four factors. If this isolation becomes possible, it can be used as another novel technique for analyzing the muscular function.

References

[1] Andreassen S, Rosenfalck A: Relationship of intracellular and extracellular action potentials of skeletal muscle fibres. CRC Crit Rev Bioeng, 6: 267-306, 1981

[2] Masuda T, Endo H, Takeda T: Magnetic fields produced by single motor units in human skeletal muscles. Electroenceph Clin Neurophysiol, in press

[3] Wikswo JP, van Egeraat JM: Cellular magnetic fields: fundamental and applied measurements on nerve axons, peripheral nerve bundles, and skeletal muscle. J Clin Neurophysiol 8: 170-188, 1991

[4] Goodgold J, Eberstein A: Electrodiagnosis of Neuromuscular Diseases. Third ed. Williams & Wilkins, Baltimore, 1983

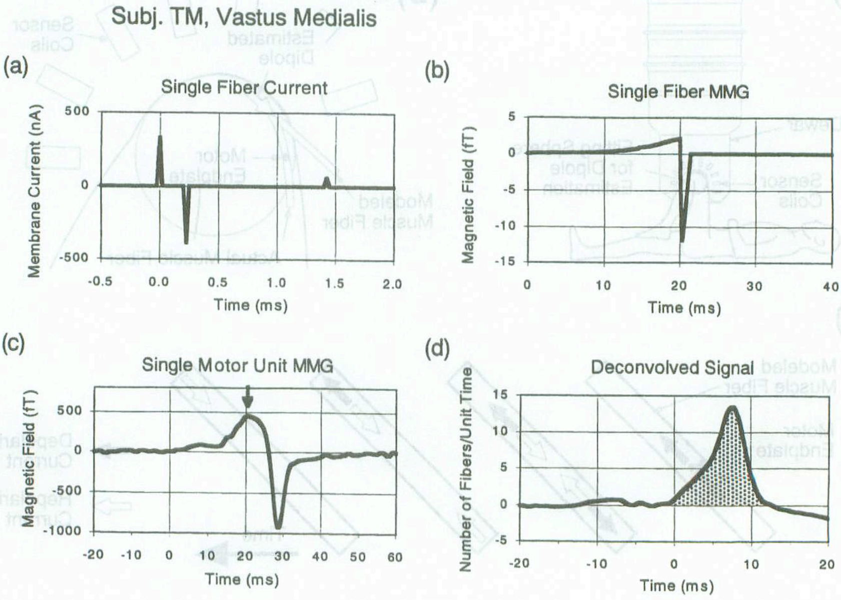

Fig. 3 (a) Action currents flowing through the muscle fiber membrane. (b) Waveform of the calculated single fiber MMG. (c) Waveform of the measured MMG that showed the maximal amplitude. The arrow indicates the time point when the depolarization current reached the fiber end. (d) Deconvolution result of the measured MMG (c) with the calculated single fiber MMG (b). An area that has a positive time shift and a positive deflection is hatched. From this area the number of active muscle fibers within a motor unit was estimated.

Models of Phagosome Motion within Cells Measured by Cytomagnetometry Incorporating Viscoelasticity

Iku Nemoto(1), Winfried Moeller(2)

(1)Tokyo Denki University, Hatoyama, Japan; (2)GSF Institute of Inhalation Biology, Gauting, Germany

Introduction

Cytomagnetormetry is a non-invasive method to investigate intracellular movements of organelles such as phagosomes by introducing magnetic particles into cells by phagocytosis, magnetizing them and measuring the field from the cells[1]. Two models(Model I and II) for intracellular phagosome motion are proposed and their behavior in terms of the magnetic field from the cells is investigated. They include an elastic body which is assumed to represent the filamentous structures surrounding the phagosomes. The magnetic relaxation phenomenon is assumed to derive from the rotationary Brownian motion.These models can simulate the experiment in which the particles are magnetized either by a pulse field or a field of long duration and then are given a twisting field which mechanically rotates the phagosomes which then will recoil toward the original position by the elasticity. In Model I the random force is given from outside the model but in Model II it is generated between the phagosome membrane and the filamentous structures. So far Model I seems to better simulate the experimental data and hence emphasis is put on the behaviors of this model. Model I was first proposed in [2] . In the present report the partial differential equation describing the time course of the distribution fuction of the angles is shown and used to calculate the cell field.

Cytomagnetometry

Cytomagnetometry is performed by applying a magnetic field to the cells which have engulfed magnetic particles and measuring the field produced by the cells. The cell field is the vector sum of the fields produced by the ensemble of magnetic particles in all the cells. The decay of the cell field after magnetization of the particles is due to the randomization of the orientations of the magnetic moments of phagosomes (see Figure 1), because the magnetization of each particle remains unchanged. We previously modeled the relaxation process by the rotationary Brownian motion.

Models

Cytomagnetometry has shown that the movement of the phagosomes are impeded not only by the apparent viscosity but also by elasticity. In these studies, at a certain time in the relaxation measurement, a medium-intensity twisting field was applied to the cells for 1-10 s either perpendicularly or in the opposite direction to the original direction of the magnetization. By 'medium', we mean, throughout this paper, that the field is strong enough to overcome (as much as possible) the influence of the randomizing force E_r and yet not so strong as to remagnetize the particels in another direction. Fig. 2 shows ModelI. It is a one-dimensional model and the equations of motion for this model are:

$$\frac{d\theta_1}{dt} = -\sigma(\theta_1(t) - \tilde{\theta}_1) + \frac{1}{k_2}\left(\frac{dW}{dt} + f(t,\theta)\right), \quad \frac{d\theta_2}{dt} = \frac{1}{k_1}\left(\frac{dW}{dt} + f(t,\theta)\right) \tag{1}$$

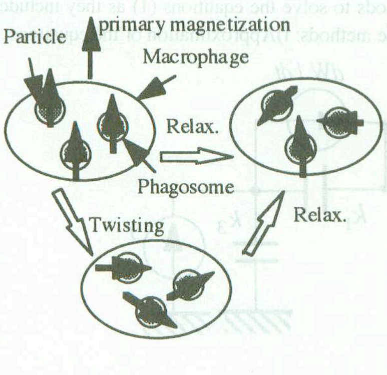

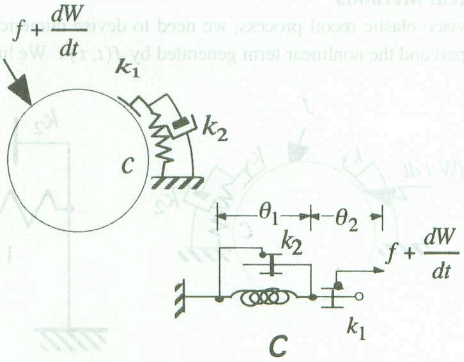

Fig. 1 Principle of Cytomagnetometry.

Fig. 2 Visco-elastic model of Phagosome motion.(Model

©1999, Tohoku University Press

Recent Advances in Biomagnetism
T. Yoshimoto et al. (Eds)

where $\sigma = c / k_2$. The angles θ_1, θ_2 are defined such that $\theta = \theta_1 + \theta_2$ is the direction of the magnetic moment of the phagosome measured from that of the measurement. $\tilde{\theta}_1$ corresponds to the natural length of the elastic body. $f(t,\theta)$ is the force exerted by the external field chosen to achieve a particular purpose in each experiment. For the perpendicular twisting where an external field H_T is given perpendicular to the direction of the primary magnetization, it is given by $f(t,\theta) = \mu H_T \cos(\theta_1 + \theta_2)$ and for the reverse twisting where the twisting field is applied in the opposite direction to the primary magnetization, cosine is replace by sine. W is the Wiener process whose mean is 0 and the variance is given by αt where $\alpha = 2E_r\kappa$, $\kappa = (k_1^{-1} + k_2^{-1})^{-1}$. Fig. 3 shows Model II which is also illustrated by an equivalent electric circuit. It has another viscus component so that the random force dW/dt is specified to act between the phagosome membrane and the elastic body. The equations of motion for this model are:

$$\frac{d\theta_1}{dt} = -\sigma_1(\theta_1(t) - \tilde{\theta}_1) + \frac{1}{K}\left(k_3\frac{dW}{dt} - k_1 f(t,\theta)\right), \quad \frac{d\theta_2}{dt} = -\frac{1}{k_1 + k_3}\left(k_3\frac{d\theta_1}{dt} + \frac{dW}{dt} - f(t,\theta)\right) \tag{2}$$

where $K = k_1k_2 + k_1k_3 + k_2k_3$, $\sigma_1 = c(k_1 + k_3)/K$.

Relaxation is the decay of the field caused by the increasing variance $V[\theta(t)]$ after magnetization of the particles as described by

$$B(t) = \frac{1}{\sqrt{2\pi V[\theta(t)]}}\int_{-\infty}^{\infty} \cos\xi \exp\left\{-\frac{\xi^2}{2V[\theta(t)]}\right\} d\xi = \exp\left\{-\frac{V[\theta(t)]}{2}\right\} \tag{3}$$

In Model I, the variance $V[\theta(t)]$ is given by

$$V[\theta(t)] = E[\tilde{\theta}_1^{\,2}](1 - e^{-\sigma t})^2 + \alpha\left\{\frac{1 - e^{-2\sigma t}}{2\sigma k_2^2} + \frac{2(1 - e^{-\sigma t})}{\sigma k_1 k_2} + \frac{t}{k_1^2}\right\} \tag{4}$$

For pulse magnetization, where the particle-containing phagosomes are magnetized by a pulse magetizing field, $E[\tilde{\theta}_1^{\,2}] = \alpha / 2\sigma k_2^2$, and for fixed magnetization, where the phagosomes are kept in position by a strong DC field for a sufficiently long period of time ($t \to \infty$), we have $\tilde{\theta}_1 = 0$. In Model II, the variance is given by

$$V(t) = E[\tilde{\theta}_1^{\,2}]\frac{k_1^2(1 - e^{-2\sigma_1 t})^2}{(k_1 + k_3)^2} + \frac{\alpha}{(k_1 + k_3)^2}\left\{\frac{k_3^2 k_1^2 (1 - e^{-2\sigma_1 t})^2}{2cK(k_1 + k_3)} - \frac{2k_1k_3(1 - e^{-\sigma_1 t})}{c(k_1 + k_3)} + t\right\} \tag{5}$$

and α in this case is given by $\alpha = 2E_r K(k_1 + k_2)/k_2^2$.

The partial differential equation for the probability density function $p_t(\theta_1, \theta_2)$ for Model I is given by

$$\frac{dp_t}{dt} = \frac{1}{2\Delta t}\left(\Theta_1^2\frac{\partial^2 p_t}{\partial\theta_1^2} + 2\Theta_1\Theta_2 + \Theta_2^2\right) - \frac{\partial}{\partial\theta_1}\left\{p_t(\theta_1,\theta_2)\left(\frac{f(\theta)}{k_2} - \sigma\theta_1\right)\right\} - \frac{\partial}{\partial\theta_2}\left\{p_t(\theta_1,\theta_2)\frac{f(\theta)}{k_1}\right\}. \tag{6}$$

where $\Theta_1 = \sqrt{\alpha\Delta t} / k_2$, $\Theta_2 = \sqrt{\alpha\Delta t} / k_1$. This is for the case $\tilde{\theta}_1 = 0$, and we have not been successful in deriving one for distributed $\tilde{\theta}_1$.

Numerical Methods

For the visco-elastic recoil process, we need to devise numerical methods to solve the eqautions (1) as they include the random part and the nonlinear term generated by $f(t,\tau)$. We have three methods: i)Approximation of the equaitons: The

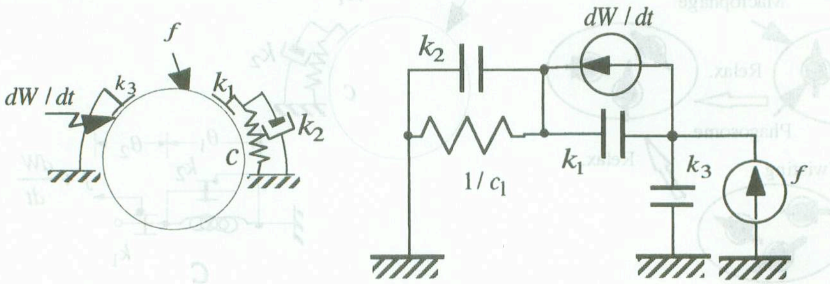

Fig. 3 Model II.

Brownian motion term is neglected during the twisting process and the nonlinear equations without the random term are solved numerically (Rnge-Kutta); ii)Monte Carlo simulation: The equations are solved 4000-5000 times by Runge-Kutta method each time with the Brownian motion term simulated by an independent series of random numbers, and the results are averaged. This gives exact solution (except for the variance caused by the finite number of simulations) for any experimental scheme and thus can be used to evaluate the other numerical methods; iii)The partial differntial equation (6) is numerically solved the calculate $B(t) = \int \cos(\theta_1 + \theta_2) p_t(\theta_1, \theta_2) d\theta_1 d\theta_2 / \int p_t(\theta_1, \theta_2) d\theta_1 d\theta_2$.

Normalization of the Parameters

The parameters $k_1, k_2, c, \mu H_T$ are normalized by dividing them by E_r . This way, E_r is eliminated from the equations. Hereafter the parameters are understood to be normalized. The normalized parameters k_1, k_2 are related to the apparent viscosities η_1, η_2 by $k_1 = 8\pi r^3 \eta_1 E_r$, etc. If we subsitute $k_1 = 100\,\mathrm{Nms}$, $r = 10^{-6}\,\mathrm{m}$, $E_r = 5 \times 10^{-18}\,\mathrm{J}$[1], for example, we get apparent viscosity $\eta_1 = 10\,\mathrm{N \cdot s/m^2}$. In [1] we obtained the apparent viscosity of the order of 10^2 Poise. Therefore, we may set $10^1 - 10^3$ as the rough range for the normalized values for k_1, k_2. Changing the Hook's law in the force form into the torque form gives the relation $\gamma = c / r^2$ where γ is the elasticity coefficient for the Hook's law. In our case we have $\gamma = 5 \times 10^{-6}\,\mathrm{Nm}$ which means that 5pN is required to extend the elastic body by 1μ m.

Numerical Results and Discussion

Fig. 4 shows several relaxation curves calculated from (3)(4) plotted in the logarithmic scale. In (a) $k_1 = 200$, $k_2 = 80$, $\mu H_T = 10$ and in (b) $k_1 = 80$, $k_2 = 200$, $\mu H_T = 10$. Relaxation curves are compared for different values of c and for three magnetization schemes; pulse magnetization (PM), fixed magnetization with infinete (FMI) and finite (FMF) values of μH_T. The derivation of $E[\tilde{\theta}_1^2]$ for FMF is not given in this paper. Fig. 5 shows visco-elastic recoil curves obtained with the three numerical methods described above. In (a) perpendicular twisting field is applied 10 s after the primary magnetization. In (b) reverse twisting field is applied 120s after the primary magnetization. EqM curves are obtained by method (i) above, MC by (ii), DF by (iii). It is seen that the three methods agree for the situation in (a) but not in (b). This is due to the large error in the approximation taken by method (i) for this situation. This also shows the validity of both the Monte Carlo simulation and the PDE(partial differential equation) approach. Fig.6 showsthe curves obtained by the PDE solution. In (a) the perpendicular twisting field is applied 10s after primary magnetization. and in (b) reverse twisting field is applied 2 minutes after the primary magnetization. Each have three curves corresponding to three values of c.

Conclusion

It is at this stage not clear how the visco-elastic element can be incorporated into the spherical Brownian motion model proposed in [1] . The present treatment of the model shows that this simple one-dimensional model can have interesting

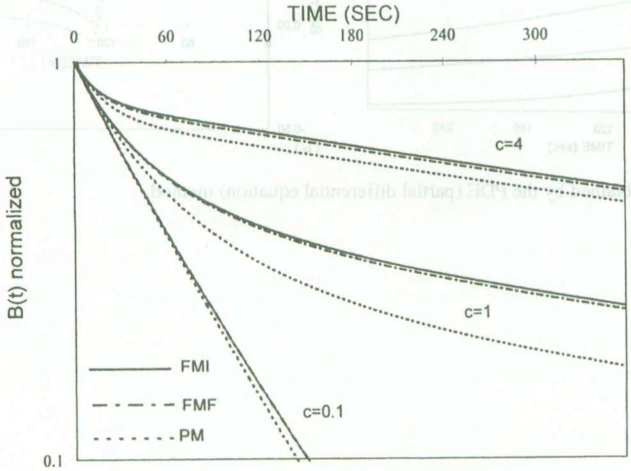

Fig. 4 Relaxation curves for different values of c and magnetization schemes.

features and thus should be studied along with experimental results. Our next problem is to find a good way for parameter estimation for the experimental data. Furthermore, it would be an interesting theoretical question whether it is possible to derive some partial differential equation describing the time course of $p_t(\theta_1,\theta_2)$ when θ_1 is distributed.

References

[1] Nemoto I: A model of magnetization and relaxation of ferrimagnetic particles in the lung. IEEE Trans BME-29: 745-752, 1982.

[2] Nemoto I: A model of phagome motion within cells incorporating visco-elasticity based on cytomagnetometric measurements. Abstracts of Biomag96, p.194, 1996.

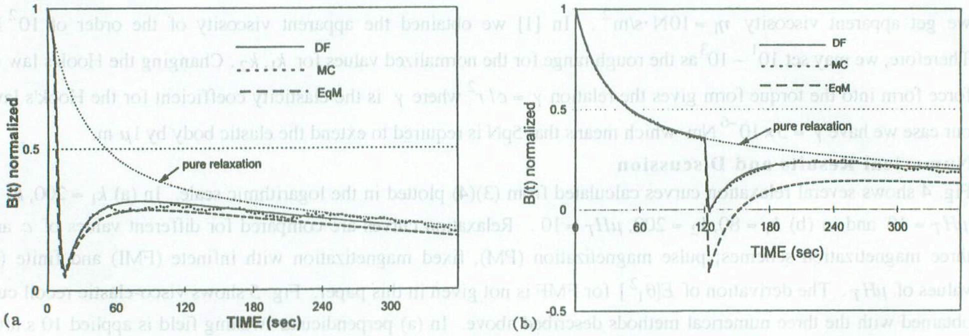

Fig. 5 Visco-elastic curves obtained by the three numerical methods.

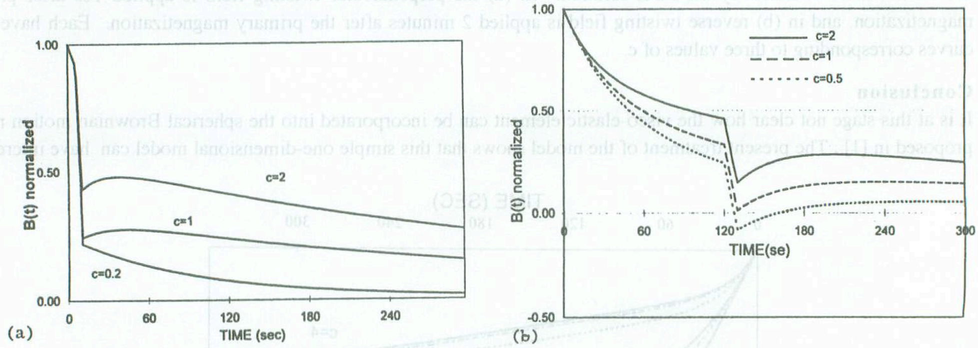

Fig. 6 Visco-elastic curves obtained by the PDE (partial differential equation) method.

Iron Quantification by Biomagnetic Liver Susceptometry in Childhood Acute Lymphoblastic Leukemia before and after Induction Chemotherapy

Engelhardt R[1], Dürken M[2], Kim SZ[2], Fischer R[1], Gabbe, EE[1], Janka, GE[2]
Abteilung Medizinische Biochemie[1]; Kinderklinik[2], UKE, University Hamburg, Germany

Introduction

Acute lymphoblastic leukemia (ALL) in childhood is treated by chemotherapy, which has been shown to cause disturbed iron homeostasis with temporary plasma iron overload. Liver iron stores, however have not yet been studied in patients with leukemia undergoing chemotherapy.

Currently, the classical liver biopsy with histologic determination of Prussian blue stainable iron in liver slices and the chemical determination of iron in the liver biopsy specimens is still the standard method in the diagnosis of a clinical relevant iron overload.

During the past decade, several methods for non invasive liver iron quantification (CT, MRI, nuclear resonance scattering, SQUID biomagnetic susceptometry) have been studied mostly in smaller groups of patients. Among this, only MRI and biomagnetic susceptometry have the principle capability to measure liver iron concentration (LIC) sensitive enough to be of clinical use.

In the last years (1989 - 1998) SQUID biosusceptometry has been used to assess iron stores in more than 1500 patients suspected for iron overload [1]. In the present study, the benefit of noninvasive iron quantification by biomagnetic liver susceptometry (BLS) under clinical conditions was used in a group of pediatric patients with acute lymphoblastic leukemia, to study the disturbed iron metabolism due to the induction chemotherapy. In this group of patients one could not expect liver iron concentrations far above the normal range (0.1 - 0.5 $\mathrm{mg/g_{liver}}$).

Methods

The iron status was studied in 8 children with acute lymphoblastic leukemia (age 3 - 13 y) undergoing chemotherapy. The liver iron concentrations were determined from biomagnetic susceptibility measurements. The patients were measured before the onset of daunorubicin (DNR) induction chemotherapy and 28 - 38 days later (only 7 children). The induction chemotherapy consisted of four 24-h-daunorobicin infusions with 36 $\mathrm{mg/m^2}$ each.

Biomagnetic liver susceptometry was performed by lowering the patient in the known localized magnetic dc-field (B_{max}= 20 mT, gradiometer 1st order) of the Hamburg Biosusceptometer (BTi) with water as the reference medium. The fluxintegral contributions for the liver and torso were calculated in advance for certain distances and radii (3 - 25 cm) as ellipsoids (liver) and as hemispheres or cylinders (torso). The calculated fluxintegrals were fitted over distances and radii and the coefficients were tabulated and stored in the computer for the analyzing of measurements.

In BLS, the magnetic flux change (rf-SQUID voltage output) detected by two 2nd order gradiometer pickup coils was fitted by torso tissue (ribs, muscle, fat; near field) and liver tissue (far field) flux integral contributions simultaneously in a 2-layer model [2]. From bedside sonography, the actual distance from the liver to the torso surface was determined.

From multiple saggital sonographic imaging, covering the abdomen with the liver below, the liver area of each image could be determined. Because the images were taken at equidistant horizontal distances, the total liver volumes could be calculated, by summing up all liver areas, multiplied by the distance. The total liver iron stores were calculated by multiplying the biomagnetically measured liver iron concentration (the major storage organ), with the respective organ volume obtained by sonography.

Biochemical parameters as serum ferritin and serum iron were determined by standard methods. Non-transferrin-bound iron (NTBI) in serum was analyzed as previously described [3].

Results

The liver iron concentrations of 8 children with acute lymphoblastic leukemia before and after induction chemotherapy, achieved with biomagnetic liver susceptometry, are shown in Fig. 1. Liver iron concentrations above the normal range (0.1 - 0.5 $\mathrm{mg/g_{liver}}$) were found in 3 patients (no. 2, 3 and 6).

After chemotherapy we found increased liver iron concentrations in 5/7 patients. Four of them received 1 (patient no. 4 and 7) or 2 (patient no. 1 and 2) erythrocyte transfusions during that time. In one patient however, who received no transfusion (no. 5), a pronounced increase in liver iron concentration was also found after chemotherapy. There were 2 patients with a decreased LIC. Patient no. 3 who received 1 erythrocyte transfusion had a twofold liver iron concentration as normal. In the patient no. 6, who received no transfusion we measured before chemotherapy a

©1999, Tohoku University Press
Recent Advances in Biomagnetism
T. Yoshimoto et al. (Eds)

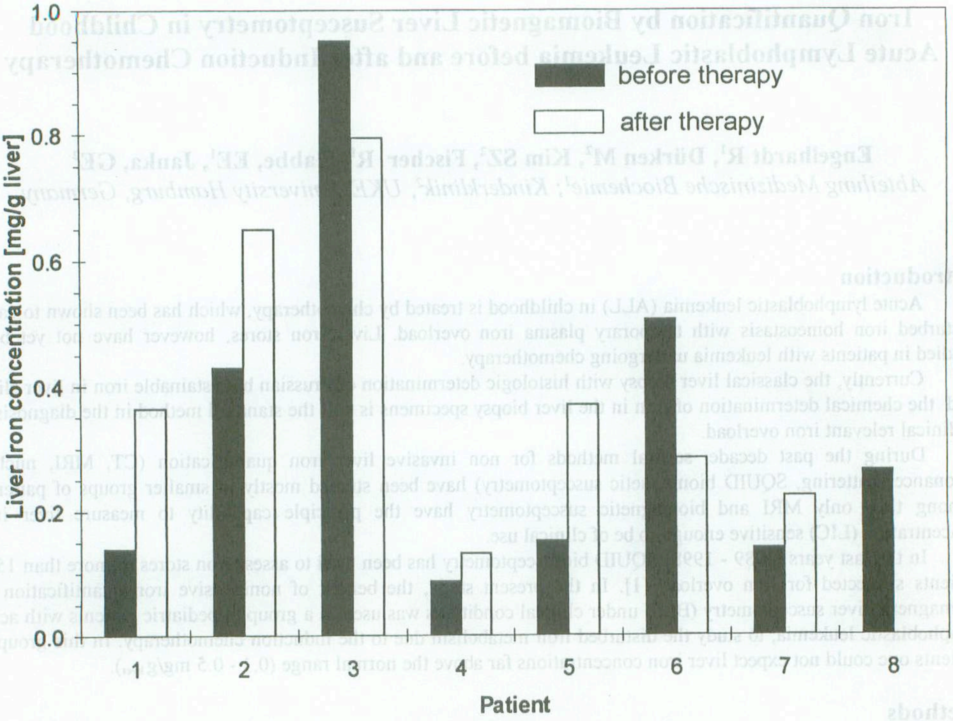

Fig. 1 Liver iron concentration of 8 patients before and after induction chemotherapy

liver iron concentration slightly above the normal range and after the therapy an iron concentration in the normal range. In patient no. 8 only an initial measurement was possible.

All patients revealed increased liver volumes (min: 580 ml, max: 2250 ml) in comparison to values derived from body weight measurements. In the mean, the liver volumes were increased by a factor of two. Due to the increased liver volumes, contributions from the lung or intestine to the measured SQUID liver signals in the young and small sized patients could be neglected.

Because ferritin is an acute phase protein, elevated serum ferritin levels were found before chemotherapy as shown in Fig. 2. ferritin levels after induction chemotherapy (28 to 38 days after onset) decreased to normal values. Only a weak correlation of serum ferritin levels with liver iron concentrations obtained from data before and after chemotherapy exist. However, these two data sets are significantly separated as show in Fig. 2. The paired t-test has the result of $p < 0.05$.

Consideration of total liver iron stores calculated from sonographic volume estimations and liver iron concentration measurements does not exhibit a better correlation. Non-transferrin-bound iron was found to fluctuate with significantly increased NTBI levels after DNR infusions in the time between the two biomagnetic investigations (data not shown).

Discussion

From the experimental point of view, these relatively slim patients were ideal subjects. The short distances between body surfaces and liver surfaces (measured by sonography) leads to low torso tissue contribution (due to fat). Finally this results in very precise iron concentration in the analysis of the measured SQUID data. Due to the low torso tissue contribution it was possible to detect even weak changes of liver iron concentrations, because the amount of transported iron indicated by NTBI-measurements was low (data not show) in the time before and after therapy.

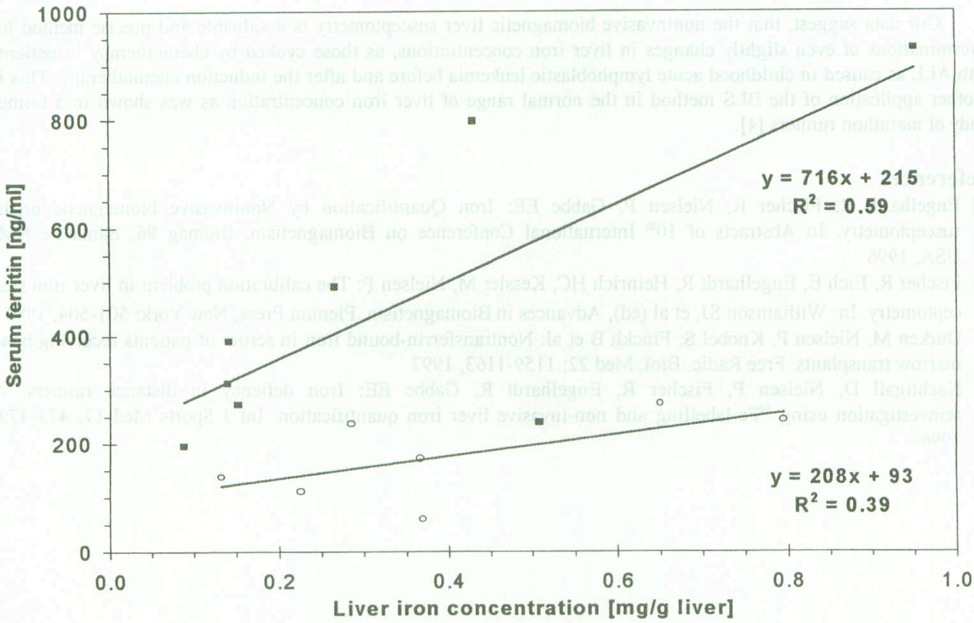

Fig. 2 Serum ferritin levels as a function of liver iron concentration of 8 patients before (dark squares) and after induction chemotherapy (open circles).

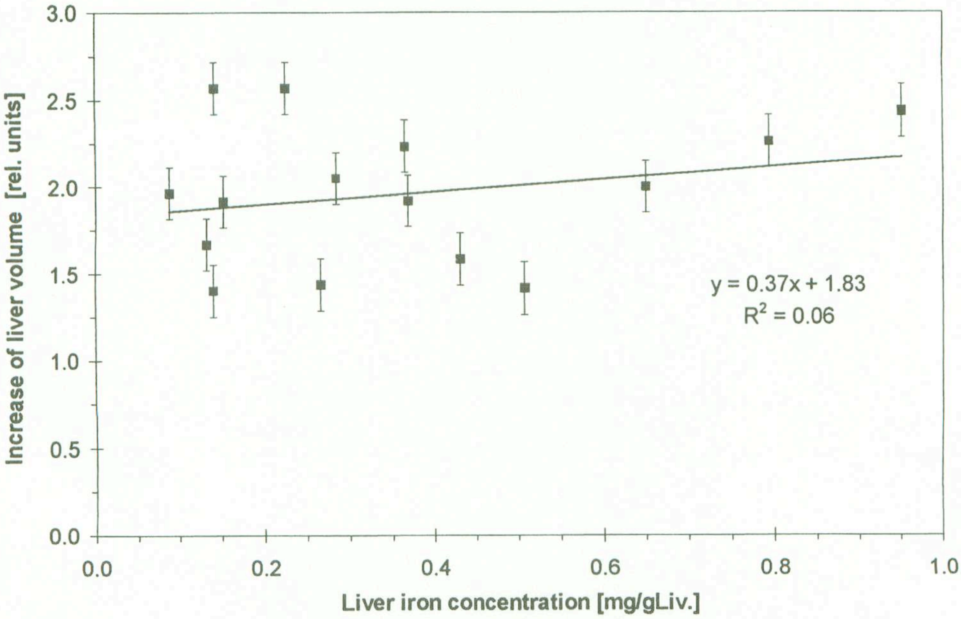

Fig. 3. Liver volumes as a function of liver iron concentration of 8 patients before and after induction chemotherapy (7 patients).

Our data suggest, that the noninvasive biomagnetic liver susceptometry is a valuable and precise method for determinations of even slightly changes in liver iron concentrations, as those evoked by chemotherapy in patients with ALL as caused in childhood acute lymphoblastic leukemia before and after the induction chemotherapy. This is another application of the BLS method in the normal range of liver iron concentration as was shown in a former study of marathon runners [4].

References

[1] Engelhardt R, Fischer R, Nielsen P, Gabbe EE: Iron Quantification by Noninvasive biomagnetic organ susceptometry. In Abstracts of 10th International Conference on Biomagnetism, Biomag 96, Santa Fe NM, USA, 1996

[2] Fischer R, Eich E, Engelhardt R, Heinrich HC, Kessler M, Nielsen P: The calibration problem in liver iron susceptometry. In: Williamson SJ, et al (ed), Advances in Biomagnetism, Plenum Press, New York; 501-504, 1989

[3] Dürken M, Nielsen P, Knobel S, Finckh B et al: Nontransferrin-bound iron in serum of patients receiving bone marrow transplants. Free Radic. Biol. Med 22; 1159-1163, 1997

[4] Nachtigall D, Nielsen P, Fischer R, Engelhardt R, Gabbe EE: Iron defiency in distance runners. A reinvestigation using ^{59}Fe-labelling and non-invasive liver iron quantification. Int J Sports Med 17; 473-479, 1996